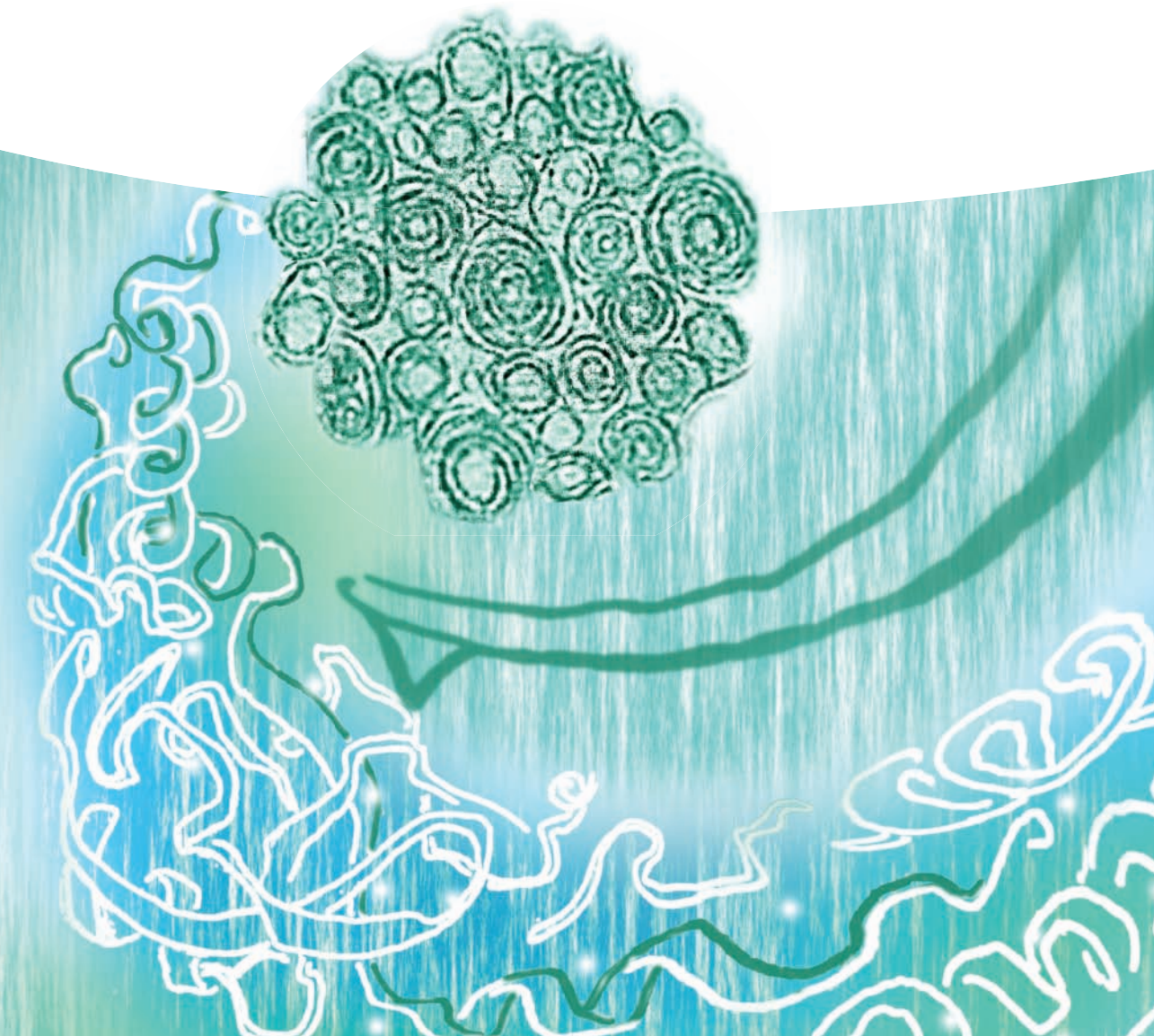


Edited by
Xiaodong Chen and Harald Fuchs

Soft Matter Nanotechnology

From Structure to Function



Edited by
Xiaodong Chen and
Harald Fuchs

**Soft Matter
Nanotechnology**

Related Titles

Picart, C., Caruso, F., Voegel, J. (eds.)

Layer-by-Layer Films for Biomedical Applications

2015

Print ISBN: 978-3-527-33589-3

Caironi, M., Noh, Y. (eds.)

Large Area and Flexible Electronics

2015

Print ISBN: 978-3-527-33639-5

Schramm, L.L.

Emulsions, Foams, Suspensions, and Aerosols

Microscience and Applications

2nd Edition

2014

Print ISBN: 978-3-527-33706-4

Someya, T. (ed.)

Stretchable Electronics

2013

Print ISBN: 978-3-527-32978-6

Liu, X.Y., Li, J.L. (eds.)

Soft Fibrillar Materials Fabrication and Applications

2013

Print ISBN: 978-3-527-33162-8

Lyon, L.A., Serpe, M.J. (eds.)

Hydrogel Micro and Nanoparticles

2012

Print ISBN: 978-3-527-33033-1

Liu, B., Bazan, G.C. (eds.)

Conjugated Polyelectrolytes Fundamentals and Applications

2012

Print ISBN: 978-3-527-33143-7

Klauk, H. (ed.)

Organic Electronics II More Materials and Applications

2012

Print ISBN: 978-3-527-32647-1

Tsukruk, V.V., Singamaneni, S.

Scanning Probe Microscopy of Soft Matter Fundamentals and Practices

2012

Print ISBN: 978-3-527-32743-0

Urban, M.W. (ed.)

Handbook of Stimuli-Responsive Materials

2011

Print ISBN: 978-3-527-32700-3

Edited by Xiaodong Chen and Harald Fuchs

Soft Matter Nanotechnology

From Structure to Function

WILEY-VCH
Verlag GmbH & Co. KGaA

Editors

Prof. Xiaodong Chen

Nanyang Technology University
Materials Science and Engineering
50 Nanyang Av.
639798 Singapore
Singapore

Prof. Harald Fuchs

Westfälische Wilhelms-Universität
Department of Physics
Wilhelm-Klemm- Str. 10
48149 Münster
Germany

Cover

Cover picture by Miss Xinran Zhou.
With permission.

All books published by **Wiley-VCH** are carefully produced. Nevertheless, authors, editors, and publisher do not warrant the information contained in these books, including this book, to be free of errors. Readers are advised to keep in mind that statements, data, illustrations, procedural details or other items may inadvertently be inaccurate.

Library of Congress Card No.: applied for

British Library Cataloguing-in-Publication Data

A catalogue record for this book is available from the British Library.

Bibliographic information published by the Deutsche Nationalbibliothek

The Deutsche Nationalbibliothek lists this publication in the Deutsche Nationalbibliografie; detailed bibliographic data are available on the Internet at <<http://dnb.d-nb.de>>.

© 2015 Wiley-VCH Verlag GmbH & Co. KGaA,
Boschstr. 12, 69469 Weinheim, Germany

All rights reserved (including those of translation into other languages). No part of this book may be reproduced in any form – by photoprinting, microfilm, or any other means – nor transmitted or translated into a machine language without written permission from the publishers. Registered names, trademarks, etc. used in this book, even when not specifically marked as such, are not to be considered unprotected by law.

Print ISBN: 978-3-527-33722-4

ePDF ISBN: 978-3-527-68214-0

ePub ISBN: 978-3-527-68216-4

Mobi ISBN: 978-3-527-68213-3

oBook ISBN: 978-3-527-68215-7

Typesetting Thomson Digital, Noida, India

Printing and Binding Markono Print Media Pte Ltd, Singapore

Printed on acid-free paper

Contents

List of Contributors XIII

Preface XIX

- 1 Chemical Reactions for the Synthesis of Organic Nanomaterials on Surfaces 1**
Hong-Ying Gao, Oscar Díaz Arado, Harry Möning, and Harald Fuchs
 - 1.1 Introduction 1
 - 1.1.1 Ullmann Coupling 2
 - 1.1.2 Condensation Reactions 5
 - 1.2 Alkane Polymerization 6
 - 1.3 Azide–Alkyne Cycloaddition 6
 - 1.4 Glaser Coupling 9
 - 1.5 Decarboxylative Polymerization of Acids 13
 - 1.6 Conclusions 16
 - Acknowledgments 17
 - References 17
- 2 Self-Assembly of Organic Molecules into Nanostructures 21**
Long Qin, Kai Lv, Zhaocun Shen, and Minghua Liu
 - 2.1 Introduction 21
 - 2.2 Classification of Nanostructures 22
 - 2.3 General Self-Assembly Method for the Construction of Nanostructures 23
 - 2.3.1 Reprecipitation 24
 - 2.3.2 Gelation 26
 - 2.3.3 Langmuir–Blodgett Technique 27
 - 2.3.4 Layer-by-Layer Assembly 29
 - 2.3.5 Self-Assembly in Solution 31

2.4	Molecular Design and Building Blocks	33
2.4.1	Amphiphiles	33
2.4.1.1	Typical Amphiphiles	35
2.4.1.2	Bolaamphiphiles	35
2.4.1.3	Gemini Amphiphiles	37
2.4.1.4	Triangular Amphiphiles	38
2.4.1.5	Supra-amphiphiles	40
2.4.2	Gelators	41
2.4.2.1	Cholesterol-Based Gelators	41
2.4.2.2	Alkane- and Fatty Acid-Based Gelators	43
2.4.2.3	Nucleoside-Based Gelators	43
2.4.2.4	Amino Acid- and Peptide-Based Gelators	45
2.4.2.5	Carbohydrate-Based Gelators	50
2.4.3	π -Functionalized System	51
2.4.3.1	Porphyrin	51
2.4.3.2	Molecular Graphene	53
2.4.3.3	π -Conjugated Gelators	54
2.4.4	Dendrimers	55
2.5	Functions of Some Typical Nanostructures	56
2.5.1	Vesicles/Hollow Spheres	56
2.5.2	Nanotubes	62
2.5.2.1	Self-Assembled Lipid Nanotubes	62
2.5.2.2	Self-Assembled Peptide Nanotubes	65
2.5.2.3	Functionalization of Nanotubes	69
2.5.3	Nanofibers	74
2.6	Conclusions and Outlook	79
	References	80
3	Supramolecular Nanotechnology: Soft Assembly of Hard Nanomaterials	95
	<i>Katsuhiko Ariga, Qingmin Ji, and Jonathan P. Hill</i>	
3.1	Introduction	95
3.2	Soft Cell-Like Structures with Hard Nanomaterials	96
3.2.1	Cerasome: Inorganic Surface Cell	96
3.2.2	Flake–Shell Capsule	98
3.2.3	Metallic Cells	100
3.3	For Hierarchical Assembly: LbL and Others	101
3.3.1	Mesoporous Carbon in Hierarchical Assembly	101
3.3.2	Mesoporous Carbon Capsule in Layer-by-Layer Film	103
3.3.3	Layer-by-Layer Assembly of Graphene and Ionic Liquids	104
3.3.4	LbL Films of Mesoporous Silica Capsule for Controlled Release	105
3.4	Summary	107
	Acknowledgments	107
	References	107

4	Nanoparticles: Important Tools to Overcome the Blood–Brain Barrier and Their Use for Brain Imaging	<i>109</i>
	<i>Ruirui Qiao, Mingyuan Gao, and Hans-Joachim Galla</i>	
4.1	Introduction	<i>109</i>
4.2	Physiology of the Blood–Brain Barrier	<i>110</i>
4.2.1	The Endothelial Blood–Brain Barrier	<i>110</i>
4.2.2	The Blood–CSF Barrier	<i>111</i>
4.2.3	Regulation of the Barrier Tightness	<i>112</i>
4.2.4	Transport Routes and Drug Permeability across the Blood–Brain Barrier	<i>112</i>
4.2.5	<i>In vitro</i> Models of the BBB and Blood–CSF Barrier	<i>114</i>
4.3	Definition and Type of Nanoparticles and Nanocarriers for Brain Uptake	<i>115</i>
4.3.1	Organic Nanoparticles	<i>115</i>
4.3.1.1	Polymeric Nanoparticles	<i>116</i>
4.3.1.2	Liposomes and Lipidic Nanoparticles	<i>117</i>
4.3.1.3	Nanomicelles, Emulsions, and Nanogels	<i>117</i>
4.3.1.4	Carbohydrates	<i>118</i>
4.3.2	Inorganic Nanoparticles	<i>118</i>
4.3.2.1	Magnetic Nanoparticles	<i>119</i>
4.3.2.2	Semiconductor Nanoparticles	<i>119</i>
4.3.2.3	Gold Nanoparticles	<i>120</i>
4.3.3	Surface Functionalization of Nanoparticles for BBB Transport	<i>120</i>
4.4	Nanoparticles and Imaging	<i>122</i>
4.4.1	Magnetic Resonance Imaging (MRI)	<i>122</i>
4.4.2	Optical Imaging	<i>123</i>
4.5	Conclusion and Outlook	<i>124</i>
	Acknowledgment	<i>124</i>
	References	<i>125</i>
5	Organic Nanophotonics: Controllable Assembly of Optofunctional Molecules toward Low-Dimensional Materials with Desired Photonic Properties	<i>131</i>
	<i>Yongli Yan and Yong Sheng Zhao</i>	
5.1	Introduction	<i>131</i>
5.2	From Molecules to Assembly	<i>132</i>
5.2.1	Inherent Intermolecular Interactions	<i>133</i>
5.2.2	Influences of External Factors	<i>137</i>
5.2.2.1	Solvent Effect in Assembly	<i>137</i>
5.2.2.2	Site-Selected Assembly on Specific Substrates	<i>138</i>
5.3	From Assembly to Structures	<i>139</i>
5.3.1	Structure Control through Intermolecular Interactions	<i>140</i>
5.3.1.1	Controlling the Structures via Molecular Design	<i>140</i>
5.3.1.2	Structures Obtained from the Synergistic Assembly of Different Compounds	<i>141</i>

5.3.2	Structure Modulation through External Factors	143
5.3.2.1	Structures versus Aging Time	143
5.3.2.2	Heterostructures through Site-Specific Epitaxial Growth	144
5.4	From Structures to Photonic Properties	145
5.4.1	Nanowire Heterojunctions	145
5.4.1.1	Dendritic Heterostructures as Optical Routers	146
5.4.1.2	Nanowire p–n Junctions as Photoelectric Transducers	146
5.4.2	Doped Nanostructures	149
5.4.2.1	Uniformly Doped Structures	149
5.4.2.2	Gradiently Doped Structures	151
5.4.2.3	Core/Sheath Structures	153
5.5	Conclusions	154
	Acknowledgments	157
	References	157
6	Functional Lipid Assemblies by Dip-Pen Nanolithography and Polymer Pen Lithography	<i>161</i>
	<i>Michael Hirtz, Sylwia Sekula-Neuner, Ainhoa Urtizberea, and Harald Fuchs</i>	
6.1	Introduction	161
6.2	Techniques and Methods	161
6.2.1	Dip-Pen Nanolithography	161
6.2.2	Polymer Pen Lithography	163
6.3	Ink Transfer Models	164
6.3.1	DPN of Liquid Inks	165
6.3.2	DPN of Diffusive Inks	165
6.3.3	DPN of Lipid Inks	166
6.3.4	Ink Transfer in PPL	170
6.4	Applications	172
6.4.1	Applications in Sensing	172
6.4.2	Biological Applications	176
6.5	Conclusions	182
	Acknowledgments	182
	References	182
7	PEG-Based Antigen-Presenting Cell Surrogates for Immunological Applications	<i>187</i>
	<i>Ilia Platzman, Gerri Kannenberg, Jan-Willi Janiesch, Jovana Matić, and Joachim P. Spatz</i>	
7.1	Introduction	187
7.2	Elastic Nanopatterned and Specifically Biofunctionalized 2D PEG-DA Hydrogels: General Properties	189
7.2.1	Block Copolymer Micellar Nanolithography (BCML)	189
7.2.2	Fabrication and Characterization of Nanopatterned PEG-DA Hydrogels	191
7.2.3	Biofunctionalization	194

7.2.4	Cell Experiments	195
7.2.4.1	T-Cells Isolation	195
7.2.4.2	T-Cells Stimulation	195
7.2.4.3	T-Cells Proliferation	196
7.2.4.4	Results	196
7.3	Nanostructured PEG-DA Hydrogel Beads: General Properties	198
7.3.1	Surfactant Synthesis	200
7.3.2	Fabrication of Nanostructured PEG-DA Hydrogel Beads by Droplet-Based Microfluidics	201
7.3.3	Characterization of Nanostructured PEG-DA Hydrogel Beads	203
7.3.4	Biofunctionalization	204
7.4	Nanostructured and Specifically Biofunctionalized Droplets of Water-in-Oil Emulsion: General Properties	205
7.4.1	Surfactant Synthesis	207
7.4.2	Droplet-Based Microfluidics	209
7.4.3	Characterization of the Gold Nanostructured Droplets of Water-in-Oil Emulsion	209
7.4.4	Biofunctionalization of the Nanostructured Droplets	209
7.4.5	Cell Experiments	211
7.4.5.1	Cell Culture	211
7.4.5.2	Cell Recovery and Live/Dead Staining	212
7.4.5.3	Results	212
7.5	Summary and Outlook for the Future	213
	Acknowledgments	213
	References	213
8	Soft Matter Assembly for Atomically Precise Fabrication of Solid Oxide	217
	<i>Norifusa Satoh</i>	
8.1	Introduction	217
8.2	The Ultimate Goal of Nanotechnology: Atomically Precise Fabrication	217
8.3	Soft Mater Assembly for Atomically Precise Oxide Layers	220
8.4	Soft Matter Assembly for Atomically Precise Oxide Dots	221
8.5	Summary for the Future Works	224
	References	225
9	Conductive Polymer Nanostructures	233
	<i>Lin Jiang, Carsten Hentschel, Bin Dong, and Lifeng Chi</i>	
9.1	Introduction	233
9.2	Solution-Based Synthesis of Conducting Polymer Nanostructures	234
9.2.1	Soft Template Synthesis	234
9.2.2	Hard Template Method	236

9.3	Substrate-Based Fabrication of Conducting Polymer Nanostructures	237
9.3.1	Add to Surface	237
9.3.1.1	Direct Writing	237
9.3.1.2	<i>In Situ</i> Synthesis or Assembly	238
9.3.2	Remove from Surface	242
9.3.2.1	Nanoscratching	242
9.3.2.2	Etching	243
9.4	Electrospinning Technique of Conducting Polymer	245
9.5	Summary and Outlook	250
	References	251
10	DNA-Induced Nanoparticle Assembly	259
	<i>Anne Buchkremer and Ulrich Simon</i>	
10.1	Introduction	259
10.2	DNA as a Template Material	262
10.2.1	On Modified Linear DNA Strands	262
10.2.2	On DNA Origami Structures	265
10.2.3	On Geometrically Tailored DNA	266
10.3	DNA as Ligand	267
10.3.1	DNA Functionalization of Gold Nanoparticles and Network Formation	267
10.3.2	Extended Superstructures	271
10.3.3	Finite Size DNA–AuNP Assemblies	273
10.3.4	Aggregates Composed of Different Particle Geometries and Morphologies	279
10.4	Applications	282
10.5	Summary	286
	References	287
11	Nanostructured Substrates for Circulating Tumor Cell Capturing	293
	<i>Jingxin Meng, Hongliang Liu, and Shutao Wang</i>	
11.1	Introduction	293
11.2	Nanostructured Substrates for CTC Capturing	294
11.2.1	Nanoparticles	295
11.2.2	Nanofractals	297
11.2.3	Nanowires	298
11.2.4	Nanoposts/pillars	300
11.2.5	Nanotubes	302
11.2.6	Nanofibers	303
11.2.7	Nanopores	304
11.3	Nanostructured Substrates for Other Cells Capturing	306
11.4	Conclusions and Perspectives	306
	References	307

12	Organic Nano Field-Effect Transistor	309
	<i>Yonggang Zhen and Wenping Hu</i>	
12.1	Introduction	309
12.2	The Fabrication of Organic Semiconductor Nanostructures	310
12.2.1	Vapor-Phase Method	310
12.2.2	Solution Process	317
12.2.3	Other Methods	328
12.3	Device Structures of Organic Nano Field-Effect Transistor	332
12.4	The Preparation of Organic Nano Field-Effect Transistor	335
12.4.1	The Transfer of Organic Nanocrystals	335
12.4.2	Electrode of Organic Semiconductor Nanocrystal Field-Effect Transistor	339
12.5	Properties of Organic Nanoscale Field-Effect Transistor	345
12.6	Application of Organic Nano-FETs	347
12.7	Summary and Outlook	350
	References	351
13	Advanced Dynamic Gels	357
	<i>Rekha G. Shrestha and Masanobu Naito</i>	
13.1	Introduction	357
13.2	Gels in Nature	358
13.3	Characterization of VEGs	359
13.3.1	Rheometer	359
13.3.2	Small-Angle Scattering	360
13.3.3	Transmission Electron Microscopy	361
13.4	Redox-Responsive VEGs	362
13.5	pH-Responsive VEGs	363
13.6	Temperature-Responsive VEGs	364
13.7	Photoresponsive VEGs	369
13.8	Applications	373
13.9	Conclusions	374
13.10	Theory	375
	References	379
14	Micro/Nanocrystal Conversion beyond Inorganic Nanostructures	385
	<i>Jiansheng Wu, Li Junbo, and Qichun Zhang</i>	
14.1	Introduction	385
14.2	Micro/Nanostructure Conversion through Charge Transfer Complex Formation	385
14.3	Micro/Nanostructure Conversion through Ion and Ligand Exchange	388
14.4	Micro/Nanostructure Conversion through Reduction	391
14.5	Micro/Nanostructure Conversion through Photoinduced Reaction	392

14.6	Micro/Nanostructure Conversion through Thermal-induced Reaction	394
14.7	Properties and Applications	395
14.7.1	Optical Properties	395
14.7.2	Electronic Properties and Information Storage	396
14.7.3	Mechanical Properties and Photomechanical Actuator	397
14.8	Summary and Outlook	397
	References	398
15	Self-Healing Electronic Nanodevices	<i>401</i>
	<i>Li Zhang, Bevita K. Chandran, and Xiaodong Chen</i>	
15.1	Introduction	401
15.2	Self-Healing Materials	402
15.3	Self-Healing Electrical Conductors	403
15.4	Self-Healing in Energy Storage Devices	408
15.5	Self-Healing Electronic Skin	414
15.6	Conclusive Remarks and Outlook	415
	References	416

Index 419

List of Contributors

Oscar Díaz Arado

Westfälische Wilhelms-Universität
Münster
Physikalisches Institut
Wilhelm-Klemmstrasse 10
48149 Münster
Germany

Katsuhiko Ariga

National Institute for Materials
Science (NIMS)
World Premier International (WPI)
Research Center for Materials
Nanoarchitectonics (MANA)
1-1 Namiki
Tsukuba 305-0044
Japan

Anne Buchkremer

RWTH Aachen University
Institute of Inorganic Chemistry
Landoltweg 1
52056 Aachen
Germany

Bevita K. Chandran

Nanyang Technological University
School of Materials Science and
Engineering
50 Nanyang Avenue
Singapore 639798
Singapore

Xiaodong Chen

Nanyang Technological University
School of Materials Science and
Engineering
50 Nanyang Avenue
Singapore 639798
Singapore

Lifeng Chi

Soochow University
Institute of Functional Nano & Soft
Materials (FUNSOM)
Ren-Ai street, 199
Suzhou, 215123 Jiangsu
China

Bin Dong

Soochow University
Institute of Functional Nano & Soft
Materials (FUNSOM)
Ren-Ai street, 199
Suzhou, 215123 Jiangsu
China

Harald Fuchs

Karlsruhe Institute of Technology
(KIT)
Karlsruhe Nano Micro Facility
(KNMF)
Institute of Nanotechnology (INT)
KIT Campus North
76021 Karlsruhe
Germany

and

Westfälische Wilhelms-Universität
Münster
Physical Institute and Center for
Nanotechnology (CeNTech)
48149 Münster
Germany

Hans-Joachim Galla

University of Münster
Institute for Biochemistry
Wilhelm Klemm Str.2
Münster 48149
Germany

and

Chinese Academy of Science Beijing
Institute of Chemistry
Bei Yi Jie 2, Zhong Guan Cun
Beijing 100190
China

Hong-Ying Gao

Westfälische Wilhelms-Universität
Münster
Physikalisches Institut
Wilhelm-Klemmstrasse 10
48149 Münster
Germany

Mingyuan Gao

Chinese Academy of Science Beijing
Institute of Chemistry
Bei Yi Jie 2, Zhong Guan Cun
Beijing 100190
China

Carsten Hentschel

Soochow University
Institute of Functional Nano & Soft
Materials (FUNSOM)
Ren-Ai street, 199
Suzhou, 215123 Jiangsu
China

Jonathan P. Hill

National Institute for Materials
Science (NIMS)
World Premier International (WPI)
Research Center for Materials
Nanoarchitectonics (MANA) 1-1
Namiki
Tsukuba 305-0044
Japan

Michael Hirtz

Karlsruhe Institute of Technology
(KIT)
Karlsruhe Nano Micro Facility
(KNMF)
Institute of Nanotechnology (INT)
KIT Campus North
76021 Karlsruhe
Germany

Wenping Hu

Institute of Chemistry, Chinese
Academy of Sciences
Beijing National Laboratory for
Molecular Sciences (BNLMS)
Zhongguancun North First Street 2
Beijing 100190
China

Jan-Willi Janiesch

Max Planck Institute for Intelligent Systems
 Department of New Materials and Biosystems
 Heisenbergstr.3
 70569 Stuttgart
 Germany

and

University of Heidelberg
 Department of Biophysical Chemistry
 Im Neuenheimer Feld 253
 69120 Heidelberg
 Germany

Qingmin Ji

National Institute for Materials Science (NIMS)
 World Premier International (WPI)
 Research Center for Materials Nanoarchitectonics (MANA)
 1-2 Namiki
 Tsukuba 305-0044
 Japan

Lin Jiang

Soochow University
 Institute of Functional Nano & Soft Materials (FUNSOM)
 Ren-Ai street, 199
 Suzhou, 215123 Jiangsu
 China

Li Junbo

Nanyang Technological University
 School of Materials Science and Engineering
 50 Nanyang Avenue
 Singapore 639798
 Singapore

Gerri Kannenberg

Max Planck Institute for Intelligent Systems
 Department of New Materials and Biosystems
 Heisenbergstr.3
 70569 Stuttgart
 Germany

and

University of Heidelberg
 Department of Biophysical Chemistry
 Im Neuenheimer Feld 253
 69120 Heidelberg
 Germany

Hongliang Liu

Technical Institute of Physics and Chemistry, Chinese Academy of Sciences
 Laboratory of Bio-Inspired Smart Interface Science
 29 Zhongguancun East Road,
 Haidian District
 Beijing 100190
 China

Minghua Liu

Institute of Chemistry, Chinese Academy of Sciences
 CAS Key Laboratory of Colloid, Interface and Chemical Thermodynamics
 Beijing National Laboratory for Molecular Science (BNLMS)
 Zhongguancun North First Street 2
 Beijing 100190
 China

Kai Lv

Institute of Chemistry, Chinese Academy of Sciences
 CAS Key Laboratory of Colloid, Interface and Chemical Thermodynamics
 Beijing National Laboratory for Molecular Science (BNLMS)
 Beijing 100190
 Zhongguancun North First Street 2
 China

Jovana Matic

Max Planck Institute for Intelligent Systems
 Department of New Materials and Biosystems
 Heisenbergstr.3
 70569 Stuttgart
 Germany

and

University of Heidelberg
 Department of Biophysical Chemistry
 Im Neuenheimer Feld 253
 69120 Heidelberg
 Germany

Jingxin Meng

Technical Institute of Physics and Chemistry, Chinese Academy of Sciences
 Laboratory of Bio-Inspired Smart Interface Science
 29 Zhongguancun East Road,
 Haidian District
 Beijing 100190
 China

Harry Möning

Westfälische Wilhelms-Universität Münster
 Physikalisches Institut
 Wilhelm-Klemmstrasse 10
 48149 Münster
 Germany

Masanobu Naito

National Institute for Materials Science
 Environment and Energy Materials Division
 Environmental Remediation Materials Unit
 Catalytic Materials Group
 1-1 Namiki
 Tsukuba, Ibaraki 305-0044
 Japan

Ilia Platzman

Max Planck Institute for Intelligent Systems
 Department of New Materials and Biosystems
 Heisenbergstr.3
 70569 Stuttgart
 Germany

and

University of Heidelberg
 Department of Biophysical Chemistry
 Im Neuenheimer Feld 253
 69120 Heidelberg
 Germany

Ruirui Qiao

Chinese Academy of Science Beijing Institute of Chemistry
 Bei Yi Jie 2, Zhong Guan Cun
 Beijing 100190
 China

Long Qin

Institute of Chemistry, Chinese Academy of Sciences
 CAS Key Laboratory of Colloid, Interface and Chemical Thermodynamics
 Beijing National Laboratory for Molecular Science (BNLMS)
 Zhongguancun North First Street 2
 Beijing 100190
 China

Norifusa Satoh

National Institute for Materials
Science (NIMS)
Environment and Energy Materials
Division
1-1 Namiki
Tsukuba, Ibaraki 305-0044
Japan

Sylwia Sekula-Neuner

Karlsruhe Institute of Technology
(KIT)
Karlsruhe Nano Micro Facility
(KNMF)
Institute of Nanotechnology (INT)
KIT Campus North
76021 Karlsruhe
Germany

Zhaocun Shen

Institute of Chemistry, Chinese
Academy of Sciences
CAS Key Laboratory of Colloid,
Interface and Chemical
Thermodynamics
Beijing National Laboratory for
Molecular Science (BNLMS)
Zhongguancun North First Street 2
Beijing 100190
China

Rekha G. Shrestha

National Institute for Materials
Science
Environment and Energy Materials
Division
Environmental Remediation
Materials Unit
Catalytic Materials Group
1-1 Namiki
Tsukuba, Ibaraki 305-0044
Japan

Ulrich Simon

RWTH Aachen University
Institute of Inorganic Chemistry
Landoltweg 1
52056 Aachen
Germany

Joachim P. Spatz

Max Planck Institute for Intelligent
Systems
Department of New Materials and
Biosystems
Heisenbergstr.3
70569 Stuttgart
Germany

and

University of Heidelberg
Department of Biophysical
Chemistry
Im Neuenheimer Feld 253
69120 Heidelberg
Germany

Ainhoa Urtizberea

Karlsruhe Institute of Technology
(KIT)
Karlsruhe Nano Micro Facility
(KNMF)
Institute of Nanotechnology (INT)
KIT Campus North
76021 Karlsruhe
Germany

Shutao Wang

Technical Institute of Physics and
Chemistry, Chinese Academy of
Sciences
Laboratory of Bio-Inspired Smart
Interface Science
29 Zhongguancun East Road,
Haidian District
Beijing 100190
China

Jiansheng Wu

Nanyang Technological University
School of Materials Science and
Engineering
50 Nanyang Avenue
Singapore 639798
Singapore

Qichun Zhang

Nanyang Technological University
School of Materials Science and
Engineering
50 Nanyang Avenue
Singapore 639798
Singapore

Yongli Yan

Institute of Chemistry, Chinese
Academy of Sciences
CAS Key Laboratory of
Photochemistry
Beijing National Laboratory for
molecular Sciences (BNLMS)
Zhongguancun North First Street 2
Beijing 100190
China

Yong Sheng Zhao

Institute of Chemistry, Chinese
Academy of Sciences
CAS Key Laboratory of
Photochemistry
Beijing National Laboratory for
molecular Sciences (BNLMS)
Zhongguancun North First Street 2
Beijing 100190
China

Li Zhang

Nanyang Technological University
School of Materials Science and
Engineering
50 Nanyang Avenue
Singapore 639798
Singapore

Yonggang Zhen

Institute of Chemistry, Chinese
Academy of Sciences
Beijing National Laboratory for
Molecular Sciences (BNLMS)
Zhongguancun North First Street 2
Beijing 100190
China

Preface

In Nature, nanoscale components of a cell are organized into highly dynamic hierarchical structures and in a way that we call life. This self-organization mainly includes modular design, fault tolerance, and the ability to self-repair damage and even to reproduce itself. The precise and spatiotemporal dynamic arrangement of the individual building blocks causes the biological functionality. This inspires us to develop a controlled mastery of natural functioning in synthetic, biomimetic nanosystems. However, we are still at the infant stages of learning how to design and master the control of soft nanoscale structures with specific properties. Both technical and basic thermodynamic processes need to be understood by learning from Nature before higher degrees of complexity and functions such as self-replication and self-healing can be targeted.

Soft matter nanotechnology is a multidisciplinary area of chemistry, physics, biology, medicine, and materials science. It essentially deals with matter such as amphiphiles, liquid crystals, colloids, polymers, and a number of hierarchically ordered biological molecular systems, using the well-honed tools of nanotechnology. This book reflects some representative examples and advanced fruitful synergies between soft matter science and nanotechnology. Bringing together 15 contributions from many leading scientists, it covers the following aspects of soft matter nanotechnology: (1) structuring soft-materials at the nanoscale; (2) fabrication of complex or composite nanomaterials; (3) nanotechnology tools to study soft nanostructures, (4) nano–bio interface, and (5) applications of soft nanomaterials.

We hope that this book will provide stimulating concepts on the design, fabrication, and exploitation of soft nanomaterials. New soft nanoscale materials and structures, responsive and active soft nanomaterials and devices, functional organic nanoelectronics, integrated nano–bio interface, and energy-related issues are several key areas to be addressed in this book. In addition, recent methodological aspects such as nanoanalytical methods are also displayed.

We are extremely grateful to the authors for their high-quality contributions to this collection. We would also like to thank the production team of Wiley-VCH, in particular Dr. Waltraud Wüst, Dr. Martin Preuss, and Dr. Gudrun Walter, for continuous and dedicated help during the production of this book.

Singapore
Münster
March 2015

*Xiaodong Chen
Harald Fuchs*

1

Chemical Reactions for the Synthesis of Organic Nanomaterials on Surfaces

Hong-Ying Gao, Oscar Díaz Arado, Harry Möning, and Harald Fuchs

1.1

Introduction

The bottom-up growth of covalently connected organic networks is a fascinating approach for the development of new functional nanomaterials with tunable mechanical and optoelectronic properties [1–5]. Hereby, organic molecules are the building blocks, which can be deposited on a substrate by evaporation under ultrahigh vacuum (UHV) conditions or by solution growth in liquid environments. By the proper design of the precursor molecules and by controlling the parameters such as deposition rates, concentrations, and substrate temperature or irradiation, chemical reactions can be induced. This can lead to the formation of either conjugated polymers or 2D covalently connected networks [6–8]. The structural and optoelectronic properties of these products can be adjusted by the manifold possibilities of organic chemistry, which allows tailoring the reactive end groups, and the geometry as well as the electronic properties of the reactants. Following this idea, nanoscale devices ranging from simple wires to transistors, capacitors, or solar cells can be envisioned. Although recent years have shown significant progress in this field, there are only a few established on-surface reaction mechanisms that actually lead to covalent coupling directly at surfaces. Therefore, there are still considerable scientific challenges at play, making it a current hot topic in nanotechnology [2,5,6].

To study the chemical processes involved in the synthesis of such materials, experimental techniques with high lateral resolution are particularly desirable. Therefore, scanning probe microscopy and in particular scanning tunneling microscopy (STM) and noncontact atomic force microscopy (NC-AFM) have become the standard characterization tools providing direct insight into reaction mechanisms. These techniques offer topographic and electronic information of single molecules and on-surface chemical processes with high resolution [9–11], and the probe tip itself can be used to trigger chemical reactions [12–14] or to manipulate molecular species at surfaces [15,16]. Furthermore, both STM and NC-AFM experiments can be performed under different environmental

conditions, such as in UHV, in liquids, or in gaseous environments, providing further versatility to the targeted experiments. Many studies also rely on complementary experimental techniques such as X-ray photoelectron spectroscopy (XPS) or temperature-programmed desorption (TPD). From the theory side, density functional theory (DFT) is applied to describe adsorption geometries and chemical processes that take place on various substrates.

In the following, the so far established on-surface reaction mechanisms are reviewed, which potentially can be utilized for the bottom-up growth of covalently connected organic networks. Other approaches where surfaces are exclusively involved to catalyze reactions and where the products do not stay on the surface are not considered in this chapter. Besides a general overview of the various reaction types, we present a compilation of the results obtained by our group at the University of Münster, which contributed to this exciting research field.

1.1.1

Ullmann Coupling

This particular reaction is the most studied one in the recent years. It involves the thermal activation of precursor molecules with halogenated moieties after or during deposition on a substrate, which, by the supply of heat, leads to the formation of C–C bonds between the radicalized reactants. This reaction has been performed mostly on metal substrates. However, recently it has been shown to also proceed on insulators [17], which represents a significant step forward toward potential applications of the Ullmann coupling mechanism. The halogen species mostly studied is bromine [18–24], although successful covalent coupling after scission of terminal iodine [19,25–27] and chlorine [17,28] has also been reported. The difference in activation temperature for the different carbon–halogen species has allowed to hierarchically control the formation of two-dimensional networks [19,24]. Another interesting nanomaterial with functional electronic properties developed with this method is based on graphene nanoribbons. These are obtained by a two-step reaction sequence where after initial on-surface Ullmann coupling, a further annealing step at a higher temperature leads to cyclodehydrogenation of adjacent aromatic species [23,29]. In particular, graphene nanoribbons were also successfully grown on a stepped Au(788) surface, which form well-defined (111) terraces with a width of about 3.8 nm along the [01–1] direction (Figure 1.1). This allows to gain control over the orientation of the nanoribbons, which predominantly grow along the terraces. High-resolution direct and inverse photoemission experiments of occupied and unoccupied states allowed to determine the energetic position and momentum dispersion of electronic states, which showed a bandgap of several electronvolts for different types of graphene nanoribbons [23,29].

It has been demonstrated that in general it is possible to achieve covalent bonding between organic molecules and metal atoms on surfaces [11,30].

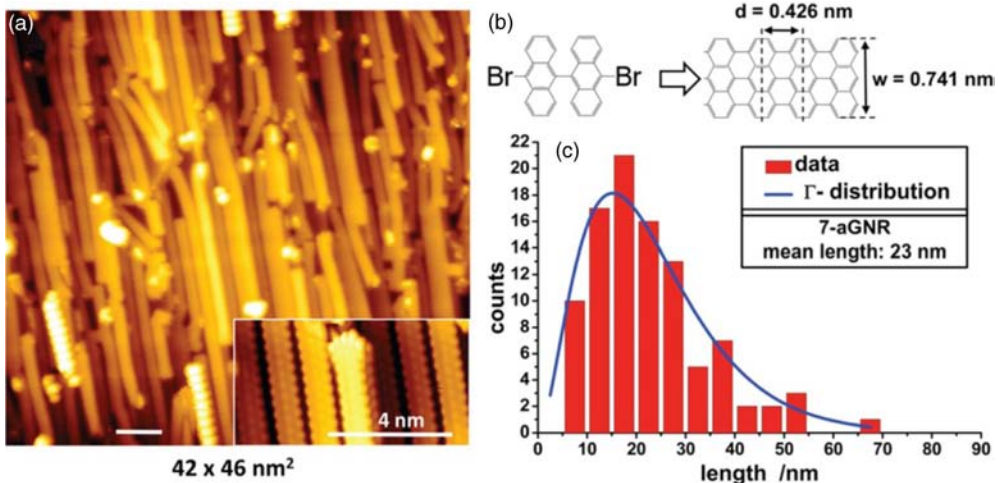


Figure 1.1 (a) STM image of spatially aligned graphene nanoribbons on a Au(788) surface. (b) After initial Ullmann coupling at a substrate temperature of 440–470 K, an additional heating step at 590 K results in a

dehydrogenation process leading to the formation of the nanoribbons. (c) Statistical distribution of the ribbon length. (Reprinted figure with permission from [29]. Copyright (2012) by the American Physical Society.)

Therefore, there are also efforts to not directly bind the organic building blocks for supramolecular structures, but instead use metal atoms to mediate the coupling. Following this approach under UHV conditions, covalent bonding between tetracyanobenzene molecules and Mn atoms was accomplished to form Mn-phthalocyanine [31]. In another study, strong bonds between metal atoms and dehalogenated reactants have been shown to play an important role in the on-surface Ullmann coupling, stabilizing two-dimensional networks [24]. Furthermore, an on-surface chemical reaction between copper ions and quinone ligands at the liquid/solid interface of a Au(111) surface has been shown to successfully form two-dimensional metal–organic polymers [32].

The results on metal–organic materials lead to further developments, which use Ullmann coupling to form gold–organic hybrids, where chemical bonding between organic precursor molecules is mediated by bonding to a substrate gold atom. With this approach, the on-surface synthesis of gold–organic linear polymers by the dehalogenation of chloro-substituted perylene-3,4,9,10-tetracarboxylic acid bisimides (PBIs) was accomplished on the Au(111) and Au(100) surfaces [17,28]. Figure 1.2a shows an STM image after depositing the PBIs at room temperature on a Au(111) surface, leading to a self-assembled monolayer of the unreacted molecules. The STM contrast features a combination of two small bumps and a big rod corresponding to the short alkyl chains and the aromatic core of the PBI molecule, respectively. The bright spots on both sides of the core correspond to the twisted two chlorine atoms. Linear molecular chains were formed via depositing the precursor molecules on a 490 K preheated

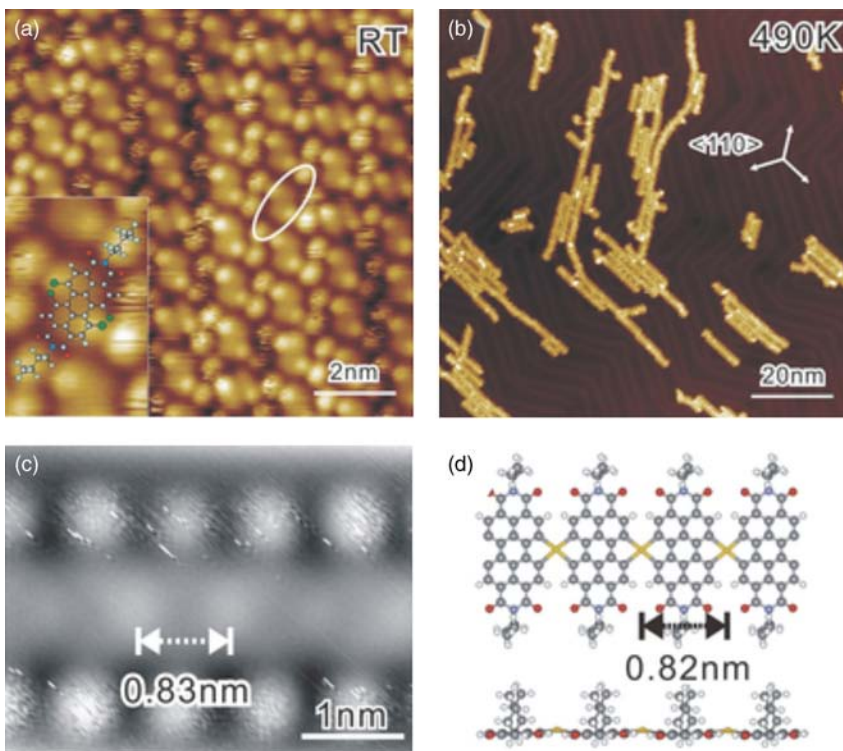


Figure 1.2 Ullmann reaction to form gold-organic hybrids. (a) The self-assembly structures of tetrachloro-PBI at a Au(111) surface ($10\text{ nm} \times 10\text{ nm}$). (b) Polymerized molecular chains of tetrachloro-PBI on a Au(111) surface (via depositing molecules onto the hot surface

of a substrate at 490 K). (c) High-resolution STM image of a polymerized PBI–Au chain and (d) its proposed chemical structure. (Reproduced with permission from Wiley-VCH Verlag GmbH [28].)

Au(111) surface at a deposition rate of about 0.1 monolayer per hour. Figure 1.2b is a representative STM image of the reaction products, in which polymers with a length of up to 70 nm can be observed. Interestingly, the orientation of the molecular chains was found mainly along $\langle 110 \rangle$ directions on the Au(111) surface. A high-resolution STM image of such a polymer is shown in Figure 1.2c, with its proposed chemical structure shown in Figure 1.2d. The measured periodic distance along the chain is $(0.83 \pm 0.04)\text{ nm}$, which matches well with the theoretical distance of 0.82 nm as determined by DFT calculations. Further experiments with the PBI deposited on the reconstructed Au(100) surface showed that on this surface the polymerization occurs exclusively along the $[011]$ direction [28]. Further DFT calculations on a simplified model system confirmed that the reaction mechanism involves an intermediate state where a PBI radical generated from the homolytic C–Cl bond dissociation binds to a surface

gold atom, which partially is pulled out from the surface to form a stable PBI–gold hybrid species.

1.1.2

Condensation Reactions

Condensation reactions are commonly referred to as dehydration synthesis, which involves the combination of two functional groups to form a unique covalently bound product, together with a small molecular by-product, following an addition–elimination mechanism. Several condensation reactions have been proven to be suitable candidates for on-surface synthesis and have received increased attention due to their reversibility by simply adding a solution with a certain concentration of the by-product [33,34]. Successful polyimide condensation [35,36] was accomplished on a Au(111) surface by reacting anhydrides and amines with H₂O as a by-product, where the careful design of the reactants allowed to obtain both polymeric strands and porous networks. Moreover, by reacting aldehydes and amines on Au(111) [37,38], successful polyimine condensation was accomplished to produce 1D and 2D polymers on a substrate, together with H₂O as a by-product. This process has also been successfully accomplished at a liquid–solid interface on highly oriented pyrolytic graphite (HOPG) [34]. Furthermore, with HCl as a by-product, two on-surface condensation reactions have been performed to successfully form 2D porous covalent networks: polyester condensation [39] by reacting alcohols and acyl chlorides on a Au(111) surface and polyamide condensation [40] by reacting acid chlorides with amines.

However, despite the versatility of these condensation processes, the on-surface condensation of boronic acids has received most of the attention to grow nanostructures on surfaces. This chemical reaction is a good example of how noncovalent interactions controlling self-assembly processes can be used to later initiate covalent coupling between adsorbed molecules on a substrate. Furthermore, given their capability to form reversible covalent complexes, boronic acids are extensively used in organic chemistry. Taking these factors into consideration, successful on-surface covalent coupling between boronic acids has been accomplished on a large variety of substrates, such as Ag (111) [41,42], Ag(100) [41,43], Cu(111) [41], at the liquid–solid interface on HOPG [33], and Au(111) [41,44]. These studies have demonstrated not only the reversibility of the on-surface reaction, but also that the pore size and quality of the 2D networks can be tailored through careful control over the kinetic parameters of the reaction and the design of the reactants. Moreover, successful attempts to combine the success of the condensation of boronic acids and the Ullmann coupling have been carried out on Au(111) [44]. By the reaction of a single reactant charged with boronic acid and bromine moieties, subsequent stepwise activation leads to an optimization of the growth mechanism of the 2D network on that substrate, with the polymerization yield reaching almost 100%.

1.2

Alkane Polymerization

To study the on-surface polymerization of alkanes, the Au(110) surface was found to be a suitable substrate [45]. After the treatment of several sputtering–annealing cycles, this surface reconstructs to form a missing row structure along the [1–10] direction. Acting as one-dimensional constraint, the reconstruction of the surface efficiently confines the diffusion of adsorbed molecules in the [1–10] direction within the atomic channels. In the first step, *n*-dotriacontane ($C_{32}H_{66}$) was used as a precursor molecule, which was deposited under UHV conditions onto the gold substrate held at room temperature. Shorter alkane chains can easily desorb, whereas the strong interaction of *n*-dotriacontane with the surface inhibits desorption at elevated temperatures. The monomers adsorb on the Au(110) surface exclusively along the atomic channels (Figure 1.3a). After subsequent annealing at 440 K, the alkane monomers were bonded end to end, forming long molecular chains within the atomic channels of the Au(110) substrate (Figure 1.3b). The successful polymerization was checked by controlled manipulation experiments with the STM tip, showing that sections of the reacted chains could be pulled out from the substrate grooves (Figure 1.3c) and providing further evidence that the products are covalently bound. It was found that most of the reacted polymers have a length of more than 200 nm. In TPD experiments, the desorption of H_2 could be verified during the thermally activated polymerization pointing to a dehydrogenation polymerization process. This was further confirmed by testing the reaction with 1,4-di(eicosyl)benzene and eicosylbenzene monomers, which both have a phenylene moiety as a marker connecting the alkyl chains (for more details see Ref. [45]). Results from DFT calculations provide a reasonable mechanism for the activation of the monomers, which exclusively takes place at the terminal CH_3 or penultimate CH_2 groups. Furthermore, the DFT results confirm that the orientational constraint of the reconstructed Au(110) surface is a major factor for the reaction to proceed.

1.3

Azide–Alkyne Cycloaddition

Among the many conceivable reactions that have potential to be performed as on-surface processes, azide–alkyne cycloadditions (often referred to as “click” reactions) are interesting candidates due to their strong covalently linked products and their low activation energies [46]. Such reactions are free of by-products and performed as solution-phase processes that have been widely used for the modification of surfaces and materials [47–49] as well as for the preparation of biologically active compounds in pharmaceutical research [50]. The most commonly used “click” reaction is the azide–alkyne 1,3-dipolar cycloaddition [51,52] leading to 1,4- and 1,5-triazoles. Whereas the classical thermal process (Huisgen azide–alkyne [3 + 2]-cycloaddition), which proceeds under

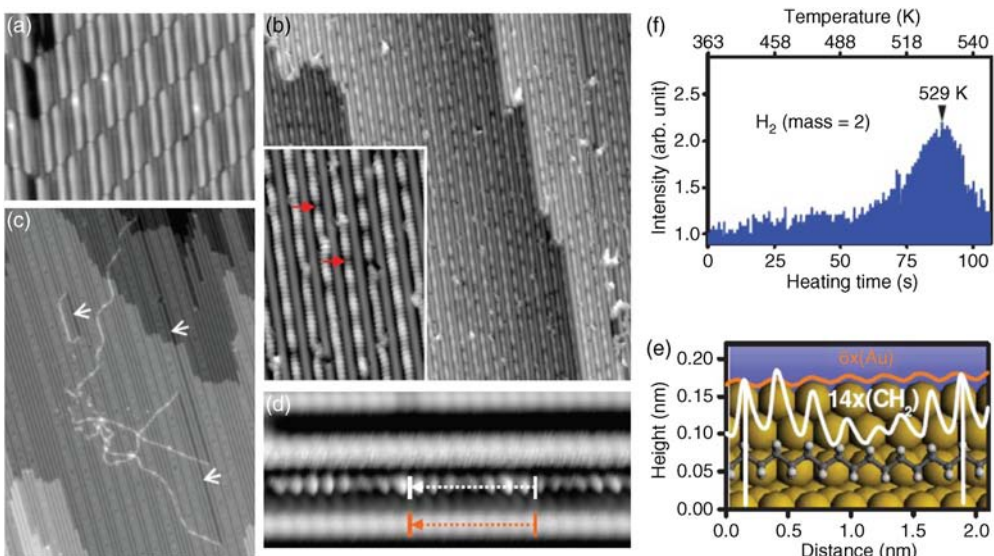


Figure 1.3 Dehydrogenative polymerization of *n*-dotriacontane ($C_{32}H_{66}$). (a) STM image of $C_{32}H_{66}$ monomers on the Au(110)-(1 \times 2) surface (20 nm \times 15 nm). (b) Parallel polyethylene chains after annealing up to 440 K for 30 min (50 nm \times 50 nm; inset: 9 nm \times 13 nm). (c) Several polyethylene chains partially released from the grooves by the STM tip

manipulations (50 nm \times 70 nm). (d) High-resolution STM image of Au atomic rows and polyethylene chain (6 nm \times 2.5 nm). (e) Height profiles at the dotted lines in (d). (f) H_2 signal detected by mass spectrometry during the annealing process (heating power: 1.2 A by 10.25 V). (Reprinted with permission from AAAS [45].)

harsh conditions, that is, high temperatures, generally delivers a mixture of the two regioisomers, the use of a copper catalyst provides 1,4-triazoles with high efficiency and regioselectivity under ambient conditions (CuAAC) [51].

Resembling the CuAAC mechanism in solution, a successful cycloaddition of alkynes and azides was recently accomplished on a Cu(111) surface with complete regioselectivity toward the formation of the corresponding 1,4-triazoles [53]. As for the solution-phase process, the high regioselectivity was discussed considering the involvement of a copper acetylidyde (C–H activation) and bonding of the alkyne group to the Cu(111) surface. However, a strong interaction between the Cu atoms of the surface and the azide moiety causes the degradation of the latter, limiting its reactivity considerably.

In an own recent study, STM experiments and DFT simulations were combined to investigate on-surface cycloaddition reactions of *N*-(4-azidophenyl)-4-ethynylbenzamide (AEB) monomers on a Au(111) surface under UHV conditions [54]. The design of the AEB monomers (Figure 1.4a) is a combination of two phenyl rings connected through an amide linker as backbone, allowing the monomers to be thermally deposited on the surface, where they can lay flat and diffuse, thus increasing the probability of the alkyne and azide groups to meet

with each other and react. The selection of the Au(111) surface as a template is based on an attempt to diminish/prevent the degradation of the azides on the surface, thus enhancing the reactivity.

The deposition of the AEB molecules on the Au(111) surface was carried out by sublimation at a crucible temperature of 85°C in UHV, while the surface was kept at room temperature. The covered surface usually showed a first layer mixture of reactants mixed with already reacted dimers as well as trimers, surrounded by a disordered molecular phase (Figure 1.4b(i)). Such phase could be ascribed to the azide end group degradation on Au(111) [53]. The quantitative assessment of the yield of the observed cycloaddition revealed that from the total of intact molecules found for four different deposition runs, about 29% reacted to dimers and about 8% to trimers. Around 63% were found as nonreacted monomers. It is interesting to note that the dimerization yield for the cycloaddition on

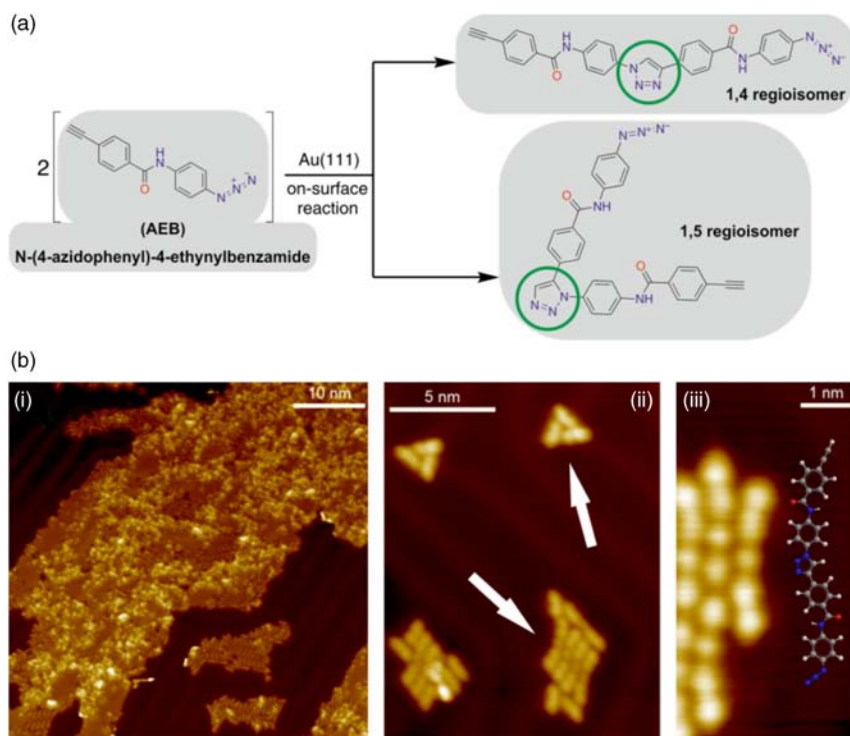


Figure 1.4 (a) Scheme of the proposed on-surface azide–alkyne cycloaddition reaction. Green circles enclose the triazole moieties. (b) STM images of AEB monomer deposition on Au(111) at room temperature. (i) Large coverage deposition (50 nm × 50 nm). (ii) Self-assembly of monomers and dimers

(13 nm × 17 nm). (iii) Dimers and trimers formed as a result of the successful azide–alkyne “click” reaction (3.5 nm × 7 nm). Inset: Molecular structure of the 1,4-triazole dimer. (Adapted with permission from Ref. [54]. Copyright 2013, American Chemical Society.)

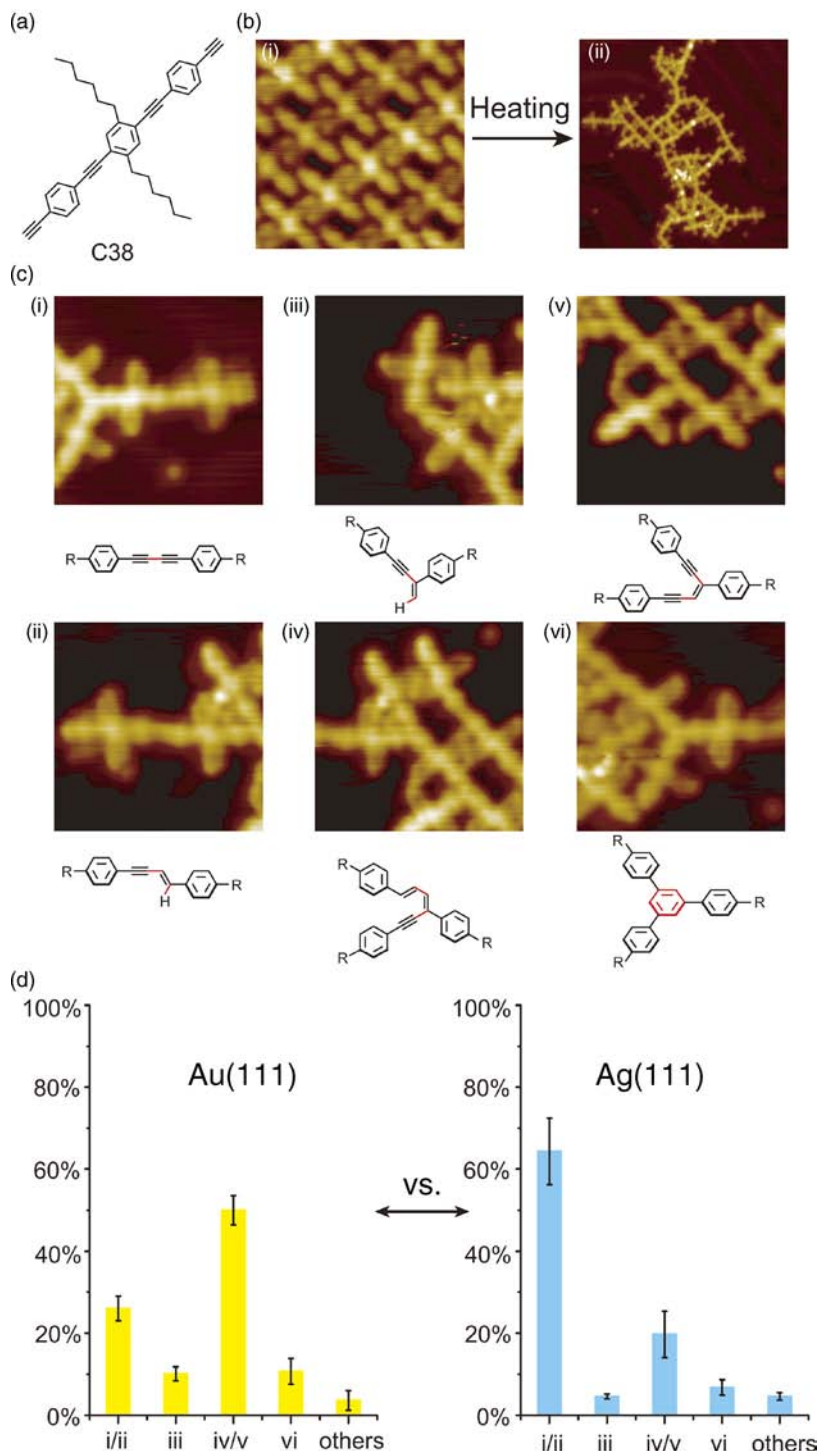
Au(111) is considerably larger than the one observed on Cu(111) [53], which one would expect larger due to the potential catalytic activity of copper. To confirm the covalent linkage of the reactants, controlled manipulations with the STM tip were carried out on the dimers and the trimers. Triazoles are known for their robustness and their high torsional degree of freedom and such features are also displayed by the on-surface coupling products on Au(111).

For a successful on-surface reaction to proceed, two monomers have to diffuse toward each other so that the reactive alkyne and azide functionalities are close enough for successful cycloaddition. Therefore, the self-assembled structure obtained after initial deposition must somehow relate to the reactivity. In our experimental studies, we found the unreacted AEB monomers to be present in three different configurations: (i) nucleation along the step edges, which is in agreement with the alkyne group high affinity for highly reactive sites, such as step edges; (ii) agglomeration adjacent to molecular islands as a result of diffusion of the molecules on the Au(111) surface and self-assembly driven by van der Waals forces; most likely those observed monomers are unreacted remnants, which did not find a counterpart to react with (lower section of Figure 1.4b(ii)); and (iii) self-assembled arrangement of three monomers in a stable triangular shaped island (upper section of Figure 1.4b(ii)). We found this configuration quite frequently (~27% of the monomers that remain intact after the deposition), being the only configuration where exclusively monomers self-assembled independently.

The inset in Figure 1.4b(iii) represents the molecular structure of a 1,4-triazole dimer. This structure matches very well the STM observations, since the alternative 1,5-regioisomer would present a significant tilt (L-shaped structure, see scheme in Figure 1.4a) instead of the observed linear structure. In these experiments, only the formation of the 1,4-regioisomer was observed. DFT calculations showed that the Au substrate (i) lowers the activation energy, which causes the reaction to proceed at room temperature, (ii) does not act as a catalyst but merely as a two-dimensional constraint, and (iii) steers the complete 1,4-regioselectivity of the [3 + 2] on-surface cycloaddition reaction by means of surface-induced steric effects preventing the formation of the 1,5-regioisomer. The fact that the regioselectivity of the azide–alkyne cycloaddition can be controlled by the surface constraint and the reactants’ design provides an efficient method to develop well-defined nanostructures at surfaces, without the requirement of a catalyst or additional thermal activation.

1.4 Glaser Coupling

Another interesting coupling mechanism involves the halogen-free reaction of aryl alkynes (Glaser coupling), which was studied at gold and silver surfaces [55]. For initial investigations, the diethynyl-substituted π -system C38, as shown in Figure 1.5a, was studied. Figure 1.5b(i) shows an STM image of the C38 molecule, which forms a self-assembled structure dominated by Van der Waals



interactions between the C6-alkane chains. After thermal annealing, the C38 molecules form a covalent bound nanostructure via reactions of the alkynes (Figure 1.5b(ii)). However, due to various possible reaction pathways, several side products were identified: Glaser coupling (Figure 1.5c(i)), formal hydroalkynylation of the terminal alkyne functionality either at the α -position or at the β -position (Figure 1.5c(ii) and (iii)), dieyne products (Figure 1.5c(iv)), enediyne moiety (Figure 1.5c(v)), and diyne polycyclotrimerization (Figure 1.5c(vi)). To further study the catalytic role of the metal surface, the relative frequency of occurrence of the reaction pathways (i)–(vi) was determined on the Au(111) and Ag(111) surfaces. As in some cases the reactions (i) and (ii), as well as (iv) and (v), were undistinguishable, they were combined in this analysis. However, it is important to note that the Glaser reaction (i) is the main reaction type within the (i)/(ii) pair of the statistical analysis. It was found that the reaction pathways (i)/(ii) and (iv)/(v) occurred with frequencies of (26 ± 3) and $(50 \pm 3.6)\%$ on the Au(111) surface, while frequencies of (64.3 ± 8.1) and $(19.7 \pm 5.7)\%$ were found on the Ag(111) surface, respectively. Thus, Glaser coupling seems to be more efficient on Ag(111) than on Au(111) surfaces, while the side reactions (iv)/(v) reverse.

To further improve the selectivity toward Glaser coupling, dimers of 1,4-diethynylbenzene having no alkane chains on its side (C20, Figure 1.6a(i)) were tested as alternative reactants. Deposited on the Au(111) surface, they formed ordered (Figure 1.6a(ii)) as well as disordered self-assembled structures [55]. After annealing, branched covalent bound nanostructures can be observed (Figure 1.6a(iii)). In a similar statistical analysis as for the C38 case, Glaser coupling events occurred at a frequency of $(43.3 \pm 4.3)\%$ on the Au(111) surface. The selectivity toward this reaction type could be further improved by performing the experiment on the Ag(111) surface, where a frequency of $(67 \pm 3.8)\%$ could be achieved. At the same time, the side reactions (iv)/(v) were slightly reduced to $(40.8 \pm 4.1)\%$ on the Au(111) surface and $(21.6 \pm 3.6)\%$ on the Ag(111) surface.

By further optimization of the precursor molecules, the side reactions of alkynes could be completely suppressed. Figure 1.6b(i) shows the structure of the resulting C22 molecule with an *ortho*-substituent next to the alkyne functionality, which suppresses side reactions due to steric reasons. As shown in Figure 1.6b (ii), STM images of the self-assembled C22 molecules on Au(111) match its chemical structure very well. After reaction, C22 molecules were mainly connected one by one through Glaser coupling (Figure 1.6b(iii)). The length of the

Figure 1.5 Glaser coupling of the C38 molecule. (a) Molecular chemical structure. (b) High-resolution STM image of C38 precursors at a Au(111) surface (i: $6 \text{ nm} \times 6 \text{ nm}$), as well as high-resolution image of C38 oligomers after thermal annealing at $123\text{--}140^\circ\text{C}$ (ii: $25 \text{ nm} \times 25 \text{ nm}$). (c) Rationalization of the different observed covalent bonding types in on-surface oligomerization by STM images

(all with $6 \text{ nm} \times 6 \text{ nm}$) and the corresponding chemical structures. (d) Corresponding statistical analysis for the distribution of the observed products on Au(111) and Ag(111) surfaces, which clearly prove that the Ag(111) surface works more efficiently toward the Glaser coupling. (Redrawn with permission from Wiley-VCH Verlag GmbH [55].)

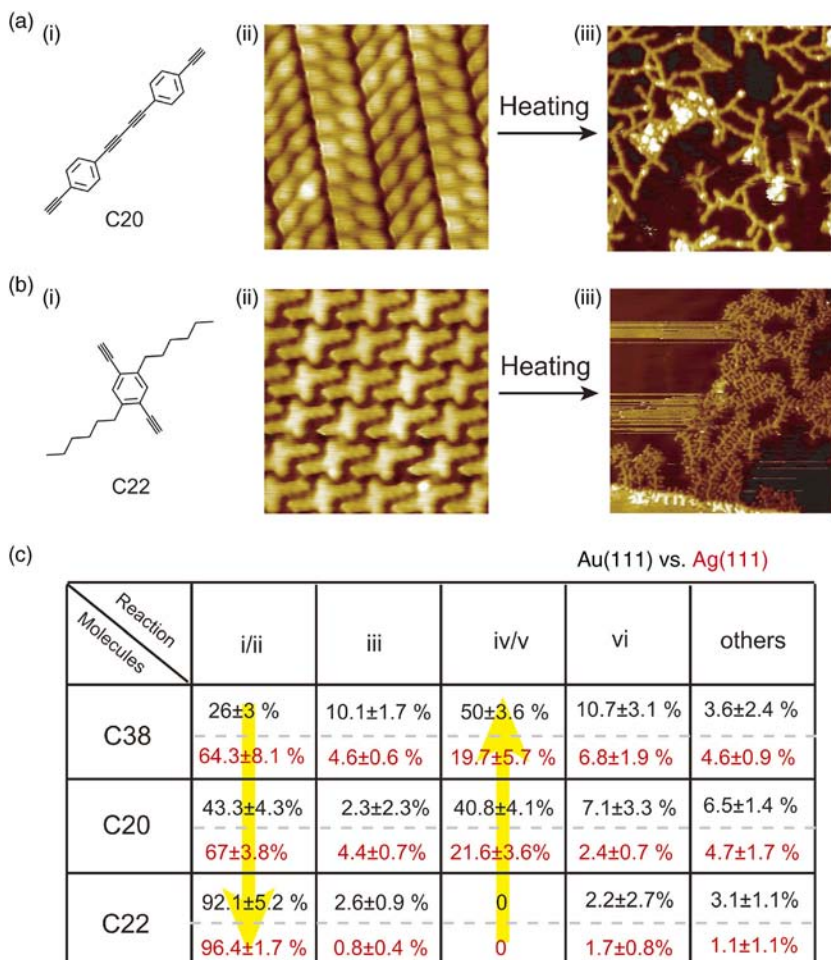


Figure 1.6 Glaser coupling of C20 and C22 molecules. (a) Chemical structure of the C20 molecule (i) and its high-resolution STM images before (ii: 6 nm × 6 nm) and after (iii: 25 nm × 25 nm) the Glaser coupling reaction on the Au(111) substrate. (b) Chemical structure of the C22 molecule (i) and its high-resolution STM images before (ii: 6 nm × 6 nm) and after (iii: 25 nm × 25 nm) reaction on the Au(111) substrate. (c) Summary of the

statistical analysis for the distribution of the observed products on the different substrates allowing the comparison of the catalytic abilities of Au(111) and Ag(111) surfaces toward Glaser coupling, side cross-coupling, and the influences of chemical structures from C38 to C20 and C22. ((a) Adapted with permission from Ref. [56]. Copyright 2013, American Chemical Society. (b) Redrawn with permission from Wiley-VCH Verlag GmbH [55].)

polymers could be increased up to 59 monomers when Ag(111) was used as a substrate. The statistical analysis revealed that the Glaser coupling was optimized up to $(92.1 \pm 5.1)\%$ on Au(111) and $(96.4 \pm 1.7)\%$ on Ag(111). At the same time, the side reactions (iv)/(v) were completely suppressed.

Figure 1.6c shows a summary of the statistical frequencies for the different tested reactants C38, C20, and C22. As indicated by the yellow arrow, the *ortho*-substituent next to the alkyne works very efficiently toward chemical selectivity of Glaser coupling in alkyne reactions. Another important point is that the Ag (111) surface has a stronger catalytic effect toward Glaser coupling than the Au (111) surface, where the latter leads to more side reactions. To understand the different catalytic effects of on-surface Glaser coupling on metal surfaces, DFT simulations were conducted [56]. The results suggest a model with two possible reaction pathways: C–C coupling via direct C–H activation and C–C coupling via alkynyl activation by π -complex formation. On both Au and Ag surfaces, the alkyne direct C–H activation was found to be a high-energy pathway (1.64 and 1.85 eV on Au and Ag, respectively), which is very unlikely to occur in experiments. The alternative low-energy route (0.79 and 0.9 eV on Au and Ag, respectively) comprises interaction of the alkyne functionality with the surface and direct C–C bond formation as the rate-determining step.

In a subsequent study on the (111) surfaces of Ag, Au, and Cu, photoinduced effects on the Glaser coupling were investigated by exposing self-assembled monolayers of the C22 molecule to UV irradiation [57]. As shown in Figure 1.7a, the formation of aryl alkyne dimers at the Ag(111) surface could be induced after UV irradiation for 67 h at a wavelength of 375 nm. This photochemical aryl alkyne dimerization occurred also on Cu(111), but with a significantly reduced efficiency compared with Ag(111). On the gold surface, no photoinduced effects could be observed at all, emphasizing the catalytic role of the substrate also for the photoinduced approach of the Glaser coupling. Short aryl alkyne oligomers such as trimers and tetramers could be observed on the Ag(111) surface as shown in Figure 1.7b. The statistical analysis of the oligomer length distribution shows that the main products of photochemical reaction of the C22 molecules are the dimers with an abundance of $(87.4 \pm 2.1)\%$, which significantly differs from the products of the thermally induced C22 reactions on Ag(111). In comparison with the thermal process, the major advantage of the photochemical on-surface reaction at room temperature is that the self-assembly of the reactants after initial deposition may be restored, allowing spatiotemporal control of the C–C bond formation. The DFT simulations indicate why the Ag surface is more efficient than Au. This is because the gold surface interacts stronger with the alkynyl groups resulting in a reduced mobility of the molecules on the substrate and a longer trapping of C–C coupled intermediates to branching reactions.

1.5

Decarboxylative Polymerization of Acids

The metal-catalyzed polymerization of 2,6-naphthalenedicarboxylic acid (NDCA) is another important recent achievement in the research field [58]. The C–C coupling of NDCA was found to occur via a three-step process, which is visualized in the scheme in Figure 1.8a: step 1 is a dehydrogenation process to

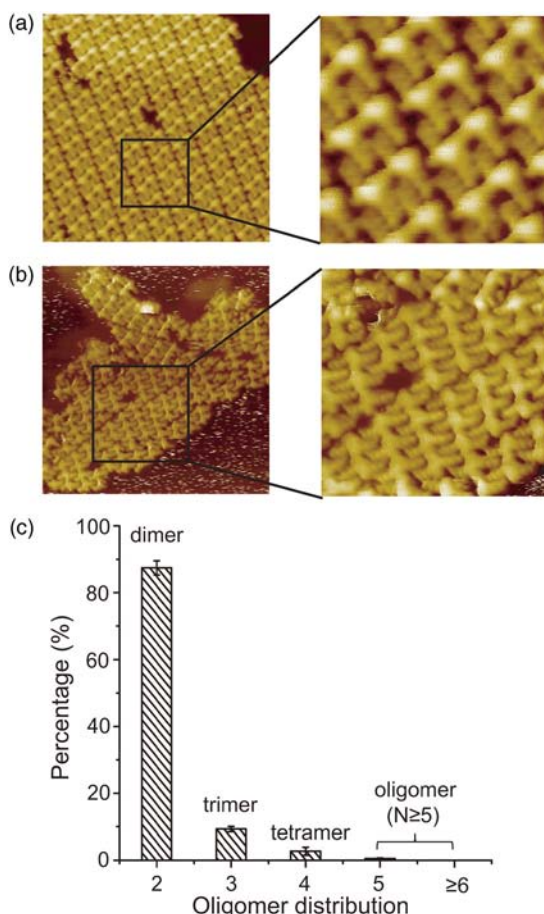


Figure 1.7 Photochemical Glaser coupling of the C22 molecule after UV irradiation (67 h) on Ag(111). (a) STM image of C22 dimers (17 nm \times 17 nm), with a high-resolution image shown in the inset (5 nm \times 5 nm). (b) STM image of short C22 oligomers (20 nm \times 20 nm), with an inset image (8.4 nm \times 8.4 nm). (c) The corresponding statistical analysis for the oligomer distribution. (Adapted with permission from Ref. [57]. Copyright 2014, American Chemical Society.)

provide the corresponding metal carboxylate; in step 2, a decarboxylative process leads to the formation of polymeric bisnaphthalene-Cu as an intermediate species; and step 3 finally leads to C–C coupling forming poly-2,6-naphthalene chains via decarboxylation. First of all, it was found that this reaction seems generally not to proceed on the Au(111) surface. Switching to the Ag(111) surface, the interaction of the carboxyl group with the substrate could be increased and covalent coupling of NDCAs occurred after thermal annealing to 156 °C. However, due to the desorption of NDCA during annealing, the efficiency toward poly-bisnaphthalene-Ag intermediates as well as the oligo-2,6-naphthalene was

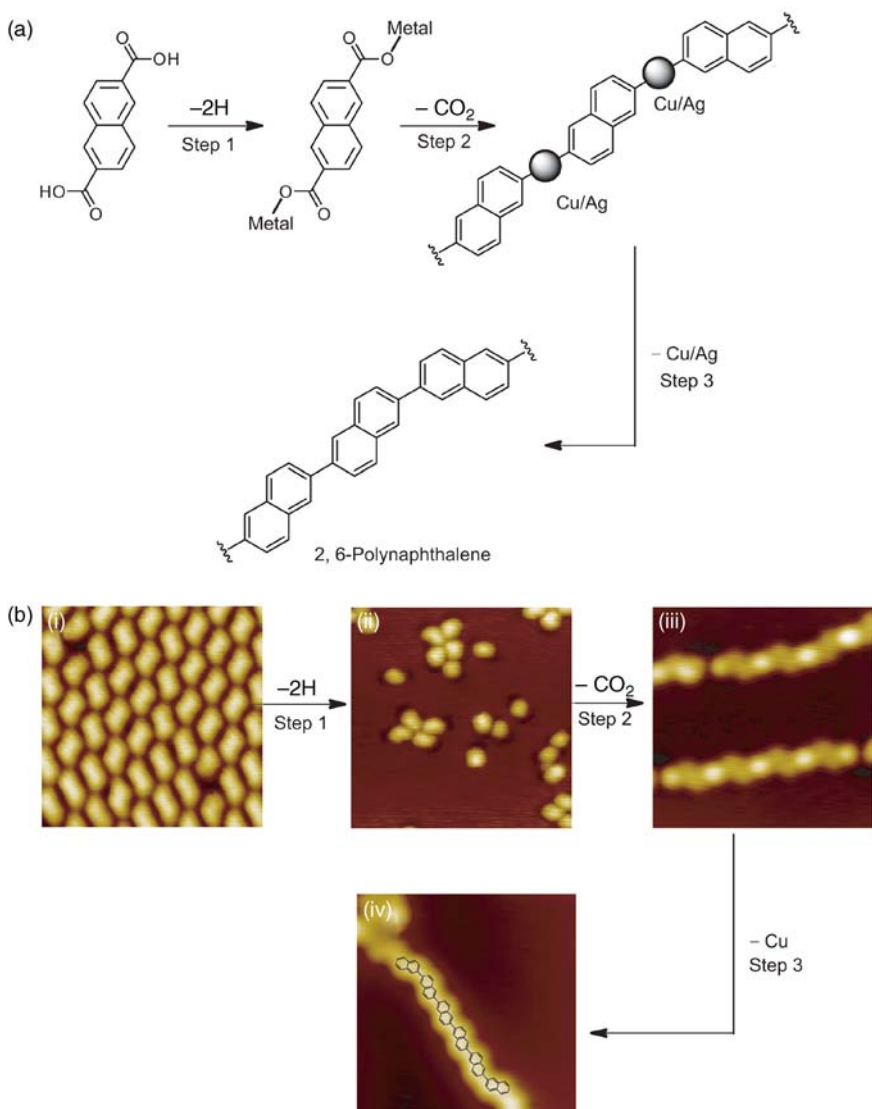


Figure 1.8 Metal-catalyzed on-surface polymerization of NDCA. (a) Schematic illustration of the reaction pathway. (b) STM images for the polymerization of NDCA on Cu(111) from unreacted precursor molecules (i: $6 \text{ nm} \times 6 \text{ nm}$), to their dehydrogenated state (ii: $10 \text{ nm} \times 10 \text{ nm}$), via the bisnaphthyl-Cu intermediates (iii: $4.24 \text{ nm} \times 4.24 \text{ nm}$), and finally to poly-2,6-naphthalene (iv: $4.2 \text{ nm} \times 4.2 \text{ nm}$). (Adapted with permission from Ref. [58]. Copyright 2014, American Chemical Society.)

rather low. Therefore, Cu(111) was tested as substrate for the reaction, as it shows the strongest interaction with carboxyl groups compared with the Au(111) or Ag(111) surfaces. Expectedly, a hydrogen-bonded self-assembly structure (one of the different phases is shown in Figure 1.8b(i)), dehydrogenated product (Figure 1.8b(ii)), bisnaphthyl-Cu species (Figure 1.8b(iii)), and final polynaphthalenes (Figure 1.8b(iv)) were obtained with high efficiency. Moreover, the differences of Cu(111), Cu(100), and Cu(110) surfaces were compared toward such decarboxylative polymerization. Surprisingly, the following reactivity order was observed: Cu(111) > Cu(100) > Cu(110), which likely relates to the ability of metal atoms being pulled out of the surface. The experiments also revealed that the organometallic polymers (bisnaphthalene-Cu species) on the Cu(100) surface were grown only in [001] and [010] directions, while organometallic polymers on the Cu(111) surface grow in [110], [011], and [101] directions. This substrate dependence indicates that the metal atoms part of the organometallic polymers should have a specific interaction with the metal surfaces.

1.6

Conclusions

An interesting feature of on-surface chemical reactions is the possibility of targeted conjugation in more than one direction on a substrate, extending 1D polymerization to the growth of 2D organic networks. Thereby, on-surface reactions performed under UHV conditions benefit from the lack of solvents required, which allows us to gain insight into chemical processes under well-defined conditions. The recent achievements in this research field allow to identify some important prerequisites for a successful covalent coupling, which are summarized in the following.

An important aspect is the flat adsorption geometry of the reactants, where the adsorption strength is crucial to avoid desorption when the system is supplied with additional energy by thermal annealing and/or light illumination. In particular, it has been observed to impact directly the ordering of the products after the on-surface coupling [55,59,60]. Too strongly adsorbed molecules might inhibit a reaction by reduced diffusion, which is vital for the reactive moieties to meet in the desired geometry on a surface. Therefore, reduced diffusion can lead to poor reactivity and stereocontrol [55,59,60]. For experiments under UHV conditions, the design of the reactants should enable a straightforward deposition, which in most cases is done by thermal sublimation. Potential issues could be the decomposition of the molecules or reactive end groups due to the elevated sublimation temperatures in the crucible. For the proper design of the reactants, steric effects on the surface should be considered, providing further control on the reaction mechanism, for example, in view of regioselectivity of the anticipated bond formation. Another important aspect is the choice of the substrate. As shown earlier, a surface can act as both a two-dimensional spatial constraint [54] and an active catalytic agent in a specific reaction mechanism [28,45]. Therefore, a

simple transfer of reaction mechanisms from solution-phase chemistry to on-surface reactions is not straightforward. Furthermore, surface orientation, reconstructions, or well-oriented stepped surfaces can help to provide directional alignment of the products [23,28,29,45]. Finally, reaction by-products are usually detrimental for the properties of a highly defined nanomaterial and can hinder the studied process or even suppress it [26].

Given the remarkable achievements of the last few years in the field of on-surface reactions with organic molecules, a promising approach for the development of novel nanomaterials with tailored optoelectronic properties and potential applications in devices emerged. The current major challenges are to determine the critical parameters to control reaction pathways and material properties in the two-dimensional environment of a surface. However, future work should also focus on extending the existing tool kit of on-surface chemistry by finding additional reaction pathways.

Acknowledgments

The authors acknowledge support by the Deutsche Forschungsgemeinschaft (DFG) through the Collaborative Research Center SFB 858, project B2, and TRR 61, projects B3 and B7.

References

- 1 Barth, J.V. (2007) Molecular architectonic on metal surfaces. *Annu. Rev. Phys. Chem.*, **58**, 375–407.
- 2 Champness, N.R. (2012) Surface chemistry making the right connections. *Nat. Chem.*, **4** (3), 149–150.
- 3 Gourdon, A. (2008) On-surface covalent coupling in ultrahigh vacuum. *Angew. Chem., Int. Ed.*, **47** (37), 6950–6953.
- 4 Mendez, J., Lopez, M.F., and Martin-Gago, J.A. (2011) On-surface synthesis of cyclic organic molecules. *Chem. Soc. Rev.*, **40** (9), 4578–4590.
- 5 Zhang, X.M., Zeng, Q.D., and Wang, C. (2013) On-surface single molecule synthesis chemistry: a promising bottom-up approach towards functional surfaces. *Nanoscale*, **5** (18), 8269–8287.
- 6 Franc, G. and Gourdon, A. (2011) Covalent networks through on-surface chemistry in ultra-high vacuum: state-of-the-art and recent developments. *Phys. Chem. Chem. Phys.*, **13** (32), 14283–14292.
- 7 Sakamoto, J., van Heijst, J., Lukin, O., and Schluter, A.D. (2009) Two-dimensional polymers: just a dream of synthetic chemists? *Angew. Chem., Int. Ed.*, **48** (6), 1030–1069.
- 8 Perepichka, D.F. and Rosei, F. (2009) Chemistry. Extending polymer conjugation into the second dimension. *Supramol. Sci.*, **323** (5911), 216–217.
- 9 de Oteyza, D.G., Gorman, P., Chen, Y.C., Wickenburg, S., Riss, A., Mowbray, D.J., Etkin, G., Pedramrazi, Z., Tsai, H.Z., Rubio, A., Crommie, M.F., and Fischer, F.R. (2013) Direct imaging of covalent bond structure in single-molecule chemical reactions. *Supramol. Sci.*, **340** (6139), 1434–1437.
- 10 Swart, I., Gross, L., and Liljeroth, P. (2011) Single-molecule chemistry and physics explored by low-temperature scanning probe microscopy. *Chem. Commun.*, **47** (32), 9011–9023.
- 11 Repp, J., Meyer, G., Paavilainen, S., Olsson, F.E., and Persson, M. (2006) Imaging bond

- formation between a gold atom and pentacene on an insulating surface. *Supramol. Sci.*, **312** (5777), 1196–1199.
- 12 Okawa, Y., Akai-Kasaya, M., Kuwahara, Y., Mandal, S.K., and Aono, M. (2012) Controlled chain polymerisation and chemical soldering for single-molecule electronics. *Nanoscale*, **4** (10), 3013–3028.
- 13 Okawa, Y., Mandal, S.K., Hu, C., Tateyama, Y., Goedecker, S., Tsukamoto, S., Hasegawa, T., Gimzewski, J.K., and Aono, M. (2011) Chemical wiring and soldering toward all-molecule electronic circuitry. *J. Am. Chem. Soc.*, **133** (21), 8227–8233.
- 14 Hla, S.W., Bartels, L., Meyer, G., and Rieder, K.H. (2000) Inducing all steps of a chemical reaction with the scanning tunneling microscope tip: towards single molecule engineering. *Phys. Rev. Lett.*, **85** (13), 2777–2780.
- 15 Zhao, A., Tan, S.J., Li, B., Wang, B., Yang, J.L., and Hou, J.G. (2013) STM tip-assisted single molecule chemistry. *Phys. Chem. Chem. Phys.*, **15** (30), 12428–12441.
- 16 Custance, O., Perez, R., and Morita, S. (2009) Atomic force microscopy as a tool for atom manipulation. *Nat. Nanotechnol.*, **4** (12), 803–810.
- 17 Kittelmann, M., Nimmrich, M., Lindner, R., Gourdon, A., and Kuhnle, A. (2013) Sequential and site-specific on-surface synthesis on a bulk insulator. *ACS Nano*, **7** (6), 5614–5620.
- 18 Grill, L., Dyer, M., Lafferentz, L., Persson, M., Peters, M.V., and Hecht, S. (2007) Nano-architectures by covalent assembly of molecular building blocks. *Nat. Nanotechnol.*, **2** (11), 687–691.
- 19 Lafferentz, L., Eberhardt, V., Dri, C., Africh, C., Comelli, G., Esch, F., Hecht, S., and Grill, L. (2012) Controlling on-surface polymerization by hierarchical and substrate-directed growth. *Nat. Chem.*, **4** (3), 215–220.
- 20 Saywell, A., Schwarz, J., Hecht, S., and Grill, L. (2012) Polymerization on stepped surfaces: alignment of polymers and identification of catalytic sites. *Angew. Chem., Int. Ed.*, **51** (21), 5096–5100.
- 21 Lafferentz, L., Ample, F., Yu, H., Hecht, S., Joachim, C., and Grill, L. (2009) Conductance of a single conjugated polymer as a continuous function of its length. *Supramol. Sci.*, **323** (5918), 1193–1197.
- 22 Gutzler, R., Walch, H., Eder, G., Kloft, S., Heckl, W.M., and Lackinger, M. (2009) Surface mediated synthesis of 2D covalent organic frameworks: 1,3,5-tris(4-bromophenyl)benzene on graphite(001), Cu(111), and Ag(110). *Chem. Commun.*, **29**, 4456–4458.
- 23 Cai, J.M., Ruffieux, P., Jaafar, R., Bieri, M., Braun, T., Blankenburg, S., Muoth, M., Seitsonen, A.P., Saleh, M., Feng, X.L., Mullen, K., and Fasel, R. (2010) Atomically precise bottom-up fabrication of graphene nanoribbons. *Nature*, **466** (7305), 470–473.
- 24 Eichhorn, J., Strunskus, T., Rastgoo-Lahrood, A., Samanta, D., Schmittel, M., and Lackinger, M. (2014) On-surface Ullmann polymerization via intermediate organometallic networks on Ag(111). *Chem. Commun. (Camb.)*, **50** (57), 7680–7682.
- 25 Eder, G., Smith, E.F., Cebula, I., Heckl, W.M., Beton, P.H., and Lackinger, M. (2013) Solution preparation of two-dimensional covalently linked networks by polymerization of 1,3,5-tri(4-iodophenyl) benzene on Au(111). *ACS Nano*, **7** (4), 3014–3021.
- 26 Schlogl, S., Heckl, W.M., and Lackinger, M. (2012) On-surface radical addition of triply iodinated monomers on Au(111): the influence of monomer size and thermal post-processing. *Surf. Sci.*, **606** (13–14), 999–1004.
- 27 Lipton-Duffin, J.A., Ivasenko, O., Perepichka, D.F., and Rosei, F. (2009) Synthesis of polyphenylene molecular wires by surface-confined polymerization. *Small*, **5** (5), 592–597.
- 28 Zhang, H., Franke, J.H., Zhong, D., Li, Y., Timmer, A., Díaz Arado, O., Möning, H., Wang, H., Chi, L., Wang, Z., Mullen, K., and Fuchs, H. (2014) Surface supported gold–organic hybrids: on-surface synthesis and surface directed orientation. *Small*, **10** (7), 1361–1368.
- 29 Linden, S., Zhong, D., Timmer, A., Aghdassi, N., Franke, J.H., Zhang, H., Feng, X., Mullen, K., Fuchs, H., Chi, L., and Zacharias, H. (2012) Electronic structure of spatially aligned graphene

- nanoribbons on Au(788). *Phys. Rev. Lett.*, **108** (21), 216801.
- 30** Nazin, G.V., Qiu, X.H., and Ho, W. (2003) Visualization and spectroscopy of a metal–molecule–metal bridge. *Supramol. Sci.*, **302** (5642), 77–81.
- 31** Koudia, M. and Abel, M. (2014) Step-by-step on-surface synthesis: from manganese phthalocyanines to their polymeric form. *Chem. Commun.*, **50**, 8565–8567.
- 32** Zhang, H.-M., Zhao, W., Xie, Z.-X., Long, L.-S., Mao, B.-W., Xu, X., and Zheng, L.-S. (2007) One step fabrication of metal–organic coordination monolayers on Au(111) surfaces. *J. Phys. Chem. C*, **111** (21), 7570–7573.
- 33** Dienstmaier, J.F., Medina, D.D., Dogru, M., Knochel, P., Bein, T., Heckl, W.M., and Lackinger, M. (2012) Isoreticular two-dimensional covalent organic frameworks synthesized by on-surface condensation of diboronic acids. *ACS Nano*, **6** (8), 7234–7242.
- 34** Xu, L.R., Zhou, X., Yu, Y.X., Tian, W.Q., Ma, J., and Lei, S.B. (2013) Surface-confined crystalline two-dimensional covalent organic frameworks via on-surface Schiff-base coupling. *ACS Nano*, **7** (9), 8066–8073.
- 35** Treier, M., Fasel, R., Champness, N.R., Argent, S., and Richardson, N.V. (2009) Molecular imaging of polyimide formation. *Phys. Chem. Chem. Phys.*, **11** (8), 1209–1214.
- 36** Treier, M., Richardson, N.V., and Fasel, R. (2008) Fabrication of surface-supported low-dimensional polyimide networks. *J. Am. Chem. Soc.*, **130** (43), 14054–14055.
- 37** Weigelt, S., Busse, C., Bombis, C., Knudsen, M.M., Gothelf, K.V., Laegsgaard, E., Besenbacher, F., and Linderoth, T.R. (2008) Surface synthesis of 2D branched polymer nanostructures. *Angew. Chem., Int. Ed.*, **47** (23), 4406–4410.
- 38** Weigelt, S., Busse, C., Bombis, C., Knudsen, M.M., Gothelf, K.V., Strunskus, T., Woll, C., Dahlbom, M., Hammer, B., Laegsgaard, E., Besenbacher, F., and Linderoth, T.R. (2007) Covalent interlinking of an aldehyde and an amine on a Au(111) surface in ultrahigh vacuum. *Angew. Chem., Int. Ed.*, **46** (48), 9227–9230.
- 39** Marele, A.C., Mas-Balleste, R., Terracciano, L., Rodriguez-Fernandez, J., Berlanga, I., Alexandre, S.S., Otero, R., Gallego, J.M., Zamora, F., and Gomez-Rodriguez, J.M. (2012) Formation of a surface covalent organic framework based on polyester condensation. *Chem. Commun.*, **48** (54), 6779–6781.
- 40** Schmitz, C.H., Ikonomov, J., and Sokolowski, M. (2011) Two-dimensional polyamide networks with a broad pore size distribution on the Ag(111) surface. *J. Phys. Chem. C*, **115** (15), 7270–7278.
- 41** Faury, T., Dumur, F., Clair, S., Abel, M., Porte, L., and Gigmes, D. (2013) Side functionalization of diboronic acid precursors for covalent organic frameworks. *CrystEngComm*, **15** (11), 2067–2075.
- 42** Zwaneveld, N.A.A., Pawlak, R., Abel, M., Catalin, D., Gigmes, D., Bertin, D., and Porte, L. (2008) Organized formation of 2D extended covalent organic frameworks at surfaces. *J. Am. Chem. Soc.*, **130** (21), 6678–6679.
- 43** Clair, S., Abel, M., and Porte, L. (2014) Growth of boronic acid based two-dimensional covalent networks on a metal surface in ultrahigh vacuum. *Chem. Commun.*, **50**, 9627–9635.
- 44** Faury, T., Clair, S., Abel, M., Dumur, F., Gigmes, D., and Porte, L. (2012) Sequential linking to control growth of a surface covalent organic framework. *J. Phys. Chem. C*, **116** (7), 4819–4823.
- 45** Zhong, D.Y., Franke, J.H., Podiyacharai, S.K., Blomker, T., Zhang, H.M., Kehr, G., Erker, G., Fuchs, H., and Chi, L.F. (2011) Linear alkane polymerization on a gold surface. *Supramol. Sci.*, **334** (6053), 213–216.
- 46** Kolb, H.C., Finn, M.G., and Sharpless, K.B. (2001) Click chemistry: diverse chemical function from a few good reactions. *Angew. Chem., Int. Ed.*, **40** (11), 2004–2021.
- 47** Binder, W.H. and Sachsenhofer, R. (2007) ‘Click’ chemistry in polymer and materials science. *Macromol. Rapid Commun.*, **28** (1), 15–54.
- 48** Li, Y. and Cai, C.Z. (2011) Click chemistry-based functionalization on non-oxidized silicon substrates. *Chem. Asian J.*, **6** (10), 2592–2605.

- 49** Yao, K.J. and Tang, C.B. (2013) Controlled polymerization of next-generation renewable monomers and beyond. *Macromolecules*, **46** (5), 1689–1712.
- 50** Kolb, H.C. and Sharpless, K.B. (2003) The growing impact of click chemistry on drug discovery. *Drug Discov. Today*, **8** (24), 1128–1137.
- 51** Rostovtsev, V.V., Green, L.G., Fokin, V.V., and Sharpless, K.B. (2002) A stepwise Huisgen cycloaddition process: copper(I)-catalyzed regioselective “ligation” of azides and terminal alkynes. *Angew. Chem., Int. Ed.*, **41** (14), 2596–2599.
- 52** Tornoe, C.W., Christensen, C., and Meldal, M. (2002) Peptidotriazoles on solid phase: [1,2,3]-triazoles by regiospecific copper(I)-catalyzed 1,3-dipolar cycloadditions of terminal alkynes to azides. *J. Org. Chem.*, **67** (9), 3057–3064.
- 53** Bebensee, F., Bombis, C., Vadapoo, S.R., Cramer, J.R., Besenbacher, F., Gothelf, K. V., and Linderoth, T.R. (2013) On-surface azide–alkyne cycloaddition on Cu(111): does it “click” in ultrahigh vacuum? *J. Am. Chem. Soc.*, **135** (6), 2136–2139.
- 54** Diaz Arado, O., Mönig, H., Wagner, H., Franke, J.H., Langewisch, G., Held, P.A., Studer, A., and Fuchs, H. (2013) On-surface azide–alkyne cycloaddition on Au (111). *ACS Nano*, **7** (10), 8509–8515.
- 55** Gao, H.Y., Wagner, H., Zhong, D., Franke, J.H., Studer, A., and Fuchs, H. (2013) Glaser coupling at metal surfaces. *Angew. Chem., Int. Ed.*, **52** (14), 4024–4028.
- 56** Gao, H.Y., Franke, J.H., Wagner, H., Zhong, D.Y., Held, P.A., Studer, A., and Fuchs, H. (2013) Effect of metal surfaces in on-surface Glaser coupling. *J. Phys. Chem. C*, **117** (36), 18595–18602.
- 57** Gao, H.Y., Zhong, D.Y., Mönig, H., Wagner, H., Held, P.A., Timmer, A., Studer, A., and Fuchs, H. (2014) Photochemical Glaser coupling at metal surfaces. *J. Phys. Chem. C*, **118** (12), 6272–6277.
- 58** Gao, H.-Y., Held, P.A., Knor, M., Mück-Lichtenfeld, C., Neugebauer, J., Studer, A., and Fuchs, H. (2014) Decarboxylative polymerization of 2,6-naphthalenedicarboxylic acid at surfaces. *J. Am. Chem. Soc.*, **136** (27), 9658–9663.
- 59** Pinardi, A.L., Otero-Irurueta, G., Palacio, I., Martinez, J.I., Sanchez-Sanchez, C., Tello, M., Rogero, C., Cossaro, A., Preobrajenski, A., Gomez-Lor, B., Jancarik, A., Stará, I.G., Stary, I., Lopez, M.F., Mendez, J., and Martin-Gago, J.A. (2013) Tailored formation of N-doped nanoarchitectures by diffusion-controlled on-surface (cyclo)dehydrogenation of heteroaromatics. *ACS Nano*, **7** (4), 3676–3684.
- 60** Bieri, M., Nguyen, M.T., Groning, O., Cai, J., Treier, M., Ait-Mansour, K., Ruffieux, P., Pignedoli, C.A., Passerone, D., Kastler, M., Mullen, K., and Fasel, R. (2010) Two-dimensional polymer formation on surfaces: insight into the roles of precursor mobility and reactivity. *J. Am. Chem. Soc.*, **132** (46), 16669–16676.

2

Self-Assembly of Organic Molecules into Nanostructures

Long Qin, Kai Lv, Zhaocun Shen, and Minghua Liu

2.1

Introduction

A molecule is defined as a sufficiently stable, electrically neutral unit of at least two atoms in a definite arrangement held together by very strong chemical bonds [1,2]. It is generally regarded as the basic unit for expressing structures and functions of the materials. While research works on the design and properties of molecules are very important, it is also the key issue that how small molecules could be assembled together into larger entities since the real properties of materials are related to not only the molecules but also their arrangement manner. During last three decades, with the rapid development of supramolecular chemistry and nanoscience and technology, we obtained a deep understanding of how molecules of subnanometer size gather together to form real macroscopic materials at different scales. Although from subnano- to nano- and to micro- and macroscales there are unique features at each scale, the formation of nanostructures or the self-assembly of small molecules into nanosized nanostructures plays an important role [3,4]. It is the key to understand the molecular interactions and to control or regulate the size, shape, and even the properties of nanomaterials.

Nanomaterials, with at least one of the three dimensions in the range of 1–100 nm, have been attracting great interest during the past three decades [5]. Nanomaterials can be divided into inorganic materials and organic or bio-nanomaterials based on their chemical composition. In addition, the hybrid nanomaterials composed of inorganic and organic or biological parts are also attractive. These materials can be fabricated through the bottom-up or top-down methods. The bottom-up method is particularly useful for the fabrication of organic materials, in which various noncovalent interactions and the self-assembly process could be efficiently utilized. Although inorganic nanomaterials have been mostly investigated from the very beginning of the rise of nanoscience, self-assembled organic or biological nanomaterials, which had a longer history, have also been attracting great interest. In this chapter, we will focus on how small organic molecules could be self-assembled into nanostructures and their potential applications.

Organic molecules are one of the most promising candidates to perform self-assembly with versatility in molecular design and tailorability. These could be composed of lower molecular weight organic molecules, π -conjugated systems, macromolecules or polymers, dendrimers, and so on, all of which have also been investigated extensively during the past decade. In the self-assembly process, the organic molecules are held together by a combination of weak forces, such as hydrogen bonding, $\pi-\pi$ stacking, and van der Waals interactions. The nanostructures formed by the organic molecules can be diverse in both their morphology and function. As a consequence of the diversity, multifunctionality, designability, and tailorability of small organic molecules, ever more work is being carried out to extend research on nanostructured materials into the organic molecule area.

In this chapter, we intend to first describe the classification of the nanostructures and then introduce the self-assembly method to form the organized nanostructures. Third, we will discuss the basic forces to glue the organic molecules together by showing several typical examples of the molecules. Fourth, we will introduce the application of the nanostructures, in particular, their differences from the single molecules or their solution properties. Finally, we will provide an outlook on the self-assembly of organic molecules.

2.2

Classification of Nanostructures

Nanostructures can be classified in various ways based on different standards [6–10]. One classification of nanostructured materials is based on their dimensions. A confinement of nanostructures in a particular direction generally leads to changes in physical properties of the system in that direction, and the nanostructures almost exhibit high regularity in size and shape. Hence, we constitute our classification of nanostructures based on their dimensionality. It may be one of the four, namely, 0D, 1D, 2D, and 3D, as described in Figure 2.1.

Zero-dimensional (0D) organic nanoparticles with amorphous structures have been widely studied. The organic nanoparticles are expected for promising organic optoelectronic devices. It is more ideal to precisely control the size-dependent properties of organic nanoparticles for high potential applications, due to their much better processing/mechanical and readily tunable optoelectronic properties. Besides the inorganic nanoparticles, the nanosized organic structures also exhibited size-dependent electronic and optical properties, with changes on a scale larger than those of the inorganic ones.

Among the organic nanomaterials, one-dimensional (1D) nanostructures have been attracting considerable attention, because they are expected to play important roles as both interconnects and functional units. 1D nanomaterials include nanowires, nanotubes, nanobelts, nanoribbons, and so on. Self-assembly of small molecules into one-dimensional nanostructures offers

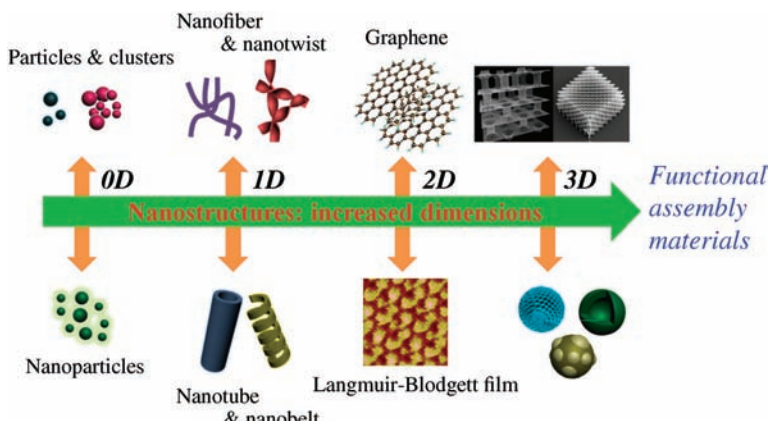


Figure 2.1 Typical nanostructures based on their dimensions.

many possibilities to obtain and control the 1D nanostructures, which find widespread applications in electronically and biologically active materials.

Two-dimensional (2D) nanostructures include graphene, discs or platelets, ultrathin films on a surface, and multilayered materials. The Langmuir–Blodgett (LB) technique is used as a graceful method to fabricate well-defined 2D organic nanostructures with molecular-level precision. While graphene itself is a good example of 2D materials showing excellent properties, the self-assembly of other organic molecules could also afford 2D nanomaterials. Besides graphene with rich functionalities, the well-defined, highly ordered 2D porous networks also caused widespread concern. The existence of highly ordered cavities in the 2D network nanostructures offers the potential to immobilize functional nano-objects as guest molecules into the 2D porous networks, which would provide a feasible way to obtain the controllable patterns of 2D nanostructures.

Three-dimensional (3D) nanostructures refer to the materials that consist of consolidated nanoparticles of 0D, 1D, and 2D nanomaterials. The 3D nanostructures exhibit three-dimensional confinement above 100 nm and include 3D superlattices, 3D networks, spheres, vesicles, and so on. The 3D nanostructures play important roles in the nanomaterials and exhibit wide applications in various fields.

2.3

General Self-Assembly Method for the Construction of Nanostructures

Although self-assembly is defined as the spontaneous and reversible association of two or more components to form a larger, noncovalently bound aggregate, the precondition such as where these molecules undergo self-assembly, in solution or on a solid surface, is also very important for the performance of such process. In fact, there are many external factors and the assembly method could affect the



Figure 2.2 The process of the reprecipitation method.

self-assembly process besides the molecular structures. The selection of the assembly methods is sometimes very important to obtain certain nanostructures. Here, we will introduce several general self-assembly methods for the construction of nanostructures.

2.3.1

Reprecipitation

Reprecipitation, which was first reported by Nakanishi and coworkers [11–13], is a solvent displacement method. The method involves a rapid mixing of a small amount of concentrated stock solution of the molecules dissolved in a good solvent with excess of a poor solvent, and it provides a very simple and versatile method to prepare organic nanoparticle dispersions. The process of the reprecipitation method can be seen in Figure 2.2. This method not only is simple (no requirement for temperature, pressure, or complicated templates) but also involves no chemical reactions (no impurity is brought to the single organic molecule self-assembly). The essential requirement for this method is the great disparity between the solubility of the target compound in the good and poor solvents. The organic molecules can dissolve in the good solvents, but when the poor solvent is rapidly mixed into the good solvents, the microenvironment of the target compound changes. The molecules are exposed to the poor solvent surroundings in a very short time, inducing the nucleation and growth of the molecules to nanoparticles. This method is usually used to obtain zero-dimensional and one-dimensional nanostructures.

A collection of organic nanostructures was successfully prepared using this facile method. Among all the nanostructures, fluorescent organic molecular nanomaterials occupy a large proportion in the field of chemistry, materials, and biology due to their excellent performance in organic electronic and biological sensing. As the pioneering work on this method, Nakanishi and coworkers prepared perylene nanoparticles and observed the emission from both free excitons and self-trapped excitons [14,15]. They prepared microcrystals of perylene and polydiacetylene and found that polydiacetylene microcrystals were a new type of material for third-order nonlinear optics [16,17]. Park and

coworkers [18] found a new class of organic nanoparticles (CN-MBE: 1-cyano-*trans*-1,2-bis-(4'-methylbiphenyl)ethylene) with a mean diameter of about 30–40 nm, which exhibit a strongly enhanced fluorescence emission. The intensity is increased by almost 700 times in the nanoparticles compared with that in solution. Then, Fang and coworkers [19] found that ethynyl-linked benzofuran–naphthyridine compounds show high-yield fluorescence with solvatochromic properties. Neckers' group [20] synthesized carbazole-based donor–acceptor compounds and found that the compounds show negative solvatochromic absorption behavior, but both positive and negative solvatochromic behavior in the fluorescence spectra. Organic dye nanoparticles were prepared by using the reprecipitation method by Barbara's group [21]. Also, Majima's group [22] directly observed the growth processes of fluorescent perylene nanocrystals using *in situ* and *ex situ* single-particle fluorescence spectroscopies. Recently, Yao's group also systematically investigated the size-tunable optical properties of organic nanoparticles prepared from a series of aromatically substituted pyrazoline compounds [23–26].

In recent years, the functionalities of the nanostructures are attracting great attention. For example, Li and Yan [27] developed a new class of “naked-eye” and ratiometric fluorescent Hg²⁺ sensors based on thiourea–thiadiazole–pyridine (TTP)-linked fluorescent organic nanoparticles. Warner's group [28] also reported a nontemplated method for controlling the aggregation in near-infrared cyanine-based nanoparticles derived from a group of uniform materials based on organic salts. Their study can help to overcome the restrictions of using a particular dye for a definite purpose and enhance the potential of a single dye for multiple applications. Recently, the nanostructures fabricated by using this method have been further developed. For example, Singh and coworkers [29] reported for the first time the use of perylene-3-ylmethanol fluorescent organic nanoparticles. The nanoparticles acted as both the nanocarrier for the drug and the phototrigger for the drug release. Schenning and coworkers [30] reported a facial and highly reproducible one-step method for generating functionalized fluorescent organic nanoparticles via the self-assembly of prefunctionalized π-conjugated oligomers. They successfully combined pre- and postfunctionalization of fluorescent oligomer nanoparticles with readily tailored optical properties to imaging applications in biology and medicine. Herz's group [31] investigated molecular nanoparticles formed by fast injection of a small volume of molecularly dissolved fluorine derivative amphiphilic molecules into a polar solvent, which resulted in solid spherical particles of ~80 nm diameter with high stability. Energy transfer studies were carried out on two-component nanoparticles that contained mixtures of various fractions of donor and acceptor amphiphiles.

Various nanostructures can be fabricated by using the reprecipitation method. Because of the diversity and potential of optical properties of organic molecules in the solid-state light-emitting diodes, organic lasers, sensors, and so on, small organic molecules have attracted wide interest for scientists. Although the control of the size and morphology of nanostructures

has been much developed, there is still a long way to the design and realization of the functions to be useful and stable.

2.3.2

Gelation

For the past few years, researchers from various fields of chemistry have been trying to develop novel methods through which the shape and size of nanostructured materials can be controlled at the nanoscopic level. From this point, the gelation process can be regarded as templates to generate the anisotropic nanostructures and composite materials. Gel-phase materials are generated when molecular building blocks assemble into nanoscale architectures, usually “one-dimensional” fibrils, which hierarchically assemble into bundles and subsequently form an entangled sample spanning network, capable of preventing the flow of bulk solvent.

Although gel has been recognized for a long time, it is often noted that a gel is actually easier to recognize than define. In 1974, Flory gave a definition that a gel has a continuous structure that is permanent on the analytical timescale and is solid-like in its rheological behavior [32], which deepened our understanding of the gels. In particular, there has been a great development in the supramolecular gels, which are made of lower molecular weight molecules through the noncovalent bonds. Such gels are easy to prepare and are thermoreversible. A common method of preparing a supramolecular gel is as follows. A certain amount of compound is dissolved in a solvent with the aid of a few drops of good solvent and heated till a transparent solution is obtained. The solution is then allowed to cool down to room temperature under ambient conditions. Gel formation is confirmed by the inverted test tube method. If there is no fluid in the upside-down tube, then the gel is formed. The organic building blocks can self-assemble into a wide variety of supramolecular gels having diversity in their morphology and function as found in many synthetic systems. A combination of weak forces, such as hydrogen bonding, $\pi-\pi$ stacking, and van der Waals interactions, hold the organic molecules together and lead to the formation of a three-dimensional network in the supramolecular gels. The schematic representation of the self-assembly of gelators into nanostructures is shown in Figure 2.3.

Using gelation to prepare nanostructured materials is very simple and various nanostructures have been obtained by using this method. One-dimensional nanostructures, such as nanowires, nanofibers, nanorods, nanobelts, and nanotubes, can be easily prepared by using this method. The controlled structures of materials lead to a variety of functions such as mechanical and optical properties that are not conceivable from the components [33]. For example, the well-defined self-assembled nanostructures based on electroactive molecules have diverse applications such as field-effect transistors, photovoltaics, and sensors, where the morphology and size of the active materials play a key role in determining the electrical properties of the final device.

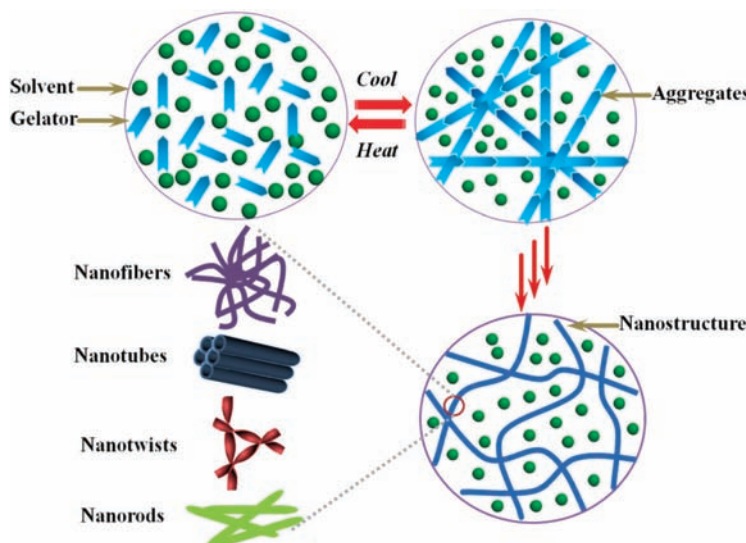


Figure 2.3 Schematic representation of the self-assembly of gelators into one-dimensional aggregates and subsequent entanglement to form a network that immobilizes the solvents.

It is remarkable that supramolecular assembly yields spectacular morphologies with molecular-level precision in the gel systems using simple noncovalent interactions. Gelation is a very important method to fabricate special nanostructures. The use of these soft nanomaterials with adjustable morphology in practical applications will be extensively investigated.

2.3.3

Langmuir–Blodgett Technique

When a water-insoluble molecule is spread at the air–water interface, it can form a thin layer of film with molecular thickness, which is called the Langmuir monolayer. Upon transfer of such monolayer onto the solid substrate, the so-called Langmuir–Blodgett (LB) film could be obtained, the technique of which was named after Irving Langmuir and Katharine Blodgett. Although the golden research age of the LB film is past, the method and the principle can be applied to fabricate nanostructures rather than uniform but usually unstable molecular films.

With the LB technique, an insoluble monolayer of amphiphilic molecules is first spread on the surface of a water phase that is usually referred to as the subphase. After compressing the monolayer into a highly condensed state, it is transferred onto a solid support in a layer-by-layer manner. In the LB technique, the monolayer-forming materials could be extended to nanomaterials such as nanoparticles, nanotubes, and nanowires, not necessary to limit those amphiphiles. Now this technique is a graceful method for the fabrication

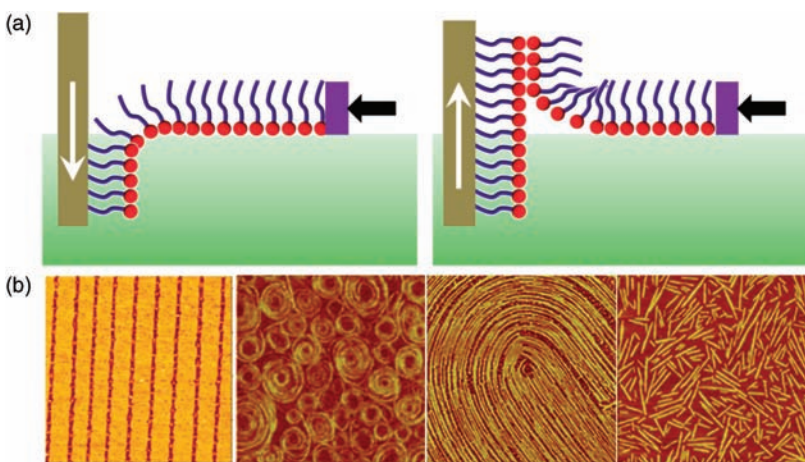


Figure 2.4 (a) Vertical dipping method (Langmuir-Blodgett deposition) of Langmuir monolayers. (a) Different nanostructures from LB technology.

of well-defined nanostructures with molecular-level precision. Furthermore, this method is a well-established and sophisticated method to control interfacial molecular orientation and packing. It is also an efficient approach toward the controllable fabrication of laterally patterned structures on solid supports. Laterally structured LB monolayers are normally generated by the deposition of ordered 2D nanostructures formed at the air–water interface onto solid substrates. In the past few years, the LB technique has made great progress in the fields of surface science, physical chemistry, materials chemistry, and nanotechnology. Many functional materials with nanometer-sized dimensions could be obtained by using the LB method. The fabrication processes of functional materials have been proved very important in the recent development of several key technologies, including nanotechnology and advanced materials technology.

The typical vertical dipping method is shown in Figure 2.4, in which the solid support is first pushed down and then pulled up through the condensed monolayer. A constant surface pressure is applied during the transfer process and the monolayer is transferred to the support with the hydrophobic tail side. The method has been used to fabricate the nanostructures and then uniform films. For example, the amphiphilic barbituric acid was found to form spiral nanoarchitectures in the LB film. Chi and coworkers [34–42] used this technique to control the alignment, size, shape, and periodicity of self-organized phospholipid monolayer patterns over surface areas of square centimeters. Then, the patterns can be used as templates to direct the self-assembly of molecules and nanocrystals. Furthermore, the pattern transfer procedures were used for directing cell growth and nanocrystal patterning.

From the viewpoint of potential device applications with electronic and optical functions, assemblies of functional 1D nanostructures are important research

targets in physical, chemical, and biological research fields. The LB approach has been used successfully for the formation of organized assemblies of nanowires and nanotubes. Dai and coworkers [43] reported the preparation of densely packed Langmuir monolayers of aligned noncovalently functionalized single-walled carbon nanotubes from an organic solvent. Kim's group [44] developed a combined method involving both soft lithography and the LB method for patterning of densely packed and aligned single-walled carbon nanotubes on silicon and flexible poly(ethylene terephthalate) substrates. Yu and coworkers [45] reported the self-assembly of hydrophilic silver nanowires with a high aspect ratio through processes at the oil–water–air interface. This approach based on the three-phase interface process represents a general method for the preparation of a variety of ordered films of nanowires. Besides the works discussed earlier, the two-dimensional water surface can serve as an ideal platform for the fabrication of 2D thin films. Dai's group [46] reported the exfoliation–intercalation–expansion process of graphite that can be used to produce high-quality single-layer grade sheets stably suspended in organic solvents. This method allows us to spread graphene sheets at the air–water interface to fabricate their LB films. Huang and coworkers [47] demonstrated that single layers of graphite oxide can float on a water surface without the aid of surfactants or stabilizing agents. Sasaki, Haga, and coworkers [48] prepared LB films of densely packed exfoliated nanosheet films on solid substrates without any amphiphilic additives. This LB transfer method for nanosheet assembly has many advantages such as wide availability of substrates and the resulting densely packed states of the nanosheet films.

2.3.4

Layer-by-Layer Assembly

Layer-by-layer (LbL) assembly has emerged as the most popular and versatile approach. LbL assembly, established by Iler in 1966 [49], was based on the LB membrane invented by Blodgett and Langmuir [50,51]. Decher and Hong were the first researchers to fully characterize the buildup of LbL films composed of positively and negatively charged bolaform molecules in 1991 [52]. Then, this technology was largely developed by Decher, Lvov, and Möhwald in the 1990s [53]. As one of the most effective synthesis tools, LbL self-assembly technology can provide a strong noncovalent integration between homo- or hetero-phase compounds or oppositely charged polyelectrolytes, resulting in highly ordered nanostructures or patterns with excellent functionalities and activities [54]. There are many advantages using the LbL self-assembly process to prepare various nanomaterials, such as simple operation, low cost, and variability of applicable materials. Thus, this method has been employed to prepare a range of nanostructured materials, including films, capsules, nanotubes, nanoporous particles, and macroporous and biomimetic structures.

Figure 2.5 shows a typical LbL self-assembly process of a multilayer thin film structure by sequential adsorption of oppositely charged polyelectrolytes.

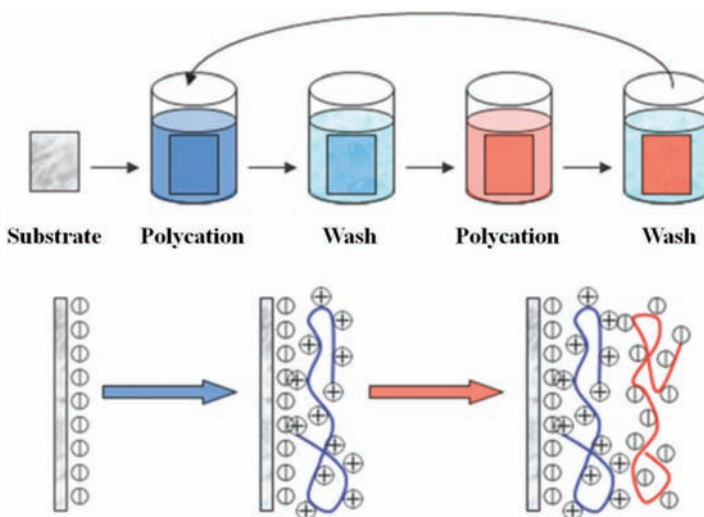


Figure 2.5 Schematic of LbL self-assembly of a multilayer coating by sequential adsorption of oppositely charged polyelectrolytes. (Reproduced with permission from Ref. [62]. Copyright 2012, The Royal Society of Chemistry.)

However, the driving forces of the LbL assemblies are not limited to electrostatic interactions. A variety of interactions have been reported. For example, Stockton and Rubner [55] reported the molecular-level LbL processing of polyaniline with a variety of different nonionic water-soluble polymers, and this type of LbL adsorption process is driven by hydrogen bonding interactions. Since the covalent reaction must take place rapidly at each deposition step, strategies involving click reactions are quite popular: oxime chemistry was introduced in 2002 by Chan's group [56], azlactone chemistry was used by Lynn's group [57], and the Huisgen–Sharpless click reaction was first used by Caruso and coworkers [58]. Haga *et al.* [59] reported the fabrication and functions of surface nanomaterials based on multi-layered or nanoarrayed assembly using metal coordination interactions. Anzai and coworkers [60] used the LbL method to construct protein architectures through avidin–biotin and lectin–sugar interactions for biosensor applications. Ariga and coworkers introduced the electrochemical-coupling layer-by-layer assembly as a novel fabrication methodology for preparing layered thin films [61]. This method allows us to covalently immobilize functional units into thin films having desired thicknesses and designable sequences for both homo- and heteroassemblies while ensuring efficient layer-to-layer electronic interactions.

The conventional LbL assembly with other microfabrication methods usually related to the final nanostructures. In recent years, many novel approaches have been reported to fabricate nanostructures, for example, spin coating, spraying, photolithography, electrochemical deposition, and microcontact printing [63–78]. Mamedov and Kotov [79] deposited alternating layers of magnetite nanoparticles and polyelectrolytes onto glass slides coated with cellulose acetate

(CA), and then freestanding films were obtained by dissolving the initial CA layer with acetone. Later, Tsukruk and coworkers [62,73,80,81] fabricated free-standing PE multilayer films doped with gold nanoparticles using this method. Kim and coworkers [82] have reported the dynamic assembly of LbL structures within microfluidic channels. Caruso and coworkers [83] used polycarbonate Nuclepore membranes with well-defined cylindrical pores as templates for the fabrication of nanotubes. Similarly, Bai and coworkers [84] used commercial anodic aluminum oxide membranes as templates and synthesized TiO₂ composite nanotubes. Microcapsules can also be obtained by using the LbL method. Shchukin *et al.* [85] used a “photocatalytic” approach to fabricate hollow metal microspheres based on the spatially confined metallization of the shell or interior of the LbL microcapsules.

Various nanostructured materials could be obtained by using the LbL technique. The simple and highly versatile LbL assembly method can be combined with other approaches to yield complex assemblies, the structures and properties of which may be readily controlled. We believe that with further development, the nanostructured materials obtained by this method will play an important role in a range of different applications.

2.3.5

Self-Assembly in Solution

With the development of supramolecular chemistry and nanotechnology, chemical self-assembly has become an important “bottom-up” approach to create intriguing materials of nano- and microstructures. Self-assembly not only is a practical approach for creating a variety of nanostructures, but also shows great superiority in building hierarchical structures at different length scales. Therefore, in the preparation of nanostructures, the self-assembly in solution also plays a very important role. There are many types of self-assembly ranging in dimensions from molecular level to supramolecular level (Figure 2.6).

In order to perform the self-assembly of organic molecules, an important step is to design the starting molecules. Amphiphiles, which possess the hydrophilic and hydrophobic parts within a molecule, are one of the most widely used building blocks. They can self-assemble in solution into structurally well-defined aggregates, as governed by a delicate balance between different noncovalent interactions. Also, they can self-assemble with other compounds to form different nanostructures, such as host–guest inclusion. Huang and coworkers have reported the self-assembly of some organic molecules into one-dimensional soft nanostructures using this method. For example, ionic surfactant sodium dodecyl sulfate (SDS) and β-CD were mixed at a molar ratio of 1:2 to form an inclusion complex. Vesicles, multilamellar microtubes, and lamellae can be realized by increasing the overall concentration of the system [86,87]. They found that this is a general phenomenon in the inclusion system of ionic surfactants with α- or β-CDs [88]. Furthermore,

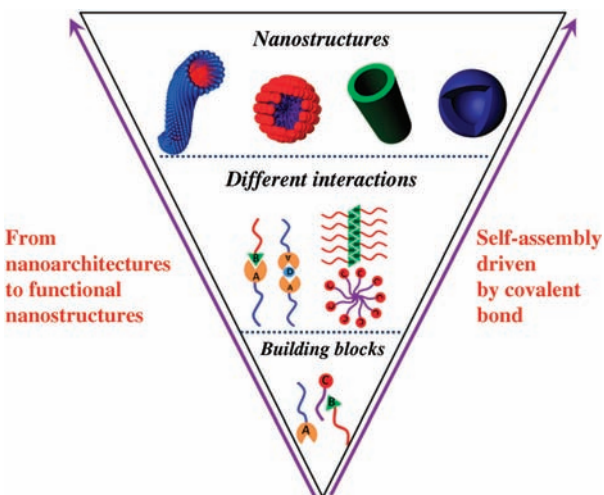


Figure 2.6 Self-assembly in solution: from building blocks to nanostructures.

Hao and coworkers have done some meaningful work on the self-assembly of surfactants and many critical reviews were presented [89,90].

On the other hand, surfactant-assisted self-assembly (SAS) is one of the most common approaches to obtain ordered architectures [91,92]. In the SAS process, organic units, dissolved in a guest solvent, are organized with the assistance of surfactants that are dispersed in a host solvent. Under most circumstances, the employed guest and host solvents have similar polarity and good compatibility. Considering the generally good solubility of organic units in apolar or low-polar medium, SAS using oil/aqueous medium is a topic of broad interest. Our group has demonstrated that various novel porphyrin-containing nanostructures, including hollow nanospheres, solid nanospheres, nanorods, nanotubes, and nanofibers, can be easily manufactured by using SAS, where an oil/aqueous medium is used. The morphologies of the nanostructures displayed distinct dependence on the aging time and surfactant concentration, which enabled the controlled production of the nanostructures [93].

During the self-assembly in solution, many factors can influence the final self-assembled nanostructure. On the one hand, the molecular structures play an important role. A large number of different nanostructures with various shapes are accessible using the self-assembly process and related molecular structures through the wide choice of commercial and designer components. On the other hand, the solvent effect is crucial for regulating the assembly process. For example, the solvent polarity and the solvent–solute interactions can influence the assembled nanostructures in terms of their size, shape, and morphology.

The self-assembly method has a number of possibilities for preparing nanostructures because of their soft and malleable nature. Therefore, many excellent results and relevant works are ongoing.

Table 2.1 Summary of noncovalent interactions.

Interaction	Bond energy (kJ mol^{-1})	Examples
van der Waals interaction	0.4–4	Figure 2.7a
Hydrophobic interaction	<40	Figure 2.7b
π – π stacking	0–50	Figure 2.7c
Cation– π interaction	5–80	Figure 2.7d
Anion– π interaction	20–70	Figure 2.7e
Hydrogen bonding	4–120	Figure 2.7f
Dipole–dipole interaction	5–50	Figure 2.7g
Halogen bonding	10–200	Figure 2.7h
Ion–dipole interaction	50–200	Figure 2.7i
Ion pairing	100–350	Figure 2.7j
Metal coordination	—	Figure 2.7k

2.4

Molecular Design and Building Blocks

Noncovalent interactions are important for obtaining nanostructures through supramolecular chemistry and self-assembly. In order to self-assemble molecules into certain nanostructures, it is very important to design the building blocks based on the knowledge of noncovalent bonding, the strength of the intermolecular interactions, and the noncovalent bonding sites.

Table 2.1 shows some typical interaction modes based on noncovalent bonding [3,94–96]. Keeping these in mind, one can design various molecules for self-assembly. Here, we show several typical organic building blocks for the self-assembly (Figure 2.7) [97].

2.4.1

Amphiphiles

As we know, self-assembly in solution is a very important method to obtain nanostructures. The most important building block is amphiphile. A typical amphiphilic molecule consists of a polar hydrophilic group, usually called the *head*, joined to a nonpolar hydrophobic moiety called the *tail*; the two parts are linked through covalent bonds. However, the number of the polar head(s) and hydrophobic tail(s) and the kind of connection among them can vary, which leads to different classes of amphiphiles [98]. The most common amphiphiles are surfactants, such as detergents, soaps, and fatty acids. Amphiphiles are usually classified according to different criteria, for example, the charge of the head group upon its dissociation in water, the number and kind of connection of polar head/hydrophobic tail, and the chemical nature of the polar head. The self-aggregation of amphiphilic molecules has long been known to yield a rich

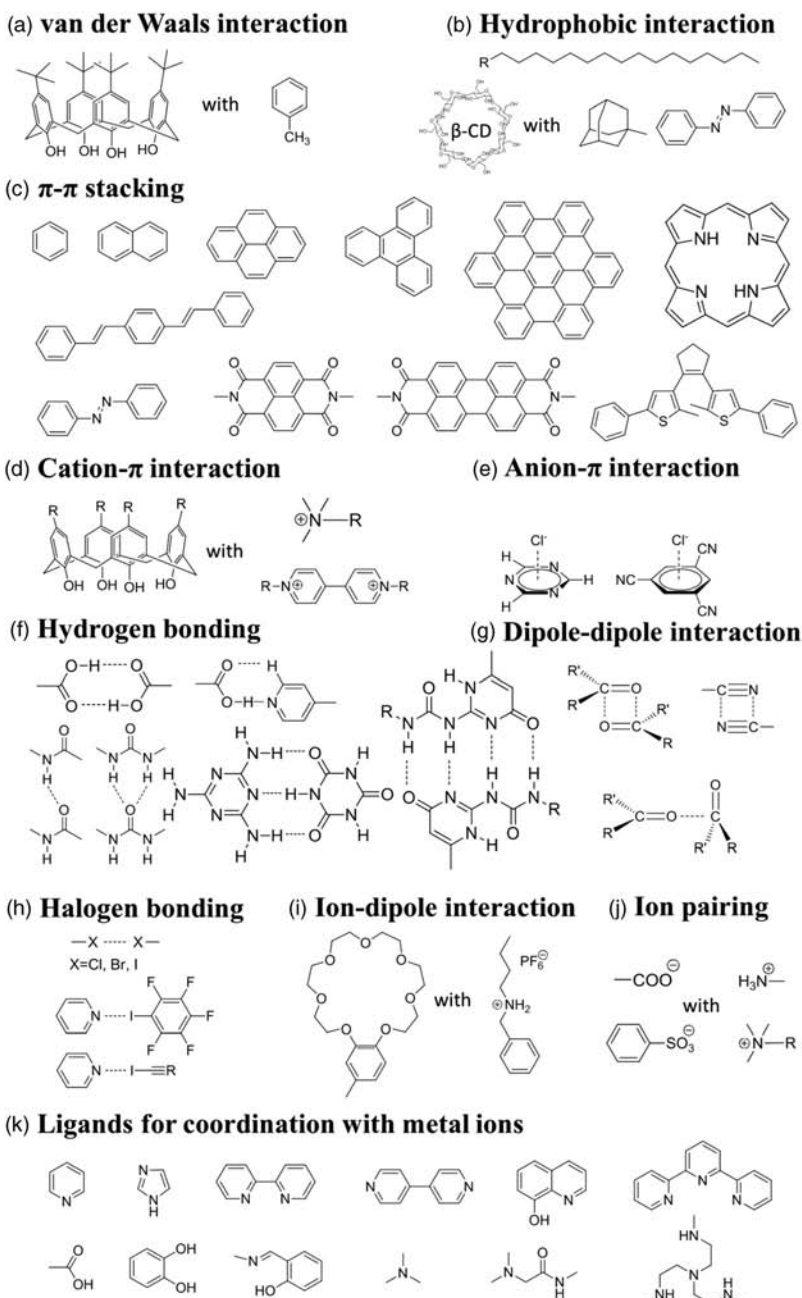


Figure 2.7 Some typical building blocks for self-assembly.

number of assemblies, depending on the molecular structure of the amphiphile and the experimental conditions. The micelles and vesicles are the most common self-assemblies for the amphiphilic molecules formed in solution. Herein, we describe several common amphiphilic molecules.

2.4.1.1 Typical Amphiphiles

The typical amphiphile is the most conventional amphiphile, which has single head and single tail. Common amphiphiles are single-chain surfactants such as fatty acids and dialkylated species such as phospholipids, the latter being the main constituents of, for instance, cell membranes. According to different polar heads, the typical amphiphilic molecules can be divided into various categories such as ionic amphiphiles and nonionic amphiphiles. However, amphiphilic behavior is also quite regularly observed in proteins and peptides. There is often a clear relationship between the amphiphilic character of a protein or peptide and its self-assembled nanostructure (Figure 2.8). For example, the *N*-octylgluconamide amphiphile **1** can form micellar rods that intertwine into quadruple helices [99]. The rationally designed sugar amphiphile **2** can self-assemble into a double-stranded helix [100]. The robust helical nanostructures result from cooperative noncovalent interactions, such as hydrophobic effect, π – π stacking, and multiple H-bonds between the sugar heads. Different chain structures can also affect the self-assembled nanostructures. For example, different number of *cis* double bonds from long-chain phenyl glucosides and *N*-gluconamide derivatives **3–5** can affect the self-assembled structures [101,102]. Another example is the photoresponsive peptide amphiphile **6**, which can self-assemble into a nanosized quadruple helix [103]. Upon irradiation at 350 nm, a light-triggered dissociation of the superhelix into single fibers was observed as a consequence of the photochemical cleavage of the bulky 2-nitrobenzyl substituent.

2.4.1.2 Bolaamphiphiles

Bolaamphiphilic molecules contain a hydrophobic skeleton (e.g., one, two, or three alkyl chains, a steroid, or a porphyrin) and two water-soluble groups on both ends [104]. Bolaamphiphiles are related to and often combined with “edge amphiphiles,” where one flank of a hydrophobic core carries hydrophilic groups whereas the other edge is hydrophobic. Since bolaamphiphiles exhibit unique hierarchically self-assembled structures both at interfaces and in solutions, the synthesis and application of bolaamphiphiles have been extensively studied. During the past two decades, various nanostructures have been developed using bolaamphiphilic molecules (Figure 2.9). The application of the hierarchically organized structures has been used in various fields. A new bolaamphiphile **7** (EDGA) based on L-glutamic acid has been reported. It is an efficient gelator and can self-assemble into a novel helical spherical nanotube with a molecular monolayered structure within the tubular wall [105]. Furthermore, this bolaamphiphilic molecule could form helical nanotubes through the compression of the spreading Langmuir film at the air–water interface [106]. Except for this traditional

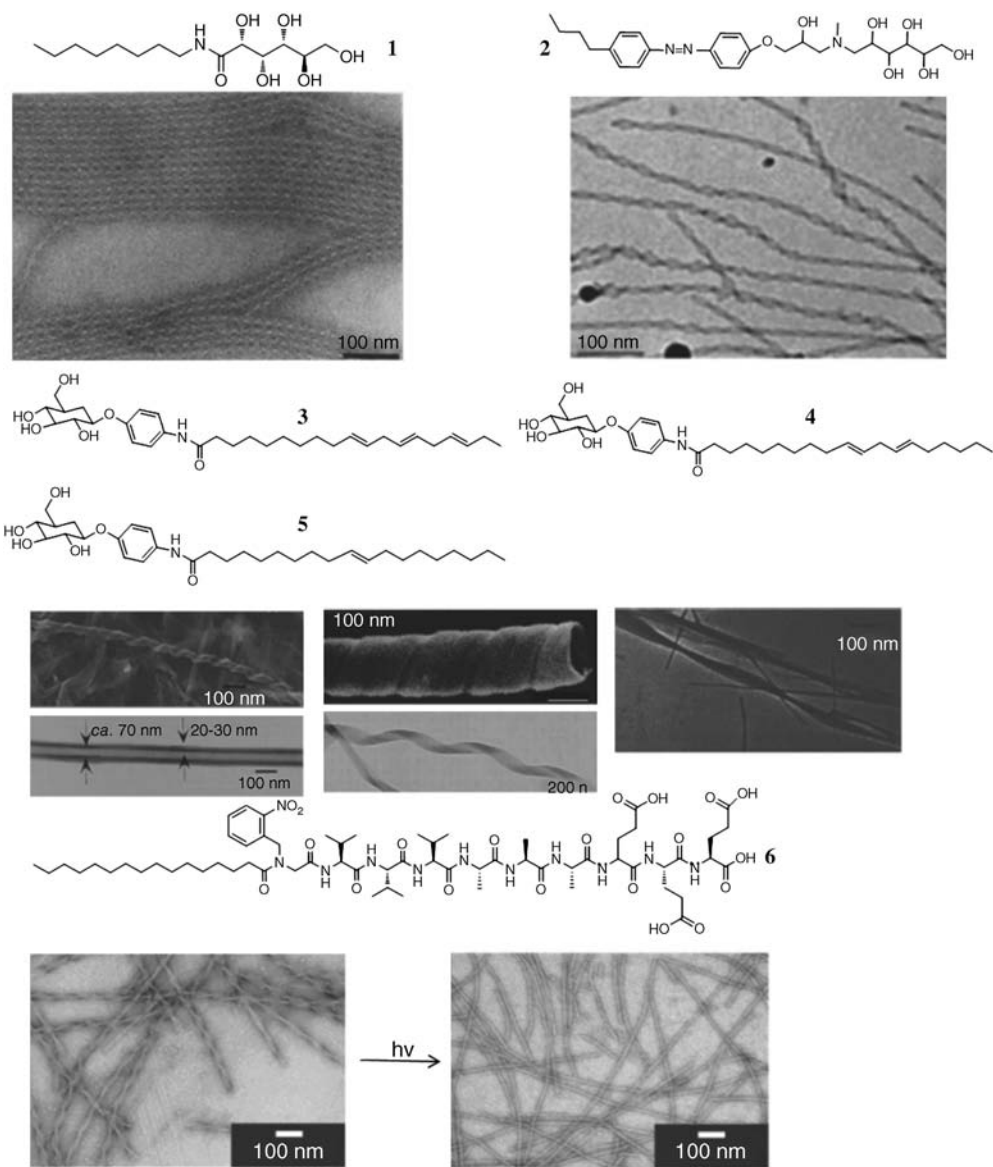


Figure 2.8 Some typical amphiphiles and the corresponding self-assembled nanostructures.

bolaamphiphile, the cationic bolaamphiphiles have been developed in recent years. Cationic bolaamphiphiles **8** and **9** bearing different counterions have been synthesized and these bolaamphiphiles can lead to different self-assembled morphologies as well as distinctive solution colors, which reveal that the morphologies are found to be related to the molecular structures of both the hydrotropic

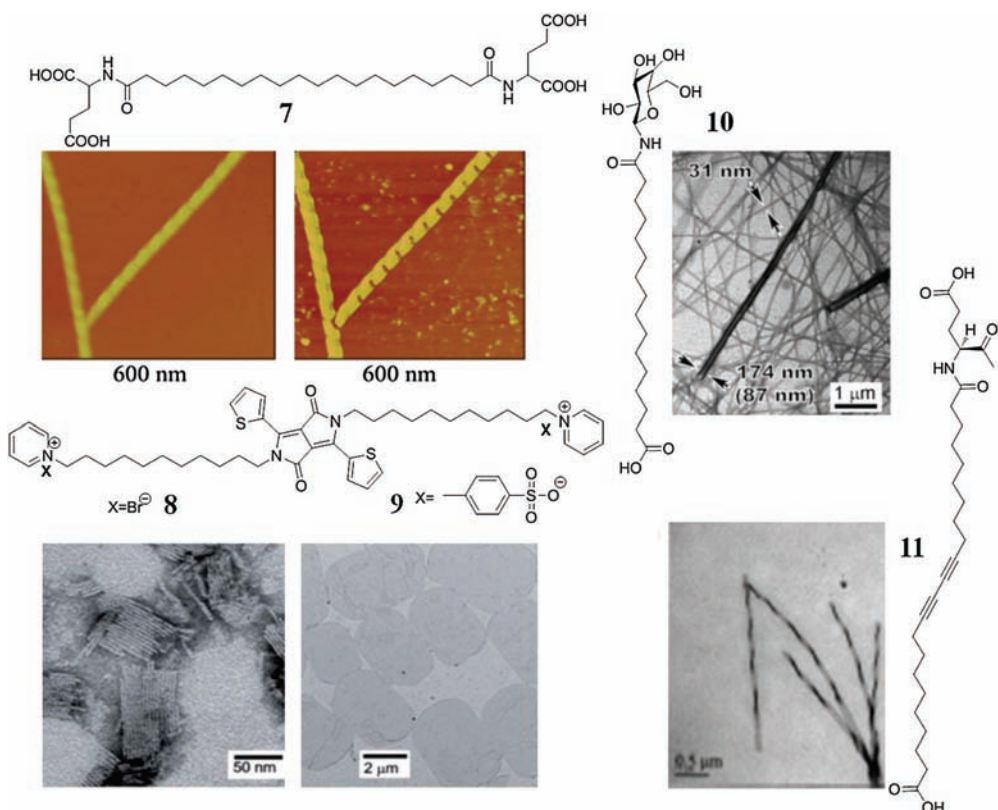


Figure 2.9 Some typical bolaamphiphiles and the corresponding self-assembled nanostructures.

anions and embedded conjugated moieties [107]. Besides the symmetrical bolaamphiphiles discussed earlier, unsymmetrical bolaamphiphilic molecules can also self-assemble into various nanostructures. Unsymmetrical bolaamphiphiles with two hydrophilic moieties of different sizes are usually assembled into two types of polymorphs depending on the molecular packing of symmetrical and unsymmetrical monolayer membranes [108]. For example, unsymmetrical bolaamphiphile **10** with one lactose head group and one carboxylic head group can self-assemble into nanotubular structures [109]. Another unsymmetrical bolaamphiphile **11** can form right-handed helical ribbon structures under mild conditions, with micron-scale length and nanoscale thickness [110].

2.4.1.3 Gemini Amphiphiles

Gemini amphiphilic molecules are made up of two hydrocarbon tails and two ionic groups linked by a spacer (Figure 2.10). They are generally composed of two identical sets of a hydrophilic head group and a hydrophobic tail. The head groups can be cationic, anionic, zwitterionic, or nonionic in nature, whereas the

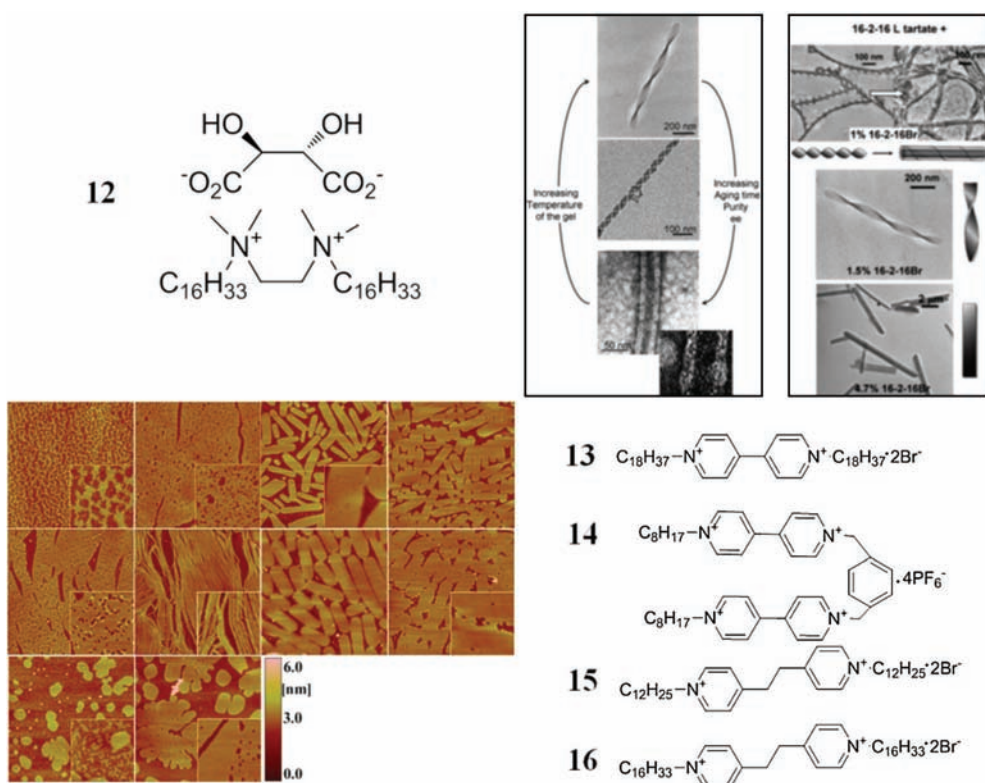


Figure 2.10 Some typical gemini amphiphiles and the corresponding self-assembled nanostructures.

spacer further defines the amphiphile's properties through variations in its size, shape, rigidity, and polarity [111]. For example, the gemini amphiphile **12** bearing the chiral tartrate as the counteranion has been found to self-assemble in water to form twisted multilayered chiral ribbons and behaves as a hydrogelator [112]. This gemini molecule can also form helical ribbons and tubules and the morphology and the dimensions of such assemblies can be finely tuned by varying external parameters such as aging time and temperature [113]. Gemini amphiphiles are also used to study the interfacial assemblies. For example, a series of gemini amphiphiles **13–16** with pyridinium head group and rigid spacers were designed, and their interfacial assemblies with cyanine dyes through the air–water interface were investigated [114]. Different nanostructure morphologies can be formed in the complex film.

2.4.1.4 Triangular Amphiphiles

The triangular amphiphilic molecule contains three peripheric parts and the core part, just like a C₃ symmetric molecule. The peripheric parts consist of the hydrophilic and hydrophobic parts, and the core part is always a benzene ring or

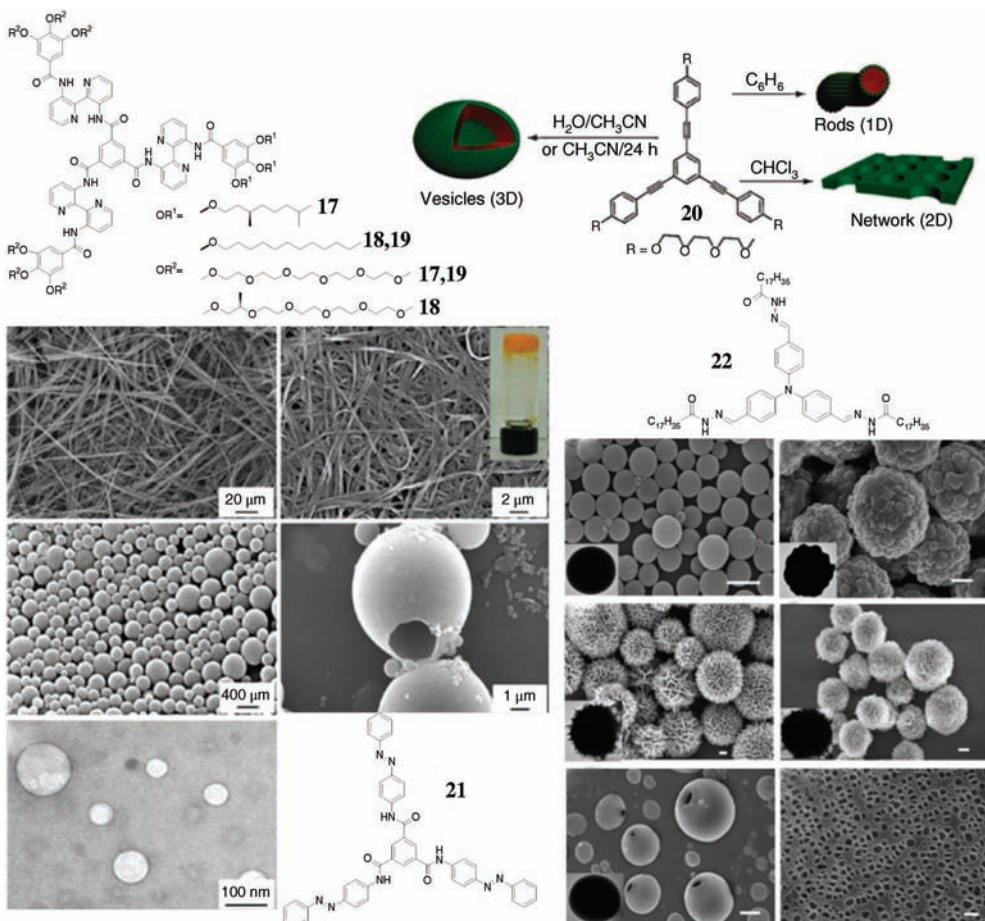


Figure 2.11 Some typical triangular amphiphiles and the corresponding self-assembled nanostructures.

only a nitrogen atom. The triangular amphiphile plays a very important role in the construction of novel nanostructures because the triangular structure provides more acting sites in the self-assembly process (Figure 2.11). For example, a set of chiral, amphiphilic, self-assembling triangular molecules based on the 3,3'-bis(acylamino)-2,2'-bipyridine-substituted benzene-1,3,5-tricarboxamide motif was prepared [115]. The morphology of aggregates of **17–19** can be tuned by the properties of the solvent mixture and with the help of π - π stacking and hydrophobic interactions the triangular molecules can self-assemble into triple helical fibers. In many of the assembled structures, the triangular molecules easily form the spherical structure, for example, the self-assembly of tripodal squaraines from acetonitrile into hollow spherical structures that change to form linear structures upon binding with Ca^{2+} or Mg^{2+} [116]. A triangular oligo

(phenylene ethynylene) amphiphilic molecule **20** can self-assemble into nanoaggregates of different morphologies – hollow vesicles, a planar network, or rod-like objects – depending on the nature of the solvent used [117]. Another triangular amphiphile **21**, tris(4-(*E*-phenyldiazaryl)phenyl)benzene-1,3,5-tricarboxamide (Azo-1), can self-assemble into different nanostructures, microfibers in DMSO, gels in DMF, and hollow spheres in THF [118]. The core part of these triangular molecules, as discussed earlier, is all the same – a benzene ring. If the benzene ring is replaced with other component, the triangular amphiphile can also self-assemble into different nanostructures. For example, if the core part of the molecule is a nitrogen atom, the triangular amphiphile **22** can self-assemble into various nanostructures in different organic solvents [119].

2.4.1.5 Supra-amphiphiles

The supramolecular amphiphile is a concept developed by Zhang, which allows the construction of structural motifs with more complexity and tenability [120]. Supra-amphiphiles refer to amphiphiles that are formed by noncovalent interactions. The rich topology of supra-amphiphiles is shown in Figure 2.12. The supra-amphiphile represents a new development of traditional colloid science. It functions as a new building block for the self-assembly of supramolecular nanostructures. For example, Zhang and coworkers [121] reported that X-shaped and H-shaped supra-amphiphiles, which are very difficult to realize in conventional amphiphiles, have been successfully constructed on the basis of directional charge transfer complexes of naphthalene diimide and naphthalene. The X-shaped supra-amphiphiles can self-assemble into one-dimensional nanorods,

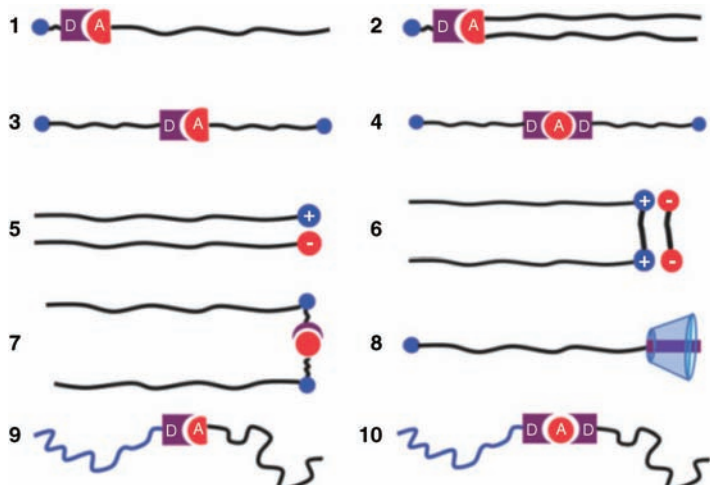


Figure 2.12 Different topologies of supra-amphiphiles. “D” and “A” refer to donor and acceptor, respectively. (Reprinted with permission from Ref. [120]. Copyright 2011, The Royal Society of Chemistry.)

while the H-shaped supra-amphiphiles can self-assemble into two-dimensional nanosheets. The functional moieties can also be linked to the supra-amphiphiles such as the stimuli-responsive group. Zhang and coworkers used a water-soluble charge transfer complex to fabricate supra-amphiphiles for assembling pH-responsive one-dimensional nanostructures [122]. Also, they designed and prepared a photoresponsive supra-amphiphile using a double hydrophilic block copolymer, poly(ethylene glycol)-*b*-poly(L -lysine hydrochloride) (PEG-*b*-PLKC), and a small organic amphiphile containing a positively charged head group and malachite green (MG) at the end [123].

2.4.2

Gelators

As discussed earlier, gelation is a very simple and efficient method to fabricate various uniform nanostructures in large area. The general process for the gelation mainly consists of heating to dissolve and cooling to form nanostructures. During cooling of the solution, the solute molecules can form different kinds of aggregates, including (i) highly ordered crystals, (ii) disordered precipitates, and (iii) relatively ordered gels, which contain entangled nanostructures to immobilize the solvent molecules in the networks. Therefore, whether the gelation can occur depends on the gelator structure and design. Feringa has proposed the following factors to design an effective gelator molecule: (i) the control of fiber–solvent interfacial energy to tune solubility and prevent crystallization, (ii) the presence of fiber–fiber interactions to achieve cross-linking and subsequently network formation; and (iii) the presence of multiple self-complementary and unidirectional interactions to achieve anisotropic self-assembly [124]. Therefore, the gelator molecule always contains some complementary groups, which drive the molecule to hierarchically self-assemble into different nanostructures through noncovalent interactions. In the following, we will discuss the gelator design based on some typical groups.

2.4.2.1 Cholesterol-Based Gelators

Steroid is a class of natural compounds made in living cells and widely found in animals, fungi, plants, and elsewhere, including cholesterol, sex hormones, vitamin D, and adrenal hormones. Cholesterol, a prototypical animal sterol, was first discovered in solid form in gallstones in 1769 and then found mainly distributed in fats, blood, brain, and bone marrow of humans and animals. Therefore, cholesterol is essential to life. As one of the steroids, cholesterol has four rings fused together, one five-membered and three six-membered with the chair conformation. As a consequence, the cholesterol skeleton is rigid, flat, and straight. Due to these typical structural features, cholesterol and its derivatives possess the unique molecular aggregation mode and have been extensively studied in supramolecular chemistry and materials chemistry, particularly in liquid crystal materials. Weiss's group first reported the low molecular weight organogel based on cholesterol [125–127]. They showed that molecular systems comprising an

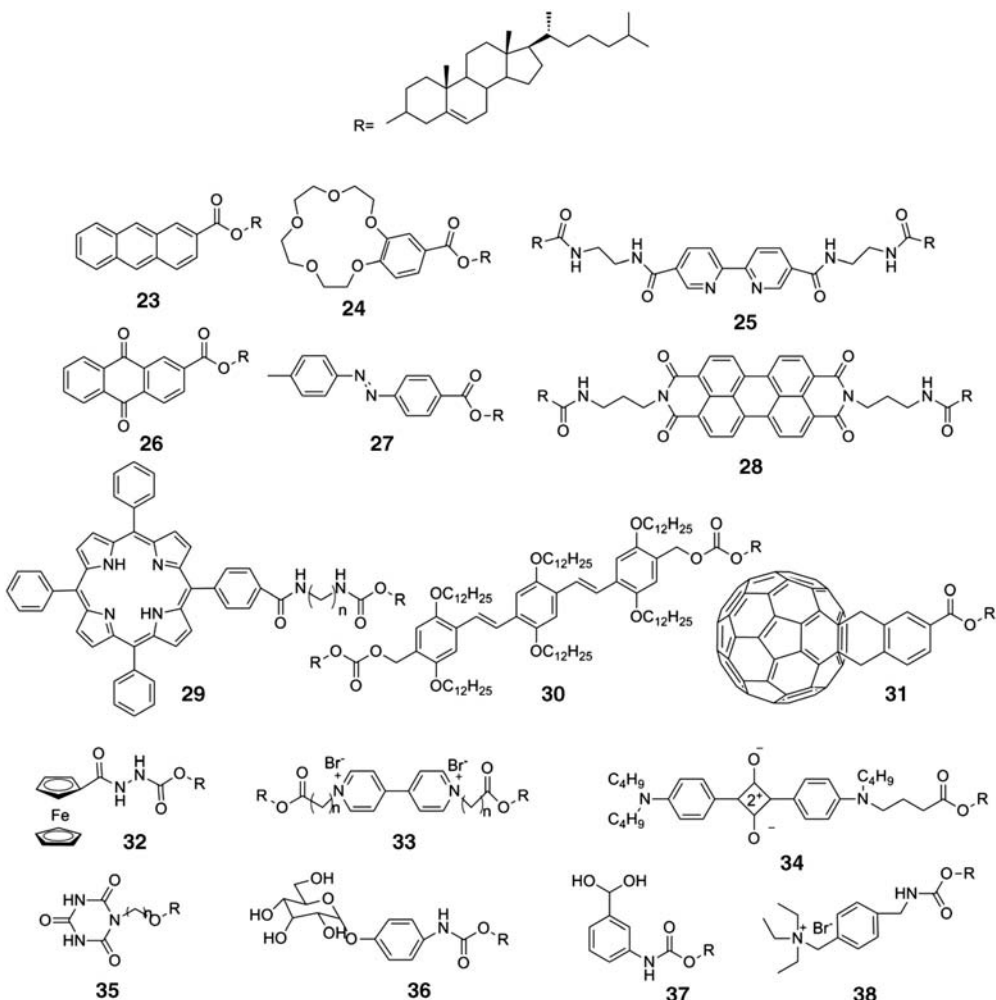


Figure 2.13 Cholesterol-based gelators.

aromatic (A) moiety connected to a steroidal (S) group through a functionalized link (L) could display effective, and somewhat predictable, gelation ability. A large number of such ALS gelators, in which every component varied, especially the aromatic moieties, have been synthesized and investigated during the last decade. By covalently appending some functional groups, including crown ethers for ion recognition [128], azobenzene groups for photoisomerization [129], melamine [130], boric acid [131], sugar moieties [132], or conjugated π -molecules, various low molecular weight gelators (LMWGs) with specific functions and properties can be prepared (Figure 2.13). Meanwhile, a more complicated cholesterol-based gelator denoted as A(LS)₂ appeared. It contains two cholesterol units symmetrically connected to the central aromatic fragment. Due to the

strong symmetric synergetic interaction and stacking between the two cholesterol compounds, the A(LS)₂-type gelators were found to offer new potentialities for the construction of novel supramolecular gels with enhanced gel properties and unique functionalities.

2.4.2.2 Alkane- and Fatty Acid-Based Gelators

The generic name for linear aliphatic hydrocarbons and cyclic hydrocarbons (except for the aromatic compounds) and their derivatives is aliphatic compounds. They cover a variety of organic compounds such as alkenes, alkanes, alcohols, ethers, ketones, aldehydes, and esters. Alkanes and fatty acids are the typical aliphatic compounds, which can serve as the simplest gelators.

It is generally believed that a molecule must be able to self-associate through interactions that are more specific and stronger than London dispersion forces to be a successful gelator [133]. However, the reported structurally simplest class of LMWGs, long *n*-alkanes, can also gelate shorter and other liquids alone. Abdallah and Weiss have found that long *n*-alkanes with chain lengths from 24 to 36 carbon atoms can be used as efficient gelators [134]. The stability of the gel depends on the time period that a gel persists in a sealed tube at room temperature without macroscopic phase separation or flowing when inverted. Furthermore, the gel stability increases with the chain length of the gelator. This work demonstrates that London dispersion forces alone can provide colloidal networks whose strength is sufficient to immobilize liquids against the gravitational pull.

Long-chain saturated fatty acids and their salts with alkali metals, alcohols, and esters are known to form hardened materials from organic liquids. Among these, 12-hydroxyoctadecanoic acid (**39**) and its related salts are the earlier fatty acid LMWGs reported to gelate a variety of organic liquids. Tachibana *et al.* have reported the formation of thermally reversible jellies of optically active **39** in CCl₄ or aromatic solvents [135,136], which showed circular dichroism (CD) absorption band, indicating that the jellies have a supramolecular helicoidal structure. X-ray examination revealed the formation of lamellar structure within the gel networks, which is related to supramolecular helicoidal structure. In contrast, Terech *et al.* have reported fatty acid-based organogels prepared by cooling dilute solutions of both racemic and chiral forms of **39** and found no difference in the gelation ability (Figure 2.14). The gels are three-dimensional networks of fibers of rectangular cross-sectional shape with varying aspect ratio and thickness and strengthen by junction points. Head-to-head contacts between the carboxylic acid groups and the multiple hydrogen sequence are ubiquitous within the gel fibrillar networks [137].

2.4.2.3 Nucleoside-Based Gelators

Nucleobases are nitrogen-containing heterocyclic compounds found within nucleotides – the basic component of DNA and RNA. Since the disclosing of structural mysteries of DNA and discovery of genetic code in the last century, the significant role of nucleobases in life sciences was recognized. There are five primary nucleobases, including guanine (G), adenine (A), thymine (T), cytosine

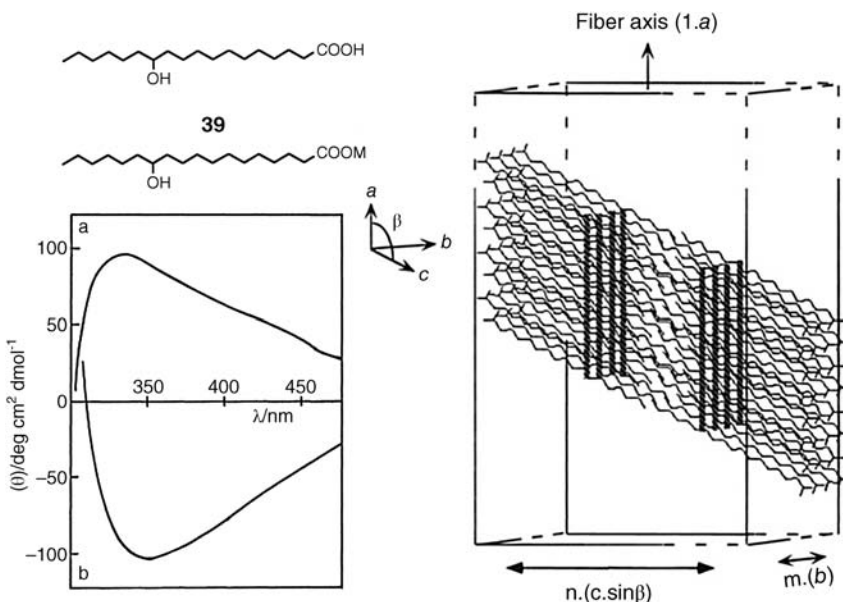


Figure 2.14 Fatty acid-based gelators: 12-hydroxyoctadecanoic acid (HOA), enantiomeric CD band, and structural model of HOA aggregates.

(C), and uracil (U). In normal spiral DNA, the A–T and C–G pairs are usually required to match the hydrogen bonds between the amine and carbonyl groups on the complementary bases. Due to the plurality of complementary hydrogen bonding sites in the horizontal plane and π – π stacking interaction in the vertical plane, nucleobases are often used as the building blocks to construct supramolecular assemblies.

Some early reports found that the guanosine derivatives can form gels in aqueous solutions at relatively high concentration in the presence of alkali metal ions [138]. The multiple hydrogen bond donor and acceptor sites within the guanine units allowed the guanosine derivatives to form the hydrogen-bonded G-quartet or continuous helix in the presence of alkali metal ions as a template and finally stacked to the hierarchical structures. However, since nucleobases are only slightly soluble in organic solvents and cannot effectively pair by hydrogen bonding in water, it is necessary to introduce some hydrophobic moieties in order to assist the self-assembly of nucleobase derivatives. Based on this consideration, a series of different lipid nucleosides were rationally designed as hydrogelators to construct supramolecular hydrogels, as shown in Figure 2.15. Shimizu and coworkers have reported the self-assemblies of the bolaamphiphiles having nucleobases at their head groups [139–142] or nucleotide bolaamphiphiles **40–43**, which showed excellent gelation ability in water and only required 0.2 wt% to form the stable translucent gel under neutral or mild alkaline conditions [143].

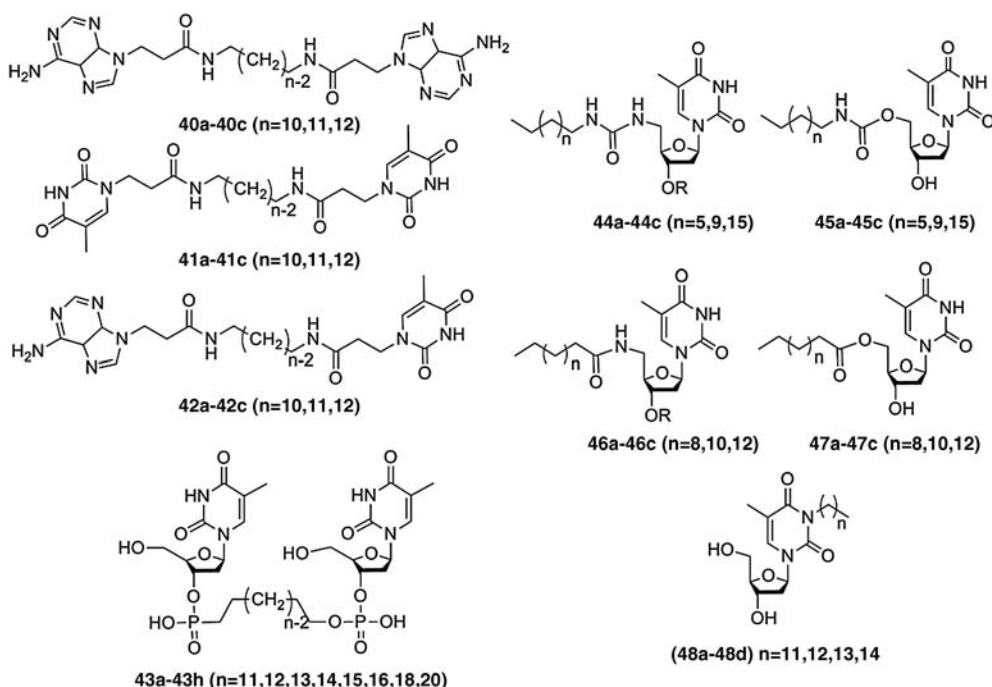


Figure 2.15 Nucleoside-based gelators.

Kim and coworkers have already reported a family of thymidine-based organogelators **44–48** and studied their gelation abilities in relation to gelator molecules and solvents [144]. They found that the urea- (**44**) and amide-linked (**45**) derivatives gave robust and translucent gels in alkanes, while the carbamate- (**46**) and ester-linked (**47**) derivatives yielded opaque gels in toluene and tetrahydronaphthalene (THN). The *N*-alkylated derivatives (**48**) formed opaque gels in benzene, toluene, and THN. SEM images showed that the different self-assembled structures such as fibrous structure, woven structure, and lamellar structure were observed. Interestingly, by changing gelation solvents, gel formed by **48b** aggregated in different patterns due to differences in hydrogen bonding interaction, van der Waals interaction, and $\pi-\pi$ stacking.

2.4.2.4 Amino Acid- and Peptide-Based Gelators

Amino acids are biologically important amphiprotic compounds composed of amine and carboxylic acid functional groups and are the structural units to make up proteins. They join together through condensation between amine and carboxylic acid groups to form short or long polymer chains called peptides or polypeptides, which can further fold into supersecondary or higher structure with specific three-dimensional cavity. Through the simple reaction at the amine

and carboxylic acid groups, some active sites with strong hydrogen bonding interaction, such as amide and urea, can be appended to amino acids. Meanwhile, depending upon the amino acid sequence, the structural properties of peptides can be rationally tailored. Therefore, a number of amino acid- or peptide-based building blocks have been designed and developed for generating molecular gels with well-defined nanostructures and their possible applications in biology and nanotechnology are explored. On the other hand, most of the amino acids are chiral molecules. Induction of molecular chirality to the gelators can not only efficiently enhance their gelation capability, but also endow the corresponding molecular gels with intriguing chiral function, such as chiral switch, sensing, and recognition.

The earliest peptide gelator that has been studied is gelatin, a mixture produced by partial hydrolysis of collagen extracted from the skin, bones, and connective tissues of animals, which is probably best known as a gelling agent in cooking. It melts to a liquid when heated and solidifies when cooled again. Due to its semisolid form and biodegradability and biocompatibility in physiological environments, gelatin is widely used for pharmaceutical and medical applications. Peptide-based scaffolds with unique molecular structures have been widely studied as interesting candidates for hydrogelation and organogelation in recent years.

Suzuki and Hanabusa have reviewed the development of L-lysine-based LMWGs and the influence of discrepancy in gelator molecular structure on their gelation properties [145]. Figure 2.16 illustrates some classes of synthesized lysine-based gelators modified by various functional groups, which can efficiently immobilize organic solvents and water to construct molecular gels. It was found that organogelators having a urea bond have better organogelation ability than those with an amide bond. This is attributed to the fact that the urea group undergoes a stronger hydrogen bonding interaction than the amide group. The gelation property also depends on the alkyl chain length and degree of branching. While some charged or noncharged hydrophilic groups were involved in lysine-based gelators, the gelation of water under low concentration would be realized.

Based on the glutamic acid, we have developed a series of gelators through rational design. The initial and the simple organogelator, dioctadecyl-substituted L-Boc-glutamic diamide (LBG) (Figure 2.17), revealed a universal gelation ability to immobilize more than 40 kinds of organic solvents from polar to nonpolar. In addition, it can cogel many organic compounds, which were not gelators. After the Boc group was replaced by some functional groups, a variety of molecular gelators with good gelation ability, multiple responsiveness, and diverse functionality can be developed [146–152]. For example, three isomeric pyridine-containing organogelators were designed; different 1D nanostructure from nanofibers to twists and nanotubes was obtained in DMSO gels depending on the molecular structure [146]. L- or D-glutamic acid-based lipids could self-assemble into ultralong chemical nanotubes in ethanol through gel formation [147]. Terephthalic acid-substituted amphiphilic L-glutamide was found to

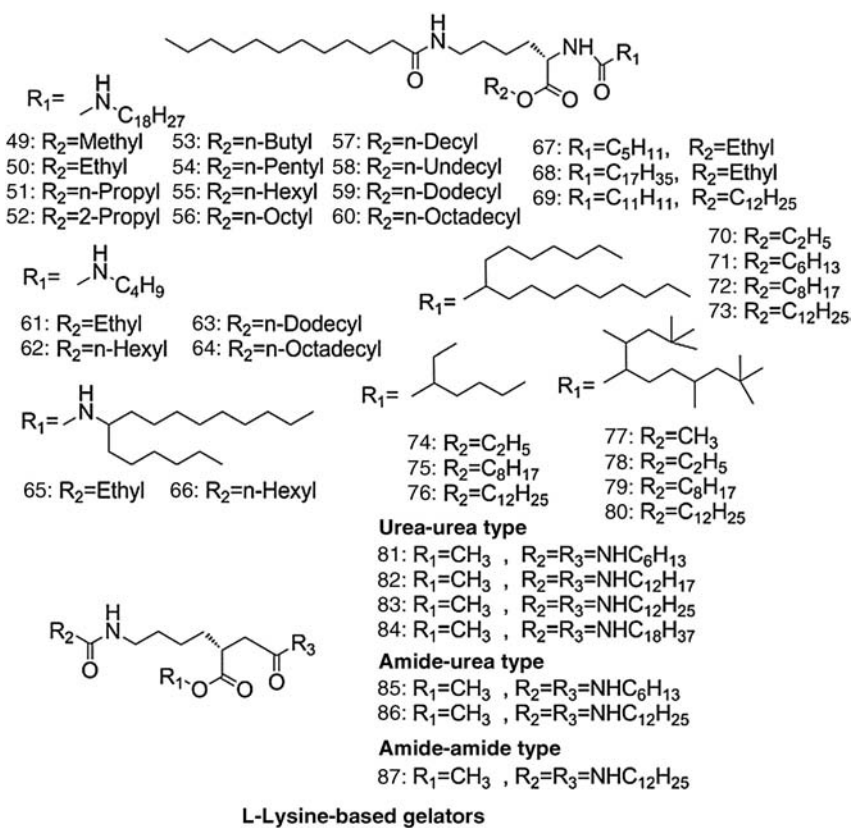


Figure 2.16 L-Lysine-based gelators.

form organogels in DMSO and a broad range of metal ions could tune the self-assembled nanostructure into a uniform helical twist [148].

On the other hand, the gel system is formed by the self-assembly of gelators by weak noncovalent interactions; thus, they may be easily disassembled in response to external stimuli. Then, the nanostructures can be changed by external stimuli. For example, we have reported an organogelator that can self-assemble into various nanostructures, from nanofibers to nanoribbons, nanotwists, and nanotubes, depending on the solvent polarity. Such morphological changes can even occur for the xerogels upon treatment with solvent vapors [151].

Besides the single amino acid-containing gelators, there are a number of works about gelation induced by peptide-based gelators, especially aromatic peptides that contain a short peptide sequence with the N-terminus capped by a synthetic aromatic moiety. Ulijn's group reported a series of Fmoc dipeptide hydrogels, whose self-assembly is driven by hydrogen bonding and $\pi-\pi$ interactions between π -electrons in the aromatic fluorenyl rings. Such hydrogels may be used as biomimetic fibrous scaffolds for three-dimensional cell culture [153–155].

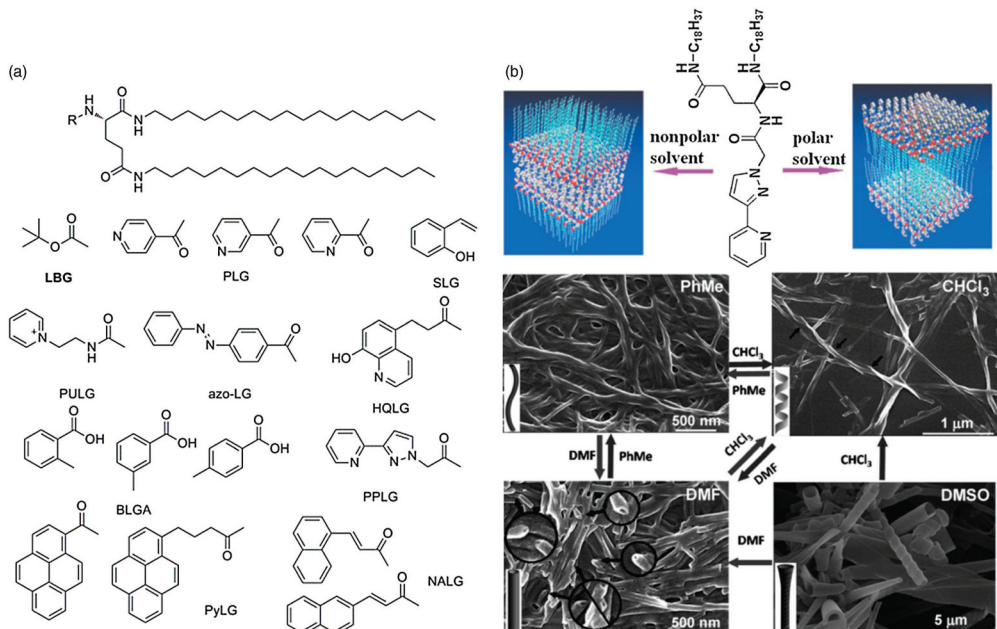


Figure 2.17 L-Glutamic acid-based gelators (a) and schematic illustration of solvent-polarity-tuned morphology inversion of PPLG and the reversible morphological transition treated by solvent vapors (b).

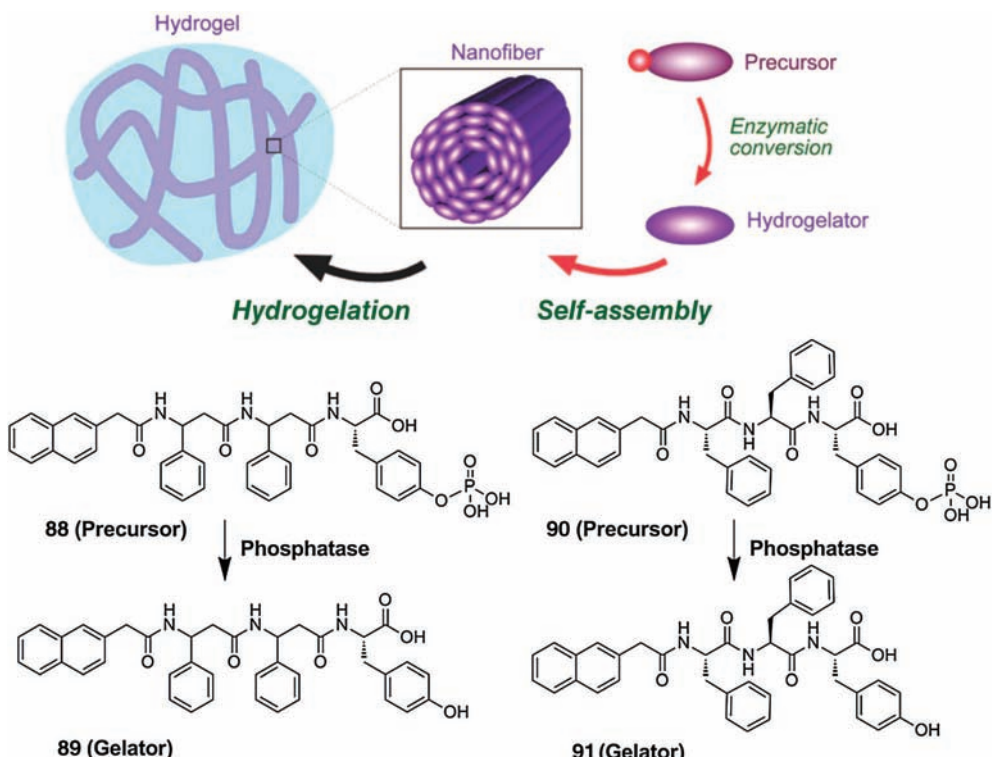


Figure 2.18 Procedure of the enzymatic hydrogelation of peptide-based gelators and the molecular structures and schematic gelation process for α - or β -peptide derivatives.

Using phosphatase, thermolysin, β -lactamase, and phosphatase/kinase as triggers, Xu and coworkers developed the enzyme-controlled self-assembly of a series of Fmoc peptides for hydrogelation (Figure 2.18) [156]. Their work illustrated a new strategy for the design and application of enzyme-catalyzed and -regulated formation of supramolecular hydrogels and offered a new approach for detecting the activity of enzymes, screening for enzyme inhibitors, typing bacteria, developing drug delivery systems, and controlling the fate of cells. By replacing the Fmoc protecting group with other aromatic rings, such as pyrene, naphthalene, and pyridine, conjugated oligopeptides can be designed that showed good gelation behavior in organic solvents or water.

Peptide amphiphiles (PAs) are another kind of peptide-based gelators, which are a class of molecules consisting of a hydrophobic nonpeptidic tail covalently conjugated to a peptide sequence. The PAs always contain three segments (Figure 2.19), including (i) a hydrophobic sequence to provide hydrophobic interaction, (ii) a β -sheet-forming peptide to promote nanofiber formation, and (iii) a peptide segment that contains ionizable side chains and usually has an amino acid sequence of interest for biological signaling [157]. Stupp and

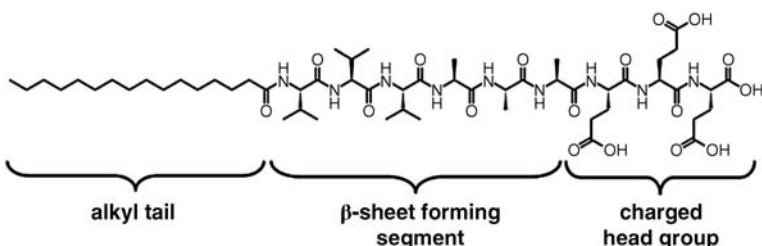


Figure 2.19 Molecular structure of a typical peptide amphiphile.

coworkers have extensively studied bioactive scaffolds composed of PAs that self-assemble into nanofiber networks. The self-assembly of PAs in water is driven by the hydrophobic collapse of alkyl tail domains and hydrogen bonding between β -sheet regions of neighboring PA molecules. These peptides that decorate the outer surface of the nanofibers can be designed to contain amino acids that serve as signals to the surrounding cells. PA fibers with bioactive epitopes have previously been used to promote bone growth [158], neural cell differentiation [159], and angiogenesis [160]. This part of the work will be well discussed subsequently.

2.4.2.5 Carbohydrate-Based Gelators

Carbohydrates, as one of the most important biological compounds, perform numerous roles in living organisms and are the main source of energy to maintain vital movement in living cells. This term is most common in biochemistry and they can also be called saccharides. The carbohydrates are divided into four groups: monosaccharides, disaccharides, oligosaccharides, and polysaccharides. Due to the structural diversity and important biological significance of carbohydrates, the design and fabrication of carbohydrate-based gelators have attracted great interest. Especially, the monosaccharide, an aldehyde and ketone with many hydroxyl groups, is very soluble in water and tends to aggregate through intermolecular hydrogen bonding interaction. With the proper modification, carbohydrate derivatives always can be used as gelators to construct molecular gels.

Shinkai and coworkers have done the pioneering work based on carbohydrate derivative integrated gelators. A series of 1-*O*-methyl-4,6-*O*-benzylidene derivative substituted monosaccharides were synthesized (Figure 2.20, 92–103) and served as gelators with different gelation properties and different three-dimensional network structures [161–164]. It is very interesting that a slight change in the configuration of saccharide as well as the presence of substituents on the sugar unit results in a drastic change in the solubility and gelation ability. Some derivatives can act as “supergelators,” which can gelate hydrocarbon solvents with 0.03–0.05 wt%. Moreover, due to the existence of a chiral component in the saccharide moiety, the gelation behavior will be affected and some chiral nanostructures (e.g., helical nanobelts, nanotubes, and nanofibers) can be

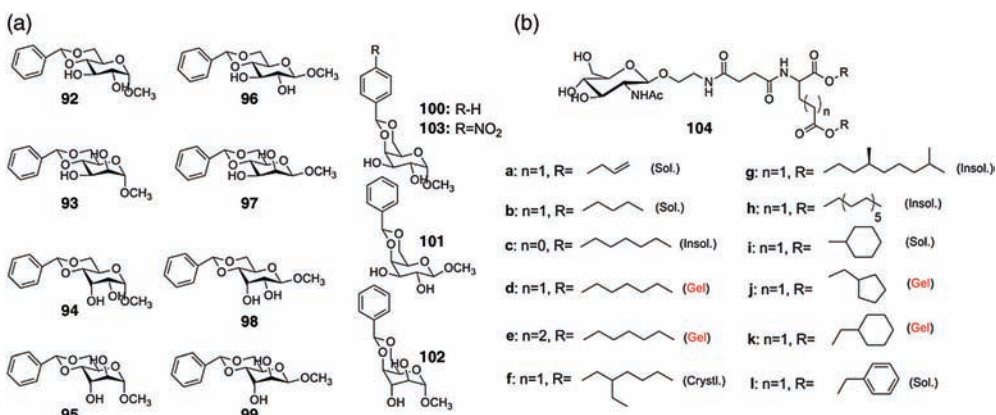


Figure 2.20 Carbohydrate-based gelators. (a) Methyl 4,6-O-benzylidene monosaccharides as gelators; (b) *N*-acetylgalactosamine-appended amino acid (GalNAc-aa) derivatives and their corresponding gelation abilities.

formed. Hamachi *et al.* developed a new solid-phase (glyco)lipid synthesis method [165,166] and synthesized a series of glycosylated glutamic acid derivatives (as shown in Figure 2.20, **104a–104l**). It was found that the obtained small library of these molecules showed different hydrogelation capability. More interestingly, the hydrogel formed by **104k** exhibited reversible swelling and shrinkage in response to temperature and pH variation [167–169]. Based on its hydrogelation ability, a new semi-wet peptide/protein gel array in which peptides or proteins are entrapped in the active form was constructed and this supramolecular protein/peptide chip is envisioned to be applicable to protein/enzyme analyses based on high-throughput activity [170–172].

2.4.3

π -Functionalized System

A π -functionalized system with large delocalized π -electrons is the most interesting building block since most of the nanostructures based on this system could show electronic properties, including luminescence, charge carrier mobility, and electronic conductivity. Therefore, π -conjugated molecules are extensively used in organic electronic devices such as LEDs [173], FETs [174,175], and PVDs [176,177]. Herein, the self-assembly of π -functionalized system from some small typical π -conjugated molecules to their derivatives used as gelators to construct molecular gels is discussed.

2.4.3.1 Porphyrin

Porphyrin, a group of heterocyclic macrocycle organic compounds, which is composed of four modified pyrrole subunits interconnected at their α carbon atoms via methine bridges, is one of the most important functional dyes in life

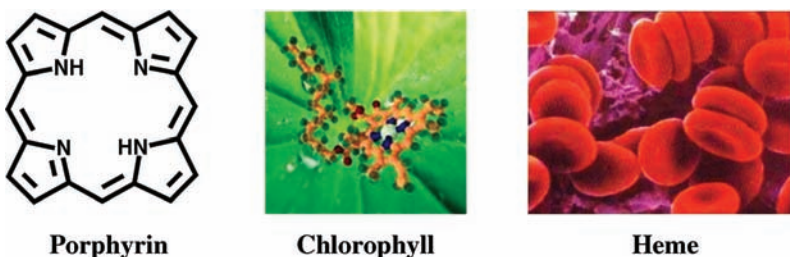


Figure 2.21 Molecular structures of porphyrin and its derivatives in nature.

and plays an essential role in the biological systems, such as heme, a cofactor of the hemoglobin responsible for oxygen transport, and chlorophyll, the main component of the antenna system for light harvesting (Figure 2.21). Due to the well-understood rigid and planar geometric structures and electronic features, porphyrin and its derivatives were always used as building blocks to self-assemble into varied supramolecular nanoarchitectures. For example, Hasobe *et al.* have reported supramolecular nanorods of *meso*-diaryl-substituted porphyrins formulated by a sonication method [178]. Shelnutt's group has synthesized porphyrin nanotubes and nanofiber bundles by ionic self-assembly of two oppositely charged porphyrins [179–181], and they have also manufactured square porphyrin nanosheets using a reprecipitation method [182]. Choi and coworkers have recently reported the synthesis of single-crystal porphyrin rectangular nanotubes by a vaporization–condensation–recrystallization process [183]. These obtained porphyrin-based self-assemblies further showed potential applications in photo- or opto-related areas, including photoelectronics, nonlinear optical devices, photocatalysts, energy conversion, chiroptical systems, and mimicking the photosynthetic process occurring in natural systems [184–186]. Meanwhile, some of the functions of porphyrins are strongly related to their supramolecular assemblies. Therefore, it is still an essential issue to study the relationship between molecular structures of porphyrin and physicochemical properties of their supramolecular assemblies.

On the other hand, porphyrin nanomaterials have also been widely studied by SAS methodologies. For example, Wan and coworkers have found that porphyrin-based hollow hexagonal nanoprisms could be prepared in a DMF/water system in the presence of surfactants [187]. Moreover, they have also shown that the hollow nanostructures could be further organized into an ordered, three-dimensional architecture. Hupp, Nguyen, and coworkers have demonstrated that porphyrin nanoplates and nanorods could be produced through a self-assembly process in an ethanol/water system. These nanostructures were hierarchically organized to form nanowires and macroscopic columnar structures with the assistance of surfactants [188,189]. Hasobe's group has constructed fullerene-encapsulated porphyrin hexagonal nanorods in a DMF/acetonitrile system mixed with surfactant [184]. Interestingly, our group extended the SAS method to a new mixed solvent system where the employed solvents are immiscible,

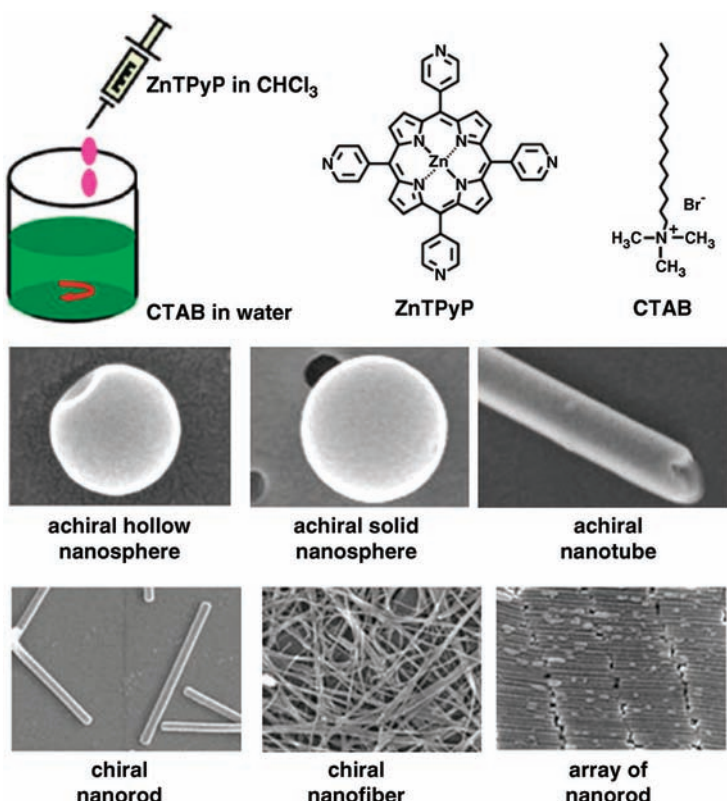


Figure 2.22 Molecular structures and the schematic illustration showing the controlled synthesis of various porphyrin nanostructures by using SAS.

especially the oil/aqueous system in which chloroform is the guest solvent and water is the host solvent. By well controlling the concentration of CTAB aqueous solution and aging time, various self-assembled porphyrin nanostructures, including hollow nanospheres, solid nanospheres, nanotubes, nanorods, and nanofibers, were successfully fabricated (Figure 2.22) [93].

2.4.3.2 Molecular Graphene

Graphene is a crystalline allotrope of carbon with two-dimensional properties. In graphene, carbon atoms are densely packed in a regular sp^2 -bonded atomic-scale chicken wire (hexagonal) pattern. Graphene can be described as a one-atom thick layer of graphite. It can also be considered as an indefinitely large aromatic molecule, the limiting case of the family of flat polycyclic aromatic hydrocarbons. Graphene is considered as one of the most promising materials, as it combines high electron mobility with atomic thickness. Some molecular graphene-related gelators can also be designed and are interesting from the viewpoint of their architectural and functional properties that can be significantly modulated

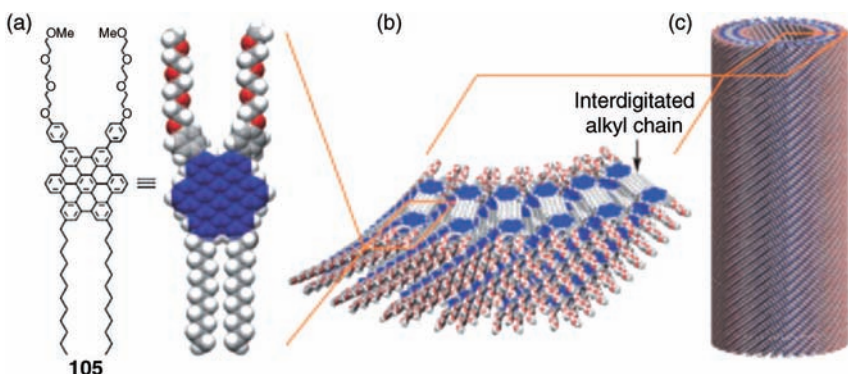


Figure 2.23 Self-assembly of gemini-shaped amphiphilic molecular graphene.

by self-assembly and gelation. Fukushima, Aida, and coworkers have synthesized a series of polycyclic aromatic hydrocarbons such as HBC derivatives, which consist of 13 fused benzene rings considered as a smallest fragment of a graphene sheet, and studied the self-assembly of these gemini-shaped amphiphilic HBCs (Figure 2.23). It was found that the graphitic nanotubes were formed by helical rolling of bilayer tapes composed of π -stacked HBC units [190–193]. The chiral self-assembly resulted in right and left helical graphitic nanotubular assemblies [194] when the chiral oxyalkylene side chains were incorporated.

2.4.3.3 π -Conjugated Gelators

$\pi-\pi$ stacking is one of the effective intermolecular interactions in supramolecular self-assembly and an important driving force for the formation of molecular gels. The induction of a large π -conjugated system is a basic strategy to design the LMWGs. Many conjugated π -systems, such as anthracene, pyrene, perylene, and other fused aromatics, oligo-phenylenevinylene, oligo-polythiophene, and oligo-polymeric pyrrole groups with photoelectric properties, and large conjugated molecules such as porphyrin, phthalocyanine, and fullerene have been widely applied to the design of LMWGs [195]. The strong $\pi-\pi$ stacking between these conjugated molecules facilitates the formation of linear aggregates and gelation. The functionalization of molecular gels can be easily achieved through rationally designing the gelators with selective π -conjugated systems; for instance, some azobenzene- [196–199], phenanthroline- [200], or porphyrin-based [201–208] gelators suffer reversible assembly-disassembly under light, protons, metal ions, and thermal treatment to realize the construction of intelligent materials. On the other hand, the induction of π -conjugated systems such as oligo-*p*-phenylenevinylenes [209], oligo-polythiophene, and oligo-polymeric pyrrole groups with specific optical, electrical, and magnetic properties to LMWGs leads to gelation of organic solvents and allows the design of a new class of photonically and electronically active supramolecular architectures.

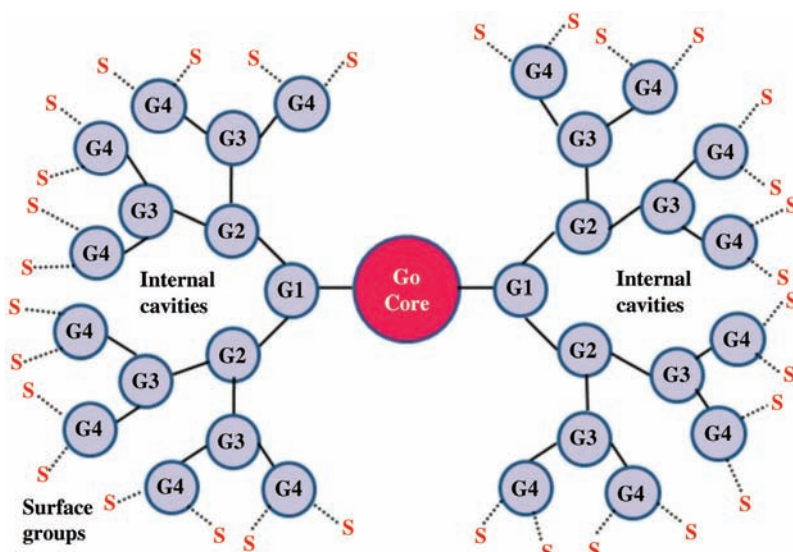


Figure 2.24 Schematic representation of general structure of a dendrimer.

2.4.4

Dendrimers

Dendritic molecules with hyperbranched globular architectures are widely found in nature and have emerged as a new class of polymers called “cascade” molecules, first synthesized by Vögtle’s group [210]. Dendrimer is derived from a Greek term *dendron* that means “tree,” which is nanosized macromolecule with a particular architecture composed of three distinct domains: a core, internal branches with repeat units called “generations,” and multivalent surface with many terminal functional groups (Figure 2.24). Dendritic structures can be chemically synthesized by using two different approaches, the divergent method and the convergent method. In the divergent approach, the dendrimer is synthesized from the core as the starting point and built up generation by generation. On the contrary, in the case of the convergent approach, the synthesis of dendrimer starts from the surface and ends up at the core, where the dendrimer segments are coupled together. Based on the large variety of linkages, the dendrimers can be classified into the following types: polyamines (PPI dendrimers), a mix of polyamides and amines (PAMAM dendrimers), dendrimers built up by more hydrophobic poly(aryl ether) subunits, peptide dendrimers, glycodendrimers, or silicon-based dendrimers.

From the viewpoint of structural features, the three parts of the dendrimer can be rationally tailored to exhibit unique properties, including unparalleled molecular uniformity, multifunctional end groups, and occurrence of numerous internal cavities. Due to these architectural properties, dendrimers are

well suited for the encapsulation of guest molecules and hold immense potential over other carrier systems in the field of drug delivery [211–213]. On the other hand, dendrimers and dendrons have been widely used as building blocks in the self-assembly of supramolecular gel-phase materials. Aida and coworkers performed the pioneering work to introduce a dipeptide into the focal point of an ester-terminated Fréchet-type dendritic organogelator and demonstrated that the hydrogen bonding interaction is the main driving force for the gelation [214,215]. Smith and coworkers then systematically studied both one-component and two-component dendritic organogels based on poly(lysine) dendrimers with amide dendritic branches [216–218]. Fan and coworkers developed a series of poly(benzyl ether) dendritic organogelators that were found to efficiently gelate various apolar and polar organic solvents (Figure 2.25). Interestingly, these dendritic organogels exhibited multiple stimuli-responsive behaviors upon exposure to environmental stimuli, including temperature, sonication, light, and shear stress [219–222]. Liu and coworkers designed and synthesized an amphiphilic dendrimer based on L-glutamic acid. It can form the hydrogel over a wide pH range from 2 to 13 and various self-assembled nanostructures ranging from helical nanotubes to coiled superhelix and dendrite nanostructures were obtained accompanying the pH change [223].

2.5

Functions of Some Typical Nanostructures

Molecular self-assembly is the main bottom-up approach for the affordable production of bulk quantities of well-defined nanostructures, such as nanotubes, nanofibers, nanobelts, and other chiral nanostructures. The driving forces for these self-assembled nanostructures are mainly based on multiple weak interactions such as van der Waals interactions, hydrogen bonds, coordination bonds, and $\pi-\pi$ stacking. Altering these noncovalent interactions in the self-assembly process, the formed nanostructures will be easily regulated and the functions of assemblies will be realized.

2.5.1

Vesicles/Hollow Spheres

As discussed earlier, the self-aggregation behavior of amphiphilic molecules can yield a rich variety of assemblies, and the most common self-assemblies of colloid dimensions are micelles and vesicles. Micelles are small, ill-defined assemblies of 50–100 unimers that feature an external polar surface made of hydrophilic head groups and a more or less disordered hydrophobic core formed by the amphiphilic tails, usually regarded as a small volume of liquid hydrocarbon [98]. Vesicles are spherical or ellipsoidal closed amphiphilic bilayer structures with an internal cavity containing the aqueous solution in which they are

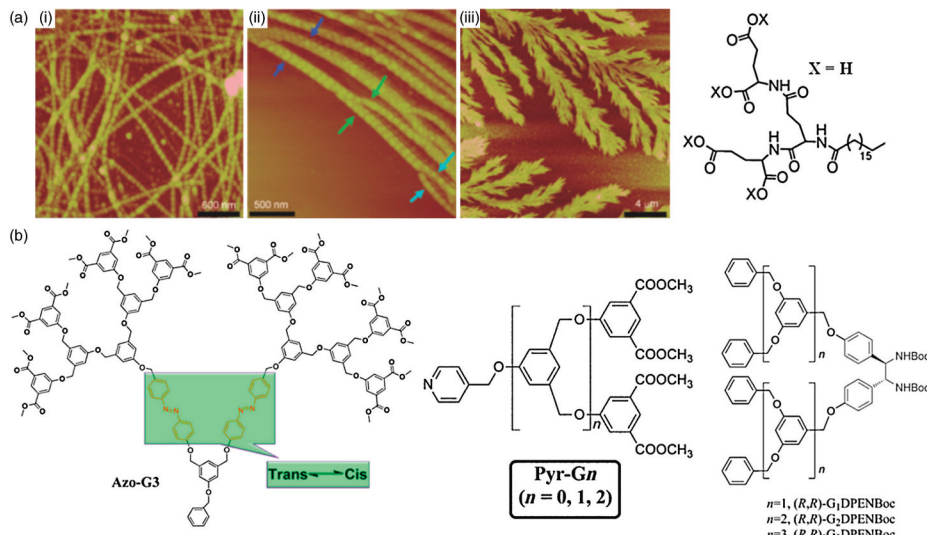


Figure 2.25 (a) Amphiphilic dendrimer based on L-glutamic acid and its pH-responsive self-assembly. (b) Poly(benzyl ether) dendritic organogelators.

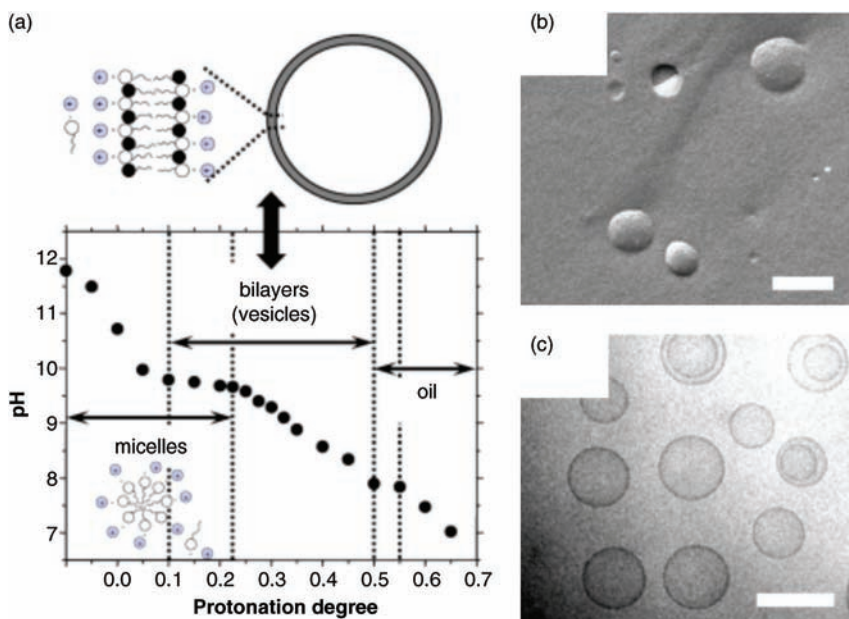


Figure 2.26 (a) Titration curve for 80 mM oleic acid/sodium oleate. The regions for the formation of micelles, vesicles, and oil droplets are indicated. The schematic drawing of the amphiphile with the empty head representing the ionized form of oleic acid (oleate); the neutral form (oleic acid) is represented with a

filled head group. (b) A freeze fracture electron microscopy image of vesicles. Scale bar: 100 nm. (c) A cryo-transmission electron microscopy image of vesicles. Scale bar: 100 nm. (Reprinted with permission from Ref. [9]. Copyright 2007, Elsevier Science.)

dispersed (Figure 2.26). In contrast to conventional amphiphiles, supra-amphiphiles constructed on the basis of noncovalent interactions or dynamic covalent bonds could also form the colloidal and vesicular structures. In recent years, some reviews based on colloid particles and vesicles have been reported [224–230].

The vesicles can be used in many applications, but the most commonly used investigated aspect of the hollow sphere is the application of drug delivery. A key factor in conventional drug delivery is the release profile of the payload. For example, Liu and coworkers [231] reported that PEG-*b*-PCPTM polyprodrug amphiphiles, where PEG is poly(ethylene glycol) and PCPTM is polymerized block of reduction-cleavable camptothecin (CPT) prodrug monomer, with >50 wt% CPT loading content can self-assemble into four types of uniform nanostructures, including spheres, large vesicles, sooth disks, and unprecedented staggered lamellae with spiked periphery. Four types of self-assembled nanostructures provide prototype models for shape-regulated cellular internalization, trafficking, and drug delivery (Figure 2.27). Devarajan and coworkers [232] reported multilamellar vesicles (onion phases) of a biodegradable surfactant PEG-8 distearate, which has been studied for the encapsulation of sumatriptan, an antimigraine

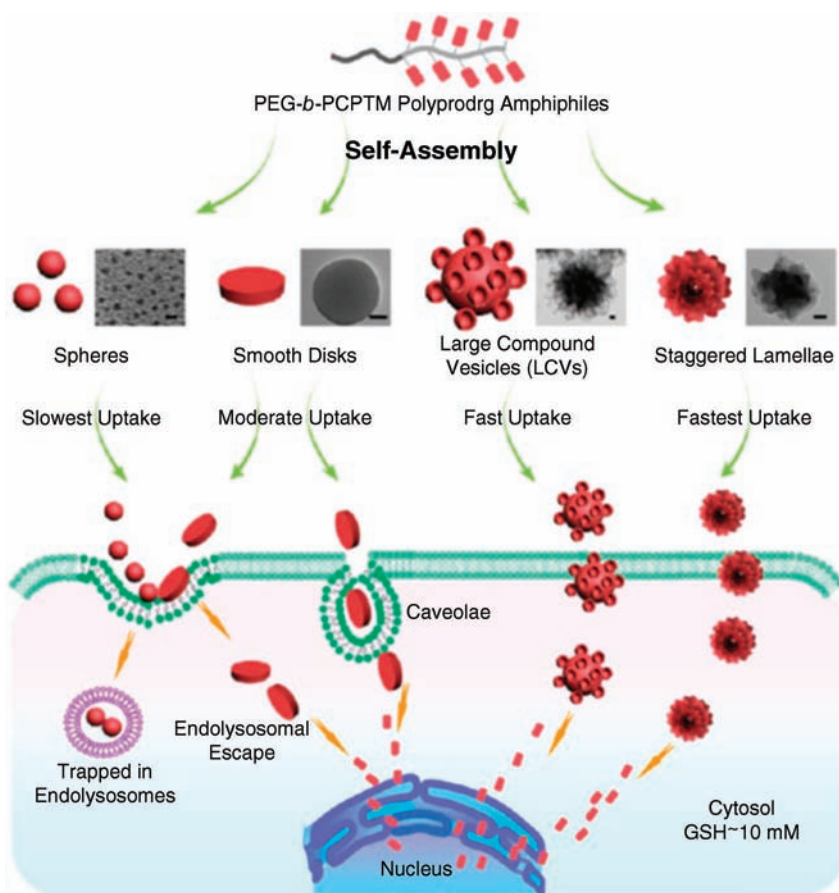


Figure 2.27 Schematic illustration for the self-assembly of polyprodrug amphiphiles into four types of uniform nanostructures, which exhibit shape-dependent performance in the context of blood circulation, cellular

internalization and transport, subcellular distribution, and degradation kinetics. (Reprinted with permission from Ref. [10]. Copyright 2013, American Chemical Society.)

drug. The drug encapsulation efficiency of the onion phases was found to be very high (90%) and *in vitro* drug release was rapid (>90% in 10 min).

Polypeptide-based vesicles are usually used for drug delivery because the polypeptides are ideal biomaterials due to high biocompatibility and biodegradability. For example, Lecommandoux and coworkers [233] reported nanovesicles that present a controlled size, excellent colloidal stability, and a high loading capacity for hydrophilic and hydrophobic drugs (Figure 2.28). Cytotoxicity study showed that controlled poly(γ -benzyl-L-glutamate)-*b*-hyaluronan vesicles without drug had nearly no influence on the viability of C6 glioma tumor cell lines in the concentration range of 0.1–700 $\mu\text{g ml}^{-1}$ according to the results of the MTT assay.

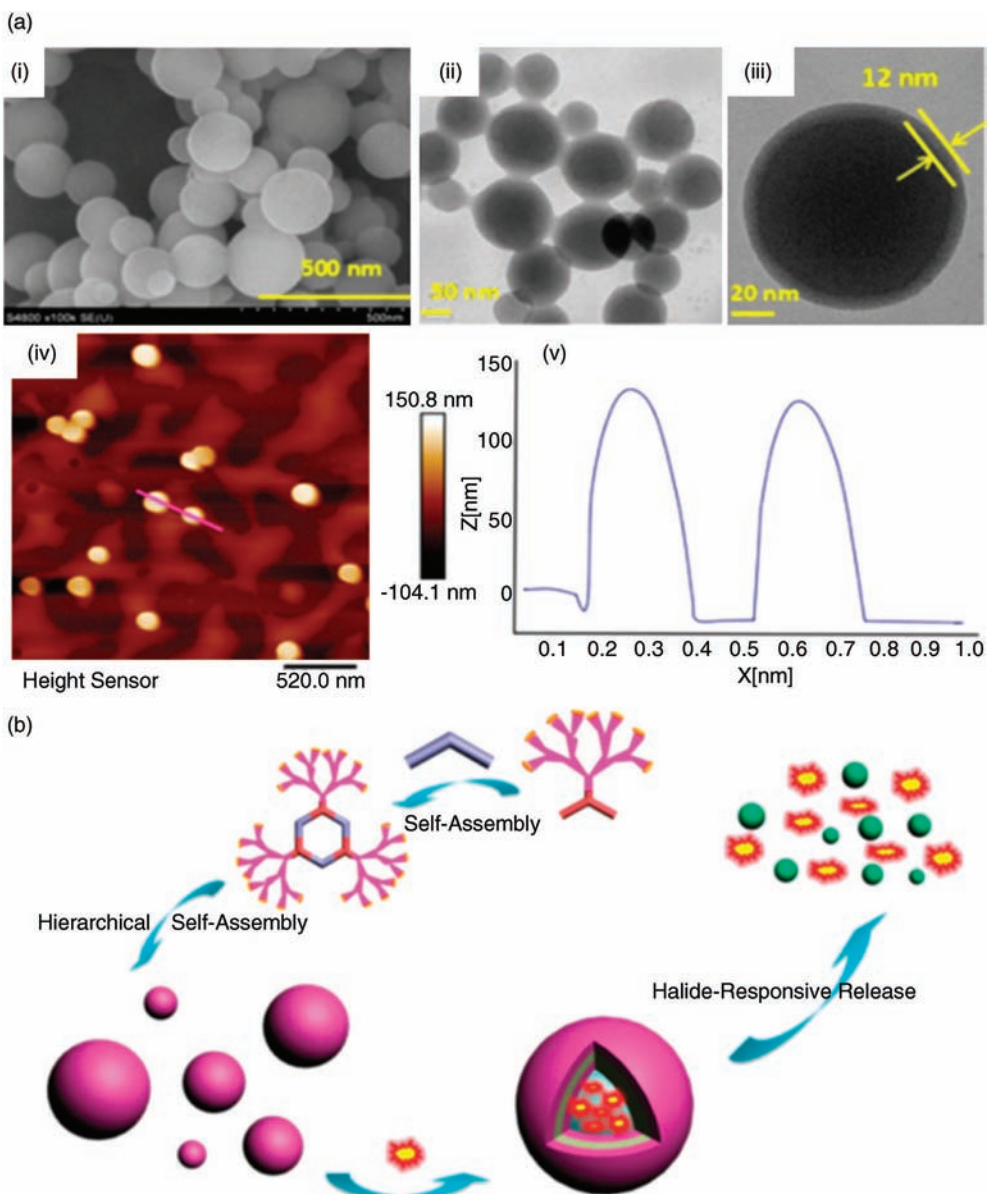


Figure 2.28 (a) SEM, TEM, and AFM images of the vesicles. (b) Schematic illustration for the self-assembly and the process of halide-responsive release of fluorescent molecules. (Reprinted with permission from Ref. [13]. Copyright 2014, American Chemical Society.)

Except for the vesicles, hollow structured materials, a kind of nanostructures with unique morphology, have been of great interest in the past decade because of the subtle combination of the hollow architecture with other molecules, such as fluorescent dyes, amphiphilic surfactants, drugs, and proteins, and can realize the encapsulation and release process of the molecules. For example, Yang and coworkers [234] designed and constructed a series of supramolecular poly(benzyl ether) metallocendrimers featuring a well-defined hexagonal metallacycle at their cores via coordination-driven self-assembly. One of the metallocendrimers was able to hierarchically self-assemble into regular vesicle-like structures. Such supramolecular vesicle-like structures could encapsulate some fluorescent molecules, such as BODIPY and SRB. Then, by taking advantage of the dynamic nature of metal–ligand bonds, the controlled release of fluorescence dye can be successfully realized by the halide-induced vesicle–micelle transition. Huang and coworkers [235] reported a new amphiphilic pillar[5]arene that could self-assemble to form vesicles and multiwalled microtubes in water. With the hollow sphere structures, the vesicles could encapsulate calcein within their interiors under neutral conditions and release it in response to a decrease in pH.

Meanwhile, when some groups with catalytic activities were incorporated into the amphiphiles, the functional self-assembled vesicles can be designed and used as nanoreactors to catalyze the asymmetric reactions. Our group found that compressed CO₂ can induce the amphiphilic proline derivatives to self-assemble into vesicles in water (Figure 2.29) [236]. Based on the pressure of compressed

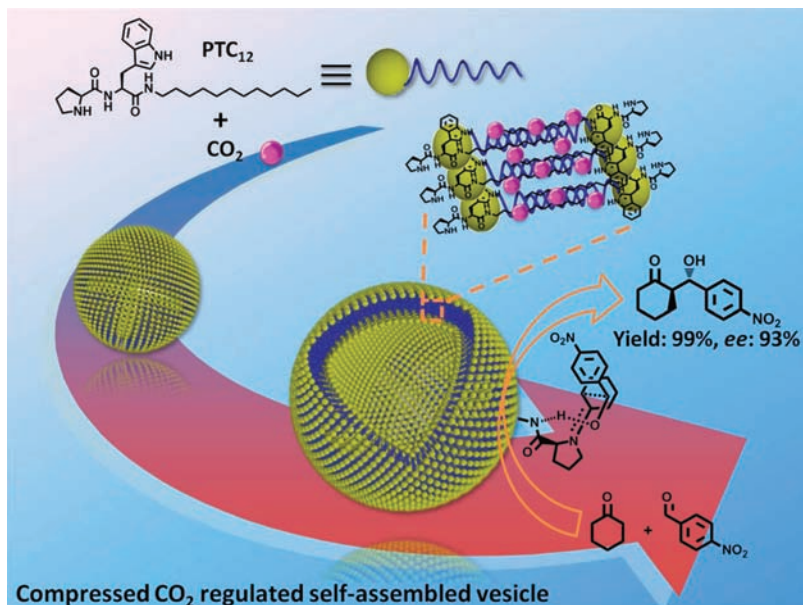


Figure 2.29 Compressed CO₂ regulated self-assembled vesicle used as a nanoreactor to catalyze asymmetric aldol reaction.

CO₂, the generated vesicle was tunable and turned out to be an efficient nano-reactor for catalyzing asymmetric aldol reaction in the absence of additives. Under optimal reaction conditions, the yield and ee value reached 99 and 93%, respectively. Furthermore, simple separation of products was realized by removing reaction medium followed with the release of CO₂. The recycling of organo-catalyst was realized over several cycles with constant catalytic activity and enantioselectivity at a high level.

2.5.2

Nanotubes

Tube-shaped proteins are among the most intriguing class of self-assembled functional molecules found in nature, such as motor proteins, tubulins, ion channels, and aquaporins. These series of proteins contain hollow cavity involved in many biological processes and activities. Driven by the sophisticated structures and a variety of functions of these natural proteins, many scientists were inspired to design artificial nanotubular structures with a hollow cylinder on the nano-scale to mimic the biofunction of natural compounds based on molecular self-assembly in supramolecular chemistry. As reported, the well self-assembled artificial nanotubes can be formed from a variety of different organic molecules such as peptides, lipids, carbohydrates, synthetic polymers, and other organic systems.

2.5.2.1 Self-Assembled Lipid Nanotubes

Usually, the main component of cell membrane and the membrane of cellular organelle are phospholipid molecules that contain two hydrophobic alkyl tail chains and a hydrophilic polar head group. With this structural feature, the phospholipid molecules have a strong self-assembling capacity to form the bilayer structure in a polar environment (e.g., water and alcohol), to maintain differences between intracellular and extracellular microenvironments. Inspired by the structural characteristics of phospholipid molecules, a series of similar compounds (lipids) were synthesized and used to construct some nanotubes with hollow structures, which were called self-assembled lipid nanotubes (LNTs) [237].

Through the chemical synthesis and bottom-up approaches, the artificial lipid nanotubes can be fabricated with hollow cylindrical supramolecular objects consisting of many identical lipid molecules as building blocks. The diameters of characteristic LNTs range between 10 and 1000 nm, which are larger than the diameters of circular molecules such as cyclodextrin, cyclic peptides (less than 1 nm), and single-walled carbon nanotubes (1–10 nm). Due to these unique structural features [99,238,239], LNTs can be widely used in the area of materials science, bionics, biomedicine, and so on. The artificial self-assembled LNTs were first reported by three independent research groups of Japan and the United States and they found that the formed bilayer structures in water derived from glutamic acid dialkyl amide derivatives [240,241] and diacetylenic phospholipid derivatives [242] were crucial for the formation of highly ordered tubular structures. Since then, various organic amphiphiles such as phospholipids, glycolipids,

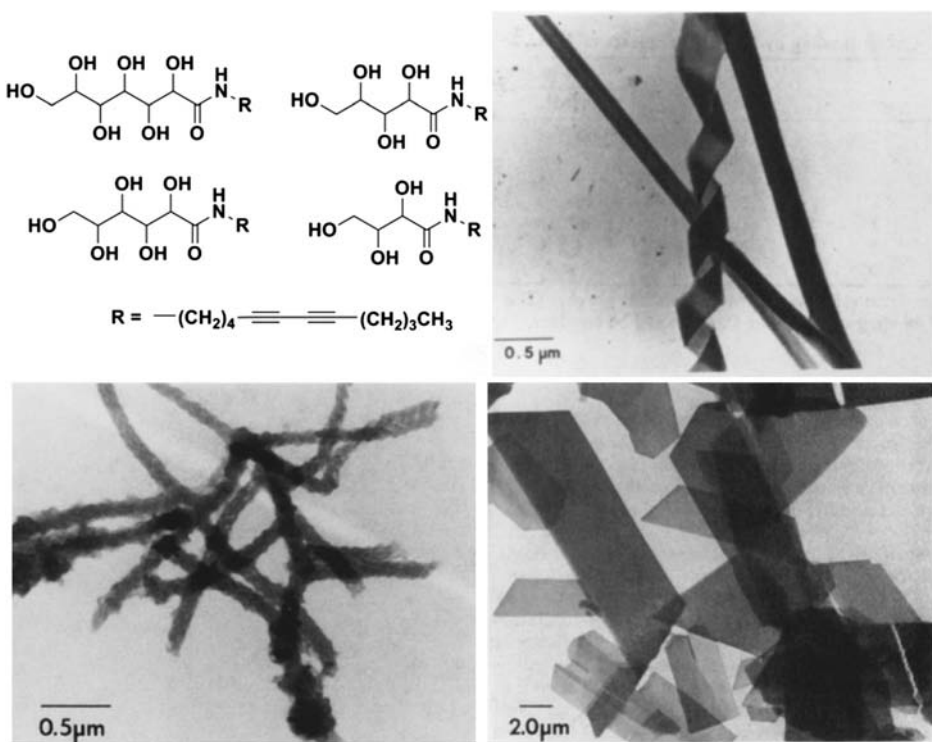


Figure 2.30 Glycolipids with the open-chain sugar head groups and their self-assembled nanostructures.

cholesterol, and cholesterol ester (steroids) have been designed to construct LNTs. In particular, by making rational alterations to the molecular structure of precursor amphiphiles to precisely control the inner and outer diameters of self-assembled LNTs that directly determine their properties and applications has been attracting great interest.

Self-assembly of a series of glycolipids by introducing various hydrophilic sugar moieties as head groups, such as glucose, galactose, other aldopyranose-type sugars, and noncyclic sugars, to the well-formed nanotubes has been reported by Frankel and O'Brien. Figure 2.30 summarizes the synthesis of a series of diacetylenic aldonamides, which differ in the structure of open-chain sugar head groups. They found that the head group can provide strong hydrogen bonds for the formation of LNTs, which effectively increases the stability of self-assembled objects. Therefore, the selection of head group tends to have an effect on the molecular packing mode. Head-to-head bilayer packing facilities the nanotube formation, whereas head-to-tail packing mode and “dromic” hydrogen bonding patterns lead to the formation of nanofibrillar assemblies [243–245].

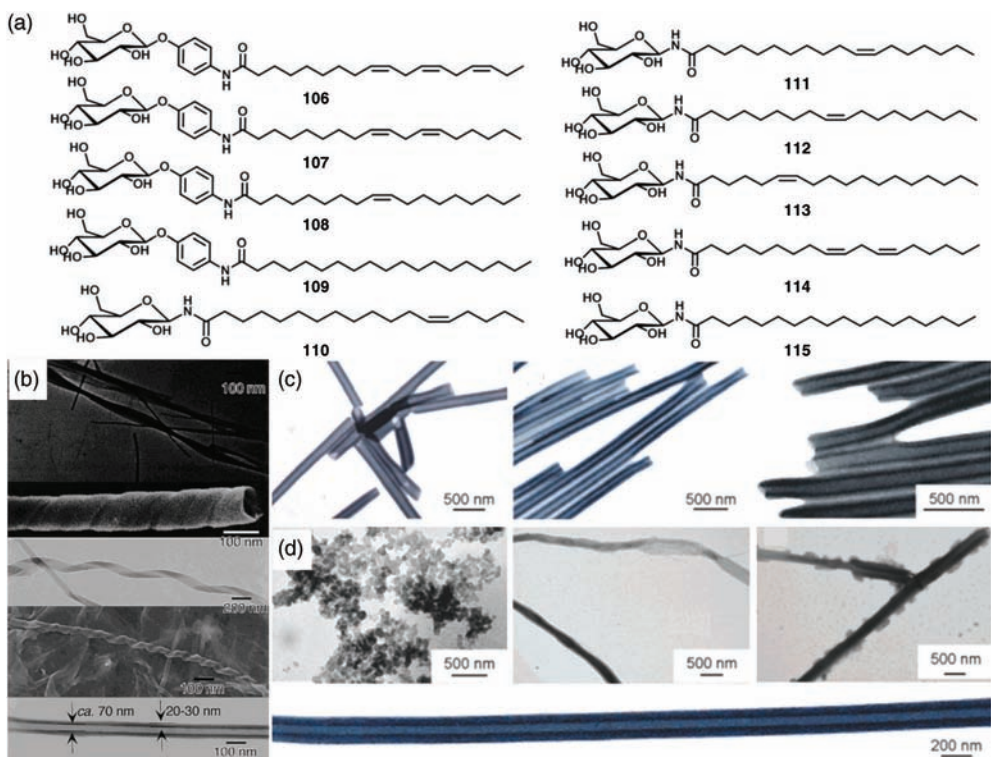


Figure 2.31 (a) Glycolipids with cyclic sugar head groups and varied hydrophobic chains.
(b-d) The corresponding self-assembled nanostructures of these glycolipids.

The length and position of double bonds in the hydrophobic chain also have a significant influence on the self-assembly behavior of glycolipids (Figure 2.31). Shimizu *et al.* found that the self-assembly of a series of long-chain amphiphilic glucosides **106–115** depended on the number and position of *cis* double bonds in the hydrocarbon chain [101,246]. Self-assembled nanotubes, helical ribbons, and twisted nanofibers were obtained from **106**, **107**, and **108**, respectively. Moreover, **110–112** can self-assemble into nanotubular structures of different sizes, but the amorphous aggregates were obtained from **114** and **115**. Using CD and X-ray diffraction, it was found that the difference in the hydrophobic chain affected the tightness of packing between tail chains and the chiral stacking of the glucoside moieties, which is crucial for the nanotube formation by chiral assembly.

Another typical class of lipid molecules that self-assemble into nanotubes is peptide lipids. Numerous reports about the self-assembled peptide lipid nanotubes, which were formed through multiple intermolecular noncovalent interactions such as hydrogen bonding and hydrophobic interactions, are available. There is a clear distinction between peptide lipid and small molecular peptide that the N-terminal of a peptide sequence is always appended by a long hydrophobic chain, which can provide strong hydrophobic interaction during

assembly. Hence, the peptide lipids can also be called lipopeptides. A typical example of natural peptide lipids is surfactin, a cyclic lipopeptide produced by the Gram-positive bacteria *Bacillus subtilis*. Similarly to the phospholipids *in vivo*, the peptide lipids comprising hydrophilic or hydrophobic amino acid residues and having a long hydrophobic chain can show a good self-assembling behavior to form LNTs. Shimizu *et al.* reported a series of synthesized oligopeptide-based bolaamphiphiles (as shown in Figure 2.32). The sodium or potassium salts of the bolaamphiphiles **116a**, **116c**, **116e**, **117a**, and **117b** produced well-defined vesicle-encapsulated microtubes with closed ends and a uniform diameter (1–3 µm). It is very interesting to find that the tube formation strongly depends on the connecting alkylene chain length and constituent amino acid residues. The microtubular structures were formed only when the oligomethylene chain had an even number of carbons and the amino acid residues Gly–Gly and Gly–Gly–Gly were used. Vectorial formation of acid–anion dimers and loose interpeptide hydrogen bond networks are responsible for the microtube self-assembly [247]. Besides the bola-type peptide lipid, the single-tail-type peptide like the typical amphiphiles can also produce tubular structures; for example, some additive transition metal cations were proved to coordinate with the peptide amphiphiles to produce self-assembled nanotubes. The nanotubes can be formed through precipitation after the addition of metal ions to a weakly alkaline aqueous solution of these single-tail-type peptide amphiphiles [248–250]. Boettcher *et al.* found that hot solutions of *N*-dodecanoyl-(D- or L-)serine in toluene or water were cooled to room temperature to give gels. Cryo-TEM investigations revealed that the bilayer structures were spontaneously formed in both media but appeared differently as multilayered vesicles and tubules in toluene or ribbons and tubules in water. With respect to the polarity of the solvent, such lamellae must be regarded either as “normal” bilayers with the hydrophilic head groups in the aqueous environment or as “inverse” bilayers orientating their alkyl chains to the hydrophobic toluene phase [251].

2.5.2.2 Self-Assembled Peptide Nanotubes

Due to the extensive chemical, conformational, and functional diversity, proteins and peptides are the most versatile natural molecular building blocks. Self-assembly of peptides plays an important role in biological systems and the well understanding of the procedure of peptide self-assembly is important for exploring the life phenomenon and origin. In the past decade, great efforts have been devoted to the development of nanotubes based on artificial synthetic peptides, which may show potential applications in nanoreactors, sensors, electronics, and stimulus-responsive materials. At the fore, we have discussed the self-assembled peptide lipid nanotubes. Herein, we review the emerging field of self-assembled nanotubes made of simple molecular peptides, including dipeptides, linear peptides, and cyclic peptides.

Görbitz's group first reported the simplest dipeptide crystals that the free hydrophobic dipeptide L-Val–L-Ala can link to hexagonal tubular channels by hydrogen bonds. These empty channels aligned in parallel along the hexagonal

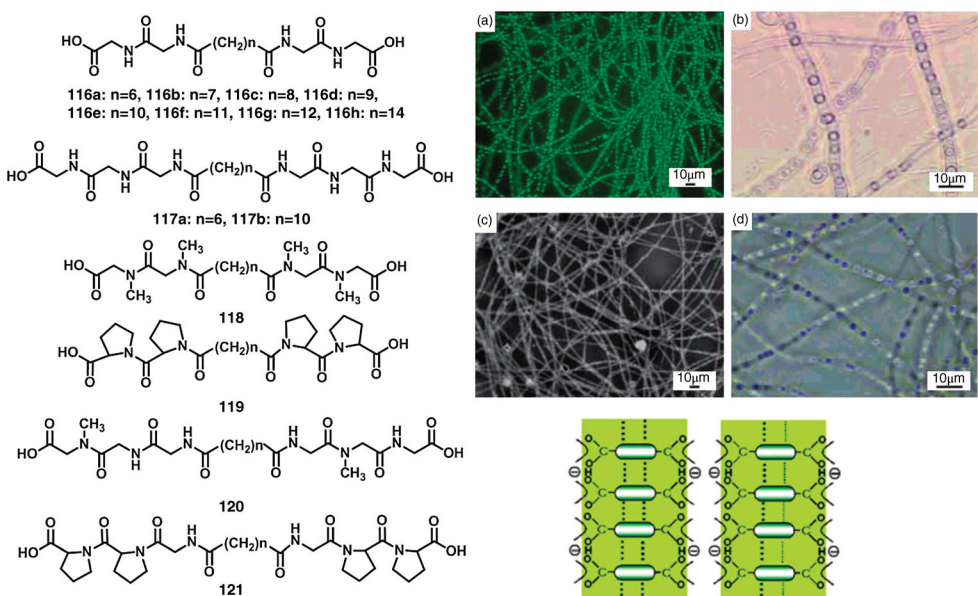


Figure 2.32 Peptide lipid-based gelators and self-assembled well-defined vesicle-encapsulated microtubes and schematic representation of the intralayer acid–anion interaction that is responsible for the microtube formation.

axis and the apparent diameter of the channel was about 5.2 Å. Further research showed that other hydrophobic dipeptides can also form crystal structures with variable hexagonal tubular channels, such as L-Ala-L-Ile, L-Ile-L-Ala, L-Val-L-Val, L-Val-L-Ile, and L-Ile-L-Val. It was found that the hydrophobic side chains form the inner surfaces of channels parallel to the hexagonal axes in these structures. By changing the bulk of the side chains, the van der Waals diameter of the channels can be regulated within the range of 3.3–5.2 Å [252,253].

The larger self-assembled tube on the nanoscale formed by dipeptide from the diphenylalanine motif of the Alzheimer's β-amyloid peptide was reported by Gazit (Figure 2.33a). When this peptide is dissolved in 1,1,1,3,3,3-hexafluoro-2-propanol (HFIP) and then diluted with water, a rapid assembly into ordered semicrystalline structures was observed visually within seconds after dilution of the aqueous solution at a final μM concentration range. TEM analysis with negative staining indicated that the peptide forms well-ordered, tubular, and elongated assemblies [254]. However, when a thiol is introduced into the diphenylalanine peptide, the spherical particles were formed instead of the nanotubes [255]. By solvent evaporation on siliconized glass, vertically aligned nanoforests were formed by axial unidirectional growth of a dense array of dipeptide nanotubes. They also achieved the horizontal alignment of the tubes through noncovalent coating of the tubes with a ferrofluid and the application of an external magnetic field (Figure 2.33b and c). These results demonstrate the ability to form a two-dimensional dense array of these nanotubes with either vertical or horizontal patterns [256].

Meanwhile, Gazit *et al.* found that these well-ordered nanotubes exhibited notable thermal and chemical stability both in aqueous solution and under dry conditions or in a wide range of organic solvents and pH. Circular dichroism spectra do not change from room temperature up to 90 °C; dry tubes heated to 150 °C are stable. The nanotubes also displayed remarkable mechanical rigidity. Indentation atomic force microscopy experiments on the mechanical properties of dried NTs on mica give an estimated average point stiffness of 160 N m⁻¹ and a high Young's modulus of ~19 GPa. This makes them among the stiffest known biological materials [257,258].

The longer designed peptides approximately 2–3 nm in length, with a hydrophilic head of one or two charged amino acids and a hydrophobic tail of four or more consecutive hydrophobic ones, for example, A₆D, V₆D, G₈DD, and KV₆, form a network of cationic or anionic open-ended nanotubes with diameters of 30–50 nm, upon dissolution in water at 4–5 mM [259–261]. These tubes are stabilized by hydrophobic effects and have smaller diameter than the tubes formed by lipids. The seven-residue peptide Aβ(16–22), CH₃CO-KLVFFAE-NH₂, derived from the Alzheimer's disease peptide was synthesized via standard Fmoc solid-phase protocols with both N- and C-termini capped and found to assemble into parallel β-sheets that produce micron-long highly homogeneous hollow tubes at pH 2. These tubes have a cross-sectional diameter of 52 nm and are bounded by 4 nm walls. Lynn and coworkers further found that through protein "salting out" strategies, simple oligopeptides that self-assemble into homogeneous nanotubes can be directed to further assemble into macroscale parallel

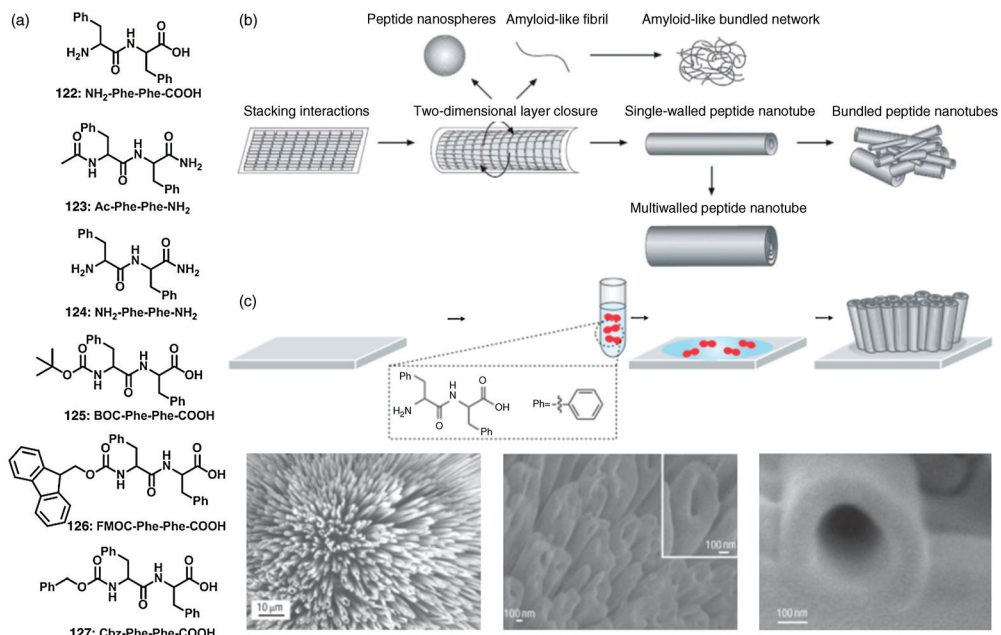


Figure 2.33 (a) The chemical structure of the diphenylalanine peptide analogues. (b) Schematic of the formation of tubular (single or multiwalled), spherical, or fibrillar structures via dipeptide self-assembly. (c) Proposed model for the formation of aligned peptide nanotube arrays.

arrays. This is a simple and generic strategy to produce higher order assemblies of homogeneous nanotubes [262,263].

The conformationally fixed cyclic peptides are one of the most important secondary building blocks for self-assembled nanotubes. The continuous hollow nanostructures formed by stacking of these cyclic peptides and stabilization by hydrogen bonds have attracted great interest due to the tunable tubular diameters and adjustable inner or outer tube properties depending on the cyclic peptide sequence and length. A well-characterized example is the naturally occurring lanreotide growth hormone inhibitor peptide, which adopted a closed compact β -hairpin-like conformation through a disulfide bond to form nanotubes when it was dissolved in water at a concentration of 3–20 wt% [264]. The formation of cyclic peptide nanotubes was first proposed by DeSantis in 1974 and the pioneering work on cyclic peptide nanotubular structures was carried out by Ghadiri and coworkers. They demonstrated a new class of organic nanotubes based on rationally designed heterochiral cyclic peptides. These peptides formed extended β -sheet-like structures, and stacked on top of each other to form hollow and extended cylinders. The peptide nanotubes were formed by using the sequence cyclo-[$(D\text{-Ala-L-Glu-D-Ala-L-Gln})_2$]. The following studies found that β - or δ -cyclic peptides, α,γ - or α,ϵ -mixed cyclic peptides, and cystine- or serine-containing cyclic peptides can also self-assemble into nanotubes [265–270]. Based on Ghadiri's report, Undén and coworkers presented a first step toward a new strategy for the stereochemical control of peptide nanotube formation by imposing sterical restrictions upon the hydrogen bonding pattern. Their model studies of the stacking of the backbone hydrogen bonds in nanotubes by the peptide cyclo[$-(L\text{-Gln-D-Tle-L-Glu-D-Tle})_2$] suggested that peptides incorporating the bulky amino acid *tert*-leucine in every second position could not readily be sampled into nanotubes by the formation of either parallel or antiparallel hydrogen bonds. However, its interaction with its enantiomer could readily be modeled into nanotubes with close antiparallel hydrogen bonding [271].

2.5.2.3 Functionalization of Nanotubes

Since LNTs possess a well-defined 10–100 nm wide hollow cylinder, the synthetic LNTs are useful especially for encapsulating some organic and inorganic guest substances. In addition, both the inner and outer surfaces of LNTs are hydrophilic. These characteristics are favorable for the 1D encapsulation of hydrophilic biomacromolecules such as DNA and proteins. Furthermore, after the guest substances are encapsulated in the confined hollow cylinders, some new functional materials with desired optical, electronic, magnetic, drug delivery, and transportation properties can be developed.

Shimizu *et al.* have reported that a series of unsymmetrical bolaamphiphiles (Figure 2.34), *N*-(2-aminoethyl)-*N'*-(β -D-glucopyranosyl)alkane diamide, can self-assemble to nanotubes in alkaline aqueous solutions. The obtained nanotubes were found to have different inner and outer surfaces covered with amino and glucose head groups, which can encapsulate negatively charged nanoparticles and ferritin into the hollow cylinder [272–274]. Moreover, through the chemical

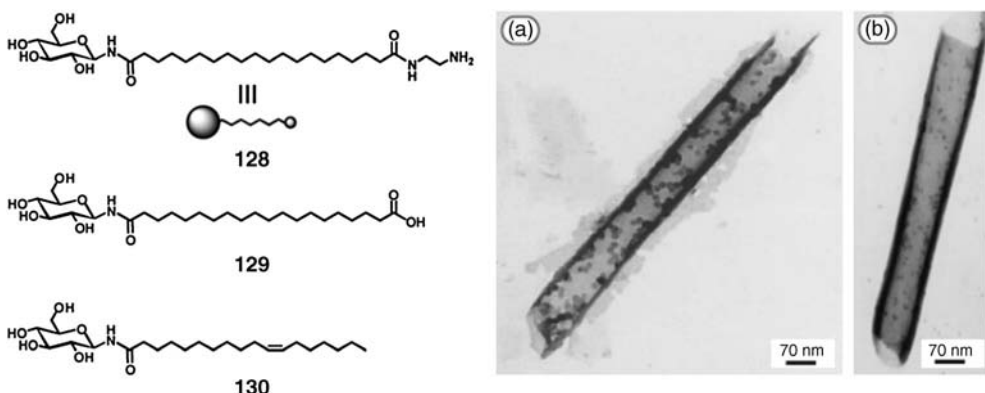


Figure 2.34 Molecular structures of the unsymmetrical bolaamphiphiles and TEM images for lipid nanotubes encapsulating (a) sulfate-latex beads and (b) ferritin in the hollow cylinder.

modification of the inner surface of nanotubes formed by unsymmetrical bolaamphiphiles with a fluorescent molecule as an optical sensing moiety, the visualized dynamic encapsulation guest molecules in the hollow channel of the resultant nanotubes can be achieved. Time-lapse fluorescence microscopy combined with the fluorescence resonance energy transfer (FRET) system realized the optical dynamic encapsulation and nanofluidic behavior of the spherical protein ferritin, gold nanoparticles, and a label reagent in the nanochannels shaped by the nanotube hollow cylinders (Figure 2.35) [275].

A simple and general approach for the encapsulation of functional species within self-assembled organic nanotubes through instant gelation was presented by our group [276]. A C₃ symmetric gelator with a 1,3,5-benzenetricarbonyl core was found to show instant gelation ability at room temperature by injecting the antisolvent into the gelator-dissolved solvent (Figure 2.36b). SEM shows that the well-developed hexagonal nanotubes were formed in a series of mixed solutions. If guest molecules were predissolved with the gelator in the good solvents, the guests could be encapsulated simultaneously during the gelation. Since the instant nanotube formation should be generated in a broad range of mixed solvents, many guest molecules, including biomacromolecules, synthetic polymers, and simple dyes, can be efficiently encapsulated (Figure 2.36c–f). This provides a universal system for the encapsulation of a wide range of guest molecules into the self-assembled organic nanotubes.

The transport of small molecules and ions across the nanometer-scaled channels, created by natural or artificial molecules, is an intriguing phenomenon and demonstrates great practical significance. The most sophisticated biological channels made by nature possess extraordinary properties in molecular transport. For instance, potassium ion channels, the most widely distributed type of ion channel found in virtually all living organisms [277], can rapidly and selectively conduct potassium ions down their electrochemical gradient, which is critically important for the maintenance of cell membrane potential. Aquaporins, the plumbing

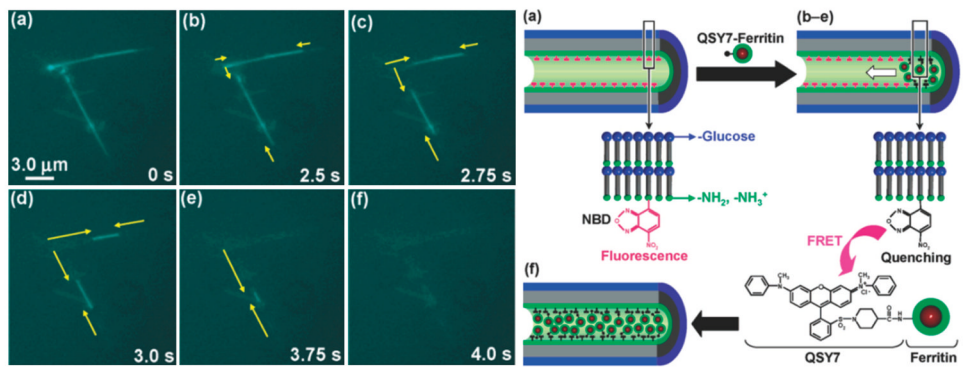


Figure 2.35 Time-lapse fluorescence microscopic images of the NBD nanotubes upon addition of QSY7-ferritin and visualized encapsulation process of ferritin in nanochannels.

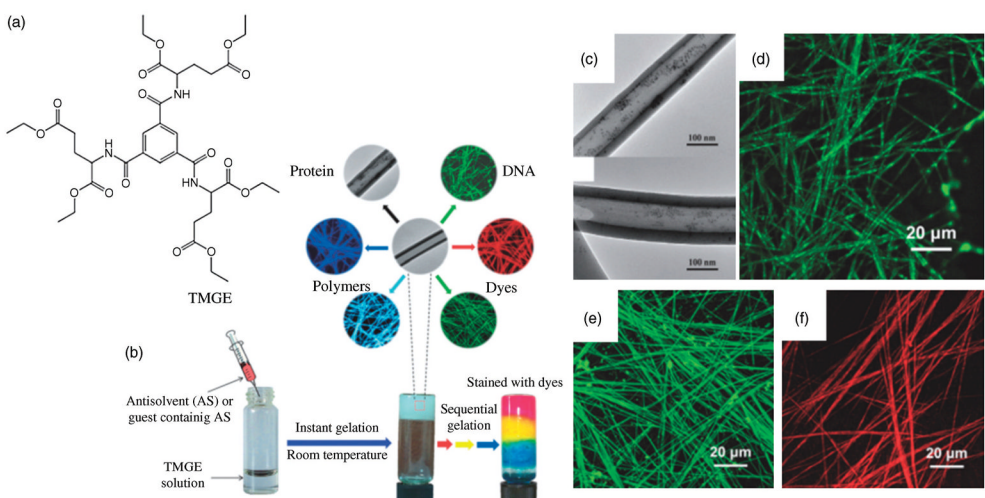


Figure 2.36 (a) Molecular structure of TMGE. (b) Schematic illustration of the process of instant gelation. (c–f) TEM and CLSM images of nanotubes obtained from TMGE instant gel encapsulated with ferritin, ethidium bromide-labeled DNA, ethidium bromide, and rhodamine B.

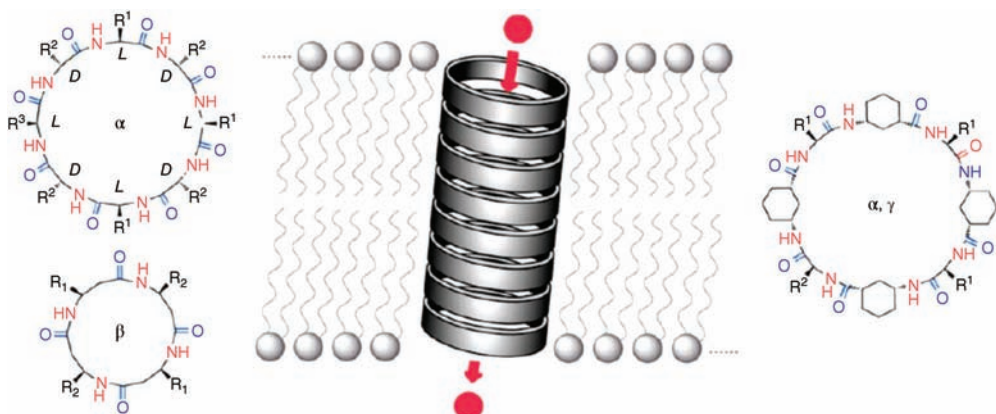


Figure 2.37 Self-assembly of conformationally flat cyclic peptides (CPs) into supramolecular nanotubes and their utilization as the artificial ion channel models.

system for cells, are responsible for selective conduction of water molecules in and out of the cell, while preventing the passage of ions and other solutes to maintain the osmotic homeostasis of a cell. A great revolution will occur in various technical fields if such highly specific and efficient mass transport or separation can be achieved by the artificial systems in a controlled manner. However, in order to simulate the mass transport in the biological channels, creating controllable nanosized pores by efficient methodologies still remains a daunting challenge. With the synthetic modifiability, organic nanotubes with allowed inner and outer diameters, especially formed by cyclic peptide building blocks, were the ideal candidates for constructing the artificial mass transport channels [278].

A simple strategy for the design of artificial membrane ion channels based on the self-assembled cylindrical β -sheet peptide architecture was reported by Ghadiri *et al.* (Figure 2.37). According to the work, the eight-residue cyclic peptide cyclo[-(Trp-D-Leu)₃Gln-D-Leu-], which proved to be ideal for the integration of the nanotube in the nonpolar environment of membrane, was designed. In addition, the driving force for the self-assembly is primarily provided by the enthalpic contribution of H-bonding and the side chain–membrane lipid interactions. After the incorporation of the peptide into the membrane of large unilamellar vesicles, the proton transport ability of the channel was addressed by using a pH-sensitive dye 5(6)-carboxyfluorescein (CF)-loaded vesicles with an induced pH gradient ($pH_{out} = 5.5$; $pH_{in} = 6.5$). The results showed that addition of the peptide to such vesicle suspensions caused a rapid collapse of the pH gradient, suggesting the apparent ion transport activity generated by the cyclic peptide channel. By using micropatch clamp techniques, the transport efficiency and the single-channel conductance of the membrane channel were quantified. The results showed that the stacking of peptide rings displayed good channel-mediated ion transport activity with rates exceeding 10^7 ions s⁻¹.

Since the chiral information can be recognized by the chiral hollow assemblies, the supramolecular assemblies with tubular architecture formed via metal

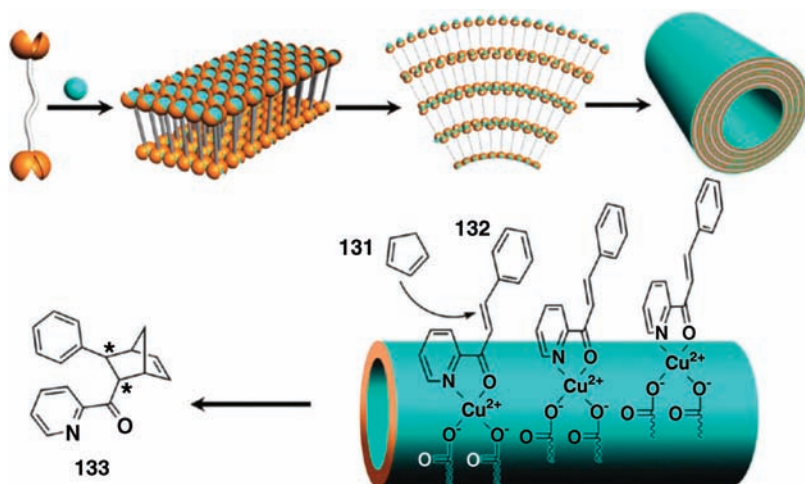


Figure 2.38 Self-assembly of Cu^{2+} -L-HDGA nanotube and its asymmetric catalysis for the Diels–Alder reaction.

coordination interaction and hydrogen bonding are believed to possess an enzyme-like pocket for the arrangement of substrates for asymmetric reaction within a well-defined cavity. Our group has reported the self-assembly of several low molecular weight L-glutamic acid-based gelators, which individually formed helical nanotube or nanofiber structures. As shown in Figure 2.38, in the presence of copper ions, the self-assembly method of these gelators changed significantly [279]. In the case of a bolaamphiphilic glutamic acid, *N,N'*-hexadecanedioyl-di-L-glutamic acid (L-HDGA), the nanotube with a multilayer wall was formed. Such nanotubes showed enhanced-asymmetry catalytic behavior and accelerated the asymmetric Diels–Alder cycloaddition between cyclopentadiene and azachalcone. Although a modest ee value was obtained, the enantiomeric selectivity of the product was still much higher than that of the control experiment without tubular structures under identical conditions. In addition, the Cu^{2+} -mediated nanotubular structure showed a more predominant enantioselectivity than other nanostructures, which suggested that the alignment of the catalytic site on the surface of the nanotube and the stereochemical environment played an important role in producing such enantioselectivity.

2.5.3

Nanofibers

Nanofibers are defined as fibrillar structures with a diameter between 1 and 100 nm. Generally, according to reports, fibers with diameters of less than 1000 nm can also be called nanofibers. The distinct difference between nanofibers and nanotubes is that nanofibers are cylindrical solid structures. At the same time, the nanofibers have larger aspect ratios and specific surface area. Due to

their structural properties, various materials with nanofiber structures based on the self-assembly of organic molecules can be rationally designed and showed broad applications in various fields (e.g., biomedicine, sensors, electronic nano-devices, and catalysis). Herein, we discuss the nanofibers mainly formed by PAs and peptides with alternating hydrophobic and hydrophilic amino acids.

Peptides have been recognized as very useful building blocks for creating different self-assembled nanostructures, in particular β -sheet-forming peptides demonstrating the extraordinary ability to assemble into one-dimensional nanostructures through intermolecular hydrogen bonding. Over the past decade, Stupp and coworkers have designed and synthesized a broad range of peptide amphiphiles. These molecules combining the structural features of amphiphilic surfactants with the functions of bioactive peptides are apt to self-assemble into high aspect ratio nanofibers under specific solution conditions (pH, ionic strength, and temperature). Figure 2.39 shows the chemical structure of a representative PA molecule and its structural features have been discussed earlier. The driving forces that govern the self-assembly of PAs in water arise

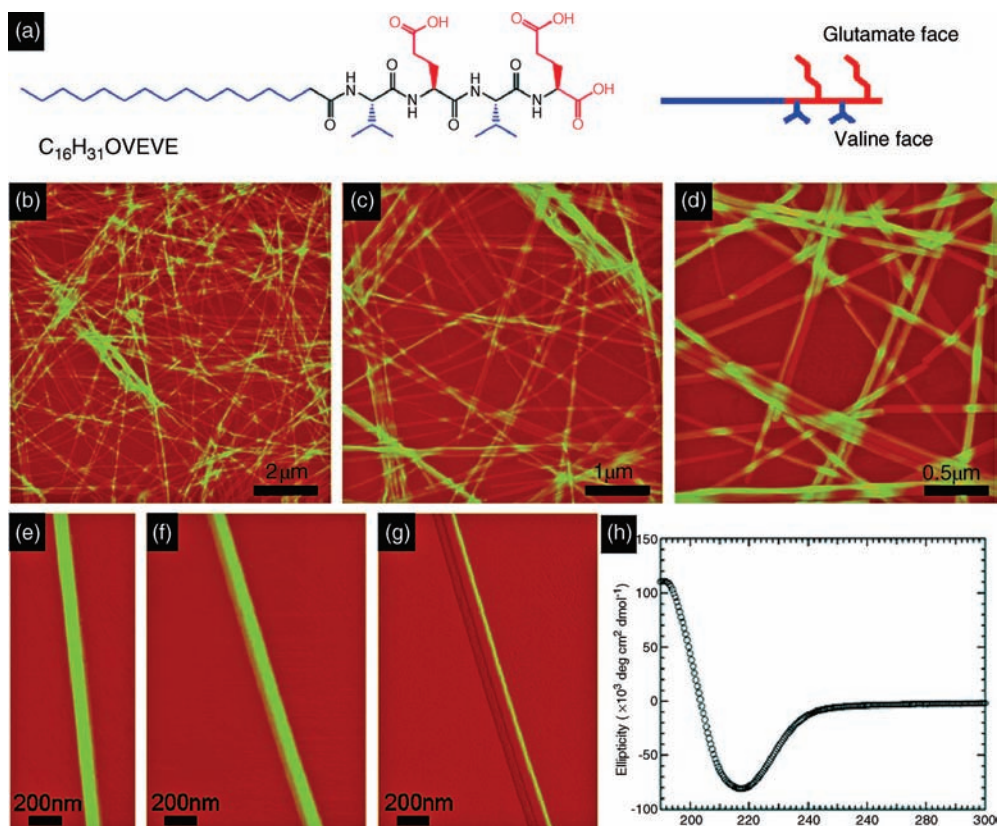


Figure 2.39 Giant nanobelts assembled from a PA containing four amino acids and an alkyl tail.

from at least three major energy contributions: hydrophobic interactions of the alkyl tails, hydrogen bonding among the middle peptide segments, and electrostatic repulsions between the charged amino acids. Molecular simulations of self-assembly behavior of PAs in water revealed that the combination of intermolecular hydrogen bonding among the peptide segments and the hydrophobic collapse of alkyl tails leads to the formation of cylindrical nanofibers in dilute aqueous solutions [280,281]. Through the manipulation of molecular forces that contribute to the self-assembly process, the self-assembled nanofibrillar structures of PAs and their subsequent gelation behavior can be well controlled. This can be effectively realized through (i) the rational molecular design, such as altering the length of the hydrophobic tail and the number of charged groups affecting the self-assembly and gelation behavior [282], the design of the PAs with different middle peptide segments inducing the self-assembled nanostructure transition from nanofibers to nanobelts [283]; (ii) variation of the assembly environment to affect the PA assembly kinetics (pH, ionic strength, concentration, electronic structure, and hydration of counterions) [284]; and (iii) introduction of coassembling molecules [285].

Our group synthesized a peptide amphiphilic dendron that can be used as an efficient hydrogelator and we interestingly found that the incorporation of a series of divalent metal ions can trigger the shrinkage of the hydrogel formed by this PA (Figure 2.40a) [286,287]. Morphological investigation indicated that nanofibers with diameters from 13 to 25 nm were obtained in the shrunken gel. Experimental results demonstrated that the gradual cross-linking between the metal ions and protonated carboxylic acid groups facilitates the formation of nanofibers and promotes the transition of hydration water from carboxyl-bound water to free water to finally undergo macroscopic volume phase transition. Further investigation revealed that the shrinkage of the hydrogel is pH dependent and the gel showed selective shrinkage upon addition of positively charged species while it remained in the gel state when negatively charged species were incorporated. Based on this property, the gel could be used as a matrix to efficiently separate ionic dye mixtures and also can be used as a model drug delivery vehicle for the stepwise release of a two-component drug system (Figure 2.40b).

On the other hand, peptides containing alternating hydrophilic and hydrophobic amino acid residues without long alkyl chains are also known to have a strong tendency to generate nanofiber structures. Short peptide KFE8 (FKFEFKFE) formed a helical ribbon initially, which transformed into fibrillar structures. Molecular dynamics simulation revealed the possibility of double helical β -sheet formation [288]. A peptide Ac-C(FKFE)₂CG-NH₂ sequence flanked with a cysteine (Cys) residue formed macrocyclic structure via disulfide bonding and prevented the β -sheet formation that was needed for self-assembly. On reduction of this disulfide bond, the peptide transformed into the stable β -sheet conformation, which resulted in self-assembled fibrillar structures. At sufficient peptide concentration, it formed rigid hydrogels with viscoelastic properties [289].

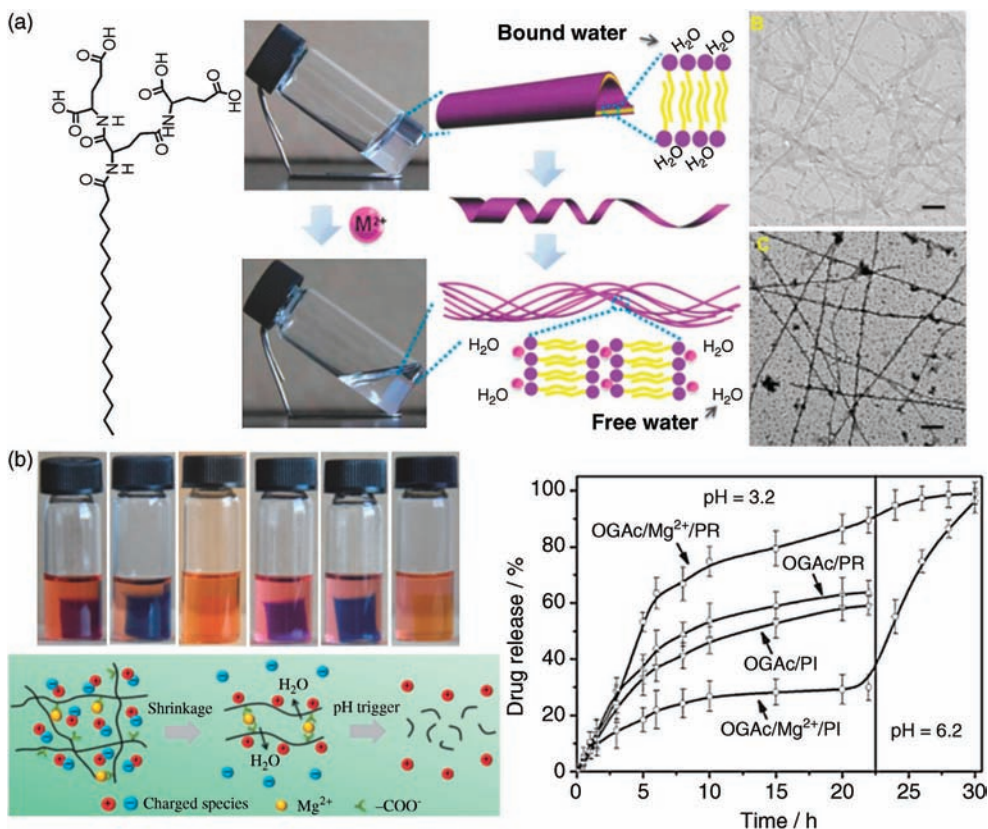


Figure 2.40 (a) Divalent metal ions triggered hydrogel volume shrinkage and the morphological transition during the shrinkage. (b) The shrinkable hydrogel was used as the matrix to realize the dye mixture separation and step release of two-component drugs.

Given the unique structural features and their inherent biocompatibility and biodegradability, the assembled nanofibers formed by β -sheet-forming peptides, in particular, PA molecules, which consist of a hydrophobic core and a hydrophilic shell in aqueous condition, show potential applications in biomedicine. One obvious application is the encapsulation of small molecules, including hydrophobic drugs [290] and semiconducting organic molecules [291], or the surface decoration of other hydrophobic nanostructures such as carbon nanotubes [292]. Another important application of PA nanofibers is the utilization of its charged surface to guide the assembly of inorganic nanoparticles and template inorganic mineralization [293,294].

PA nanofibers can bundle and entangle to form self-supporting 3D networks under physiological conditions, which enables the encapsulation of cells within the nanofiber matrix (Figure 2.41) [295]. The experimental results showed that cells entrapped within PA nanofiber matrices have been found to be viable for

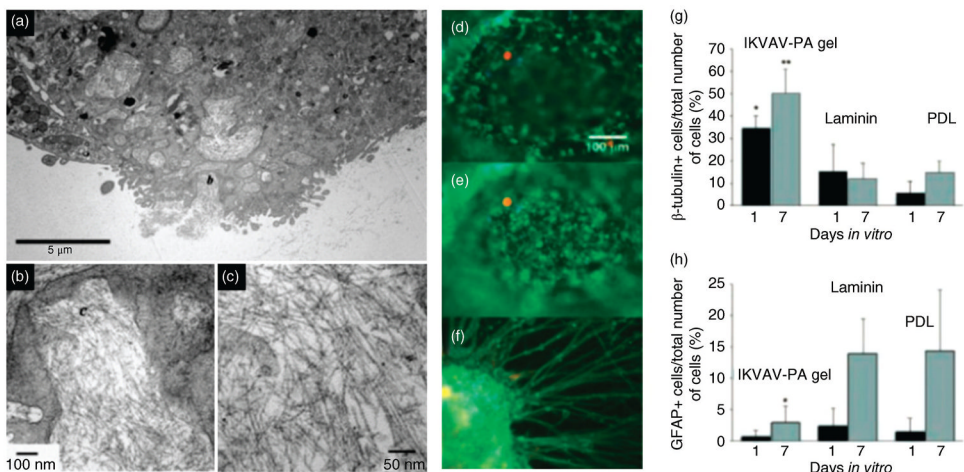


Figure 2.41 TEM micrograph of a cell entrapped in the nanofibrillar matrix internalizing the PA nanofibers and neural progenitor cells (NPCs) cultured under different experimental conditions that showed selective and rapid differentiation.

weeks and can continue to proliferate. They also found that the murine neural progenitor cells cultured within the IKVAV PA quickly undergo selective and rapid differentiation into neurons, while the formation of astrocytes was largely suppressed [159]. Interestingly, this observed selective differentiation was more obvious when cells are cultured with laminin. This rapid selective differentiation is linked to the amplification of bioactive epitope presentation to cells by the nanofibers. The PA nanofibers can be further used to functionalize titanium implants for bone replacement [296,297], angiogenesis [160,298], and regeneration of bone and enamel [299].

2.6

Conclusions and Outlook

Various self-assembly methods and the concepts of the molecular design using covalent and noncovalent bonds have shown their great potential to formulate small molecules into nanostructured entity with the characteristic feature of structural diversity and adjustability, and find widespread applications in many fields. Considering the future development of this field, several challenges should be considered. One is the structural control. Although it seemed that small molecules can be controlled to some extent in their nanostructures based on the molecular design and the utilization of the various noncovalent bonds between molecules, their further growth or self-assembly into larger architectures remains a great challenge. In many material and biological systems, the hierarchical structure plays an important role. Therefore, the structural control of the self-assembly system cannot be stopped at the nanoscale level. It should be extended to larger scale through hierarchical self-assembly.

The second challenge is how to combine multiple components into organized complex architectures. Although we have acquired much knowledge about the intermolecular interactions, structural control, and function development, many of these are limited to one to two components because of the lack of understanding regarding assembly of many different molecules into a complex system in a cooperative or syndetic way such as in the cell. Although there is still a long way to go before we can realize the sophisticated structures such as a cell, a step forward is to fabricate the nanosystem with adaptation and transportation ability.

The third consideration should be the intermolecular interaction and the chemical bonding. As we know, in the development history of chemistry, the covalent bond has occupied a central position. Due to the concept of the supramolecular chemistry, the noncovalent bonds deepened our understanding of natural biological systems, materials, in particular, supra or soft materials, and nanosystems. Chemistry witnessed a great development with these concepts. At present, the concept of dynamic covalent bonds, which is developed following the molecular and supramolecular chemistry, has gained much attention. The stability of covalent bonds and the flexibility of noncovalent bonds showed the feasibility of dynamic covalent chemistry to build more complex structures and

find many applications. The coordination bond, which is sometimes included in the noncovalent bond or dynamic covalent bond, is unique, which combined the molecule (ligand) and metal or metal ions and played an important role in the self-assembly. Full understanding and utilization of all these chemical bonds will help to assemble various small molecules into larger and complex entities beyond nanostructures.

References

- 1 McNaught, A.D. and Wilkinson, A. (1997) *IUPAC Compendium of Chemical Terminology (the Gold Book)*, 2nd edn, Blackwell Scientific Publications, Oxford.
- 2 Puling, L. (1970) *General Chemistry*, Dover Publications, Inc., New York.
- 3 Steed, J.W., Turner, D.R., and Wallace, K.J. (2007) *Core Concepts in Supramolecular Chemistry and Nanochemistry*, John Wiley & Sons, Ltd, Chichester, UK.
- 4 Whitesides, G.M. and Boncheva, M. (2002) Beyond molecules: self-assembly of mesoscopic and macroscopic components. *Proc. Natl. Acad. Sci. USA*, **99** (8), 4769–4774.
- 5 Bai, C. and Liu, M. (2013) From chemistry to nanoscience: not just a matter of size. *Angew. Chem., Int. Ed.*, **52**, 2678–2683.
- 6 Kelsall, R.W., Hamley, I.W., and Geoghegan, M. (eds) (2005) *Nanoscale Science and Technology*, John Wiley & Sons, Ltd, Chichester, UK.
- 7 Pokropivny, V.V. and Skorokhd, V.V. (2008) New dimensionality classifications of nanostructures. *Physica E*, **40**, 2521–2525.
- 8 Pokropivny, V.V. and Skorokhd, V.V. (2007) Classification of nanostructures by dimensionality and concept of surface forms engineering in nanomaterial science. *Mater. Sci. Eng. C*, **27**, 990–993.
- 9 Kustov, E.F. and Nefedov, V.I. (2008) Nanostructures: compositions, structure, and classification. *Russ. J. Coord. Chem.*, **53**, 2103–2170.
- 10 Kharissov, B.I., Kharissova, O.V., and Jose-Yacaman, M. (2010) Nanostructures with animal-like shapes. *Ind. Eng. Chem. Res.*, **49**, 8289–8309.
- 11 Kasai, H., Nalwa, H.S., Oikawa, H., Okada, S., Matsuda, H., Minami, N., Kakuta, A., Ono, K., Mukoh, A., and Nakanishi, H. (1992) A novel preparation method of organic microcrystals. *Jpn. J. Appl. Phys.*, **31**, L1132–L1134.
- 12 Nalwa, H.S., Kasai, H., Kamatani, H., Okada, S., Oikawa, H., Matsuda, H., Kakuta, A., Mukoh, A., and Nakanishi, H. (1993) Fabrication of organic nanocrystals for electronics and photonics. *Adv. Mater.*, **5**, 758–760.
- 13 Kasai, H., Oikawa, H., and Nakanishi, H. (1999) In *Organic Mesoscopic Chemistry* (eds H. Masuhara and F.C. Schryver), Blackwell Science, Oxford, pp. 145–170.
- 14 Kasai, H., Kamatani, H., Yoshikawa, Y., Okada, S., Oikawa, H., Watanabe, A., Itoh, O., and Nakanishi, H. (1997) Crystal size dependence of emission from perylene microcrystals. *Chem. Lett.*, **26**, 1181–1182.
- 15 Oikawa, H., Mitsui, T., Onodera, T., Kasai, H., Nakanishi, H., and Sekiguchi, T. (2003) Crystal size dependence of fluorescence spectra from perylene nanocrystals evaluated by scanning near-field optical microscopy. *Jpn. J. Appl. Phys.*, **42**, L111.
- 16 Kasai, H., Kamatani, H., Okada, S., Oikawa, H., Matsuda, H., and Nakanishi, H. (1996) Size-dependent colors and luminescences of organic microcrystals. *Jpn. J. Appl. Phys. Part 2*, **35** (2B), L221–L223.
- 17 Nakanishi, H. and Katagi, H. (1998) Microcrystals of polydiacetylene derivatives and their linear and nonlinear optical properties. *Supramol. Sci.*, **5**, 289–295.
- 18 An, B.K., Kwon, S.K., Jung, S.D., and Park, S.Y. (2002) Enhanced emission and its switching in fluorescent organic

- nano particles. *J. Am. Chem. Soc.*, **124**, 14410–14415.
- 19** Sun, Y.Y., Liao, J.H., Fang, J.M., Chou, P.T., Shen, C.H., Hsu, C.W., and Chen, L.C. (2006) Fluorescent organic nanoparticles of benzofuran–naphthyridine linked molecules: formation and fluorescence enhancement in aqueous media. *Org. Lett.*, **8**, 3713–3716.
- 20** Palayangoda, S.S., Cai, X., Adhikari, R.M., and Neckers, D.C. (2008) Carbazole-based donor–acceptor compounds: highly fluorescent organic nanoparticles. *Org. Lett.*, **10**, 281–284.
- 21** Gesquiere, A.J., Uwada, T., Asahi, T., Masuhara, H., and Barbara, P.F. (2005) Single molecule spectroscopy of organic dye nanoparticles. *Nano Lett.*, **5**, 1321–1325.
- 22** Tachikawa, T., Chung, H.R., Masuhara, A., Kasai, H., Oikawa, H., Nakanishi, H., Fujitsuka, M., and Majima, T. (2006) *In situ* and *ex situ* observations of the growth dynamics of single perylene nanocrystals in water. *J. Am. Chem. Soc.*, **128**, 15944–15945.
- 23** Fu, H. and Yao, J. (2001) Size effects on the optical properties of organic nanoparticles. *J. Am. Chem. Soc.*, **123**, 1434–1439.
- 24** Xiao, D., Xi, L., Yang, W., Fu, H., Shuai, Z., Fang, Y., and Yao, J. (2003) Size-tunable emission from 1,3-diphenyl-5-(2-anthryl)-2-pyrazoline nanoparticles. *J. Am. Chem. Soc.*, **125**, 6740–6745.
- 25** Fu, H., Loo, B.H., Xiao, D., Xie, R., Ji, X., Yao, J., Zhang, B., and Zhang, L. (2002) Multiple emissions from 1,3-diphenyl-5-pyrenyl-2-pyrazoline nanoparticles: evolution from molecular to nanoscale to bulk materials. *Angew. Chem., Int. Ed.*, **41**, 962–965.
- 26** Xiao, D., Yang, W., Yao, J., Xi, L., Yang, X., and Shuai, Z. (2004) Size-dependent exciton chirality in (*R*)-(+)1,1'-bi-2-naphthol dimethyl ether nanoparticles. *J. Am. Chem. Soc.*, **126**, 15439–15444.
- 27** Li, H. and Yan, H. (2009) Ratiometric fluorescent mercuric sensor based on thiourea–thiadiazole–pyridine linked organic nanoparticles. *J. Phys. Chem. C*, **113**, 7526–7530.
- 28** Das, S., Bwambok, D., El-Zahab, B., Monk, J., de Rooy, S.L., Challa, S., Li, M., Hung, F.R., Baker, G.A., and Warner, I.M. (2010) Nontemplated approach to tuning the spectral properties of cyanine-based fluorescent nanoGUMBOS. *Langmuir*, **26**, 12867–12876.
- 29** Jana, A., Devi, K.S.P., Maiti, T.K., and Singh, N.D.P. (2012) Perylene-3-ylmethanol: fluorescent organic nanoparticles as a single-component photoresponsive nanocarrier with real-time monitoring of anticancer drug release. *J. Am. Chem. Soc.*, **134**, 7656–7659.
- 30** Petkau, K., Kaeser, A., Fischer, I., Brunsved, L., and Schenning, A.P.H.J. (2011) Pre- and postfunctionalized self-assembled π-conjugated fluorescent organic nanoparticles for dual targeting. *J. Am. Chem. Soc.*, **133**, 17063–17071.
- 31** Stevens, A.L., Kaeser, A., Schenning, A.P.H.J., and Herz, L.M. (2012) Morphology-dependent energy transfer dynamics in fluorene-based amphiphile nanoparticles. *ACS Nano*, **6**, 4777–4787.
- 32** Flory, P.J. (1974) Introductory lecture. *Faraday Discuss. Chem. Soc.*, **57**, 7–18.
- 33** Babu, S.S., Möhwald, H., and Nakanishi, T. (2010) Recent progresses in morphology control of supramolecular fullerene assemblies and its applications. *Chem. Soc. Rev.*, **39**, 4021–4035.
- 34** Gleiche, M., Chi, L.F., and Fuchs, H. (2000) Nanoscopic channel lattices with controlled anisotropic wetting. *Nature*, **403**, 173–175.
- 35** Lenhert, S., Gleiche, M., Fuchs, H., and Chi, L.F. (2005) Mechanism of regular pattern formation in reactive dewetting. *ChemPhysChem*, **6**, 2495–2498.
- 36** Chen, X.D., Hirtz, M., Fuchs, H., and Chi, L.F. (2005) Self-organized patterning: regular and spatially tunable luminescent submicrometer stripes over large areas. *Adv. Mater.*, **17**, 2881–2885.
- 37** Chen, X.D., Hirtz, M., Fuchs, H., and Chi, L.F. (2007) Fabrication of gradient mesostructures by Langmuir–Blodgett rotating transfer. *Langmuir*, **23**, 2280–2283.
- 38** Lu, N., Gleiche, M., Zheng, J.W., Lenhert, S., Xu, B., Chi, L.F., and Fuchs, H. (2002)

- Patterned surfaces based on template-directed self-assembly. *Adv. Mater.*, **14**, 1812–1815.
- 39** Chen, X.D., Rogach, A.L., Talapin, D.V., Fuchs, H., and Chi, L.F. (2006) Hierarchical luminescence patterning based on multiscaled self-assembly. *J. Am. Chem. Soc.*, **128**, 9592–9593.
- 40** Zhang, M.Z., Lenhert, S., Wang, M., Chi, L.F., Lu, N., Fuchs, H., and Ming, N.B. (2004) Regular arrays of copper wires formed by template-assisted electrodeposition. *Adv. Mater.*, **16**, 409–413.
- 41** Lenhert, S., Meier, M.B., Meyer, U., Chi, L.F., and Wiesmann, H.P. (2005) Osteoblast alignment, elongation and migration on grooved polystyrene surfaces patterned by Langmuir–Blodgett lithography. *Biomaterials*, **26**, 563–570.
- 42** Wu, X.C., Lenhert, S., Chi, L.F., and Fuchs, H. (2006) Interface interaction controlled transport of CdTe nanoparticles in the microcontact printing process. *Langmuir*, **22**, 7807–7811.
- 43** Li, X., Zhang, L., Wang, X., Shimoyama, I., Sun, X., Seo, W.S., and Dai, H. (2007) Langmuir–Blodgett assembly of densely aligned single-walled carbon nanotubes from bulk materials. *J. Am. Chem. Soc.*, **129**, 4890–4891.
- 44** Choi, S.W., Kang, W.S., Lee, J.H., Najeeb, C.K., Chun, H.S., and Kim, J.H. (2010) Patterning of hierarchically aligned single-walled carbon nanotube Langmuir–Blodgett films by microcontact printing. *Langmuir*, **26**, 15680–15685.
- 45** Shi, H.Y., Hu, B., Yu, X.C., Zha, R.L., Re, X.F., Liu, S.L., Liu, J.W., Feng, M., Xu, A.W., and Yu, S.H. (2010) Ordering of disordered nanowires: spontaneous formation of highly aligned, ultralong Ag nanowire films at oil–water–air interface. *Adv. Funct. Mater.*, **20**, 958–964.
- 46** Li, X., Zhang, G., Bai, X., Su, X., Wang, X., Wang, E., and Dai, H. (2008) Highly conducting graphene sheets and Langmuir–Blodgett films. *Nat. Nanotechnol.*, **3**, 538–542.
- 47** Cote, L.J., Kim, F., and Huang, J. (2009) Langmuir–Blodgett assembly of graphite oxide single layers. *J. Am. Chem. Soc.*, **131**, 1043–1049.
- 48** Muramatsu, M., Akatsuka, K., Ebina, Y., Wang, K., Sasaki, T., Ishida, T., Miyake, K., and Haga, M. (2005) Fabrication of densely packed titania nanosheet films on solid surface by use of Langmuir–Blodgett deposition method without amphiphilic additives. *Langmuir*, **21**, 6590–6595.
- 49** Iler, R.K. (1966) Multilayers of colloidal particles. *J. Colloid Interface Sci.*, **21**, 569–594.
- 50** Blodgett, K.B. (1934) Monomolecular films of fatty acids on glass. *J. Am. Chem. Soc.*, **56**, 495.
- 51** Blodgett, K.B. and Langmuir, I. (1937) Built-up films of barium stearate and their optical properties. *Phys. Rev.*, **51**, 0964–0982.
- 52** Decher, G. and Hong, J.-D. (1991) Buildup of ultrathin multilayer films by a self-assembly process. I. Consecutive adsorption of anionic and cationic bipolar amphiphiles. *Makromol. Chem. Macromol. Symp.*, **46**, 321–327.
- 53** Decher, G. (1997) Fuzzy nanoassemblies: toward layered polymeric multicomposites. *Science*, **277**, 1232–1237.
- 54** Xiang, Y., Lu, S., and Jiang, S. (2012) Layer-by-layer self-assembly in the development of electrochemical energy conversion and storage devices from fuel cells to supercapacitors. *Chem. Soc. Rev.*, **41**, 7291–7321.
- 55** Stockton, W.B. and Rubner, M.F. (1997) Molecular-level processing of conjugated polymers. 4. Layer-by-layer manipulation of polyaniline via hydrogen-bonding interactions. *Macromolecules*, **30**, 2717–2725.
- 56** Chan, E.W.L., Lee, D.C., Ng, M.K., Wu, G., Lee, K.Y.C., and Yu, L. (2002) A novel layer-by-layer approach to immobilization of polymers and nanoclusters. *J. Am. Chem. Soc.*, **124**, 12238–12243.
- 57** Buck, M.E., Zhang, J., and Lynn, D.M. (2007) Layer-by-layer assembly of reactive ultrathin films mediated by click-type reactions of poly(2-alkenyl azlactone)s. *Adv. Mater.*, **19**, 3951–3955.

- 58** Such, G.K., Quinn, J.F., Quinn, A., Tjipto, E., and Caruso, F. (2006) Assembly of ultrathin polymer multilayer films by click chemistry. *J. Am. Chem. Soc.*, **128**, 9318–9319.
- 59** Haga, M., Kobayashi, K., and Terada, K. (2007) Fabrication and functions of surface nanomaterials based on multilayered or nanoarrayed assembly of metal complexes. *Coord. Chem. Rev.*, **251**, 2688–2701.
- 60** Takahashi, S., Sato, K., and Anzai, J. (2012) Layer-by-layer construction of protein architectures through avidin–biotin and lectin–sugar interactions for biosensor applications. *Anal. Bioanal. Chem.*, **402**, 1749–1758.
- 61** Li, M., Ishihara, S., Akada, M., Liao, M., Sang, L., Hill, J.P., Krishnan, V., Ma, Y., and Ariga, K. (2011) Electrochemical-coupling layer-by-layer (ECC-LbL) assembly. *J. Am. Chem. Soc.*, **133**, 7348–7351.
- 62** Jiang, C. and Tsukruk, V.V. (2006) Freestanding nanostructures via layer-by-layer assembly. *Adv. Mater.*, **18**, 829–840.
- 63** Cho, J., Char, K., Hong, J.D., and Lee, K.B. (2001) Fabrication of highly ordered multilayer films using a spin self-assembly method. *Adv. Mater.*, **16**, 1076–1078.
- 64** Chiarelli, P.A., Johal, M.S., Carron, J.L., Roberts, J.B., Robinson, J.M., and Wang, H.L. (2001) Controlled fabrication of polyelectrolyte multilayer thin films using spin-assembly. *Adv. Mater.*, **16**, 1167–1171.
- 65** Campbell, V.E., Chiarelli, P.A., Kaur, S., and Johal, M.S. (2005) Coadsorption of a polyanion and an azobenzene dye in self-assembled and spin-assembled polyelectrolyte multilayers. *Chem. Mater.*, **17**, 186–190.
- 66** Schlenoff, J.B., Dubas, S.T., and Farhat, T. (2000) Sprayed polyelectrolyte multilayers. *Langmuir*, **26**, 9968–9969.
- 67** Zhao, N., Shi, F., Wang, Z., and Zhang, X. (2005) Combining layer-by-layer assembly with electrodeposition of silver aggregates for fabricating superhydrophobic surfaces. *Langmuir*, **21**, 4713–4716.
- 68** Jiang, X., Zheng, H., Gourdin, S., and Hammond, P.T. (2002) Polymer-on-polymer stamping: universal approaches to chemically patterned surfaces. *Langmuir*, **18**, 2607–2615.
- 69** Zheng, H., Rubner, M.F., and Hammond, P.T. (2002) Particle assembly on patterned “plus/minus” polyelectrolyte surfaces via polymer-on-polymer stamping. *Langmuir*, **18**, 4505–4510.
- 70** Tokuhisa, H., and Hammond, P.T. (2004) Nonlithographic micro- and nanopatterning of TiO₂ using polymer stamped molecular templates. *Langmuir*, **20**, 1436–1441.
- 71** Shi, F., Wang, Z., Zhao, N., and Zhang, X. (2005) Patterned polyelectrolyte multilayer: surface modification for enhancing selective adsorption. *Langmuir*, **21**, 1599–1602.
- 72** Sun, J., Gao, M., Zhu, M., Feldmann, J., and Möhwald, H. (2002) Layer-by-layer depositions of polyelectrolyte/CdTe nanocrystal films controlled by electric fields. *J. Mater. Chem.*, **12**, 1775–1778.
- 73** Jiang, C., Markutsya, S., and Tsukruk, V.V. (2004) Compliant, robust, and truly nanoscale free-standing multilayer films fabricated using spin-assisted layer-by-layer assembly. *Adv. Mater.*, **16**, 157–161.
- 74** Jiang, C., Lio, W.Y., and Tsukruk, V.V. (2005) Surface enhanced Raman scattering monitoring of chain alignment in freely suspended nanomembranes. *Phys. Rev. Lett.*, **95**, 115503.
- 75** Izquierdo, A., Ono, S.S., Voegel, J.C., Schaaf, P., and Decher, G. (2005) Dipping versus spraying: exploring the deposition conditions for speeding up layer-by-layer assembly. *Langmuir*, **21**, 7558–7567.
- 76** Michel, M., Izquierdo, A., Decher, G., Voegel, J.C., Schaaf, P., and Ball, V. (2005) Layer by layer self-assembled polyelectrolyte multilayers with embedded phospholipid vesicles obtained by spraying: integrity of the vesicles. *Langmuir*, **21**, 7854–7859.
- 77** Park, J., Fouché, L.D., and Hammond, P.T. (2005) Multicomponent patterning of layer-by-layer assembled polyelectrolyte/nanoparticle composite thin films with controlled alignment. *Adv. Mater.*, **17**, 2575–2579.
- 78** Jiang, C., Markutsya, S., Shulha, H., and Tsukruk, V.V. (2005) Freely suspended

- gold nanoparticle arrays. *Adv. Mater.*, **17**, 1669–1673.
- 79** Mamedov, A.A. and Kotov, N.A. (2000) Free-standing layer-by-layer assembled films of magnetite nanoparticles. *Langmuir*, **16**, 5530–5533.
- 80** Jiang, C., Markutsya, S., Pikus, Y., and Tsukruk, V.V. (2004) Freely suspended nanocomposite membranes as highly sensitive sensors. *Nat. Mater.*, **3**, 721–728.
- 81** Markutsya, S., Jiang, C., Pikus, Y., and Tsukruk, V.V. (2005) Freely suspended layer-by-layer nanomembranes: testing micromechanical properties. *Adv. Funct. Mater.*, **15**, 771–780.
- 82** Kim, H.J., Lee, K., Kumar, S., and Kim, J. (2005) Dynamic sequential layer-by-layer deposition method for fast and region-selective multilayer thin film fabrication. *Langmuir*, **21**, 8532–8538.
- 83** Liang, Z., Susha, A.S., Yu, A., and Caruso, F. (2003) Nanotubes prepared by layer-by-layer coating of porous membrane templates. *Adv. Mater.*, **15**, 1849–1853.
- 84** Guo, Y.G., Hu, J.S., Liang, H.P., Wan, L.J., and Bai, C.L. (2005) TiO₂-based composite nanotube arrays prepared via layer-by-layer assembly. *Adv. Funct. Mater.*, **15**, 196–202.
- 85** Shchukin, D.S., Ustinovich, E.A., Sukhorukov, G.B., Möhwald, H., and Sviridov, D.V. (2005) Metallized polyelectrolyte microcapsules. *Adv. Mater.*, **17**, 468–472.
- 86** Jiang, L.X., Peng, Y., Yan, Y., and Huang, J.B. (2011) Aqueous self-assembly of SDS@2β-CD complexes: lamellae and vesicles. *Soft Matter*, **7**, 1726–1731.
- 87** Jiang, L.X., Yan, Y., and Huang, J.B. (2011) Zwitterionic surfactant/cyclodextrin hydrogel: microtubes and multiple responses. *Soft Matter*, **7**, 10417–10423.
- 88** Jiang, L.X., Yan, Y., and Huang, J.B. (2011) Versatility of cyclodextrins in self-assembly systems of amphiphiles. *Adv. Colloid Interface Sci.*, **169**, 13–25.
- 89** Dong, R. and Hao, J. (2010) Complex fluids of poly(oxyethylene) monoalkyl ether nonionic surfactants. *Chem. Rev.*, **110**, 4978–5022.
- 90** Ma, H. and Hao, J. (2011) Ordered patterns and structures via interfacial self-assembly: superlattices, honeycomb structures and coffee rings. *Chem. Soc. Rev.*, **40**, 5457–5471.
- 91** Palmer, L.C. and Stupp, S.I. (2008) Molecular self-assembly into one-dimensional nanostructures. *Acc. Chem. Res.*, **41**, 1674–1684.
- 92** Zang, L., Che, Y., and Moore, J.S. (2008) One-dimensional self-assembly of planar π-conjugated molecules: adaptable building blocks for organic nanodevices. *Acc. Chem. Res.*, **41**, 1596–1608.
- 93** Qiu, Y.F., Chen, P.L., and Liu, M.H. (2010) Evolution of various porphyrin nanostructures via an oil/aqueous medium: controlled self-assembly, further organization, and supramolecular chirality. *J. Am. Chem. Soc.*, **132**, 9644–9652.
- 94** Atwood, J.L. and Steed, J.W. (eds) (2004) *Encyclopedia of Supramolecular Chemistry*, Marcel Dekker, New York.
- 95** Robertazzi, A., Krull, F., Knapp, E.-W., and Gamez, P. (2011) Recent advances in anion–π interactions. *CrystEngComm*, **13**, 3293–3300.
- 96** Steed, J.W. and Atwood, J.L. (2009) *Supramolecular Chemistry*, 2nd edn, John Wiley & Sons, Ltd, Chichester, UK.
- 97** Frontera, A., Quiñonero, D., and Deyà, P.M. (2011) Cation–π and anion–π interactions. *Wiley Interdiscip. Rev.: Comput. Mol. Sci.*, **1**, 440–459.
- 98** Sorenti, A., Illa, O., and Ortúño, R.M. (2013) Amphiphiles in aqueous solution: well beyond a soap bubble. *Chem. Soc. Rev.*, **42**, 8200–8219.
- 99** Fuhrhop, J.H. and Helfrich, W. (1993) Fluid and solid fibers made of lipid molecular bilayers. *Chem. Rev.*, **93**, 1565–1582.
- 100** Lin, Y., Wang, A., Qiao, Y., Gao, C., Drechsler, M., Ye, J., Yan, Y., and Huang, J. (2010) Rationally designed helical nanofibers via multiple non-covalent interactions: fabrication and modulation. *Soft Matter*, **6**, 2031–2036.
- 101** Jung, J.H., John, G., Yoshida, K., and Shimizu, T. (2002) Self-assembling structures of long-chain phenyl glucoside influenced by the introduction of double bonds. *J. Am. Chem. Soc.*, **124**, 10674–10675.

- 102** Kamiya, S., Minamikawa, H., Jung, J.H., Yang, B., Masuda, M., and Shimizu, T. (2005) Molecular structure of glucopyranosylamide lipid and nanotube morphology. *Langmuir*, **21**, 743–750.
- 103** Muraoka, T., Cui, H., and Stupp, S.I. (2008) Quadruple helix formation of a photoresponsive peptide amphiphile and its light-triggered dissociation into single fibers. *J. Am. Chem. Soc.*, **130**, 2946–2947.
- 104** Fuhrhop, J.H. and Wang, T. (2004) Bolaamphiphiles. *Chem. Rev.*, **104**, 2901–2938.
- 105** Zhan, C., Gao, P., and Liu, M. (2005) Self-assembled helical spherical-nanotubes from an L-glutamic acid based bolaamphiphilic low molecular mass organogelator. *Chem. Commun.*, **41**, 462–464.
- 106** Gao, P. and Liu, M. (2006) Compression induced helical nanotubes in a spreading film of a bolaamphiphile at the air/water interface. *Langmuir*, **22**, 6727–6729.
- 107** Wu, G., Thomas, J., Smet, M., Wang, Z., and Zhang, X. (2014) Controlling the self-assembly of cationic bolaamphiphiles: hydrotropic counteranions determine aggregated structures. *Chem. Sci.*, **5**, 3267–3274.
- 108** Nuraje, N., Bai, H., and Su, K. (2013) Bolaamphiphilic molecules: assembly and applications. *Prog. Polym. Sci.*, **38**, 302–343.
- 109** Masuda, M. and Shimizu, T. (2004) Lipid nanotubes and microtubes: experimental evidence for unsymmetrical monolayer membrane formation from unsymmetrical bolaamphiphiles. *Langmuir*, **20**, 5969–5977.
- 110** Song, J., Cheng, Q., Kopta, S., and Stevens, R.C. (2001) Modulating artificial membrane morphology: pH-induced chromatic transition and nanostructural transformation of a bolaamphiphilic conjugated polymer from blue helical ribbons to red nanofibers. *J. Am. Chem. Soc.*, **123**, 3205–3213.
- 111** Maran, U., Conley, H., Frank, M., Arif, A.M., Orendt, A.M., Britt, D., Hlady, V., Davis, R., and Stang, P.J. (2008) Giant micelles of organoplatinum(II) gemini amphiphiles. *Langmuir*, **24**, 5400–5410.
- 112** Brizard, A., Oda, R., and Huc, I. (2005) Chirality effects in self-assembled fibrillar networks. *Top. Curr. Chem.*, **256**, 167–218.
- 113** Delclos, T., Aimé, C., Pouget, E., Brizard, A., Huc, I., Delville, M.H., and Oda, R. (2008) Individualized silica nanohelices and nanotubes: tuning inorganic nanostructures using lipidic self-assemblies. *Nano Lett.*, **8**, 1929–1935.
- 114** Zhang, G. and Liu, M. (2008) Interfacial assemblies of cyanine dyes and gemini amphiphiles with rigid spacers: regulation and interconversion of the aggregates. *J. Phys. Chem. B*, **112**, 7430–7437.
- 115** Gillissen, M.A., Koenigs, M.M., Spiering, J.J., Vekemans, J.A., Palmans, A.R., Voets, I.K., and Meijer, E.W. (2014) Triple helix formation in amphiphilic discotics: demystifying solvent effects in supramolecular self-assembly. *J. Am. Chem. Soc.*, **136**, 336–342.
- 116** Ajayaghosh, A., Chithra, P., and Varghese, R. (2007) Self-assembly of tripodal squaraines: cation-assisted expression of molecular chirality and change from spherical to helical morphology. *Angew. Chem., Int. Ed.*, **46**, 230–233.
- 117** Fernández, G., García, F., and Sánchez, L. (2008) Morphological changes in the self-assembly of a radial oligo-phenylene ethynylene amphiphilic system. *Chem. Commun.*, **44**, 6567–6569.
- 118** Lee, S., Oh, S., Lee, J., Malpani, Y., Jung, Y.S., Kang, B., Lee, J.Y., Ozasa, K., Isoshina, T., Lee, S.Y., Hara, M., Hashizume, D., and Kim, J.M. (2013) Stimulus-responsive azobenzene supramolecules: fibers, gels, and hollow spheres. *Langmuir*, **29**, 5869–5877.
- 119** Lv, K., Zhang, L., and Liu, M. (2014) Self-assembly of triangular amphiphiles into diverse nano/microstructures and release behavior of the hollow sphere. *Langmuir*, **30**, 9295–9302.
- 120** Zhang, X. and Wang, C. (2011) Supramolecular amphiphiles. *Chem. Soc. Rev.*, **40**, 94–101.
- 121** Liu, K., Wang, C., Li, Z., and Zhang, X. (2011) Superamphiphiles based on directional charge-transfer interactions: from supramolecular engineering to

- well-defined nanostructures. *Angew. Chem., Int. Ed.*, **50**, 4952–4956.
- 122** Wang, C., Guo, Y., Wang, Y., Xu, H., Wang, R., and Zhang, X. (2009) Supramolecular amphiphiles based on a water-soluble charge-transfer complex: fabrication of ultralong nanofibers with tunable straightness. *Angew. Chem., Int. Ed.*, **48**, 8962–8965.
- 123** Han, P., Li, S., Wang, C., Xu, H., Wang, Z., Zhang, X., Thomas, J., and Smet, M. (2011) UV-responsive polymeric superamphiphile based on a complex of malachite green derivative and a double hydrophilic block copolymer. *Langmuir*, **27**, 14108–14111.
- 124** de Loos, M., Feringa, B.L., and van Esch, J.H. (2005) Design and application of self-assembled low molecular weight hydrogels. *Eur. J. Org. Chem.*, 3615–3631.
- 125** Lin, Y.C. and Weiss, R.G. (1987) A novel gelator of organic liquids and the properties of gels. *Macromolecules*, **20**, 414–417.
- 126** Terech, P., Ostuni, E., and Weiss, R.G. (1996) Structural study of cholesteryl anthraquinone-2-carboxylate (CAQ) physical organogels by neutron and X-ray small angle scattering. *J. Phys. Chem.*, **100**, 3759–3766.
- 127** Lin, Y., Kachar, B., and Weiss, R.G. (1989) Liquid-crystalline solvents as mechanistic probes. Part 37. Novel family of gelators of organic fluids and the structure of their gels. *J. Am. Chem. Soc.*, **111**, 5542–5551.
- 128** Murata, K., Aoki, M., Nishi, T., Ikeda, A., and Shinkai, S. (1991) New cholesterol-based gelators with light-responsive and metal-responsive functions. *J. Chem. Soc., Chem. Commun.*, 1715–1718.
- 129** Murata, K., Aoki, M., Suzuki, T., Harada, T., Kawabata, H., Komori, T., Ohseto, F., Ueda, K., and Shinkai, S. (1994) Thermal and light control of the sol–gel phase transition in cholesterol-based organic gels. Novel helical aggregation modes as detected by circular dichroism and electron microscopic observation. *J. Am. Chem. Soc.*, **116**, 6664–6676.
- 130** Jeong, S.W., Murata, K., and Shinkai, S. (1996) Dual-component cholesterol-based gelators bearing complementary hydrogen-bonding sites. *Supramol. Sci.*, **3**, 83–86.
- 131** Shinkai, S. and Murata, K. (1998) Cholesterol-based functional tectons as versatile building-blocks for liquid crystals, organic gels and monolayers. *J. Mater. Chem.*, **8**, 485–495.
- 132** Amaike, M., Kobayashi, H., and Shinkai, S. (2000) New organogelators bearing both sugar and cholesterol units. An approach toward molecular design of universal gelators. *Bull. Chem. Soc. Jpn.*, **73**, 2553–2558.
- 133** Terech, P. and Weiss, R.G. (1997) Low molecular mass gelators of organic liquids and the properties of their gels. *Chem. Rev.*, **97**, 3133–3159.
- 134** Abdallah, D.J. and Weiss, R.G. (2000) *n*-Alkanes gel *n*-alkanes (and many other organic liquids). *Langmuir*, **16**, 352–355.
- 135** Tachibana, T., Mori, T., and Hori, K. (1980) Chiral mesophases of 12-hydroxyoctadecanoic acid in jelly and in the solid state. I. A new type of lyotropic mesophase in jelly with organic solvents. *Bull. Chem. Soc. Jpn.*, **53**, 1714–1719.
- 136** Tachibana, T., Mori, T., and Hori, K. (1981) Chiral mesophases of 12-hydroxyoctadecanoic acid in jelly and in the solid state. II. A new type of mesomorphic solid state. *Bull. Chem. Soc. Jpn.*, **54**, 73–80.
- 137** Terech, P., Rodriguez, V., Barnes, J.D., and McKenna, G.B. (1994) Organogels and aerogels of racemic and chiral 12-hydroxyoctadecanoic acid. *Langmuir*, **10**, 3406–3418.
- 138** Araki, K. and Yoshikawa, I. (2005) Nucleobase-containing gelators. *Top. Curr. Chem.*, **256**, 133–165.
- 139** Shimizu, T. (2002) Bottom-up synthesis and structural properties of self-assembled high-axial-ratio nanostructures. *Macromol. Rapid Commun.*, **23**, 311–331.
- 140** Shimizu, T., Iwaura, R., Masuda, M., Hanada, T., and Yase, K. (2001) Internucleobase-interaction-directed self-assembly of nanofibers from homo- and heteroditopic 1,ω-nucleobase bolaamphiphiles. *J. Am. Chem. Soc.*, **123**, 5947–5955.

- 141** Iwaura, R., Yoshida, K., Masuda, M., Ohnishi-Kameyama, M., Yoshida, M., and Shimizu, T. (2003) Oligonucleotide-templated self-assembly of nucleotide bolaamphiphiles: DNA-like nanofibers edged by a double-helical arrangement of A-T base pairs. *Angew. Chem., Int. Ed.*, **42**, 1009–1012.
- 142** Iwaura, R., Ohnishi-Kameyama, M., Yoshida, M., and Shimizu, T. (2002) Detection of complementary hydrogen bond complexes in water by electrospray ionization-Fourier-transform ion cyclotron resonance mass spectrometry. *Chem. Commun.*, **38**, 2658–2659.
- 143** Iwaura, R., Yoshida, K., Masuda, M., Yase, K., and Shimizu, T. (2002) Spontaneous fiber formation and hydrogelation of nucleotide bolaamphiphiles. *Chem. Mater.*, **14**, 3047–3053.
- 144** Park, S.M., Lee, Y.S., and Kim, B.H. (2003) Novel low-molecular-weight hydrogelators based on 2'-deoxyuridine. *Chem. Commun.*, 2912–2913.
- 145** Suzuki, M. and Hanabusa, K. (2009) L-Lysine-based low-molecular-weight gelators. *Chem. Soc. Rev.*, **38**, 967–975.
- 146** Duan, P., Zhu, X., and Liu, M. (2011) Isomeric effect in the self-assembly of pyridine-containing L-glutamic lipid: substituent position controlled morphology and supramolecular chirality. *Chem. Commun.*, **47**, 5569–5571.
- 147** Zhu, X., Li, Y., Duan, P., and Liu, M. (2010) Self-assembled ultralong chiral nanotubes and tuning of their chirality through the mixing of enantiomeric components. *Chem. Eur. J.*, **16**, 8034–8040.
- 148** Wang, X., Duan, P., and Liu, M. (2012) Universal chiral twist via metal ion induction in the organogel of terephthalic acid substituted amphiphilic L-glutamide. *Chem. Commun.*, **48**, 7501–7503.
- 149** Liu, C., Jin, Q., Lv, K., Zhang, L., and Liu, M. (2014) Water tuned the helical nanostructures and supramolecular chirality in organogels. *Chem. Commun.*, **50**, 3702–3705.
- 150** Cao, H., Yuan, Q., Zhu, X., Zhao, Y.P., and Liu, M. (2012) Hierarchical self-assembly of achiral amino acid derivatives into dendritic chiral nanotwists. *Langmuir*, **28**, 15410–15417.
- 151** Jin, Q., Zhang, L., and Liu, M. (2013) Solvent-polarity-tuned morphology and inversion of supramolecular chirality in a self-assembled pyridylpyrazole-linked glutamide derivative: nanofibers, nanotwists, nanotubes, and microtubes. *Chem. Eur. J.*, **19**, 9234–9241.
- 152** Duan, P.F., Li, Y.G., and Liu, M.H. (2010) Preparation of optical active polydiacetylene through gelating and the control of supramolecular chirality. *Sci. China Chem.*, **53**, 432–437.
- 153** Jayawarna, V., Ali, M., Jowitt, T.A., Miller, A.F., Saiani, A., Gough, J.E., and Ulijn, R.V. (2006) Nanostructured hydrogels for three-dimensional cell culture through self-assembly of fluoresylmethoxycarbonyl-dipeptides. *Adv. Mater.*, **18**, 611–614.
- 154** Zhou, M., Smith, A.M., Das, A.K., Hodson, N.W., Collins, R.F., Ulijn, R.V., and Gough, J.E. (2009) Self-assembled peptide-based hydrogels as scaffolds for anchorage-dependent cells. *Biomaterials*, **30**, 2523–2530.
- 155** Jayawarna, V., Richardson, S.M., Hirst, A.R., Hodson, N.W., Saiani, A., Gough, J.E., and Ulijn, R.V. (2009) Introducing chemical functionality in Fmoc-peptide gels for cell culture. *Acta Biomater.*, **5**, 934–943.
- 156** Yang, Z., Liang, G., and Xu, B. (2008) Enzymatic hydrogelation of small molecules. *Acc. Chem. Res.*, **41**, 315–326.
- 157** Tomasini, C. and Castellucci, N. (2013) Peptides and peptidomimetics that behave as low molecular weight gelators. *Chem. Soc. Rev.*, **42**, 156–172.
- 158** Hartgerink, J.D., Beniash, E., and Stupp, S.I. (2001) Self-assembly and mineralization of peptide-amphiphile nanofibers. *Science*, **294**, 1684–1688.
- 159** Silva, G.A., Czeisler, C., Niece, K.L., Beniash, E., Harrington, D.A., Kessler, J.A., and Stupp, S.I. (2004) Selective differentiation of neural progenitor cells by high-epitope density nanofibers. *Science*, **303**, 1352–1355.
- 160** Rajangam, K., Behanna, H.A., Hui, M.J., Han, X.Q., Hulvat, J.F., Lomasney, J.W.,

- and Stupp, S.I. (2006) Heparin binding nanostructures to promote growth of blood vessels. *Nano Lett.*, **6**, 2086–2090.
- 161** Yoza, K., Amanokura, N., Ono, Y., Akao, T., Shimori, H., Takeuchi, M., Shinkai, S., and Reinhoudt, D.N. (1999) Sugar-integrated gelators of organic solvents: their remarkable diversity in gelation ability and aggregate structure. *Chem. Eur. J.*, **5**, 2722–2729.
- 162** Gronwald, O. and Shinkai, S. (2001) Sugar-integrated gelators of organic solvents. *Chem. Eur. J.*, **7** (20), 4328–4334.
- 163** Gronwald, O., Sakurai, K., Luboradzki, R., Kimura, T., and Shinkai, S. (2001) Further evidence for the gelation ability–structure correlation in sugar-based gelators. *Carbohydr. Res.*, **331**, 307–318.
- 164** Jung, J.H., John, G., Masuda, M., Yoshida, K., Shinkai, S., and Shimizu, T. (2001) Self-assembly of a sugar-based gelator in water: its remarkable diversity in gelation ability and aggregate structure. *Langmuir*, **17**, 7229–7232.
- 165** Hamachi, I., Kiyonaka, S., and Shinkai, S. (2000) Solid phase lipid synthesis (SPLS) for construction of an artificial glycolipid library. *Chem. Commun.*, **36**, 1281–1282.
- 166** Hamachi, I., Kiyonaka, S., and Shinkai, S. (2001) Solid-phase lipid synthesis (SPLS)-2: incidental discovery of organogelators based on artificial glycolipids. *Tetrahedron Lett.*, **42**, 6141–6145.
- 167** Kiyonaka, S., Sugiyasu, K., Shinkai, S., and Hamachi, I. (2002) First thermally responsive supramolecular polymer based on glycosylated amino acid. *J. Am. Chem. Soc.*, **124**, 10954–10955.
- 168** Zhou, S.L., Matsumoto, S., Tian, H.D., Yamane, H., Ojida, A., Kiyonaka, S., and Hamachi, I. (2005) pH-responsive shrinkage/swelling of a supramolecular hydrogel composed of two small amphiphilic molecules. *Chem. Eur. J.*, **11**, 1130–1136.
- 169** Kiyonaka, S., Zhou, S.L., and Hamachi, I. (2003) pH-responsive phase transition of supramolecular hydrogel consisting of glycosylated amino acetate and carboxylic acid derivative. *Supramol. Chem.*, **15**, 521–528.
- 170** Kiyonaka, S., Sada, K., Yoshimura, I., Shinkai, S., Kato, N., and Hamachi, I. (2004) Semi-wet peptide/protein array using supramolecular hydrogel. *Nat. Mater.*, **3**, 58–64.
- 171** Tamaru, S.I., Kiyonaka, S., and Hamachi, I. (2005) Three distinct read-out modes for enzyme activity can operate in a semi-wet supramolecular hydrogel. *Chem. Eur. J.*, **11**, 7294–7304.
- 172** Koshi, Y., Nakata, E., Yamane, H., and Hamachi, I. (2006) A fluorescent lectin array using supramolecular hydrogel for simple detection and pattern profiling for various glycoconjugates. *J. Am. Chem. Soc.*, **128**, 10413–10422.
- 173** Müllen, K. and Scherf, U. (2006) *Organic Light Emitting Devices*, Wiley-VCH Verlag GmbH, Weinheim, Germany.
- 174** Muccini, M. (2006) A bright future for organic field-effect transistors. *Nat. Mater.*, **5**, 605–613.
- 175** Mas-Torrent, M. and Rovira, C. (2011) Role of molecular order and solid-state structure in organic field-effect transistors. *Chem. Rev.*, **111**, 4833–4856.
- 176** Hains, A.W., Liang, Z., Woodhouse, M.A., and Gregg, B.A. (2010) Molecular semiconductors in organic photovoltaic cells. *Chem. Rev.*, **110**, 6689–6735.
- 177** Sun, S.-S. and Sariciftci, N.S. (2005) *Organic Photovoltaics: Mechanisms, Materials and Devices*, Taylor & Francis, Boca Raton, FL.
- 178** Hasobe, T., Oki, H., Sandanayaka, A.S.D., and Atula, S.D. (2008) Sonication-assisted supramolecular nanorods of meso-diaryl-substituted porphyrins. *Chem. Commun.*, 724–726.
- 179** Wang, Z., Ho, K.J., Medforth, C.J., and Shelnutt, J.A. (2006) Porphyrin nanofiber bundles from phase-transfer ionic self-assembly and their photocatalytic self-metallization. *Adv. Mater.*, **18**, 2557–2560.
- 180** Wang, Z., Medforth, C.J., and Shelnutt, J.A. (2004) Self-metallization of photocatalytic porphyrin nanotubes. *J. Am. Chem. Soc.*, **126**, 16720–16721.
- 181** Wang, Z., Medforth, C.J., and Shelnutt, J.A. (2004) Porphyrin nanotubes by ionic self-assembly. *J. Am. Chem. Soc.*, **126**, 15954–15955.

- 182** Wang, Z., Li, Z., Medforth, C.J., and Shelnutt, J.A. (2007) Self-assembly and self-metallization of porphyrin nanosheets. *J. Am. Chem. Soc.*, **129**, 2440–2441.
- 183** Yoon, S.M., Hwang, I.C., Kim, K.S., and Choi, H.C. (2009) Synthesis of single-crystal tetra(4-pyridyl)porphyrin rectangular nanotubes in the vapor phase. *Angew. Chem., Int. Ed.*, **48**, 2506–2509.
- 184** Hasobe, T., Sandanayaka, A.S.D., Wada, T., and Araki, Y. (2008) Fullerene-encapsulated porphyrin hexagonal nanorods. An anisotropic donor–acceptor composite for efficient photoinduced electron transfer and light energy conversion. *Chem. Commun.*, 3372–3374.
- 185** Ji, H.X., Hu, J.S., and Wan, L.J. (2008) ZnOEP based phototransistor: signal amplification and light-controlled switch. *Chem. Commun.*, 2653–2655.
- 186** Schwab, A.D., Smith, D.E., Bond-Watts, B., Johnston, D.E., Hone, J., Johnson, A.T., de Paula, J.C., and Smith, W.F. (2004) Photoconductivity of self-assembled porphyrin nanorods. *Nano Lett.*, **4**, 1261–1265.
- 187** Hu, J.S., Guo, Y.G., Liang, H.P., Wan, L.J., and Jiang, L. (2005) Three-dimensional self-organization of supramolecular self-assembled porphyrin hollow hexagonal nanoprisms. *J. Am. Chem. Soc.*, **127**, 17090–17095.
- 188** Lee, S.J., Malliakas, C.D., Kanatzidis, M.G., Hupp, J.T., and Nguyen, S.T. (2008) Amphiphilic porphyrin nanocrystals: morphology tuning and hierarchical assembly. *Adv. Mater.*, **20**, 3543–3549.
- 189** Lee, S.J., Hupp, J.T., and Nguyen, S.T. (2008) Growth of narrowly dispersed porphyrin nanowires and their hierarchical assembly into macroscopic columns. *J. Am. Chem. Soc.*, **130**, 9632–9633.
- 190** Aida, T. and Fukushima, T. (2007) Soft materials with graphitic nanostructures. *Philos. Trans. R. Soc. A*, **365**, 1539–1552.
- 191** Yamamoto, Y. (2011) Electroactive nanotubes from π -conjugated discotic molecules. *Bull. Chem. Soc. Jpn.*, **84**, 17–25.
- 192** Hill, J.P., Jin, W., Kosaka, A., Fukushima, T., Ichihara, H., Shimomura, T., Ito, K., Hashizume, T., Ishii, N., and Aida, T. (2004) Self-assembled hexa-*peri*-hexabenzocoronene graphitic nanotube. *Science*, **304**, 1481–1483.
- 193** Jin, W., Yamamoto, Y., Fukushima, T., Ishii, N., Kim, J., Kato, K., Takata, M., and Aida, T. (2008) Systematic studies on structural parameters for nanotubular assembly of hexa-*peri*-hexabenzocoronenes. *J. Am. Chem. Soc.*, **130**, 9434–9440.
- 194** Jin, W., Fukushima, T., Niki, M., Kosaka, A., Ishii, N., and Aida, T. (2005) Self-assembled graphitic nanotubes with one-handed helical arrays of a chiral amphiphilic molecular graphene. *Proc. Natl. Acad. Sci. USA*, **102**, 10801–10806.
- 195** Babu, S.S., Praveen, V.K., and Ajayaghosh, A. (2014) Functional π -gelators and their applications. *Chem. Rev.*, **114**, 1973–2129.
- 196** Ishi-I, T. and Shinkai, S. (2005) Dye-based organogels: stimuli-responsive soft materials based on one-dimensional self-assembling aromatic dyes. *Top. Curr. Chem.*, **258**, 119–160.
- 197** Mamiya, J., Kanie, K., Hiyama, T., Ikeda, T., and Kato, T. (2002) A rodlike organogelator: fibrous aggregation of azobenzene derivatives with a *syn*-chiral carbonate moiety. *Chem. Commun.*, 1870–1871.
- 198** Hamada, K., Yamada, K., Mitsuishi, M., Ohira, M., and Miyazaki, K. (1992) Gelation of an aqueous fluorinated dye solution. *J. Chem. Soc., Chem. Commun.*, 544–545.
- 199** Kobayashi, H., Friggeri, A., Koumoto, K., Amaike, M., Shinkai, S., and Reinhoudt, D.N. (2002) Molecular design of “super” hydrogelators: understanding the gelation process of azobenzene-based sugar derivatives in water. *Org. Lett.*, **4**, 1423–1426.
- 200** Kobayashi, H., Koumoto, K., Jung, J.H., and Shinkai, S. (2002) Sol–gel phase transition induced by fiber–vesicle structural changes in sugar-based bolaamphiphiles. *J. Chem. Soc., Perkin Trans. 2*, 1930–1936.

- 201** Sugiyasu, K., Fujita, N., Takeuchi, M., Yamadab, S., and Shinkai, S. (2003) Proton-sensitive fluorescent organogels. *Org. Biomol. Chem.*, **1**, 895–899.
- 202** Terech, P., Gebel, G., and Ramasseul, R. (1996) Molecular rods in a zinc(II) porphyrin/cyclohexane physical gel: neutron and X-ray scattering characterizations. *Langmuir*, **12**, 4321–4323.
- 203** Tamaru, S., Nakamura, M., Takeuchi, M., and Shinkai, S. (2001) Rational design of a sugar-appended porphyrin gelator that is forced to assemble into a one-dimensional aggregate. *Org. Lett.*, **3**, 3631–3634.
- 204** Tamaru, S., Uchino, S., Takeuc, H.M., Ikeda, M., Hatano, T., and Shinkai, S. (2002) A porphyrin-based gelator assembly which is reinforced by peripheral urea groups and chirally twisted by chiral urea additives. *Tetrahedron Lett.*, **43**, 3751–3755.
- 205** Tanaka, S., Shirakawa, M., Kaneko, K., Takeuchi, M., and Shinkai, S. (2005) Porphyrin-based organogels: control of the aggregation mode by a pyridine-carboxylic acid interaction. *Langmuir*, **21**, 2163–2172.
- 206** Shirakawa, M., Kawano, S., Fujita, N., Sada, K., and Shinkai, S. (2003) Hydrogen-bond-assisted control of H versus J aggregation mode of porphyrins stacks in an organogel system. *J. Org. Chem.*, **68**, 5037–5044.
- 207** Setnicka, V., Urbanova, M., Pataridis, S., Kral, V., and Volka, K. (2002) Sol-gel phase transition of brucine-appended porphyrin gelator: a study by vibrational circular dichroism spectroscopy. *Tetrahedron: Asymmetry*, **13**, 2661–2666.
- 208** Kral, V., Pataridis, S., Setnicka, V., Zaruba, K., Urbanova, M., and Volka, K. (2005) New chiral porphyrin-brucine gelator characterized by methods of circular dichroism. *Tetrahedron*, **61**, 5499–5506.
- 209** Ajayaghosh, A. and Praveen, V.K. (2007) π -Organogels of self-assembled *p*-phenylenevinylenes: soft materials with distinct size, shape, and functions. *Acc. Chem. Res.*, **40**, 644–656.
- 210** Buhleier, E., Wehner, W., and Vögtle, F. (1978) “Cascade”- and “nonskid-chain-like” syntheses of molecular cavity topologies. *Synthesis (Stuttgart)*, **2**, 155–158.
- 211** Boas, U. and Heegaard, P.M.H. (2004) Dendrimers in drug research. *Chem. Soc. Rev.*, **33**, 43–63.
- 212** Kesharwani, P., Jain, K., and Jain, N.K. (2014) Dendrimer as nanocarrier for drug delivery. *Prog. Polym. Sci.*, **39**, 268–307.
- 213** Agrawal, A., Asthana, A., Gupta, U., and Jain, N.K. (2008) Tumor and dendrimers: a review on drug delivery aspects. *J. Pharm. Pharmacol.*, **60**, 671–688.
- 214** Jang, W.D., Jiang, D.L., and Aida, T. (2000) Dendritic physical gel: hierarchical self-organization of a peptide-core dendrimer to form a micrometer-scale fibrous assembly. *J. Am. Chem. Soc.*, **122**, 3232–3233.
- 215** Jang, W.D. and Aida, T. (2003) Dendritic physical gels: structural parameters for gelation with peptide-core dendrimers. *Macromolecules*, **36**, 8461–8469.
- 216** Partridge, K.S., Smith, D.K., Dykes, G.M., and McGrail, P.T. (2001) Supramolecular dendritic two-component gel. *Chem. Commun.*, 319–320.
- 217** Hirst, A.R., Smith, D.K., Feiters, M.C., Geurts, H.P.M., and Wright, A.C. (2003) Two-component dendritic gels: easily tunable materials. *J. Am. Chem. Soc.*, **125**, 9010–9011.
- 218** Huang, B.Q., Hirst, A.R., Smith, D.K., Castellett, V., and Hamley, I.W. (2005) A direct comparison of one- and two-component dendritic self-assembled materials: elucidating molecular recognition pathways. *J. Am. Chem. Soc.*, **127**, 7130–7139.
- 219** Liu, Z., Feng, Y., Yan, Z., He, Y., Liu, C., and Fan, Q. (2012) Multistimuli responsive dendritic organogels based on azobenzene-containing poly(aryl ether) dendron. *Chem. Mater.*, **24**, 3751–3757.
- 220** Liu, J., Feng, Y., Yan, Z., He, Y., Liu, C., and Fan, Q. (2013) *N*-Boc-protected 1,2-diphenylethylene diamine-based dendritic organogels with multiple-stimulus-responsive properties. *Chem. Asian J.*, **8**, 572–581.

- 221 Feng, Y., Liu, Z., Chen, H., Yan, Z., He, Y., Liu, C., and Fan, Q. (2014) A systematic study of peripherally multiple aromatic ester-functionalized poly(benzyl ether) dendrons for the fabrication of organogels: structure–property relationships and thixotropic property. *Chem. Eur. J.*, **20**, 7069–7082.
- 222 Liu, Z., Feng, Y., Zhao, Z., Yan, Z., He, Y., Luo, X., Liu, C., and Fan, Q. (2014) A new class of dendritic metallogeles with multiple stimuli-responsiveness and as templates for the *in situ* synthesis of silver nanoparticles. *Chem. Eur. J.*, **20**, 533–541.
- 223 Duan, P., Qin, L., Zhu, X., and Liu, M. (2011) Hierarchical self-assembly of amphiphilic peptide dendrons: evolution of diverse chiral nanostructures through hydrogel formation over a wide pH range. *Chem. Eur. J.*, **17**, 6389–6395.
- 224 Hao, R., Liu, W., and Hao, J. (2012) Soft vesicles in the synthesis of hard materials. *Acc. Chem. Res.*, **45**, 504–513.
- 225 Wang, C., Wang, Z., and Zhang, X. (2012) Amphiphilic building blocks for self-assembly: from amphiphiles to supra-amphiphiles. *Acc. Chem. Res.*, **45**, 608–618.
- 226 Tanner, P., Baumann, P., Enea, R., Onaca, O., Palivan, C., and Meier, W. (2011) Polymeric vesicles: from drug carriers to nanoreactors and artificial organelles. *Acc. Chem. Res.*, **44**, 1039–1049.
- 227 Sarti, S. and Bordi, F. (2013) Polymeric hollow micro and nanospheres for biotechnological applications: a focused review. *Mater. Lett.*, **109**, 134–139.
- 228 Verma, G. and Hassan, P.A. (2013) Self-assembled materials: design strategies and drug delivery perspectives. *Phys. Chem. Chem. Phys.*, **15**, 17016–17028.
- 229 Sasidharan, M. and Nakashima, K. (2014) Core–shell–corona polymeric micelles as a versatile template for synthesis of inorganic hollow nanospheres. *Acc. Chem. Res.*, **47**, 157–167.
- 230 Morigaki, K. and Walde, P. (2007) Fatty acid vesicles. *Curr. Opin. Colloid Interface Sci.*, **12**, 75–80.
- 231 Hu, X., Hu, J., Tian, J., Ge, Z., Zhang, G., Luo, K., and Liu, S. (2013) Polyprodrug amphiphiles: hierarchical assemblies for shape-regulated cellular internalization, trafficking, and drug delivery. *J. Am. Chem. Soc.*, **135**, 17617–17629.
- 232 Redkar, M., Hassan, P.A., Aswal, V., and Devarajan, P. (2007) Onion phases of PEG-8 distearate. *J. Pharm. Sci.*, **96**, 2436–2445.
- 233 Upadhyay, K.K., Meins, J.F.L., Misra, A., Voisin, P., Bouchaud, V., Ibarboure, E., Schatz, C., and Lecommandoux, S. (2009) Biomimetic doxorubicin loaded polymersomes from hyaluronan-*block*-poly(gamma-benzyl glutamate) copolymers. *Biomacromolecules*, **10**, 2802–2808.
- 234 Chen, L., Zhao, G., Jiang, B., Sun, B., Wang, M., Xu, L., He, J., Abliz, Z., Tan, H., Li, X., and Yang, H. (2014) Smart stimuli-responsive spherical nanostructures constructed from supramolecular metallocendrimers via hierarchical self-assembly. *J. Am. Chem. Soc.*, **136**, 5993–6001.
- 235 Yao, Y., Xue, M., Chen, J., Zhang, M., and Huang, F. (2012) An amphiphilic pillar[5]arene: synthesis, controllable self-assembly in water, and application in calcein release and TNT adsorption. *J. Am. Chem. Soc.*, **134**, 15712–15715.
- 236 Qin, L., Zhang, L., Jin, Q., Zhang, J., Han, B., and Liu, M. (2013) Supramolecular assemblies of amphiphilic L-proline regulated by compressed CO₂ as a recyclable organocatalyst for the asymmetric aldol reaction. *Angew. Chem., Int. Ed.*, **52**, 7761–7765.
- 237 Shimizu, T., Masuda, M., and Minamikawa, H. (2005) Supramolecular nanotube architectures based on amphiphilic molecules. *Chem. Rev.*, **105**, 1401–1443.
- 238 Shimizu, T., Masuda, M., and Minamikawa, H. (2005) Supramolecular nanotube architectures based on amphiphilic molecules. *Chem. Rev.*, **105**, 1401–1444.
- 239 Schnur, J.M. (1993) Lipid tubules: a paradigm for molecularly engineered structures. *Science*, **262**, 1669–1676.
- 240 Yamada, K., Ihara, H., Ide, T., Fukumoto, T., and Hirayama, C. (1984) Formation of helical super structure from single-walled bilayers by amphiphiles with

- oligo-L-glutamic acid-head group. *Chem. Lett.*, **10**, 1713–1716.
- 241** Nakashima, N., Asakuma, S., and Kunitake, T. (1985) Optical microscopic study of helical superstructures of chiral bilayer membranes. *J. Am. Chem. Soc.*, **107**, 509–510.
- 242** Yager, P. and Schoen, P.E. (1984) Formation of tubules by a polymerizable surfactant. *Mol. Cryst. Liq. Cryst.*, **106**, 371–381.
- 243** Frankel, D.A. and O'Brien, D.F. (1991) Supramolecular assemblies of diacetylenic aldonamides. *J. Am. Chem. Soc.*, **113**, 7436–7437.
- 244** Frankel, D.A. and O'Brien, D.F. (1994) Effect of headgroup on the supramolecular morphology of diacetylenic aldonamides. *Macromol. Symp.*, **77**, 141–148.
- 245** Frankel, D.A. and O'Brien, D.F. (1994) Supramolecular assemblies of diacetylenic aldonamides. *J. Am. Chem. Soc.*, **116**, 10057–10069.
- 246** Kamiya, S., Minamikawa, H., Jung, J.H., Yang, B., Masuda, M., and Shimizu, T. (2005) Molecular structure of glucopyranosylamide lipid and nanotube morphology. *Langmuir*, **21**, 743–750.
- 247** Kogiso, M., Ohnishi, S., Yase, K., Masud, M., and Shimizu, T. (1998) Dicarboxylic oligopeptide bolaamphiphiles: proton-triggered self-assembly of microtubes with loose solid surfaces. *Langmuir*, **14**, 4978–4986.
- 248** Kogiso, M., Okada, Y., Hanada, T., Yase, K., and Shimizu, T. (2000) Self-assembled peptide fibers from valylvaline bolaamphiphiles by a parallel beta-sheet network. *Biochim. Biophys. Acta: Gen. Subjects*, **1475**, 346–352.
- 249** Kogiso, M., Yoshida, K., Yase, K., and Shimizu, T. (2002) One-dimensional organization of copper nanoparticles by chemical reduction of lipid–copper hybrid nanofibers. *Chem. Commun.*, **21**, 2492–2493.
- 250** Kogiso, M., Okada, Y., Yase, K., and Shimizu, T. (2004) Metal-complexed nanofiber formation in water from dicarboxylic valylvaline bolaamphiphiles. *J. Colloid Interface Sci.*, **273**, 394–399.
- 251** Boettcher, C., Schade, B., and Fuhrhop, J. (2001) Dicarboxylic oligopeptide bolaamphiphiles: proton-triggered self-assembly of microtubes with loose solid surfaces. *Langmuir*, **17**, 873–877.
- 252** Görbitz, C.H. and Gundersen, E. (1996) L-Valyl-L-alanine. *Acta Crystallogr. C*, **52**, 1764–1767.
- 253** Görbitz, C.H. (2003) Nanotubes from hydrophobic dipeptides: pore size regulation through side chain substitution. *New J. Chem.*, **27**, 1789–1793.
- 254** Reches, M. and Gazit, E. (2003) Casting metal nanowires within discrete self-assembled peptide nanotubes. *Science*, **300**, 625–627.
- 255** Reches, M. and Gazit, E. (2006) Designed aromatic homo-dipeptides: formation of ordered nanostructures and potential nanotechnological applications. *Phys. Biol.*, **3**, S10–S19.
- 256** Reches, M. and Gazit, E. (2006) Controlled patterning of aligned self-assembled peptide nanotubes. *Nat. Nanotechnol.*, **1**, 195–200.
- 257** Adler-Abramovich, L., Reches, M., Sedman, V.L., Allen, S., Tendler, S.J.B., and Gazit, E. (2006) Thermal and chemical stability of diphenylalanine peptide nanotubes: implications for nanotechnological applications. *Langmuir*, **22**, 1313–1320.
- 258** Kol, N., Adler-Abramovich, L., Barlam, D., Shneck, R.Z., Gazit, E., and Rousso, I. (2005) Self-assembled peptide nanotubes are uniquely rigid bioinspired supramolecular structures. *Nano Lett.*, **5**, 1343–1346.
- 259** Vauthay, S., Santoso, S., Gong, H., Watson, N., and Zhang, S. (2002) Molecular self-assembly of surfactant-like peptides to form nanotubes and nanovesicles. *Proc. Natl. Acad. Sci. USA*, **99**, 5355–5360.
- 260** Zhang, S.G. and Zhao, X.J. (2004) Design of molecular biological materials using peptide motifs. *J. Mater. Chem.*, **14**, 2082–2086.
- 261** Zhao, X.J. and Zhang, S.G. (2006) Self-assembling nanopeptides become a new type of biomaterial. *Polym. Regen. Med.*, **203**, 145–170.

- 262** Lu, K., Guo, L., Mehta, A.K., Childers, W.S., Dublin, S.N., Skanthakumar, S., Conticello, V.P., Thiagarajan, P., Apkarian, R.P., and Lynn, D.G. (2007) Macroscale assembly of peptide nanotubes. *Chem. Commun.*, **26**, 2729–2731.
- 263** Lu, K., Jacob, J., Thiagarajan, P., Conticello, V.P., and Lynn, D.G. (2003) Exploiting amyloid fibril lamination for nanotube self-assembly. *J. Am. Chem. Soc.*, **125**, 6391–6393.
- 264** Valery, C., Paternostre, M., Robert, B., Gulik-Krzywicki, T., Narayanan, T., Dedieu, J., Keller, G., Torres, M., Cherif-Cheikh, R., Calvo, P., and Artzner, F. (2003) Biomimetic organization: octapeptide self-assembly into nanotubes of viral capsid-like dimension. *Proc. Natl. Acad. Sci. USA*, **100**, 10258–10262.
- 265** Clark, T.D., Buehler, L.K., and Ghadiri, M.R. (1998) Self-assembling cyclic β -peptide nanotubes as artificial transmembrane ion channels. *J. Am. Chem. Soc.*, **120**, 651–656.
- 266** Gauthier, D., Baillargeon, P., Drouin, M., and Dory, Y.L. (2001) Self-assembly of cyclic peptides into nanotubes and then into highly anisotropic crystalline materials. *Angew. Chem., Int. Ed.*, **40**, 4635–4638.
- 267** Amorín, M., Castedo, L., and Granja, J.R. (2003) New cyclic peptide assemblies with hydrophobic cavities: the structural and thermodynamic basis of a new class of peptide nanotubes. *J. Am. Chem. Soc.*, **125**, 2844–2845.
- 268** Seth, H.W., David, S.C., and Ghadiri, M.R. (2003) A heterocyclic peptide nanotube. *J. Am. Chem. Soc.*, **125**, 9372–9376.
- 269** Ranganathan, D., Lakshmi, C., and Karle, I.L. (1999) Hydrogen-bonded self-assembled peptide nanotubes from cystine-based macrocyclic bisureas. *J. Am. Chem. Soc.*, **121**, 6103–6107.
- 270** Ranganathan, D., Haridas, V., Gilardi, R., and Karle, I.L. (1998) Self-assembling aromatic-bridged serine-based cyclodepsipeptides (serinophanes): a demonstration of tubular structures formed through aromatic π – π interactions. *J. Am. Chem. Soc.*, **120**, 10793–10800.
- 271** Rosenthal, A.K., Svensson, G., and Undén, A. (2004) Self-assembling peptide nanotubes from enantiomeric pairs of cyclic peptides with alternating D and L amino acid residues. *J. Am. Chem. Soc.*, **126**, 3372–3373.
- 272** Kameta, N., Masuda, M., Minamikawa, H., Goutev, N.V., Rim, J.A., Jung, J.H., and Shimizu, T. (2005) Selective construction of supramolecular nanotube hosts with cationic inner surfaces. *Adv. Mater.*, **17**, 2732–2736.
- 273** Kameta, N.M., Minamikawa, H., and Shimizu, T. (2007) Self-assembly and thermal phase transition behavior of unsymmetrical bolaamphiphiles having glucose- and amino-hydrophilic headgroups. *Langmuir*, **23**, 4634–4641.
- 274** Yui, H., Shimizu, Y., Kamiya, S., Yamashita, I., Masuda, M., Ito, K., and Shimizu, T. (2005) Encapsulation of ferritin within a hollow cylinder of glycolipid nanotubes. *Chem. Lett.*, **34**, 232–233.
- 275** Shimizu, T. (2007) Self-assembled organic nanotubes: toward attoliter chemistry. *Chem. Mater.*, **19**, 3553–3560.
- 276** Cao, H., Duan, P.F., Zhu, X.F., Jiang, J., and Liu, M.H. (2012) Self-assembled organic nanotubes through instant gelation and universal capacity for guest molecule encapsulation. *Chem. Eur. J.*, **18**, 5546–5550.
- 277** Littleton, J.T. and Ganetzky, B. (2000) Ion channels and synaptic organization: analysis of the *Drosophila* genome. *Neuron*, **26**, 35–43.
- 278** Montenegro, J., Ghadiri, M.R., and Granja, J.R. (2013) Ion channel models based on self-assembling cyclic peptide nanotubes. *Acc. Chem. Res.*, **46**, 2955–2965.
- 279** Zhu, X.F., Jiang, J., and Liu, M.H. (2011) Self-assembly of copper(II) ion-mediated nanotube and its supramolecular chiral catalytic behavior. *Langmuir*, **27**, 13847–13853.
- 280** Velichko, Y.S., Stupp, S.I., and de la Cruz, M.O. (2008) Molecular simulation study of peptide amphiphile self-assembly. *J. Phys. Chem. B*, **112**, 2326–2334.

- 281** Paramonov, S.E., Jun, H.W., and Hartgerink, J.D. (2006) Self-assembly of peptide-amphiphile nanofibers: the roles of hydrogen bonding and amphiphilic packing. *J. Am. Chem. Soc.*, **128**, 7291–7298.
- 282** Hartgerink, J.D., Beniash, E., and Stupp, S.I. (2002) Peptide-amphiphile nanofibers: a versatile scaffold for the preparation of self-assembling materials. *Proc. Natl. Acad. Sci. USA*, **99**, 5133–5138.
- 283** Cui, H., Muraoka, T., Cheetham, A.G., and Stupp, S.I. (2009) Self-assembly of giant peptide nanobelts. *Nano Lett.*, **9**, 945–951.
- 284** Stendahl, J.C., Rao, M.S., Guler, M.O., and Stupp, S.I. (2006) Intermolecular forces in the self-assembly of peptide amphiphile nanofibers. *Adv. Funct. Mater.*, **16**, 499–508.
- 285** Behanna, H.A., Rajangam, K., and Stupp, S.I. (2007) Modulation of fluorescence through coassembly of molecules in organic nanostructures. *J. Am. Chem. Soc.*, **129**, 321–327.
- 286** Qin, L., Xie, F., Duan, P.F., and Liu, M.H. (2013) A metal ion triggered shrinkable supramolecular hydrogel and controlled release by an amphiphilic peptide dendron. *Chem. Commun.*, **49**, 10823–10825.
- 287** Qin, L., Xie, F., Duan, P.F., and Liu, M.H. (2014) A peptide dendron-based shrinkable metallo-hydrogel for charged species separation and stepwise release of drugs. *Chem. Eur. J.* doi: 10.1002/chem.201404035.
- 288** Marini, D.M., Wang, W.H., Lauffenburger, D.A., Zhang, S., and Kamm, R.D. (2002) Left handed helical ribbon intermediates in the self-assembly of a β -sheet peptide. *Nano Lett.*, **2**, 295–299.
- 289** Bowerman, C.J. and Nilsson, B.L. (2010) A reductive trigger for peptide self-assembly and hydrogelation. *J. Am. Chem. Soc.*, **132**, 9526–9527.
- 290** Guler, M.O., Claussen, R.C., and Stupp, S.I. (2005) Encapsulation of pyrene within self-assembled peptide amphiphile nanofibers. *J. Mater. Chem.*, **15**, 4507–4512.
- 291** Tovar, J.D., Rabatic, B.M., and Stupp, S.I. (2007) Conducting polymers confined within bioactive peptide amphiphile nanostructures. *Small*, **3**, 2024–2028.
- 292** Arnold, M.S., Guler, M.O., Hersam, M.C., and Stupp, S.I. (2005) Encapsulation of carbon nanotubes by self-assembling peptide amphiphiles. *Langmuir*, **21**, 4705–4709.
- 293** Palmer, L.C., Newcomb, C.J., Kaltz, S.R., Spoerke, E.D., and Stupp, S.I. (2008) Biomimetic systems for hydroxyapatite mineralization inspired by bone and enamel. *Chem. Rev.*, **108**, 4754–4783.
- 294** Sone, E.D. and Stupp, S.I. (2004) Semiconductor-encapsulated peptide-amphiphile nanofibers. *J. Am. Chem. Soc.*, **126**, 12756–12757.
- 295** Beniash, E., Hartgerink, J.D., Storrie, H., Stendahl, J.C., and Stupp, S.I. (2005) Self-assembling peptide amphiphile nanofiber matrices for cell entrapment. *Acta Biomater.*, **1**, 387–397.
- 296** Sargeant, T.D., Guler, M.O., Oppenheimer, S.M., Mata, A., Satcher, R.L., Dunand, D.C., and Stupp, S.I. (2008) Hybrid bone implants: self-assembly of peptide amphiphile nanofibers within porous titanium. *Biomaterials*, **29**, 161–171.
- 297** Sargeant, T.D., Oppenheimer, S.M., Dunand, D.C., and Stupp, S.I. (2008) Titanium foam-bioactive nanofiber hybrids for bone regeneration. *Tissue Eng. Regen. Med.*, **2**, 455–462.
- 298** Rajangam, K., Arnold, M.S., Rocco, M.A., and Stupp, S.I. (2008) Peptide amphiphile nanostructure-heparin interactions and their relationship to bioactivity. *Biomaterials*, **29**, 3298–3305.
- 299** Huang, Z., Sargeant, T.D., Hulvat, J.F., Mata, A., Bringas, P., Koh, C.Y., Stupp, S.I., and Snead, M.L.J. (2008) Bioactive nanofibers instruct cells to proliferate and differentiate during enamel regeneration. *Bone Miner. Res.*, **23**, 1995–2006.

3

Supramolecular Nanotechnology: Soft Assembly of Hard Nanomaterials

Katsuhiko Ariga, Qingmin Ji, and Jonathan P. Hill

3.1

Introduction

It is well known that nanotechnology contributes to the development of current science and technology. Ultrasmall devices with high density of functional structures are the products of advanced microfabrication and nanofabrication techniques. Most existing technologies depend heavily on so called top-down fabrication techniques. However, at the current rate of miniaturization, silicon-based technology will encounter the physical limits of device dimensions in the very near future according to Moore's law [1,2]. Therefore, alternative way for nanotechnological techniques involving the bottom-up approach should be considered, where functional systems can be constructed through spontaneous and/or directed assembly of small building blocks. Bottom-up approaches include the important concept of supramolecular chemistry using noncovalent molecular associations [3–10]. Thus, nanotechnology ought to incorporate supramolecular chemistry to make up the important new methodology of supramolecular nanotechnology.

Supramolecular chemistry involves organic and bioorganic materials in most of the well-known or well-investigated cases. Although organic molecules are of a "softly" adjustable nature and possess great structural and functional diversity, they have a large drawback in their relative physical instability under the harsh conditions currently required for precise fabrication. Therefore, use of supramolecular chemistry based on organic molecules might not be compatible with current nanotechnology. In order to solve this dilemma, extension of supramolecular concepts to hard inorganic nanomaterials should be considered.

In this chapter, we describe briefly the recent challenges involving the above-mentioned research concept of supramolecular nanotechnology with soft assembly of hard nanomaterials. Although there is a wide variety in the corresponding subjects, we have focused especially on two topics: (i) soft cell-like structures with hard nanomaterials and (ii) hierarchical assemblies. Formation of hollow spherical structures through sol–gel linkage, self-assemblies of inorganic structures, and layer-by-layer (LbL) assemblies of hard mesoporous materials were

selected and are described together with their unusual functions in sensing, catalysis, and drug delivery. From the contents in this chapter, readers should better appreciate the wide applicability of supramolecular concepts even as far as their application to inorganic nanomaterials.

3.2

Soft Cell-Like Structures with Hard Nanomaterials

Of the various self-assembly systems available in nature and in the laboratory, living cells can be regarded as highly sophisticated and functional self-assembly systems. Of the known cellular structures, cell membrane structures can be regarded as well-functionalized soft assemblies. Mimicking cell membrane systems by using hard nanomaterials could be an attractive approach in the design and fabrication of artificial functional materials.

3.2.1

Cerasome: Inorganic Surface Cell

Cell-like hollow spherical assemblies composed of lipid bilayer, which are known as liposomes and vesicles, have been investigated as artificial cells in the fields of biochemistry, biology, medical science, and supramolecular chemistry. Although their soft and flexible nature is suitable for some applications such as controlled drug release, the limited mechanical stability of conventional lipid liposomes and vesicles is often disadvantageous. Spherical lipid assemblies composed of a hard inorganic framework may be useful due to their flexible functionalities and mechanical stabilities.

In a pioneering example, Katagiri *et al.* reported preparation of lipid bilayer vesicles with hard silica framework through covalent linkage (Figure 3.1) [11–13], which are known as cerasomes (ceramics + soma). Dispersion of alkoxy silane-bearing amphiphiles under moderately acidic conditions resulted in the formation of stable cerasomes. The formation of siloxane bonds was confirmed by the presence of peaks assigned to the Si–O–Si and Si–OH groups in their FT-IR spectra. Observation by transmission electron microscopy (TEM) revealed multilamellar cerasomes with a bilayer thickness of about 4 nm and vesicular diameter of 150 nm. The cerasomes sometimes aggregated without causing destruction of their vesicular structures, although aggregation of conventional vesicles often leads to their fusions into multilayer flat structures following vesicle destruction. The greater stability of the cerasome structure may originate from the formation of an intra- and intermembrane siloxane network. Cerasome aggregates may become good models of multicellular structures.

Subjecting the cerasome structure to the LbL technique (see later part of this chapter) leads to preparation of multicellular mimics in a predesigned order (Figure 3.2) [14,15]. Successful LbL assembly between anionic cerasomes and cationic polyelectrolyte (poly(diallyldimethylammonium chloride) (PDDA)) was

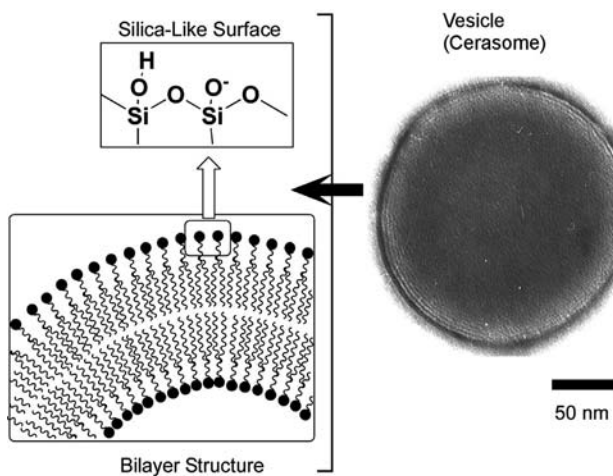


Figure 3.1 Cerasome, lipid bilayer vesicles with a hard silica framework.

confirmed using a quartz crystal microbalance (QCM). The QCM device is known to allow sensitive mass detection of materials deposited on the surface from its frequency shifts. Direct LbL assemblies between small cationic cerasomes and large anionic cerasomes were also possible. The closely packed cerasome particles were clearly observed like a stone pavement in both layers by atomic force microscopy (AFM). Functionalization of the cerasome surface

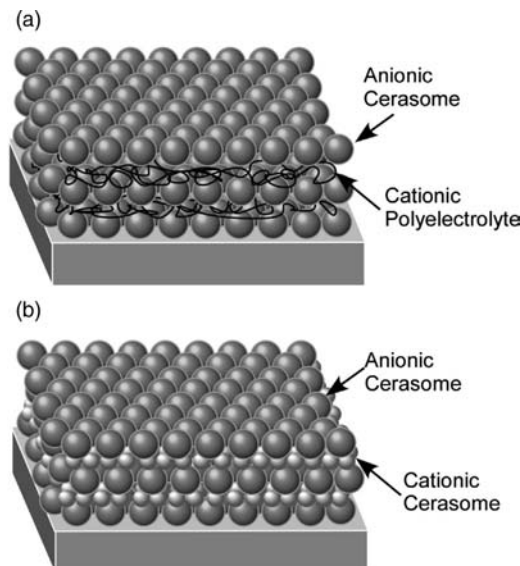


Figure 3.2 LbL films of cerasome. (a) Anionic cerasome and cationic polyelectrolyte. (b) Anionic cerasome and cationic cerasome.

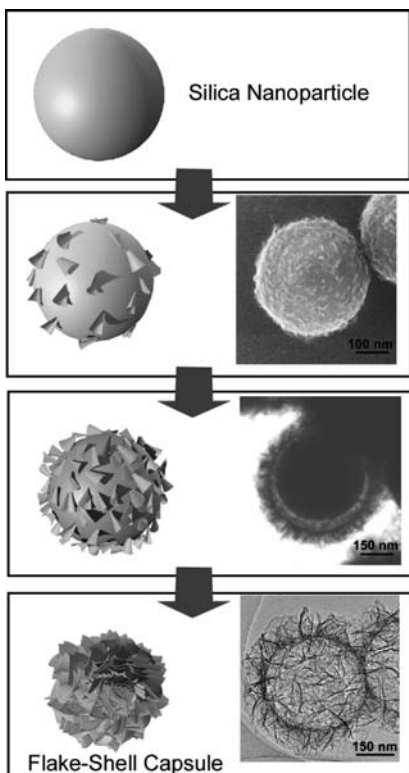


Figure 3.3 Formation of flake–shell capsule, soft capsules with a shell structure composed solely of assembled silica nanosheets.

would be useful for immobilization of various biomolecules such as enzymes and antibodies, leading to the creation of various types of biomimetic silica nanohybrids.

3.2.2

Flake–Shell Capsule

For a more advanced cell-like spherical assembly composed of inorganic nanomaterials, Ji *et al.* recently developed soft capsules with a shell structure assembled from silica nanosheets [16–18]. The resulting soft silica capsules are known as flake–shell capsules (Figure 3.3) and are formed by a spontaneous self-templating mechanism. Exposure of silica nanoparticles to hydrothermal conditions induced gradual dissolution of silica from the nanoparticle surface and precipitation as nanosheets in the vicinity of the original nanoparticles. These spontaneous processes result in formation of flake–shell capsules. Although they are formed by assembly of inorganic silica nanosheets, they possess some structural flexibility as confirmed by the shrinking behavior caused by the incident beam during

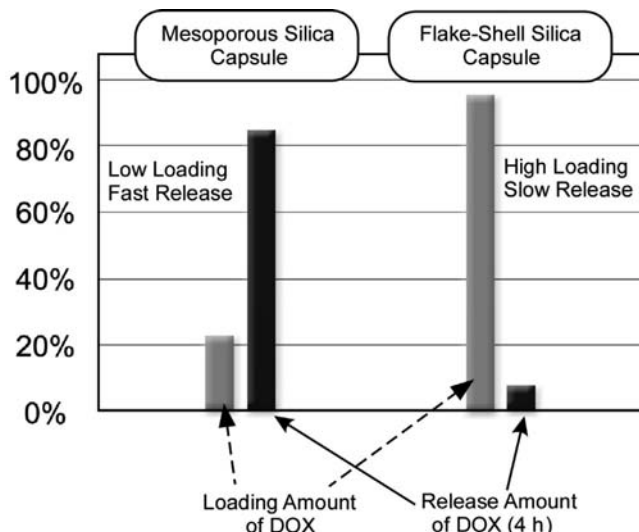


Figure 3.4 Storage and release processes of the anticancer drug DOX were compared between conventional mesoporous silica capsule and flake–shell silica capsule.

observation by scanning electron microscopy (SEM). The diameter of flake–shell capsules reduced from 560 to 440 nm upon heating of the capsule by focusing of the electron beam at their position for 5 min. In addition, modulation of Si–O–Si networks by appropriate pH treatments could be used to induce structural changes of the flake–shell capsules.

Depending on the structural changes made, the size of the pores between the silica nanosheets in the outer wall could be controlled over a wide range by adjusting pH. This modification leads to variation in the molecular diffusion route that might be applied for controlling drug storage and release. It eventually leads to an effective control of drug release duration, that is, sustained drug release. In a typical example, storage and release processes of the anticancer drug DOX were compared for conventional mesoporous silica capsules and flake–shell silica capsules (Figure 3.4). Storage efficiency exceeded 80% (by weight) for the flake–shell capsules after appropriate pH treatment, while only 20% of DOX drug could be contained in structurally inflexible mesoporous silica spheres. Enhanced loading efficiency of the drug was achieved by maintaining the pores in an open state between the nanosheet assemblies. The porous structure of flake–shell capsules could then be tuned again by a subsequent pH treatment following loading of DOX molecules. Release rate of DOX from the flake–shell capsule could be drastically decreased by the closing of pores in the silica nanosheet assemblies. While more than 90% of the stored DOX was released within 4 h from the nonflexible conventional silica capsules under standard conditions, only 10% of the loaded drug was released from flake–shell capsules under the same conditions. High loading and slow release from flake–shell capsules resulted in sustained DOX release on a timescale of days. The use of

structural adjustments of flake–shell capsules is advantageous for sustained drug release with the possibility of adjustment of the release rate, which could find application in various medical scenarios.

3.2.3

Metallic Cells

Capsule structures have great potential to provide sophisticated functions depending on differentiation between their interiors and exteriors as can be found in living cells. However, most artificial cell mimics including lipid vesicles, polymer capsules, and hollow spheres composed of hybrids and inorganic materials have been used to explore functions that rely only on permeation control through the capsule membrane and/or specific interactions at their outer surfaces. Thus, it is not surprising that functionalities at the interior surfaces of these capsule structures have not been fully explored. Use of capsular interior surfaces might be used to double the available functionality relative to those with functions only at their exterior surfaces. In addition, it is expected that the interior surface environment is not susceptible to particle agglomeration effects.

In a rare example of cell-like capsule materials where effective use can be made of interior functionality, Abe and coworkers developed platinum micro-capsules with open-mouthed structures, which were named “metallic cells” (Figure 3.5) [19]. Metallic cells are prepared through deposition of Pt onto a polystyrene sphere template followed by thermal removal of the templating polystyrene. The latter process is accompanied by vaporization of the organic components, which results in formation of open-mouthed structures. Because access to the interior surfaces of metallic cells is unobstructed, the metallic cells showed a significant enhancement of their electrode capability for methanol oxidation. In addition, superior catalytic activity for carbon monoxide (CO) oxidation over both Pt on polymer spheres and Pt powder was demonstrated with the metallic cells. The very high CO oxidation activity observed for the metallic cells is due to the agglomeration-free nature of their interior surfaces. Generally, such particles tend to form aggregates at high reaction temperature, which often causes serious difficulties in the access of reaction substrates to active catalytic sites. In contrast, catalytic sites at the inside of metallic cells are free from such

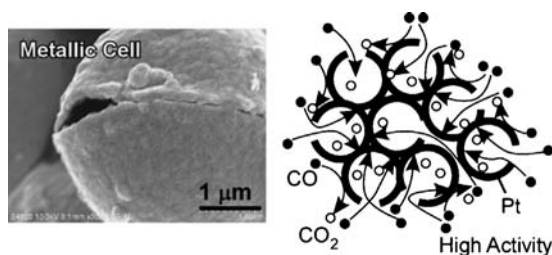


Figure 3.5 Metallic cells with superior catalytic activities for carbon monoxide (CO) oxidation.

particle aggregation and maintain their activities under reaction conditions. The concept of metallic cells could be used to improve practical applications such as exhaust catalysts for automobile technologies. Because the synthetic strategy of metallic cells could be widely applicable to alloys of Pt, Pd, and/or Rh, superior activities relative to the materials currently in use are expected to be demonstrated.

3.3

For Hierarchical Assembly: LbL and Others

Hierarchical structures play important roles in many biological functional systems. Such hierarchical structures are usually constructed through spontaneous self-assembly based on the appropriate selection of soft components. Application of such natural processes to inorganic hard nanomaterials could be used to create highly functional systems. However, to mimic entire natural processes by using nonbiochemical approaches is usually difficult. Selected multistep processes for synthesis of nanostructured materials followed by subsequent assembly into organized structures might also be possible. For example, a two-step process including (i) synthesis of mesoporous structures and (ii) LbL assembly would be one possible approach to construct hierarchical functional systems from hard nanomaterials.

Alternative LbL assembly is now regarded as one of the most versatile techniques to fabricate layered organized structures [20–25]. LbL assembly is applicable to a large variety of materials from organic and biological substances to inorganic materials. In initial research activity on LbL assemblies, electrostatic interaction was used as the main assembly driving force. This has been expanded to involve various interactions, including hydrogen bonding, metal coordination, stereocomplex formation, charge transfer, bio-specific interactions, covalent bonding, and electrochemical coupling. Apart from thin films, multilayered three-dimensional structures such as spheres, capsules, and tubes can also be fabricated using LbL assembly.

3.3.1

Mesoporous Carbon in Hierarchical Assembly

Ariga *et al.* developed sensor systems using LbL films composed of polyelectrolytes and mesoporous carbon materials, CMK-3 (Figure 3.6) [26]. Introduction of negative charges upon partial surface oxidation of CMK-3 enabled LbL assembly with countercharged polyelectrolytes on a QCM plate. For investigation of sensing performances, the QCM plate covered with a LbL film of CMK-3 was immersed into an aqueous phase where guest molecules were injected. QCM frequency shifts upon binding of tannic acid strongly exceeded frequency shifts for catechin and caffeine. The presence of multiple phenyl rings in the tannic acid molecule is advantageous for its adsorption into carbon mesopores through

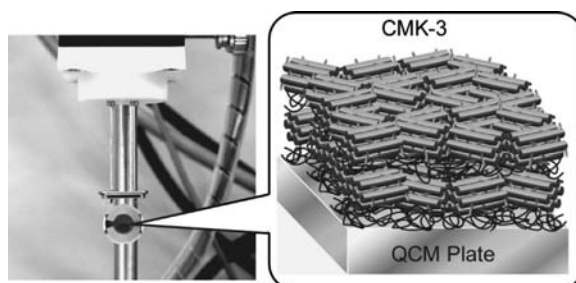


Figure 3.6 QCM sensor system with LbL films of polyelectrolytes with mesoporous carbon materials, CMK-3.

$\pi-\pi$ interactions and hydrophobic effects. In addition, size matching of tannic acid to the CMK-3 nanochannel would result in enhanced adsorption. Interestingly, adsorption quantities of tannic acid to the CMK LbL film at equilibrium showed a sigmoidal profile in the low concentration regions. This highly cooperative behavior may be similarly explained by enhanced guest–guest interaction through $\pi-\pi$ and/or hydrophobic interactions in confined environment.

A sensing system containing mesoporous carbon with more highly advanced structures was also investigated. Vinu *et al.* invented a novel type of nanocarbon, carbon nanocage, that can be synthesized using three-dimensional large cage-type face-centered cubic mesoporous silica materials (KIT-5) as inorganic templates [27–32]. Carbon nanocage prepared under optimized condition has pores with pore diameters of 5.2 nm and cage diameter of 15.0 nm, specific surface areas of $1600\text{ m}^2\text{ g}^{-1}$, and specific pore volumes of $2.10\text{ cm}^3\text{ g}^{-1}$. These structural characteristics are very advantageous for guest adsorption compared with other conventional mesoporous carbon materials. Carbon nanocage materials actually showed a higher capacity of lysozyme adsorption than that observed for CMK-3. Carbon nanocage materials exhibit larger adsorption capacities for tannic acid over catechin, resulting in a highly selective adsorption of tannic acid (~95%) in a simple one-pot process. In addition, carbon nanocage is capable of selective adsorption of nucleosides and DNA intercalators.

This carbon nanocage material can be assembled into hierarchical structures for sensor applications. For example, fabrication of a cage-in-fiber-type nanoporous carbon sensor was reported by Ishihara and coworkers who demonstrated selective sensing of aniline (Figure 3.7) [33]. Carbon nanocage was doped into electrospun nanofibrous films of poly(methyl methacrylate) (PMMA) on QCM mass sensors. Larger surface area and a porous membrane structure advantageous for sensitive and rapid sensing are guaranteed using this hierarchical construction. This sensing device was introduced into a gas flow system. Detection of aniline at the ppm level was possible with high selectivity over many other substances in their vapor phases, including benzene, ammonia, and water. Since aromatic amines such as aniline can be carcinogenic and are found in cigarette smoke, broiled meats, some vegetables,

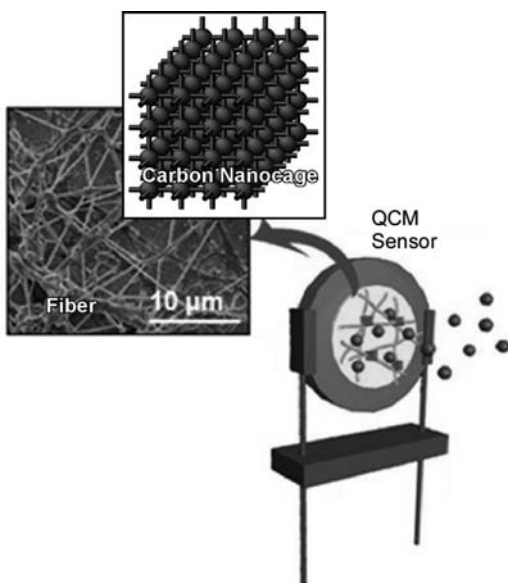


Figure 3.7 A cage-in-fiber-type nanoporous carbon sensor.

and industrial emissions, the real-time sensing realized in this research would certainly be useful for cancer risk management.

3.3.2

Mesoporous Carbon Capsule in Layer-by-Layer Film

Selectivity-tunable sensors were demonstrated using hierarchical assembly of mesoporous carbon capsules. Carbon capsules with homogeneous dimensions ($1000 \times 700 \times 300 \text{ nm}^3$) and 35 nm thick mesoporous walls of a uniform pore size distribution centered at 4.3 nm in diameter and a specific surface area of $918 \text{ m}^2 \text{ g}^{-1}$ were synthesized. Electrostatic LbL assembly for uncharged carbon capsules was performed through surfactant covering of mesoporous carbon capsules with the aid of a counterionic polyelectrolyte.

In vapor-saturated atmospheres, adsorption behaviors of various volatile substances onto the LbL films of mesoporous carbon capsules were monitored by *in situ* frequency shift of the QCM device (Figure 3.8) [34]. Interestingly, aromatic hydrocarbons exhibited higher adsorption values than aliphatic compounds. For example, adsorbed quantities of benzene at equilibrium was about five times greater than that of cyclohexane, although these two guest molecules have similar vapor pressures, molecular weights, and structures. Differentiation between aromatic and aliphatic compounds could be derived from effective $\pi-\pi$ interactions within the mesoporous carbon structures.

One of the pronounced advantages of the capsule structure is selectivity tuning by impregnation with an additional recognition component. Although

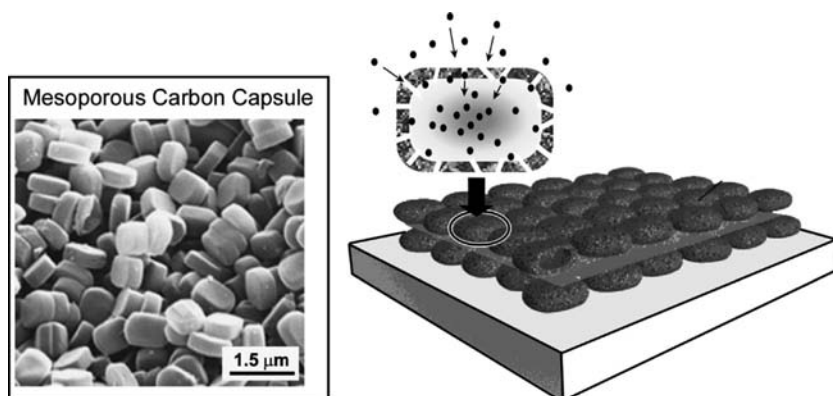


Figure 3.8 LbL films of mesoporous carbon capsules for QCM sensor device.

undoped carbon capsule sensor had high affinities for aromatic carbons, impregnation with lauric acid lead to the greatest affinities for nonaromatic amines based on acid–base interactions. Similarly, a selectivity shift to strong preference for acetic acid was induced by impregnation of dodecylamine into the mesoporous carbon capsule in LbL films. As can be seen in these examples, hierarchical nanostructures of LbL films of mesoporous carbon capsules result in selectivity tuning of sensors. These systems will find widespread applications as sensors or filters because of their tunable guest selectivity.

3.3.3

Layer-by-Layer Assembly of Graphene and Ionic Liquids

As already illustrated, nanostructured carbon assemblies are effective media for detection of toxic aromatic substances because of enhanced or accumulated π – π interaction. If increasingly π -electron-rich nanocarbon materials are used as components of sensing materials, sensor systems more sensitive to aromatic guest may be constructed. For this purpose, graphene is one of the most attractive component materials because it is an ideal two-dimensional π -electron-rich carbon.

For preparation of LbL assembled films, graphene oxide sheet prepared through oxidization of graphite under acidic conditions was reduced to graphene sheet in the presence of ionic liquids. The resulting charged composites of graphene and ionic liquids were then assembled into LbL films with poly(sodium styrenesulfonate) (PSS) on the surface of a QCM plate (Figure 3.9) [35].

Gas sensing capabilities of the LbL films prepared were similarly investigated by exposure of the LbL QCM system to vapors of the target gases. In this case, adsorption of benzene onto the LbL films of graphene nanosheet and ionic liquid was clearly observed, while a similar system containing no interlayer ionic liquid exhibited almost no adsorption capability. In addition, the 10-fold selectivity for benzene over cyclohexane indicates the enhanced selectivity for aromatic vapors of the well-designed π -electron-rich nanospace within the LbL films. Repeated

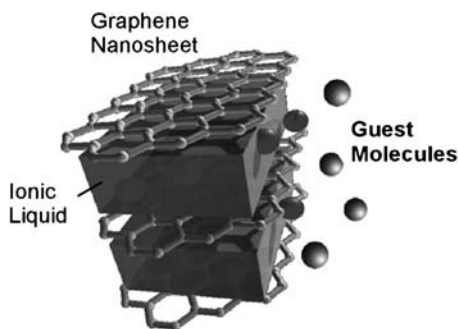


Figure 3.9 LbL film of graphene and ionic liquid for selective gas sensing.

detection of vapors was observed upon alternate exposure and removal of the target gases with gradual degradation of the On/Off response probably due to too strong interactions between aromatic compounds and the graphene layer.

These LbL films can be applied to sensors based on electrical resistance that are sensitive to gas adsorption. In addition, adsorption of CO₂ vapors from a saturated sodium hydrogen carbonate solution into the LbL films of graphene nanosheet and ionic liquid was also confirmed. These experimental results also suggest the great potential for practical applications in a variety of environmental situations.

3.3.4

LbL Films of Mesoporous Silica Capsule for Controlled Release

Hierarchical assembly of inorganic nanomaterials can be used in other applications, such as drug delivery systems (DDS), because structural hierarchy and complexity provide an opportunity to create novel functions and combined properties. Ji *et al.* fabricated LbL films of mesoporous silica capsules that were prepared using pseudohexagonal prismatic zeolite cores as template [36,37]. The resulting mesoporous silica capsules have internal void microspaces ($1000 \times 700 \times 300 \text{ nm}^3$) at the interior and mesopores (average diameter of 2.2 nm) in their silica walls.

Although these silica capsules are negatively charged, mixing with anionic silica nanoparticles simplifies their LbL assembly. The anionic mixture of mesoporous silica capsules and silica nanoparticles was assembled alternately with cationic polyelectrolytes as LbL films on QCM plate (Figure 3.10). As the initial demonstration of material release from the LbL films of mesoporous silica capsule, quantitative analyses of water evaporation from the films were carried out through monitoring frequency shifts of a QCM system. Interestingly, water evaporation from the LbL films of mesoporous silica capsules exhibited stepwise profiles even though no external stimulus was applied.

The unusual profiles of water release observed, referred to as automodulated release of water, can be explained by the following model (Figure 3.11). It is based on combination of two processes: water evaporation from mesopore nanospaces and capillary penetration into the pores. Water entrapped in pores at the

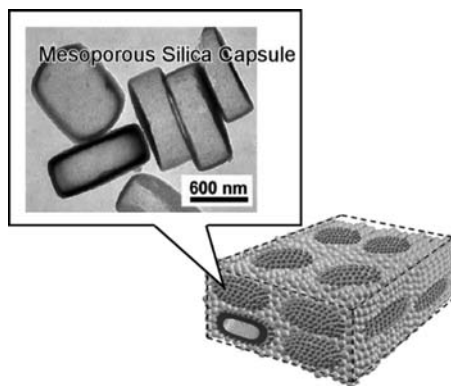


Figure 3.10 LbL film of mesoporous silica capsules (with silica nanoparticles) on QCM plate.

exterior shells initially evaporates in the first step (On stage). Because water molecules at the interior cannot penetrate into the exterior pores under this condition, water evaporates with a decreasing evaporation rate. Therefore, water release slows down (Off stage). Only after the channels between exteriors and interiors are formed upon release of the majority of the water contained in the exterior pores can water enter from the capsules' interiors to refill the pores in the capsule walls. Refilling of water into the exterior mesopores leads to

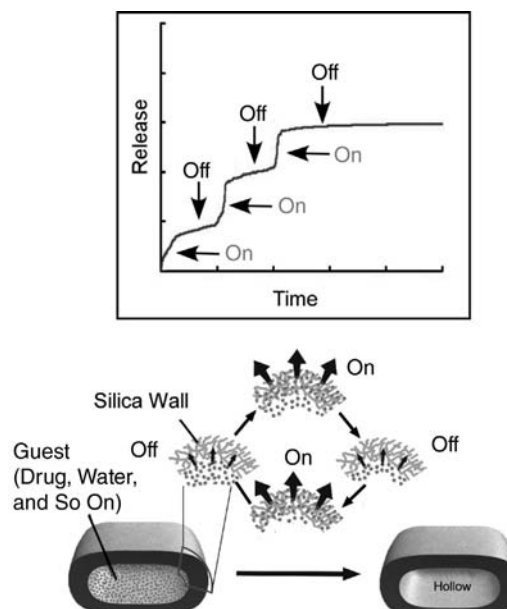


Figure 3.11 Automodulated (periodic On and Off) materials release from mesoporous silica capsules.

resumption of water release to the exterior (second On stage). Repetition of these processes results in automodulated On and Off water release profiles even in the absence of an external stimulus.

Similarly, automodulated release profile from the LbL films of mesoporous silica capsules was observed for various liquid-phase materials such as fragrance molecules. Nonequilibrated concurrent evaporation and capillary penetration can also occur with these rather viscous liquid molecules. Therefore, it is expected that the unusual drug release behaviors observed can be generalized in many cases. In most of the currently available drug release systems, some external stimulus is required for release control. However, the present system can be regarded as a rare example of a stimulus-free controlled release system. It may be used to realize stepwise drug release with prolonged release efficiency, which is of great utility for energy-less and clean controlled drug release applications.

3.4 Summary

In this chapter, various examples of soft assemblies of hard inorganic nanomaterials based on supramolecular concepts have been introduced. Although the building blocks are not strictly organic components, they behave in a similar fashion to organic molecules in that they can be assembled into organized structures. As a result, unusual functions such as enhanced catalytic properties, sensing with tunable selectivity, and automodulated drug release have been realized using the structures fabricated. These examples strikingly indicate that supramolecular chemistry is not only for organic molecules but is also highly applicable to inorganic nanomaterials. Because there is a huge selection of functional nanomaterials available, supramolecular nanotechnology with soft assembly of hard inorganic nanomaterials will be used to create various functional systems and materials in the very near future.

Acknowledgments

We thank World Premier International Research Center Initiative (WPI Initiative), MEXT, Japan and Core Research for Evolutionary Science and Technology (CREST) program of Japan Science and Technology Agency (JST), Japan.

References

- 1 Lundstrom, G. (2003) *Science*, **299**, 210.
- 2 Thompson, S.E. and Parthasarathy, S. (2006) *Mater. Today*, **9**, 20.
- 3 Ariga, K., Nakanishi, T., and Hill, J.P. (2007) *Curr. Opin. Colloid Interface Sci.*, **12**, 106.
- 4 Ariga, K., Hill, J.P., Lee, M.V., Vinu, A., Charvet, R., and Acharya, S. (2008) *Sci. Technol. Adv. Mater.*, **9**, 014109.
- 5 Ariga, K., Lee, M.V., Mori, T., Yu, X.-Y., and Hill, J.P. (2010) *Adv. Colloid Interface Sci.*, **154**, 20.

- 6 Ramanathan, M., Kilbey, S.M., II, Ji, Q., Hill, J.P., and Ariga, K. (2012) *J. Mater. Chem.*, **22**, 10389.
- 7 Li, M., Ishihara, S., Ji, Q., Akada, M., Hill, J.P., and Ariga, K. (2012) *Sci. Technol. Adv. Mater.*, **13**, 053001.
- 8 Ramanathan, M., Tseng, Y.-C., Ariga, K., and Darling, S.B. (2013) *J. Mater. Chem. C*, **1**, 2080.
- 9 Shrestha, L.K., Shrestha, R.G., Hill, J.P., and Ariga, K. (2013) *J. Oleo Sci.*, **62**, 541.
- 10 Hill, J.P., Shrestha, L.K., Ishihara, S., Ji, Q., and Ariga, K. (2014) *Molecules*, **19**, 8589.
- 11 Katagiri, K., Ariga, K., and Kikuchi, J. (1999) *Chem. Lett.*, 661.
- 12 Katagiri, K., Hamasaki, R., Ariga, K., and Kikuchi, J. (2003) *J. Sol-Gel Sci. Technol.*, **26**, 393.
- 13 Katagiri, K., Hashizume, M., Ariga, K., Terashima, T., and Kikuchi, J. (2007) *Chem. Eur. J.*, **13**, 5272.
- 14 Katagiri, K., Hamasaki, R., Ariga, K., and Kikuchi, J. (2002) *Langmuir*, **18**, 6709.
- 15 Katagiri, K., Hamasaki, R., Ariga, K., and Kikuchi, J. (2002) *J. Am. Chem. Soc.*, **124**, 7892.
- 16 Ji, Q., Guo, C., Yu, X., Ochs, C.J., Hill, J.P., Caruso, F., Nakazawa, H., and Ariga, K. (2012) *Small*, **8**, 2345.
- 17 Manoharan, Y., Ji, Q., Yamazaki, T., Chinnathambi, S., Chen, S., Singaravelu, G., Hill, J.P., Ariga, K., and Hanagata, N. (2012) *Int. J. Nanomed.*, **7**, 3625.
- 18 Terentyeva, T.G., Matras, A., Van Rossom, W., Hill, J.P., Ji, Q., and Ariga, K. (2013) *J. Mater. Chem. B*, **1**, 3248.
- 19 Mandal, S., Sathish, M., Saravanan, G., Datta, K.K.R., Ji, Q., Hill, J.P., Abe, H., Honma, I., and Ariga, K. (2010) *J. Am. Chem. Soc.*, **132**, 14415.
- 20 Ariga, K., Hill, J.P., and Ji, Q. (2007) *Phys. Chem. Chem. Phys.*, **9**, 2319.
- 21 Ariga, K., Ji, Q., Hill, J.P., and Vinu, A. (2009) *Soft Matter*, **5**, 3562.
- 22 Ariga, K., Ji, Q., and Hill, J.P. (2010) *Adv. Polym. Sci.*, **229**, 51.
- 23 Ariga, K., McShane, M., Lvov, Y.M., Ji, Q., and Hill, J.P. (2011) *Expert Opin. Drug Deliv.*, **8**, 633.
- 24 Ariga, K., Lvov, Y.M., Kawakami, K., Ji, Q., and Hill, J.P. (2011) *Adv. Drug Deliv. Rev.*, **63**, 762.
- 25 Ariga, K., Yamauchi, Y., Rydzek, G., Ji, Q., Yonamine, Y., Wu, K.C.-W., and Hill, J.P. (2014) *Chem. Lett.*, **43**, 36.
- 26 Ariga, K., Vinu, A., Ji, Q., Ohmori, O., Hill, J.P., Acharya, S., Koike, J., and Shiratori, S. (2008) *Angew. Chem. Int. Ed.*, **47**, 7254.
- 27 Vinu, A., Miyahara, M., Sivamurugan, V., Mori, T., and Ariga, K. (2005) *J. Mater. Chem.*, **15**, 5122.
- 28 Vinu, A., Miyahara, M., Mori, T., and Ariga, K. (2006) *J. Porous Mater.*, **13**, 379.
- 29 Ariga, K., Vinu, A., Miyahara, M., Hill, J.P., and Mori, T. (2007) *J. Am. Chem. Soc.*, **129**, 11022.
- 30 Srinivasu, P., Balasubramanian, V.V., Kumaresan, L., Sawant, D.P., Jin, X., Alam, S., Ariga, K., Mori, T., and Vinu, A. (2007) *J. Nanosci. Nanotechnol.*, **7**, 3250.
- 31 Datta, K.K.R., Vinu, A., Mandal, S., Al-deyab, S., Hill, J.P., and Ariga, K. (2011) *J. Nanosci. Nanotechnol.*, **11**, 3084.
- 32 Datta, K.K.R., Vinu, A., Mandal, S., Al-deyab, S., Hill, J.P., and Ariga, K. (2011) *J. Nanosci. Nanotechnol.*, **11**, 3959.
- 33 Kosaki, Y., Izawa, H., Ishihara, S., Kawakami, K., Sumita, M., Tateyama, Y., Ji, Q., Krishnan, V., Hishita, S., Yamauchi, Y., Hill, J.P., Vinu, A., Seime, S., and Ariga, K. (2013) *ACS Appl. Mater. Interface*, **5** 2930.
- 34 Ji, Q., Yoon, S.B., Hill, J.P., Vinu, A., Yu, J.-S., and Ariga, K. (2009) *J. Am. Chem. Soc.*, **131**, 4220.
- 35 Ji, Q., Honma, I., Paek, S.-M., Akada, M., Hill, J.P., Vinu, A., and Ariga, K. (2010) *Angew. Chem. Int. Ed.*, **49**, 9737.
- 36 Ji, Q., Miyahara, M., Hill, J.P., Acharya, S., Vinu, A., Yoon, S.B., Yu, J.-S., Sakamoto, K., and Ariga, K. (2008) *J. Am. Chem. Soc.*, **130**, 2376.
- 37 Ji, Q., Acharya, S., Hill, J.P., Vinu, A., Yoon, S.B., Yu, J.-S., Sakamoto, K., and Ariga, K. (2009) *Adv. Funct. Mater.*, **19**, 1792.

4

Nanoparticles: Important Tools to Overcome the Blood–Brain Barrier and Their Use for Brain Imaging

Ruirui Qiao, Mingyuan Gao, and Hans-Joachim Galla

4.1

Introduction

The treatment of neurological diseases is often limited by the low permeation of drugs into the brain due to the existence of highly impermeable and selective cellular barriers separating the blood stream from the brain parenchyma, thereby not only maintaining the homeostasis of the brain but also protecting the central nervous system (CNS) against invading organisms and hydrophilic as well as large hydrophobic substrates [1]. Thus, the brain import of a variety of drugs and therapeutic agents such as antibodies, recombinant proteins, and enzymes in enzyme replacement therapy or small interfering RNAs is hampered. The two important gateways to enter the brain parenchyma targeting mainly the neurons as the transducing cellular unit are the blood stream and the cerebrospinal fluid (CSF) [2].

The endothelial cells of the cerebral microvessels form the so-called blood–brain barrier (BBB). Due to their low number of fenestrations, reduced pinocytosis, and almost impermeable intercellular connections called tight junctions, this endothelial monolayer provides a strong physical barrier. The cells of the neurovascular unit (astrocytes, pericytes, and neurons) contribute to the tightness of the barrier via cell–cell interaction, gap junction communication, and/or soluble factors [3]. One major component has been found recently to be the extracellular matrix (ECM) produced and assembled by all the cells that are involved in the making of the barrier [4–6]. It seems to be important to note that the total length of the capillaries in the brain is roughly 650 km, covering an impressive area of about 20 m^2 [7].

The second important barrier is the blood–CSF barrier (BCSFB), which is morphologically as well as functionally different from the BBB [8]. The barrier is formed within the choroid plexus covering the two laterals as well as the third and fourth ventricles [9]. This highly branched network of vessels is also lined by endothelial cells, which, however, are fenestrated and thus highly leaky. However, polarized epithelial cells in a sandwich-like structure facing the CSF with their apical side form a tight barrier, restricting the movement of ions and

molecules. Besides their barrier forming properties, their main function is the production of the CSF [10].

Since passive diffusion into the brain is almost impossible except for small hydrophilic compounds, controlled transport processes have to be provided not only to provide the brain nutrition, vitamins, and nucleotides but also to remove metabolic degradation products. Moreover, proton and ion gradients have to be maintained, for example, to allow CSF secretion [11]. For these processes, passive as well as active (ATP-dependent) transporters are needed and thus are present in both the endothelial cells of the BBB [12] and in the epithelial cells of the BCSFB [13,14]. Of major importance for drug delivery to the brain are ATP-binding cassette transporters (ABC transporters) with multidrug resistance that act as efflux pumps, pumping pharmaceutical agents back to the blood stream at the BBB. Application of specific inhibitors of these ABC transporters is one strategy toward drug delivery to the brain. Chemical modification of the substrates making them unspecific is another strategy. Finally, using nanocontainers as camouflage helps to bypass the barrier.

4.2

Physiology of the Blood–Brain Barrier

4.2.1

The Endothelial Blood–Brain Barrier

The blood–brain barrier is located within the cerebral capillaries and is formed by the endothelial cells lining the vessel wall. Pericytes, astrocytes, and neurons are part of the so-called cerebrovascular unit (CVU), although they do not contribute directly to the barrier but indirectly by inducing barrier properties in the endothelial cell layer and by including the extracellular matrix (Figure 4.1) as mediator in between those cells. Composition of the matrix as well as its assembly is of major importance for the maintenance of the BBB [15].

The paracellular diffusion through the intercellular cleft is strongly limited by the formation of tight junctions and assisted by both adherens and gap junctions. Since diffusion of hydrophilic substances is limited, the supply of nutrition to the brain is through transporters. Hydrophobic and membrane-soluble substrates can however pass through the physical barrier by diffusion. Efflux pumps of ABC transporter families, however, protect the brain against uncontrolled invasion of a large variety of foreign substances by actively pumping them out of the endothelial cells and back into the blood stream.

Tight junctions are formed by a belt of so-called tight junction proteins such as occludins and claudins [16] and may include lipidic assemblies [17]. They do not only form the physical barrier leading to high electrical resistances up to $2000 \Omega \text{ cm}^2$ as a measure for the barrier that leads to a gate function but also guarantee the polarity of cells by their fence function hindering diffusion of membrane components from the apical to the basolateral side and vice versa [18,19].

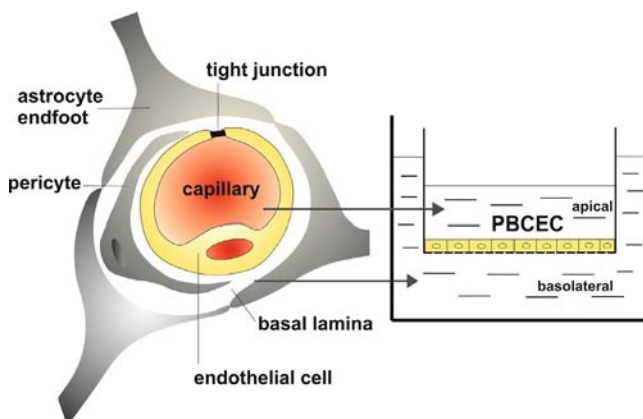


Figure 4.1 The cells of the neurovascular unit forming the blood–brain barrier. (Adapted with permission from Ref. [3]). The endothelial cells (yellow) are lining the lumen of the brain capillary, thus sealing the intercellular cleft by tight junctions. Astrocytic end feet contact the endothelial surface but do not contribute to the physical barrier. However, the extracellular matrix (basal lamina) separates the astrocytes from the endothelial cells. Pericytes are embedded into the extracellular matrix. *In vitro* models can be engineered where the

endothelial cells grow on a permeable filter (here porcine brain endothelial cells). This arrangement allows the coculture with pericytes and/or astrocytes by growing them on the lower side of the filter or on the bottom of the well. The polarized endothelial cells form the apical and the basolateral sides corresponding to the blood and the brain sides *in vivo*. The filter might be coated by extracellular matrix material. This arrangement allows transport experiments in both directions.

4.2.2

The Blood–CSF Barrier

The blood–CSF barrier separates the CSF from the blood stream and is located in the choroid plexus of the two laterals and the third and fourth ventricles. The endothelium in the choroid plexus is highly fenestrated and thus leaky. However, an epithelial layer attached to the basolateral (brain) endothelial side in a sandwich-like arrangement is joined together by tight junctions [11]. Thus, this epithelial layer forms the barrier that restricts the diffusion of hydrophilic molecules and ions between the blood and the cerebrospinal fluid. Moreover, epithelial cells secrete the CSF [20], thus maintaining the homeostasis within the CSF but in parallel provide a drainage system to the brain. Similar to the endothelial cells of the blood–brain barrier, the epithelial cells of the blood–CSF barrier exhibit a polarized expression of transporters. These transporters contribute to the neuroprotective function of the blood–CSF barrier and are also responsible for influx and efflux of drugs and metabolites, including solute carriers as well as ABC transporters [14]. The blood–CSF barrier also serves as an entrance for drugs into the brain and may thus be a target for nanoparticles loaded with drugs, for example, to overcome the multidrug resistance.

4.2.3

Regulation of the Barrier Tightness

The blood–brain barrier regulates the influx/efflux of a large variety of endogenous and exogenous compounds such as nutrition, hormones, nucleotides, vitamins, and ions, to name a few. The crucial elements for all transport processes and for the passive inward and outward flux of compounds by diffusion are the tight junctions with their junctional proteins (e.g., zonula occludens (ZO), occludin, and claudin proteins) in a serial arrangement to the adherens junction containing the junctional adhesion molecules as well as the catenin/cadherin complex. This special arrangement [21], although different for different members of the corresponding protein families (e.g., claudins 1 and 5 in endothelial cells and claudins 1, 2, and 11 in epithelial cells), causes barrier properties with electrical resistances up to $2000 \Omega \text{ cm}^2$, restricting the passive paracellular entry of even small hydrophilic compounds and ions. The tightness of the barrier is strongly regulated by other cells belonging to the CVU, the astrocytes and the pericytes. It is especially important to note that the extracellular matrix secreted by all the cells of the CVU is one of the major regulators for barrier tightness. Both the composition and the assembly of the ECM are crucial for the barrier development, including the action of matrix metalloproteinases (MMP) and their inhibitors, the tissue inhibitors of MMPs (TIMPs) [22,23]. It has been reported that under pathophysiological conditions, MMPs are even able to cleave occludin and thus open the junctions [24]. Moreover, mediators of the signal transduction cascades are involved in the regulation of tight junctions mainly by phosphorylation and dephosphorylation as well as by the modulation of intra- or extracellular Ca^{2+} content. Thus, in summary, the tight junctions are highly dynamic structures sensitively regulated by a complex and interconnected interaction network. This topic has been reviewed in detail elsewhere [25].

4.2.4

Transport Routes and Drug Permeability across the Blood–Brain Barrier

As already indicated, the influx/efflux of compounds across the BBB is strongly regulated. Tight junction permeability, membrane transporters, and metabolic enzymes modulate the barrier permeability by permitting or inhibiting the transcellular traffic.

Three different routes have to be considered (Figure 4.2):

- 1) Passive diffusion following a concentration gradient that needs no metabolic energy. However, even if such a concentration gradient exists, molecular weight and low lipophilicity may limit the diffusion. Only lipophilic molecules with molecular weight below 400 Da may cross the BBB via diffusion along the cellular membrane. However, it has to be considered that ABC transporters act as efflux pumps to export membrane-soluble molecules out of the brain.

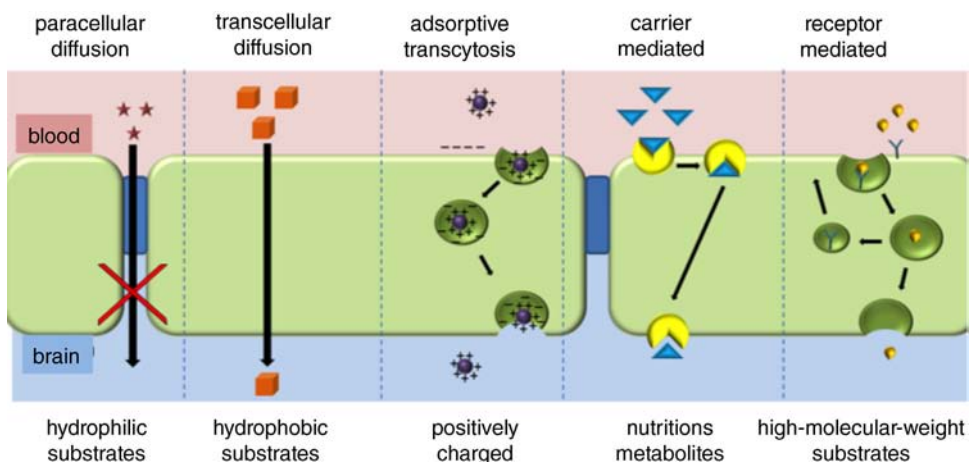


Figure 4.2 The transport barrier of brain capillaries strictly regulates the transcellular passage of substrates differing in size, charge, and hydrophobicity. Hydrophilic substances may cross the barrier passively via the tight junctions by paracellular diffusion. Small hydrophobic substrates with high lipid solubility may be taken up across the cellular membrane, again by passive diffusion. This pathway is strictly controlled by the ABC transporters acting as efflux pumps and thus transporting those substrates back into the blood stream. Adsorptive transcytosis followed by endocytosis allows the uptake of positively charged molecules such as cationized albumin

catalyzed by electrostatic interaction. Solute carriers are responsible for cellular supply with essential nutrients such as glucose, amino acids, nucleosides, organic ions, monocarboxylates, and metabolites. This mediated transport requires specific binding to the corresponding carrier. The solute carriers might act uni- or bidirectionally and be an active process. Receptor-mediated transcytosis and endocytosis are responsible for the transfer of macromolecules, mainly proteins. Note that both adsorptive and receptor-mediated transcytosis demand the formation of vesicles enclosing the cargo.

- 2) Carrier-mediated transport involving proteins that facilitate either passive diffusion or using ATP hydrolysis for active transport.
- 3) Endocytosis combined with transcytosis demands for an internalization of molecules from the circulation by the formation of vesicles. Endocytosis targets the endosomes or lysosomes; transcytosis is responsible for a transcellular transport. Both processes can be either adsorptive or receptor mediated. Adsorptive processes are mainly induced by electrostatic binding of the positively charged large molecules (proteins) with the negatively charged membrane surface. Receptor-mediated uptake begins either with the specific interaction of a ligand with its receptor on the luminal membrane surface targeting the endosomes or lysosomes or with the externalization of a ligand at the abluminal membrane.

The nanoparticles are used as carriers mainly to mediate endocytic ways to transfer drugs across the BBB by circumventing the multidrug resistance using a “camouflage concept.”

4.2.5

In vitro Models of the BBB and Blood–CSF Barrier

Most of the present knowledge about barrier properties, the regulation of the barrier tightness, tight junctions, and transport processes comes from studies using *in vitro* models. Besides using isolated brain capillaries as *ex vivo* models, *in vitro* cell culture models are also used due to their easy availability and the possibility to grow them on filter devices, thus getting access to both the apical (blood) and basolateral (brain) sides. However, cell culture conditions have to be selected to allow polarized cell growth and proper development of barrier properties, for example, tight junctions [26]. This is basically fulfilled only in primary cells. Most of the cell lines that have been generated do not express all transport systems and none of them develops barrier properties as are expected from *in vivo* measurements. One of the best models with respect to barrier properties is a porcine model (porcine brain capillary endothelial cells (PBCEC) Figure 4.1), where cells are grown to confluence and then transferred into serum-free medium generating electrical resistances up to $2000\Omega\text{ cm}^2$ and a permeability down to 10^{-7} cm s^{-1} [27]. Immortalized cell lines obtained from the brain of different sources, including humans, have the advantage of long-term availability due to the possibility of almost unlimited passages. However, they develop only reduced barrier properties with electrical resistances far below $100\Omega\text{ cm}^2$, which does not represent the *in vivo* situation. They are however useful in investigating general cellular events. With regard to transport measurements, especially of small molecules, the barrier is far too weak. The same is true for choroid plexus epithelial cells. We have shown that these epithelial cells in culture develop in serum-free medium barrier properties that are high enough to secrete on their apical side CSF-like fluid that is able to build up a water column of 4 cm [28]. This was possible only if the tight junctions are tight enough to prevent backflow of ions and protons, because their gradient is essential to secrete actively the CSF-like fluid. Another advantage of cell cultures is, as already said, their access to both the apical and basolateral side. This is especially important for the choroid plexus epithelial cells, where the upper apical membrane represents the brain side (CSF-oriented). For the study of cell transfer into the brain, one has to realize that this is possible only if the substrate under investigation is added to the basolateral side, which normally is the lower filter compartment. Thus, for transfer of nanoparticles or for transmigration studies with microorganisms or inflammatory cells, one has to use an inverted design that has been developed by Tenenbaum *et al.* [29].

It is well known that the barrier properties could be improved by coculturing the endothelial cells of the BBB with astrocytes and/or pericytes. In case of pericytes, it is important to note that their barrier-inducing effect strongly depends on their differentiation [30]. Besides, for the coculture model, using only extracellular matrix produced by astrocytes and/or pericytes is a very new approach, which makes transport studies easier [5]. Finally, one has to consider that the models mentioned so far are mainly used in a static system. Within the vessels,

however, endothelial cells are exposed to shear stress. Thus, dynamic models are thought to better mimic the *in vivo* situation [31].

Finally, we will discuss the use of noncerebral endothelial or epithelial cell lines in place of BBB barrier cells. Although this is not studied here in detail, it should be however stated that MDCK (Madin Darby canine kidney) cells or CaCo (colon carcinoma) cells develop tight junction but by no means represent the brain and thus should not be used as brain surrogates.

4.3

Definition and Type of Nanoparticles and Nanocarriers for Brain Uptake

Different neuroinvasive strategies have been applied to enhance the brain uptake of therapeutic drugs, including direct injection into the parenchyma, implantation of drug-loaded polymeric matrices, polymeric wafers, and microcapsules with controlled release. Nonsurgical strategies, such as opening of the BBB with hyperosmotic solution, for example mannitol and combined addition of drugs, have been applied. Recently, using polymeric butyl cyanoacrylate nanoparticles as both a nanocarrier and an “opener” for the blood–brain barrier has been proposed to reduce temporarily the electrical resistance and thus increase the permeability for a short time (hours) followed by a recovery period resealing the opened barrier [32].

Nanoparticles are mainly used as nanocontainers to target the brain and to release their carriage there. Drugs may be incorporated in or attached to the nanoparticles. Endogenous recognition molecules such as receptor ligands or antibodies could be attached to the outer surface mediated by linkers such as polyethylene glycol (PEG), which not only fulfill the role of spacer molecules but also increase the biocompatibility and water solubility of nanoparticles.

Nanoparticles may be classified by their chemical nature into organic and inorganic carriers. Since the preparation, the nature, and the coating of organic nanoparticles have been described extensively in the last years, we will here mainly focus on inorganic nanoparticles and their use in medical diagnosis and as transport facilitators. The organic nanoparticles will be summarized only in brief and references will be given to recent reviews for further information [6,25,33,34] to avoid repetitions.

4.3.1

Organic Nanoparticles

Organic nanoparticles are built mainly by polymers of either synthetic or natural origin. The monomeric units may be covalently coupled or self-assembly processes may be used to create nanocontainers that could be filled with drugs, or drugs could be adsorbed or attached to the surface. The surface itself could be modified [35] with respect to its charge, rendering it positive to promote cellular surface adsorption, and/or by linking recognition molecules for targeting purposes (Figure 4.3).

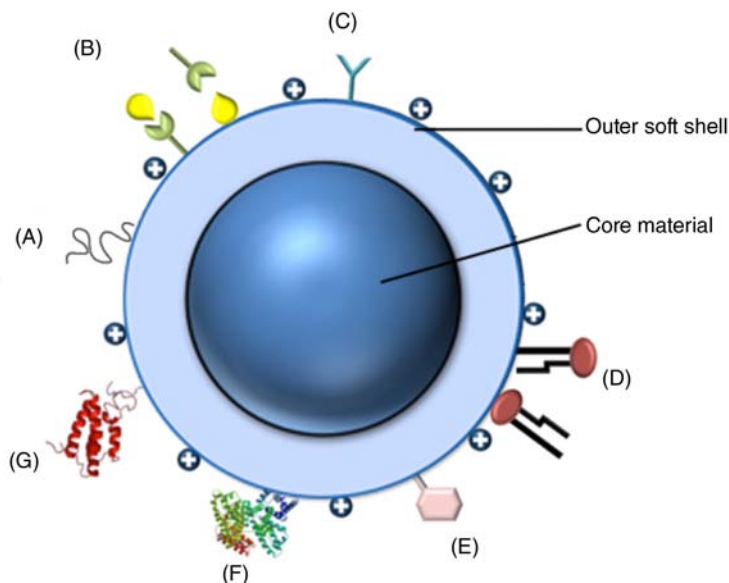


Figure 4.3 Schematic and integrated view of a nanoparticle exhibiting different material properties related to the inner core, outer shell, and functionalization. For drug delivery, the core is mainly aqueous or filled with soft materials such as hydrogels. For imaging techniques, the core might be a solid-state material such as iron oxides, quantum dots, or other inorganic materials. The outer soft shell might be a lipidic monolayer or bilayer, a protein corona or a polymer matrix. The surface might be functionalized by (A) surface functionalization ligands with terminal groups

such as $-COOH$, $-NH_2$, maleimide, and so on for further bioconjugation with molecules, (B) receptor molecules such as lactoferrin and transferrin, (C) antibodies, (D) lipids, oriented with their head groups to the surface for hydrophilic and with their fatty acid tails for hydrophobic shell material. They might form close monolayer and/or bilayers. Detergents are eligible as well: (E) carbohydrates, (F) cationic proteins for adsorptive transcytosis, and (G) cell-penetrating proteins or peptides to facilitate transcytosis.

4.3.1.1 Polymeric Nanoparticles

Nanoparticles made of acrylic acid derivatives have been widely used for CNS drug delivery and are described extensively in a recent review by Kreuter [33]. The crucial requirement for nanoparticles for brain delivery is that they should be biodegradable and nontoxic. This is perfectly fulfilled by poly(butyl-cyanoacrylate) nanoparticles, mostly overcoated with surfactants such as polysorbate 80 (Tween 80) or poloxamer 188 (Pluronic F68). These particles are reported to be taken up by endocytosis followed by transcytosis (discussed in detail in Refs [36,37]), or they may temporarily open tight junction as has been shown in BBB models [38]. Furthermore, it has been demonstrated that apolipoprotein E (apoE) adsorbed to the surface further enhances brain uptake probably by interacting with the scavenger SR-BI and/or the LDL-receptor (LRP1). Polylactic acid and its copolymeric compounds (D,L -lactide-*co*-glycolide and D,L -lactic-*co*-

glycolic acid) have also been used as a promising material due to their prevailing fast degradation by lipases, whereas esterases are responsible for the degradation of cyanoacrylates. It is important to note that not only the surface properties, the size, the composition of the core, and the incorporated drug but also the stabilizers such as surfactants, lipids, dextrans, proteins, or even polyvinyl alcohol that might have been used during nanoparticle preparation play a major role in the envisaged drug delivery efficacy [39,40].

4.3.1.2 Liposomes and Lipidic Nanoparticles

Many lipids in aqueous dispersion form closed spherical bilayer membranes incorporating an aqueous core. Depending on their hydrophilicity/hydrophobicity, drugs could be trapped within the aqueous interior or embedded into the hydrophobic membrane bilayer. Most of the lipid vesicles unfortunately are not suitable to be used in targeting the brain because they are mainly taken up by the liver [34]. However, even small amounts reaching the brain may be favorable for drug delivery to the brain. Antineoplastic agents may be incorporated into the membranes to enhance the circulation time. The lipid composition, for example, addition of cholesterol, strongly influences the biodistribution and the release efficacy. Some lipids exhibit thermotropic phase transition from the so-called quasi-crystalline (below the phase transition temperature) to the fluid state (above the phase transition temperature). Thus, thermosensitive liposomes can be fabricated to allow the release of an encapsulated drug under temperatures above the phase transition temperature crossing the BBB and releasing the content by hyperthermia [41]. Membrane-spanning ligands can be incorporated for selective targeting [42].

Liposomes should not be confused with lipid nanoparticles. These include lipid nanocapsules consisting of an oily core (e.g., fluid short-chain triacylglycerols) and a shell of lipids being oriented with their fatty acid chains toward the lipophilic surface and with their hydrophilic head groups toward the aqueous phase rendering these hydrophobic droplets hydrophilic (Figure 4.3). Solid lipid nanoparticles also contain a hydrophobic core made up of long-chain triacylglycerols and waxes, which are solid at physiological temperatures. Detergent to make it soluble in aqueous solutions then covers this hydrophobic core. The solid lipid nanoparticles are more stable, better protect the enclosed drug, and are biodegradable. However, the loading capacity is low due to the limited solubility of hydrophobic drugs in the rigid inner core.

A third approach besides using lipids as a building block to engineer nanocarrier is the coating of nanoparticles with lipids. With such a lipid corona, the possible cytotoxicity of nanoparticles could be decreased and their brain permeation could be increased by using appropriate lipids to mask unfavorable properties of the nanoparticle itself.

4.3.1.3 Nanomic Emulsions, Micelles, and Nanogels

Nanomic emulsions are closely related to the already discussed lipidic nanoparticles. However, they are smaller in size consisting of nanosized droplets of

biological oils (e.g., flaxseed oil) in stable dispersion. They are mainly used to improve the drug bioavailability for oral administration, but have also been shown to improve brain delivery. This should not be confused with nanosuspensions, which are simply formulations of highly dispersed solid particles, sometimes in the presence of surfactants. The advantage of such a formulation is the increased effective surface area allowing better bioavailability.

Micelles are aggregates of amphiphilic molecules dispersed in water and able to incorporate small hydrophobic molecules into the micellar core and thus improve drug transport of poorly water-soluble lipophilic compounds.

Nanogels are nanoparticles composed of hydrogels consisting of a cross-linked polymer network. Similar to hydrogels, the pores of the nanogels can be filled up with molecules fitting to the size of the mesh of the polymer. They are used not only as drug delivery matrices but also as a matrix to enclose contrast agents for medical imaging.

4.3.1.4 Carbohydrates

Many receptors carry moieties that specifically recognize sugars or sugar derivatives. The improved endocytosis by the mannose-6-phosphate receptor, for example, has been used to increase the brain delivery of an enzyme needed to compensate for an enzyme deficiency-related disease behind the BBB [43,44]. Approaches that use nanoparticles with sugar moieties as recognition unit are numerous. Carbohydrates, however, are also used as nanoparticulate systems to incorporate drugs. Among such well-known nanoparticles are those that are build up by chitosan or those coated with chitosan, the product of the enzymatic digest of chitin, the major compound of the crustaceans cytoskeleton [45]. This natural product is best suited to incorporate not only drugs but also proteins, nucleic acids, and even cells. Due to the high water content of their structures and the possibility to form self-assembled aggregates with different kinds of polysaccharides, they are closely related to hydrogels already discussed. A summary of the state of the art is given in Ref. [46].

Dextran is another well-known highly branched polysaccharide used to coat nanoparticles. The linear cyclic form, the cyclodextrin, composed of at least six alpha-bonded glucopyranose units, has long been used to separate stereoisomers. Their inner cavity is hydrophobic and the outer surface is hydrophilic, which enables it to best suit the noncovalent inclusion complexes [47,48]. Other carbohydrates such as hyaluronic acid, gelatin, or even micelle-forming lipopolysaccharides have been used to coat or to form nanoparticles.

Besides the formation of nanoparticles, carbohydrates are often used to functionalize nanoparticles of different composition.

4.3.2

Inorganic Nanoparticles

Inorganic nanoparticles with intrinsic magnetic, optical, thermal, or electrical properties have provided great opportunities for imaging or therapeutic

applications. With the development of the synthesis and surface functionalization, inorganic nanoparticles such as magnetic nanoparticles, semiconductor nanoparticles, and gold nanoparticles have shown prominent potential for brain disease detection, drug delivery along with BBB transport abilities, and their novel applications.

4.3.2.1 Magnetic Nanoparticles

Magnetic nanoparticles in the form of iron oxide nanoparticles (Fe_3O_4 and $\gamma\text{-Fe}_2\text{O}_3$) have received great attention for medical applications as MRI contrast agent since 1980's [49]. Due to its unique superparamagnetic property, iron oxide nanoparticles can greatly enhance the contrast in T_2 -weighted images. In principle, superparamagnetism occurs when the core size of iron oxide nanoparticles is smaller than 20–30 nm [50]. More recent studies demonstrated that if the size is further reduced to less than 4 nm, paramagnetism would be the dominant property, which enables the enhancement in T_1 -weighted images [51].

In vivo application of iron oxide nanoparticles strongly relies on their hydrodynamic size. In general, superparamagnetic iron oxide (SPIO) (larger than 50 nm) can be quickly taken up by the reticuloendothelial system (RES), leading to the application as contrast agents for diagnosis of liver and spleen diseases [49,52]. On the contrary, ultrasmall superparamagnetic iron oxides (USPIOs) (smaller than 50 nm) were used for lymph node metastases diagnosis for their longer plasma circulating time, which also favors accumulation at tumor site by the enhanced permeability and retention (EPR) effect [53–57].

Recently, paramagnetic inorganic nanoparticles such as gadolinium-based nanoparticles (e.g., GdF_3 [58], GdPO_4 [59], Gd_2O_3 [60], and NaGdF_4 [61]) and manganese-based nanoparticles (e.g., MnO [62] and Mn_3O_4) as alternatives of paramagnetic chelate-based T_1 contrast agents have received great attention in the past few years. Benefiting from the large size and variable surface functional ligands, paramagnetic nanoparticles not only prolong the circulating time but also enable the targeting imaging by conjugating with biomolecules. In addition, doping with rare-earth (RE) elements with luminescent property, such as Yb^{3+} and Er^{3+} , could further enable the utilization for MRI/optical dual-modality imaging.

4.3.2.2 Semiconductor Nanoparticles

Semiconductor nanoparticles or quantum dots (QDs) are fluorescent probes with outstanding optical properties arising from the quantum confinement effect. In comparison with organic dyes, the optical properties of QDs exhibit valuable features extremely useful for *in vivo* bioapplications, such as broad excitation range, narrow and symmetrical emission, and photochemical stability [63,64]. Moreover, the emission of QDs is tunable from visible to near-infrared (NIR) by changing their size or composition, allowing for in-depth fluorescence detections with greater signal/background ratio [64].

Besides the innately low spatial resolution, optical signal also suffers from low penetration in passing through the skull for brain disease detection [65].

Incorporation of paramagnetic ions such as Mn²⁺ into QDs has been used to create fluorescent/paramagnetic dual-modality probes [66], allowing for *in vivo* optical and MRI detection [65,67].

4.3.2.3 Gold Nanoparticles

Gold nanoparticles (GNPs) are well known as attractive nanoplatform for imaging, drug delivery, and therapeutic applications. GNPs exhibit strong surface-plasmon-enhanced absorption and scattering effects at both the visible and the NIR spectrum range [68], thereby allowing its utilization as optical imaging probe as well as photothermal therapy [69,70]. In addition, GNPs are also ideal CT contrast agents owing to their much higher attenuation attributed to their large atomic number and electron density of gold [71–73]. During the past few decades, tremendous efforts have been made in the field of GNPs-based brain delivery [74–79]. Moreover, GNPs also have favorable biocompatibility owing to their nontoxicity and inertness profiles, making them as ideal nanoplatform for targeting diseases within the CNS.

Although a size-dependent distribution of GNPs in the brain has been reported, showing that smaller GNPs (15 and 50 nm) are more likely to pass through BBB in comparison to their larger counterparts (100 and 200 nm) [80], the relatively low concentration in the brain depending on the administrated dose is far from being enough for brain delivery applications. Therefore, functional modifications of GNPs for increasing BBB transport efficacy are essential to enhance the accumulation in brain.

4.3.3

Surface Functionalization of Nanoparticles for BBB Transport

Surface functionalization of nanoparticles is one of the predominant factors determining the biological behavior as well as the biomedical application of nanoparticles. In general, physicochemical properties of nanoparticles mainly contributed by charge and hydrophilicity/hydrophobicity of surface coating strongly affect the biodistribution of nanoparticles. Obviously, a sufficient circulating time is favorable for increasing the chance of BBB transport and then enhancing the brain delivery.

With respect to the surface charge, the cationic lipid nanoparticles have been demonstrated to effectively increase the permeability of BBB on an *in vitro* model in comparison to the neutral nanoparticles [81]. However, the *in vivo* effectiveness is still debatable for the reason that cationic charged particles are easily taken up by RES before reaching the target tissues [82].

Actually, intravenously injected nanoparticles are first recognized by opsonins (i.e., circulating plasma proteins, including various subclasses of immunoglobulins, complement proteins, and fibronectin) and then taken up by the RES. Therefore, to avoid the absorption of opsonins, antibiofouling polymers such as PEG are commonly used [57,83–85]. The highly flexible and hydrated PEG chain has an effective opsonins-resistant property for providing a presumed steric

barrier to plasma protein adsorption [86]. Furthermore, as verified by the improving BBB transport of PEGylated Fe₃O₄ nanoparticles, the amphiphilic nature of PEG could further enhance the BBB permeation [57,84].

Apart from the chemical coating on the particle surface, specifically transport through BBB is further required to increase the BBB delivery. Therefore, functionalization of nanoparticles with appropriate targeting ligands (e.g., antibody, protein, peptide, sugar moiety, folate, or carbohydrates) is widely applied for the BBB transport. In principle, selection of transport ligands is commonly based on the already-mentioned transport routes, including the adsorption-mediated transcytosis (AMT) and receptor-mediated transcytosis (RMT).

For BBB transport through AMT, cationized proteins, including bovine serum albumin (BSA), insulin, and immunoglobulin (IgG), showed greater enhanced of brain penetration in comparison to the natural counterparts. By covalently binding with cationic BSA (CBSA), Lu *et al.* systematically investigated the brain delivery of PEG–PLA nanoparticles on both *in vitro* and *in vivo* models [87]. Importantly, a rational density of CBSA on the surface of PEG–PLA nanoparticles (110 per nanoparticle) could lead to a 2.3-fold increase in brain in comparison to PEG–PLA nanoparticles. The increased number of CBSA showed compromised blood half-time consistent with another study that the blood half-time of cationized rat albumin (2.5 h) was around 50% of native rat albumin (4.8 h) [88]. Therefore, a balance between surface charges for acquiring prolonged circulating behavior and enhancing BBB transport through AMT needs to be taken into consideration for brain delivery nanocarrier design.

Cell-penetrating peptides (CPPs), positively charged peptides with short sequences between 10 and 27 amino acid residues, are another group of ligands for BBB transport through AMT [89]. Although the mechanism of BBB transport by CPPs is still under debate (AMT or RMT), the cationic nature of CCPs plays a crucial role owing to their translocation ability associated with AMT approach [90]. SynB3 (RRLSYSRRRF) and transactivator of transcription (TAT) (HIV-1 transactivating transcriptor) are two notable CPPs for increasing BBB delivery of drugs or nanoparticles. To date, only TAT was found to couple with nanoparticles for BBB transport [91,92]. TAT-coupled polymeric micelles self-assembled from cholesterol-conjugated PEG [92], liposomes fabricated from cholesterol-PEG2000 [93], and QDs [65] showed effective enhancement of brain delivery, indicating that nanocarriers conjugated with TAT could be a promising carrier system for BBB transport.

Apparently, due to the cationic charge of the surface, AMT-based BBB transport systems can potentially accumulate in nontargeted organs, particularly RES, suffering from the lack of selectivity. Based on the RMT route, active targeting through BBB can be achieved. Benefiting from the endogenous RMT systems, ligands can be easily selected from the molecules with specific receptors on the BBB. Transferrin (Tf), OX26 (antibody against Tf receptor), lactoferrin (Lf), and angiopep-2 have been utilized for BBB transport of nanoparticles. Among them, Tf has been conjugated with multiple nanocarriers such as PEG liposomes [94,95], poly(lactide)-D-alpha-tocopheryl polyethylene glycol succinate

(PLA-TPGS) diblock copolymer [96], and magnetic nanoparticles [97] for brain targeting. Particularly, the Tf receptor has been demonstrated to be overexpressed not only on brain capillary endothelium but also on brain malignant tumors [98], making it a very attractive tool for enhancing simultaneously the brain permeation as well as the tumor targeting ability.

4.4

Nanoparticles and Imaging

4.4.1

Magnetic Resonance Imaging (MRI)

For brain disease imaging, MRI is one of the primary imaging modalities used in the clinic for providing high spatial and temporal resolution. Normally, contrast agents such as gadolinium chelates are used to further generate hyperintense regions for shortening the longitudinal (T_1) relaxation time of water, increasing the contrast between normal and disease tissues. By using relatively high-molecular-weight gadolinium-based macromolecular contrast agent, brain tumors could be enhanced by passing through the disrupted BBB [99]. However, gadolinium-based contrast agents suffer from the inability of BBB transport, which limits their utility for brain disease diagnosis [100].

Nanoplatforms have been developed for enhancing the delivery of contrast agent. Spires-Jones and coworkers reported a biodegradable nanoparticle-based BBB transport system to deliver BBB-impermeable molecular imaging probes into brain for targeted neuroimaging. MRI contrast agent gadobutrol (Gadovist) was adsorbed onto the polysorbate 80-coated (poly(*n*-butyl-cyanoacrylate) (PBCA) nanoparticles and the obtained nanoparticle showed several hundred-fold increase in comparison to the gadobutrol [101]. The prolonged blood half-time (2.5 h) of the PBCA nanoparticles combined with the apoE adsorption facilitated BBB crossing through a receptor-mediated transcytosis route.

Gd-based inorganic nanoparticles were also investigated for increasing the longitudinal relaxivity as well as promoting the longer retention time at tumor site [61,102]. Fortin and coworkers developed a synthesis route of PEGylated ultrasmall gadolinium oxide nanoparticles for brain tumor cell labeling and tracking with MRI. The implanted tumor cells labeled with nanoparticles showed positive contrast for 48 h *in vivo* [103]. Manganese-based nanoparticle is another group of T_1 contrast agent. Na *et al.* reported the construction of nanoprobe based on the MnO nanoparticles for brain tumor detection. They further applied the probe on a breast cancer brain metastatic tumor model for *in vivo* MR imaging, which showed enhancement at the tumor site on T_1 -weighted images [62]. However, the impedimental function of BBB was not taken into consideration by using this nanoprobe for brain tumor targeting.

Based on the unique physicochemical properties, iron oxide nanoparticles (IONPs) have been developed as T_2 contrast agent for MRI imaging [104].

Intrinsic superparamagnetism combined with multiple surface binding sites of the IONPs enables the *in vivo* tumor targeting at an early stage [54–56]. For brain tumor imaging, Zhang and coworkers built a selectively targeting nanoprobe (NPCP-CTX-Cy5.5) based on the PEGylated chitosan-coated IONPs. *In vivo* MRI and optical imaging on a ND2:SmoA1 mouse model showed the specific targeting of brain tumor with the intact BBB, indicating a BBB traverse ability of this probe [57].

As already mentioned, receptor-mediated transport has been demonstrated to be one of the most effective approaches for BBB crossing. Based on this mechanism, Qiao and coworkers investigated the Lf-mediated BBB transport of IONPs in both *in vitro* and *in vivo* models. Lf was bonded with Fe₃O₄ through the amide reaction between amine group of the Lf and carboxylic group of the PEGylated Fe₃O₄ nanoparticles. For *in vivo* BBB transport studies, the integrity of the PBCECs BBB model was monitored by transendothelial electrical resistance (TEER). It has been demonstrated that the Lf-conjugated Fe₃O₄ nanoparticles (Fe₃O₄-Lf) showed improved transfer efficacy through the receptor-mediated transcytosis compared with the PEGylated Fe₃O₄ nanoparticles. Meanwhile, the PEG modification on the particle surface ensured a relatively longer blood half-time and the amphiphilic nature also provided an increased BBB transport effect [84].

4.4.2

Optical Imaging

Optical imaging has been shown to be one of the most feasible imaging technologies to be translated into the clinics owing to its high sensitivity and low cost facilities. The optical probes serve as the essential signal source for imaging. Owing to the intrinsic optical property and multiple surface binding sites for combining with targeting molecules, semiconductor nanoplatforms such as quantum dots and quantum rods (QRs) have been demonstrated to be useful for BBB transport and brain tumor imaging [105,106]. Santra *et al.* addressed TAT-mediated transport of QDs across the BBB. Amine-modified CdS:Mn@ZnS QDs were covalently conjugated with cell-penetrating TAT peptide, and the conjugates were administered into a rat for brain delivery study. The staining of brain parenchyma and blood vessels revealed the BBB penetration of this probe [65]. Although MRI was not actively utilized in that study, it clearly demonstrated the potential for the delivery of diagnostic and therapeutic agents for brain diseases. Cai *et al.* first reported arginine-glycine-aspartic acid (RGD) peptide-labeled QDs for brain tumor imaging as well as the tumor vasculature visualization [106]. The recognition of the integrin α_vβ₃ by the RGD on the surface greatly enhanced the accumulation at the tumor site on a subcutaneous tumor model, which was obviously irrelevant to BBB transport. For the purpose of brain disease diagnosis across BBB, Xu *et al.* used Tf-conjugated QRs probes that showed BBB transmigration ability on a primary brain microvascular endothelial cells *in vitro* model [105]. Although 80% cell viability was maintained with the probes

below a certain concentration, the author failed to provide evidence for BBB integrity. Nevertheless, the receptor-mediated transport by Tf was verified by the increased affinity to these endothelial cells and the blocking effect of free Tf [105].

In addition to the diagnosis of brain diseases, optical imaging can also be a promising approach for image-guided surgical resection of brain tumors. Driven by the long circulating behavior of cross-linked iron oxide nanoparticles (CLIO), a near-infrared fluorescence(NIRF) dye Cy5.5-attached probe Cy5.5-CLIO has been demonstrated to be useful for delineating brain tumors in a model intra-operative setting [107]. In a more recent study, Nie *et al.* designed a Coomassie Brilliant Blue G-250 (CB) dye-loaded polyacrylamide (PAA) conjugated with F3 peptides for brain tumor targeting. PEG-containing cross-linkers were also used in the nanoplatform for increasing the stability and preventing nonspecific binding. Benefiting from the blue color of the nanoprobe, tumor delineation could be visualized by the naked eyes.

4.5

Conclusion and Outlook

Nanoparticles are important tools for brain disease diagnoses and treatment. In both cases, either used for imaging or for the transfer of drugs, they have to cross the blood–brain or the blood–CSF barrier in order to reach the brain parenchyma. Thus, nanocarriers have to be fabricated allowing the transfer of therapeutic agents like simple drugs, but also proteins or nucleic acids or complete genes to the brain. To enhance most specific uptake by the brain, the nanoparticles have to be modified mainly chemically to reduce uptake by peripheral organs, to increase their biocompatibility and to reduce their cytotoxicity as well as to increase the residence time within the body. With respect to imaging, the physical properties have to be tuned corresponding to the technique applied. Although tremendous progress in nanotechnology is made, the “magic bullet” demanded and searched for by Paul Ehrlich, who reasoned that “if a compound could be made that selectively targeted a disease-causing organism,” then a toxin for that organism could be delivered along with the agent of selectivity, is not yet found. However, considering the complexity of the brain, the progress in brain targeting nanomedicine is already impressive. Although still in an infant stage, strong progress has been made in nanocarrier formulation toward the general clinical application.

Acknowledgment

As full professor and director at the University of Münster, Dr. Hans-Joachim Galla has been awarded a Visiting Professorship for Senior International Scientists by the Chinese Academy of Sciences, Beijing. This honor gave us the opportunity to write this chapter.

References

- 1 Pardridge, W.M. (2005) Molecular biology of the blood–brain barrier. *Mol. Biotechnol.*, **30**, 57–70.
- 2 Neuwelt, E., Abbott, N.J., Abrey, L., Banks, W.A., Blakley, B., Davis, T. et al. (2008) Strategies to advance translational research into brain barriers. *Lancet Neurol.*, **7**, 84–96.
- 3 Abbott, N.J., Ronnback, L., and Hansson, E. (2006) Astrocyte–endothelial interactions at the blood–brain barrier. *Nat. Rev. Neurosci.*, **7**, 41–53.
- 4 Abbott, N.J., Patabendige, A.A., Dolman, D.E., Yusof, S.R., and Begley, D.J. (2010) Structure and function of the blood–brain barrier. *Neurobiol. Dis.*, **37**, 13–25.
- 5 Kroll, S., El-Gindi, J., Thanabalanusundaram, G., Panpumthong, P., Schrot, S., Hartmann, C. et al. (2009) Control of the blood–brain barrier by glucocorticoids and the cells of the neurovascular unit. *Ann. N.Y. Acad. Sci.*, **1165**, 228–239.
- 6 Thanabalanusundaram, G., Pieper, C., Lischper, M., and Galla, H.J. (2010) Regulation of the blood–brain barrier integrity by pericytes via matrix metalloproteinases mediated activation of vascular endothelial growth factor *in vitro*. *Brain Res.*, **1347**, 1–10.
- 7 Pardridge, W.M. (2003) Blood–brain barrier drug targeting: the future of brain drug development. *Mol. Interv.*, **3**, 90–105.
- 8 Angelow, S., Wegener, J., and Galla, H.J. (2003) Transport and permeability characteristics of the blood–CSF barrier *in vitro*, in *Blood–Spinal Cord and Brain Barriers in Health and Disease* (ed. S. Sharma), Academic Press, Amsterdam.
- 9 Spector, R. and Johanson, C. (1989) *The Mammalian Choroid Plexus: Structure, Development and Function*, Scientific American.
- 10 Angelow, S., Zeni, P., and Galla, H.J. (2004) Usefulness and limitation of primary cultured porcine choroid plexus epithelial cells as an *in vitro* model to study drug transport at the blood–CSF barrier. *Adv. Drug Deliv. Rev.*, **56**, 1859–1873.
- 11 Angelow, S. and Galla, H.J. (2005) Junctional proteins of the blood–CSF barrier, in *The Blood–Cerebrospinal Fluid Barrier*, Taylor & Francis, Boca Raton, FL.
- 12 Begley, D.J. (2004) ABC transporters and the blood–brain barrier. *Curr. Pharm. Des.*, **10**, 1295–1312.
- 13 de Lange, E.C. (2004) Potential role of ABC transporters as a detoxification system at the blood–CSF barrier. *Adv. Drug Deliv. Rev.*, **56**, 1793–1809.
- 14 Ghersi-Egea, J.F. and Strazielle, N. (2002) Choroid plexus transporters for drugs and other xenobiotics. *J. Drug Target.*, **10**, 353–357.
- 15 Abbott, N.J. (2005) Dynamics of CNS barriers: evolution, differentiation, and modulation. *Cell. Mol. Neurobiol.*, **25**, 5–23.
- 16 Krause, G., Winkler, L., Piehl, C., Blasig, I., Piontek, J., and Muller, S.L. (2009) Structure and function of extracellular claudin domains. *Ann. N.Y. Acad. Sci.*, **1165**, 34–43.
- 17 Wegener, J. and Galla, H.J. (1996) The role of non-lamellar lipid structures in the formation of tight junctions. *Chem. Phys. Lipids*, **81**, 229–255.
- 18 Franke, H., Galla, H.J., and Beuckmann, C.T. (1999) An improved low-permeability *in vitro*-model of the blood–brain barrier: transport studies on retinoids, sucrose, haloperidol, caffeine and mannitol. *Brain Res.*, **818**, 65–71.
- 19 Franke, H., Galla, H.J., and Beuckmann, C.T. (2000) Primary cultures of brain microvessel endothelial cells: a valid and flexible model to study drug transport through the blood–brain barrier *in vitro*. *Brain Res. Protoc.*, **5**, 248–256.
- 20 Haselbach, M., Wegener, J., Decker, S., Engelbertz, C., and Galla, H.J. (2001) Porcine choroid plexus epithelial cells in culture: regulation of barrier properties and transport processes. *Microsc. Res. Tech.*, **52**, 137–152.
- 21 Haseloff, R.F., Piontek, J., and Blasig, I.E. (2010) The investigation of *cis*- and *trans*-interactions between claudins. *Curr. Top. Membr.*, **65**, 97–112.

- 22** Hartmann, C., Zozulya, A., Wegener, J., and Galla, H.J. (2007) The impact of glia-derived extracellular matrices on the barrier function of cerebral endothelial cells: an *in vitro* study. *Exp. Cell Res.*, **313**, 1318–1325.
- 23** Zeni, P., Doepker, E., Topphoff, U.S., Huwel, S., Tenenbaum, T., and Galla, H.J. (2007) MMPs contribute to TNF-alpha-induced alteration of the blood–cerebrospinal fluid barrier *in vitro*. *Am. J. Physiol. Cell Physiol.*, **293**, C855–C864.
- 24** Lischper, M., Beuck, S., Thanabalanadaram, G., Pieper, C., and Galla, H.J. (2010) Metalloproteinase mediated occludin cleavage in the cerebral microcapillary endothelium under pathological conditions. *Brain Res.*, **1326**, 114–127.
- 25** Chen, Y. and Liu, L. (2012) Modern methods for delivery of drugs across the blood–brain barrier. *Adv. Drug Deliv. Rev.*, **64**, 640–665.
- 26** Gath, U., Hakvoort, A., Wegener, J., Decker, S., and Galla, H.J. (1997) Porcine choroid plexus cells in culture: expression of polarized phenotype, maintenance of barrier properties and apical secretion of CSF-components. *Eur. J. Cell Biol.*, **74**, 68–78.
- 27** Galla, H.-J., Thanabalanadaram, G., Wedel-Parlow, M., Rempe, R., Kramer, S., El-Gindi, J. *et al.* (2011) The blood–brain barrier *in vitro*: regulation, maintenance and quantification of the barrier properties by impedance spectroscopy, in *Horizons in Neuroscience Research* (eds A. Costa and E. Villalba), Nova, New York, pp. 1–14.
- 28** Angelow, S., Zeni, P., and Galla, H.J. (2004) Usefulness and limitation of primary cultured porcine choroid plexus epithelial cells as an *in vitro* model to study drug transport at the blood–CSF barrier. *Adv. Drug Deliv. Rev.*, **56**, 1859–1873.
- 29** Tenenbaum, T., Steinmann, U., Friedrich, C., Berger, J., Schwerk, C., and Schroten, H. (2013) Culture models to study leukocyte trafficking across the choroid plexus. *Fluids Barriers CNS*, **10**, 1.
- 30** Thanabalanadaram, G., Schneidewind, J., Pieper, C., and Galla, H.J. (2011) The impact of pericytes on the blood–brain barrier integrity depends critically on the pericyte differentiation stage. *Int. J. Biochem. Cell Biol.*, **43**, 1284–1293.
- 31** Garcel, A., Martel, S., Carrupt, P.A., Doelker, E., and Delie, F. (2010) *In vitro* blood–brain barrier models as a screening tool for colloidal drug delivery systems and other nanosystems. *Int. J. Biomed. Nanosci. Nanotechnol.*, **1**, 133–163.
- 32** Rempe, R., Cramer, S., Qiao, R., and Galla, H.J. (2014) Strategies to overcome the barrier: use of nanoparticles as carriers and modulators of barrier properties. *Cell Tissue Res.*, **355**, 717–726.
- 33** Kreuter, J. (2014) Drug delivery to the central nervous system by polymeric nanoparticles: what do we know? *Adv. Drug Deliv. Rev.*, **71**, 2–14.
- 34** Wong, H.L., Wu, X.Y., and Bendayan, R. (2012) Nanotechnological advances for the delivery of CNS therapeutics. *Adv. Drug Deliv. Rev.*, **64**, 686–700.
- 35** Voigt, N., Henrich-Noack, P., Kockstedt, S., Hintz, W., Tomas, J., and Sabel, B.A. (2014) Surfactants, not size or zeta-potential influence blood–brain barrier passage of polymeric nanoparticles. *Eur. J. Pharm. Biopharm.*, **87**, 19–29.
- 36** Kreuter, J. (2012) Nanoparticulate systems for brain delivery of drugs. *Adv. Drug Deliv. Rev.*, **47**, 65–81.
- 37** Kreuter, J. (2013) Mechanism of polymeric nanoparticle-based drug transport across the blood–brain barrier (BBB). *J. Microencapsul.*, **30**, 49–54.
- 38** Rempe, R., Cramer, S., Huwel, S., and Galla, H.J. (2011) Transport of poly (*n*-butylcyano-acrylate) nanoparticles across the blood–brain barrier *in vitro* and their influence on barrier integrity. *Biochem. Biophys. Res. Commun.*, **406**, 64–69.
- 39** Gelperina, S., Maksimenko, O., Khalansky, A., Vanchugova, L., Shipulo, E., Abbasova, K. *et al.* (2010) Drug delivery to the brain using surfactant-coated poly(lactide-*co*-glycolide) nanoparticles: influence of the

- formulation parameters. *Eur. J. Pharm. Biopharm.*, **74**, 157–163.
- 40** Wohlfart, S., Gelperina, S., and Kreuter, J. (2012) Transport of drugs across the blood–brain barrier by nanoparticles. *J. Control Release*, **161**, 264–273.
- 41** Gong, W., Wang, Z., Liu, N., Lin, W., Wang, X., Xu, D. *et al.* (2011) Improving efficiency of Adriamycin crossing blood–brain barrier by combination of thermosensitive liposomes and hyperthermia. *Biol. Pharm. Bull.*, **34**, 1058–1064.
- 42** Georgieva, J.V., Brinkhuis, R.P., Stojanov, K., Weijers, C.A., Zuilhof, H., Rutjes, F.P. *et al.* (2012) Peptide-mediated blood–brain barrier transport of polymersomes. *Angew. Chem., Int. Ed.*, **51**, 8339–8342.
- 43** Matthes, F., Wolte, P., Bockenhoff, A., Huwel, S., Schulz, M., Hyden, P. *et al.* (2011) Transport of arylsulfatase A across the blood–brain barrier *in vitro*. *J. Biol. Chem.*, **286**, 17487–17494.
- 44** Bockenhoff, A., Cramer, S., Wolte, P., Knieling, S., Wohlenberg, C., Giesemann, V. *et al.* (2014) Comparison of five peptide vectors for improved brain delivery of the lysosomal enzyme arylsulfatase A. *J. Neurosci.*, **34**, 3122–3129.
- 45** Fazil, M., Md, S., Haque, S., Kumar, M., Baboota, S., Sahni, J.K. *et al.* (2012) Development and evaluation of rivastigmine loaded chitosan nanoparticles for brain targeting. *Eur. J. Pharm. Sci.*, **47**, 6–15.
- 46** Cramer, S., Rempe, R., and Galla, H.J. (2012) Exploiting the properties of biomolecules for brain targeting of nanoparticulate systems. *Curr. Med. Chem.*, **19**, 3163–3187.
- 47** Gil, E.S., Wu, L., Xu, L., and Lowe, T.L. (2012) Beta-cyclodextrin-poly(beta-amino ester) nanoparticles for sustained drug delivery across the blood–brain barrier. *Biomacromolecules*, **13**, 3533–3541.
- 48** Ye, Y., Sun, Y., Zhao, H., Lan, M., Gao, F., Song, C. *et al.* (2013) A novel lactoferrin-modified beta-cyclodextrin nanocarrier for brain-targeting drug delivery. *Int. J. Pharm.*, **458**, 110–117.
- 49** Stark, D.D., Weissleder, R., Elizondo, G., Hahn, P.F., Saini, S., Todd, L.E. *et al.* (1988) Superparamagnetic iron oxide: clinical-application as a contrast agent for MR imaging of the liver. *Radiology*, **168**, 297–301.
- 50** Dunlop, D.J. (1973) Superparamagnetic and single-domain threshold sizes in magnetite. *J. Geophys. Res.*, **78**, 1780–1793.
- 51** Kim, B.H., Lee, N., Kim, H., An, K., Park, Y.I. *et al.* (2011) Large-scale synthesis of uniform and extremely small-sized iron oxide nanoparticles for high-resolution T1 magnetic resonance imaging contrast agents. *J. Am. Chem. Soc.*, **133**, 12624–12631.
- 52** Weissleder, R., Stark, D.D., Rummeny, E.J., Compton, C.C., and Ferrucci, J.T. (1988) Splenic lymphoma: ferrite-enhanced MR imaging in rats. *Radiology*, **166**, 423–430.
- 53** Harisinghani, M.G., Barentsz, J., Hahn, P.F., Deserno, W.M., Tabatabaei, S., van de Kaa, C.H. *et al.* (2003) Noninvasive detection of clinically occult lymph-node metastases in prostate cancer. *N. Engl. J. Med.*, **348**, 2491–2499.
- 54** Hu, F.Q., Wei, L., Zhou, Z., Ran, Y.L., Li, Z., and Gao, M.Y. (2006) Preparation of biocompatible magnetite nanocrystals for *in vivo* magnetic resonance detection of cancer. *Adv. Mater.*, **18**, 2553–2556.
- 55** Liu, S.J., Jia, B., Qiao, R.R., Yang, Z., Yu, Z.L., Liu, Z.F. *et al.* (2009) A novel type of dual-modality molecular probe for MR and nuclear imaging of tumor: preparation, characterization and *in vivo* application. *Mol. Pharm.*, **6**, 1074–1082.
- 56** Lee, J.H., Huh, Y.M., Jun, Y., Seo, J., Jang, J., Song, H.T. *et al.* (2007) Artificially engineered magnetic nanoparticles for ultra-sensitive molecular imaging. *Nat. Med.*, **13**, 95–99.
- 57** Veiseh, O., Sun, C., Fang, C., Bhattacharai, N., Gunn, J., Kievit, F. *et al.* (2009) Specific targeting of brain tumors with an optical/magnetic resonance imaging nanoprobe across the blood–brain barrier. *Cancer Res.*, **69**, 6200–6207.
- 58** Evanics, F., Diamente, P.R., van Veggel, F.C.J.M., Stanisz, G.J., and Prosser, R.S. (2006) Water-soluble GdF₃ and GdF₃/LaF₃ nanoparticles: physical

- characterization and NMR relaxation properties. *Chem. Mater.*, **18**, 2499–2505.
- 59** Hifumi, H., Yamaoka, S., Tanimoto, A., Citterio, D., and Suzuki, K. (2006) Gadolinium-based hybrid nanoparticles as a positive MR contrast agent. *J. Am. Chem. Soc.*, **128**, 15090–15091.
- 60** Bridot, J.L., Faure, A.C., Laurent, S., Riviere, C., Billotey, C., Hiba, B. *et al.* (2007) Hybrid gadolinium oxide nanoparticles: multimodal contrast agents for *in vivo* imaging. *J. Am. Chem. Soc.*, **129**, 5076–5084.
- 61** Hou, Y., Qiao, R.R., Fang, F., Wang, X.X., Dong, C.Y., Liu, K. *et al.* (2013) NaGdF₄ nanoparticle-based molecular probes for magnetic resonance imaging of intraperitoneal tumor xenografts *in vivo*. *ACS Nano.*, **7**, 330–338.
- 62** Na, H.B., Lee, J.H., An, K.J., Park, Y.I., Park, M., Lee, I.S. *et al.* (2007) Development of a T-1 contrast agent for magnetic resonance imaging using MnO nanoparticles. *Angew Chem., Int. Ed.*, **46**, 5397–5401.
- 63** Alivisatos, P. (2004) The use of nanocrystals in biological detection. *Nat. Biotechnol.*, **22**, 47–52.
- 64** Cassette, E., Helle, M., Bezdetnaya, L., Marchal, F., Dubertret, B., and Pons, T. (2013) Design of new quantum dot materials for deep tissue infrared imaging. *Adv. Drug Deliv. Rev.*, **65**, 719–731.
- 65** Santra, S., Yang, H.S., Holloway, P.H., Stanley, J.T., and Mericle, R.A. (2005) Synthesis of water-dispersible fluorescent, radio-opaque, and paramagnetic CdS:Mn/ZnS quantum dots: a multifunctional probe for bioimaging. *J. Am. Chem. Soc.*, **127**, 1656–1657.
- 66** Wang, S.Z., Jarrett, B.R., Kauzlarich, S.M., and Louie, A.Y. (2007) Core/shell quantum dots with high relaxivity and photoluminescence for multimodality imaging. *J. Am. Chem. Soc.*, **129**, 7702.
- 67** Ding, K., Jing, L.H., Liu, C.Y., Hou, Y., and Gao, M.Y. (2014) Magnetically engineered Cd-free quantum dots as dual-modality probes for fluorescence/magnetic resonance imaging of tumors. *Biomaterials*, **35**, 1608–1617.
- 68** Jain, P.K., Lee, K.S., El-Sayed, I.H., and El-Sayed, M.A. (2006) Calculated absorption and scattering properties of gold nanoparticles of different size, shape, and composition: applications in biological imaging and biomedicine. *J. Phys. Chem. B.*, **110**, 7238–7248.
- 69** Jain, P.K., Huang, X.H., El-Sayed, I.H., and El-Sayed, M.A. (2008) Noble metals on the nanoscale: optical and photothermal properties and some applications in imaging, sensing, biology, and medicine. *Acc. Chem. Res.*, **41**, 1578–1586.
- 70** Murphy, C.J., Gole, A.M., Stone, J.W., Sisco, P.N., Alkilany, A.M., Goldsmith, E. C. *et al.* (2008) Gold nanoparticles in biology: beyond toxicity to cellular imaging. *Acc. Chem. Res.*, **41**, 1721–1730.
- 71** Hainfeld, J.F., Slatkin, D.N., Focella, T.M., and Smilowitz, H.M. (2006) Gold nanoparticles: a new X-ray contrast agent. *Br. J. Radiol.*, **79**, 248–253.
- 72** Reuveni, T., Motiei, M., Romman, Z., Popovtzer, A., and Popovtzer, R. (2011) Targeted gold nanoparticles enable molecular CT imaging of cancer: an *in vivo* study. *Int. J. Nanomed.*, **6**, 2859–2864.
- 73** Popovtzer, R., Agrawal, A., Kotov, N.A., Popovtzer, A., Balter, J., Carey, T.E. *et al.* (2008) Targeted gold nanoparticles enable molecular CT imaging of cancer. *Nano. Lett.*, **8**, 4593–4596.
- 74** Cheng, Y., Dai, Q., Morshed, R., Han, Y., Auffinger, B., Wainwright, D. *et al.* (2013) Gold nanoparticles as a drug delivery system for malignant brain tumors. *Neuro-Oncology*, **15**, 39–40.
- 75** Prades, R., Guerrero, S., Araya, E., Molina, C., Salas, E., Zurita, E. *et al.* (2012) Delivery of gold nanoparticles to the brain by conjugation with a peptide that recognizes the transferrin receptor. *Biomaterials*, **33**, 7194–7205.
- 76** Sousa, F., Mandal, S., Garrovo, C., Astolfo, A., Bonifacio, A., Latawiec, D. *et al.* (2010) Functionalized gold nanoparticles: a detailed *in vivo* multimodal microscopic brain distribution study. *Nanoscale*, **2**, 2826–2834.
- 77** Guerrero, S., Araya, E., Fiedler, J.L., Arias, J.I., Adura, C., Albericio, F. *et al.* (2010) Improving the brain delivery of gold

- nano particles by conjugation with an amphipathic peptide. *Nanomedicine*, **5**, 897–913.
- 78** Hainfeld, J.F., Smilowitz, H.M., O'Connor, M.J., Dilmanian, F.A., and Slatkin, D.N. (2013) Gold nanoparticle imaging and radiotherapy of brain tumors in mice. *Nanomedicine*, **8**, 1601–1609.
- 79** Masserini, M. (2013) Nanoparticles for brain drug delivery. *ISRN Biochem.*, **2013**, 18.
- 80** Sonavane, G., Tomoda, K., and Makino, K. (2008) Biodistribution of colloidal gold nanoparticles after intravenous administration: effect of particle size. *Colloids Surf. B*, **66**, 274–280.
- 81** Fenart, L., Casanova, A., Dehouck, B., Duhem, C., Slupek, S., Cecchelli, R. *et al.* (1999) Evaluation of effect of charge and lipid coating on ability of 60-nm nanoparticles to cross an *in vitro* model of the blood–brain barrier. *J. Pharmacol. Exp. Ther.*, **291**, 1017–1022.
- 82** Papisov, M.I., Bogdanov, A., Jr., Schaffer, B., Nossiff, N., Shen, T., Weissleder, R. *et al.* (1993) Colloidal magnetic resonance contrast agents: effect of particle surface on biodistribution. *J. Magn. Magn. Mater.*, **122**, 383–386.
- 83** Kim, D., Park, S., Lee, J.H., Jeong, Y.Y., and Jon, S. (2007) Antibiofouling polymer-coated gold nanoparticles as a contrast agent for *in vivo* X-ray computed tomography imaging. *J. Am. Chem. Soc.*, **129**, 7661–7665.
- 84** Qiao, R., Jia, Q., Huewel, S., Xia, R., Liu, T., Gao, F. *et al.* (2012) Receptor-mediated delivery of magnetic nanoparticles across the blood–brain barrier. *ACS Nano*, **6**, 3304–3310.
- 85** Nance, E.A., Woodworth, G.F., Sailor, K. A., Shih, T.Y., Xu, Q.G., Swaminathan, G. *et al.* (2012) A dense poly(ethylene glycol) coating improves penetration of large polymeric nanoparticles within brain tissue. *Sci. Transl. Med.*, **4**, 119.
- 86** Woodle, M.C. (1995) Sterically stabilized liposome therapeutics. *Adv. Drug Deliv. Rev.*, **16**, 249–265.
- 87** Lu, W., Wan, J., She, Z.J., and Jiang, X.G. (2007) Brain delivery property and accelerated blood clearance of cationic albumin conjugated pegylated nanoparticle. *J. Control Release*, **118**, 38–53.
- 88** Pardridge, W.M., Triguero, D., Buciak, J., and Yang, J. (1990) Evaluation of cationized rat albumin as a potential blood–brain barrier drug transport vector. *J. Pharmacol. Exp. Ther.*, **255**, 893–899.
- 89** Herve, F., Ghinea, N., and Scherrmann, J. M. (2008) CNS delivery via adsorptive transcytosis. *AAPS J.*, **10**, 455–472.
- 90** Vives, E., Richard, J.P., Rispal, C., and Lebleu, B. (2003) TAT peptide internalization: seeking the mechanism of entry. *Curr. Protein Pept. Sci.*, **4**, 125–132.
- 91** Kanazawa, T., Taki, H., Tanaka, K., Takashima, Y., and Okada, H. (2011) Cell-penetrating peptide-modified block copolymer micelles promote direct brain delivery via intranasal administration. *Pharm. Res.*, **28**, 2130–2139.
- 92** Liu, L., Venkatraman, S.S., Yang, Y.Y., Guo, K., Lu, J., He, B. *et al.* (2008) Polymeric micelles anchored with TAT for delivery of antibiotics across the blood–brain barrier. *Biopolymers*, **90**, 617–623.
- 93** Qin, Y., Chen, H., Yuan, W., Kuai, R., Zhang, Q., Xie, F. *et al.* (2011) Liposome formulated with TAT-modified cholesterol for enhancing the brain delivery. *Int. J. Pharm.*, **419**, 85–95.
- 94** Hatakeyama, H., Akita, H., Maruyama, K., Suhara, T., and Harashima, H. (2004) Factors governing the *in vivo* tissue uptake of transferrin-coupled polyethylene glycol liposomes *in vivo*. *Int. J. Pharm.*, **281**, 25–33.
- 95** Eavarone, D.A., Yu, X., and Bellamkonda, R.V. (2000) Targeted drug delivery to C6 glioma by transferrin-coupled liposomes. *J. Biomed. Mater. Res.*, **51**, 10–14.
- 96** Gan, C.W. and Feng, S.S. (2010) Transferrin-conjugated nanoparticles of poly(lactide)-D-alpha-tocopheryl polyethylene glycol succinate diblock copolymer for targeted drug delivery across the blood–brain barrier. *Biomaterials*, **31**, 7748–7757.
- 97** Yan, F., Wang, Y., He, S., Ku, S., Gu, W., and Ye, L. (2013) Transferrin-conjugated,

- fluorescein-loaded magnetic nanoparticles for targeted delivery across the blood–brain barrier. *J. Mater. Sci. Mater. Med.*, **24**, 2371–2379.
- 98** Tortorella, S. and Karagiannis, T.C. (2014) Transferrin receptor-mediated endocytosis: a useful target for cancer therapy. *J. Membr. Biol.*, **247**, 291–307.
- 99** Fries, P., Runge, V.M., Bucker, A., Schurholz, H., Reith, W., Robert, P. *et al.* (2009) Brain tumor enhancement in magnetic resonance imaging at 3 tesla: intraindividual comparison of two high relaxivity macromolecular contrast media with a standard extracellular GD-chelate in a rat brain tumor model. *Invest. Radiol.*, **44**, 200–206.
- 100** Cheng, Y., Morshed, R.A., Auffinger, B., Tobias, A.L., and Lesniak, M.S. (2014) Multifunctional nanoparticles for brain tumor imaging and therapy. *Adv. Drug Deliv. Rev.*, **66**, 42–57.
- 101** Koffie, R.M., Farrar, C.T., Saidi, L.J., William, C.M., Hyman, B.T., and Spires-Jones, T.L. (2011) Nanoparticles enhance brain delivery of blood–brain barrier-impermeable probes for *in vivo* optical and magnetic resonance imaging. *Proc. Natl. Acad. Sci. USA*, **108**, 18837–18842.
- 102** Liu, C.Y., Gao, Z.Y., Zeng, J.F., Hou, Y., Fang, F., Li, Y.L. *et al.* (2013) Magnetic/upconversion fluorescent NaGdF₄:Yb, Er nanoparticle-based dual-modal molecular probes for imaging tiny tumors *in vivo*. *ACS Nano*, **7**, 7227–7240.
- 103** Faucher, L., Tremblay, M., Lagueux, J., Gossuin, Y., and Fortin, M.A. (2012) Rapid synthesis of PEGylated ultrasmall gadolinium oxide nanoparticles for cell labeling and tracking with MRI. *ACS Appl. Mater. Int.*, **4**, 4506–4515.
- 104** Qiao, R.R., Yang, C.H., and Gao, M.Y. (2009) Superparamagnetic iron oxide nanoparticles: from preparations to *in vivo* MRI applications. *J. Mater. Chem.*, **19**, 6274–6293.
- 105** Xu, G., Yong, K.T., Roy, I., Mahajan, S.D., Ding, H., Schwartz, S.A. *et al.* (2008) Bioconjugated quantum rods as targeted probes for efficient transmigration across an *in vitro* blood–brain barrier. *Bioconjug. Chem.*, **19**, 1179–1185.
- 106** Cai, W.B., Shin, D.W., Chen, K., Gheysens, O., Cao, Q.Z., Wang, S.X. *et al.* (2006) Peptide-labeled near-infrared quantum dots for imaging tumor vasculature in living subjects. *Nano Lett.*, **6**, 669–676.
- 107** Kircher, M.F., Mahmood, U., King, R.S., Weissleder, R., and Josephson, L. (2003) A multimodal nanoparticle for preoperative magnetic resonance imaging and intraoperative optical brain tumor delineation. *Cancer Res.*, **63**, 8122–8125.

5

Organic Nanophotonics: Controllable Assembly of Optofunctional Molecules toward Low-Dimensional Materials with Desired Photonic Properties

Yongli Yan and Yong Sheng Zhao

5.1

Introduction

Nanophotonics, which deals with the generation, transfer, modulation, and detection of photons in a confined system, was first introduced in the near-field optics/spectroscopy, and subsequently generalized in other fields such as photonic crystals and surface plasmon optics and materials [1]. In comparison with electrons, photons exhibit great superiority as information carriers, including speed, bandwidth, and capacity. Thus, nanophotonics provides an effective solution to the current obstacles that seriously limit the further improvement of modern electronics. Utilizing inorganic/organic nanostructures as photonic materials becomes an ascendant branch of nanophotonics. There is no existing guidance for the design and synthesis of photonic materials and functional devices due to the vast differences between photons and electrons in fundamental physical properties at the moment. Chemists and material scientists, in this respect, contribute enormously to the achievement of novel optical properties with inorganic materials, such as ZnO, CdSe, and noble metal nanostructures, especially gold and silver [2]. During the flourish of their inorganic counterparts, organics are gradually becoming a better choice as nanophotonic materials due to numerous advantages. Organic compounds possess high photoluminescence quantum yields, tunable optical properties, and rapid photoresponses. The excellent flexibility and processability are also big pluses in the construction and assembly of functional photonic devices. Taken together, it is no doubt that organic molecular materials would bring great innovation in the design and fabrication of functional elements toward photonic integrated circuits [3].

For organic compounds, the interactions among molecules, such as hydrogen bonds, van der Waals forces, $\pi-\pi$ interactions, and electrostatic forces, are of weak type [4]. These weak intermolecular interactions allow for more facile and mild conditions in the fabrication of crystalline low-dimensional structures through a spontaneous or nonspontaneous assembly process. There have been numerous efforts in the preparation of organic nanostructures through a variety of methods, which can be divided into assembly in the liquid phase, epitaxial

growth in the vapor phase, and template-based methods [5]. It has been demonstrated that molecular interactions play a crucial role in dominating the assembly characteristics [6]. In general, participation of a single force will induce a one-dimensional (1D) molecular packing along a preferential direction. The simultaneous participation of two or more kinds of interactions would complicate the assembly behavior and nanostructures with various geometries are expected. It is increasingly necessary to summarize the relationship between the intermolecular interactions and the final structural features to further guide the molecular design and construction strategy optimization.

One of the most important reasons why organic nanomaterials have become so attractive in the photonics field is their unique optical properties and light–matter interactions, which are fundamentally different from the inorganic counterparts [7]. The optical properties of assembled molecular nanocrystals depend not only on the properties of molecules constituting them, but also on the morphologies of aggregated products [8]. Aggregation-induced enhanced photoluminescence [9], which arises from the reduced vibration–rotation in the solid state, has been widely reported in various compounds. In addition, those as-prepared nanostructures with regular shapes exhibit remarkable photon confinements, including but not limiting to cavity effect and waveguide behavior. Moreover, the strong coupling between photons and Frenkel-type excitons would generate a new type of quasiparticles, called exciton polaritons (EPs), which can significantly influence the original properties and give rise to a number of new phenomena [10]. The fruitful excited-state processes among different molecules, that is, energy/charge transfer, exciton diffusion, separation, conversion, and recombination [11], could bring much flexibility in the construction of complex photonic elements. Therefore, an in-depth understanding of the relationship between photonic properties and aggregated structures is essential to direct the material design, synthesis, and application.

In this chapter, we mainly concentrate on the relationships among molecules, assembly, structures, and photonic properties, which are divided into three parts (Figure 5.1). We begin with how optofunctional molecules start to assemble under various intermolecular forces (part 2). Then, we put emphasis on the relationship between assembly behavior and final morphologies of the obtained low-dimensional structures, with the aim of fabricating diverse nanostructures through rational control of intermolecular interactions (part 3). In the following part, we will focus on the structural design and corresponding cooperative assembly method of multiple molecules toward complex photonic functions and high performance (part 4). Finally, we summarize the recent contributions as well as challenges in this field and put forward the prospects and directions for future development.

5.2

From Molecules to Assembly

A facile strategy to construct organic low-dimensional structures is essential to further investigate the optofunctions. There are several well-understood methods

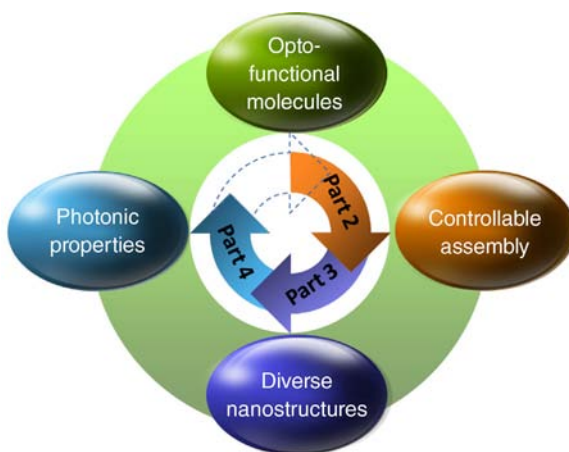


Figure 5.1 Organization of this chapter. Part 2: morphologies through the modulated assembly processes. Part 4: optical properties and photonic applications of the assembled complex structures.

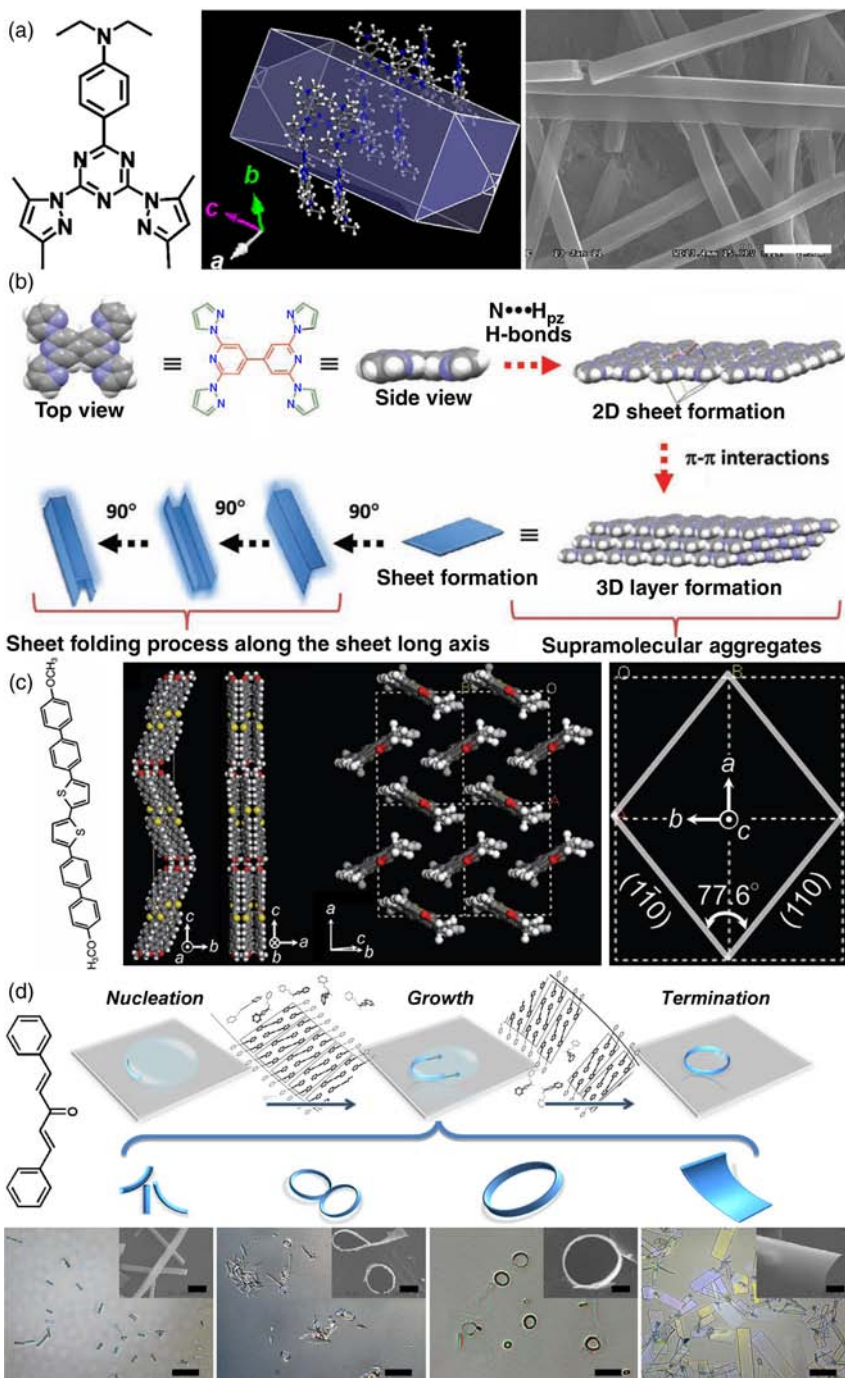
for inorganic materials, which are not suitable for organic materials because of the vicious reaction conditions, such as high pressure, high temperature, and various solvents. Fortunately, some meaningful attempts for synthesizing organic nanostructures have been made in the past few years and assembly has been demonstrated to be a facile and universal route to the acquisition of organic solid materials [12]. This bottom-up method starts from the aggregation of individual molecules and ends up with dynamic balance in the liquid phase or depletion of raw materials in the vapor phase.

Organic molecules could assemble into micro-/nanocrystals on some occasions if the nucleation and crystal growth processes coexist in a system. The tiny aggregations assembled at the initial stage can serve as stable nuclei once they reach a critical size. Then the crystals grow larger and larger until the whole system reaches dynamic equilibrium. The assembly process is fundamentally different from a crystallization process, although the final products of the two processes are all crystals. The main difference is the driving force behind the formation of solids. The crystallization process, which consists of nucleation and crystal growth stages, is driven by supersaturation, while the driving forces in the assembly process come from either the inherent weak intermolecular interactions or the influences from the environment. Here, we elaborate on how these interactions affect the molecular behavior in the assembly process.

5.2.1

Inherent Intermolecular Interactions

Among numerous construction strategies for organic micronanostructures, the most widespread one is assembly in the liquid phase, because of the simplicity,



flexibility, and easy controllability. By carefully controlling the molecular assembly behavior, we can obtain multiple aggregated materials with regular shapes. For small molecules, the weak interactions among molecules, such as π - π interactions, van der Waals forces, and hydrogen bonds, play a key role in dominating the aggregation behavior. Continuous efforts have been made to explore the relationship between the intermolecular interactions and the pattern modes of molecules in crystalline structures with smooth surfaces and flat end facets.

Figure 5.2 summarizes several typical molecular structures (fibers, tubes, sheets, and rings) fabricated through the assembly behavior of distinct organic molecules. Shown in Figure 5.2a is a representative formation mechanism of the 1D structures, which are assembled from a π -conjugated compound, 2-(*N,N*-diethylanilin-4-yl)-4,6-bis(3,5-dimethylpyrazol-1-yl)-1,3,5-triazine (DBPT) [13]. It is indicated in the middle of Figure 5.2a that the DBPT molecule has a preferential packing direction along the *c* crystal axis due to the strong π - π interaction stemming from the middle core. Therefore, DBPT molecules stack one by one along the [001] direction, leading to the formation of wire-like nanostructures. The SEM image displayed in Figure 5.2a (right) further confirms that the 1D structures growing along a single direction are smooth surfaced. The end facets are flat enough to serve as reflectors of high-quality Fabry-Pérot cavities.

Things change if there are more than one kind of intermolecular interactions during the assembly process. Figure 5.2b schematically elucidates the formation mechanism of tubular structures from a novel back-to-back coupled 2,6-dipyrazol-1-ylpyridine compound [14]. As shown in Figure 5.2b, the molecule is near planar (demonstrated by the optimized top-view and side-view images). The hydrogen bond formed by pyrazole ring nitrogen and pyrazole ring proton facilitates a head-to-tail packing mode and thus forms a 1D chain-like structure, which is then closely packed and forms a pseudo-sheet-like structure. These sheet-like structures could aggregate into a 3D multilayered supramolecular structure via intermolecular π - π interactions of the pyridine rings. These supramolecular aggregates are not thermodynamically stable, and an upfolding of 90° along the sheet axis occurs to minimize the surface energy. After a subsequent seaming process, these triple-folded nanosheets formed a rectangular tube-like

Figure 5.2 Formation mechanisms of four representative structures. (a) Nanowire: (left) molecular structure of DBPT; (middle) predicted growth morphology of DBPT crystalline structure; and (right) SEM image of the DBPT nanowires. Scale bar is 2 μm . (b) Schematic elucidation of the possible formation mechanism of tubular structures via supramolecular assembly of 2,6-dipyrazol-1-ylpyridine. (c) Nanosheet: (left) molecular structure of BP2T-OMe; (middle) crystal structures of BP2T-OMe with projections of *bc*-plane, *ac*-plane, and herringbone packing mode along the *c*-axis,

respectively; and (right) crystal lattice in the *ab*-plane. (d) Microring: (top) molecular structure of DPPDO and illustration of assembling mechanism of microrings; and (bottom) optical microscopy images of nanowires, small/large rings, and tiles by using DPPDO solutions with different concentrations. Scale bars are 25 μm . Insets show the corresponding SEM images. Scale bars are 2 μm . ((a) Ref. [13], copyright 2011, American Chemical Society; (b) Ref. [14], copyright 2011, Wiley; (c) Ref. [15], copyright 2012, Wiley; (d) Ref. [17], copyright 2013, Wiley.)

structure. The further growth of the tube along the axis was steered by the rapid growth of the tube walls.

Figure 5.2c shows a molecular structure and the stacking pattern in the corresponding low-dimensional crystals with a consequent rhombus shape [15]. This model compound, 5,5'-bis(4'-methoxybiphenyl-4-yl)-2,2'-bithiophene (BP2T-OMe), has a long-chain core of thiophene/phenylene co-oligomer (Figure 5.2c, left), which has been used extensively as gain medium for lasing. In the middle of Figure 5.2c, it is indicated that the molecules are tilted against the *ab*-plane, which is governed by the interactions between peripheral methoxy groups. The molecular axes are alternately declined in the opposite direction to the *c*-axis in the stacked molecular layers because of the zigzag molecular shape. When projected along the molecular axis in one molecular layer in parallel to the *ab*-plane, a classic herringbone packing is clearly observed. The π -stacking and interactions between neighboring methoxy groups are responsible for the two-dimensional shape, because hydrogen atoms on the molecular terminals do not contribute to the stabilization of an orthorhombic form [16]. The angle between the (110) and (1 $\bar{1}$ 0) faces of the crystal is determined to be 77.6°, which is close to the edge angle of the rhombus shape of the sheet.

Recently, Zhao's group succeeded in a controllable construction of ring-shaped structures with an organic compound named 1,5-diphenyl-1,4-penta-dien-3-one (DPPDO) [17]. Such a molecule, whose structure is displayed in Figure 5.2d, exhibits a good tolerance for structural distortion due to the rearrangement of molecules in the loose crystal lattice. The molecular planes are perpendicular to the *c*-axis and the distance between adjacent molecules along the *c*-axis is a bit large, affording a buffer space for the slight movement of DPPDO molecules. As a result, the assembled DPPDO 1D structures are of remarkable flexibility, implying bendable characteristics in the preferential growth directions. Therefore, it is likely to achieve microrings from the assembly of DPPDO molecules, as long as an appropriate driving force could be applied for the circular growth during the assembly process.

The crystalline microrings were fabricated with the action of the liquid tension during the assembly process. As shown in Figure 5.2d, the DPPDO molecules concentrate preferentially first at the contact line between microsized droplet and substrate, where the solvent evaporated faster than that in other areas. The solution droplet was therefore confined within the inner surface, acting as a circular template for the assembly. Along with the enlargement of DPPDO segments, molecular packing starts to bend, which is induced by the force of liquid tension at the contact line. With the further evaporation of solvent, the segments gradually grow into a curved belt. The formation of the rings heavily depends on the amount of DPPDO units in the microdroplets (Figure 5.2d, bottom). If there are no sufficient molecules, only short rods would appear. With the increase of DPPDO amount, the products gradually develop into incomplete and perfect microrings. However, only large tiles emerge if excess DPPDO were put in a droplet, because of the huge mechanical resistance that needs to be overcome for the wide tiles to bend. From this result, we can infer that although intermolecular

forces dominate the assembly behavior and thus the final morphology, other influences, such as the amount of DPPDO [18], should not be ignored.

5.2.2

Influences of External Factors

Except for inherent intermolecular forces, some other external conditions, including solvent, humidity [19], surface tension, temperature [20], aging time [21], and ultrasonic action [22], also play a role in determining the assembly behavior of molecules. For example, a highly humid condition would be crucial to the formation of ring-shaped structures for thiacyanine derivatives [19]. Zhang *et al.* reported that by changing the process temperature, three kinds of single-crystal nanostructures, for example, nanoribbons, nanotubes, and nanowires, can be controllably prepared with a single intramolecular charge transfer organic compound [20].

5.2.2.1 Solvent Effect in Assembly

Figure 5.3 illustrates an example of solvent effect on the assembly and final products with distinct morphologies, for example, solid rods and hollow tubes, respectively. Both the structures were formed by assembly in the liquid phase with the same compound [21]. Briefly, dilute 9,10-bis(phenylethynyl)anthracene (BPEA) solution was injected into boiling water under vigorous agitation and then cooled to room temperature. The assembled products are rod-like crystals, as proved by the SEM image in Figure 5.3a. The magnified image of a single rod tip shown in the inset indicates that the end face is relatively flat. If the boiling system was kept refluxed for a period before cooling, the assembled products would be perfectly hollow tubes (Figure 5.3b), which were further confirmed by the TEM image (Figure 5.3c). The preferential growth directions of the two distinct structures are the same (Figure 5.3c, inset), revealing some inherent connections. The reason why reflux enables the formation of hollow structure was explored through a variation of reflux time. It is the etching of BPEA molecules by the small amount of ethanol (the good solvent) during the reflux period that resulted in the formation of the hollow tubular structures [23].

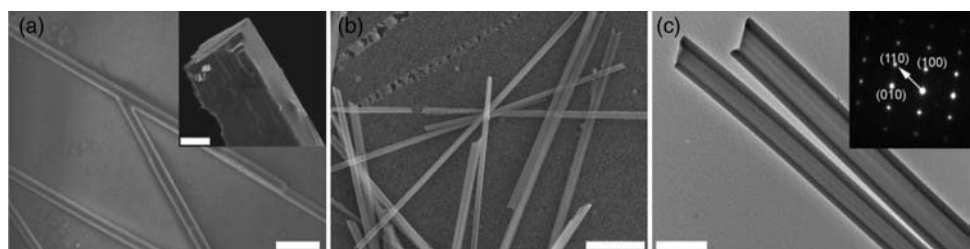


Figure 5.3 Solvent etching effect on the assembly. (a) SEM image of the BPEA micro-rods prepared with a regular liquid-phase assembly. Scale bar is 5 μm . *Inset:* SEM image of a single rod tip. (b) SEM image of BPEA

microtubes prepared through an assembly process under reflux. Scale bar is 10 μm . (c) TEM image of the typical BPEA microtubes. Scale bar is 2 μm . (*Inset:* SAED pattern. Copyright 2008, Wiley.)

5.2.2.2 Site-Selected Assembly on Specific Substrates

For assembly in the liquid phase, the solvent is especially significant mainly because of the fact that some other factors come into play through it, such as temperature, solubility, aging time, and surface tension. In contrast, the most important factor for assembly in the vapor phase is the parameters of vaporized organic molecules. The supersaturation degree of the vaporized molecules has been demonstrated to be the key factor in deciding the morphology and monodispersity of aggregates [24]. Maintaining the vapor saturation at an appropriate level will facilitate the assembly of most organic compounds into uniform low-dimensional structures. Thus, it is increasingly important to be able to control such a parameter.

It was reported that the introduction of adsorbent would improve the quality remarkably in vapor-phase deposition [25]. The adsorbents, which can be neutral aluminum oxide or silica gel, are extremely effective in controlling the degree of supersaturation. The mechanism is considered to be associated with an adsorption–desorption equilibrium between the adsorbents and the organic sources. A variety of organic nanocrystals have been fabricated with this improved method. Taking tris(8-hydroxyquinoline)aluminum (Alq_3) as an example, Figure 5.4a illustrates a typical assembly process in the gas phase. The material source, which is a mixture of Alq_3 and adsorbent, is heated to the deposition temperature with a furnace. The sublimed Alq_3 vapor with proper flux translates

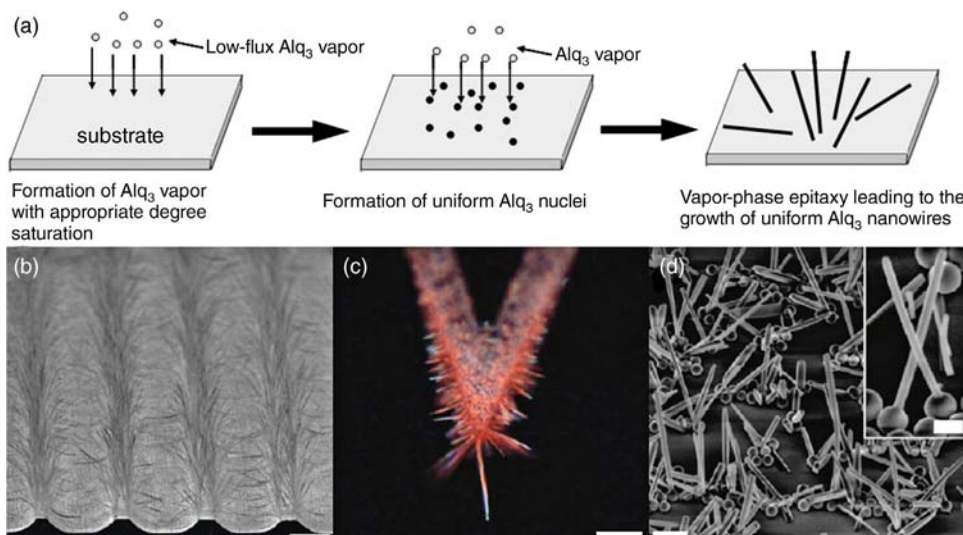


Figure 5.4 Substrate effect on the assembly of organic molecules in the vapor phase. (a) Growth mechanism of Alq_3 nanowires with the assistance of adsorbents to improve the uniformity and crystallinity. (b) Patterned growth of DAAQ nanowire arrays on silicon wafers with periodic ridge–groove patterns.

Scale bar is 25 μm . (c) Optical microscopy image of the DAAQ nanowires grown at an AFM tip. Scale bar is 10 μm . (d) SEM image of the DAAQ nanowires grown on silica spheres. Inset is the magnified image. Scale bars are 2 μm . ((a) Copyright 2006, Wiley; (b–d) copyright 2010, American Chemical Society.)

into small Alq₃ crystal nuclei with high uniformity on the substrates. Then subsequent Alq₃ molecules adsorbed onto the nuclei through intermolecular interactions and grew into uniform 1D structures.

The acquisition of nanowire arrays has been actively pursued because of the improved properties for wide applications, such as efficient solar cells, high-capacity batteries, and light-emitting diodes. Previous works on array materials mostly concentrated on inorganic semiconductors [26] or materials fabricated through various templates [27,28]. Since organic materials have been widely used in the photoelectric area, it is necessary to acquire crystalline organic nanowire arrays. Huang and coworkers reported a direct fabrication method of vertically aligned organic nanowire arrays [29]. It was found that 1,5-diaminoanthraquinone (DAAQ) tends to preferably nucleate and grow faster on sites with high surface energy. This site-selected growth enables a patterned growth on modified substrates. Figure 5.4b is the tilted view SEM image of DAAQ arrays grown on a silicon plate with alternating ridge edges and grooves. Here, DAAQ molecules selectively nucleate and grow on ridge edges where the surface energy is much higher than that of grooves. For the same reason, DAAQ molecules could also grow on AFM tips (Figure 5.4c) with a much longer wire near the very end tip, which possesses the highest surface energy. This reminds us that introducing extra sites with high surface energy should be an effective way to control the distribution of the obtained nanostructures. It has been proved that the size of growth site affects the number and orientation of DAAQ nanowires. As demonstrated in Figure 5.4d, only one nanowire grew on each silica sphere with a proper diameter of 520 nm. The ease of the oriented vertical growth and modulation provides convenience for the fabrication of complex structures as well as direct integration of nanowires into devices.

5.3

From Assembly to Structures

Organic nanostructures have become so attractive in recent decades mainly because of their unique optical and electronic properties. To our knowledge, the optical performances of organic nanostructures are determined by both the intrinsic properties of molecules constituting them and the optical confinement arising from the structural features. Organic aggregates assembled from small molecules are usually crystals with regular geometric shape, where the ordered molecular arrangements present good photon confinement. From the previous section, we know that the molecular assembly behaviors directly determine the final structures of tiny crystals. That is to say, the acquisition of distinct structures can be reasonably expected through a fine control of the assembly process. In this section, we will discuss the achievements of nanomaterials with specific structures either through rational molecular design or through construction strategy selection.

5.3.1

Structure Control through Intermolecular Interactions

We know that molecules would aggregate into various low-dimensional structures if appropriate forces were introduced during the assembly process. Since the optical properties are strongly structure dependent, a controllable synthesis is of particular significance. In most cases, aromatic molecules could assemble into 1D structures through strong π -stacking if there are no other intermolecular interactions. Modifying molecular structure by tailoring the constituent groups may introduce extra forces, causing different preferential packing modes, such as direction, planarity, and steric hindrance effect. Thus, the rational design of molecular components with different intermolecular recognition patterns would be promising for the acquisition of nanostructures with predefined morphologies, which can manipulate photons in specific ways.

5.3.1.1 Controlling the Structures via Molecular Design

Very recently, Zhao's group constructed 1D and 2D nanoarchitectures through assembly by varying the molecular components, affording a guideline to the function-guided molecular design and morphology control (Figure 5.5) [30]. The only difference between 2-acetyl-6-dimethylaminonaphthalene (ADN, Figure 5.5a) and 2-acetyl-6-methylaminonaphthalene (AMN, Figure 5.5e) is the peripheric substituents on the naphthalene core. The secondary amine in AMN could afford less steric repulsion with neighboring molecules and an extra hydrogen bonding site, hindering the 1D packing. It is predicted from the thermodynamical perspective that the stable morphology for ADN is wire-like, while AMN molecules would be

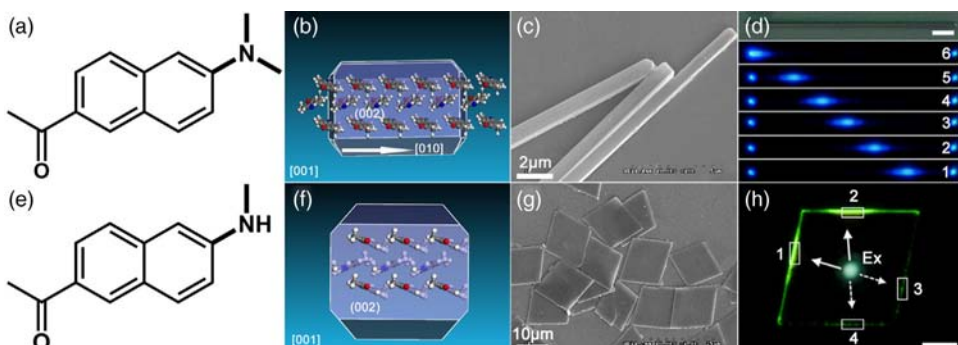


Figure 5.5 Assembled structures with 1D and 2D features through molecular design. (a and e) Molecular structures of ADN and AMN compounds, respectively. (b and f) Predicted growth morphologies based on the attachment energies of ADN and AMN molecules, respectively. (c and g) SEM images of 1D

nanowires aggregated from ADN and 2D rhombic plates from AMN molecules, respectively. (d and h) Distinct waveguide behaviors of 1D and 2D structures, respectively. Scale bars in (d) and (h) are 5 and 10 μm , respectively. (Copyright 2013, Wiley.)

arranged in a slip-stack mode to form sheet-like structure (Figure 5.5b and f, respectively).

The 1D growth of ADN (Figure 5.5c) was determined to be along [010] direction, which can be attributed to the $\pi-\pi$ interactions. These wires can serve as active waveguides where the emitted light is confined within the nanowire and propagates along the axis in two predominant directions (Figure 5.5d). There is no obvious light loss from the light intensities for positions 1–6 (labeled in Figure 5.5d) with the increase of propagation length, indicating a low-loss transmission. Similarly, the two preferential growth directions of the 2D rhombic sheets (Figure 5.5g) are [100] and [010], which are associated with the $\pi-\pi$ interaction and hydrogen bond interactions, respectively. When a focused laser beam irradiated the center of the rhombus plate, the neighboring two outcoupled edges (marked with 1 and 2, Figure 5.5h) have large, bright fluorescence emissions, which show significant contrast with the small, obscure outcouplings at the opposite edges (3 and 4). The remarkable intensity difference between edges of an acute angle implies an asymmetric light propagation, which may play a fundamental role in creating new types of devices.

For organic compounds, not only the differences of substituent groups [19,31], but also their positions may significantly influence the major driving forces in the assembly process, and thus the structures of final products [32]. It has been proved that three isometric molecules of bis(iminopyrrole)benzene could assemble into well-defined spheres, wires, and cubes, respectively, although the intermolecular forces are the same. Different interactions for aggregate stacking at the supramolecular level caused by the isomeric molecular structures are most likely responsible for the different morphological evolution.

5.3.1.2 Structures Obtained from the Synergistic Assembly of Different Compounds

Intermolecular interactions between different compounds can be utilized to fabricate multicomponent structures through their cooperative assembly [33]. In general, the selected compounds constitute a donor–acceptor pair with efficient energy transfer, where a small amount of energy acceptor would quench the donor emission heavily. The energy transfer process through either dipole–dipole interaction or electron exchange would be very effective for organic solid systems due to the reduced intermolecular distance. Benefiting from the fruitful excited-state dynamics, the doped structures could not only maintain the advantages of each component, but also provide novel optical performances, for example, tunable color emission or white light emission [34]. Therefore, exploration of construction strategy to binary systems has a far-reaching consequence to the overall manipulation of photon parameters.

Figure 5.6 presents two typical 1D binary structures obtained by the co-assembly of different molecules. The well-defined nanorods shown in Figure 5.6a were prepared through the adsorbent-assisted epitaxial growth method with two dyes, a blue light emitter (1,3,5-triphenyl-2-pyrazoline, TPP) and an orange light emitter (rubrene). The dopant was determined to be uniformly distributed in the TPP host, ensuring an efficient Förster resonant energy transfer (FRET) process.

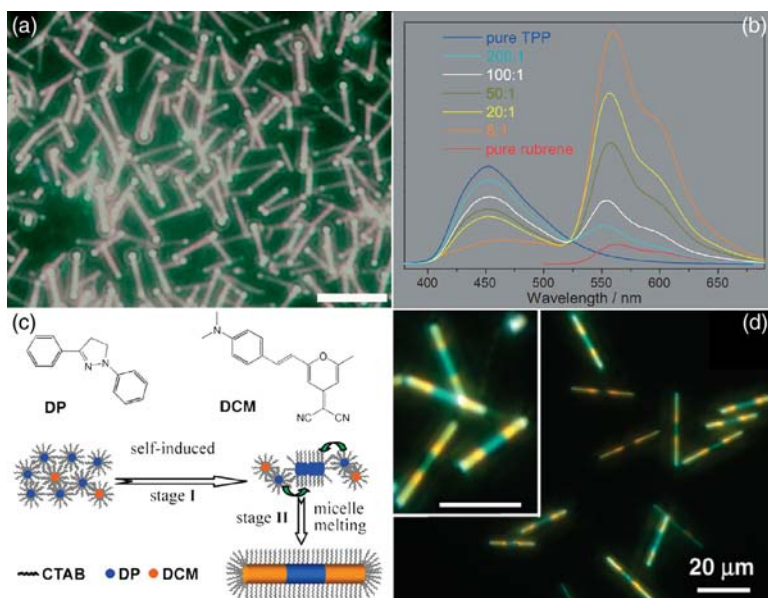


Figure 5.6 Composite structures fabricated from the synergistic assembly of different molecules. (a) PL microscopy image of TPP/rubrene nanorods with controllable doping ratios. Scale bar is 5 μm . (b) Emission spectra of the TPP/rubrene nanostructures with different doping contents. (c) Molecular structures

of DP and DCM as well as the illustration for formation mechanism of the gradiantly doped microrods. (d) PL microscopy image of the microrods under UV illumination. ((a and b) Copyright 2008, Wiley; (c and d) copyright 2010, American Chemical Society.)

The emission color varies significantly with the rubrene doping content, which was modulated by changing the molar ratio of the source materials (Figure 5.6b). At first, there was only one characteristic fluorescence band for pure TPP nanostructures. With the increase of rubrene amount, the emission of TPP was quenched gradually, while the emission corresponding to the rubrene rose up rapidly. When the TPP/rubrene molar ratio was fixed at 100:1, a stable white light emission can be reached from these 1D nanostructures.

Yao and coworkers reported a supramolecular synthesis of triblock microrods constituted with 1,3-diphenyl-2-pyrolidine (DP) and 4-(dicyanomethylene)-2-methyl-6-(*p*-dimethylaminostyryl)-4H-yan (DCM) [35], as illustrated in Figure 5.6c. With the assistance of cetyltrimethylammonium bromide (CTAB) micelles, the DCM molecules could selectively deposit at both ends of the DP rods. During the synergistic assembly process, DP molecules first dissolved into the hydrophobic core of the spherical CTAB micelles due to the solubilization effect (stage I). The dissolution of DP molecules helps in the formation of rod-like micelles that in turn act as templates directing the primary growth of DP molecules. Finally, DCM molecules started to codeposit with DP molecules, generating the tri-block microrods (Figure 5.6d). Although these microrods exhibit microarea heterogeneity, they show macroscopic high-quality white light emission properties.

5.3.2

Structure Modulation through External Factors

From the above discussion, we know that the environment plays a complementary role in the assembly process. Utilizing this point, we could intervene in the molecular assembly behavior by adjusting ambients on the basis of a clear aggregation picture. For example, both the rod and wire structures can be obtained with the same *fac*-tris(2-phenylpyridine)iridium ($\text{Ir}(\text{ppy})_3$) compound, but using different methods. The assembled structures from solvent exchange and solvent evaporation methods are of different crystalline forms [36]. Also, reversible nanostructure conversion from nanospheres to nanorods and nanosheets has also been realized [37].

5.3.2.1 Structures versus Aging Time

Recently, a partly reversible shape shifting of 1,4-bis(1,2':6',1''-bis(3-butyl-1*H*-3,4,5-triazolyl)pyridin-4'-yl)benzene nanostructures was reported by Chandrasekar's group, as shown in Figure 5.7 [38]. The molecule has a rod-shaped arrange-

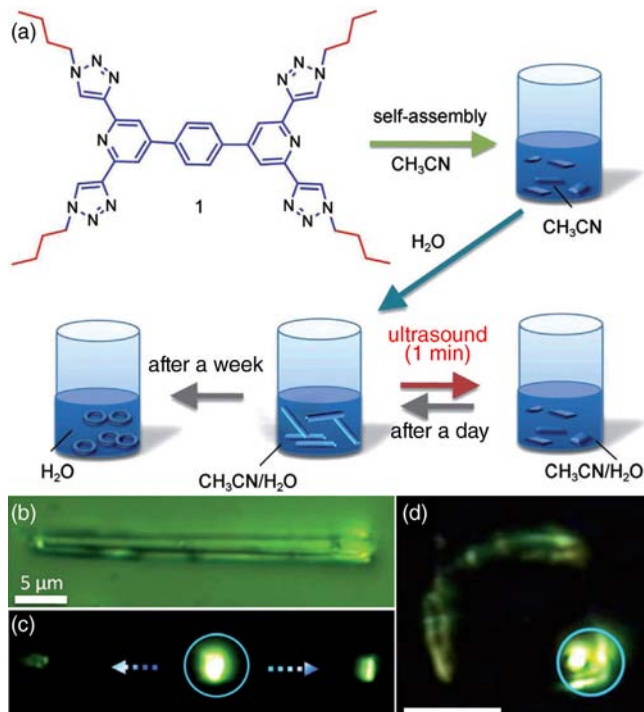


Figure 5.7 Various assembled nanostructures and corresponding optical properties obtained with different assembly conditions. (a) Sketch map of the formation of 2D rectangular plates, 1D nanotubes, and 0D nanorings of the compound under different conditions.

(b and c) Optical bright-field and photoluminescence microscopy images of an identical microtube, respectively. (d) Photoluminescence microscopy image of a single nanosheet with a laser excitation at the corner. (Copyright 2012, Wiley.)

ment of three aromatic rings in the center (Figure 5.7a), which ensures a nice molecular planarity. The nitrogen atom in triazole ring (N_2) would participate in two hydrogen bond interactions with phenyl ring protons, playing a major role in the supramolecular ordering. Homogeneous rectangular sheets are easily achieved through an assembly process in solution. Those microsized plates could switch into tubes via a rolling mechanism in the presence of water, while sonication could induce a reverse transformation of the tubes back into plates. The nanorings were obtained from the tube solution after a week and the transformation process is irreversible.

The absence of any external interference during the whole structural evolution process suggests that the critical activation energy needed to overcome the intermolecular binding forces is very low. For this case, the driving force behind the structural deformation was ascribed to the hydrophobic surface effect, which propels these sheets to curve to avoid the exposure to water. Anisotropy optical waveguide was observed with the excitation of a focused laser beam, demonstrating a possibility of switching the wave guiding behavior through light propagating direction in both 1D (Figure 5.7b and c) and 2D (Figure 5.7d) structures. This work announces again that various optical performances for different application can be achieved even from the same compound as long as an appropriate assembly condition is predesigned. Before that, a careful analysis of the relationship between intermolecular/environmental interactions and structures is indispensable to choose proper assembly strategies.

5.3.2.2 Heterostructures through Site-Specific Epitaxial Growth

The site-specific nucleation characteristics of organic molecules are promising in fabricating some complex structures, for example, organic–metal nanowire heterojunctions, which were realized recently by our group via the vapor deposition of organic compounds on silicon substrates with predispersed silver nanowires (Figure 5.8) [39]. Figure 5.8a is the SEM image of crystalline silver nanowires with convex vertices, which ensure an overwhelming superiority in attracting vaporized BPEA molecules. During the deposition process, the sharp wire tips serve as nuclei centers for the condensation of BPEA vapor. Finally, BPEA molecules nucleated specifically adjacent to the tips of the silver wires to form heterojunctions (Figure 5.8b), which is confirmed by the TEM image of a single BPEA–silver nanowire junction area (Figure 5.8c).

Shown in Figure 5.8d and e are the bright-field and photoluminescence microscopy images of an identical organic–silver nanowire heterojunction. The great contrast in Figure 5.8d reveals that the two wires are of different quality. Both tips of the BPEA wire and the joint point emit bright yellow light under an excitation of a focused laser beam, which is a characteristic of active waveguide. The red emission, emitted from the end of silver nanowire, can be modulated through the polarization of the incident beam, which is attributed to the direct exciton polariton–plasmon coupling. The distinct characteristic of EPs in organic nanowires supplies a new idea to realize logic operations with an individual heterojunction. This facile two-step growth strategy provides a remarkable

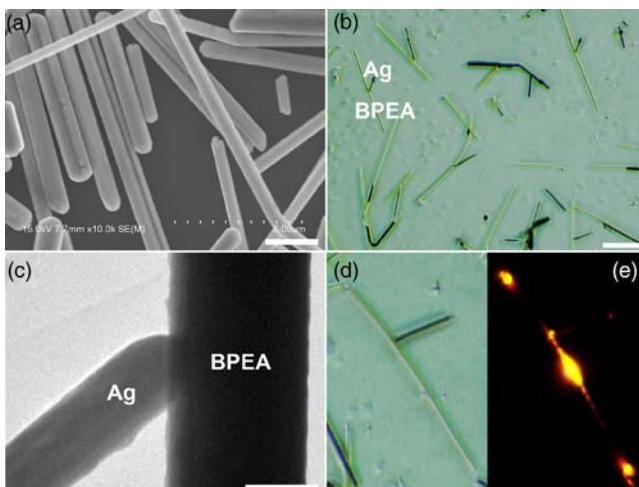


Figure 5.8 Preparation of organic–metal nanowire heterojunctions through substrate modification. (a) SEM image of the silver nanowires with convex tips. Scale bar is 2 μm . (b) Optical microscopy image of the BPEA–silver

heterojunctions. Scale bar is 20 μm . (c) TEM image of the junction area. Scale bar is 200 nm. (d and e) Optical bright-field and PL microscopy images of an identical junction, respectively. (Copyright 2012, Wiley.)

convenience for incorporating plasmonic modules as practical components into high-capacity photonic circuits.

5.4

From Structures to Photonic Properties

Low-dimensional structures constructed from single kind of compounds offer an ideal model to study the assembly characteristics as well as structure-related light confinement and electronic properties [40]. Now we have reached a preliminary comprehension in the relationships among molecule, assembly, and structure from the previous two sections. The abundant interactions among different materials, such as energy/charge transfer, exciton migration and conversion, and EP–SPP coupling, have a fair chance of generating a series of novel properties in complex structures. An ingenious utilization of these new mechanisms would be of great significance to the realization of photonic devices with desired functions [11]. Thus, in this section, we will focus on the optical properties and corresponding applications of three representative complex structures assembled from organic molecules.

5.4.1

Nanowire Heterojunctions

In comparison with uniformly doped structures, heterostructured materials with a clear interface are much more flexible in the manipulation of photons at the

micro-/nanoscale. Some innovative effects could be utilized to finely tune the light–matter interactions and thus bring out meaningful optical properties. For example, multiple segmented nanostructures show broad multifunctionality in photonic applications, including nanobarcodes [35], p–n junctions [41], and multiluminescent light sources. However, these phase-separated low-dimensional structures were mainly prepared via hard template or electrochemical deposition techniques, with a great weakness of photoelectric properties due to the amorphous structures. Along with our knowledge on the controllable assembly, heterostructures could also be prepared via modified assembly [42].

5.4.1.1 Dendritic Heterostructures as Optical Routers

Organic dendritic structures have been actively investigated due to their potential applications in one-to-many, many-to-one, and many-to-many photonic devices. Inspired by the fact that vaporized organic molecules tend to nucleate preferentially and grow more rapidly on sites with smaller curvature radii or higher surface energies [29], Zhao and coworkers proposed a two-step deposition method to create organic wire-on-wire structures (Figure 5.9a) [43]. In a typical synthesis, assembled crystalline Alq₃ microwires (step 1) with hexagonal cross sections (Figure 5.9b) were used as nucleation centers for the vertical epitaxial growth of DAAQ molecules (step 2). DAAQ molecules concentrate selectively on the Alq₃ microwires to form isolated clusters, seeding subsequent molecular deposition to form the final vertical nanowire branches. Such a growth mechanism has been testified by the SEM images of different growth stages (Figure 5.9c–e). Both the branch density and length can be precisely controlled by deposition time and temperature, respectively, illustrating the versatility and universality of the fabrication method. The green emission from Alq₃ trunk and red emission from DAAQ branches are clearly observed in corresponding positions (Figure 5.9f), verifying the phase-separated component distribution and existence of clear interfaces.

The obtained heterostructures function as optical routers with many output channels so that the guided light can be output simultaneously from the trunk tips and each branch under an excitation (Figure 5.9g). The spatially resolved PL spectra (Figure 5.9h) from different branches demonstrate the propagation length-dependent outputs as well as color changes (inset). In comparison with the PL of Alq₃ (curve I in Figure 5.9h), the spectra taken locally from the trunk tip (curve V) show a red shift due to the variation in the energy transfer process. The other three curves are all superpositions of the green and red emissions from the two compositions, indicating the simultaneous occurrence of efficient FRET processes and the direct guidance of Alq₃ emission in DAAQ branches at the interfaces. The decreased fluorescence lifetime of Alq₃ emission at different positions (Figure 5.9h) further confirmed the different energy transfer efficiency.

5.4.1.2 Nanowire p–n Junctions as Photoelectric Transducers

If both the nucleation spots and the growth direction can be simultaneously controlled with a high accuracy, where only one wire grows vertically on the

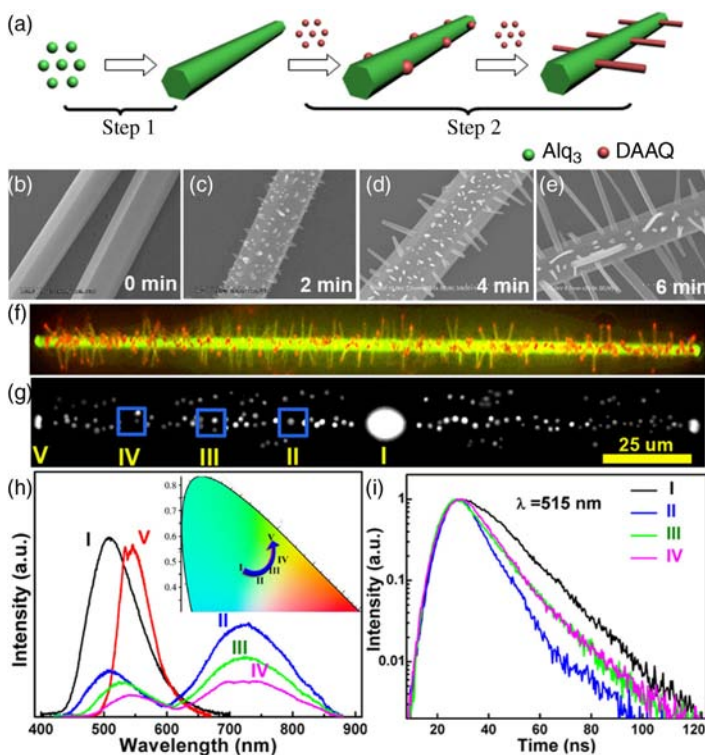


Figure 5.9 Growth processes and photonic properties of the dendritic organic–metal nanowire heterojunctions. (a) Schematic illustration of the growth mechanism. Step 1: Alq₃ microwire prepared through assembly in the liquid phase. Step 2: site-specific nucleation and epitaxial growth of DAAQ molecules on the Alq₃ microwires. (b–e) SEM images of different growth stages of DAAQ in step 2. (f) PL microscopy image of a single nanowire heterojunction under the illumination of unfocused

UV light. (g) PL microscopy image of the heterostructure under the excitation of a focused laser beam. (h) Spatially resolved photoluminescence spectra of the excited spot (I), output signals from the DAAQ branches (II–IV), and the Alq₃ tip (V) labeled in (g). (i) Photoluminescence decay profiles of Alq₃ emissions at different propagation lengths. (Copyright 2012, American Chemical Society.)

predispersed wire, crystalline heterojunctions, even arrays, would be available [44]. The preparation method might be a two-step process as previously discussed or just a one-step process, for example, epitaxial growth via vapor-phase codeposition, as illustrated in Figure 5.10a [41]. Here, two compounds with similar molecular structures, the p-type material (copper phthalocyanine, CuPc) and the n-type material (5,10,15,20-tetra(4-pyridyl)porphyrin, H₂TPyP), were selected for the synthesis of coaxial p–n junction nanowire arrays. Both compounds were put in a tube furnace at different positions to be coevaporated with a varied evaporation rate. During the deposition process, H₂TPyP forms vertically aligned hollow structures first, which provide nucleation sites for

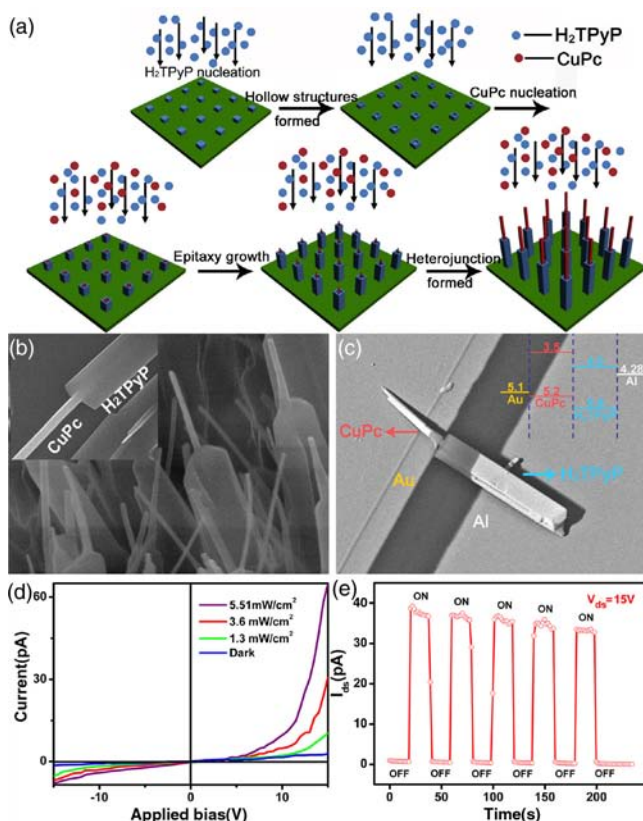


Figure 5.10 Formation and photoelectric properties of the coaxial organic p–n heterojunctions. (a) Schematic illustration of the assembly processes of the CuPc–H₂TPyP p–n junction nanowire arrays. (b) SEM image of the as-prepared nanowire junctions. Scale bar is 1 μm. Inset shows a single heterojunction.

(c) SEM image of a photoelectric device based on a single junction. Inset shows the energy level diagram of the device. (d) Current–voltage (I – V) curves of the device shown in (c). (e) Photo-switching characteristics of the p–n junction device. (Copyright 2012, Wiley.)

subsequent CuPc vapor concentration. Then, the two molecules codeposited for some time to form the heterojunction nanowire arrays (Figure 5.10b).

The strong π – π interactions between the two planar compounds ensure good connections at the junction area that endow each coaxial heterojunction nanowire with excellent photoelectric properties. Shown in Figure 5.10c is a single device with the prepared p–n junction. Such a device acts as a good photoelectric transducer, as depicted in Figure 5.10d and e. The repeatable photo-current under the light illumination indicates a reversible and stable response to external illumination. The large energy difference between the lowest unoccupied molecular orbital of H₂TPyP and the highest occupied molecular orbital of CuPc at the heterointerface enables a great opportunity for the further

improvement of device efficiency. Commonly, the larger the wire diameters, the higher the device efficiency. Owing to the unique cable-type structure and the large interfacial gap, the single-junction device shows better optoelectronic conversion performance than single-component nanowires and thin film sandwiched devices, which can be applied as highly sensitive photoelectrical transducers in nanoscale photonic circuits.

5.4.2

Doped Nanostructures

The signal sources for an integrated photonic circuit might be a nanolaser with a narrow linewidth or broadband emissions, and even white light, since they provide more possibilities in novel optical signal processing. Doping is a general technique in organic materials to obtain color-tunable emissions due to the efficient energy transfer process. However, the emission colors of the doped structures are usually not stable because of slight acceptor content variation caused by external stimuli. Therefore, developing an intelligent mechanism that can adjust the output automatically, regardless of doping ratio and environmental variation, is necessary and challenging.

5.4.2.1 Uniformly Doped Structures

The combination of FRET downconversion and triplet–triplet energy transfer (TTET) upconversion in an organic system is supposed to fulfill the requirement. Zhao and coworkers fabricated uniform 1D nanostructures with 9,10-diphenylanthracene (DPA) and iridium(III) bis(2-phenylbenzothiozolato-*N,C*²) acetylacetone ((BT)₂Ir(acac)) through assembly [45]. In these composite nanowires, the bidirectional energy transfer, that is, the FRET from DPA to (BT)₂Ir(acac) and the reverse TTET from (BT)₂Ir(acac) to DPA coexist, causing the energy fluctuations between the singlet and triplet states during the light propagation. The excitons can fluctuate between the blue emission of DPA and the orange emission of (BT)₂Ir(acac) in the binary nanowire. The color ratios of two outcoupling colors from either low- or high-doped wires can reach the same value after the light transmission over a certain distance (Figure 5.11a), resulting in a self-modulated white light outcoupling at wire tips. Such an optical waveguide behaves like a regulator that converts different input colors into a standard output, as displayed in Figure 5.11b. These results provide a comprehensive understanding of exciton polariton conversion in active waveguiding and effective strategies for developing novel multicomponent waveguide building blocks.

Optical switcher is indispensable to perform some ordinary functions in photonic signal processing. The achievement of ON/OFF state for photons is not an easy thing because external activities can hardly intervene in the behavior of photons. Fortunately, various light–matter interactions as well as optical confinement in different tiny structures could be used to solve the problem. Organic molecules, which were endowed with diverse photoresponses, could be conveniently utilized to realize specific functions. For example, photochromism [46], a

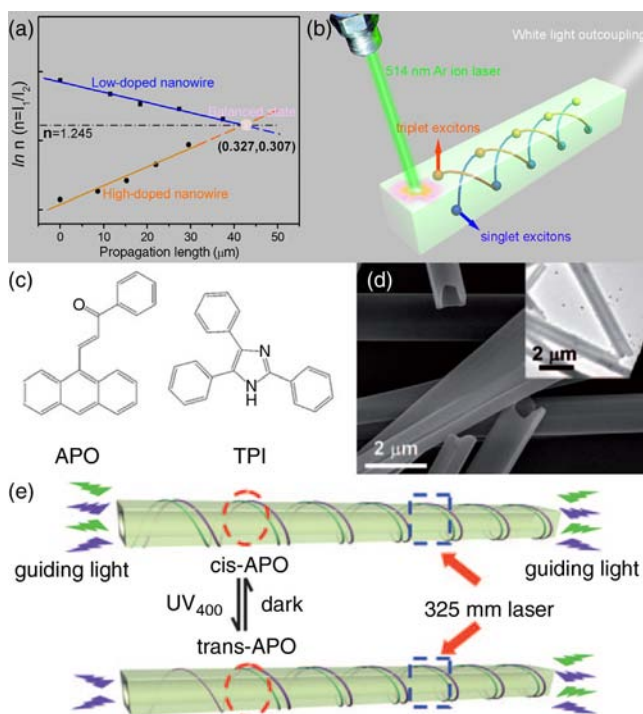


Figure 5.11 Fabrication of uniformly doped structures for light sources with tunable emission colors. (a) The exponential relationship between the contribution ratio of donor to acceptor emission, n , and the propagation length in the low- and high-doped nanowires. (b) Schematic illustration of the mechanism for the self-modulated white light outcoupled emission. (c) Molecular structures of APO and

TPI. (d) SEM and TEM (inset) images of the 1D doped tubular structures. (e) The principle of the microtubes as optical waveguide switch. The circled areas represent the photoisomerization regions induced by UV irradiation. The squares indicate the excited spots for waveguide measurement. ((a and b) Copyright 2011, Wiley; (c and e) copyright 2011, Wiley.)

reversible change in absorption band governed by the light irradiation, can be applied for the construction of waveguide switcher [47]. Figure 5.11c presents two molecular structures: a photochromic molecule 3-(anthracen-10-yl)-1-phenylpro-2-en-1-one (APO) and 2,4,5-triphenylimidazole (TPI). Homogeneous tubular structures (Figure 5.11d) can be obtained through the synergistic assembly of these two model compounds mediated by hydrogen bonding.

When excited with a focused laser at the squared area (Figure 5.11e), the 1D tube would emit intense fluorescence and self-guide to both tips. After the illumination of 400 nm beam (UV₄₀₀), the guided light from the left tip decreased dramatically while the emission with a peak of 540 nm disappeared completely. Meanwhile, there is no obvious change in the outcouplings from the right tip before and after the UV irradiation. That is to say, selective switching of the waveguide had been successfully achieved in such a binary structure. The

outcoupled light can be turned on again by keeping the sample in the dark. This switching behavior can be reversibly switched over many cycles without any fatigue, demonstrating a good repeatability and reliability as practical photonic devices. This work also enlightens a way to control the waveguide behavior through the particular properties of molecules.

5.4.2.2 Gradiently Doped Structures

Precise design and fabrication of chemical heterogeneous structures is another good alternative to obtain specific photonic functions. Benefiting from the flexible synthesis through cooperative assembly, the spatial excitonic emission during the light propagation path could be finely engineered through the donor–acceptor energy transfer in organic heterogeneous composites. A template-free method for heterostructures with tunable compositions in the axial direction was developed by Zhao and coworkers [48]. The axial segments were acquired through a proper control of intermolecular interactions between the host and the guest, TPI was selected as the host material, and two compounds – a sphere-like organometallic complex $(BT)_2Ir(acac)$ and a planar molecule BPEA – were selected as typical guest materials. In the assembly process (Figure 5.12a), TPI molecules quickly aggregate into short rod-like hollow structures and then the guest molecules start to enter into the TPI host matrix subsequently. The major difference between the two molecules lies in the host–guest interaction strength, that is, the π – π interaction in the BPEA–TPI pair is much stronger than the van der Waals force in the $(BT)_2Ir(acac)$ –TPI pair. Such a divergence results in the axially distinct distribution of the two dopants.

For $(BT)_2Ir(acac)$, the great mismatch with TPI in molecular planarity brings a large steric hindrance, which terminates the further growth of TPI molecules. Therefore, the final products were characterized as three blocks, where the doped components are distributed mostly in both ends (Figure 5.12b). Comparatively, the nice similarity in molecular structures between BPEA and TPI molecules ensures a better molecular compatibility, which allows for the continuous packing of TPI molecules. The consumption of BPEA ends up its aggregation on the TPI host, and then the growth of TPI restarts and becomes predominant. These processes took place repeatedly until the depletion of molecules. The alternant accumulation of TPI and BPEA molecules resulted in the multiblock structures with tunable colors (Figure 5.12c).

This cooperative assembly strategy is universal, which can be generalized and expanded to achieve some complex structures toward practical functions, such as full-color emission in a single tube [14] or triode for signal processing [41,49]. Soon afterward, 3-(2-benzothiazoly)-7-diethylaminocoumarin (coumarin 6) was adopted as the guest compound to acquire nanostructures with distensible color tunability on the basis of the above results. Besides the intrinsic green emission from monomer, coumarin 6 also emits red fluorescence from the charge transfer state in aggregates, as shown in Figure 5.12d. Therefore, red–green–blue full colors in an individual luminescent structure would be accomplished with the TPI–coumarin 6 pair via controllable doping in the assembly process.

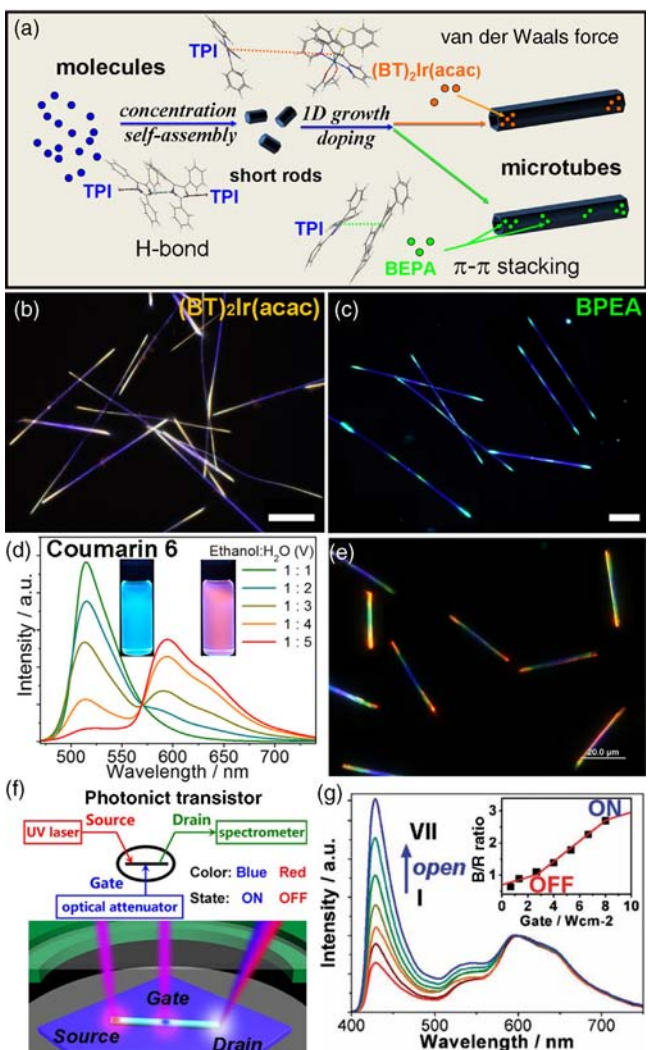


Figure 5.12 Formation and optical properties of the gradiently doped 1D nanostructures. (a) Schematic illustration for the formation of doped TPI tubes with different guest molecules. (b and c) PL microscopy images of the triblock and multiblock doped TPI microtubes. (d) Fluorescence spectra of coumarin 6 aggregates with different contents in the ethanol/water mixture. (e) PL microscopy image of coumarin 6-doped TPI microtubes. (f)

Schematic illustrations of the design concept (top) and realization (down) of a photonic transistor in rainbow colored microtubes. (g) Outcoupled emission spectra from the drain port under various gate controls. Inset shows the relationship between outputted blue to red light ratio and the power of the gate laser. ((a–c) Copyright 2012, Wiley; (d–g) copyright 2013, Wiley.)

The formation mechanism of the TPI–coumarin 6 microstructures is similar to that of the TPI–(BT)₂Ir(acac) pair. The doping gradient of coumarin 6 in the axial direction induced the full-colored photoluminescence along these microtubes (Figure 5.12e). Upon an unfocused UV light excitation, both TPI and coumarin 6 could be excited and emit fluorescence with different colors. A part of the emitted fluorescence is confined and self-guided in both directions. During the light propagation along the tubes, the irreversible energy transfer from the donor to the acceptor ensures a unidirectional light transfer in the optical materials. Such a characteristic is of great importance in the development of essential photonic devices, especially all-optical diodes and triodes.

The design concept and experimental verification of a photonic triode are illustrated in Figure 5.12f. The optical triode also constitutes source, drain, and gate components, which is similar to an electronic analogy. The incident laser excitation with a fixed intensity at the left end acts as the source, while the outcoupled light from the right tip is regarded as the drain. The gate beam with different attenuations is located at the middle part of the individual tube to control the conducting signal from the source to the drain. The outcouplings from the drain (Figure 5.12g) are gradually altered from red (blue/red < 1, OFF) to blue (blue/red > 1, ON) with increased gate intensity. The continuous blue/red ratio suggests a precise gate-modulated output of the transistor.

5.4.2.3 Core/Sheath Structures

Assembled organic crystalline nanomaterials are all excellent waveguides as the fluorescence can be well confined and propagated within the 1D structure due to the difference in refractive index between material and surrounding medium, which is mostly air. Ambient environmental changes could be recorded by the transmitted light in form of light parameters. Since light transmission in nano-sized structures is very sensitive to the surrounding variance, such a mechanism could be applied to fabricate ingenious sensors. Figure 5.13 gives an example of photonic gas transducer with a single core/sheath nanowire, which was fabricated by decorating the single crystalline BPEA nanowire with chemoreactive bis(2,4,5-trichloro-6-carbopentoxyphenyl) oxalate (CPPO) [50]. A cooperative assembly method was put forward to get this core/sheath nanostructure (Figure 5.13a). The cable-like structures appeared with the proper ratio of BPEA to CPPO quantity so that the BPEA nanowires can be totally wrapped by the dye-doped CPPO shell, as testified by the TEM image in Figure 5.13b. The CPPO in the peripheral layer is highly sensitive and selective to the H₂O₂ gas as a typical chemiluminescent compound. Such a core/sheath structure could not only keep the high chemical activity of CPPO, but also improve its mechanical and optical properties through the introduction of BPEA crystalline wire in the inner core.

A single nanowire heterostructure was employed as a gas sensor based on a gas concentration-dependent evanescent energy leakage (Figure 5.13c). The fluorescence under a laser excitation serves as the input signal while the outcoupled light is regarded as the output signal. Once the surrounding medium contains trace amounts (several ppm) of H₂O₂, the output coupling is drastically attenuated

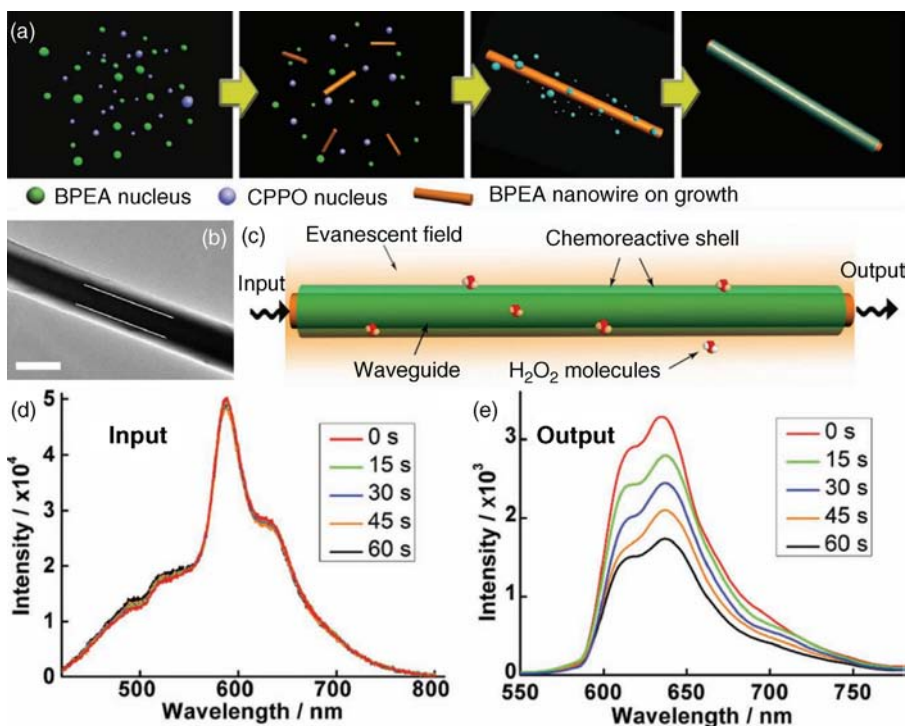


Figure 5.13 Formation and photonic sensing performance of the core/sheath nanostructure. (a) Scheme of the growth mechanism. (b) TEM image of a single core/sheath nanowire. Scale bar is 1 μm . (c) Schematic illustration for the evanescent field sensing of the core/

sheath optical waveguide. Light is coupled into the cavity and travels through the sensing region coated with chemoreactive shell. (d) and (e) Time-dependent PL intensities of the input and output light on exposure to 6 ppm H₂O₂ vapor. (Copyright 2012, Wiley.)

(about 50%) while the input intensity remains unchanged (Figure 5.13d and e). The characteristic response of the nanowires exposed to the gas vapors is remarkably fast (tens of seconds). This cable-like optical waveguide sensing platform complements the present gas sensor with the ability of rapidly and specifically monitoring the amplified environmental variations, demonstrating the great potential of a single nanocable for on-chip optical probes. The use of a facile assembly method to obtain cable-like composites not only bestows the transducer with a defect-free structure and high sensitivity, but also enables the large-scale preparation, which is a key point to commercial products.

5.5

Conclusions

The ever-increasing demand of multifunctional photonic devices at micro-/nanoscale greatly promotes the development of chemistry and materials.

Organic materials are promising building blocks due to the huge advantages of flexible design, tailored properties, easy processability, and low cost. Small molecules tend to assemble into low-dimensional crystals impelled by the weak intermolecular interactions, resulting in unique photophysical and photochemical characteristics with large differences from their inorganic counterparts. Structure-dependent photonic properties have been demonstrated with these organic nanocrystals, suggesting a way to obtain desired functionalities. Till date, various improved construction strategies starting from organic molecules have been proposed continuously for the acquisition of functional materials.

However, systemic studies on the relationships among molecular design, assembly process control, morphological modulation, and optical performance manipulation of final products are rather scattered and suffer from an in-depth summarization. Considering these aspects, we began with a comprehensive introduction of the assembly process of several representative molecules, highlighting the influences of molecular interactions and environmental conditions on the molecular packing mode. Either aggregation in the liquid phase or epitaxial growth in the vapor phase has been proved to be a universal and facile preparation method to achieve diverse nanostructures.

Rational molecular design and targeted assembly method selection are higher demands of function-oriented material synthesis. On the basis of an in-depth understanding of basic assembly rules, we could tailor the intermolecular interactions by modifying the molecular structure or altering the environmental conditions, which may affect both the structures and properties of organic aggregations. A good way to obtain multifunctional materials is the construction of crystalline nanocomposites through cooperative assembly of several compounds, due to the ease of preparation and flexibility. Multi-component materials, with the guest molecules uniformly or gradually distributed in the nanostructures, have been demonstrated to be beneficial for high quality and performance in the application of the devices. Before that, it is imperative to precisely design and control the structures according to the desired properties. Besides photonic elements, the resulting composite nanomaterials could also be used in biomedicine, sensors, automation, optoelectronics, and so on.

So far, the development of organic nanomaterials is still far behind that of the inorganic counterparts, although considerable attention has been paid in the past few decades. The preparation of micro-/nanocrystals is still in its early stage, not to mention controllability. For this reason, a continuous investigation of molecular assembly would be necessary to develop improvements in reproducibility, uniformity, structural controllability, crystalline quality, and performances. In this sense, we hope to promote a comprehensive understanding of the relationships among molecules, assembly, structures, and properties to speed up the spiraling development of organic nanophotonic materials (Figure 5.14). Benefiting from the present developments, we know that optical performances of organic aggregates can be finely

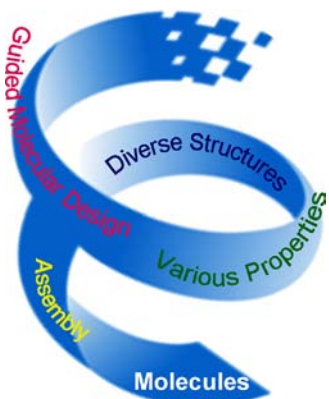


Figure 5.14 A spiraling cognition of the relationships among molecules, assembly, structures, and properties to power the following development of organic nanophotonic materials and devices.

tuned through rational molecular design and fabrication strategy selection. New efforts based on current cognitions would help us to achieve a better comprehension of the function-oriented assembly behavior as well as structure evolution, which would further stimulate progress in this area. A reasonable theoretical model, which is not limited to several molecules, will be beneficial for obtaining overall knowledge of the assembly process and structural confinement effect.

Present photonic devices primarily take advantage of the linear optical properties only, especially photoluminescence. It is not an easy thing to realize some sophisticated applications solely with the linear response, such as ultrafast switcher or signal amplifier. Thus, organic nanostructures consisting of large nonlinear optical molecules would be an appropriate alternative in such areas. The response time of nonlinear effect is usually on the order of femtoseconds to picoseconds. Such a rapid response pledges a good signal processing speed. Moreover, the nonlinear properties of organic materials might be magnified at micro-/nanoscale due to the size-dependent optical confine effect, facilitating the design and realization of nonlinear photonic devices.

Considering the vast number of organic species and great possibilities of their structure-related optical properties, it is reasonable to believe that there will be a brighter future for the organic assemblies as photonic materials. To achieve this goal, we need to devote ourselves to explore this promising field, especially the relationships among molecule, morphology, and performance. There are still many challenges, for example, synthesis of hierarchical structures, acquisition of complex functions, and synergistic effects among different compositions. We hope that the bottom-up assembly method will open up a new prospect for the creation of novel photonic materials.

Acknowledgments

This work was supported by the National Natural Science Foundation of China (Nos. 21125315 and 21373241), the Ministry of Science and Technology of China (2012YQ120060), and the Strategic Priority Research Program of the Chinese Academy of Sciences (Grant No. XDB12020300).

References

- 1 Kirchain, R. and Kimerling, L. (2007) A roadmap for nanophotonics. *Nat. Photon.*, **1** (6), 303–305.
- 2 Piccione, B., Cho, C.-H., van Vugt, L.K., and Agarwal, R. (2012) All-optical active switching in individual semiconductor nanowires. *Nat. Nanotechnol.*, **7** (10), 640–645.
- 3 Clark, J. and Lanzani, G. (2010) Organic photonics for communications. *Nat. Photon.*, **4** (7), 438–446.
- 4 Zhao, Y.S., Fu, H., Peng, A., Ma, Y., Liao, Q., and Yao, J. (2009) Construction and optoelectronic properties of organic one-dimensional nanostructures. *Acc. Chem. Res.*, **43** (3), 409–418.
- 5 Zhao, Y.S., Fu, H., Peng, A., Ma, Y., Xiao, D., and Yao, J. (2008) Low-dimensional nanomaterials based on small organic molecules: preparation and optoelectronic properties. *Adv. Mater.*, **20** (15), 2859–2876.
- 6 Avestro, A.-J., Belowich, M.E., and Stoddart, J.F. (2012) Cooperative self-assembly: producing synthetic polymers with precise and concise primary structures. *Chem. Soc. Rev.*, **41** (18), 5881–5895.
- 7 Lehn, J.-M. (2002) Self-organization and complex matter. *Supramol. Sci.*, **295** (5564), 2400–2403.
- 8 Cordovilla, C. and Swager, T.M. (2012) Strain release in organic photonic nanoparticles for protease sensing. *J. Am. Chem. Soc.*, **134** (16), 6932–6935.
- 9 Hong, Y., Lam, J.W.Y., and Tang, B.Z. (2011) Aggregation-induced emission. *Chem. Soc. Rev.*, **40** (11), 5361–5388.
- 10 Yan, Y. and Zhao, Y.S. (2012) Exciton polaritons in 1D organic nanocrystals. *Adv. Funct. Mater.*, **22** (7), 1330–1332.
- 11 Yan, Y., Zhang, C., Yao, J., and Zhao, Y.S. (2013) Recent advances in organic one-dimensional composite materials: design, construction, and photonic elements for information processing. *Adv. Mater.*, **25** (27), 3627–3638.
- 12 Zang, L., Che, Y., and Moore, J.S. (2008) One-dimensional self-assembly of planar π-conjugated molecules: adaptable building blocks for organic nanodevices. *Acc. Chem. Res.*, **41** (12), 1596–1608.
- 13 Zhang, C., Zou, C.-L., Yan, Y., Hao, R., Sun, F.-W., Han, Z.-F., Zhao, Y.S., and Yao, J. (2011) Two-photon pumped lasing in single-crystal organic nanowire exciton polariton resonators. *J. Am. Chem. Soc.*, **133** (19), 7276–7279.
- 14 Basak, S. and Chandrasekar, R. (2011) Multiluminescent hybrid organic/inorganic nanotubular structures: one-pot fabrication of tricolor (blue–red–purple) luminescent parallelepipedic organic superstructure grafted with europium complexes. *Adv. Funct. Mater.*, **21** (4), 667–673.
- 15 Mizuno, H., Haku, U., Marutani, Y., Ishizumi, A., Yanagi, H., Sasaki, F., and Hotta, S. (2012) Single crystals of 5,5'-bis(4'-methoxybiphenyl-4-yl)-2,2'-bithiophene for organic laser media. *Adv. Mater.*, **24** (42), 5744–5749.
- 16 Bernstein, J., Sarma, J.A.R.P., and Gavezzotti, A. (1990) Generation of unknown crystal phases for aromatic hydrocarbons by packing energy calculations. *Chem. Phys. Lett.*, **174** (3–4), 361–368.
- 17 Zhang, C., Zou, C.-L., Yan, Y., Wei, C., Cui, J.-M., Sun, F.-W., Yao, J., and Zhao, Y.S. (2013) Self-assembled organic crystalline microrings as active

- whispering-gallery-mode optical resonators. *Adv. Opt. Mater.*, **1** (5), 357–361.
- 18** Huang, L., Liao, Q., Shi, Q., Fu, H., Ma, J., and Yao, J. (2010) Rubrene micro-crystals from solution routes: their crystallography, morphology and optical properties. *J. Mater. Chem.*, **20** (1), 159–166.
- 19** Takazawa, K. (2007) Micrometer-sized rings self-assembled from thiacyanine dye molecules and their waveguiding properties. *Chem. Mater.*, **19** (22), 5293–5301.
- 20** Zhang, X., Zhang, X., Zou, K., Lee, C.-S., and Lee, S.-T. (2007) Single-crystal nanoribbons, nanotubes, and nanowires from intramolecular charge-transfer organic molecules. *J. Am. Chem. Soc.*, **129** (12), 3527–3532.
- 21** Zhao, Y.S., Xu, J., Peng, A., Fu, H., Ma, Y., Jiang, L., and Yao, J. (2008) Optical waveguide based on crystalline organic microtubes and microrods. *Angew. Chem., Int. Ed.*, **47** (38), 7301–7305.
- 22** Zhao, Y.S., Yang, W., and Yao, J. (2006) Organic nanocrystals with tunable morphologies and optical properties prepared through a sonication technique. *Phys. Chem. Chem. Phys.*, **8** (28), 3300–3303.
- 23** Zhang, X., Zhang, X., Shi, W., Meng, X., Lee, C., and Lee, S. (2007) Single-crystal organic microtubes with a rectangular cross section. *Angew. Chem., Int. Ed.*, **46** (9), 1525–1528.
- 24** Dai, Z.R., Pan, Z.W., and Wang, Z.L. (2003) Novel nanostructures of functional oxides synthesized by thermal evaporation. *Adv. Funct. Mater.*, **13** (1), 9–24.
- 25** Zhao, Y.S., Xiao, D., Yang, W., Peng, A., and Yao, J. (2006) 2,4,5-Triphenylimidazole nanowires with fluorescence narrowing spectra prepared through the adsorbent-assisted physical vapor deposition method. *Chem. Mater.*, **18** (9), 2302–2306.
- 26** Huang, M.H., Mao, S., Feick, H., Yan, H., Wu, Y., Kind, H., Weber, E., Russo, R., and Yang, P. (2001) Room-temperature ultraviolet nanowire nanolasers. *Supramol. Sci.*, **292** (5523), 1897–1899.
- 27** O'Carroll, D., Lieberwirth, I., and Redmond, G. (2007) Microcavity effects and optically pumped lasing in single conjugated polymer nanowires. *Nat. Nanotechnol.*, **2** (3), 180–184.
- 28** Briseno, A.L., Mannsfeld, S.C.B., Ling, M. M., Liu, S., Tseng, R.J., Reese, C., Roberts, M.E., Yang, Y., Wudl, F., and Bao, Z. (2006) Patterning organic single-crystal transistor arrays. *Nature*, **444** (7121), 913–917.
- 29** Zhao, Y.S., Zhan, P., Kim, J., Sun, C., and Huang, J. (2010) Patterned growth of vertically aligned organic nanowire waveguide arrays. *ACS Nano*, **4** (3), 1630–1636.
- 30** Yao, W., Yan, Y., Xue, L., Zhang, C., Li, G., Zheng, Q., Zhao, Y.S., Jiang, H., and Yao, J. (2013) Controlling the structures and photonic properties of organic nanomaterials by molecular design. *Angew. Chem., Int. Ed.*, **52** (33), 8713–8717.
- 31** Cantekin, S., Balkenende, D.W.R., Smulders, M.M.J., Palmans, A.R.A., and Meijer, E.W. (2011) The effect of isotopic substitution on the chirality of a self-assembled helix. *Nat. Chem.*, **3** (1), 42–46.
- 32** Wang, Y., Fu, H., Peng, A., Zhao, Y., Ma, J., Ma, Y., and Yao, J. (2007) Distinct nanostructures from isomeric molecules of bis(iminopyrrole) benzenes: effects of molecular structures on nanostructural morphologies. *Chem. Commun.*, **16**, 1623–1625.
- 33** Park, S.K., Varghese, S., Kim, J.H., Yoon, S.-J., Kwon, O.K., An, B.-K., Gierschner, J., and Park, S.Y. (2013) Tailor-made highly luminescent and ambipolar transporting organic mixed stacked charge-transfer crystals: an isometric donor–acceptor approach. *J. Am. Chem. Soc.*, **135** (12), 4757–4764.
- 34** Zhao, Y.S., Fu, H.B., Hu, F.Q., Peng, A.D., Yang, W.S., and Yao, J. (2008) Tunable emission from binary organic one-dimensional nanomaterials: an alternative approach to white-light emission. *Adv. Mater.*, **20** (1), 79–83.
- 35** Lei, Y., Liao, Q., Fu, H., and Yao, J. (2010) Orange–blue–orange triblock one-dimensional heterostructures of organic microrods for white-light emission. *J. Am. Chem. Soc.*, **132** (6), 1742–1743.

- 36** Wang, H., Liao, Q., Fu, H., Zeng, Y., Jiang, Z., Ma, J., and Yao, J. (2009) Ir(ppy)₃ phosphorescent microrods and nanowires: promising micro-phosphors. *J. Mater. Chem.*, **19** (1), 89–96.
- 37** Liu, T., Li, Y., Yan, Y., Li, Y., Yu, Y., Chen, N., Chen, S., Liu, C., Zhao, Y., and Liu, H. (2012) Tuning growth of low-dimensional organic nanostructures for efficient optical waveguide applications. *J. Phys. Chem. C*, **116** (26), 14134–14138.
- 38** Chandrasekhar, N. and Chandrasekar, R. (2012) Reversibly shape-shifting organic optical waveguides: formation of organic nanorings, nanotubes, and nanosheets. *Angew. Chem., Int. Ed.*, **51** (15), 3556–3561.
- 39** Yan, Y., Zhang, C., Zheng, J.Y., Yao, J., and Zhao, Y.S. (2012) Optical modulation based on direct photon–plasmon coupling in organic/metal nanowire heterojunctions. *Adv. Mater.*, **24** (42), 5681–5686.
- 40** Palermo, V., Schwartz, E., Finlayson, C.E., Liscio, A., Otten, M.B.J., Trapani, S., Müllen, K., Beljonne, D., Friend, R.H., Nolte, R.J.M., Rowan, A.E., and Samori, P. (2010) Macromolecular scaffolding: the relationship between nanoscale architecture and function in multichromophoric arrays for organic electronics. *Adv. Mater.*, **22** (8), E81–E88.
- 41** Cui, Q.H., Jiang, L., Zhang, C., Zhao, Y.S., Hu, W., and Yao, J. (2012) Coaxial organic p–n heterojunction nanowire arrays: one-step synthesis and photoelectric properties. *Adv. Mater.*, **24** (17), 2332–2336.
- 42** Bu, L., Pentzer, E., Bokel, F.A., Emrick, T., and Hayward, R.C. (2012) Growth of polythiophene/perylene tetracarboxydiimide donor/acceptor shish-kebab nanostructures by coupled crystal modification. *ACS Nano*, **6** (12), 10924–10929.
- 43** Zheng, J.Y., Yan, Y., Wang, X., Zhao, Y.S., Huang, J., and Yao, J. (2012) Wire-on-wire growth of fluorescent organic heterojunctions. *J. Am. Chem. Soc.*, **134** (6), 2880–2883.
- 44** Zhang, Y., Dong, H., Tang, Q., Ferdous, S., Liu, F., Mannsfeld, S.C.B., Hu, W., and Briseno, A.L. (2010) Organic single-crystalline p–n junction nanoribbons. *J. Am. Chem. Soc.*, **132** (33), 11580–11584.
- 45** Zhang, C., Zheng, J.Y., Zhao, Y.S., and Yao, J. (2011) Self-modulated white light outcoupling in doped organic nanowire waveguides via the fluctuations of singlet and triplet excitons during propagation. *Adv. Mater.*, **23** (11), 1380–1384.
- 46** Zhang, J., Zou, Q., and Tian, H. (2013) Photochromic materials: more than meets the eye. *Adv. Mater.*, **25** (3), 378–399.
- 47** Liao, Q., Fu, H., Wang, C., and Yao, J. (2011) Cooperative assembly of binary molecular components into tubular structures for multiple photonic applications. *Angew. Chem., Int. Ed.*, **50** (21), 4942–4946.
- 48** Zhang, C., Yan, Y., Jing, Y.-Y., Shi, Q., Zhao, Y.S., and Yao, J. (2012) One-dimensional organic photonic heterostructures: rational construction and spatial engineering of excitonic emission. *Adv. Mater.*, **24** (13), 1703–1708.
- 49** Zhang, C., Yan, Y., Yao, J., and Zhao, Y.S. (2013) Manipulation of light flows in organic color-graded microstructures towards integrated photonic heterojunction devices. *Adv. Mater.*, **25** (20), 2854–2859.
- 50** Zheng, J.Y., Yan, Y., Wang, X., Shi, W., Ma, H., Zhao, Y.S., and Yao, J. (2012) Hydrogen peroxide vapor sensing with organic core/sheath nanowire optical waveguides. *Adv. Mater.*, **24** (35), OP194–OP199.

6

Functional Lipid Assemblies by Dip-Pen Nanolithography and Polymer Pen Lithography

Michael Hirtz, Sylwia Sekula-Neuner, Ainhoa Urtizberea, and Harald Fuchs

6.1

Introduction

Phospholipids are the main constituents of cell membranes and therefore are of vast importance in biological systems. Because of their natural tendency to organize in membrane structures, phospholipids found diverse applications in nanotechnology [1], for example, as liposomal cargo carriers delivering drugs in medical applications [2] or genetic material for transfection in cell experiments [3] and as interface in cell biology studies [4]. As the lipid membrane is a key component in biological signaling and sensing (as it separates the cell interior from the outside environment), it has also great prospects in the field of bio-inspired sensing especially in conjunction with other micro- and nanostructures [5].

Here, we will focus on surface-bound lipid assemblies generated by two techniques, dip-pen nanolithography (DPN) and polymer pen lithography (PPL). In recent years, these two methods (and related stamping techniques based on DPN setups) have emerged into sophisticated platforms for the generation of functional lipid assemblies and supported lipid membranes.

6.2

Techniques and Methods

6.2.1

Dip-Pen Nanolithography

After the introduction of atomic force microscopes (AFMs), these instruments were gradually adopted not only for imaging but also for lithography. While scratching of surfaces and thin films was already exploited for lithography in the early 1990s, it took several more years until the transfer of organic molecules from an AFM tip and assembly into a film on the substrate was observed [6]. Mirkin and coworkers exploited this phenomenon for a novel additive AFM-based lithographic method and coined the term dip-pen nanolithography in

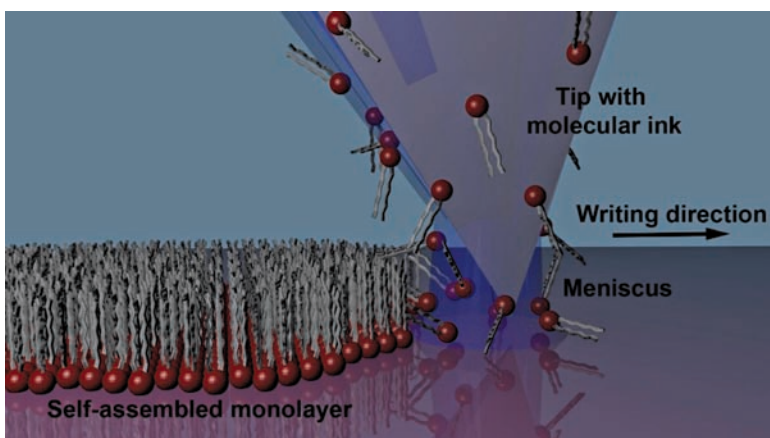


Figure 6.1 Scheme of DPN. A tip coated with molecular ink is brought into contact with a substrate. Over the bridging water meniscus, molecules transfer to the surface and assemble into a monolayer.

1999 [7]. They demonstrated a line resolution of 30 nm with ODT as “ink” for writing on a gold substrate and arbitrary control over the patterning process resulting in diverse line and dot patterns. The basic principle behind DPN is the coating of an AFM tip with the desired ink or molecules, and then bringing the coated tip into contact with a surface and allowing the ink/molecules to transfer from the tip onto the substrate surface in a controlled fashion (Figure 6.1).

Typical control parameters for the ink transfer are relative humidity, dwell time of the tip on the substrate surface, and writing speed (see Section 6.3). The achievable resolution depends on the interplay between ink and substrate in terms of wetting properties and stability, but typically submicron resolution is readily achieved. By introducing parallel arrays of tips instead of using a single tip, the lithography process can be substantially accelerated and larger areas can be patterned in practical timescales. In addition, multiplexing (i.e., the incorporation of different inks within one micro- or nanopattern) with high precision and registry is enabled by the use of cantilever arrays [8,9]. Due to its generally mild processing parameters, DPN has also induced much interest in the field of biomolecular patterning as an alternative and complementary technique to traditional or soft lithographic methods [10]. One of the extensions of this technique specializing in the writing of biomimetic lipid membranes is lipid DPN (L-DPN) [11].

The patterning process in a classical DPN experiment can be divided into three elementary processes: the first step is the dissolution of ink from the tip apex. Then, secondly, a transport from the tip to the substrate over a meniscus (either ink or water) is taking place. The third step is ink adsorption onto the surface and feature formation. Both the transport and adsorption of ink molecules generally depend on several physical parameters, including temperature, relative humidity (RH), physicochemical properties of the ink and surface,

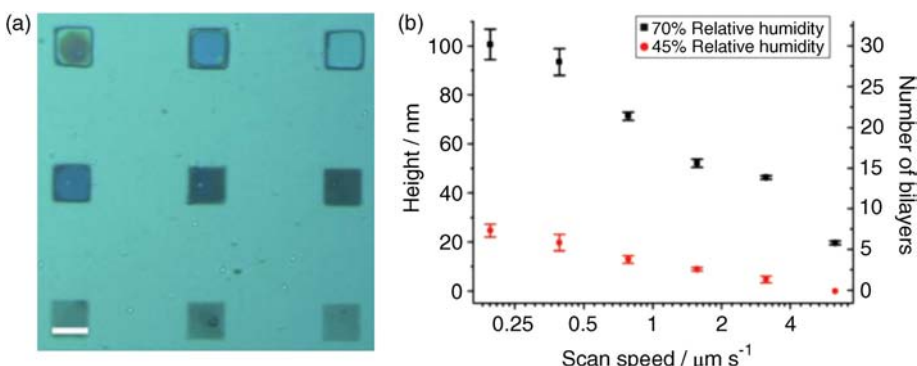


Figure 6.2 Control of multilayer stacking. (a) Reflection-mode optical micrograph of phospholipid squares patterned on plasma-oxidized silicon at various speeds (scale bar = 5 μm). (b) The height of phospholipid multilayers (and the corresponding number of bilayer stacks) measured by AFM is plotted

as a function of scan speed (on a logarithmic scale) at two different relative humidities. Error bars represent the standard deviation between the heights of eight different cross sections of a single square. Reproduced with permission from Ref. [11].

writing speed, and tip–substrate contact force. Rather than spreading laterally over the surface to form a monolayer like covalent DPN inks, the phospholipid ink in L-DPN can also stack as multilayers in air (with lateral resolution down to 100 nm). The heights of the phospholipid features measured by AFM exhibit a strong correlation with the tip velocity and the relative humidity (Figure 6.2).

After performing the L-DPN procedure, ordered stacks of membranes are formed on the substrate [12]. The main carrier ink in L-DPN is 1,2-dioleoyl-*sn*-glycero-3-phosphocholine (DOPC), which is conveniently neutral in regard to biological signaling and interaction with proteins and living cells. Depending on the substrate surface energy in solution, phospholipid patterns either remain stable as multilayers under water (partial wetting) or spread to form supported lipid bilayers (or monolayers on hydrophobic surfaces) of homogeneous thickness (complete wetting) [13–15]. Specific functionalities can be introduced into the lipid patches by admixing modified lipids or other lipid-affine molecules into the ink prior to writing. The technique was applied in a variety of applications ranging from biological presentation of allergens to different kinds of sensor functionalization (see Section 6.4).

6.2.2

Polymer Pen Lithography

Polymer pen lithography emerged as a combination of DPN and microcontact printing (μCP). In this technique, the stamp usually utilized in μCP is replaced with an elastomeric array of tips that is put into a DPN system for precise control of movement and position during the printing process (Figure 6.3) [16,17].

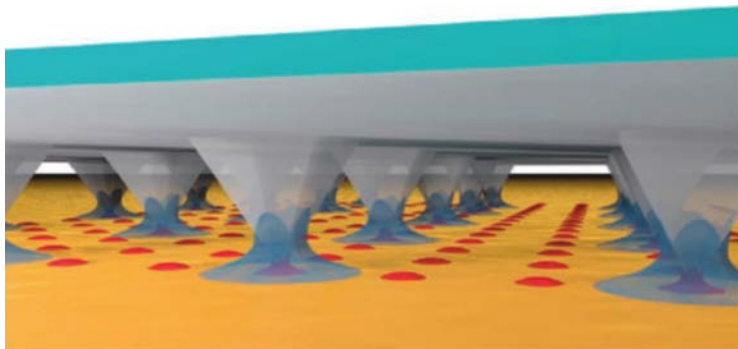


Figure 6.3 Scheme of the PPL process. A 2D array of elastomeric pens is brought into contact with a substrate in a well-controlled manner in regard to position and applied pressure. Ink coated on the PPL stamp can

transfer over a water meniscus onto the substrate to form the desired features. Reprinted by permission from Macmillan Publishers Ltd: Nature Protocols Ref. [18], copyright 2013.

Depending on the ink/substrate combination, high resolutions below 100 nm can be reached, while patterning over square centimeter areas in parallel. Due to the elastomeric tips, feature size can be additionally controlled by the applied pressure, because the tips deform elastically upon contact yielding a bigger contact area when more pressure is applied. Different approaches allow for multiplexing in PPL, either by selectively covering neighboring polymer tips with different inks by a combination of inkjet printing and inking in matching molds [19], by microfluidic networks similar to inkwells [20], or by employing an alternative writing strategy with whole segments of the stamp inked in the respective ink [21]. Especially the latter ones, demonstrating multiplexed patterning capabilities in subcellular resolution, allow to present more than one chemical cue to a single cell in a controlled fashion over large sample areas, as often desirable in cell culture experiments.

6.3 Ink Transfer Models

Although a wide variety of inks can be patterned with DPN, most of the analytical models and simulations have been developed for DPN of molecular alkanethiol inks on gold. More recent additions to the DPN ink arsenal are liquid and polymer-based inks, which encompass a different transport mechanism, and empirical models have also been proposed for them. Lipid inks resemble some characteristics present in liquid inks but also keep some attributes of molecular diffusive ones. Following the classification presented in Ref. [22], lipid inks settle between diffusive inks and liquid inks in terms of writing behavior. Their transport can be subsequently described by models based on both types of inks, but each one has to be modified to include the particularities of the lipid inks. Much

less theoretical work was done on describing the ink flow in the PPL process. As in DPN, ink and substrate properties decide the transport mode. However, one striking difference from DPN is that feature size is now strongly dependent on the applied force, because the PPL pens can be elastically deformed upon contact with the substrate, yielding differently sized contact areas.

In both patterning techniques, depending on the physicochemical properties of the ink, molecular diffusion or bulk fluid flow is expected to dominate the transport. Accordingly, the process is better described by the molecular or fluid ink models, respectively.

6.3.1

DPN of Liquid Inks

In DPN of liquid inks, transfer occurs by the growth of an ink droplet over a meniscus that becomes snapped off upon tip retraction leaving behind a droplet of ink on the substrate. Transport is governed by the fluid dynamics of the capillary rupture process and the meniscus volume, and depends strongly on the contact angle, viscosity, retraction speed, dwell time, and volume of ink at the pen [23–25]. The process can be seen as a competition between surface energy and ink viscosity connected by a variable shaped meniscus.

Polymer inks are also classified as liquid inks due to the fact that their transport proceeds by a bulk liquid flow, which could be also termed capillary mass transport. In this case, meniscus transport and surface diffusion are strongly dependent on the ink viscosity. The polymer chains perturb a molecular entanglement absent in liquid inks yielding higher viscosity. The viscosity dependence promotes that already patterned features even influence the meniscus flow [26]. Contrary to liquid inks whose fluidity provides a volume dependence that increases exponentially with time [23], patterned features of polymer inks show a volume dependence with dwell time that “saturates” at long dwell times [26], probably due to the increased viscosity.

Both systems can be described within the growth mechanism of a bulk flow, and some empirical models have been proposed [25,26]. However, a complete analytical model has not been fully developed yet. In the following, we propose a model based on the spreading kinetics of a liquid droplet that includes the particular properties of lipid spreading. Due to these basic principles, this model may also be used to describe the transport of liquid inks.

6.3.2

DPN of Diffusive Inks

In DPN of diffusive molecular inks, the transport generally follows three stages [27,28]. (i) The ink is chemically dissolved from a solid state into the water meniscus at the meniscus/tip interface. The rate of forward reaction (ink dissolves into meniscus) depends on the amount of ink on the tip and the kinetics of the chemical dissolution; the rate of backward reaction (ink adsorbs to tip) depends on the ink concentration at the meniscus/tip interface. The net ink flow

is the balance between both. (ii) The ink is transported to the substrate through the water meniscus or over the water meniscus/air interface. The role of the meniscus in the ink transport to surface has been a controversial subject. It was shown that the transport of water-compatible inks (e.g., MHA) depends on the relative humidity [29,30], contrary to observations with water-insoluble inks (e.g., ODT) [31]. However, some studies with MHA showed transport even at very low humidity conditions (although its transport was increased with higher humidities) [29] showing that molecular inks can also diffuse directly from the tip to the surface. Still it can be said that water-compatible inks follow a meniscus-based model in the regime with higher humidity, where a water meniscus enhances the transport, and under these conditions exhibit dominantly a meniscus-dependent rate. In the last stage, (iii) ink spreads over the surface as a radially 2D uniform flow of ink, from a nonzero concentration below the tip to a zero concentration at the edge boundary.

Since the slowest transport stage dominates the whole process, in some systems one or two of these steps can be neglected, thereby transport being controlled by dissolution at the tip [32], surface diffusion [33,34], or transport and subsequent diffusion [35]. Noticeable are also the results that show that molecular systems on the surface do not always rearrange in the sometimes claimed independent fashion [36], neither spread independently [37] up to the point of showing anisotropic patterns instead of the conventionally expected round features [38]. Saha and Culpepper developed a complete analytical model that includes the three steps in the transport of molecular inks [27,28].

6.3.3

DPN of Lipid Inks

Lipids at the tip surface will become hydrated at ambient temperature and raising humidities even before brought into contact with the surface. As the tip approaches the surface of the substrate, a meniscus of water condenses between the tip and the surface, creating a water vessel in which the hydrated lipid ink can immerse. Lipids in contact with the water meniscus become fully hydrated and start spreading toward the surface, through the meniscus. This depiction is supported by DPN under water [39] and membrane spreading experiments [14]. Below the tip, where the meniscus of water contacts substrate, fluidity and permeation are enhanced. The lipid membrane is formed while its front edge uniformly advances out of the tip over the substrate, as the tips continue to feed the membrane growth from the inside. This picture is supported by Mohamad *et al.* [40], which show how lipids can transfer from multilayer membranes through dislocation places while the base layer that covers the surface progresses outward in a 2D spreading mode, keeping a circular shape. When the flow from the tip reaches a dynamic equilibrium, the spreading follows a “steady like” kinetics. Finally, when the tip is removed from the surface, there is no longer any source driving force and the only mechanism left for the spreading of the deposited ink is kinetic spreading, which is energetically unfavorable. At that point,

growth and spreading of the ink patch stop. It should be noted that within this dynamic picture the transport entails a time dependence of the difference in concentration between the tip and the surface; it is expected to be transient, until the system although yet spreading reaches a constant flow equilibrium.

In our description, lipid inks share some attributes of liquid inks as well as of diffusive inks. Lipids have the fluidity of liquid systems. Water molecules enter into the membrane, preferentially at the lipid hydrophilic head groups, and in between membranes, providing a high fluidity to the membrane [41,42], and resulting in swelling bilayers above 40% membrane hydration [41,43]. Due to this high fluidity at higher hydration, it is not surprising that L-DPN can be described by a liquid-based model. As a first approximation, Eq. (6.1) describes the energy balance in the transport-spreading processes of a liquid ink. It follows the wetting dynamics of solids [44] but includes kinetic energy arising from the tip flow and kinetic spread dragging over the surface:

$$x(t)C_d \frac{1}{2}\rho v(t)^2 = \frac{J}{t} + S + \frac{1}{2}\gamma\theta^2. \quad (6.1)$$

The first term on the right-hand side arises from the kinetic energy of the tip flow, and the last two terms describe the droplet-shape capillary energy. The term on the left-hand side describes the kinetic drag losses (for fast spreading can be assumed to be proportional to $x(t)v(t)^2$), where v is the speed of the front edge, C_d is an adimensional spreading factor, ρ is the lipid viscosity, and x is the spread length. Equation (6.1) can be analytically solved to fit the dependence of the area spread for L-DPN, as shown in Figure 6.4.

When comparing the fits with a stationary flow (dotted lines) with the fits with a time-dependant flow (full lines), it becomes obvious that a flow dependence with time is mandatory for a good description. This dependence arises from the high concentration gradient between the tip and the substrate [45] and is a consequence of the “molecular behavior” of lipid inks: their surface bonding and assembly promotes differences in concentration at the meniscus–substrate contact area [27,28,35]. This is striking for line writing in which the large concentration gradient between the tip and the surface is increased as the tip is exposed to the clean surface when it travels, thereby creating a large driving force for ink deposition [30,46]. This dynamic flow rate is absent in conventional liquid-based models.

The drag term in Eq. (6.1) can be replaced by other expressions that better describe the spreading in the particular system, for example, a membrane spreading term used in Refs. [14] and [47], a fluid viscosity dissipation term used in Ref. [44], or even be neglected, if the other energies dominate the spreading process. Each of these terms will provide different time dependences of the area spread with time, for example, a dependence of $x^2 \propto \ln(t)$, $x^2 \propto \ln^2(t)$, and $x^2 \propto t$, respectively. It should be noted in Figure 6.4 that the area spread is not proportional to dwell time, requiring drag to be incorporated into the energy balance.

Liquid ink transport does not entail an assembly of its constituents onto the surface, but rather results in a drop of liquid on the substrate, with a flow–drag–capillary energy balance. The self-assembly and spreading is the key feature of

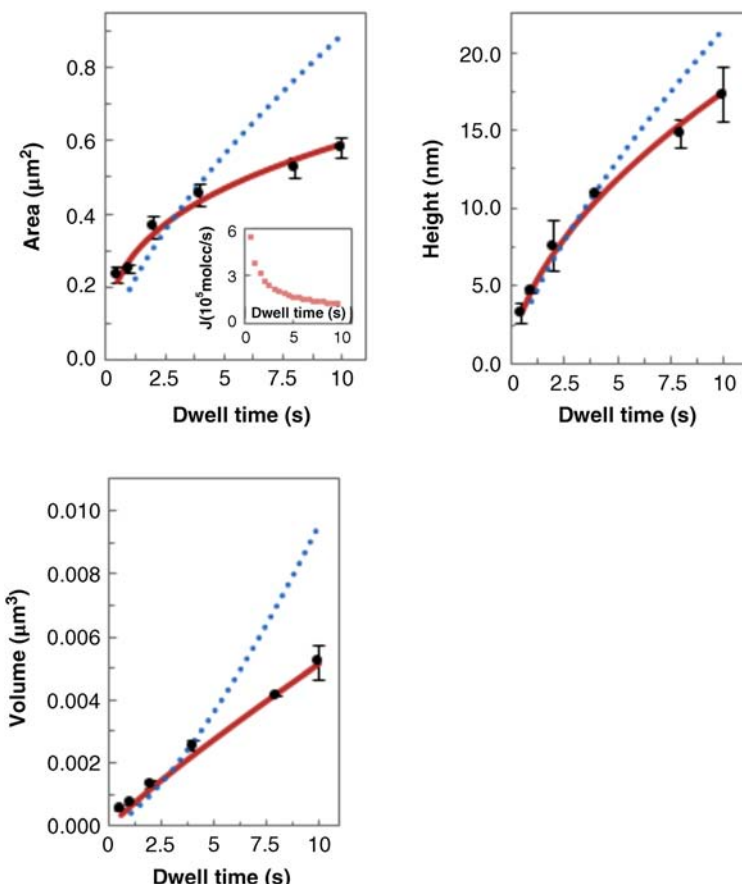


Figure 6.4 Area, height, and volume of DOPC dots patterned at $32.8 \pm 0.2\%$ RH on glass measured with an AFM. Error bars represent the average error of four samples. Dotted line

is the fit to Eq. (6.1); full line is the fit to Eq. (6.1) including the time dependence of the flow $J(t)$ determined from the experimental data, shown in the inset.

molecular systems. The nature of the bonding to the substrate can ultimately determine the geometry of the final structure. This feature is present in lipid ink systems [48], too, in which the differences in morphology depend on the interactions of lipids with the substrate. Usually, the bond between lipids and substrates is physisorption through van der Waals forces. Now, within the molecular modeling framework, the “drag” of liquid ink modeling is replaced by the “bonding” of the lipids to the substrate.

Since the lipids keep a noticeable fluidity [13,14], a noncorrelated circular spreading is expected, as shown in Ref. [40]. At long dwell times where flow rate relaxes into equilibrium kinetics (see flow dynamics in the inset of Figure 6.4), an area–time dependence t^α is expected but with an exponent smaller than that in membrane water/lipid/hydrated surface spreading experiments [14], leading to

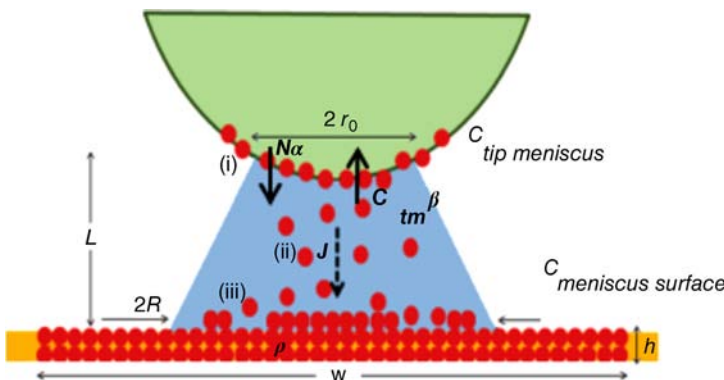


Figure 6.5 Scheme of the ink transport in DPN showing three stages: (i) ink dissolution into the meniscus at the tip/water meniscus interface of size $2r_0$, with a forward flow $N\alpha$, where α accounts for the solubility of the N lipids, and a backward flow $C_{tip \text{ meniscus}}\beta$, where $C_{tm} = C_{tip \text{ meniscus}}$ is the concentration at the tip/water meniscus interface and β represents the impingement and attachment rate; (ii) flow (J) transport via meniscus of size R and

height L to the water meniscus/surface with an ink diffusivity D_1 , as a 1D Fickian diffusion due to differences in concentration $C_{tip \text{ meniscus}}$ and the concentration at the water meniscus/surface interface, $C_{meniscus \text{ surface}}$; and (iii) spreading over the surface creates a 3D circular feature with density β , width w , and height h . Adapted with permission from Ref. [27]. Copyright 2010 American Chemical Society.

$\alpha < 1$, due to asymmetric air/lipid/hydrated surface spreading in L-DPN. This behavior resembles the spread of some molecular systems [35].

The lacking feature for the description of lipid inks in molecular modeling is that, as in liquid inks, L-DPN can also form 3D piled structures, not necessarily a self-assembled monolayer. The height of the feature, controlled by the minimization of the interfacial ink/substrate/air energies, is $h = w \tan(\theta/2)$, θ being the droplet contact angle, as usually found in droplet-shaped features. In order to account for this feature, the model developed for molecular systems [27,28] has been modified.

A representative picture in this model for L-DPN transport is shown in Figure 6.5. With the definitions of Figure 6.5, we can describe the L-DPN process as follows. Ink dissolution at the tip/water meniscus interface generates a flow $J = N\alpha - C_{tip \text{ meniscus}}\beta$, where $\alpha = \gamma e^{-E_a/k_B T}$ and $\beta = \pi r_0^2 \sqrt{k_B T / 2\pi P_M} e^{-E_A/k_B T}$. Diffusion through the meniscus is assumed to follow Fickian transport $J = (D_1 \pi R r_0 / L)(C_{tip \text{ meniscus}} - C_{meniscus \text{ surface}})$, where $D_1 = k_B T / 6\pi\mu d$. Finally, lipids 2D spread over surface keeping a circular shape (moving boundary), with a flow $J = C_{meniscus \text{ surface}}[2\pi Z_t D_S / \ln(w/2R)]$, where Z_t is the monolayer thickness and D_S is the surface diffusion coefficient. Mass conservation leads to $J = \rho(w^2 h / t)$. Rearrangement of these expressions leads to Eq. (6.2) that can be used to fit the dependence of the area spread for L-DPN, as shown in Figure 6.6.

$$N\alpha = \rho w^2 \frac{h}{t} \frac{\beta}{2\pi Z_t D_S} \ln\left(\frac{w}{2R}\right) + \rho w^2 \frac{h}{t} \left(1 + \frac{\beta}{D_1 \pi R r_0 / L}\right). \quad (6.2)$$

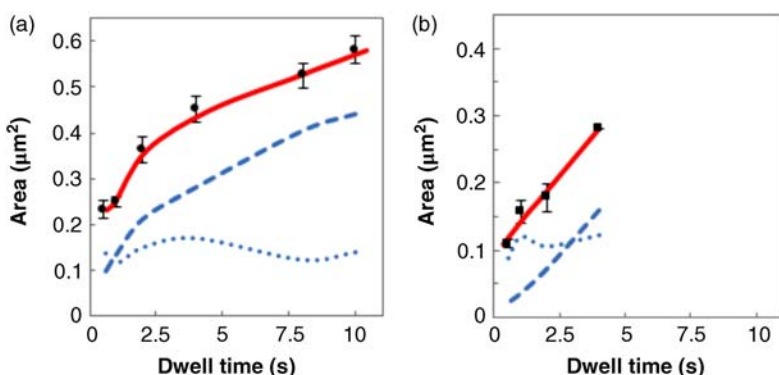


Figure 6.6 Area, height, and volume of DOPC dots patterned on glass at $32.8 \pm 0.2\%$ RH (a) and $29.2 \pm 0.2\%$ RH (b) measured by AFM. Error bars represent the average error of four

samples. Full line is the fit to Eq. (6.2). The dashed line represents the term of Eq. (6.2) representing the meniscus contribution and the dotted line that of surface spreading.

In analogy with molecular diffusion models [27,28], the first term on the right-hand side of Eq. (6.2) represent the spreading on the surface while the second term represents the meniscus transport. Note that, unlike in molecular systems, in L-DPN both transport mechanisms are present, as shown in Figure 6.6. This feature is due to the diffusive ink-like and liquid ink-like behaviors, which are simultaneously present in L-DPN. At low humidities (Figure 6.6), although the lipid ink is not depleted (when writing the pattern, larger dwell times were written first before the shorter ones), the water meniscus becomes less stable and the concentration gradient decreases, thus lowering J to extinction.

These results show that L-DPN can be described by liquid ink models as well as by molecular diffusion models. In liquid models, it is necessary to find a suitable term for the drag in the particular system analyzed, following either membrane spreading [14,47] or droplet spreading [49]. Molecular diffusion models should be modified to include the 3D growth. The flow must incorporate dynamics, either by a $J(t)$ in the liquid models or by incorporating specifically the meniscus transport influence as in the molecular models. Noticeable is that the dynamics shown by liquid ink models and molecular diffusion models are not that far apart from each other. The fundamentals of both are actually not that different: dynamics is governed by the energy balance between the meniscus kinetics and the surface energy.

6.3.4

Ink Transfer in PPL

PPL is capable of patterning almost the complete arsenal of DPN inks, excluding thermal DPN [50], which is one of the missing features in PPL yet. Liquid inks (inks with solvent carriers, hydrogels, fluid polymers, etc.) as well as non-liquid

inks (diffusive inks) can be employed. A remarkable advantage of PPL is that now a new series of inks can be printed: dry inks. This category includes high gel–liquid phase transition temperature inks and nonsoluble inks. In this transfer mode, inks neither need to be liquid nor need to be soluble in any carrier as they benefit from the “stamping” transport absent in DPN.

As PPL combines DPN and μ CP, ink–substrate physicochemical properties do not entirely define the ink transfer process. Now the lithography technique itself conditions the nature of the ink transport. When the writing mode approaches more DPN or μ CP, respectively, the ink transfer process follows closer the characteristics of one or the other [21]. Under some experimental conditions, these modes may also act in combination.

In the case of liquid inks (i.e., inks that still remain in a fluid state on the PPL stamp), ink will flow from the polymer pens and spread on the sample, depending on its wetting properties. Since the apex stamps onto the substrate, a capillary rupture process as in DPN liquid inks is expected [24]: the meniscus will snap off upon tip retraction, creating a droplet that remains on the substrate. Typical inks showing this behavior are formulations mixed with glycerol or low chain length PEG to prevent ink drying, leading to ink microdroplets on the sample surface that can act as highly localized reaction chambers and washed away later [51]. Similarly to DPN, this transport encompasses a “bulk fluid” transfer. Here, feature size depends on dwell time, since it defines how much material is allowed to transfer. It should be noted that since in this transport mode transferred volume is meniscus volume dependent [23] higher pressures of the stamps involve wider meniscus; therefore, feature sizes will increase with z-piezo extension [19]. The plastic deformation of the elastomeric tips will condition the meniscus volume and thereby the transferred volume [23,25]. Liquid ink models would describe the ink transport in these systems, incorporating the meniscus size dependence with the applied pressure (i.e., with the apex deformation).

In non-liquid inks, a further division between nonaqueous (i.e. non-water-soluble and non-hydratable) and aqueous inks is advisable. The former greatly benefit in PPL by the “stamp” transport mode. Non-liquid inks coat the PPL stamp leaving a dry surface. Small molecules (e.g., ODT) will diffuse from the tip to the substrate upon stamp contact, resembling the ink transfer suggested for nonaqueous diffusive inks in DPN [31]. If a water meniscus is formed, ink transfer may additionally proceed over the air/water meniscus interface [52]. Diffusive transport will strongly depend on the applied force as elastic deformation of the pen apex modifies the ink source size and shape (i.e., the available ink source area) [53]. Apex deformation additionally modifies the size and shape of the water meniscus, and thereby the air/water meniscus transport. Therefore, the transport of these systems may be analyzed in terms of an air/water meniscus transfer model [52] incorporating the mass transport by direct apex surface contact. The meniscus transport is expected to be negligible compared with the direct stamping in inks that are too big for extensive diffusion (e.g., proteins, nanoparticles, and molecules embedded in PEG of larger chain length). Two experimental parameters then regulate the ink transfer in nonaqueous inks:

dwell time, defining how much of the material on the stamp transfers to the surface [53], and pressure, defining how much ink source area is available and in contact with the surface [45,54]. Relative humidity is expected to play a minor role, as is the case in insoluble inks [30,33].

Non-liquid, water-compatible inks (aqueous inks) comprise the most complex ink transport mechanism. Here, ink molecules diffuse not only from the tip to the surface over the stamp but also through the water meniscus built up upon contact with the surface. Pressure and elastic properties of the pen apex [55] influence the diffusive transport, as discussed above, but they also greatly influence the meniscus shape, and thereby the transport through the water meniscus. The meniscus transfer mode can be selected to dominate the process, by patterning at low stamping pressure [21]. In this case, as a first approximation, ink transfer can be described with DPN-like models, but with a tip whose shape and size can be tuned with the z-piezo extension. Lipids are included in this category of inks. Their meniscus transport is influenced by the same parameters that control DPN ink transfer, as discussed in the previous sections. However, it should be noted that with an elastomeric tip the meniscus size can be readily modified. It would be interesting to investigate the role of the water meniscus in the transport of lipids covering a wide relative humidity range, since diffusivity strongly depends on the water content in these systems [43].

A great deal of effort has gone into understanding DPN transport. As such, there is a clearer picture of the important parameters. In contrast, there is a lack of theoretical studies as well as simulations concerning PPL. This different angle of view could actually represent an opportunity for furthering the understanding of ink transport mechanisms also in DPN, particularly for those inks whose transport is not fully understood (e.g., ODT).

6.4

Applications

6.4.1

Applications in Sensing

Lipids are an interesting material for sensing applications, especially when biological analytes such as proteins or cocktails of proteins (e.g., in serum) are targeted. The inherent biocompatibility and neutrality of DOPC layers, combined with generally very low unspecific protein adhesion, are ideal for highly targeted sensing purposes. The specific sensing functionality can be introduced by admixing modified lipids or other compounds miscible with DOPC prior to ink transfer on the surface. The general capability for parallelization and multiplexing inherent in DPN and PPL allows for the diverse functionalization of arrays of sensing devices for parallel or multivariate detection.

A very elegant way of exploiting lipid assemblies for sensing was demonstrated by Lenhert *et al.* when using lipid multilayer gratings for detecting proteins in

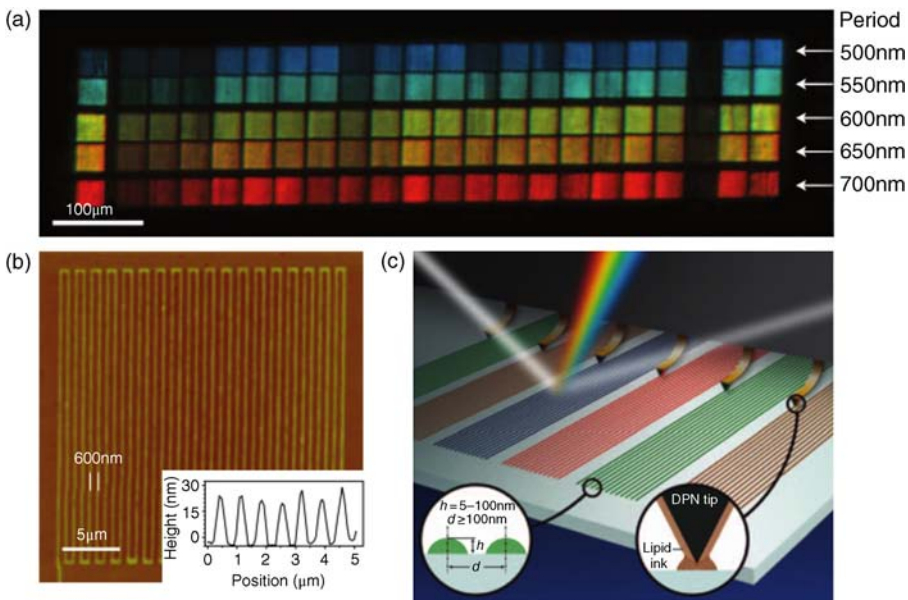


Figure 6.7 (a) Optical image of the light diffracted by lipid gratings of different periodicities. (b) AFM image of a grating with 600 nm pitch. (c) Scheme of the lipid grating

fabrication process and light diffraction.
Adapted by permission from Macmillan Publishers Ltd: Nature Nanotechnology Ref. [56], copyright 2010.

complex mixtures [56]. In this approach, L-DPN was employed to write optical gratings with a pitch in the range of visible light and controllable height between 5 and 100 nm (Figure 6.7). The resulting gratings can diffract light depending on their height and general structure, which is exploited as readout signal for sensing. By admixing a head group-modified functional lipid specifically binding a protein (here biotin-PE targeting streptavidin as model protein), the gratings were able to fish out the protein from a complex protein cocktail (fetal calf serum). The binding of the protein to the grating structures changes the wetting properties of the lipids and thus induces changes in the grating geometry by dewetting or direct changes to the geometry of the grating by intercalation, both of which influence the diffraction capability of the sensor. Thus, in the presence of the target protein the diffraction signal from the gratings diminishes, allowing for a sensitive and concentration-dependent detection. Recently, it was demonstrated that these kinds of lipid gratings can also be fabricated by stamping techniques, allowing for faster production after pitch and general layout are fixed [57].

Instead of generating the whole sensing device by L-DPN as in the case of the lipid gratings, one can also use L-DPN to functionalize already existing devices fabricated by other techniques. This offers the possibility of combining well-established sensing approaches by electrical, mechanical, or optical devices fabricated with conventional micro- and nanolithographic methods with the special

capability of L-DPN to deliver the functional lipids in a highly localized and multiplexed manner to the active sites on the devices. One example of this approach is the coating of a surface acoustic wave (SAW) sensor with functional lipid mixtures [58]. SAW sensors are based on the generation of acoustic surface waves from electric signals in interdigitated transducer (IDT) electrodes that then travel along the sensor surface before being reconverted into electric signals by another set of IDT electrodes as output. Processes at the sensor surface (e.g., adsorption of materials or a change in viscosity of the sensing medium) are reflected in changes of phase and amplitude of the acoustic wave [59]. In the work of Mitsakakis *et al.*, different parts of a SAW sensor device were functionalized with lipid mixtures containing functionalized lipids bearing dinitrophenol (DNP), Ni ions in a chelating complex, or biotin in their head groups. The functionalized areas were covered by separate microchannels of a microfluidic device allowing for controlled incubation with various analyte solutions. In this setup, the authors could clearly observe the phase change when solutions containing the corresponding binding targets were added, indicating the binding of anti-DNP antibodies, His-GFP, and streptavidin. When a mixture of all these proteins is flowed over a sensor functionalized with pure DOPC as a negative control, no phase change is registered, indicating that the DOPC layer alone can act as a good blocking layer against unspecific protein adhesion on such sensors.

Another example for the application of L-DPN to prestructured substrates is the functionalization of photonic whispering gallery mode (WGM) resonators in order to produce microlaser sensing devices [60]. WGM-based sensors have been shown to be extremely sensitive based on the small perturbation in the resonance of such devices that is created by a change in resonator geometry or in optical properties induced by binding of the target analyte. In the case of Bog *et al.*, the WGM device was generated based on goblet structures (Figure 6.8). Especially the rim of the goblet structure should be functionalized for effective sensing, since here the binding of target molecules has the greatest impact on the lasing mode resonance. In a first example, this was realized by delivering a lipid mixture exclusively to the rim of the resonator structure by L-DPN. The resulting sensor device exhibits a concentration-dependent shift in lasing mode resonance frequency when incubated with the matching protein, easily detecting nanomolar concentrations (Figure 6.8). One especially interesting feature of this approach is that the lipid mixture used for functionalization provides three functions in one: (i) it provides the optically active material to allow lasing, (ii) provides the specific binding sites for the target protein, and (iii) prevents unspecific adsorption of proteins to the rim of the goblet structure. An alternative route to achieve the rim-specific functionalization is the use of a PPL generated stamping pad [61]. A multiplexed stamp pad array is aligned and brought into contact with a WGM array to transfer the lipid mixture and functionalize the goblet structures (Figure 6.9). In this way, it is possible to functionalize a multitude of devices in parallel and with different ink mixtures, allowing for multiplexed detection and control devices on one substrate in near vicinity. It was also demonstrated that sandwich structures are feasible for detection. This allows for the detection of

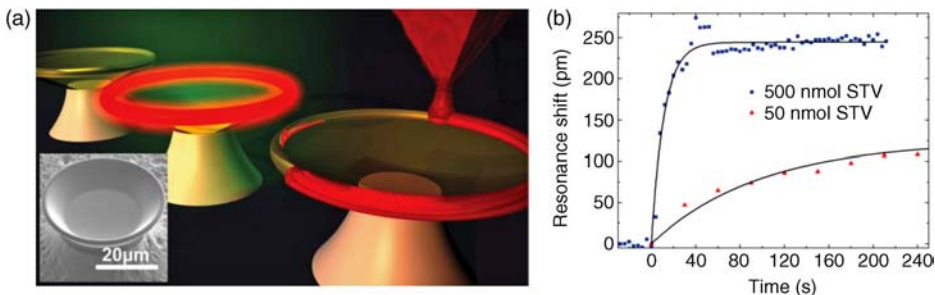


Figure 6.8 (a) Scheme of L-DPN on goblet WGM structures. The inset shows a SEM micrograph of a goblet structure. (b) Resulting resonance shift in lasing signal by incubation of

the functionalized goblet structure with the matching target protein in nanomolar concentration. Adapted from Ref. [60] with permission from The Royal Society of Chemistry.

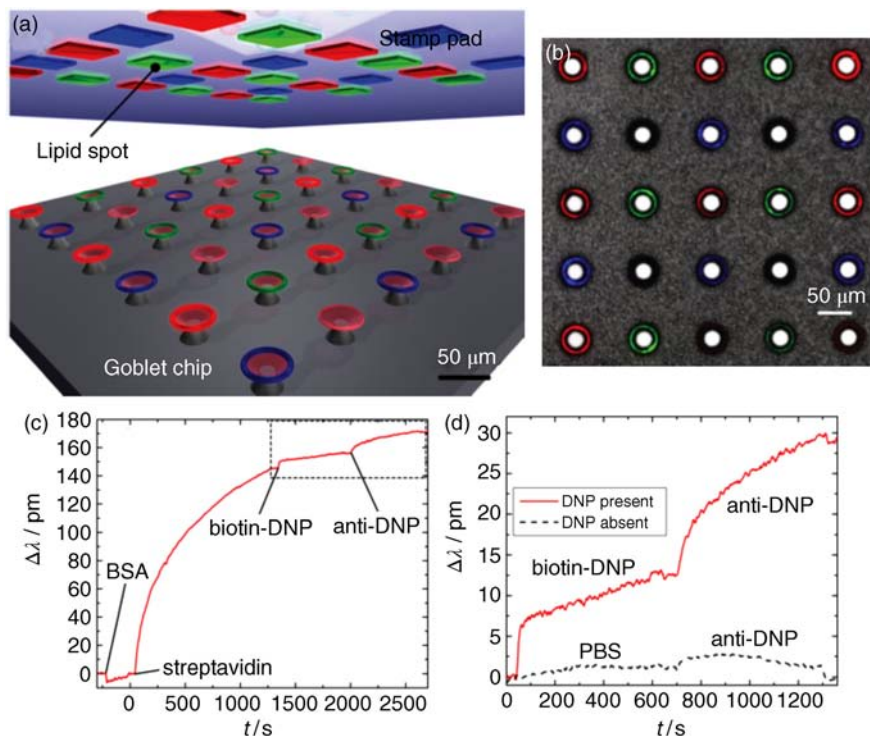


Figure 6.9 (a) Scheme of multiplexed stamp pad-based functionalization of WGM arrays. (b) Micrograph of a multiplexed functionalized WGM array. (c) Shift in lasing resonance frequency during binding of different proteins to the functionalized goblet structure: after a blocking step with BSA, streptavidin binds to

the functionalized WGM structure as binding segment for the biotin-DNP and later anti-DNP antibody. (d) Magnification of the curve segment with the protein–antibody binding and a negative control without binding of the antigen DNP as comparison. Adapted with permission from Ref. [61].

antibodies against any protein available as biotinylated species or, conversely, in case of biotinylated antibodies the detection of target proteins (Figure 6.9).

Another interesting substrate for future application of L-DPN in sensing devices is graphene [62]. Although graphene already exhibits several intrinsic sensitivities exploitable for sensing in devices, a specific functionalization will highly advance the usefulness of graphene especially in the context of complex targets, for example, proteins. L-DPN on graphene was successfully demonstrated by Hirtz *et al.* [48]. The lipid membrane stacks spread even more easily on graphene compared with silicon oxide under same writing conditions, but the stability still allows for immersion of the structures in liquid. Electronic coupling of the lipid membrane to the graphene is evident by quenching of lipid-coupled fluorophores. Specific binding sites can be introduced into the lipid membranes and analyte binding could be observed by fluorescence and AFM (Figure 6.10). Altogether, these results are very encouraging for the development of lipid-functionalized graphene-based sensors in the near future.

6.4.2

Biological Applications

Biomimetic membranes composed of lipids only, lipid–protein mixtures, or lipid–small molecule mixtures can be the basic platforms in many nanobiological applications, for example, functionalization of various surfaces, development

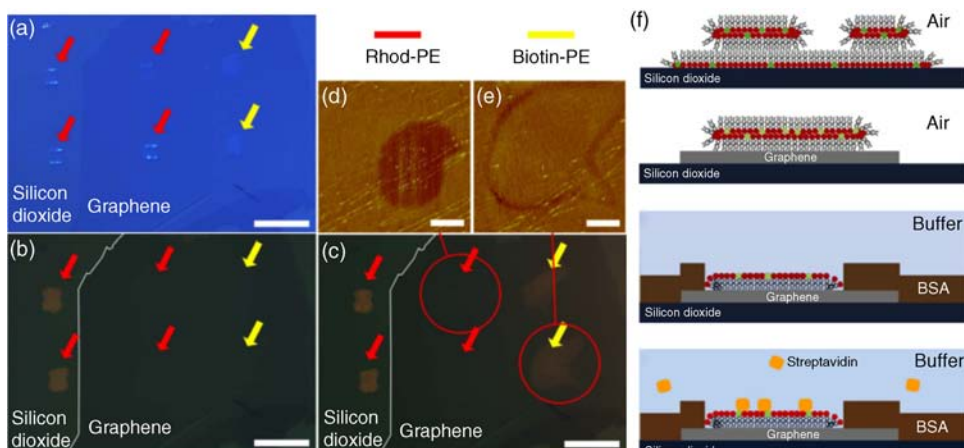


Figure 6.10 Optical micrographs of lipid patches on silicon dioxide and graphene substrates in (a) air and (b) water. The red marked patches are doped with a fluorophore that is quenched on the graphene substrate. The yellow marked patches are doped with biotinylated lipids allowing for binding of streptavidin. (c) Cy3-marked streptavidin is far

enough away from the graphene to be not completely quenched after binding. In AFM, no binding can be observed on the nonbiotinylated lipid patches (d), while the biotinylated patches get filled with streptavidin (e). (f) Scheme of the membrane organization during the experiments. Adapted with permission from Ref. [48].

of nanobiosensors, reconstruction of membrane proteins, and fabrication of nanocontainers for drug delivery. This section will present several examples of biomimetic phospholipid structures generated via L-DPN and PPL and their application in the context of biological experiments.

Generally, DPN has been used both for the direct, nanoscale deposition of functional proteins [63–65] and for the fabrication of biochemical templates for selective adsorption [66–72]. The latter approach has proven suitable for further applications, for instance, patterning antibodies for highly sensitive and specific diagnostics [66] and immobilization of entire virus particles via metal affinity interactions for cell infectivity studies [67].

In regard to biological applications, L-DPN is of special interest, since the main carrier lipid DOPC forms biomimetic lipid membranes that are biocompatible and can be tuned in many ways for specific desired functions. In order to reproducibly integrate multiple components on subcellular scales by L-DPN, it is preferable to simultaneously deposit inks from different tips in a parallel tip array. For this purpose, microfluidic inkwells capable of simultaneously delivering different lipid mixtures to different tips in a tip array are a unique tool (Figure 6.11a) [73].

Arguably, the most unique capability of multiplexed DPN is the ability to integrate different ink materials into complex, combinatorial structural and compositional libraries at high (e.g., subcellular) lateral resolution [75]. This is illustrated for phospholipids in Figure 6.11b, where a single cantilever array is used to simultaneously pattern arrays of bull's-eye type features of DOPC doped with 1 mol% of rhodamine-labeled and fluorescein-labeled lipids. When the distinct pattern compartments are connected as in the two triangle patterns in the top row, it can be seen that the patterns are contiguous and retain their lateral fluidity. Since the red/green ratios in the fluorescence of the nanostructures correspond to the amount of ink in each reservoir, this method of mixing lipids on the canvas opens the possibility of creating an arbitrary number of mixture combinations on the surface from a limited number of inks on the tips.

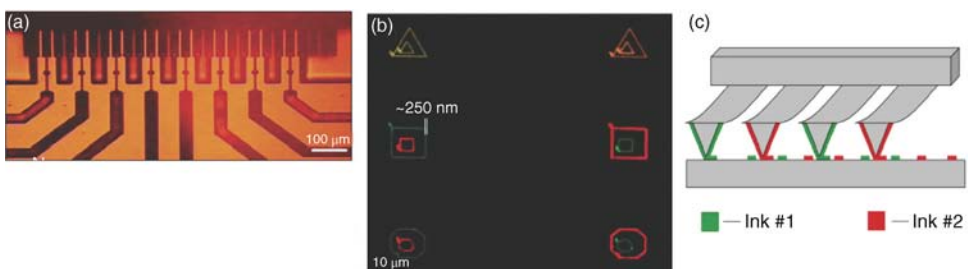


Figure 6.11 Multiplexed lipid patterning. (a) Optical micrograph of a cantilever array (top) approaching microfluidic channels for delivery of up to eight different inks on the same array. (b) Multichannel fluorescence images of multilayer structures composed of DOPC doped with two different fluorophore-labeled lipids (rhodamine (red) and fluorescein (green)) integrated with bull's eyes of different shapes and topologies on subcellular scales. (c) Schematic illustration of a method used to pattern different lipids on subcellular scales using a single multiplexing DPN cantilever array. Adapted with permission from Ref. [74].

Multiplexing can also be achieved using PPL. A piezo-based *xyz*-stage motion (digital closed loop) with a resolution of less than 100 nm and a travel range of 40 mm × 40 mm allows for the production of patterns with much higher speed than the DPN process. Multiplex PPL was shown to be an excellent tool for the integration of various bioinks with high resolution and in combinatorial patterns: phospholipids, fluorescent dyes, and proteins [21]. This demonstrated the potential of the PPL technique for highly flexible microarray fabrication.

Another way to integrate multiple different inks onto a single surface is the use of stamping techniques (“nanointaglio” in reference to the intaglio printing technique), as recently shown by Lowry *et al.* [76]. Robotic pin spotting is used to deposit lipids, dissolved in ethanol or as liposomal emulsions in water, onto an ink palette, used to ink a microstructured intaglio stamp. Coated stamp prints ink from the recesses onto the substrate. Printing of different lipids onto one substrate demonstrates the potential of scalability and material integration onto the same surface without significant cross-contamination.

Combinatorial biomimetic lipid membranes used for protein reconstruction can serve not only as a platform for protein studies but also as cell adhesion and activation modules. Selective adsorption of functionalized or recombinant proteins based on streptavidin or histidine-tag coupling onto NTA-Ni- or biotin head group-containing patterns enables the semisynthetic fabrication of arrays of peripheral membrane-bound proteins (Figures 6.12 and 6.13).

The streptavidin/biotin system is widely used because it has one of the largest free energies of association yet observed for noncovalent binding of a protein and small ligands in aqueous solution [77,78]. The complexes are also extremely stable over a wide range of temperature and pH. His-tag chelator coupling relies

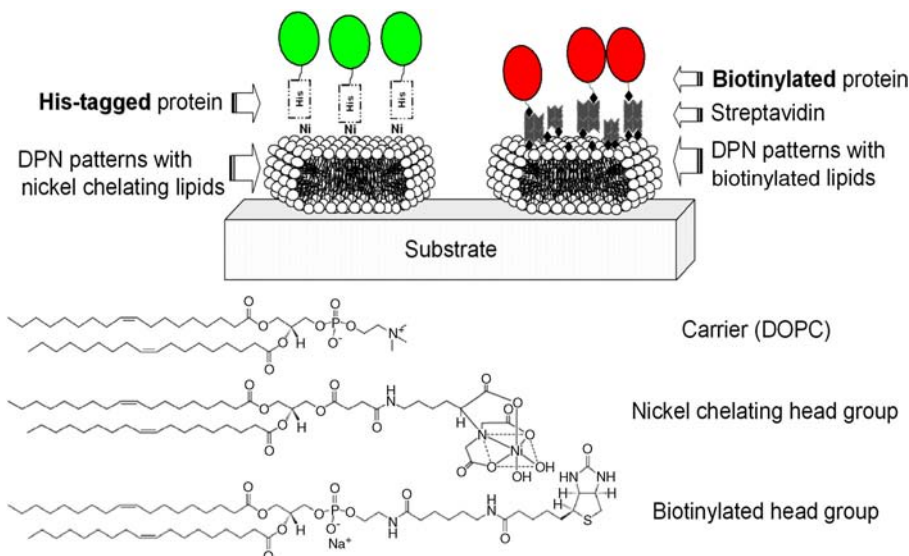


Figure 6.12 Schematic representation of protein coupling strategies to spatially patterned lipid membranes and chemical structures of the lipids. Reproduced with permission from Ref. [74].

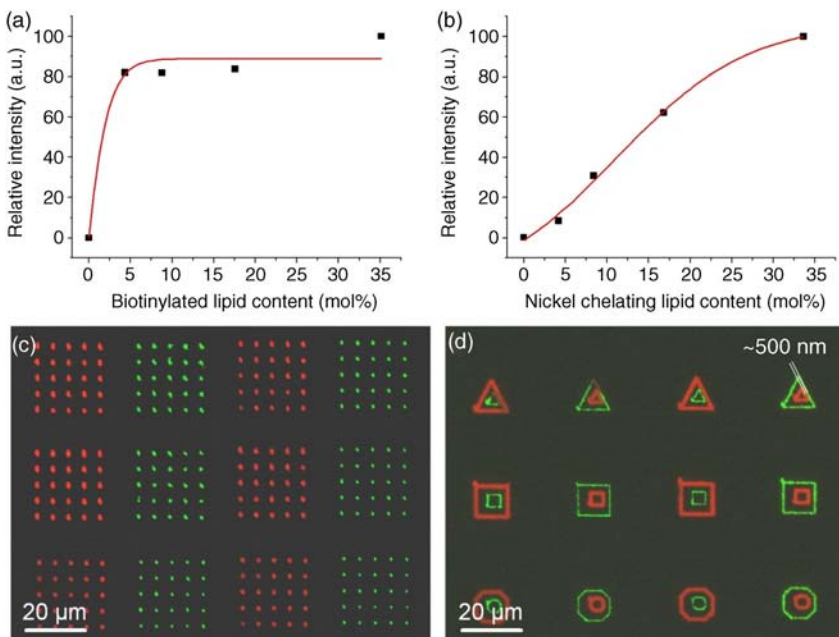


Figure 6.13 Fluorescence intensity of selectively adsorbed proteins. (a) Fluorescence intensity of selectively adsorbed Cy3-streptavidin to spread phospholipid arrays with increasing concentration of biotin head groups. (b) Fluorescence intensity of His-GFP selectively adsorbed to spread phospholipid arrays with increasing concentrations of NTA-Ni head groups. Sigmoidal curves are fit

to the data. In (a) and (b), phospholipid patterns were deposited on a plasma-treated glass surface and incubated in water to create spread lipid bilayers; (c) and (d) are finer, multilayer patterns fabricated on glass, where the lateral resolution is not increased by the bilayer spreading. Reproduced with permission from Ref. [74].

on the noncovalent interaction of histidine residues with a bivalent cation (e.g., Ni²⁺) that is complexed with nitrilotriacetate (NTA).

The biomimetic membranes doped with biotin head groups were successfully used for selective adhesion and activation of T-cells (Figure 6.14) [74]. A similar approach using supported membranes with biotin-functionalized lipids on substrate with chromium barriers was used to characterize receptor–ligand spatial organization during T-cell activation [79].

Control over the location and size of receptor clusters can also be achieved once membranes are generated with liganded lipid inks. Haptenated phospholipids, DNP-cap-PE lipid (1,2-dipalmitoyl-*sn*-glycero-3-phosphoethanolamine-*N*-[6-[(2,4-dinitrophenyl)amino]hexanoyl]), were used to create model allergen arrays. Such allergen arrays patterned on glass are a basic and straightforward platform for the detection of allergen-specific immunoglobulin E (IgE) antibodies using fluorescence-based techniques (Figure 6.15).

This approach can also be applied for mast cell activation profiling on allergen arrays [80]. Similar mode using the lift-off technique and haptenated, fluorescent

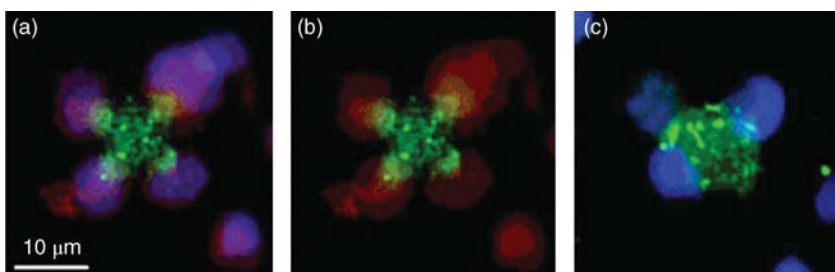


Figure 6.14 Fluorescence micrographs of T cells selectively adhered to and activated by functional proteins (anti-CD3/anti-CD28 antibodies) bound to phospholipid multilayer patterns via streptavidin. (a) A three-channel image of T cells adhering to the corners of lipid–protein DPN patterns and activated by anti-CD3/anti-CD28. The green color indicates fluorescence from a fluorescein-doped lipid pattern containing 5% biotinylated lipids. The blue fluorescence indicates the nucleus of the

cells by DAPI staining and the red fluorescence shows CD69 expression detected by subsequent staining with anti-CD69-PE and anti-PE-TRITC. (b) A two-channel image showing only the red expression and green DPN patterns from (a). (c) A control where the functional proteins were replaced with biotinylated IgG. The cells adhere to the pattern but are not activated. Reproduced with permission from Ref. [74].

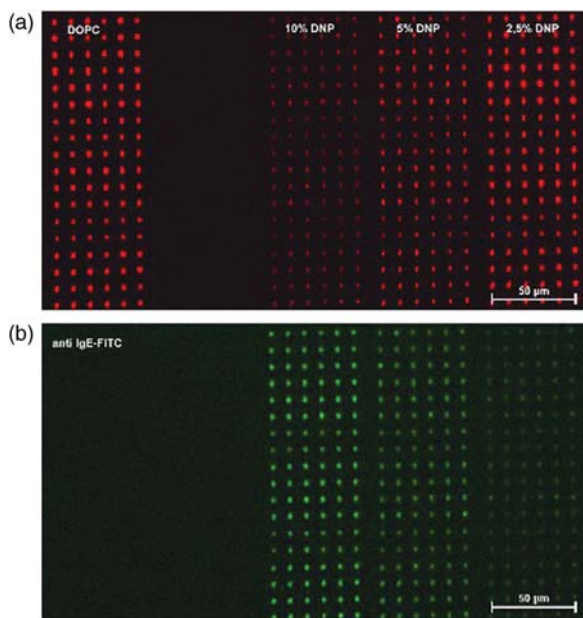


Figure 6.15 IgE reactivity profile on DNP gradient allergen arrays. (a) Fluorescence image of an allergen array containing 0, 10, 5, and 2.5 mol% DNP. The decrease in red channel fluorescence at high DNP

concentration is due to the DNP molecule affecting the rhodamine fluorescence [12]. (b) Binding of anti-DNP IgE to the DNP arrays was detected with anti-IgE FITC antibody. Reproduced with permission from Ref. [80].

lipids was used previously for spatial control over IgE receptor cluster formation in mast cells [81,82]. It enabled direct visualization of reorganization of membrane components and revealed additional interacting proteins.

Mast cells activated on allergen arrays were also shown to be an excellent platform for the visualization of events at the site of interaction of the allergen with the IgE receptor and identification of previously unknown interacting proteins. Recently, it was shown that a glucocorticoid receptor (GR) is localized at the membrane of the activated mast cells. Recruitment of GR in fusion with GFP to the site of IgE receptor cross-linking on allergen pattern was visualized and quantified (Figure 6.16) [83].

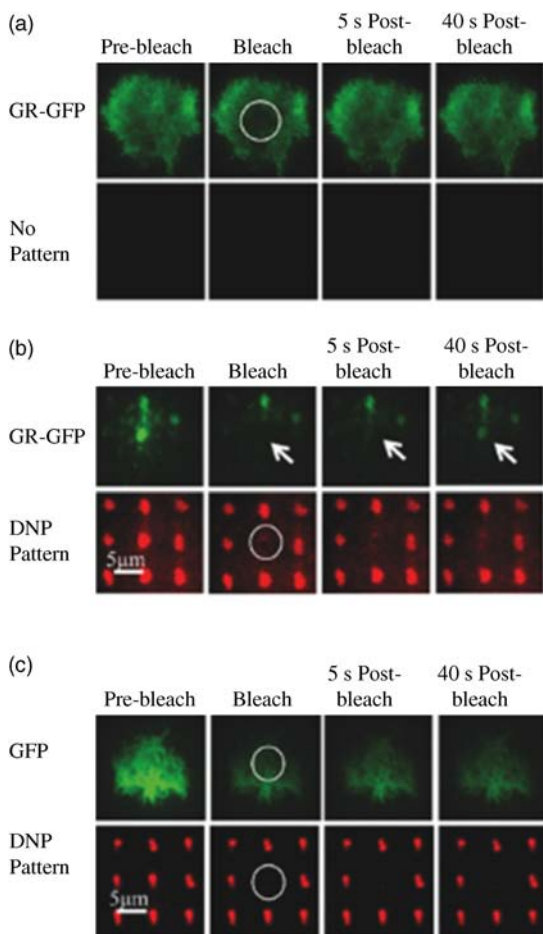


Figure 6.16 Dynamics of GR at the plasma membrane. FRAP assays of RBL-2H3 mast cells stably expressing GR-GFP (a) on cover slips without pattern and (b) on DNP patterns and (c) RBL-2H3 mast cells stably expressing GFP

on DNP patterns. White circles and arrows show bleached and recovery regions, respectively. Reproduced with permission from Ref. [83].

The same approach of using bioactive arrays of phospholipids can be extended to other target proteins and other cell types.

Besides invoking interface function, phospholipid membranes can also be applied for direct delivery of lipid-encapsulated compounds into cells. Small-molecule microarrays of phospholipid multilayers were shown to successfully deliver a rhodamine-tagged lipid and drugs to the cells. The efficacies of two drugs were assayed from the same sample, and delivered dosages were comparable to those of solution-based delivery [84].

6.5

Conclusions

The generation of functional lipid assemblies by DPN and PPL has become a powerful tool with application in biological experiments and sensor devices. The unique features of phospholipids regarding biocompatibility, suppression of unspecific binding, and specific function of modified lipids are an ideal basis for such applications.

L-DPN can be analyzed and characterized in terms of liquid ink and molecular diffusion models, but both should be modified to include the particular characteristics of lipid inks absent in liquid and molecular inks, respectively. This requires incorporating the flow dynamics in liquid ink models and the 3D growth in the molecular models.

L-DPN can create lipid assemblies in high resolution (~ 100 nm) depending on the substrate wetting properties and can create multiplexed (multicomponent) patterns on a subcellular scale on area sizes suitable for cell culture experiments. In addition, L-DPN is not limited to flat substrates, but can also be used to functionalize pre-existing three-dimensional structures and devices as long as suitable access from above for the desired functionalization sites is feasible. This was demonstrated on a range of different sensors and devices. PPL and stamping-like methods offer a complementary technique for the generation of lipid assemblies, especially when very large area coverage is desired.

Acknowledgments

A.U. acknowledges the People Programme (Marie Curie Actions) of the European Union's Seventh Framework Programme (FP7/2007–2013) under REA grant agreement no. 328163. This work was partly carried out with the support of the Karlsruhe Nano Micro Facility (KNMF, www.kmf.kit.edu), a Helmholtz Research Infrastructure at Karlsruhe Institute of Technology (KIT, www.kit.edu).

References

- 1 Mashaghi, S., Jadidi, T., Koenderink, G., and Mashaghi, A. (2013) *Int. J. Mol. Sci.*, **14**, 4242–4282.
- 2 Allen, T.M. and Cullis, P.R. (2013) *Adv. Drug Deliv. Rev.*, **65**, 36–48.
- 3 Tarahovsky, Y.S. (2010) *Biochemistry*, **74**, 1293–1304.
- 4 Jackman, J., Knoll, W., and Cho, N.-J. (2012) *Materials*, **5**, 2637–2657.

- 5 Lee, Y.K., Lee, H., and Nam, J.-M. (2013) *NPG Asia Mater.*, **5**, e48.
- 6 Jaschke, M. and Butt, H.-J. (1995) *Langmuir*, **11**, 1061–1064.
- 7 Piner, R.D., Zhu, J., Xu, F., Hong, S., and Mirkin, C.A. (1999) *Science*, **283**, 661–663.
- 8 Jang, J.-W., Smetana, A., and Stiles, P. (2010) *Scanning*, **32**, 24–29.
- 9 Martínez-Otero, A., González-Monje, P., Maspoch, D., Hernando, J., and Ruiz-Molina, D. (2011) *Chem. Commun.*, **47**, 6864.
- 10 Wu, C.-C., Reinhoudt, D.N., Otto, C., Subramaniam, V., and Velders, A.H. (2011) *Small*, **7**, 989–1002.
- 11 Lenhert, S., Sun, P., Wang, Y., Fuchs, H., and Mirkin, C.A. (2007) *Small*, **3**, 71–75.
- 12 Hirtz, M., Corso, R., Sekula-Neuner, S., and Fuchs, H. (2011) *Langmuir*, **27**, 11605–11608.
- 13 Sanii, B. and Parikh, A.N. (2007) *Soft Matter*, **3**, 974–977.
- 14 Nissen, J., Gritsch, S., Wiegand, G., and Rädler, J.O. (1999) *Eur. Phys. J. B*, **10**, 335–344.
- 15 Nissen, J., Jacobs, K., and Rädler, J. (2001) *Phys. Rev. Lett.*, **86**, 1904–1907.
- 16 Huo, F., Zheng, Z., Zheng, G., Giam, L.R., Zhang, H., and Mirkin, C.A. (2008) *Science*, **321**, 1658–1660.
- 17 Hong, J.M., Ozkeskin, F.M., and Zou, J. (2008) *J. Micromech. Microeng.*, **18**, 015003.
- 18 Eichelsdoerfer, D.J., Liao, X., Cabezas, M. D., Morris, W., Radha, B., Brown, K.A., Giam, L.R., Braunschweig, A.B., and Mirkin, C.A. (2013) *Nat. Protoc.*, **8**, 2548–2560.
- 19 Zheng, Z., Daniel, W.L., Giam, L.R., Huo, F., Senesi, A.J., Zheng, G., and Mirkin, C. A. (2009) *Angew. Chem., Int. Ed.*, **48**, 7626–7629.
- 20 Arrabito, G., Schroeder, H., Schröder, K., Filips, C., Marggraf, U., Dopp, C., Venkatachalapathy, M., Dehmelt, L., Bastiaens, P.I.H., Neyer, A., and Niemeyer, C.M. (2014) *Small*, **10** (14), 2870–2876.
- 21 Brinkmann, F., Hirtz, M., Greiner, A.M., Weschenfelder, M., Waterkotte, B., Bastmeyer, M., and Fuchs, H. (2013) *Small*, **9**, 3266–3275.
- 22 Brown, K.A., Eichelsdoerfer, D.J., Liao, X., He, S., and Mirkin, C.A. (2014) *Front. Phys.*, **9**, 385–397.
- 23 O'Connell, C.D., Higgins, M.J., Marusic, D., Moulton, S.E., and Wallace, G.G. (2014) *Langmuir*, **30**, 2712–2721.
- 24 Eichelsdoerfer, D.J., Brown, K.A., and Mirkin, C.A. (2014) *Soft Matter*, **10**, 5603–5608.
- 25 O'Connell, C.D., Higgins, M.J., Sullivan, R. P., Moulton, S.E., and Wallace, G.G. (2014) *Small*, **10**, 3717–3728.
- 26 Liu, G., Zhou, Y., Banga, R.S., Boya, R., Brown, K.A., Chipre, A.J., Nguyen, S.T., and Mirkin, C.A. (2013) *Chem. Sci.*, **4**, 2093–2099.
- 27 Saha, S.K. and Culpepper, M.L. (2010) *J. Phys. Chem. C*, **114**, 15364–15369.
- 28 Saha, S.K. and Culpepper, M.L. (2010) *Appl. Phys. Lett.*, **96**, 243105.
- 29 Peterson, E.J., Weeks, B.L., De Yoreo, J.J., and Schwartz, P.V. (2004) *J. Phys. Chem. B*, **108**, 15206–15210.
- 30 Rozhok, S., Piner, R.D., and Mirkin, C.A. (2003) *J. Phys. Chem. B*, **107**, 751–757.
- 31 Schwartz, P.V. (2002) *Langmuir*, **18**, 4041–4046.
- 32 Weeks, B.L., Noy, A., Miller, A.E., and De Yoreo, J.J. (2002) *Phys. Rev. Lett.*, **88**, 255505.
- 33 Sheehan, P. and Whitman, L. (2002) *Phys. Rev. Lett.*, **88**, 156104.
- 34 Jang, J., Hong, S., Schatz, G.C., and Ratner, M.A. (2001) *J. Chem. Phys.*, **115**, 2721–2729.
- 35 Cho, N., Ryu, S., Kim, B., Schatz, G.C., and Hong, S. (2006) *J. Chem. Phys.*, **124**, 024714.
- 36 Lee, N.-K. and Hong, S. (2006) *J. Chem. Phys.*, **124**, 114711.
- 37 Heo, D.M., Yang, M., Kim, H., Saha, L.C., and Jang, J. (2009) *J. Phys. Chem. C*, **113**, 13813–13818.
- 38 Manandhar, P., Jang, J., Schatz, G., Ratner, M., and Hong, S. (2003) *Phys. Rev. Lett.*, **90**, 115505.
- 39 Lenhert, S., Mirkin, C.A., and Fuchs, H. (2010) *Scanning*, **32**, 15–23.
- 40 Mohamad, S., Noël, O., Burraud, J.-L., Brotons, G., Fedala, Y., and Ausserré, D. (2012) *Phys. Rev. Lett.*, **109**, 248108.
- 41 Hristova, K. and White, S.H. (1998) *Biophys. J.*, **74**, 2419–2433.
- 42 Wiener, M.C. and White, S.H. (1992) *Biophys. J.*, **61**, 428–433.

- 43** Filippov, A., Orädd, G., and Lindblom, G. (2003) *Langmuir*, **19**, 6397–6400.
- 44** de Gennes, P.G. (1985) *Rev. Mod. Phys.*, **57**, 827–863.
- 45** Giam, L.R., Wang, Y., and Mirkin, C.A. (2009) *J. Phys. Chem. A*, **113**, 3779–3782.
- 46** Piner, R.D. and Mirkin, C.A. (1997) *Langmuir*, **13**, 6864–6868.
- 47** Raedler, J., Strey, H., and Sackmann, E. (1995) *Langmuir*, **11**, 4539–4548.
- 48** Hirtz, M., Oikonomou, A., Georgiou, T., Fuchs, H., and Vijayaraghavan, A. (2013) *Nat. Commun.*, **4**, 2591.
- 49** Alava, M.J. and Dubé, M. (2012) *Phys. Rev. E*, **86**, 011607.
- 50** Malshe, A.P., Rajurkar, K.P., Virwani, K.R., Taylor, C.R., Bourell, D.L., Levy, G., Sundaram, M.M., McGeough, J.a., Kalyanasundaram, V., and Samant, A.N. (2010) *CIRP Ann. – Manuf. Technol.*, **59**, 628–651.
- 51** Bian, S., He, J., Schesing, K.B., and Braunschweig, A.B. (2012) *Small*, **8** (13), 2000–2005.
- 52** Nafday, O.A., Vaughn, M.W., and Weeks, B.L. (2006) *J. Chem. Phys.*, **125**, 144703.
- 53** Liao, X., Braunschweig, A.B., Zheng, Z., and Mirkin, C.A. (2010) *Small*, **6**, 1082–1086.
- 54** John, N.S. and Kulkarni, G.U. (2007) *J. Nanosci. Nanotechnol.*, **7**, 977–981.
- 55** Xie, Z., Shen, Y., Zhou, X., Yang, Y., Tang, Q., Miao, Q., Su, J., Wu, H., and Zheng, Z. (2012) *Small*, **8**, 2664–2669.
- 56** Lenhert, S., Brinkmann, F., Laue, T., Walheim, S., Vannahme, C., Klinkhammer, S., Xu, M., Sekula, S., Mappes, T., Schimmel, T., and Fuchs, H. (2010) *Nat. Nanotechnol.*, **5**, 275–279.
- 57** Nafday, O.A., Lowry, T.W., and Lenhert, S. (2012) *Small*, **8**, 1021–1028.
- 58** Mitsakakis, K., Sekula-Neuner, S., Lenhert, S., Fuchs, H., and Gizeli, E. (2012) *Analyst*, **137**, 3076–3082.
- 59** Martin, S.J., Frye, G.C., and Senturia, S.D. (1994) *Anal. Chem.*, **66**, 2201–2219.
- 60** Bog, U., Laue, T., Grossmann, T., Beck, T., Wienhold, T., Richter, B., Hirtz, M., Fuchs, H., Kalt, H., and Mappes, T. (2013) *Lab Chip*, **13**, 2701–2707.
- 61** Bog, U., Brinkmann, F., Kalt, H., Koos, C., Mappes, T., Hirtz, M., Fuchs, H., and Köber, S. (2014) *Small*, **10**, 3863–3868.
- 62** Hill, E.W., Vijayaraghavan, A., and Novoselov, K. (2011) *IEEE Sens. J.*, **11**, 3161–3170.
- 63** Lee, K.-B., Lim, J.-H., and Mirkin, C.A. (2003) *J. Am. Chem. Soc.*, **125**, 5588–5589.
- 64** Agarwal, G., Naik, R.R., and Stone, M.O. (2003) *J. Am. Chem. Soc.*, **125**, 7408–7412.
- 65** Wilson, D.L., Martin, R., Hong, S., Cronin-Golomb, M., Mirkin, C.A., and Kaplan, D. L. (2001) *Proc. Natl. Acad. Sci. USA*, **98**, 13660–13664.
- 66** Lee, K.-B., Kim, E.-Y., Mirkin, C.A., and Wolinsky, S.M. (2004) *Nano Lett.*, **4**, 1869–1872.
- 67** Vega, R.A., Shen, C.K.-F., Maspoch, D., Robach, J.G., Lamb, R.A., and Mirkin, C.A. (2007) *Small*, **3**, 1482–1485.
- 68** Valiokas, R., Vaitekonis, S., Klenkar, G., Trinkūnas, G., and Liedberg, B. (2006) *Langmuir*, **22**, 3456–3460.
- 69** Lee, K.-B., Park, S.-J., Mirkin, C.A., Smith, J.C., and Mrksich, M. (2002) *Science*, **295**, 1702–1705.
- 70** Lee, M., Kang, D.-K., Yang, H.-K., Park, K.-H., Choe, S.Y., Kang, C., Chang, S.-I., Han, M.H., and Kang, I.-C. (2006) *Proteomics*, **6**, 1094–1103.
- 71** Kwak, S.K., Lee, G.S., Ahn, D.J., and Choi, J.W. (2004) *Mater. Sci. Eng. C*, **24**, 151–155.
- 72** Hyun, J., Ahn, S.J., Lee, W.K., Chilkoti, A., and Zauscher, S. (2002) *Nano Lett.*, **2**, 1203–1207.
- 73** Banerjee, D., Amro, N.A., Disawal, S., and Fragala, J. (2005) *J. Microlithogr. Microfabr. Microsyst.*, **4**, 023014.
- 74** Sekula, S., Fuchs, J., Weg-Remers, S., Nagel, P., Schuppler, S., Fragala, J., Theilacker, N., Franzreb, M., Wingren, C., Ellmark, P., Borrebaeck, C.A.K., Mirkin, C. A., Fuchs, H., and Lenhert, S. (2008) *Small*, **4**, 1785–1793.
- 75** Ivanisevic, A., McCumber, K.V., and Mirkin, C.A. (2002) *J. Am. Chem. Soc.*, **124**, 11997–12001.
- 76** Lowry, T.W., Kusi-Appiah, A., Guan, J., Van Winkle, D.H., Davidson, M.W., and Lenhert, S. (2014) *Adv. Mater. Interfaces.*, **1**, 1300127.
- 77** Bayer, E.A., Ben-Hur, H., and Wilchek, M. (1990) *Methods Enzymol.*, **184**, 80–89.

- 78** Helm, C.A., Knoll, W., and Israelachvili, J.N. (1991) *Proc. Natl. Acad. Sci. USA*, **88**, 8169–8173.
- 79** Salaita, K., Nair, P.M., Petit, R.S., Neve, R.M., Das, D., Gray, J.W., and Groves, J.T. (2010) *Science*, **327**, 1380–1385.
- 80** Sekula-Neuner, S., Maier, J., Oppong, E., Cato, A.C.B., Hirtz, M., and Fuchs, H. (2012) *Small*, **8**, 585–591.
- 81** Orth, R.N., Wu, M., Holowka, D.A., Craighead, H.G., and Baird, B.A. (2003) *Langmuir*, **19**, 1599–1605.
- 82** Wu, M., Holowka, D., Craighead, H.G., and Baird, B. (2004) *Proc. Natl. Acad. Sci. USA*, **101**, 13798–13803.
- 83** Oppong, E., Hedde, P.N., Sekula-Neuner, S., Yang, L., Brinkmann, F., Dörlich, R.M., Hirtz, M., Fuchs, H., Nienhaus, G.U., and Cato, A.C.B. (2014) *Small*, **10**, 1991–1998.
- 84** Kusi-Appiah, A.E., Vafai, N., Cranfill, P.J., Davidson, M.W., and Lenhert, S. (2012) *Biomaterials*, **33**, 4187–4194.

7

PEG-Based Antigen-Presenting Cell Surrogates for Immunological Applications

Ilia Platzman, Gerri Kannenberg, Jan-Willi Janiesch, Jovana Matić, and Joachim P. Spatz

7.1

Introduction

T cells play a crucial role in orchestrating the body's adaptive and innate immune system responses to foreign pathogens and mutations. This role is best illustrated by the successful treatment of various life-threatening diseases using adoptive T-cell therapy (ACT) [1–7]. ACT aims to generate a large pool of individual's T cells, resulting in a potent immune response specific to antigens on the disease-causing cells. Despite the beneficial impact of modified T cells, the road toward a broadly applicable ACT is still long and winding. Major challenges that remain include the guidance and precise regulation of immune processes *ex vivo*.

Activation, *ex vivo* expansion, and controlled differentiation of T cells into particular phenotypes are key steps in an effective ACT and represent a challenge because it is difficult to simulate T cell–antigen-presenting cell (APC) interactions during their contact with peripheral lymphoid organs. The fate of T cells is regulated not only by the presence of certain molecules on the surface of APCs but also by their density and spatial distribution on the micro- and nanometric scales [8,9]. Moreover, mechanical properties of APCs and force-dependent conformational changes during the formation of an immunological synapse (IS) (a highly organized supramolecular complex at the T cell–APC interface) play a crucial role in T-cell fate regulation [10,11]. Currently, a common clinical-grade culture system for T-cell expansion in ACT is a bead-based APC surrogate system [12]. Latex or magnetic beads endowed with antibodies can provide good control over signal delivery, but the approach has several limitations. The ability of these systems to serve as optimal APC analogues is mainly hindered by their inability to dynamically remodel their protein composition, which is in stark contrast to the natural IS [10,13,14]. Moreover, the rigid nature of the beads' material limits mechanosensing, which is an important factor for efficient and controlled T-cell differentiation [15–18]. Because of these limitations and the high complexity of APC–T cell interactions, much effort has been put into the development of new 2D and 3D simplified APC analogue

systems during the past decade. Reports describing the pros and cons of different APC analogues for T-cell stimulation have been reviewed elsewhere [10,13,14,19,20].

From an immunological point of view, it is imperative that optimal APC analogues must deliver all the physiological signals necessary for T-cell activation. Besides, when designing APC surrogates, particular attention should be given to the spatial distribution of ligands on the micro- and nanoscale levels. Spatial organization of chemical cues can be accomplished by different patterning techniques that allow the mimicry of the microscale conditions in the APC's environment *in vivo*. Higher patterning resolutions, down to single ligands (i.e., less than 10 nm), can be achieved using block copolymer self-assembly at interfaces in combination with domain-specific functionalization using proteins [21–23]. Other factors that must be considered when engineering APCs are the critical functions of protein transport regulators, namely, the cell membrane and the dynamic actin cytoskeleton; both are essential for the signaling activity of individual proteins and the cell as a whole [24]. Recent studies have shown that cytoskeleton contractility appears vital in T-cell activation, as T-cell receptors are sensitive to forces in the piconewton range [15,25]. Inspired by these observations – and considering that T cells are unlikely to encounter stimulatory surfaces with the stiffness of glass *in vivo* – much effort has been put into the development of biocompatible compliant supports that mimic more closely the physiological elasticity ranges found in living organisms. A recent study by O'Connor *et al.* [17] revealed the important, previously unrecognized, influence of the APC mechanical properties on the fate of human T cells. The main outcome of this research was that soft (Young's modulus, $E_Y < 100 \text{ kPa}$) PDMS substrates support, on average, a fourfold increase in overall T-cell expansion, compared with stiffer ($E_Y \sim 2 \text{ MPa}$) substrates. This effect was observed in both CD4+ and CD8+ T cells. Moreover, CD4+ T cells expanding on soft substrates yield an average threefold greater proportion of IFN- γ -producing type 1 helper (Th1) T cells. This observation could indicate that naive T cells expanding on soft materials can function more effectively following adoptive therapy in cancer [26].

Given the recent extensive evidence that crosstalk between different biophysical and biochemical stimuli can have a tremendous impact on T-cell fate, we describe and discuss the most recent developments in artificial APCs engineering, which have led to the production of systems with individual adjustability and control over different parameters stimulating T cells. In this chapter, we present approaches for the molecular engineering of nanopatterned poly(ethylene glycol) (PEG)-based 2D and 3D APC surrogates. We describe the following three types of recently developed nanopatterned APC surrogate systems and discuss their impact on cellular analysis:

- i) Elastic nanopatterned and specifically biofunctionalized 2D PEG-diacrylate (DA) hydrogels [27–29].

- ii) Elastic nanostructured PEG-DA hydrogel beads.
- iii) Soft gold nanostructured and specifically biofunctionalized droplets of water-in-oil emulsions [30].

7.2

Elastic Nanopatterned and Specifically Biofunctionalized 2D PEG-DA Hydrogels: General Properties

Many T-cell functions are known to depend on both the elasticity of their environment and the distribution of available stimulatory ligands. So far it has been impossible to independently control these two parameters in cell stimulation experiments *in vitro*. Here we present a method that allows individual control of substrate stiffness and ligand spacing by fabricating nanoscopically controlled biomolecule anchors (gold nanoparticles) using block copolymer micellar nanolithography (BCML), followed by transferring these anchors onto elastic PEG-DA polymers [27]. Anti-CD3 antibody was chosen to mimic the natural ligands for T-cell receptors as it triggers robust T-cell activation and expansion regardless of the affinity of their receptors. To achieve enhanced stimulation of T cells, the antibodies were immobilized on gold nanoparticles in an oriented or a site-directed manner via nitrilotriacetic acid (NTA) chemistry and hexahistidine (His6-tag) antibody-binding protein G, as previously described [23]. In order to induce the full repertoire of T-cell activation responses, an additional costimulatory antibody anti-CD28 was provided as soluble in the current system with the possibility for coimmobilization on the surface in the future experiments. On the hydrogel surface, the distance between the bound antibodies (ΔL) can be finely adjusted by varying the spacing between the gold nanoparticles ($30 \text{ nm} < \Delta L < 200 \text{ nm}$). The size of the individual anchor points was chosen not to exceed the size limit of $\sim 10 \text{ nm}$ to ensure single receptor–ligand interaction. To probe the recently proposed role of mechanosensing in T-cell activation, the stiffness of the supporting hydrogel can be tuned by changing the molecular weight of the PEG macromers and its concentration in solution prior to polymerization. The Young's modulus (E_Y) of the hydrogels ranges from 10 to 90 kPa. The spacing values were chosen to closely parallel recently reported T-cell studies on stimulatory anti-CD3 nanoarrays supported by passivated glass substrates [23], while the stiffness values were designed based on recent findings that human T cells prefer softer substrates ($< 1 \text{ MPa}$) [17].

7.2.1

Block Copolymer Micellar Nanolithography (BCML)

During the past 15 years, different semiconductor fabrication strategies have been adapted to manipulate the spatial organization of APC's key ligands on planar surfaces with the aim of developing simplified 2D APC surrogates [8,10].

Only few techniques, such as Dip-pen and e-beam lithography, have been able to achieve patterns with sub-100 nm spatial resolution, a length scale that plays a significant role in T-cell activation [31]. Higher resolution patterning, down to single ligands (i.e., less than 10 nm), may be obtained using BCML at interfaces [29,32]. The method is based on the self-assembly of amphiphilic macromolecules, which create periodic patterns of nanometer-sized gold particles. Such nanoparticle arrays serve as templates in which each individual gold particle serves as an anchor point for the selective binding of biomolecules. The basic concept behind these systems is to allow well-defined signal inputs to be delivered to the T cell and to investigate how the signal's spatial distribution and biochemical composition control T-cell activation.

Quasi-hexagonally ordered gold nanoparticle arrays on glass surfaces ($20 \times 20 \times 0.15 \text{ mm}^3$) were fabricated using *o*-xylene solution of poly(styrene)-block-poly(2-vinyl pyridine) (PS-b-P2VP) (Polymer Source Inc., Canada). Shortly, the PS-b-P2VP *o*-xylene solution was loaded with HAuCl₄ (Sigma Aldrich, Germany) at a stoichiometric loading of (P2VP/HAuCl₄) = 0.5 and stirred for at least 24 h to obtain gold nanoparticles with a diameter between 6 and 8 nm. The lateral distance between the individual gold nanoparticles was adjusted to a range of 30–200 nm by varying the molecular weight of the polystyrene units, block copolymer concentration, or the micellar coating process, such as the dipping or spinning speed. Details concerning the applied block polymers and the dip or spin casting processes are included in Table 7.1. To control the quality of the nanopatterned surfaces, at least four samples from each solution were observed by scanning electron microscopy (SEM) prior to being transferred to the hydrogel surfaces.

Table 7.1 Summary of PS-b-P2VP characteristics, parameters of the dipping and spin casting processes, and the resulting distance between the gold nanoparticles on the surface (ΔL).

Polymer PS _(units) -b-P2 VP _(units)	PDI	Polymer concentration (mg ml ⁻¹)	Dipping (V)/spinning (rpm) speed	ΔL (nm)
PS ₁₅₄ -b-P2 VP ₃₃	1.08	5	24 [V]	22 ± 5
			3000	25 ± 4
PS ₂₄₀ -b-P2 VP ₁₄₃	1.07	5	10 [V]	36 ± 8
			4	45 ± 8
PS ₄₅₁ -b-P2 VP ₂₂₈	1.07	5	4000	40 ± 3
PS ₁₀₅₆ -b-P2 VP ₄₉₅	1.15	5	3000	63 ± 8
			6000	85 ± 7
PS ₁₈₂₄ -b-P2 VP ₅₂₃	1.10	2.5	6000	100 ± 8
			4000	140 ± 17
			6000	165 ± 21

Table 7.2 Properties of PEG-DA hydrogels.

Polymer	MW (g mol ⁻¹) of PEG units	C (mg ml ⁻¹) in water
PEG(700)-DA	700	600
PEG(10 000)-DA	10 000	600, 400, 300, 200
PEG(20 000)-DA	20 000	
PEG(35 000)-DA	35 000	

7.2.2

Fabrication and Characterization of Nanopatterned PEG-DA Hydrogels

Photo-cross-linkable PEG-DA hydrogels were chosen as elastic substrates primarily due to PEG's outstanding stability and repellent properties against unspecific protein absorption [29,33,34]. Moreover, tunable elasticity over four orders of magnitude from 1 kPa to 9 MPa, controlled by varying the molecular weight of the PEG units from 35 000 to 700 g mol⁻¹, respectively, increases the potential to transfer the biophysical key functionalities of biorelevant interfaces, including those of native APCs. The molecular weight and concentration of PEG-DA molecules used in our studies are listed in Table 7.2 (not all were used for the T-cell stimulation).

Figure 7.1 depicts the entire multistep fabrication process of nanopatterned PEG-DA hydrogels [27,29,35]. First, quasi-hexagonally ordered arrays of gold nanoparticles on glass supports were functionalized with a transfer linker *N,N'*-bis(acryloyl)cysteamine (98%, Alpha Aesar, Germany). Second, an aqueous polymer solution containing the desired concentration of the chosen PEG-DA macromer and the photoinitiator 2-hydroxy-4'-(2-hydroxyethoxy)-2-methylpropiophenone (98%, Sigma-Aldrich, Germany) was cast over the nanopatterned

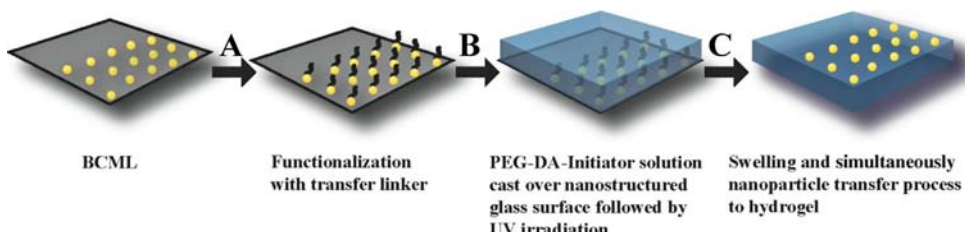


Figure 7.1 (A) Gold nanoparticles on a solid support are covalently coupled to a transfer linker. (B) After addition of a PEG-DA photoinitiator solution and irradiation by UV light, the linker is copolymerized into the PEG

meshwork. (C) Swelling caused by incubation in water induces particle detachment. The resulting PEG-DA hydrogel substrate is decorated with surface-exposed gold nanoparticles.

glass. UV irradiation initiated the polymerization process and the linker copolymerized into the PEG mesh. Subsequently, the samples were incubated in phosphate buffered saline (PBS) for at least 48 h. Lateral forces induced by the swelling process are responsible for the detachment of the gold nanoparticles from the glass surface. The swelling of the PEG-DA hydrogels is a crucial process for the particle transfer from the glass support to the hydrogel surface. During this process, the interparticle distances on the hydrogel substrates increase isotropically by a so-called swelling ratio factor [27].

To verify the successful transfer of the gold nanoparticles from the glass surface to the respective PEG-DA hydrogels, the nanopatterned hydrogels were investigated and characterized by cryo-SEM. Cross-sectional tilted view (3° tilt relative to the hydrogel surface) and top-view cryo-SEM imaging were performed under low temperature conditions (top = $-110 \pm 5^\circ\text{C}$). Low acceleration voltages of 1–1.5 kV were applied because of the low conductivity of the investigated samples. After vitrification, the PEG-DA specimen, mounted on a liquid nitrogen-cooled stage, was transferred to a BAL-TECH MED 020 (BAL-TEC AG, Balzers, Liechtenstein) preparation device via an evacuated liquid nitrogen-cooled shuttle BAL-TECH VLC 100 (BAL-TEC AG, Balzers, Liechtenstein). For cross-sectional cryo observations, the hydrogels were fractured in the 10^{-5} – 10^{-6} mbar vacuum chamber at -160°C with a cooled knife. After fracturing, the samples were heated to -90°C and kept in the vacuum for 30 min in order to allow water on the interface to sublime. For cryo-SEM, the samples were transferred immediately to the SEM chamber via an evacuated liquid nitrogen-cooled shuttle. A Zeiss Ultra 55 field-emission electron microscope was used for image acquisition.

Figure 7.2a–c shows representative cryo-SEM micrographs (top view) of the nanopatterned PEG(35 000)-DA hydrogels. It can be verified that the gold

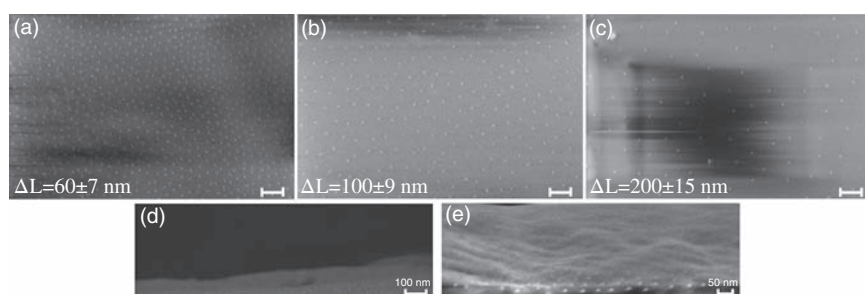


Figure 7.2 (a–c) Top-view cryo-SEM micrographs of $400 (\text{mg ml}^{-1})$ PEG(35 000)-DA hydrogels; scale bar = 100 nm. Extended gold nanoparticle patterns fabricated using the following combination: (a) 5 mg ml^{-1} PS₂₄₀-b-P2VP₁₄₃ and 10 (V), (b) 5 mg ml^{-1} PS₁₀₅₆-b-P2VP₄₉₅ and 3000 rpm, and (c) 2.5 mg ml^{-1} PS₁₈₂₄-b-P2VP₅₂₃ and 4000 rpm. Parts (d) and (e) showing cross-sectional tilted view (3° tilt relative to the hydrogel surface) of PEG35000-DA hydrogel micrographs obtained with different magnifications. In both cases, the gold nanoparticles with an interparticle spacing of $\sim 60 \text{ nm}$ and a diameter of 8 nm are clearly observable.

nano particle pattern was successfully transferred one-to-one with nanoscale precision. Qualitative data regarding the gold nanoparticle exposure on hydrogel surfaces could be provided by cross-sectional, high-resolution cryo-SEM micrographs (Figure 7.2d and e). It can be shown that the particles are partially immersed in the hydrogel. This finding was not unexpected as the nanostructured hydrogels were prepared by casting the liquid hydrogel precursor over the nanostructured glass surface leading to a partial enclosure of the gold nanoparticles.

Mechanical characterization of the PEG-DA hydrogels was performed by indentation measurements with a “Nano Wizard II” scanning probe microscope (SPM) (JPK Instruments AG, Berlin, Germany). Tipples, silicon cantilevers (CSC 12 tipples no. Al; μ masch, Estonia) were simultaneously cleaned and activated with reactive oxygen plasma (0.4 mbar O_2 ; 150 W, 5 min). Spring constants of the cantilevers were determined by the thermal noise calibration method and ranged between 1.0 and 2.5 N m^{-1} . Subsequently, a borosilicate glass microsphere with a diameter of 8 μm (SPI supplies, Westchester, PA) was glued to the cantilever with a two-component epoxy adhesive (UHU GmbH & Co. KG, Germany). To derive accurately the Young’s modulus of the PEG-DA hydrogels, force distance curves were recorded from different points on the hydrogel surfaces and fitted to the modified Hertz model [29,36].

Figure 7.3 shows the summary of the mechanical properties of different PEG-DA hydrogels. The main outcome from the indentation measurement is that the mechanical properties of the hydrogel substrates can be gradually adjusted within four orders of magnitude, covering all physiologically relevant values, by choosing an appropriate PEG-DA monomer ($35000 \text{ g mol}^{-1} > \text{MW} > 700 \text{ g mol}^{-1}$) and its concentration in water.

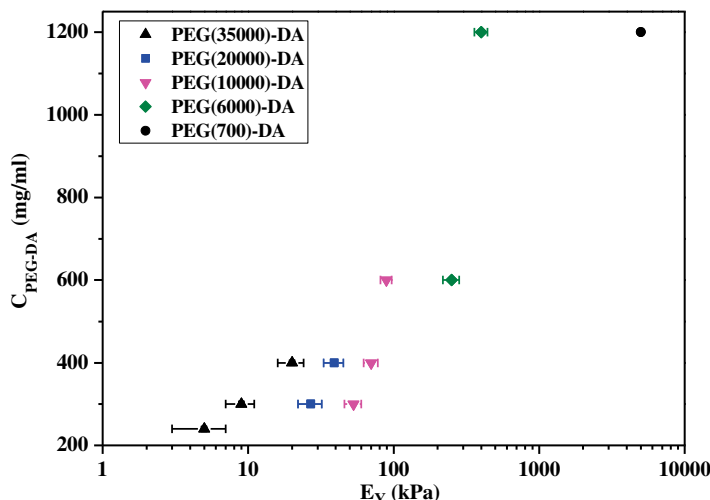


Figure 7.3 Summary of the mechanical properties of different PEG-DA hydrogels. Error bars refer to the standard error of the mean.

7.2.3

Biofunctionalization

Prior to biofunctionalization, all hydrogel substrates were sterilized by UV irradiation. For the following biofunctionalization steps, the hydrogels can be glued to the bottom of the assay wells using biocompatible ethyl-2-cyanoacrylate tissue adhesive (EPIGLU, Meyer-Haake, Germany). In order to achieve enhanced stimulation of T cells, the antibodies were immobilized on gold nanoparticles in an oriented or a site-directed manner via NTA/Ni²⁺/His chemistry and antibody-binding protein G, as has been previously described (Figure 7.4a) [23]. Briefly, hydrogels were immersed in 0.5 mM ethanolic solution (70%) of thiol-NTA linker (ProChimia, Poland) for 60 min at room temperature. Thiol-NTA linker was then loaded with 10 mM NiCl₂ solution in HBS pH 7.5 for 10 min. After rinsing steps the hydrogels were incubated in HBS solution with 10 µg ml⁻¹ of His6-Protein G (BioVision Inc., Milpitas, CA) for 1 h at room temperature and rinsed with HBS and PBS. Human anti-CD3-Alexa Fluor 488 or purified human anti-CD3e OKT3 (both purchased from eBioscience, Germany) for substrate imaging or cell activation experiments, respectively, were coupled to nanoarrays by incubating 10 µg ml⁻¹ antibody solution in PBS pH 7.4 for 1 h at room temperature. Functionalized nanoarrays were extensively rinsed with PBS overnight at 4 °C with mild shaking and immediately used for imaging or cell activation experiments. The functionalized hydrogel samples were mounted between two coverslips, sealed by common grease and imaged with an inverted laser scanning confocal microscope (LSCM) Leica TCS SP5 (Leica Microsystems,

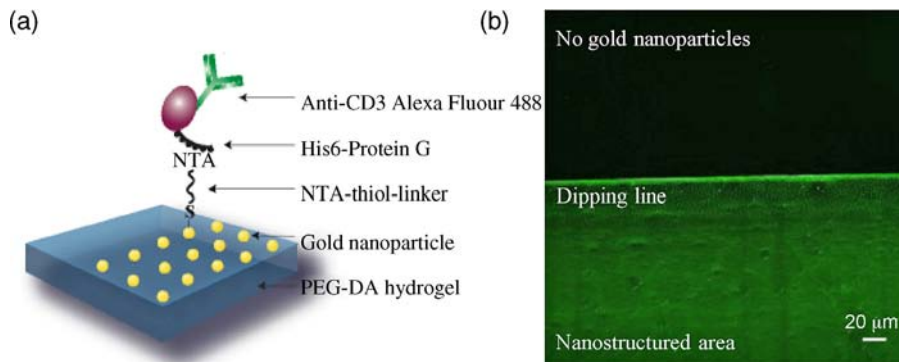


Figure 7.4 Nanopatterned hydrogels can be efficiently functionalized with anti-CD3 antibody to provide a novel stimulatory platform for T cells with tunable properties. (a) Schematic representation of the site-directed immobilization strategy based on NTA/Ni²⁺/His chemistry and antibody-binding protein G that results in oriented anti-CD3 binding to

the gold nanoparticles and preserved bioactivity on the surface. (b) Fluorescence images of nanopatterned PEG-DA hydrogel ($\Delta L = 60$ nm) surfaces biofunctionalized with Alexa Fluor 488 labeled anti-CD3. The surface consisted of a gold-nanostructured area beneath the dipping line and an area with no gold nanoparticles above the dipping line.

Germany) equipped with a HCX PL APO CS 20×/0.7 objective. A white laser was used to excite anti-CD3-Alexa Fluor 488 at 488 nm.

By using fluorescently labeled anti-CD3 antibodies, the successful biofunctionalization of the gold nanoparticles on hydrogels could be proven. Figure 7.4b clearly shows the internal control line on the substrate separating the areas with and without gold nanoparticles and the resulting difference in the functionalization signal.

7.2.4

Cell Experiments

7.2.4.1 T-Cells Isolation

Human CD4+ T cells were isolated via a two-step procedure from the peripheral blood of healthy volunteers after obtaining informed consent. Peripheral blood mononuclear cells (PBMCs) were first acquired by density gradient centrifugation on lymphocyte separation medium (PAA Laboratories, USA) according to manufacturer's instructions and were further enriched for CD4+ T cell by negative selection with CD4+ T cell isolation kit (Miltenyi Biotec, Germany). The enriched population was analyzed for purity by staining with anti-CD3-FITC, anti-CD4-PE, and the appropriate isotype controls (all purchased from Immuno-tools, Germany) and performing flow cytometry (FC 500 Cytometer, Beckman Coulter GmbH, Germany). The purity of isolated CD4+ T cells was consistently >97% and the viability >90% (based on Trypan Blue exclusion assay). CD4+ T cells were resuspended in complete RPMI medium (RPMI 1640 supplemented with 10% HI FBS, 2 mM L-glutamine, and 1% penicillin–streptomycin, all purchased from Gibco and Life Technologies, Germany) and immediately used in activation experiments.

7.2.4.2 T-Cells Stimulation

Freshly isolated human CD4+ T cells (3×10^5 per well, 0.6 ml complete RPMI medium) were cultured in a 48-well standard microplate for 4 days on anti-CD3 nanoarrays of three distinct interparticle spacings (50, 100, and 200 nm) and three different stiffnesses (10, 40, and 90 kPa) of the supporting PEG-DA hydrogel supplemented with $2 \mu\text{g ml}^{-1}$ anti-CD28 (clone 9.2, eBioscience, Germany). The spacing values were chosen to closely parallel recently reported T-cell studies on stimulatory anti-CD3 nanoarrays supported by passivated glass substrates [23], while the stiffness values were designed based on recent findings that human T cells have a preference for softer substrates (<1 MPa). To check the functionality of the isolated cell batches by their ability to respond to specific activation stimuli and account for donor-to-donor variability among the samples, sets of positive and negative controls have been performed. Standard positive (cells cultured in anti-CD3-coated plastic wells with soluble anti-CD28) and negative controls (nontreated cells or cells cultured in plastic wells coated with an anti-CD3 matching isotype) in plastic well plates were run in parallel to each experiment on functionalized nanopatterned hydrogels. After 4 days of culture,

bright field images of live T cells were acquired on Axiovert 40 CFL (Zeiss) equipped with LD A-Plan 20 \times /0.3 Ph1 objective and IL-2 concentration was determined in culture supernatants using a human IL-2 ELISA Ready-Set-Go! kit (eBioscience, Germany) according to manufacturer's instructions.

7.2.4.3 T-Cells Proliferation

For the proliferation assay, prior to seeding on hydrogels, T cells were labeled with a fluorescent dye 5-(and 6)-carboxyfluorescein diacetate succinimidyl ester CFSE (Invitrogen, Germany), as previously described for low cell numbers ($0.5\text{--}10 \times 10^6 \text{ cells ml}^{-1}$) [37]. Briefly, freshly isolated CD4+ T cells in 1 ml complete RPMI medium were stained with 5 μM dye solution in PBS for 5 min at room temperature in the dark. The labeling was stopped by adding 10 times the volume of 20 °C PBS containing 5% HI FBS, followed by centrifugation for 10 min at 300 $\times g$. The cells were washed once again with 20 °C PBS containing 5% HI FBS, resuspended in complete medium, and counted to check for viability and recovery prior to seeding. After 4 days of culture on stimulatory nanopatterned hydrogels, the cells were harvested from the substrates, washed with PBS, fixed with 4% formaldehyde in FACS buffer (PBS/0.1% HI FBS/0.1% NaN₃), and analyzed on the following day with a FC 500 Cytometer with CXP software using a blue/green laser to excite CFSE at 488 nm. Dead cells and cell debris were excluded from the analysis by forward and side scatter gating. Collected data were further analyzed by FlowJo v9.6 for different proliferation parameters, for example, percentage of proliferating cells.

7.2.4.4 Results

After 4 days of culture on stimulatory nanopatterned hydrogels, the T cells appeared healthy and activated (Figure 7.5). Elongated cell morphology could be observed where they interacted with the stimulatory surface and subsequent cell activation took place, as well as enlarged cell blasts, leading to proliferation and clusters of activated T cells. Similar observations were made on corresponding positive controls in plastic wells. On the other hand, the cells appeared rounded on blank hydrogel substrates (without AuNPs), indicating the lack of interaction with the surface and proving the preserved passivation of the background. This inactivated appearance of stimulus-deprived cells was also observed on standard negative controls.

Interparticle spacing controlling the stimulus density on the hydrogels affected T-cell activation – more cells with activated phenotype could be spotted as the spacing was decreased from 200 to 60 nm. These findings are in agreement with previous studies performed with both human and mouse T cells on stimulatory glass-supported nanoarrays presenting anti-CD3 and natural T-cell ligands, respectively [22,23]. Interestingly, the rigidity of the substrate also appeared to have an effect on cellular activation, as especially more T-cell clusters and clusters of bigger diameters could be detected on the softer hydrogels (10 kPa) at any interparticle distance. In order to get a more quantitative assessment of the cellular activation dependence on the

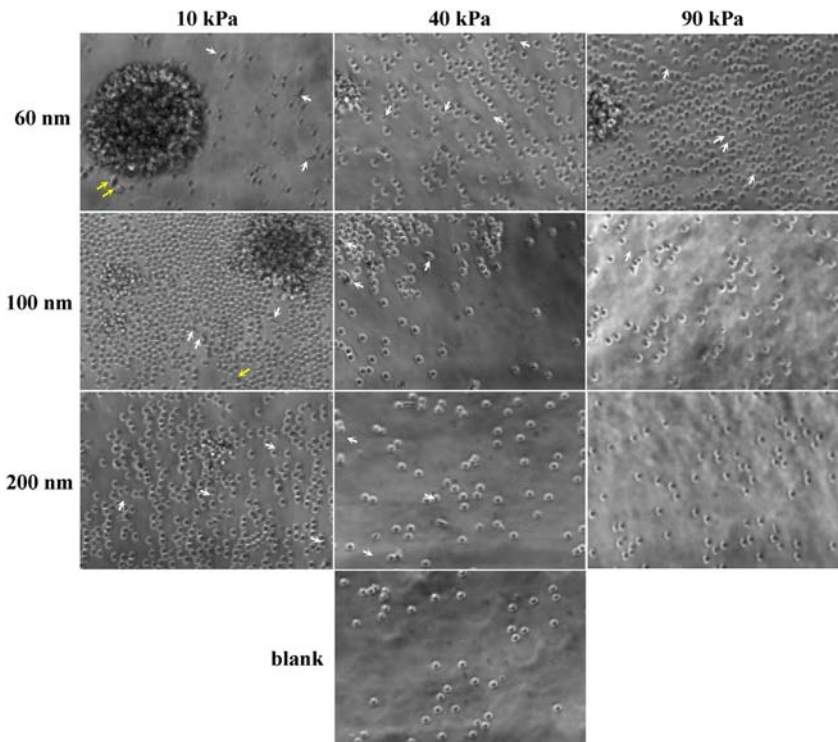


Figure 7.5 Specific T-cell appearance indicates the interaction with the stimulatory nanopatterned hydrogels. Bright field images showing characteristic T-cell morphology observed after 4 days of culture on anti-CD3 nanoarrays of different interparticle spacing supported by PEG hydrogels of varying

stiffnesses (scale bar = 20 μm). Blank substrate refers to PEG hydrogel without gold nanoparticles. Elongated cells (white arrows), enlarged T-cell blasts (yellow arrows), and clusters of activated T cells can be noticed where the surfaces induced activation.

substrate stiffness, two key T-cell activation responses were further monitored on the stimulatory nanopatterned hydrogels: the production of the IL-2 cytokine and cell proliferation. Preliminary results have again indicated that human T cells have a preference for softer substrates (Figure 7.6). Both IL-2 levels and percentage of proliferating cells were higher on stimulatory hydrogels presenting lower Young's moduli. These observations are in agreement with previous reports of enhanced human T-cell activation observed on softer PDMS substrates (<100 kPa) [17]. It is remarkable how T cells are able to use their sensing apparatus to selectively recognize and judge environmental stimuli. Although a promising proof of concept, these preliminary results need to be further validated. For example, some of the background signal in both readouts was not insignificant within these experiments, indicating the need for further experimental optimization in future studies.

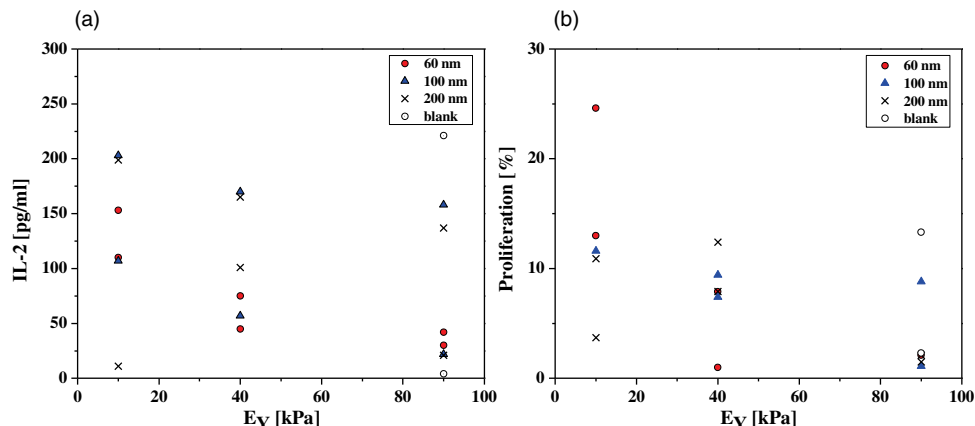


Figure 7.6 T-cell activation is sensitive to the rigidity of the underlying stimulatory substrate. Graphs showing (a) interleukin-2 (IL-2) production and (b) cell proliferation

(presented as percentage of proliferating cells) after 4 days of culture on anti-CD3 nanoarrays of different interparticle spacing supported by PEG hydrogels of varying stiffness.

7.3

Nanostructured PEG-DA Hydrogel Beads: General Properties

Bead-based APC systems combine the advantages of 2D configuration with surfaces of well-defined molecular composition and the possibility of effectively contacting a large number of T cells at once. Establishing contact between T cells and beads in suspension is considered to represent *in vivo* conditions more realistically than those mimicked on solid planar systems. Therefore, cell-size monodisperse polystyrene and magnetic iron oxide rigid bead-based APCs endowed with anti-CD3 and anti-CD28 antibodies were qualified as clinical-grade culture systems for T-cell expansion in adoptive therapy [10,12,38–40]. These APC surrogate systems can provide adequate control over signal delivery, although the approach has a remarkable limitation. The ability of these systems to optimally govern the T-cell fate is mainly hindered by their rigid nature, which is in a stark contrast to natural APC. Given the recent evidence that mechanical properties of APC surrogates can have a tremendous impact on T-cell fate – and considering that T cells are unlikely to encounter stimulatory surfaces with the stiffness of glass *in vivo* – much effort has been put by us into the development of PEG-DA hydrogel beads. This bead-based APC system will allow independent control over both biophysical (elasticity) and biochemical (distribution of stimulation ligands) properties of antigen-presenting interfaces.

In this section, we describe an easy and cost-effective method of fabricating nanostructured monodisperse PEG-DA beads ($30 \mu\text{m} > D > 15 \mu\text{m}$) for immunological applications (Figure 7.7). Toward this end, droplet-based microfluidic technology was used to create droplets of a PEG-DA_(precursor)-in-oil emulsion.

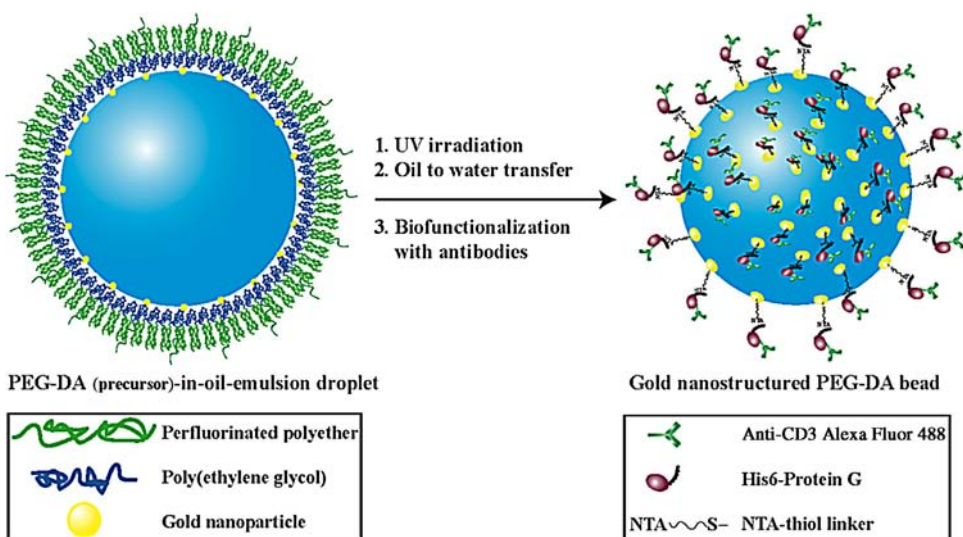


Figure 7.7 Schematic representation of gold-nanostructured PEG-DA hydrogel beads formation.

Nonionic diblock copolymer fluorosurfactants made of perfluorinated polyethers (PFPE) (hydrophobic tails) and PEG-monomethyl ether (PEG-OMe, hydrophilic head groups) were used to provide long-term stability to the PEG-DA precursor solution droplets by preventing coalescence. Moreover, gold-linked surfactants were synthesized and mixed with other surfactants (diblock surfactants) at different concentration ratios to create stable PEG-DA droplets coated with gold nanoparticles at various densities [30]. To form gold-nanostructured beads, PEG-DA precursor droplets were photopolymerized in UV light. Following the exchange of the oil phase by water, the nanostructured PEG-DA beads were characterized using cryo-SEM to quantitatively estimate the gold nanoparticle density. Moreover, indentation measurements were performed to assess the mechanical properties of the beads. Similar to 2D hydrogels (see Section 7.2), the elasticity of the PEG-DA beads can be tuned over four orders of magnitude ($4 \text{ MPa} > E_Y > 3 \text{ kPa}$). To provide bioactivity in terms of T-cell stimulation, anti-CD3 anti-CD28 antibodies were immobilized on the beads, following the same protocol as described in Section 7.2.3.

In experiments with T cells, the hydrogel beads, like the softer 2D substrates, showed the same improved stimulation on soft beads. However, it should be noted that many aspects were not explored in this work and warrant further investigation. For example, particular attention has to be devoted to the optimization of the beads' diameter. In the case of polystyrene and magnetic iron oxide rigid bead-based APC systems, the beads of 4 or 5 μm diameter were found to be the most effective for T-cell stimulation [40,41]. This, in turn, might indicate

that a reduction of the PEG-DA beads' sizes will be necessary for improved performances in T-cell stimulation.

7.3.1

Surfactant Synthesis

The synthesis of the PFPE(7000)-PEG(750)-OMe diblock followed the procedure reported earlier [30], but with several modifications (Figure 7.8). PEG(750)-OMe (750 mg, 1 mmol, Fluka, Germany) was dissolved under argon atmosphere in 70 ml of dry tetrahydrofuran (THF) and cooled to -78°C with isopropanol/dry ice. *N*-Butyl lithium (0.40 ml of a 2.5 M solution in hexane, 1 mmol, Sigma-Aldrich, Germany) was added dropwise to the PEG-OMe solution over a period of 45 min at -78°C and stirred for additional 30 min at -78°C . While continuously stirred, the reaction thawed slowly to room temperature and was stirred for another 30 min. Subsequently, PFPE(7000)-carboxylic acid (7 g, 1 mmol, molecular weight 7000 g mol $^{-1}$, DuPont, The Netherlands) was added dropwise over a period of 30 min and stirred for another 12 h. After the reaction was finished, the THF solvent with unreacted PEG-OMe was removed using a syringe. Two additional washing steps with dry THF solvent were employed to purify the crude product from the unreacted PEG-OMe. The product was dissolved in methanol (Carl Roth GmbH, Germany) to separate it from unreacted PFPE(7000)-carboxylic acid. The PFPE(7000)-PEG(750)-OMe product dissolved in methanol was transferred to a clean flask and dried with a rotary evaporator at 40°C . After removing the methanol and drying on the vacuum line, the desired PFPE(7000)-PEG(750)-OMe diblock copolymer surfactant was obtained (4.45 g, 83%).

Synthesis of gold nanoparticle-linked diblock copolymer surfactants, PFPE(2500)-PEG(350)-gold transfer linker (Figure 7.9) followed the procedure reported earlier [30] but with one additional step. To create PEG-DA beads with covalently bound gold nanoparticles, the gold nanoparticles were functionalized

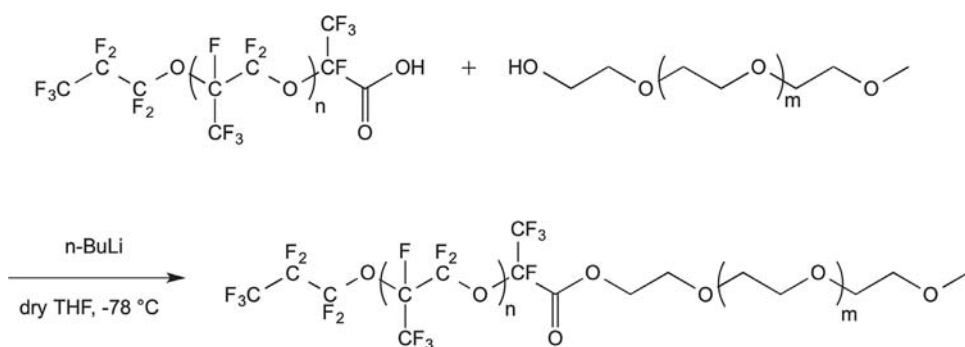


Figure 7.8 One-step esterification synthesis of PFPE(7000)-PEG(750)-OMe diblock copolymer surfactants.

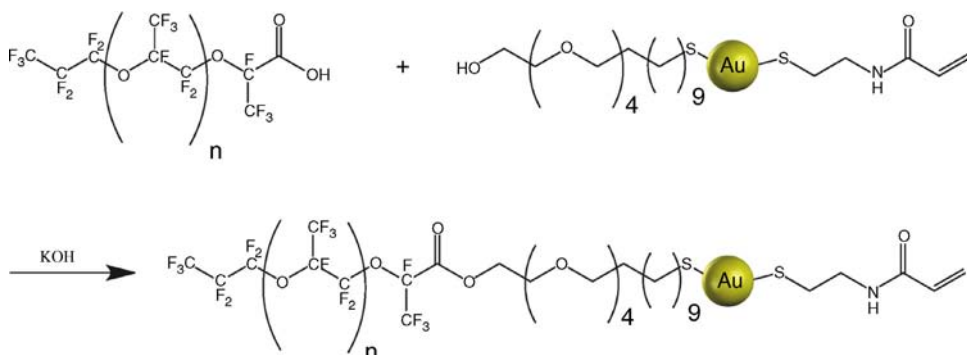


Figure 7.9 Synthesis of PFPE(2500)-PEG(350)-gold transfer linker surfactants.

first with the transfer linker (see Section 7.2.2). Toward this end, ethanolic solution of *N,N'*-bis(acryloyl)cysteamine (98%, Alpha Aesar, Germany) was added to (11-Mercaptoundecyl)tetra(ethylene glycol)-functionalized gold nanoparticle solution (2% w/w solution in water, 1 ml, Sigma Aldrich, Germany) to get final 25 µM concentration and stirred for 60 min. Subsequently, PFPE(2500)-carboxylic acid (2.5 mg, 1 µmol, DuPont, The Netherlands) and KOH (5 N, 10 µl) were added to the 1 ml of transfer linker-functionalized gold nanoparticle solution and stirred for 1 h. The PFPE-PEG-gold transfer linker and unreacted PFPE were flocculated during the reaction. The water was removed by freeze-drying for 24 h. The product was dissolved in 1 ml of fluorinated oil FC-40 (Acros Organics, Germany) and filtered with a hydrophobic filter (PTFE 0.2 µm, Roth, Germany) to remove unreacted, hydrophilic (11-Mercaptoundecyl)tetra(ethylene glycol)-functionalized gold nanoparticles, and the desired PFPE-PEG-gold transfer linker surfactant was obtained (18.35 mg, 81.5%).

To synthesize a hydrophilic diblock copolymer surfactant PFPE(2500)-PEG(5000)-OMe, which is required for a washing step (see Section 7.3.2), the PFPE(2500)-carboxylic acid (2 g, 0.8 mmol, molecular weight 2500 g mol⁻¹, DuPont, The Netherlands) was added to a 20 ml aqueous solution of PEG5000-OMe (4 g, 0.8 mmol, molecular weight 5000 g mol⁻¹, Fluka, Germany). Subsequently, KOH (5 N, 160 µl, 0.8 mmol, Sigma Aldrich, Germany) was added dropwise and stirred for 10 min. The solvent was removed at a rotary evaporator and the product dried on the vacuum line. Yield: 5.52 g, 92%.

7.3.2

Fabrication of Nanostructured PEG-DA Hydrogel Beads by Droplet-Based Microfluidics

A droplet-based microfluidic device made of PDMS (Sylgard 184, Dow Corning, Midland, MI) was prepared by standard photo and soft lithography methods, as described previously [30,42]. To create droplets of a PEG-DA_(precursor)-in-oil emulsion, the required flow rates were adjusted for the different PEG-DA

Table 7.3 Flow rate parameters successfully applied for stable droplet formation.

PEG-DA	Concentration in water (mg ml^{-1})	Aqueous phase ($\mu\text{l h}^{-1}$)	Oil phase ($\mu\text{l h}^{-1}$)	Flow ratio
PEG(700)-DA	600	50	350	1:7
PEG(6000)-DA		90	180	1:2
PEG(10 000)-DA	400	50	200	1:4
PEG(20 000)-DA		50	400	1:8
PEG(35 000)-DA		10	150	1:15

precursor solutions; an overview of the successfully applied flow rates is given in Table 7.3. (Note: Different PEG-DA precursor solutions were prepared according to the protocol described in Section 7.2.2.)

Figure 7.10a and b depict a microfluidic device and the flow-focusing junction in which the droplets were created, respectively. In all experiments, the aqueous phase contained PEG-DA precursor solution and the FC-40 oil phase contained the surfactant mixture of 20 mM PFPE(7000)–PEG(750)–OMe and PFPE(2500)–PEG(300)–gold transfer linker at three different concentrations (0.3, 3, and 30 μM). The formed droplets were collected in a pipette tip at the outlet and stored upright in Eppendorf tubes (1.5 ml) for

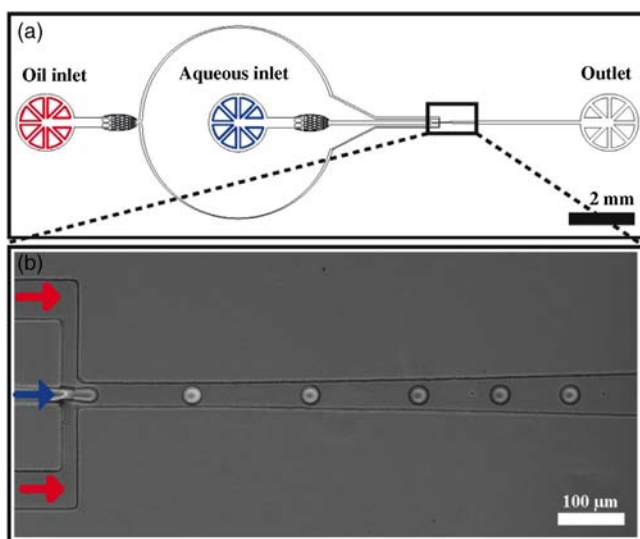


Figure 7.10 (a) Representation of the droplet-based microfluidic device. (b) Shows the flow-focusing junction with 20 μm width channels, in which the droplets are generated and flow to the outlet.

ultraviolet irradiation (intensity of 3 mW cm^{-2}) for 2 h. To transfer the beads from oil to water phase, the oil solution of PEG-DA beads was cast on a petri dish in order to evaporate the oil at 60°C over night. To remove the oil completely, PEG-DA hydrogel beads were washed with a 5 mM aqueous solution of hydrophilic diblock copolymer surfactant PFPE(2500)-PEG(5000)-OMe. Finally, hydrogel beads were sterilized in ethanol (70%) for 2 h and transferred to Milli-Q water for the subsequent biofunctionalization and characterization steps.

7.3.3

Characterization of Nanostructured PEG-DA Hydrogel Beads

To verify the successful formation of gold nanostructured PEG-DA beads and to quantitatively estimate the gold nanoparticle density, the beads were investigated by cryo-SEM (see Section 7.2.2). Figure 7.11 shows representative cryo-SEM micrographs of the nanostructured PEG-DA beads. The beads were created using different concentrations of gold-linked surfactants (30, 3, and $0.3 \mu\text{M}$). In Figure 7.11c and d, the direct correlation between gold nanoparticle density on the periphery of the beads and gold-linked surfactant concentration can be observed.

Similar to 2D hydrogels (see Section 7.2.2), indentation measurements were applied to assess the mechanical properties of the PEG-DA beads. Hydrogel beads were glued to the surface of a 60 mm petri dish using an ethyl-2-cyanoacrylate tissue adhesive (EPIGLU, Meyer Haake, Germany) to prevent movement during indentation measurements and filled with 2 ml of PBS. Prior to testing,

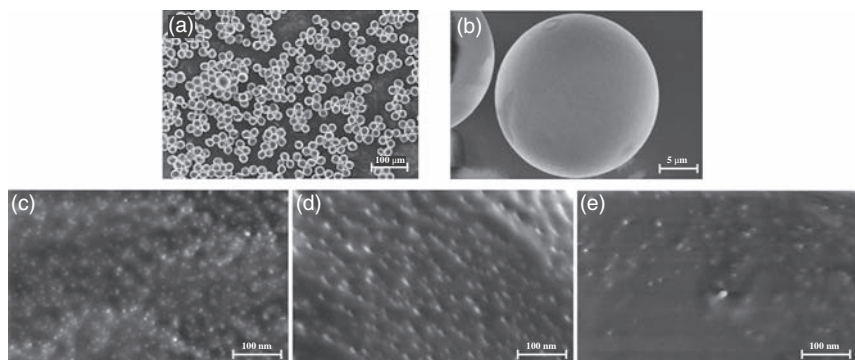


Figure 7.11 (a and b) Representative cryo-SEM micrographs of the nanostructured PEG(10 000)-DA beads, obtained with different magnifications. The different gold nanoparticle ($\sim 5 \text{ nm}$ in diameter) densities on the

beads periphery are directly related to the three different concentrations of gold-linked surfactant: 30, 3, and $0.3 \mu\text{M}$ are used for bead formation, as represented in parts (c)–(e), respectively.

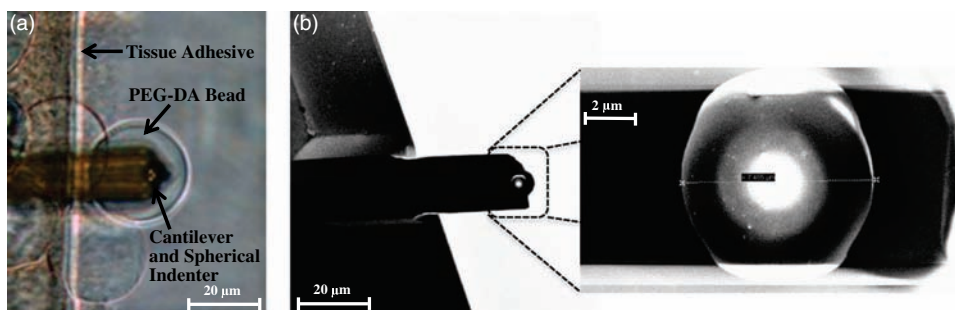


Figure 7.12 Representation of the indentation measurements. (a) Top-view bright-field image of the cantilever on top of the PEG-DA bead. (b) SEM micrographs of the cantilever used for indentation measurements with the spherical indenter of about 8 μm in diameter.

cantilever deflection sensitivity was calibrated on a bare petri dish filled with PBS. Figure 7.12a presents a top-view image of a cantilever with the spherical indenter during the indentation measurement. Indentation measurements revealed mechanical properties of the hydrogel beads similar to those of 2D hydrogel substrates (see Section 7.2.2).

7.3.4

Biofunctionalization

The beads were functionalized by immobilizing antibodies on the gold nanostructured PEG-DA beads via NTA/ Ni^{2+} /His chemistry and the antibody-binding protein G following the same protocol as described for 2D hydrogel substrates (see Section 7.2.3). In between the different biofunctionalization steps, the beads were washed with 5 ml of appropriate buffer and centrifuged ($100 \times g$, 5 min) to remove the loosely bound molecules with the supernatant. Alexa Fluor 488-labeled anti-CD3 antibodies were used to prove the successful biofunctionalization of the gold nanoparticles on hydrogels, as shown in Figure 7.13a.

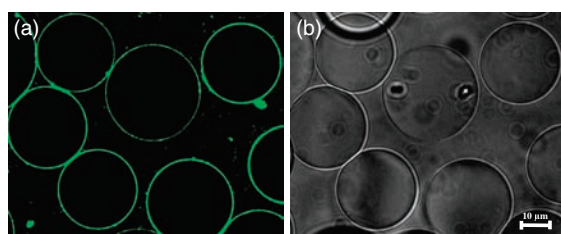


Figure 7.13 Representative (a) fluorescence and (b) bright field images of the gold-nanostructured PEG-DA beads linked with Alexa Fluor 488 labeled anti-CD3, measured 1 day after biofunctionalization.

7.4

Nanostructured and Specifically Biofunctionalized Droplets of Water-in-Oil Emulsion: General Properties

We have already highlighted the powerful role of the crosstalk between the spatial organization of chemical cues and the mechanical properties of the APC surrogates for T-cell activation studies. We showed that 2D hydrogel substrates and 3D beads can provide good control over signal delivery and that their mechanical properties resemble qualitatively the actin cytoskeleton functions. However, the ability of these systems to serve as optimal APC analogues is still hindered by their inability to dynamically remodel their protein composition, which is in stark contrast to natural APC-T cell interactions.

The most common technology used to allow the dynamic reorganization of the ligands in the case of 2D planar APC analogues is based on supported lipid bilayers (SLBs). SLBs provide a suitable model system for mimicking the cell membrane because the lateral mobility of lipids and proteins partially resembles the *in vivo* situation [43,44]. SLBs containing fluorescent-labeled APC ligands enabled the discovery of the IS and have been heralded as a powerful model for investigating the dynamically coordinated formation of micrometer-scale spatial patterns of cellular surface molecules, the so-called supramolecular activation clusters [45–48]. However, the major disadvantage of this system lies in its inability to enable T cells to exert force in all three dimensions. Unlike biological membranes, planar bilayers do not permit any pushing or pulling of proteins by force. Instead, proteins are trapped on the glass surface causing rigidity in the vertical dimension. Moreover, T-cell experiments with SLBs and the aforementioned 3D or 2D APC surrogate systems were performed on T cells cultivated in batch suspension mode. Unfortunately, this mode has several drawbacks related to the long-term dynamic analysis and control over T-cell processes using live cell imaging. First, primary T cells are nonadherent and become highly motile upon activation – this means they rapidly escape out of the microscopic field. Second, the cell's cytokine secretions become diluted and mixed in a contiguous sample. Finally, T-cell activation is considered to be a stochastic process. Therefore, analyzing individual T cells and their most proximal environment might bring new insights into different events underlying T-cell response. One promising method to avoid such difficulties is to utilize microfluidic devices to encapsulate, culture, and monitor T cells in close confinements over long periods of time.

Picoliter-sized droplets of water-in-oil emulsions created in a droplet-based microfluidic device have recently been tested and used as 3D confinements for *ex-vivo* translation, encapsulation, and incubation of different cell types [49]. Inspired by these confinements, we synthesized and developed a novel approach to form gold-nanostructured and specifically biofunctionalized droplets of water-in-oil emulsions with the potential to serve as 3D APC surrogates (Figure 7.14a). The combination of flexible biofunctionalization, the pliable soft and dynamic nature of droplets, and a controlled environment for individual T-cell analysis

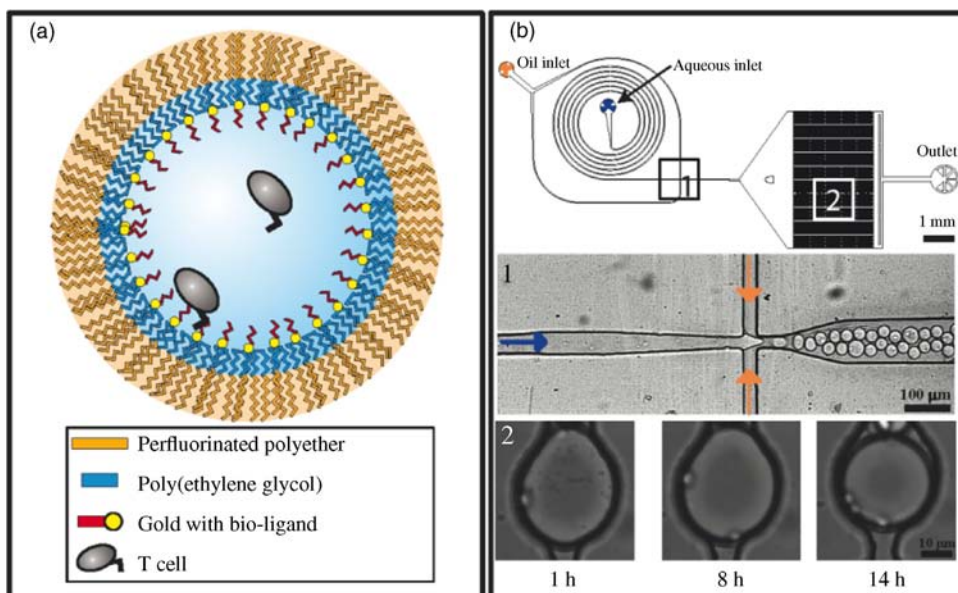


Figure 7.14 (a) Schematic representation of two encapsulated T cells inside the nanostructured and biofunctionalized water-in-oil emulsion droplet. (b) Representation of the droplet-based microfluidic device. Inset 1 shows the flow-focusing junction with 20 μm wide nozzle. Here the droplets are generated and T

cells are encapsulated. Then the cell-containing droplets flow to the analysis chamber, as represented in inset 2 for high-throughput analysis of individual T cells. Inset 2 shows the representative bright field images of Jurkat E6.1 T cells proliferating inside the cRGD-functionalized droplets.

add up to a system that combines physical and biochemical key functions of professional APCs and provides a flexible and modular system for APC–T-cell interaction analysis.

Similar to the creation of PEG-DA beads (see Section 7.3), synthesized gold-linked surfactants (Figure 7.15) were mixed with nonionic stabilizing surfactants (Figure 7.16) at different concentration ratios to form stable droplets ($\sim 30 \mu\text{m}$ in diameter) coated with gold nanoparticles at various densities. Two different approaches were used to test how efficiently the gold nanoparticles inside the droplets can serve as anchoring points and to provide the required chemical and biological key functions of APCs. The first approach was based on the functionalization of the created droplets using NTA and (His6-tag) proteins. The second approach involved two steps: the synthesis of gold-linked surfactants coupled to bioactive molecules and the subsequent creation of bioactive droplets. The nanostructured droplets were functionalized with cyclic arginine–glycine–aspartic acid peptide (cRGDfK) to establish specific interactions with Jurkat E6.1 T cells (cells that express $\alpha_4\beta_1$ and $\alpha_5\beta_1$ integrins and exhibit activation-dependent regulation of integrin-mediated adhesion). Remarkably, more than

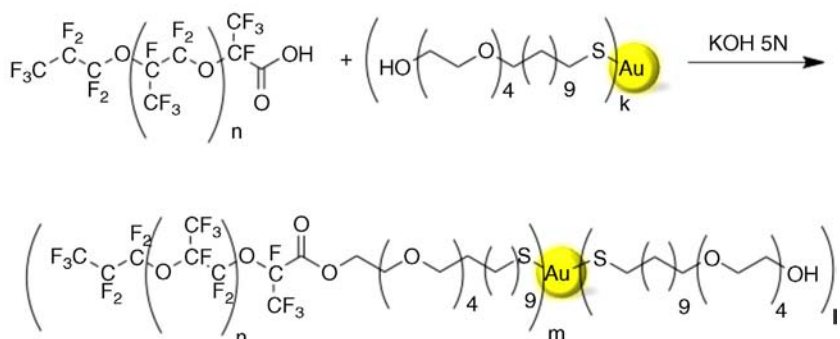


Figure 7.15 Synthesis of PFPE(7500)-PEG(350)-gold diblock copolymer surfactants.

90% of encapsulated T cells were found to be in contact with the inner periphery of the droplets, compared to less than 10% in the case of droplets without functionalization. Moreover, the cells in the functionalized droplets exhibited induced proliferation and remained viable for up to 5 days of incubation without any external nutrition. Maintaining cell viability for a longer time period would have required either enlarging the droplet size or exogenous addition of nutrients by means of picoinjection technology [50].

7.4.1

Surfactant Synthesis

Synthesis of the gold-linked diblock copolymer surfactants PFPE(7500)-PEG(350)-gold was performed in a one-step process (Figure 7.15) [30]. PFPE(7500)-carboxylic acid (7.5 mg, 1 µmol, DuPont, The Netherlands) and KOH (5 N, 10 µl) were added to 1 ml of gold nanoparticle solution (see Section 7.3.1) and stirred for 1 h. The PFPE-PEG-gold and unreacted PFPE were flocculated during the

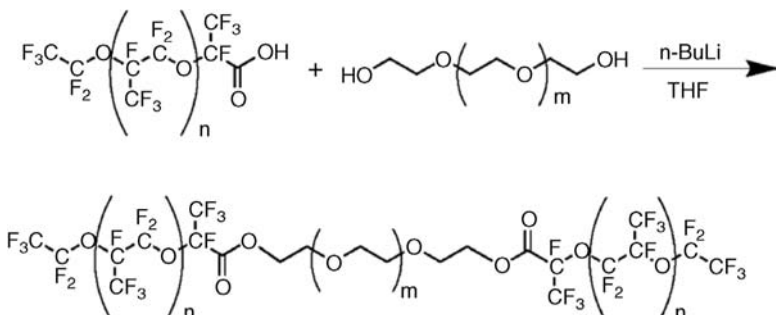


Figure 7.16 One-step esterification synthesis of PFPE(2500)-PEG(600)-PFPE(2500) triblock copolymer surfactants.

reaction. The water was removed by freeze-drying for 24 h. The product was dissolved in 1 ml of fluorinated oil FC-40 (Acros Organics, Germany) and filtered with a hydrophobic filter (PTFE 0.2 µm, Roth, Germany) to remove unreacted, hydrophilic (11-Mercaptoundecyl)tetra(ethylene glycol)-functionalized gold nanoparticles, resulting in the desired PFPE(7500)-PEG(350)-gold diblock copolymer surfactant (22 mg, 80%).

The synthesis of the PFPE-PEG-PFPE triblock followed the procedure reported earlier [51] but with several modifications [30], as shown in Figure 7.16. PEG(600) (600 mg, 1 mmol, Fluka, Germany) was dissolved under argon atmosphere in 80 ml dry THF and cooled to -78 °C. *N*-Butyl lithium (1.22 ml of a 1.6 M solution in hexane, 2 mmol, Sigma-Aldrich, Germany) was added dropwise over a period of 60 min at -78 °C to the PEG solution and stirred for additional 30 min at -78 °C. Under continuous stirring, the reaction was slowly heated to room temperature followed by additional 30 min of stirring. Then, PFPE(2500)-carboxylic acid (5 g, 2 mmol, DuPont, The Netherlands) was added dropwise over a period of 30 min and stirred for another 12 h. After the reaction was finished, the THF solvent with unreacted PEG was removed by separatory funnel. Two additional washing steps with dry THF solvent were used to purify the crude product from the unreacted PEG. The product was dissolved in methanol (Carl Roth GmbH, Germany) to separate it from unreacted PFPE(2500)-carboxylic acid. The PFPE-PEG-PFPE product, soluble in methanol, was transferred to a clean flask and dried with a rotary evaporator at 40 °C. After removing the methanol and drying on the vacuum line, the desired PFPE-PEG-PFPE triblock copolymer surfactant was obtained (4.6 g, 82%).

The synthesis of perfluorooctanyl-triethylene glycol (PFO-PEG), which was used as an emulsion destabilizer (see Section 7.4.5.2), was carried out under argon atmosphere in dry THF solvent in a heated Schlenk flask [30]. Triethylene glycol (6.36 g, 30.6 mmol, molecular weight 208.05 g mol⁻¹, Sigma-Aldrich, Germany) was added to 200 ml dry THF and cooled to -78 °C. *N*-Butyl lithium (18.5 ml of a 1.6 M solution in hexane, 29.6 mmol) was added dropwise over a period of 60 min at -78 °C to the PEG solution and stirred for additional 30 min at -78 °C. Under continuous stirring, the reaction was slowly heated to room temperature followed by an additional 30 min of stirring. Pentadecafluoroctanoyl chloride (12.97 g, 30 mmol, molecular weight 432.51 g mol⁻¹, Sigma-Aldrich, Germany) was added dropwise over a period of 30 min and stirred for another 4 h. After the reaction was finished, the THF solvent with unreacted PEG was removed by separatory funnel. The crude product was washed with 10 ml water to remove the lithium chloride. Following the washing procedures, the crude product was dried on the vacuum line and purified using column chromatography. The column was packed with silica gel and a mix of petroleum ether (40/60) and THF (mix 2 : 1) was used as mobile phase. The diblock product ($R_f = 0.28$) of bright yellow color was obtained in a yield of 9.02 g (16.02 mmol, 55%).

7.4.2

Droplet-Based Microfluidics

As described in Section 7.3.2, the droplet-based microfluidic device made of PDMS was prepared by standard photo and soft lithography methods (Figure 7.14b). To create droplets, the FC-40 oil phase contained a mixture of 20 mM triblock copolymer and gold-linked diblock copolymer surfactants at two different concentrations (3 and 30 µM, respectively). T cells in a complete RPMI medium (aqueous phase) were injected into a curved inlet microchannel (Figure 7.14b). This channel is required for Dean-coupled inertial ordering of cells and allows single-cell encapsulation per droplet in a flow-focusing junction (inset 1) [52]. Following the creation step, the droplets flow into the dropspot chamber (inset 2) for high-throughput time lapse studies of individual T cells. In the dropspot chamber, up to 1 000 000 droplets can be stored.

7.4.3

Characterization of the Gold Nanostructured Droplets of Water-in-Oil Emulsion

The thus obtained droplets were freeze-fractured and investigated by cryo-SEM to verify the successful creation of the nanostructured droplets. Toward this end, an emulsion droplet solution (5 µl) was dropped on 0.8 mm diameter gold specimen carriers assembled on a freeze-fracture holder (BAL-TEC AG, Liechtenstein) and immersed immediately in liquid nitrogen. After vitrification in liquid nitrogen, the droplets were transferred to a BAL-TECH MED 020 preparation device via an evacuated liquid nitrogen-cooled shuttle BAL-TECH VLC 100. For freeze-fracture cryo observations, the droplets were fractured in a 10^{-6} – 10^{-7} mbar vacuum chamber at -160°C with a cooled knife. After fracturing, the stage was heated to -90°C and kept in the vacuum for 60 min in order to allow the aqueous phase in the fractured droplets to sublime. For cryo-SEM imaging, the samples were transferred immediately to the SEM chamber via an evacuated liquid nitrogen-cooled shuttle.

Figure 7.17 shows representative cryo-SEM (top view) micrographs of the freeze-fractured nanostructured droplets created using two different concentrations of the gold-linked surfactants (30 and 3 µM). The gold nanoparticles of ~ 5 nm in diameter are presented on the inner periphery of the droplet. A higher density of the gold nanoparticles and their more homogeneous distribution can be observed in the droplets obtained with a higher concentration (30 µM) of the gold-linked surfactants.

7.4.4

Biofunctionalization of the Nanostructured Droplets

Two different biofunctionalization approaches were tested [30]. The first approach was based on the functionalization of the created droplets using

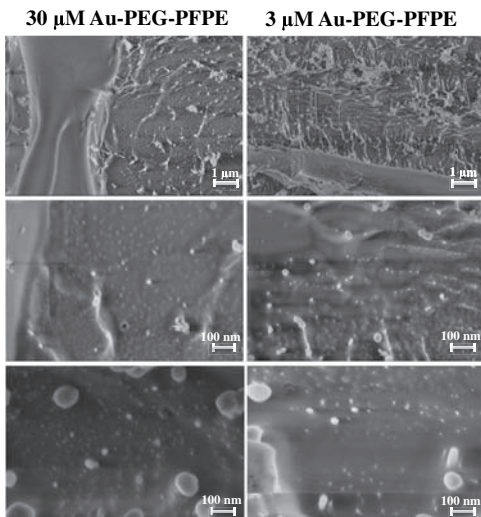


Figure 7.17 Representative cryo-SEM micrographs of the freeze-fractured nanostructured droplets created using different concentrations of gold-linked surfactants [30].

(His6-tag) proteins and NTA chemistry, and the second approach involved two steps: the synthesis of gold-linked surfactants coupled to bioactive molecules and the subsequent creation of biofunctionalized droplets. Successful functionalization of the nanostructured droplets with (His6-tag) proteins is particularly important since the chemistry behind the immobilization of these proteins is the same as is required for the immobilization of the peptide-loaded major histocompatibility complexes (pMHC) or antibodies such as anti-CD3 and anti-CD28, which are important in T-cell activation (see Sections 7.2.3 and 7.3.4).

(His6-tag)-GFP (300 µl, 30 µM) (GFP was a gift of S. Gardia Addgene plasmid #29663; protein was expressed in *Escherichia coli* using standard protocols and purified by Ni-NTA chromatography) was mixed with NiCl₂ (9 µl, 100 mM, Fluka, Germany) and NTA-thiol (300 µl, 1 mM, ProChimia, Poland) and diluted with 600 µl PBS. NTA-thiol and NiCl₂ were mixed by stirring for 20 min. Ethanol was removed to a final volume of 50 µl by nitrogen flow. Following this procedure, the (His6-tag)-GFP was added and mixed for another 1 h. PBS was added and a final GFP concentration of 8 µM was determined using the extinction coefficient $\epsilon = 30\,000$ at A_{395nm}. A similar chemistry was applied to pMHC fluorescently labeled with [moth cytochrome C 88–103 (MCC)-Alexa Fluor 568]-IEk-2xHis6 (a kind gift of Michael Dustin, Kennedy Institute of Rheumatology, Oxford, UK).

Two types of droplets were investigated; those containing only PFPE–PEG–PFPE (20 mM) surfactants and another containing a mixture of PFPE–PEG–PFPE (20 mM) and gold–PEG–PFPE (30 µM) surfactants in oil phase. Figure 7.18

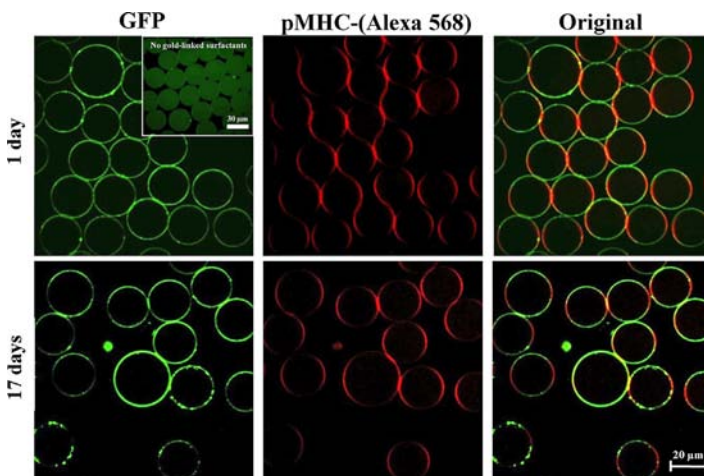


Figure 7.18 Representative fluorescence images of the (His6-tag) GFP- and (His6-tag) pMHC-linked nanostructured droplets, measured 1 day (upper row) and 17 days (lower row) after

creation. All images have the same intensity scale. The inset shows the equal distribution of the fluorescence intensity in the droplets having no gold-linked surfactants.

shows fluorescence images of the (His6-tag) GFP- and (His6-tag) pMHC-linked nanostructured droplets taken 1 day and 17 days after creation. It can be seen that the fluorescence is concentrated on the periphery of the droplets. The inset figure shows a fluorescence image of the non-gold nanostructured droplets taken 1 day after creation. It can be seen that the fluorescence intensity is distributed equally inside the droplets.

To provide cell interactions with nanostructured droplets, the two-step method was used to immobilize c(RGDfK)-PEG-(cysteine)₃ peptide (Peptide Specialty Laboratories GmbH, Germany) on gold nanoparticles via cysteine linker. The freeze-dried PFPE(7500)-PEG(350)-gold diblock copolymer surfactants (see Section 7.4.1) were dissolved in 100 µl FC-40 and then an aqueous solution of cRGD (50 µM, 100 µl) was added and stirred for 1 h. To remove the unbound cRGD peptide, the crude product solution was centrifuged. The supernatant solution was removed and the precipitant was freeze-dried for 24 h to remove completely the remaining water. Finally, the product was dissolved in 1 ml of fluorinated oil FC-40 (Acros Organics, Germany) and filtered with a hydrophobic filter (PTFE 0.2 µm) to remove unreacted peptide traces.

7.4.5

Cell Experiments

7.4.5.1 Cell Culture

The human acute T-cell leukemia cell line Jurkat E6.1 clone was purchased from ATCC (American Type Culture Collection, Manassas, VA) and maintained in

RPMI 1640 supplemented with 2 mM L-glutamine, 10% FBS, and 1% (v/v) penicillin/streptomycin at 37 °C and 5% CO₂.

For adhesion experiments, Jurkat E6.1 cells (30×10^6 cells) were suspended in 1 ml adhesion medium (RPMI 1640, 2 mM L-glutamine, 1% FBS, and 1% (v/v) penicillin/streptomycin). This cell-containing medium was used as an aqueous phase for droplet creation (Figure 7.14b, inset 1). To encapsulate T cells within the droplets at the rate of 18 000/s, the flow rates were adjusted to 1200 $\mu\text{l h}^{-1}$ for the oil phase and to 900 $\mu\text{l h}^{-1}$ for the aqueous phase (cell culture media and cells). Droplets imaging was performed using an AxioVert 40 CFL microscope (Zeiss, Germany).

7.4.5.2 Cell Recovery and Live/Dead Staining

Recovery of encapsulated cells and live/dead staining followed the procedure reported earlier [53], but with several modifications [30]. From each experiment, 1 ml of the resulting droplets emulsion was split equally between five (1 ml) falcons and incubated within the incubator condition (37 °C, 5% CO₂). After different incubation times (1, 2, 3, 4, and 5 days), the emulsion was broken by the addition of 5% v/v PFO–PEG surfactants, which function as an emulsion destabilizer (see Section 7.4.1), and the supernatant was transferred into a 15 ml centrifuge tube. The cells were washed with 10 ml PBS and centrifuged to remove serum esterase activity. Following the washing step, 100 μl of cell-containing buffer solution was added to the microplate reader flat-bottom well with a total capacity of 250–300 μl . The cells were treated for 45 min at room temperature with the 100 μl of the live/dead staining solution, containing 2 μM calcein AM and 4 μM ethidium homodimer-1 (Live/Dead Viability/Cytotoxicity Kit for mammalian cells, Invitrogen Kit L-3224, Invitrogen, Germany). After staining, the percentage of live cells was calculated from fluorescence measurements using the microplate reader.

7.4.5.3 Results

To establish specific interactions with Jurkat E6.1 T cells – cells that express $\alpha_4\beta_1$ and $\alpha_5\beta_1$ integrins and exhibit activation-dependent regulation of integrin-mediated adhesions [54] – the nanostructured droplets were functionalized with cRGDfK peptide, which is specific against $\alpha_5\beta_1$ (see Section 7.4.4). A curved inlet microchannel (Figure 7.14b) was required to allow single-cell encapsulation per droplet. Remarkably, more than 90% of encapsulated T cells were found to be in contact with the inner periphery of the droplets after 1 h of incubation, compared with less than 10% in the case of nonfunctionalized droplets [30]. Moreover, the cells proliferated in the functionalized droplets (Figure 7.14b, inset 2) and remained viable for up to 5 days of incubation without the addition of any further supplements. This study highlighted the advanced properties of emulsion droplets for use in T-cell stimulation. The combination of flexible biofunctionalization and pliable physical droplet properties can play a crucial role because it results in a flexible and modular system that closely models *in situ* APC–T cell interactions.

7.5

Summary and Outlook for the Future

In this chapter, a synthetic approach for studying the complex encounters between T cells and APCs within the lymph node has been discussed. We primarily addressed the complexity of these interactions and highlighted the important role that crosstalk between the mechanical and biochemical parameters of the antigen-presenting interfaces plays in T-cell functions. We summarized in detail our recently developed methods that allow individual control of the substrate stiffness and the distribution of available T-cell stimulatory ligands by fabricating nanoscopically controlled biomolecule anchors and their transfer to PEG-based 2D and 3D soft/elastic nanopatterned systems. It is our expectation that optimization of these and other precisely engineered APC surrogates might provide novel insights into the mechanisms underlying the ability of T cells to perform “intelligent” missions, such as acquiring, processing, and responding to environmental information.

Acknowledgments

Parts of the research leading to these results have received funding from the European Union Seventh Framework Programme (FP7/2007–2013) under grant agreement Nos. NMP4-LA-2009-229289 NanoII and NMP3-SL-2009-229294 NanoCARD, as well as from an ERC Advanced Grant under grant agreement No. 294852-SynAd. This work is also part of the MaxSynBio consortium which is jointly funded by the Federal Ministry of Education and Research of Germany and the Max Planck Society. I.P. gratefully acknowledges the support of the Alexander von Humboldt Foundation. J.P.S. is the Weston Visiting Professor at the Weizmann Institute of Science. The authors acknowledge the support of the excellence cluster CellNetworks at the University of Heidelberg. The Max Planck Society is appreciated for its general support in all aspects of our research.

References

- 1 Haile, L.A., Von, W.R., Gamrekelashvili, J., Kruger, C., Bachmann, O., Westendorf, A.M., Buer, J., Liblau, R., Manns, M.P., Korangy, F., and Greten, T.F. (2008) *Gastroenterology*, **135**, 871.
- 2 Hoxie, J.A. and June, C.H. (2012) *Cold Spring Harb. Perspect. Med.*, **2**, a007179.
- 3 Vonderheide, R.H. and June, C.H. (2014) *Immunol. Rev.*, **257**, 7.
- 4 June, C., Rosenberg, S.A., Sadelain, M., and Weber, J.S. (2012) *Nat. Biotechnol.*, **30**, 611.
- 5 Grupp, S.A., Kalos, M., Barrett, D., Aplenc, R., Porter, D.L., Rheingold, S.R., Teachey, D.T., Chew, A., Hauck, B., Wright, J.F., Milone, M.C., Levine, B.L., and June, C.H. (2013) *N. Engl. J. Med.*, **368**, 1509.
- 6 Rosenberg, S.A. and Dudley, M.E. (2009) *Curr. Opin. Immunol.*, **21**, 233.
- 7 Kalos, M. and June, C.H. (2013) *Immunity*, **39**, 49.
- 8 Manz, B.N. and Groves, J.T. (2010) *Nat. Rev. Mol. Cell Biol.*, **11**, 342.
- 9 Milone, M.C. and Kam, L.C. (2013) *Wiley Interdiscip. Rev. Nanomed. Nanobiotechnol.*, **5**, 75.
- 10 Platzman, I., Janiesch, J.W., Matic, J., and Spatz, J.P. (2013) *Isr. J. Chem.*, **53**, 655.

- 11 Huppa, J.B. and Davis, M.M. (2003) *Nat. Immunol.*, **3**, 973.
- 12 Mescher, M.F., Curtsinger, J.M., Agarwal, P., Casey, K.A., Gemer, M., Hammerbeck, C.D., Popescu, F., and Xiao, Z.G. (2006) *Immunol. Rev.*, **211**, 81.
- 13 Steenblock, E.R., Wrzesinski, S.H., Flavell, R.A., and Fahmy, T.M. (2009) *Expert Opin. Biol. Ther.*, **9**, 451.
- 14 Turtle, C.J. and Riddell, S.R. (2010) *Cancer J.*, **16**, 374.
- 15 Alon, R. and Dustin, M.L. (2007) *Immunity*, **26**, 17.
- 16 Judokusumo, E., Tabdanov, E., Kumari, S., Dustin, M.L., and Kam, L.C. (2012) *Biophys. J.*, **102**, L5.
- 17 O'Connor, R.S., Hao, X.L., Shen, K.Y., Bashour, K., Akimova, T., Hancock, W.W., Kam, L.C., and Milone, M.C. (2012) *J. Immunol.*, **189**, 1330.
- 18 Springer, T.A. and Dustin, M.L. (2012) *Curr. Opin. Cell Biol.*, **24**, 107.
- 19 Kim, J.V., Latouche, J.B., Riviere, I., and Sadelain, M. (2004) *Nat. Biotechnol.*, **22**, 403.
- 20 Oelke, M., Krueger, C., Giuntoli, R.L., and Schneck, J.P. (2005) *Trends Mol. Med.*, **11**, 412.
- 21 Polleux, J., Rasp, M., Louban, I., Plath, N., Feldhoff, A., and Spatz, J.P. (2011) *ACS Nano*, **5**, 6355.
- 22 Deeg, J., Axmann, M., Matic, J., Liapis, A., Depoil, D., Afrose, J., Curado, S., Dustin, M.L., and Spatz, J.P. (2013) *Nano Lett.*, **13**, 5619.
- 23 Matic, J., Deeg, J., Scheffold, A., Goldstein, I., and Spatz, J.P. (2013) *Nano Lett.*, **13**, 5090.
- 24 Ilani, T., Vasiliver-Shamis, G., Vardhana, S., Bretscher, A., and Dustin, M.L. (2009) *Nat. Immunol.*, **10**, 531.
- 25 Li, Y.C., Chen, B.M., Wu, P.C., Cheng, T.L., Kao, L.S., Tao, M.H., Lieber, A., and Roffler, S.R. (2010) *J. Immunol.*, **184**, 5959.
- 26 Restifo, N.P., Dudley, M.E., and Rosenberg, S.A. (2012) *Nat. Rev. Immunol.*, **12**, 269.
- 27 Aydin, D., Louban, I., Perschmann, N., Blummel, J., Lohmuller, T., Cavalcanti-Adam, E.A., Haas, T.L., Walczak, H., Kessler, H., Fiammengo, R., and Spatz, J.P. (2010) *Langmuir*, **26**, 15472.
- 28 Platzman, I., Gadomska, K.M., Janiesch, J.-W., Louban, I., Cavalcanti-Adam, E.A., and Spatz, J.P. (2014) *Methods in Cell Biology*, vol. **119** (eds M. Piel and M. Théry), Academic Press, p. 237.
- 29 Platzman, I., Muth, C.A., Lee-Thedieck, C., Pallarola, D., Atanasova, R., Louban, I., Altrock, E., and Spatz, J.P. (2013) *RSC Adv.*, **3**, 13293.
- 30 Platzman, I., Janiesch, J.-W., and Spatz, J.P. (2013) *J. Am. Chem. Soc.*, **135**, 3339.
- 31 Lillemoer, B.F., Mortelmaier, M.A., Forstner, M.B., Huppa, J.B., Groves, J.T., and Davis, M.M. (2010) *Nat. Immunol.*, **11**, 90.
- 32 Glass, R., Möller, M., and Spatz, J.P. (2003) *Nanotechnology*, **14**, 1153.
- 33 Blummel, J., Perschmann, N., Aydin, D., Drinjakovic, J., Surrey, T., Lopez-Garcia, M., Kessler, H., and Spatz, J.P. (2007) *Biomaterials*, **28**, 4739.
- 34 Dyer, M.A., Ainslie, K.M., and Pishko, M.V. (2007) *Langmuir*, **23**, 7018.
- 35 Graeter, S.V., Huang, J., Perschmann, N., Lopez-Garcia, M., Kessler, H., Ding, J., and Spatz, J.P. (2007) *Nano Lett.*, **7**, 1413.
- 36 Hertz, H. (1882) *J. Reine Angew. Math.*, **94**, 156 (English translation in miscellaneous papers by H. Hertz (1896), Jones and Schott, Macmillan, London).
- 37 Quah, B.J.C., Warren, H.S., and Parish, C.R. (2007) *Nat. Protoc.*, **2**, 2049.
- 38 Deeths, M.J., Kedl, R.M., and Mescher, M.F. (1999) *J. Immunol.*, **163**, 102.
- 39 Levine, B.L., Bernstein, W.B., Connors, M., Craighead, N., Lindsten, T., Thompson, C.B., and June, C.H. (1997) *J. Immunol.*, **159**, 5921.
- 40 Mescher, M.F. (1992) *J. Immunol.*, **149**, 2402.
- 41 Wei, X.B., Tromberg, B.J., and Cahalan, M.D. (1999) *Proc. Natl. Acad. Sci. USA*, **96**, 8471.
- 42 Duffy, D.C., McDonald, J.C., Schueller, O.J.A., Whitesides, G.M., Baroud, G.M., Delville, J.P., Gallaire, F., and Wunenburger, R. (1998) *Anal. Chem.*, **70**, 4974.
- 43 Sackmann, E. (1996) *Supramol. Sci.*, **271**, 43.
- 44 Yu, C.H. and Groves, J.T. (2010) *Med. Biol. Eng. Comput.*, **48**, 955.
- 45 Campi, G., Varma, R., and Dustin, M.L. (2005) *J. Exp. Med.*, **202**, 1031.

- 46** DeMond, A.L., Mossman, K.D., Starr, T., Dustin, M.L., and Groves, J.T. (2008) *Biophys. J.*, **94**, 3286.
- 47** Grakoui, A., BromLey, S.K., Sumen, C., Davis, M.M., Shaw, A.S., Allen, P.M., and Dustin, M.L. (1999) *Supramol. Sci.*, **285**, 221.
- 48** Groves, J.T. and Dustin, M.L. (2003) *J. Immunol. Methods*, **278**, 19.
- 49** Lagus, T.P. and Edd, J.F. (2013) *J. Phys. D Appl. Phys.*, **46**, 114005.
- 50** Abate, A.R., Hung, T., Mary, P., Agresti, J.J., and Weitz, D.A. (2010) *Proc. Natl. Acad. Sci. USA*, **107**, 19163.
- 51** Holtze, C., Rowat, A.C., Agresti, J.J., Hutchison, J.B., Angile, F.E., Schmitz, C.H.J., Köster, S., Duan, H., Humphry, K.J., Scanga, R.A., Johnson, J.S., Pisignano, D., and Weitz, D.A. (2008) *Lab Chip*, **8**, 1632.
- 52** Kemna, E.W.M., Schoeman, R.M., Wolbers, F., Vermes, I., Weitz, D.A., and van den Berg, A. (2012) *Lab Chip*, **12**, 2881.
- 53** Clausell-Tormos, J., Lieber, D., Baret, J.C., El-Harrak, A., Miller, O.J., Frenz, L., Blouwolff, J., Humphry, K.J., Koster, S., Duan, H., Holtze, C., Weitz, D.A., Griffiths, A.D., and Merten, C.A. (2008) *Chem. Biol.*, **15**, 427.
- 54** Romzek, N.C., Harris, E.S., Dell, C.L., Skronek, J., Hasse, E., Reynolds, P.J., Hunt, S.W., and Shimizu, Y. (1998) *Mol. Biol. Cell*, **9**, 2715.

8

Soft Matter Assembly for Atomically Precise Fabrication of Solid Oxide

Norifusa Satoh

8.1

Introduction

Soft matter has innovated synthetic capacity of hard matter in nano- and micro-scales (Figure 8.1). Conventional hard matter is synthesized through crystal nucleation and growth. The fine controls of these processes give diverse nanostructures such as nanoparticles [1–4], nanowires [5–9], and nanotrees [10–12]. However, the growth based on crystal faces has limited the shapes of nanostructures. Due to their flexibility, bioinspired soft matter templates provide nano/microstructures based on their assembled structures. For example, tunable length of alkyl chain in micelle templates controls pore size of the mesoporous silica [13,14]. Various types of assembling structures of block copolymer templates [15] produce a variety of nanodots [16,17], nanowire arrays [18], mesopores [19,20], nanopores [21], and trenches [22]. With a view to advance the concept, this chapter briefly reviews atomically precise fabrication in nanotechnology and then moves on to soft matter assembly for atomically precise oxide depositions.

8.2

The Ultimate Goal of Nanotechnology: Atomically Precise Fabrication

The ideas and concepts behind nanotechnology started with the lecture “There’s Plenty of Room at the Bottom” by an American physicist, Richard Feynman, in 1959 [23]. People realized the importance of manipulating the individual atoms and molecules in materials and electronic devices through a more sophisticated and direct methodology than the “mysterious” chemical synthesis mixing, shaking, and fiddling away chemical agents many times (Figure 8.2). In 1969, Esaki and Tsu proposed a new concept, superlattice structure [24], based on their observation of quantum tunneling on 10 nm thick barriers [25]. The concept led to develop a methodology, molecular beam epitaxy (MBE) [26], controlling crystal film growth with atomic precision under a high vacuum condition. MBE

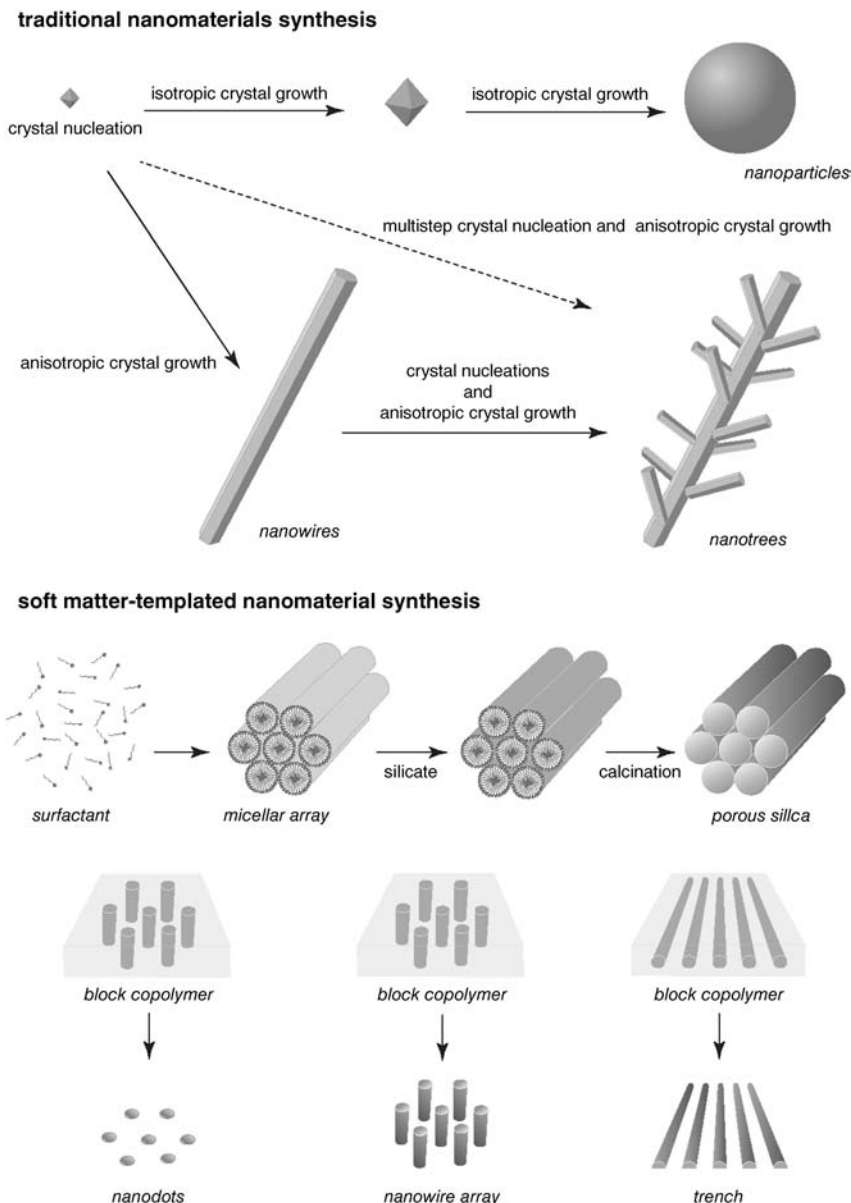


Figure 8.1 Overview of traditional and soft matter-templated inorganic synthesis of nanomaterials.

strongly aids in creating artificial materials and inventing semiconductor lasers [27,28]. In 1981, Binnig *et al.* developed scanning tunneling microscope (STM) to image surfaces with an atomic resolution [29,30]. STM also initiated manipulating atoms on surfaces [31–34]. The atomic and molecular

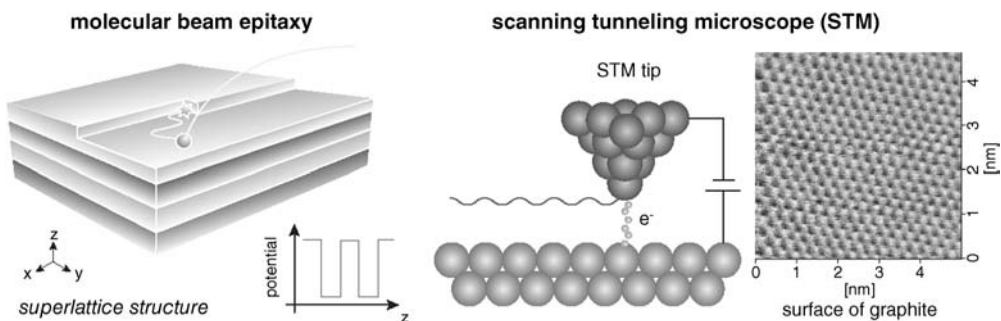


Figure 8.2 Physics-based nanotechnology for atomic manipulation.

manipulations are generally demonstrated under a high vacuum condition and at low temperatures because the surfaces are easily contaminated by air and the weakly binding atoms and molecules thermally diffuse around the surfaces at room temperature. The weak binding is necessary for STM tips to manipulate atoms and molecules. Although some researchers have reported the atom manipulation at room temperature under a high vacuum condition, the combination of atoms and substrates is limited [35,36]. There is still more room at the bottom, especially for industrializations.

Soft matter assembly has also contributed to nanoarchitectonics with atomic precision (Figure 8.3). Self-assembled monolayer (SAM) has provided a way to obtain atomically precise modified surfaces with SAM molecules [37–39]. SAM molecules are molecular chains having an anchoring head and a functionalizing tail. In SAM molecule solutions, the anchoring heads adsorb to close-pack the SAM molecules on substrate surfaces, creating the tail-functionalized surfaces of single-molecule layers [40–52]. In addition, supermolecule forms atomically

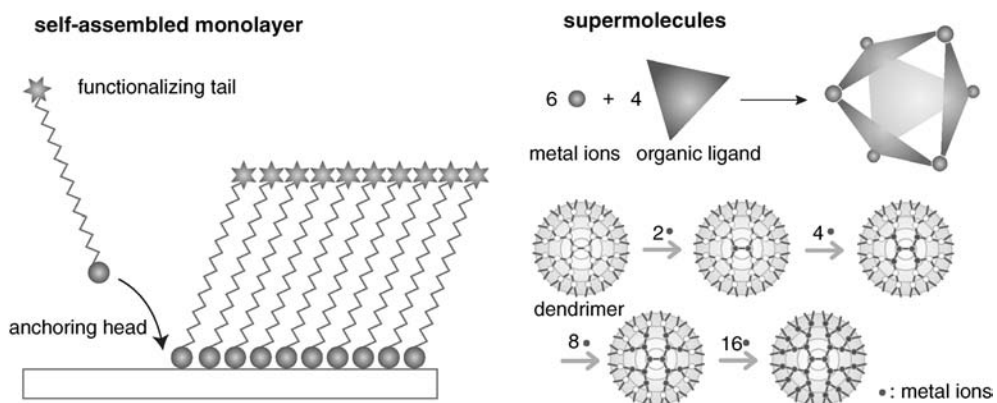


Figure 8.3 Soft matter assembly for constructing nanostructure with atomic precision.

precise nanostructures from a discrete number of molecular subunits in a controlled manner using noncovalent bonds interactions, such as hydrogen bonding, electrostatic interaction, $\pi-\pi$ interaction, van der Waals interaction, and hydrophobic interaction [53–62]. The noncovalent interactions are able to rearrange the conformation of nanostructures, resulting in a stable form. These soft matter assembly structures, including metals, give new templates for atomically precise oxides.

8.3

Soft Mater Assembly for Atomically Precise Oxide Layers

Atomic layer deposition (ALD) [63–68] is a technique to grow oxide films with atomic precision based on sequential decomposition of metallo-SAMs obtained from ALD precursors in the gas phase (Figure 8.4). Although the solution process is also possible to prepare metallo-SAMs [69–71], it takes longer time because molecules diffuse slower in solution than in gas. In addition, the ALD process is achieved by automated sequential gas change of ALD precursors and oxidants in the ALD reactor. It is more convenient than the sequential manual soaking of substrates for chemisorption, rinsing, soaking for hydrolysis, and rinsing in the solution method. To achieve the ALD process, ALD precursors need to be volatile, reactive to substrate, stable after the chemisorption to form the SAM structure, and fully oxidized by oxidants like water. The chamber temperature is set not only to activate the chemisorption and oxidation reactions but also to maintain the SAM structure, generally around 200–300 °C for water oxidant. The choice of ozone or plasma oxidants allows achieving ALD at lower temperatures in some cases.

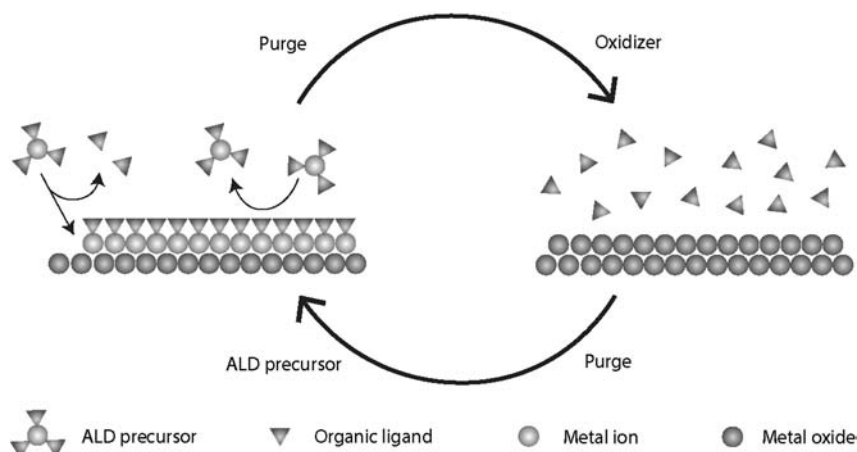


Figure 8.4 ALD processes to control thickness of oxide layer with atomic precision.

ALD precursors have been developed for most of the metal oxides, lithium to lanthanides in the periodic table [72].

ALD has a wide range of applications. One of the biggest target applications is electronics. In accordance with Moore's law [73,74], downscaling of gate oxide thickness dramatically increases the leakage current in a metal oxide semiconductor (MOS) structure. Thus, high-dielectric ALD oxides have replaced the traditional SiO_2 [75]. In addition, ALD is able to deposit the conformal film because the gas phase of the ALD precursors penetrates into small space in complex nanostructures and then forms the SAM structures. Therefore, ALD oxide will become more important for the next-generation transistors having a three-dimensional device structure surrounding the channel with gate oxides to improve the inside current controllability [68,76]. Based on the progress in downscaling, ALD is also important to fabricate memories [77–79], barrier layers [80–83], and interconnections [84–86] in electronics applications. Besides, these unique features of ALD have been applied to modifying surfaces or interfaces in energy applications. The surfaces and interfaces are the primary places for electron and mass transport. Therefore, ALD contributes to improving the efficiencies of solar cells by the fine surface passivation and electron collection [87–91] and Li batteries [92–95]. For nanostructure construction, combinations of the conformal and atomically precise coating of ALD with other nanostructures provide new opportunities for nanotubes [96], inverted opals [97], and molecule-templated cavities [98,99]. These various innovations result from the atomically precise thickness control.

8.4

Soft Matter Assembly for Atomically Precise Oxide Dots

Atomically precise thickness control of thin films has already been demonstrated by MBE, ALD, and so on, resulting in industrial innovations. However, atomically precise size control of nanodots has been challenging because of their fragility and the difficulty in controlling size growth. The toughness of nanodots depends on the volume because the specific surface area increases, which has been discussed as the melting point, indicating the significance of stability of solid state for thermal fluctuation. The size-dependent melting point $T(r)$ is described as follows:

$$T(r) \approx T_{\text{bulk}} - \frac{A}{r}, \quad (8.1)$$

where r is the radius of nanodots, T_{bulk} is the melting temperature in bulk, and A is a constant [100–105]. For example, gold nanoparticles melt at lower temperatures (2.5 nm size at $\sim 300^\circ\text{C}$) than the bulk gold (1064°C). Thus, 1 nm gold particle consisting of ~ 25 atoms would be liquefied at room temperature. In bare small particles, it is difficult to maintain the atomically precise dot structures against thermal fluctuation especially at high temperatures. Hence, molecules

and atoms have been nominated as atomically precise dots. However, as already mentioned, these demonstrations are also limited at low temperatures to suppress the thermal diffusion on substrate [106–108]. Small particles tend to aggregate or make their domains due to their high surface energy. This suggests that atomically precise dot structures need to be constructed using strong chemical bonds to increase the melting points and strongly bind with substrates. According to bond energies (600–1500 kJ mol⁻¹ for ionic bond, 60–700 kJ mol⁻¹ for covalent bond, 80–120 kJ mol⁻¹ for metal bond, 5–30 kJ mol⁻¹ for hydrogen bond, and 4–20 kJ mol⁻¹ for van der Waals bond), ionic covalent bond of oxides is a candidate for atomically precise construction. Although oxide nanodots are generally synthesized by hydrolysis of metal alkoxides, the statistical mechanics-driven nucleation and growth generate the statistical distribution in size. The strong bonding obstructs distinguishing the nucleation and growth processes. In short, weak bond is easy to manipulate but is frail; strong bond is tough but difficult to manipulate with atomic precision.

To achieve atomically precise size control of oxide dots, the number of atoms for reactions must be predetermined in a limited space. The concept has been demonstrated for the first time in controlling the size of TiO₂ with atomic precision using phenylazomethine dendrimers as molecular capsule to determine the number of Ti ions (Figure 8.5) [109,110]. The size dependence of nanosize TiO₂ on the bandgap and the initiation temperature of phase transition from anatase to rutile is important for applications to photocatalysts and electrodes for dye-sensitized solar cells [111,112]. Some reports have suggested that small TiO₂ shows blueshift in absorption edge based on confining exiton formed by photoexcitation [113–119] and much lower phase transition temperature than that of bulk TiO₂ [120–123]. However, such size dependence is unclear because the prepared samples contain contaminants that hide dependence. As the quantum energy of confined exiton in the particle-in-a-box model, the size dependence in bandgap is practically described as follows [124–126]:

$$E(r) \approx E_{\text{bulk}} + \frac{\hbar^2 \pi^2}{2r^2} \frac{1}{\mu'} - \frac{1.8e^2}{er}, \quad (8.2)$$

where $E(r)$ is the size-dependent bandgap energy, \hbar is the Planck's constant, e is the charge on the electron, E_{bulk} is the bandgap in the bulk, μ' is the *semiempirically adjusted* reduced mass, and ϵ is the dielectric constant of the bulk

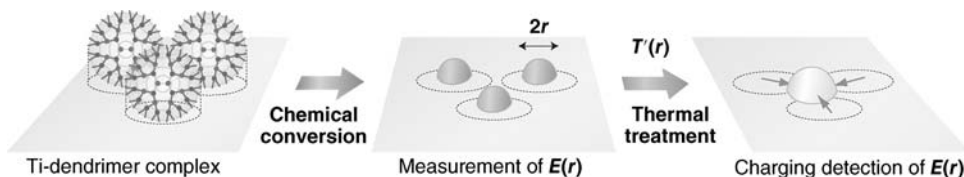


Figure 8.5 Synthetic strategy to deposit atomically precise TiO₂ dots in size.

semiconductor [127–130]. Small dots having large $E(r)$ show blueshift in absorption edge, while larger size contaminants absorb light at redder regions and hide the blueshift. Thus, the size dependence on $E(r)$ is observed when the sample does not contain any large contaminants. On the other hand, the initiation step of the irreversible phase transition is similar to the melting process: atoms obtain freedom in motion from metastable phase and then irreversibly transform into the most stable phase. Thus, the phase transition initiation temperature $T(r)'$ of nanodots has the same size dependence as given in Eq. (8.1). In the temperature-elevating experimental condition, the smallest contaminant having lower $T(r)'$ first gives the transition signal. Thus, the size dependence on $T(r)'$ is observed when the sample does not contain any small contaminants. Phenylazomethine dendrimers are able to complex in a radially stepwise manner with 6, 14, 30, and 60 metal ions based on gradient in their molecular structure [131–135]. This specifies the number and location of metal ions inside the large molecules. The single-molecule layers of the Ti dendrimer complexes formed by drop cast provide 6, 14, 30, and 60 TiO_2 (1.0, 1.2, 1.6, and 1.8 nm in size) on substrate after hydrolysis for rutile or after thermolysis for anatase. The dendrimer is removed by 500°C annealing and UV O_3 treatment. The atomically precise TiO_2 shows the clear size dependence on $E(r)$ and $T(r)'$ (Figure 8.6) suggesting no small and large contaminants. These results support the concept to deposit atomically precise dots using oxide inside a limited space. At the same time, these results deny a superstition that no quantum effect exists in TiO_2 and connect the understandings between Ti molecular oxides and nano- TiO_2 . The observation of rutile phase in small scale completely contradicts the theoretical predictions based on thermodynamics that the anatase structure favorably forms in less than 14 nm particle size because of the thermodynamical stability. Metastable anatase kinetically tends to form resulting from the kinetic stable *cis*-coordination processes (Figure 8.7). The ionic covalent bonds are too strong to free the formed structure from the metastable state to the stable state. In other words, the rutile structure also forms in small scale, depending on the experimental condition to

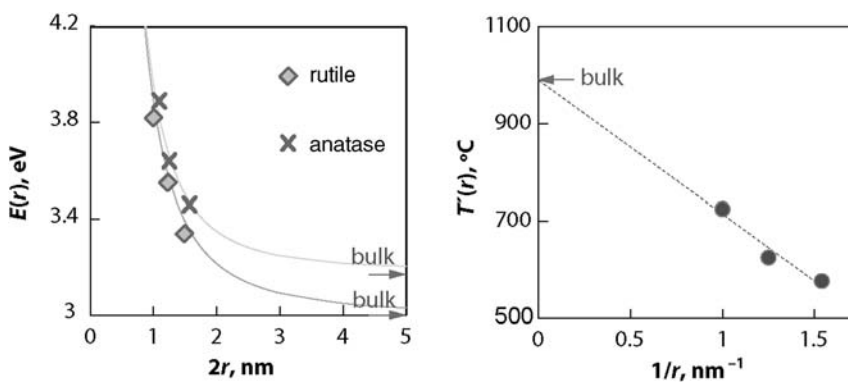


Figure 8.6 Size dependence of atomically precise TiO_2 on $E(r)$ and $T(r)'$.

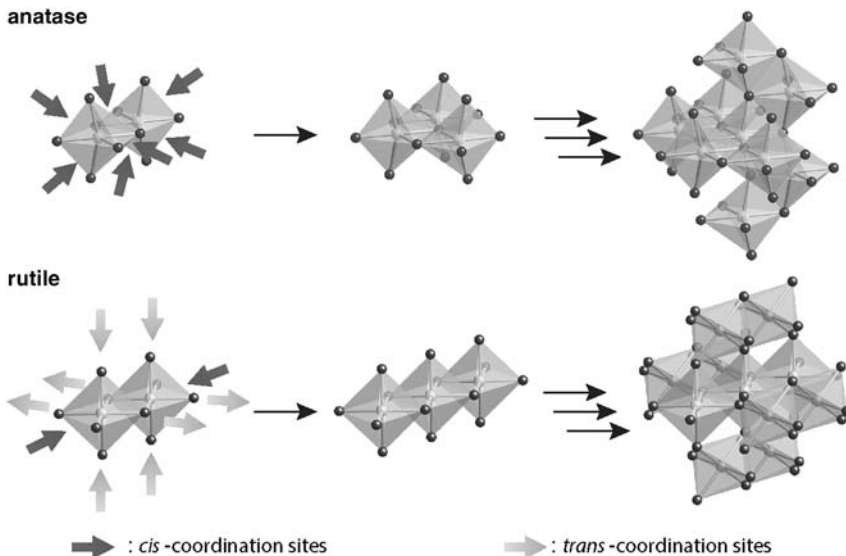


Figure 8.7 Kinetic crystal growth model of anatase and rutile TiO_2 .

control the kinetic reaction processes. The first demonstration gives an insight into the crystal growth process as well as evidences of fabricating atomically precise oxide dots at high temperatures to remove the dendrimer capsules without a high vacuum condition.

8.5

Summary for the Future Works

Chemistry-based soft matter assembly contributes to atomically precise fabrication in a different way than the one defined by Feynman. Especially, the combination of conformal ALD and atomically precise dot deposition is promising. Small dots have attracted much attention to confine electrons for single-electron manipulation and artificial atom creation [136–140]. For the purpose of confining electrons at high temperatures or at room temperature, dot size must be less than 2 nm for charging energy to excess thermal energy. Besides, the insight into molecular chemistry suggests that the charging dot also needs to be surrounded by uniform dielectrics because the surrounding media stabilize the localized charges and activate the electron transfer [141–144]. Hence, ALD conformal coating of the atomically precise oxide dots will pave way to manipulate electrons at high temperatures efficiently [145]. Compared with chemistry-based organic devices, the atomically precise oxide devices will be more stable and durable in oxygen and water in air. In addition, atomically precise oxide dots embedded in ALD oxides are considered as atomically precise dopants for ALD

host oxides. Therefore, in addition to the single-electron devices operating at room temperature, the atomically precise fabrication will lead to new functional materials based on the artificial atom concept and atomically precise doping toward the industrialization.

References

- 1 Peng, X., Wickham, J., and Alivisatos, A.P. (1998) Kinetics of II–VI and III–V colloidal semiconductor nanocrystal growth: “focusing” of size distributions. *J. Am. Chem. Soc.*, **120**, 5343–5344.
- 2 Manna, L., Scher, E.C., and Alivisatos, A.P. (2000) Synthesis of soluble and processable rod-, arrow-, teardrop-, and tetrapod-shaped CdSe nanocrystals. *J. Am. Chem. Soc.*, **122**, 12700–12706.
- 3 Jun, Y.W., Choi, J.S., and Cheon, J. (2006) Shape control of semiconductor and metal oxide nanocrystals through nonhydrolytic colloidal routes. *Angew. Chem., Int. Ed.*, **45**, 3414–3439.
- 4 Yu, Y., Zhang, Q., Xie, J., and Lee, J.Y. (2013) Engineering the architectural diversity of heterogeneous metallic nanocrystals. *Nat. Commun.*, **4**, 1454.
- 5 Morales, A.M. and Lieber, C.M. (1998) A laser ablation method for the synthesis of crystalline semiconductor nanowires. *Science*, **279**, 208–211.
- 6 Gudiksen, M.S., Lauhon, L.J., Wang, J., Smith, D., and Lieber, C.M. (2002) Growth of nanowire superlattice structures for nanoscale photonics and electronics. *Nature*, **415**, 617–620.
- 7 Tian, B., Zheng, X., Kempa, T.J., Fang, Y., Yu, N., Yu, G., Huang, J., and Lieber, C.M. (2007) Coaxial silicon nanowires as solar cells and nanoelectronic power sources. *Nature*, **449**, 885–890.
- 8 Tian, B., Xie, P., Kempa, T.J., Bell, D.C., and Lieber, C.M. (2009) Single crystalline kinked semiconductor nanowire superstructures. *Nat. Nanotechnol.*, **4**, 824–829.
- 9 Fang, X., Bando, Y., Liao, M., Gautam, U.K., Zhi, C., Dierre, B., Liu, B., Zhai, T., Sekiguchi, T., Koide, Y., and Golberg, D. (2009) Single-crystalline ZnS nanobelts as ultraviolet-light sensors. *Adv. Mater.*, **21**, 2034–2039.
- 10 Wang, D. and Lieber, C.M. (2003) Inorganic materials: nanocrystals branch out. *Nat. Mater.*, **2**, 355–356.
- 11 Wang, D., Qian, F., Yang, C., Zhong, Z., and Lieber, C.M. (2004) Rational growth of branched and hyperbranched nanowire structures. *Nano Lett.*, **4**, 871–874.
- 12 Cheng, C. and Fan, H.J. (2012) Branched nanowires: synthesis and energy applications. *Nano Today*, **7**, 327–343.
- 13 Yanagisawa, T., Shimizu, T., Kuroda, K., and Kato, C. (1990) The preparation of alkyltrimethylammonium–kanemite complexes and their conversion to microporous materials. *Bull. Chem. Soc. Jpn.*, **63**, 988–992.
- 14 Kresge, C.T., Leonowicz, M.E., Roth, W.J., Vartuli, J.C., and Beck, J.S. (1992) Ordered mesoporous molecular sieves synthesized by a liquid-crystal template mechanism. *Nature*, **359**, 710–712.
- 15 Li, M. and Ober, C.K. (2006) Block copolymer patterns and templates. *Mater. Today*, **9**, 30–39.
- 16 Park, M., Harrison, C., Chaikin, P.M., Register, R.A., and Adamson, D.H. (1997) Block copolymer lithography: periodic arrays of $\sim 10^{11}$ holes in 1 square centimeter. *Science*, **276**, 1401–1404.
- 17 Hong, A.J., Liu, C.-C., Wang, Y., Kim, J., Xiu, F., Ji, S., Zou, J., Nealey, P.F., and Wang, K.L. (2010) Metal nanodot memory by self-assembled block copolymer lift-off. *Nano Lett.*, **10**, 224–229.
- 18 Thurn-Albrecht, T., Schotter, J., Kästle, G.A., Emley, N., Shibauchi, T., Krusin-Elbaum, L., Guarini, K., Black, C.T., Tuominen, M.T., and Russell, T.P. (2000) Ultrahigh-density nanowire arrays grown in self-assembled diblock copolymer templates. *Science*, **290**, 2126–2129.

- 19** Yang, P., Zhao, D., Margolese, D.I., Chmelka, B.F., and Stucky, G.D. (1998) Generalized syntheses of large-pore mesoporous metal oxides with semicrystalline frameworks. *Nature*, **396**, 152–155.
- 20** Zhao, D., Feng, I., Huo, Q., Melosh, N., Fredrickson, G.H., Chmelka, B.F., and Stucky, G.D. (1998) Triblock copolymer syntheses of mesoporous silica with periodic 50 to 300 angstrom pores. *Science*, **279**, 548–552.
- 21** Chan, V.Z.-H., Hoffman, J., Lee, V.Y., Iatrou, H., Avgeropoulos, A., Hadjichristidis, N., Miller, R.D., and Thomas, E.L. (1999) Ordered bicontinuous nanoporous and nanorelief ceramic films from self assembling polymer precursors. *Science*, **286**, 1716–1719.
- 22** Peng, Q., Tseng, Y.-C., Darling, S.B., and Elam, J.W. (2011) A route to nanoscopic materials via sequential infiltration synthesis on block copolymer templates. *ACS Nano*, **5**, 4600–4606.
- 23** Feynman, R.P. (1960) There's plenty of room at the bottom. *Eng. Sci.*, **23**, 22–36.
- 24** Esaki, L. and Tsu, R. (1970) Superlattice and negative differential conductivity in semiconductors. *IBM J. Res. Dev.*, **14**, 61–65.
- 25** Esaki, L. (1958) New phenomenon in narrow germanium p–n junctions. *Phys. Rev.*, **109**, 603.
- 26** Cho, A.Y. and Arthur, J.R. (1975) Molecular beam epitaxy. *Prog. Solid State Chem.*, **10**, 157–192.
- 27** Alferov, Z.I. (2000) Nobel Lecture: the double heterostructure concept and its applications in physics, electronics, and technology. *Rev. Mod. Phys.*, **73**, 767–782.
- 28** Kroemer, H. (2001) Nobel Lecture: quasielectric fields and band offsets: teaching electrons new tricks. *Rev. Mod. Phys.*, **73**, 783–793.
- 29** Binnig, G., Rohrer, H., Gerber, Ch., and Weibel, E. (1982) Surface studies by scanning tunneling microscopy. *Phys. Rev. Lett.*, **49**, 57–61.
- 30** Binnig, G. and Rohrer, H. (1987) Scanning tunneling microscopy: from birth to adolescence. *Rev. Mod. Phys.*, **59**, 615–625.
- 31** Eigler, D.M. and Schweizer, E.K. (1990) Positioning single atoms with a scanning tunnelling microscope. *Nature*, **344**, 524–526.
- 32** Eigler, D.M., Lutz, C.P., and Rudge, W.E. (1991) An atomic switch realized with the scanning tunnelling microscope. *Nature*, **352**, 600–603.
- 33** Crommie, M.F., Lutz, C.P., and Eigler, D. M. (1993) Confinement of electrons to quantum corrals on a metal surface. *Science*, **262**, 218–220.
- 34** Fuechsle, M., Miwa, J.A., Mahapatra, S., Ryu, H., Lee, S., Warschkow, O., Hollenberg, L.C.L., Klimeck, G., and Simmons, M.Y. (2012) A single-atom transistor. *Nat. Nanotechnol.*, **7**, 242–246.
- 35** Fishlock, T.W., Oral, A., Egdell, R.G., and Pethica, J.B. (2000) Manipulation of atoms across a surface at room temperature. *Nature*, **404**, 743–745.
- 36** Kawai, S., Foster, A.S., Canova, F.F., Onodera, H., Kitamura, S., and Meyer, E. (2014) Atom manipulation on an insulating surface at room temperature. *Nat. Commun.*, **5**, 4403.
- 37** Ulman, A. (1996) Formation and structure of self-assembled monolayers. *Chem. Rev.*, **96**, 1533–1554.
- 38** Joachim, C., Gimzewski, J.K., and Aviram, A. (2000) Electronics using hybrid-molecular and mono-molecular devices. *Nature*, **408**, 541–548.
- 39** Love, J.C., Estroff, L.A., Kriebel, J.K., Nuzzo, R.G., and Whitesides, G.M. (2005) Self-assembled monolayers of thiolates on metals as a form of nanotechnology. *Chem. Rev.*, **105**, 1103–1170.
- 40** Maskus, M. and Abruna, H.D. (1996) Synthesis and characterization of redox-active metal complexes sequentially self-assembled onto gold electrodes via a new thiol–terpyridine ligand. *Langmuir*, **12**, 4455–4462.
- 41** Gorman, C.B., Miller, R.L., Chen, K.-Y., Bishop, A.R., Haasch, R.T., and Nuzzo, R. G.V. (1998) Semipermeable, chemisorbed adlayers of focally-substituted organothiol dendrons on gold. *Langmuir*, **14**, 3312–3319.

- 42** Zhang, L., Huo, F., Wang, Z., Wu, L., Zhang, X., Höppener, S., Chi, L., Fuchs, H., Zhao, J., Niu, L., and Dong, S. (2000) Investigation into self-assembled monolayers of a polyether dendron thiol: chemisorption, kinetics, and patterned surface. *Langmuir*, **16**, 3813–3817.
- 43** Friggeri, A., Schönher, H., van Manen, H.-J., Huisman, B.-H., Vancso, G.J., Huskens, J., van Veggel, F.C.J.M., and Reinhoudt, D.N. (2000) Insertion of individual dendrimer molecules into self-assembled monolayers on gold: a mechanistic study. *Langmuir*, **16**, 7757–7763.
- 44** Ishida, T., Fukushima, H., Mizutani, W., Miyashita, S., Ogiso, H., Ozaki, K., and Tokumoto, H. (2002) Annealing effect of self-assembled monolayers generated from terphenyl derivatized thiols on Au(111). *Langmuir*, **18**, 83–92.
- 45** Taranekar, P., Baba, A., Park, J.Y., Fulghum, T.M., and Advincula, R. (2006) Dendrimer precursors for nanomolar and picomolar real-time surface plasmon resonance/potentiometric chemical nerve agent sensing using electrochemically crosslinked ultrathin films. *Adv. Funct. Mater.*, **16**, 2000–2007.
- 46** Zhang, L., Zou, B., Dong, B., Huo, F., Zhang, X., Chi, L., and Jiang, L. (2001) Self-assembled monolayers of new dendron-thiols: manipulation of the patterned surface and wetting properties. *Chem. Commun.*, 1906–1907.
- 47** Mark, S.S., Sandhyarani, N., Zhu, C., Campagnolo, C., and Batt, C.A. (2004) Dendrimer-functionalized self-assembled monolayers as a surface plasmon resonance sensor surface. *Langmuir*, **20**, 6808–6817.
- 48** Abe, M., Michi, T., Sato, A., Kondo, T., Zhou, W., Ye, S., Uosaki, K., and Sasaki, Y. (2003) Electrochemically controlled layer-by-layer deposition of metal cluster molecular multilayers on gold. *Angew. Chem., Int. Ed.*, **42**, 2912–2915.
- 49** Kanaizuka, K., Murata, M., Nishimori, Y., Mori, I., Nishio, K., Masuda, H., and Nishihara, H. (2005) Stepwise preparation of linear π -conjugated bis(terpyridine)metal polymer chains at gold surface. *Chem. Lett.*, **34**, 534–535.
- 50** Nishimori, Y., Kanaizuka, K., Murata, M., and Nishihara, H. (2007) Synthesis of molecular wires of linear and branched bis(terpyridine)-complex oligomers and electrochemical observation of through-bond redox conduction. *Chem. Asian J.*, **2**, 367–376.
- 51** Choi, S.H., Kim, B.-S., and Frisbie, C.D. (2008) Electrical resistance of long conjugated molecular wires. *Science*, **320**, 1482–1486.
- 52** Satoh, N. and Yamamoto, K. (2009) Self-assembled monolayers of metal-assembling dendron thiolate formed from dendrimers with a disulfide core. *Org. Lett.*, **11**, 1729–1732.
- 53** Fujita, M., Oguro, D., Miyazawa, M., Oka, H., Yamaguchi, K., and Ogura, K. (1995) Self-assembly of ten molecules into nanometer sized organic host framework. *Nature*, **378**, 469–471.
- 54** Hasenknopf, B., Lehn, J.-M., Kneisel, B.O., Baum, G., and Fenske, D. (1996) Self-assembly of a circular double helicate. *Angew. Chem., Int. Ed. Engl.*, **35**, 1838–1840.
- 55** Bravo, J.A., Raymo, F.M., Stoddart, J.F., White, A.J.P., and Williams, D.J. (1998) High yielding template-directed syntheses of [2]rotaxanes. *Eur. J. Org. Chem.*, **11**, 2565–2571.
- 56** Lehn, J.-M. (1998) Supramolecular chemistry: scope and perspectives molecules, supermolecules, and molecular devices (Nobel Lecture). *Angew. Chem., Int. Ed. Engl.*, **27**, 89–112.
- 57** Whitesides, G.M., Mathias, J.P., and Seto, C.T. (1991) Molecular self-assembly and nanochemistry: a chemical strategy for the synthesis of nanostructures. *Science*, **254**, 1312–1319.
- 58** Tanaka, K., Tengeiji, A., Kato, T., Toyama, N., and Shionoya, M. (2003) A discrete self-assembled metal array in artificial DNA. *Science*, **299**, 1212–1213.
- 59** Hiraoka, S., Shiro, M., and Shionoya, M. (2004) Heterotopic assemblage of two different disk-shaped ligands through silver(I) complexation: ligand exchange driven molecular motion. *J. Am. Chem. Soc.*, **126**, 1214–1218.
- 60** Yoshizawa, M., Kusukawa, T., Kawano, M., Ohhara, T., Tanaka, I., Kurihara, K.,

- Niimura, N., and Fujita, M. (2005) Endohedral clusterization of ten water molecules into a molecular ice within the hydrophobic pocket of a self-assembled cage. *J. Am. Chem. Soc.*, **127**, 2798–2799.
- 61** Tanaka, K., Glever, G.H., Takezawa, Y., Yamada, Y., Kaul, C., Shionoya, M., and Carell, T. (2006) Programmable self-assembly of metal ions inside artificial DNA duplexes. *Nat. Nanotechnol.*, **1**, 190–194.
- 62** Ariga, K., Hill, J.P., Lee, M.V., Vinu, A., Charvet, R., and Acharya, S. (2008) Challenges and breakthroughs in recent research on self-assembly. *Sci. Technol. Adv. Mater.*, **9**, 014109.
- 63** Leskelä, M. and Ritala, M. (2003) Atomic layer deposition chemistry: recent developments and future challenges. *Angew. Chem., Int. Ed.*, **42**, 5548–5554.
- 64** Kim, H. (2003) Atomic layer deposition of metal and nitride thin films: current research efforts and applications for semiconductor device processing. *J. Vac. Sci. Technol. B*, **21**, 2231–2261.
- 65** Riikka, L.P. (2005) Surface chemistry of atomic layer deposition: a case study for the trimethylaluminum/water process. *J. Appl. Phys.*, **97**, 121301.
- 66** George, S.M. (2010) Atomic layer deposition: an overview. *Chem. Rev.*, **110**, 111–131.
- 67** Miikkulainen, V., Leskelä, M., Ritala, M., and Puurunen, R.L. (2013) Crystallinity of inorganic films grown by atomic layer deposition: overview and general trends. *J. Appl. Phys.*, **113**, 021301.
- 68** Johnson, R.W., Hultqvist, A., and Bent, S. F. (2014) A brief review of atomic layer deposition: from fundamentals to applications. *Mater. Today*, **17**, 236–246.
- 69** Ichinose, I., Senzu, H., and Kunitake, T. (1996) Stepwise adsorption of metal alkoxides on hydrolyzed surfaces: a surface sol–gel process. *Chem. Lett.*, **25**, 831–832.
- 70** Ichinose, I., Senzu, H., and Kunitake, T. (1997) A surface sol–gel process of TiO₂ and other metal oxide films with molecular precision. *Chem. Mater.*, **9**, 1296–1298.
- 71** Vallant, T., Brunner, H., Kattner, J., Mayer, U., Hoffmann, H., Leitner, T., Friedbacher, G., Schügerl, G., Svagera, R., and Ebel, M. (2000) Monolayer-controlled deposition of silicon oxide films on gold, silicon, and mica substrates by room-temperature adsorption and oxidation of alkylsiloxane monolayers. *J. Phys. Chem. B*, **104**, 5309–5317.
- 72** Lim, B.S., Rahtu, A., and Gordon, R.G. (2003) Atomic layer deposition of transition metals. *Nat. Mater.*, **2**, 749–754.
- 73** Frank, D.J., Dennard, R.H., Nowak, E., Solomon, P.M., Yuan, T., and Hen-Sum, P.W. (2001) Device scaling limits of Si MOSFETs and their application dependencies. *Proc. IEEE*, **89**, 259–288.
- 74** Chau, R., Doyle, B., Datta, S., Kavalieros, J., and Zhang, K. (2007) Integrated nanoelectronics for the future. *Nat. Mater.*, **6**, 810–812.
- 75** Ando, T. (2012) Ultimate scaling of high- κ gate dielectrics: higher- κ or interfacial layer scavenging? *Materials*, **5**, 478–500.
- 76** Si, M., Gu, J.J., Wang, X., Shao, J., Li, X., Manfra, M.J., Gordon, R.G., and Ye, P.D. (2013) Effects of forming gas anneal on ultrathin InGaAs nano wire metal-oxide-semiconductor field-effect transistors. *Appl. Phys. Lett.*, **102**, 093505.
- 77** Farmer, D.B. and Gordon, R.G. (2007) High density Ru nanocrystal deposition for nonvolatile memory applications. *J. Appl. Phys.*, **101**, 124503.
- 78** Rinkiö, M., Johansson, A., Paraoanu, G.S., and Törmä, P. (2009) High-speed memory from carbon nanotube field-effect transistors with high- κ gate dielectric. *Nano Lett.*, **9**, 643–647.
- 79** Kwon, D.-H., Kim, K.M., Jang, J.H., Jeon, J.M., Lee, M.H., Kim, G.H., Li, X.-S., Park, G.-S., Lee, B., Han, S., Kim, M., and Hwang, C.S. (2010) Atomic structure of conducting nanofilaments in TiO₂ resistive switching memory. *Nat. Nanotechnol.*, **5**, 148–153.
- 80** Rossnagel, S.M., Sherman, S.M., and Turner, F. (2000) Plasma-enhanced atomic layer deposition of Ta and Ti for interconnect diffusion barriers. *J. Vac. Sci. Technol. B*, **18**, 2016.
- 81** Becker, J.S. and Gordon, R.G. (2003) Diffusion barrier properties of tungsten nitride films grown by atomic layer

- deposition from bis(*tert*-butylimido)bis(dimethylamido) tungsten and ammonia. *Appl. Phys. Lett.*, **82**, 2239–2241.
- 82** Groner, M.D., George, S.M., McLean, R.S., and Garcia, P.F. (2006) Gas diffusion barriers on polymers using Al₂O₃ atomic layer deposition. *Appl. Phys. Lett.*, **88**, 051907.
- 83** Dameron, A.A., Davidson, S.D., Burton, B.B., Garcia, P.F., McLean, R.S., and George, S.M. (2008) Gas diffusion barriers on polymers using multilayers fabricated by Al₂O₃ and rapid SiO₂ atomic layer deposition. *J. Phys. Chem. C*, **112**, 4573–4580.
- 84** Gordon, R.G., Hausmann, D.M., Kim, E., and Shepard, J. (2003) A kinetic model for step coverage by atomic layer deposition in narrow holes or trenches. *Chem. Vapor Depos.*, **9**, 73–78.
- 85** Au, Y., Lin, Y., and Gordon, R.G. (2011) Filling narrow trenches by iodine-catalyzed CVD of copper and manganese on manganese nitride barrier/adhesion layers. *J. Electrochem. Soc.*, **158**, D248–D253.
- 86** Au, Y., Wang, Q.M., Li, H., Lehn, J.-S.M., Shenai, D.V., and Gordon, R.G. (2012) Vapor deposition of highly conformal copper seed layers for plating through-silicon vias (TSVs). *J. Electrochem. Soc.*, **159**, D382–D385.
- 87** Schmidt, J., Merkle, A., Brendel, R., Hoex, B., van de Sanden, M.C.M., and Kessels, W.M.M. (2008) Surface passivation of high-efficiency silicon solar cells by atomic-layer-deposited Al₂O₃. *Prog. Photovolt: Res. Appl.*, **16**, 461–466.
- 88** Poodt, P., Lankhorst, A., Roozeboom, F., Spee, K., Maas, D., and Vermeer, A. (2010) High-speed spatial atomic-layer deposition of aluminum oxide layers for solar cell passivation. *Adv. Mater.*, **22**, 3564–3567.
- 89** Son, H.-J., Wang, X., Prasittichai, C., Jeong, N.C., Aaltonen, T., Gordon, R.G., and Hupp, J.T. (2012) Glass-encapsulated light harvesters: more efficient dye-sensitized solar cells by deposition of self-aligned, conformal, and self-limited silica layers. *J. Am. Chem. Soc.*, **134**, 9537–9540.
- 90** Sun, L., Haight, R., Sinsermsuksakul, P., Kim, S.B., Park, H.H., and Gordon, R.G. (2013) Band alignment of SnS/Zn(O,S) heterojunctions in SnS thin film solar cells. *Appl. Phys. Lett.*, **103**, 181904.
- 91** Lee, Y.S., Heo, J., Siah, S.C., Mailoa, J.P., Brandt, R.E., Kim, S.B., Gordon, R.G., and Buonassisi, T. (2013) Ultrathin amorphous zinc–tin–oxide buffer layer for enhancing heterojunction interface quality in metal-oxide solar cells. *Energy Environ. Sci.*, **6**, 2112–2118.
- 92** Meng, X., Yang, X.-Q., and Sun, X. (2012) Emerging applications of atomic layer deposition for lithium-ion battery studies. *Adv. Mater.*, **24**, 3589–3615.
- 93** Sun, S., Zhang, G., Gauquelin, N., Chen, N., Zhou, J., Yang, S., Chen, W., Meng, X., Geng, D., Banis, M.N., Li, R., Ye, S., Knights, S., Botton, G.A., Sham, T.-K., and Sun, X. (2013) Single-atom catalysis using Pt/graphene achieved through atomic layer deposition. *Sci. Rep.*, **3**, 1775.
- 94** Lu, J., Lei, Y., Lau, K.C., Luo, X., Du, P., Wen, J., Assary, R., Das, U., Miller, D., Elam, J.W., Albishri, H., El-Hady, D., Sun, Y.K., Curtiss, L.A., and Amine, K. (2013) A nanostructured cathode architecture for low charge overpotential in lithium-oxygen batteries. *Nat. Commun.*, **4**, 2383.
- 95** Li, X., Liu, J., Banis, M.N., Lushington, A., Li, R., Cai, M., and Sun, X. (2014) Atomic layer deposition of solid-state electrolyte coated cathode materials with superior high-voltage cycling behavior for lithium ion battery application. *Energy Environ. Sci.*, **7**, 768–778.
- 96** Jin Fan, H., Knez, M., Scholz, R., Nielsch, K., Pippel, E., Hesse, D., Zacharias, M., and Gösele, U. (2006) Monocrystalline spinel nanotube fabrication based on the Kirkendall effect. *Nat. Mater.*, **5**, 627–631.
- 97** Rugge, A., Becker, J.S., Gordon, R.G., and Tolbert, S.H. (2003) Tungsten nitride inverse opals by atomic layer deposition. *Nano Lett.*, **3**, 1293–1297.
- 98** Lu, J., Fu, B., Kung, M.C., Xiao, G., Elam, J.W., Kung, H.H., and Stair, P.C. (2012) Coking- and sintering-resistant palladium catalysts achieved through atomic layer deposition. *Science*, **335**, 1205–1208.

- 99** Canlas, C.P., Lu, J., Ray, N.A., Gross-Giordano, N.A., Lee, S., Elam, J.W., Winans, R.E., Van Duyne, R.P., Stair, P.C., and Notestein, J.M. (2012) Shape-selective sieving layers on an oxide catalyst surface. *Nat. Chem.*, **4**, 1030–1036.
- 100** Buffat, P. and Borel, J.-P. (1976) Size effect on the melting temperature of gold particles. *Phys. Rev. A*, **13**, 2287–2298.
- 101** Goldstein, A.N., Echer, C.M., and Alivisatos, A.P. (1992) Melting in semiconductor nanocrystals. *Science*, **256**, 1425–1427.
- 102** Cleveland, C.L., Luedtke, W.D., and Landman, U. (1998) Melting of gold clusters: icosahedral precursors. *Phys. Rev. Lett.*, **81**, 2036–2039.
- 103** Cleveland, C.L., Luedtke, W.D., and Landman, U. (1999) Melting of gold clusters. *Phys. Rev. B*, **60**, 5065–5077.
- 104** Olson, E.A., Yu, M., Zhang, E.M., Zhang, Z., and Allen, L.H. (2005) Size-dependent melting of Bi nanoparticles. *J. Appl. Phys.*, **97**, 034304.
- 105** Dick, K., Dhanasekaran, T., Zhang, Z., and Meisel, D. (2002) Size-dependent melting of silica-encapsulated gold nanoparticles. *J. Am. Chem. Soc.*, **124**, 2313–2317.
- 106** Park, J., Pasupathy, A.N., Goldsmith, J.I., Chang, C., Yaish, Y., Petta, J.R., Rinkoski, M., Sethna, J.P., Abruna, H.D., McEuen, P.L., and Ralph, D.C. (2002) Coulomb blockade and the Kondo effect in single-atom transistors. *Nature*, **417**, 722–725.
- 107** Kubatkin, S., Danilov, A., Hjort, M., Cornil, J., Brédas, J.L., Stuhr-Hansen, N., Hedegård, P., and Bjørnholm, T. (2003) Single-electron transistor of a single organic molecule with access to several redox states. *Nature*, **425**, 698–701.
- 108** Bogani, L. and Wernsdorfer, W. (2008) Molecular spintronics using single-molecule magnets. *Nat. Mater.*, **7**, 179–186.
- 109** Satoh, N., Nakashima, T., Kamikura, K., and Yamamoto, K. (2008) Quantum size effect in TiO₂ nanoparticles prepared by finely controlled metal assembly on dendrimer templates. *Nat. Nanotechnol.*, **3**, 106–111.
- 110** Satoh, N., Nakashima, T., and Yamamoto, K. (2013) Metastability of anatase: size dependent and irreversible anatase–rutile phase transition in atomic-level precise titania. *Sci. Rep.*, **3**, 1959.
- 111** Fujishima, A. and Honda, K. (1972) Electrochemical photolysis of water at a semiconductor electrode. *Nature*, **238**, 37–38.
- 112** O'Regan, B. and Grätzel, M. (1991) A low-cost, high-efficiency solar cell based on dye-sensitized colloidal TiO₂ films. *Nature*, **353**, 737–740.
- 113** Anpo, M., Shima, T., Kodama, S., and Kubokawa, Y. (1987) Photocatalytic hydrogenation of propyne with water on small-particle titania: size quantization effects and reaction intermediates. *J. Phys. Chem.*, **91**, 4305–4310.
- 114** Kormann, C., Bahnemann, D.W., and Hoffmann, M.R. (1988) Preparation and characterization of quantum-size titanium dioxide. *J. Phys. Chem.*, **92**, 5196–5201.
- 115** Geobaldo, F., Bordiga, S., Zecchina, A., Giannello, E., Leofanti, G., and Petrini, G. (1992) DRS UV-vis and EPR spectroscopy of hydroperoxo and superoxo complexes in titanium silicalite. *Catal. Lett.*, **16**, 109–115.
- 116** Marchese, L., Gianotti, E., Dellarocca, V., Maschmeyer, T., Rey, F., Coluccia, S., and Thomas, J.M. (1999) Structure-functionality relationships of grafted Ti-MCM41 silicas: spectroscopic and catalytic studies. *Phys. Chem. Chem. Phys.*, **1**, 585–592.
- 117** Monticone, S., Tufeu, R., Kanaev, A.V., Scolan, E., and Sanchez, C. (2000) Quantum size effect in TiO₂ nanoparticles: does it exist? *Appl. Surf. Sci.*, **162–163**, 565–570.
- 118** Serpone, N., Lawless, D., and Khairutdinov, R. (1995) Size effects on the photophysical properties of colloidal anatase TiO₂ particles: size quantization versus direct transitions in this indirect semiconductor. *J. Phys. Chem.*, **99**, 16646–16654.
- 119** Hu, Y., Martra, G., Zhang, J., Higashimoto, S., Coluccia, S., and Anpo, M. (2006) Characterization of the local structures of Ti-MCM-41 and their

- photocatalytic reactivity for the decomposition of NO into N₂ and O₂. *J. Phys. Chem. B*, **110**, 1680–1685.
- 120** Zhang, H. and Banfield, J.F. (2000) Understanding polymorphic phase transformation behavior during growth of nanocrystalline aggregates: insights from TiO₂. *J. Phys. Chem. B*, **104**, 3481–3487.
- 121** Pal, M., Serrano, J.G., Santiago, P., and Pal, U. (2007) Size-controlled synthesis of spherical TiO₂ nanoparticles: morphology, crystallization, and phase transition. *J. Phys. Chem. C*, **111**, 96–102.
- 122** Zhang, H. and Banfield, J.F. (2005) Size dependence of the kinetic rate constant for phase transformation in TiO₂ nanoparticles. *Chem. Mater.*, **17**, 3421–3425.
- 123** Sun, Y., Egawa, T., Zhang, L., and Yao, X. (2002) High anatase–rutile transformation temperature of anatase titania nanoparticles prepared by metalorganic chemical vapor deposition. *Jpn. J. Appl. Phys.*, **41**, L945–L948.
- 124** Brus, L.E. (1986) Electronic wave functions in semiconductor clusters: experiment and theory. *J. Phys. Chem.*, **90**, 2555–2560.
- 125** Nosaka, Y. (1991) Finite depth spherical well model for excited states of ultrasmall semiconductor particles: an application. *J. Phys. Chem.*, **95**, 5054–5058.
- 126** Rao, C.N.R., Müller, A., and Cheetham, A.K. (2004) Chapter 11, in *The Chemistry of Nanomaterials: Synthesis, Properties and Applications*, Wiley-VCH Verlag GmbH, Weinheim.
- 127** Monticone, S., Tufeu, R., and Kanaev, A.V. (1998) Complex nature of the UV and visible fluorescence of colloidal ZnO nanoparticles. *J. Phys. Chem. B*, **102**, 2854–2862.
- 128** Vossmeyer, T., Katsikas, L., Giersig, M., Popovic, I.G., Diesner, K., Chemseddine, A., Eychmueller, A., and Weller, H. (1994) CdS nanoclusters: synthesis, characterization, size dependent oscillator strength, temperature shift of the excitonic transition energy, and reversible absorbance shift. *J. Phys. Chem.*, **98**, 7665–7673.
- 129** Malik, M.A., O'Brien, P., Noragerand, S., and Smitha, J. (2003) Gallium arsenide nanoparticles: synthesis and characterization. *J. Mater. Chem.*, **13**, 2591–2595.
- 130** Zhu, K., Shi, J., and Zhang, L. (1998) Preparation and optical absorption of InSb microcrystallites embedded in SiO₂ thin films. *Solid State Commun.*, **107**, 79–84.
- 131** Yamamoto, K., Higuchi, M., Shiki, S., Tsuruta, M., and Chiba, H. (2002) Stepwise radial complexation of imine groups in phenylazomethine dendrimers. *Nature*, **415**, 509–511.
- 132** Satoh, N., Cho, J.-S., Higuchi, M., and Yamamoto, K. (2003) Novel triarylamine dendrimers as a hole-transport material with a controlled metal-assembling function. *J. Am. Chem. Soc.*, **125**, 8104–8105.
- 133** Satoh, N., Nakashima, T., and Yamamoto, K. (2005) Metal-assembling dendrimers with a triarylamine core and their application to a dye-sensitized solar cell. *J. Am. Chem. Soc.*, **127**, 13030–13038.
- 134** Yamamoto, K., Higuchi, M., Kimoto, A., Imaoka, T., and Masachika, K. (2005) Novel functional groups with fine-controlled metal assembling function. *Bull. Chem. Soc. Jpn.*, **78**, 349–355.
- 135** Yamamoto, K., Imaoka, T., Chun, W.-J., Enoki, O., Katoh, H., Takenaga, M., and Sonoi, A. (2009) Size-specific catalytic activity of platinum clusters enhances oxygen reduction reactions. *Nat. Chem.*, **1**, 397–402.
- 136** Watababe, H. and Inoshita, T. (1986) Superatom: a novel concept in materials science. *Optoelectron.: Devices Technol.*, **1**, 33–39.
- 137** Kastner, M.A. (1993) Artificial atoms. *Phys. Today*, **64**, 24–31.
- 138** Ashoori, R.C. (1996) Electrons in artificial atoms. *Nature*, **379**, 413–419.
- 139** Oosterkamp, T.H., Fujisawa, T., van der Wiel, W.G., Ishibashi, K., Hijman, R.V., Tarucha, S., and Kouwenhoven, L.P. (1998) Microwave spectroscopy on a quantum-dot molecule. *Nature*, **395**, 873–876.

- 140 Fujisawa, T., Austing, D.G., Tokura, Y., Hirayama, Y., and Tarucha, S. (2002) Allowed and forbidden transitions in artificial hydrogen and helium atoms. *Nature*, **419**, 278–281.
- 141 Marcus, R.A. and Sutin, N. (1985) Electron transfers in chemistry and biology. *Biochim. Biophys. Acta*, **811**, 265–322.
- 142 Moser, C.C., Keske, J.M., Warncke, K., Farid, R.S., and Dutton, P.L. (1992) Nature of biological electron transfer. *Nature*, **355**, 796–802.
- 143 Bao, D., Millare, B., Xia, W., Steyer, B.G., Gerasimenko, A.A., Ferreira, A., Contreras, A., and Vullev, V.I. (2009) Electrochemical oxidation of ferrocene: a strong dependence on the concentration of the supporting electrolyte for nonpolar solvents. *J. Phys. Chem. A*, **113**, 1259–1267.
- 144 Satoh, N. and Han, L. (2012) Chemical input and I–V output: stepwise chemical information processing in dye-sensitized solar cell. *Phys. Chem. Chem. Phys.*, **14**, 16014–16022.
- 145 Satoh, N. (2014) Insight from molecular-scale electron transfer to small-scale electronics. *Chem. Lett.*, **43**, 629–630.

9

Conductive Polymer Nanostructures

Lin Jiang, Carsten Hentschel, Bin Dong, and Lifeng Chi

9.1

Introduction

Since the discovery of conductive polymers by Shirakawa, MacDiarmid, and Heeger in 1976, conductive polymers have attracted great attention in different research fields based on their outstanding properties: their electronic and optoelectronic characteristics can be reversibly controlled by doping and dedoping processes (metal–insulator transition) without losing the attractive mechanical advantages of polymers [1–3]. These have led to the production of various functional devices such as batteries, field effect transistors (FETs) [4,5], photodetectors [6], light-emitting diodes [7], and gas sensors [8], among many others [9–12]. It has also been shown that nanostructured conductive polymers exhibit significant improved physicochemical characteristics compared with their bulk counterparts, for instance, increased electrical conductivity, size-dependent excitation or emission, easier bandgap tunability, and coulomb blockade, which have led to a various new applications in electronics [13,14], optoelectronics [15,16], tissue regeneration [17], neural electrodes [18], and sensors [19,20].

In order to realize the potential applications of nanostructured conducting polymers, especially in nanodevice-related application, there are still some key questions to be clarified, for example, ordering and alignment of conducting polymer nanostructures, manipulating and positioning of conducting polymer nanostructure in nanodevices, the effects of nanocontacts on the electrical measurements, and so on [21,22]. These questions are particularly important to develop nanodevices based on individual conducting polymer nanostructure. In this chapter, we will focus on those methods that have been demonstrated to be capable of or have shown potential to produce ordered, single, and individually addressable conductive polymer nanostructure. Generally, the approaches can be characterized into the following categories: (i) solution-based synthesis, (ii) substrate-based fabrication, (iii) electrospinning technology and so on. The advantages, limitations, and future development potential of each approach will be provided.

9.2

Solution-Based Synthesis of Conducting Polymer Nanostructures

The low-cost solution preparation of conducting polymer nanostructures is of great interest for future applications. Accordingly, several template-assisted techniques were developed in the last years to increase the throughput [23]. Generally, template-assisted methods can be classified into two different groups: soft template and hard template syntheses.

9.2.1

Soft Template Synthesis

Soft template synthesis is a method that applies surfactants [24], liquid crystalline polymers [25], or functionalized polymers [26] to control the process of growth and morphologies of polymer nanomaterials. In this method, the driving forces are usually relatively weak, such as electrostatic interactions [27], π -stacking [28], hydrogen bonding [29], or van der Waals forces [30], which determine the self-assembly of the molecules.

Microemulsions are macroscopically oil–water mixtures, including amphiphile molecules, namely, surfactants, which exhibit a hydrophilic head and a hydrophobic tail, as represented in the micelle formation in Figure 9.1 [31]. Depending on the microemulsion, oil–water (a) or water–oil (b) mixture, the orientation of the surfactants can be controlled. The resulting structures called micelles produce conducting polymer nanoparticles with good control over the size, which can be influenced by the concentration of surfactant, the amount of water, and the temperature. The microemulsion polymerization process can be modified as well to synthesize nanocapsules [32], nanocomposites [33], and mesoporous structures [34] of conducting polymers. Jang *et al.* could selectively produce

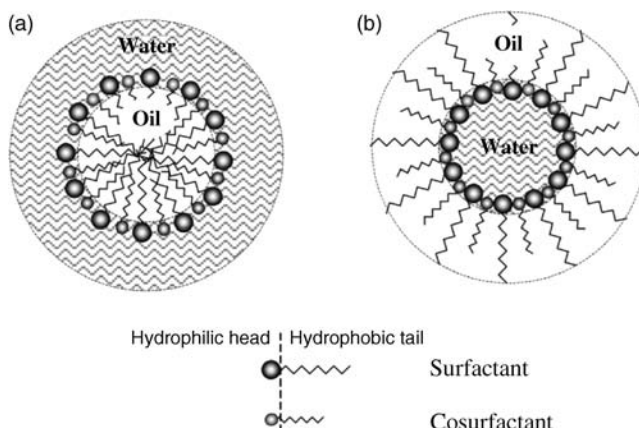


Figure 9.1 Schematic illustrations of (a) oil-in-water and (b) water-in-oil micelles. (Reprinted with permission from Ref. [31]. Copyright 2006, Springer.)

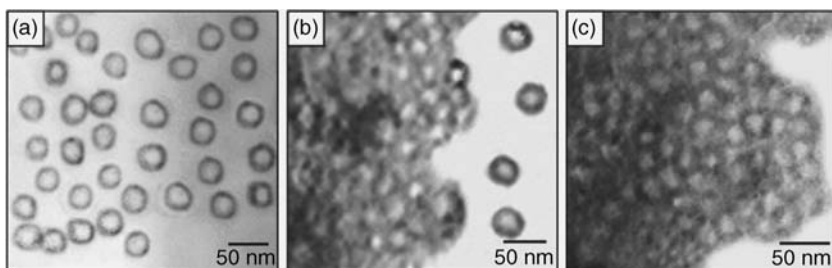


Figure 9.2 TEM images of PEDOT. (a) Nanocapsules prepared using 0.15 M DeTAB. (b) Mixture of nanocapsules and mesocellular foams obtained with 0.20 M DeTAB. (c) Mesocellular foams produced with 0.30 M DeTAB [35]. (Reprinted with permission from Ref. [35]. Copyright 2006, Wiley-VCH Verlag GmbH.)

poly(3,4-ethylenedioxythiophene) (PEDOT) nanocapsules and mesocellular foams by using surfactant-mediated interfacial polymerization (SMIP), as shown in Figure 9.2 [35]. The micelles act as porogens and serve as the polymerization sites at the micelle–water interface, which generated hollow nanostructures of conductive polymers efficiently.

Moreover, one-dimensional polymerized PEDOT structures can be produced by using sodium bis(2-ethylhexyl)sulfosuccinate (AOT) molecules with two relatively large hydrophobic tails in a reverse water-in-oil microemulsions [36–39]. The addition of FeCl_3 led to the development of AOT reverse cylindrical micelles and, finally, to the formation of ellipsoidal PEDOT nanoparticles toward PEDOT nanotubes, depending on the concentration of the FeCl_3 , as shown in Figure 9.3 [40]. Resistance measurements reveal that the PEDOT nanotubes have a high sensitivity to alcohol vapor and fast responses.

The soft template method provides a powerful and popular technique to produce conducting polymer nanostructures at low cost and in large yield. The

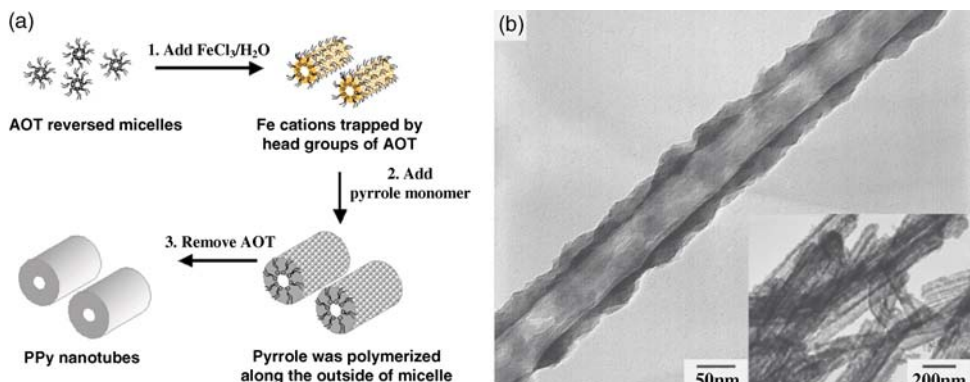


Figure 9.3 (a) Schematic diagram of PPy nanotube fabrication using reverse microemulsion polymerization. (b) TEM image of PPy nanotubes. (Reprinted with permission from Ref. [40]. Copyright 2003, American Chemical Society.)

disadvantage of this method is the poor control in morphology, orientation, and diameter of the 1D conducting polymer nanostructures. But the apparently less controllable environment of the polymerization in the soft template technique leaves room for the preparation of complex 1D as well as 3D nano- and micro-structure designs [40].

9.2.2

Hard Template Method

The hard template approach relies on the direct synthesis of conducting polymer nanostructures within the cylindrical channels of porous membranes [41]. In this case, the linear pores guide the growth of the polymer along the pore axis in perpendicular direction to the surface. Thus, after the synthesis, highly ordered 1D nanostructured arrays of nanotubes [42] and/or nanowires [43] are formed within the template (Figure 9.4) [43]. The technique of using hard templates was first introduced by Cai and Martin in the late 1980s [44]. The linear pores guide the polymer to align along the pore axis in perpendicular direction to the surface and leads to the nanofabrication of cylinders [45], fiber wires [46], and hollow tubes [47] consisting of, for example, polypyrrole (PPy) [48], poly(3,4-ethylene-di-oxythiophene) (PEDOT) [49], polyaniline (PAN) [50], and poly-(*p*-phenylen-vinylen) (PPV). Zuo *et al.* prepared PANI–Ppy binary nanotubes by using halloysite as template with a pore diameter of 200 nm and a thickness of 60 nm [51]. Chen *et al.* fabricated in a multistep procedure PEDOT–PbS–PPy heterojunction nanowires with diameters of roughly 270 nm and lengths of 26 mm by using an AAO

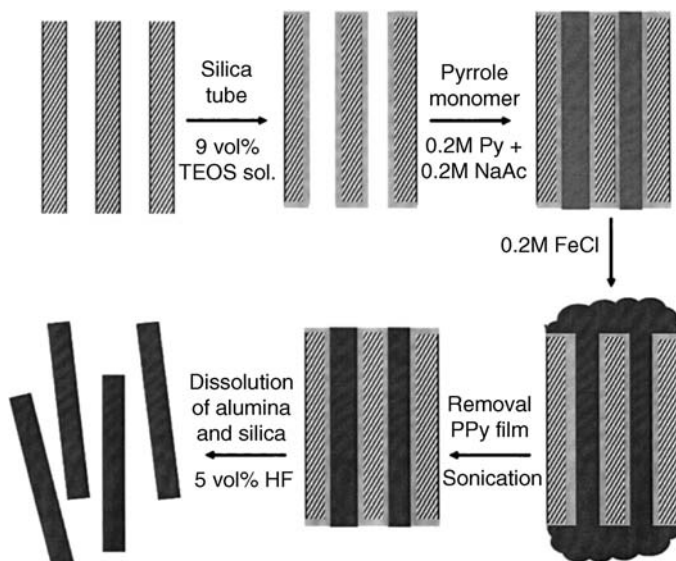


Figure 9.4 Schematic of polypyrrole nanowires synthesis. (Reprinted with permission from Ref. [43]. Copyright 2007, Wiley-VCH Verlag GmbH.)

template [52]. These types of wires represent a combination of organic/inorganic semiconductors and display a logic gate. The dimensions of synthesized nanowires using AAO templates depend mainly on two factors, polymerization time and used current [53,54], and the electrical properties can be influenced by external agents.

For the measurement of the conductivity of 1D nanowire, the solid hosting material should be removed by etching processes, which make the procedure comparatively intricate. Martin *et al.* found that the conductivity of the PPy fibrils increased with the decreased diameter of the fibrils, which were template synthesized by using porous membranes at low temperature ($<0^{\circ}\text{C}$) [55]. Their conductivity measurement was based on bundles of conducting polymer fibrils rather than on individual ones. On applying pressure on the fibrils, samples led to the reduction of the contact resistance, but might possibly destruct the samples [56,57]. The conducting polymer nanowire can also be rinsed after the removal of the alumina template and dispersed in a solvent [58]. A typical way to obtain individual nanowires on a substrate is to drop-cast a very dilute nanowire solution and place across four metal electrodes for four-point measurement [59]. However, the effect of the nanocontacts on the electrical measurements is still not resolved.

Furthermore, heterogeneous conducting nanowires can be synthesized in alumina templates. Nanowires that contain segments of different materials can be grown electrochemically inside the alumina nanopores via sequential deposition of the materials using different precursors and electrolytes [60–64]. However, regarding nanodevice requirement, the capability of variability and manipulation in position of the resulting surface structures is limited.

9.3

Substrate-Based Fabrication of Conducting Polymer Nanostructures

Due to the steady development of microelectronics toward smaller and smaller scales, such devices offer higher precision, enhanced performance, and new properties and begin to take more prominent roles. In nanodevice-related application, conducting polymer nanostructures are mainly applied to flat planar substrates. In general, strategies used to generate conducting polymer nanostructure on a substrate can be separated into two different fields: add material to the surface or remove material from it.

9.3.1

Add to Surface

9.3.1.1 Direct Writing

A scanning probe can be used in “dip-pen” lithography by direct writing conducting polymer ink onto a substrate following a programmed route to create conducting polymer nanostructure with desired patterns and shapes [65,66]. For instance, Lim and Mirkin reported the deposition of conducting polymer nanostructure on the pretreated oppositely charged substrate by electrostatic interactions (see

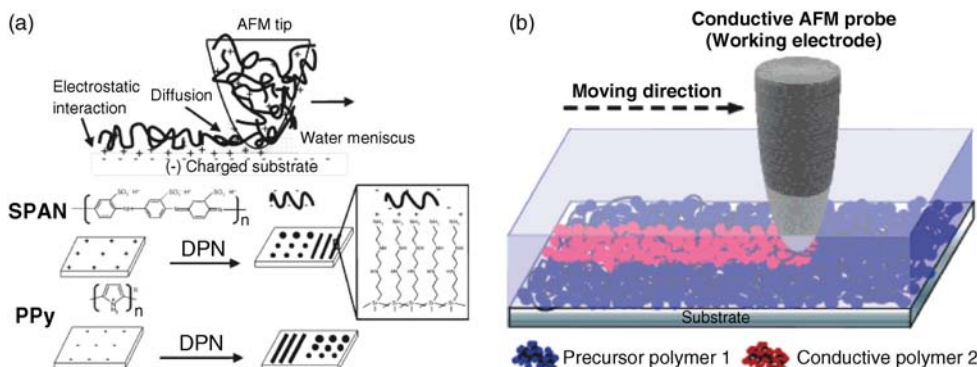


Figure 9.5 (a) Schematic representation of dip-pen nanolithography for charged conducting polymers. (Reprinted with permission from Ref. [65]. Copyright 2002, Wiley-VCH Verlag

GmbH.) (b) Electrochemical oxidative nanolithography process. (Reprinted with permission from Ref. [74]. Copyright 2004, American Chemical Society.)

Figure 9.5a). The dimensions of the transferred structures depend heavily on the probe geometry, capillary meniscus formed between tip and surface, and the velocity of the tip movement. Su *et al.* reported a slightly different method in which a monomer ink was transported from the AFM tip to the substrate while polymerizing chemically with an acid promoter to form conducting polymer nanostructure [67]. By combining DPN with other techniques [68,69], such as electrochemical DPN (e-DPN) [70] and thermal DPN (tDPN) [71], defined conducting polymer patterns with higher resolution (less than 100 nm dimensions) on semiconducting and insulating surfaces can be achieved [72,73]. Sotzing and coworkers have produced conducting polymer nanostructures on the substrate by solid-state oxidative cross-linking (SOC) (Figure 9.5b) [74]. The entire procedure is a maskless, one-step process and there is no material transfer from the tip to the substrate. The conducting polymer lines are patterned into a precursor plastic film without specific restriction in the choice of substrates.

9.3.1.2 *In Situ* Synthesis or Assembly

In situ synthesis and assembly provide a promising approach to fabricate the conducting polymer nanostructures on the substrate [75–77]. Unlike some of the inorganic nanowires, conducting polymers tend to bend and curve easily as they are grown/synthesized without any form of guidance. To achieve low-cost and high-resolution nanostructure patterning with high throughput, template-assisted techniques were developed and currently combined with *in situ* synthesis or assembly for patterning conducting polymers. Here, the term “template-assisted” implies that the surface has to display nanostructures, prepared by external pre-pattern lithography techniques (e.g., AFM, FIB, e-beam, nano- and micropainting, and photolithography) [78–80]. There are mainly two *in situ* syntheses or assembly methods for patterning: electrochemical polymerization and chemical polymerization. Physical adsorption and electrostatic interaction have also been used for fabrication of conducting polymer nanostructures [81–83].

Electrochemical Polymerization

Although there are a number of different successful approaches to fabricate conducting polymer nanostructures, they still have limitations regarding, for example, throughput, resolution of the feature size, large-scale positioning, and simplicity in the production. A simple and robust method to archive conducting polymer nanostructures on surfaces is given by a technique called electropolymerization [84,85]. This technique provides the polymerization of the monomers induced by an electric field applied between individual addressed electrodes [78,86–89]. The gold electrodes were fabricated on a silicon/silicon oxide substrate by using photolithography and electron beam deposition techniques. Combination with prepattern techniques allows a controlled number of highly aligned conducting polymer nanowires to be synthesized *in situ* – between two metal electrodes, thereby providing a simple way to incorporate single and multiple nanowires into prepatterned electrical circuits. Ramanathan *et al.* used a template-assisted electropolymerization approach [90]. Their fabrication procedure of the polymer nanowires is based on a prestructure process by etching multiple channels between the gold electrodes that provide and guide the growth of the polymer chain. Figure 9.6 displays a typical SEM image of a 100 nm wide and 4 μm long electrochemically grown PANI nanowire. It was reported that the wires revealed resistance values of 0.2–0.8 and 6–7 $\text{k}\Omega$ for a 500 nm wide nanowire, depending on whether they are wet or dry. For a 100 nm wide dry nanowire, the resistance was determined to be 1 $\text{M}\Omega$. Peng *et al.* also used the *in situ* electrochemical polymerization to specifically produce polyaniline nanoribbons and further conducted two- and four-point electrical characterization of these nanoribbons, using the built-in electrodes [89]. The *in situ* electrochemical deposition of conducting polymers within nanochannels between two electrodes makes it possible to realize individual conducting polymer nanostructure devices. However, the formed conducting polymer nanostructures by electropolymerization can easily detach from the substrate due to weak adhesion between polymer layer and substrate, thus the effects of the nanocontacts on the electrical measurements still remain [91].

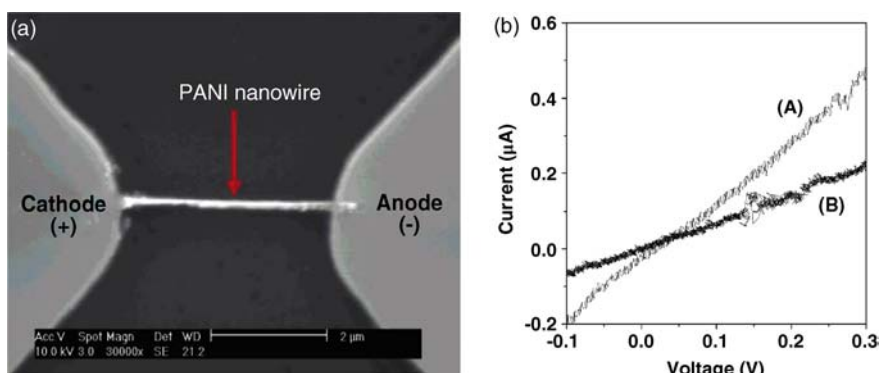


Figure 9.6 (a) SEM image of a 100 nm wide by 4 μm long PANI nanowire. (b) Current versus potential for a PANI (A) and PPy nanowire (B) at 50 mV s^{-1} scan rate. (Reprinted with permission from Ref. [90]. Copyright 2004, American Chemical Society.)

Chemical Polymerization

In order to solve the above problem, one of the key issues has to be addressed: the improvement of the adhesion of the conducting polymers onto the substrate without reducing the conductivity, especially on insulating surfaces. The Gleason group directly grafted conducting polymers onto the substrates that relied on covalent bonding between the conducting polymer and an aromatic moiety of the substrate and exhibited a dramatic increase in adhesion strength [92,93].

Dong *et al.* presented a copolymer strategy based on a nanolithography technique that is used to pattern conducting polymers with high resolution [94,95]. In order to immobilize polypyrrole on the substrate, surface-reactive reagent bearing pyrrole, for example, *N*-(3-trimethoxysilylpropyl) pyrrole (abbreviated as py-silane) was applied to increase the adhesion between polymer and substrate [95]. First, the substrate was spin coated with a thin layer of PMMA, which prestructured in the next step either with e-beam lithography or nanoimprint techniques to generate the desired pattern into the resistance layer. Then, the sample was treated with a mixture of pyrrole and py-silane and used iron-III chloride in order deposit the PPy by oxidizing the pyrrole and py-silane onto the surface. Finally, the resist layer is lifted off in acetone by sonication. The height of the polypyrrole layer can be controlled by the reaction time. Figure 9.7 shows a sample patterned with nanowire arrays with different widths and lateral distances, which is reflected by the different colors of the light diffractions. The positions labeled with 1, 2, 3, 4, 5, and 6 correspond to 100, 150, 250, 350, 320, and 220 nm wide wires separated by gaps of 150, 200, 300, 400, 380, and 280 nm. Electrical conductivity experiments of these polypyrrole revealed conductivities less than 1 S cm^{-1} , which is relatively low compared to the conductivity of PPy

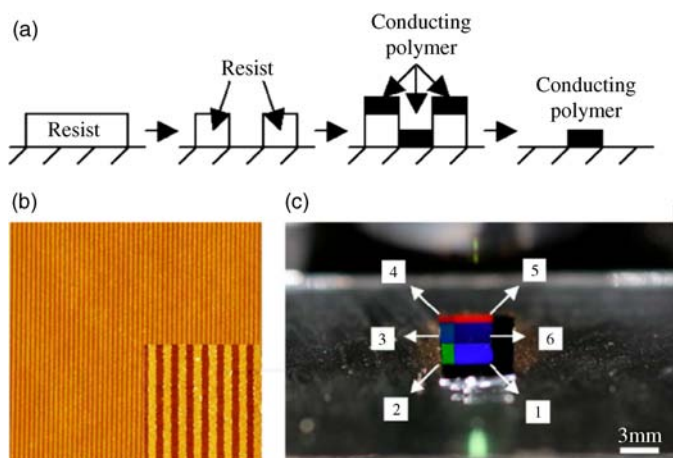


Figure 9.7 (a) Schematic representation of the fabrication process. (Reprinted with permission from Ref. [94]. Copyright 2005, Wiley-VCH Verlag GmbH.) (b) AFM image showing the high-density polypyrrole nanowires. (c) Optical image

from a CCD camera showing the light diffraction from high-density polypyrrole nanowires fabricated using NIL and a lift-off process. (Reprinted with permission from Ref. [95]. Copyright 2006, Wiley-VCH Verlag GmbH.)

film (20 S cm^{-1}) with the same py-silane incorporation. One reason could be the incorporation of surface-active monomers (py-silane) into the main chains, which inevitably decreases the conducting polymer's electrical properties, especially for the small structures [94–96].

In order to employ 1D conducting polymer nanostructures as building blocks in nanodevices, new strategies must be developed to enhance their conductivity. Jiang *et al.* first directly assembled a py-silane monolayer on top of a silicon oxide layer [97]. The initial surface functionalization of the substrate with py-silane monolayer is then used to conjugate with the chemically deposited PPy layer and enhance the adhesion between substrate and PPy layer through chemical covalent connection. After lift-off in acetone, the resistance and the PPy layer on the top of it were removed, while the PPy chemically adhered to the substrate remained, which led to the formation of PPy nanobelts, whose width depends on the feature size written by EBL. The strategy presented here offers efficient fabrication of conducting polymer structures with a resolution down to sub-50 nm. Conductance measurements demonstrated that a decrease in the width of the polymer belts caused a significant enhancement in the conductivity (up to $\sim 3200\text{ S cm}^{-1}$) as soon as the width of the belts fell below a value of roughly 80 nm due to the better alignment of the polymer chains with decreasing cross section, as shown in Figure 9.8c.

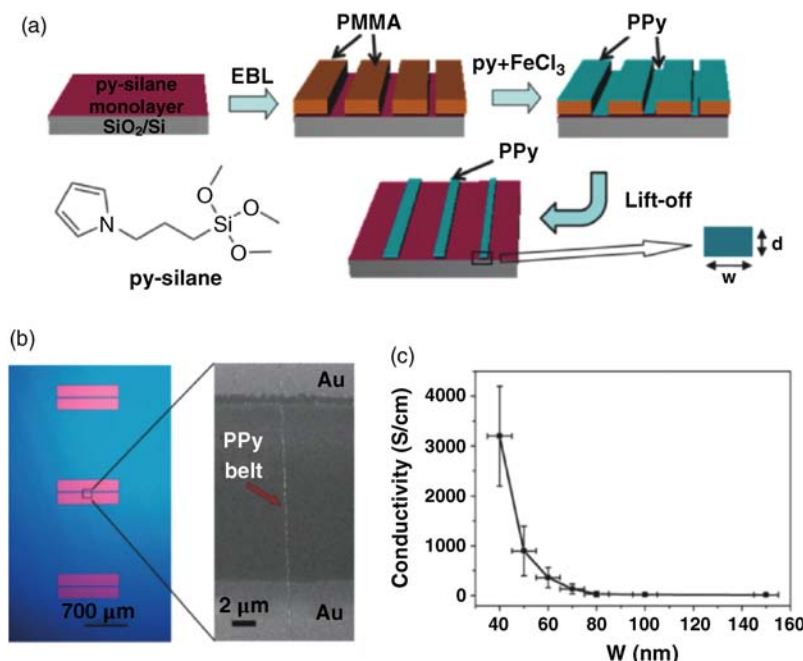


Figure 9.8 (a) Schematic illustration of the fabrication process. (b) Optical and SEM images of a PPy nanobelt bridging two Au microelectrodes. (c) Dependence of the

electrical conductivity of individual nanobelts on the width of the nanobelts. (Reprinted with permission from Ref. [97]. Copyright 2011, Wiley-VCH Verlag GmbH.)

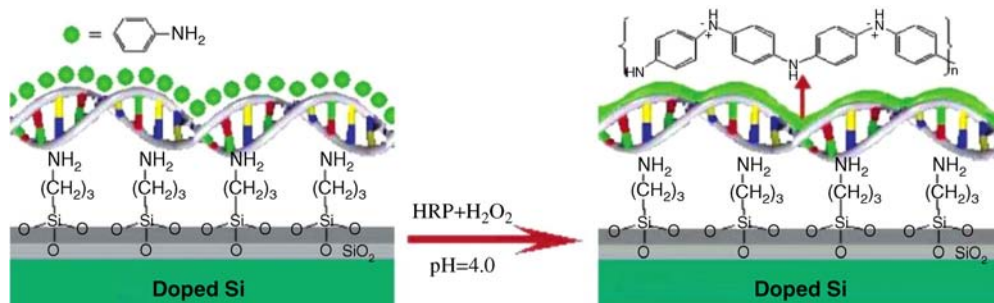


Figure 9.9 Fabrication of a polyaniline nanowire immobilized on a Si surface with stretched double-stranded DNA as a guiding template. (Reprinted with permission from Ref. [99]. Copyright 2004, American Chemical Society.)

Electrostatic Assembly

Besides electrochemical and chemical synthesis methods, electrostatic interaction has also been used for fabrication of conducting polymer nanostructures [82,83,98]. Since conducting polymers are commonly synthesized by oxidizing polymer monomers in a strongly acidic environment, using biological polyelectrolytes as template provide more mild reaction conditions. DNA can provide a soft template for the polymer wire fabrication, as demonstrated by Ma *et al.* [99–102]. In their experiments, they used DNA as growing substrate to fabricate polyaniline nanowires. Therefore, the fully stretched DNA strands were first immobilized onto a thermally oxidized silicon oxide substrate (Figure 9.9). Then, after aniline monomer solution was given to the DNA substrate, the aniline monomers organize along the DNA chain driven by electrostatic interactions. Afterward, the aniline monomers were polymerized so that polyaniline nanowires were finally formed whose positions were defined by the orientation of the immobilized DNA strands. Conductance measurements have shown high sensitivity of the DNA/PANI nanowires to doping and dedoping processes with HCl and NH₃ vapor, however, with low electrical conductivity values.

9.3.2

Remove from Surface

9.3.2.1 Nanoscratching

Instead of applying conductive polymers as ink to a substrate, AFM can be used in a reversed way by scratching [103,104]. This nanolithography technique that is cost-effective and reliable allows scratching pattern directly into a polymer film with a submicrometer until nanoscale resolution, whereas the resolution can be adjusted by varying the polymer film procedure conditions and lithography parameters [105,106].

Jones *et al.* demonstrated a high reproducibility of this technique by scratching gab structures of different dimensions ranging from 40 nm to 2.3 μm directly into films of poly(3-hexylthiophene-2,5-diyl) (P3HT) [107]. Li *et al.*, for example,

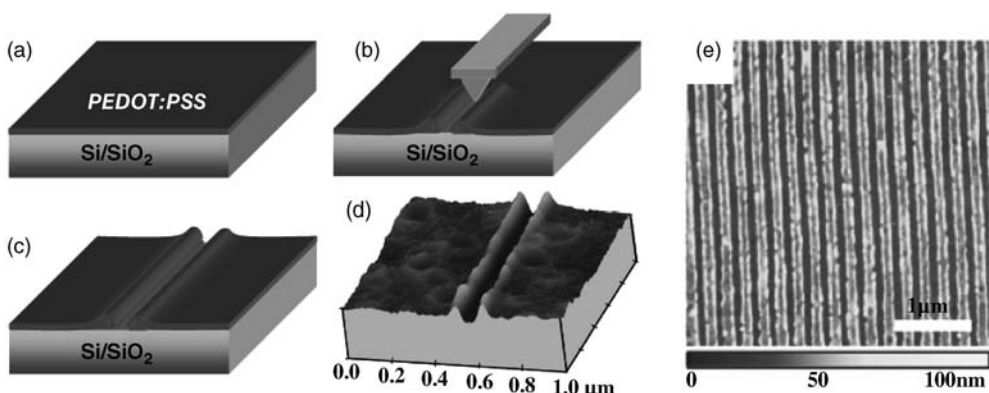


Figure 9.10 AFM nanoscratching on PEDOT:PSS. (a–c) Schematic process of AFM nanoscratching by an AFM tip on PEDOT:PSS. (d) AFM image of an exemplified groove, the groove width is about 50 nm. (e) Multiple parallel grooves and lines with a periodicity of 250 nm (100 nm groove and 150 nm line). (Reprinted with permission from Ref. [108]. Copyright 2010, Wiley-VCH Verlag GmbH.)

reported about nanoscratching experiments on poly(3,4-ethylenedioxythiophene):poly(4-styrenesulfonate) (PEDOT:PSS) on both rigid and flexible substrates [108]. Figure 9.10 shows multiple scratching patterns performed on a 15 nm thick film of PEDOT:PSS spin coated on silicon. The resulting line structure exhibits parallel well-defined 150 nm wide polymer lines surrounded by 100 nm wide grooves (smallest groove width was reported to be 50 nm). Additionally, organic transistors fabricated in this way reveal a low threshold voltage and show a negligible short-channel effect. Thus, both the high reliability and resolution suggest that PEDOT:PSS may be attractive for scratched organic electronics. Besides, PEDOT:PSS is classified as an excellent organic electrode material since the contact resistance to organic semiconductors is reported to be low [109–113]. This result proposes a feasible concept of instrument design based on mechanical scratching for patterning PEDOT:PSS for organic electronics, which may lead to the development of scratching electronics. In former experiments, the Sengupta *et al.* have exploited latter feature to fabricate PEDOT:PSS electrodes by using AFM nanolithography to study the charge transport properties of biological nanowires [114]. In comparison to other techniques, nanoscratching is a straightforward technique without any complicated procedure steps and enables to structure surfaces with a high throughput by using arrays of tips.

9.3.2.2 Etching

Another remove from surface technique for fabrication of conducting polymer nanostructures with higher resolution and high throughput is etching. Starting from a thin film spin coated on a substrate, the conducting polymer can be patterned by physical embossing [115,116], photodecomposition [117], laser ablation [118], or dry plasma etching modes [119–121] using a pattern mold or

mask. Lipomi *et al.* developed a template-free nanoskiving approach to fabricate conducting polymer nanowires by edge lithography [122]. Huang *et al.* developed an approach to reduce the lateral size of conducting polymer structures using isotropic plasma etching (IPE) combined with nanoimprint lithography [120,121], which provides a cost-effective way for fabrication of high-resolution and complex patterns of conducting polymer.

The Ross group demonstrated the large-area fabrication of an array of well-ordered 15 nm wide conducting polymer nanowires by using an etch mask consisting of self-assembled patterns of cylinder-forming poly(styrene-*b*-dimethylsiloxane) diblock copolymer confined in topographic templates. Briefly, the surface was first prestructured with a 40 nm deep gab structure that was then coated with different layers of PEDOT:PSS (20 nm), SiO₂ (5 nm), and PDMS brush (3–4 nm) and in the final step with a PS-PDMS block copolymer. After the sample was solvent annealed and etched with CF₄ or O₂ plasma, the surface exhibited a highly ordered PEDOT:PSS line structure, as can be seen in Figure 9.11. It is shown that this kind of structured polymer surface show

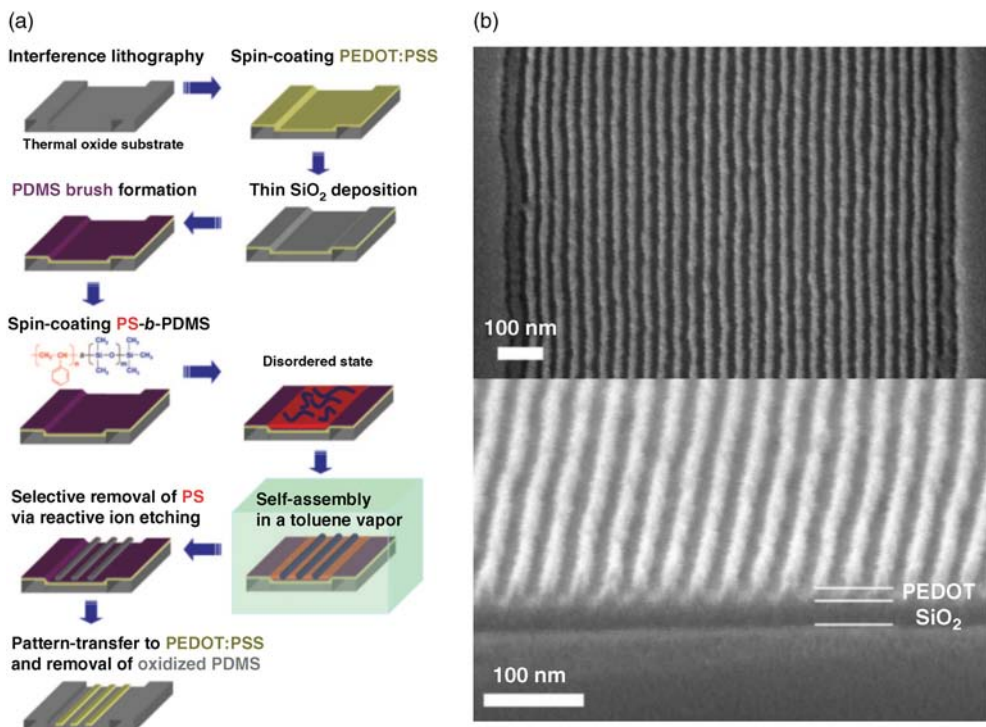


Figure 9.11 Fabrication steps of nanostructured polymer surfaces. In the first step (left), the prestructured surface of Si₂ was spin coated with PEDOT:PSS, then with PDMS brush and, finally, with a PS-PDMS block

copolymer. After the surface was ion etched, it showed highly aligned PEDOT:PSS nanowires (right). (Reprinted with permission from Ref. [119]. Copyright 2008, American Chemical Society.)

higher and more stable sensitivities to ethanol vapor than the unstructured polymer films.

9.4

Electrospinning Technique of Conducting Polymer

Electrospinning is another highly effective technique to transfer electrostatically polymer fibers or nonwoven fibers with a diameter in micrometer to nanometer range directly onto the substrate. Generally, for electrospinning, a high positive voltage, typically in the tens of kilovolts, is applied between a capillary syringe that contains the polymeric solution and a collecting surface. The induced electric field forces the polymer droplet at the end of the syringe to overcome its surface tension and, as the solution is evaporated, a charged thin polymer jet is finally ejected from the tip toward the collecting grounded surface. Within the flight time, the diameter of the polymer jet decreases steadily [123]. The morphology of the resulting polymer fibers can be controlled and influenced by several more experimental parameters, such as applied voltage and distance between the syringe tip and the collecting substrate, the flow rate of the solution, molecular weight, polymer solution concentration, and so on, to name a few [124]. Figure 9.12 shows the typical electrospinning setup, where the polymer solution was loaded to the syringe, which is pumped out at a constant rate

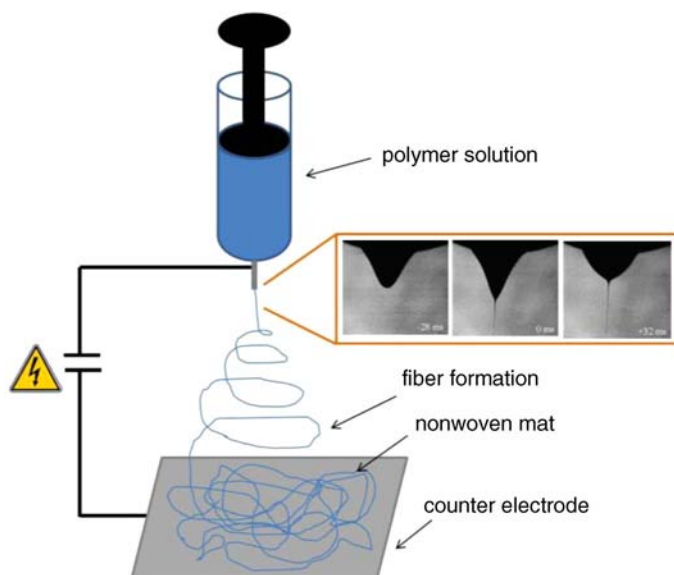


Figure 9.12 Schematic illustration of the electrospinning apparatus. (Reprinted with permission from Ref. [123]. Copyright 2008, Elsevier.)

by a syringe pump. Upon the application of a high voltage, a Taylor cone, as indicated by the optical microscopic image in Figure 9.12, is formed, which is key to the successful electrospinning.

Though electrospinning was first developed to be a technique to obtain the polymeric fibers, it has now been widely utilized to fabricate functional nanofibers composed of functional materials, such as conducting polymers. The conducting polymer nanofiber fabricated by electrospinning technique has a diameter in the range of several tens of nanometers to several hundreds of nanometers, depending on the fabrication condition. Due to the rigidity of the conducting polymer structure originating from the conjugated backbone, the electrospinning of conducting polymer is not easily achievable. The fabrication of tiny conducting polymer nanofibers, particularly those smaller than 100 nm, normally requires the utilization of a carrier polymer, for example, polyethylene oxide. The function of the carrier polymer is to render higher viscosity to the solution and increase the polymer chain entanglement, which increase the electrospinnability of the conducting polymer. Figure 9.13 listed the common conducting polymer structures that have been utilized for electrospinning and the corresponding polymers that were utilized as the carrier polymers [125].

The conductivity of the electrospun conducting polymer nanofibers considerably varies, depending on the composition of the resulting nanofibers [126]. As can be seen from Figure 9.14, the higher the content of the conducting polymer, the higher the conductivity, with the highest value being around 10 S cm^{-1} .

Because of the elongation stress caused by the high electrical field during the electrospinning process, the conducting polymer inside the electrospun fiber often exhibits orientations. For example, Tu *et al.* [128] have reported the electrospinning of poly[2-methoxy-5-(2-ethylhexyloxy)-1,4-phenylenevinylene] (MEHPPV). MEHPPV is a light-emitting p-type polymeric semiconductor with intermediate charge mobility. MEHPPV was first dissolved in chloroform and then electrospun into defect-free fibers, uniform and smooth as observed by SEM and AFM. The diameter of the resulting polymeric fiber is about 300 nm. As observed by polarized photoluminescence spectroscopy (Figure 9.15), there is strong molecular orientation inside the electrospun nanofiber due to the elongation strength and the size confinement inside the nanofiber. Such orientation also leads to the electrical performances comparable to the best thin films in literature observed, with μ value about $1 \times 10^{-3}\text{ cm}^2\text{ V}^{-1}\text{ s}^{-1}$.

Electrospun conducting polymer nanofibers have been demonstrated to possess a variety of different applications. They can be utilized as the active material for the FET. Due to the sensitivity of the conducting polymer itself when exposed to external analyte, conducting polymer nanofibers were also utilized in various nanosensors. Other electronic applications involving conducting polymer nanofibers include logic circuit and phototransistor.

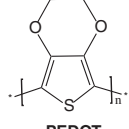
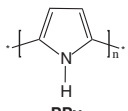
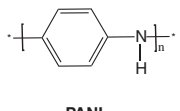
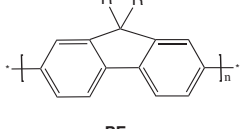
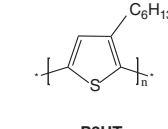
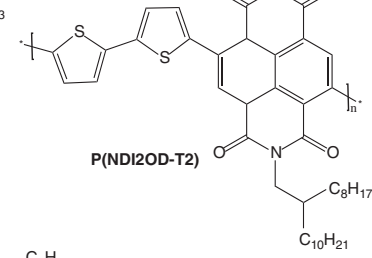
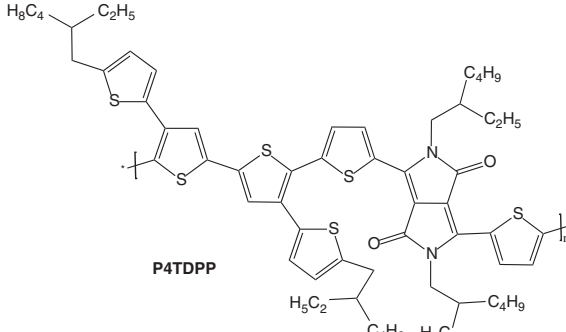
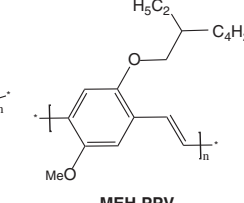
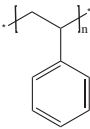
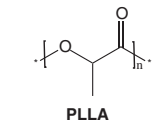
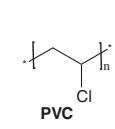
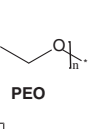
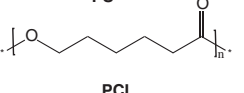
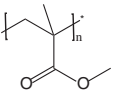
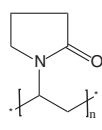
Conductor and semiconductor conjugated polymers	 PEDOT  PPy  PANI  PF  P3HT  P(NDI2OD-T2)  P4TDPP  MEH-PPV
Insulating/supporting polymers	 PS  PLLA  PVC  PEO  PCL  PMMA  PVP

Figure 9.13 Conducting polymer structure and the carrier polymers utilized in electrospinning process. (Reprinted with permission from Ref. [125]. Copyright 2014, Multidisciplinary Digital Publishing Institute.)

As shown in Figure 9.16, Pinto *et al.* [129] have reported a camphorsulfonic acid-doped polyaniline/polyethylene oxide nanofiber, which is fabricated by electrospinning at low voltage of about 8 kV. This nanofiber can be used as the active material for the FET. The thinnest nanofiber they have tested has a diameter of approximately 120 nm. They found that the conductivity of the nanofiber can reach $10^{-3} \text{ S cm}^{-1}$, and the hole mobility is $1.4 \times 10^{-4} \text{ cm}^2 \text{ V}^{-1} \text{ s}^{-1}$. This work

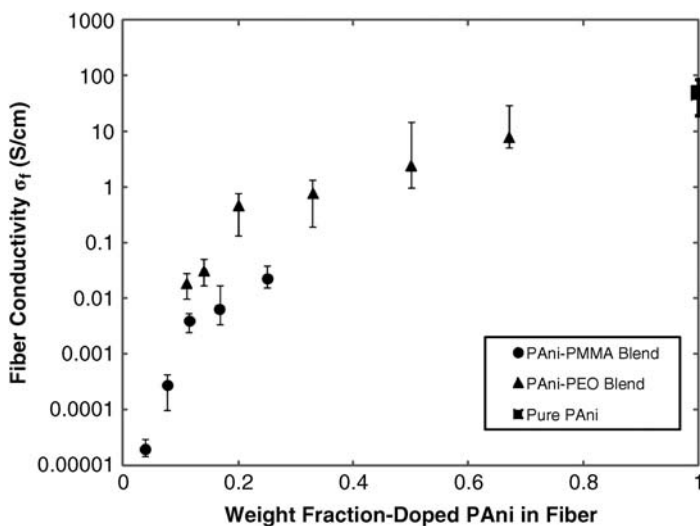


Figure 9.14 Conductivity of the electrospun conducting polymer nanofiber as a function of conducting polymer content. (Reprinted with permission from Ref. [127]. Copyright 2012, American Chemical Society.)

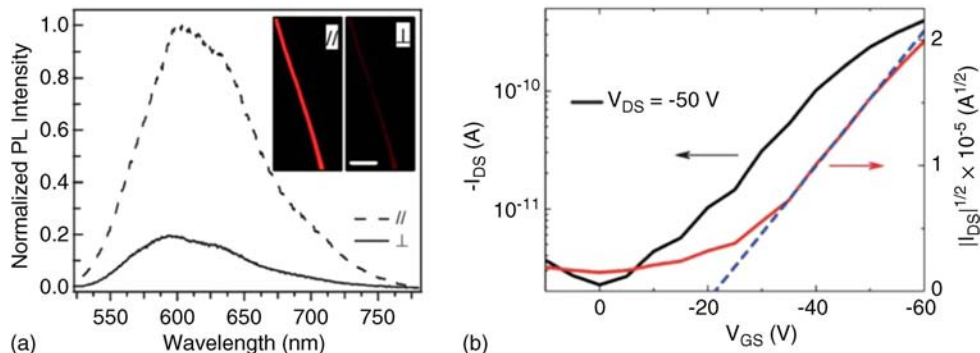


Figure 9.15 (a) Polarized photoluminescence (PL) spectroscopy of single MEH-PPV nanofiber showing clear molecular orientation along the fiber axis. PL spectra parallel to the fiber axis (PL//, dashed line) and perpendicular to the fiber axis (PL \perp , solid line) are reported. Insets: Corresponding fluorescence micrographs. Marker = 20 nm. (b) $-I_{DS}$ (left vertical scale) and

$|I_{DS}|^{1/2}$ (right scale) versus V_{GS} for $V_{DS} = 50$ V of MEH-PPV nanofiber FET (channel length of 20 μ m and fiber diameter of 500 nm). The dashed curve is a linear fit to data in the saturation region. (Reprinted with permission from Ref. [128]. Copyright 2010, Royal Society of Chemistry.)

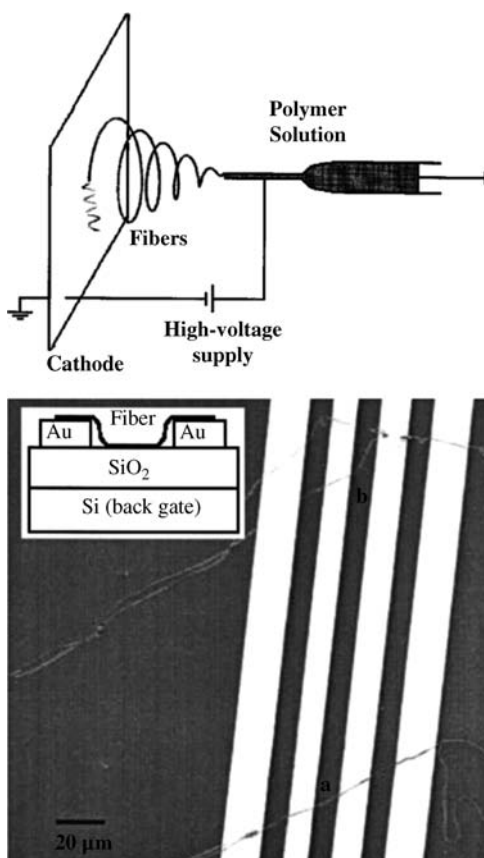


Figure 9.16 SEM image showing the polyaniline nanofiber bridging the gap between the metal electrodes. Fibers a and b have direct contact with the electrodes. *Inset:* Schematic

illustration showing the configuration.
(Reprinted with permission from Ref. [129].
Copyright 2003, American Institute of Physics.)

implies that a simple method to fabricate polymer FET may have potential for low-cost FET circuits.

Liu *et al.* [130] used electrospinning technique to fabricate polyaniline nanowires with diameters of 100 nm on substrate electrically connected to four gold electrodes, as illustrated in Figure 9.17. The carrier polymer utilized during electrospinning process is based on polyethylene oxide. Single polyaniline nanofiber can be laid between electrodes. The conductivity of the resulting structure is very high, which is measured to be around 0.5 S cm^{-1} . Conducting polymers, such as polyaniline, are p-type doped materials. They are sensitive to molecules that are rich in electron, such as ammonia gas. Therefore, by exposing this device to the ammonia gas, it can function as a nanosensor. These devices showed characteristics of a gas sensor that is able

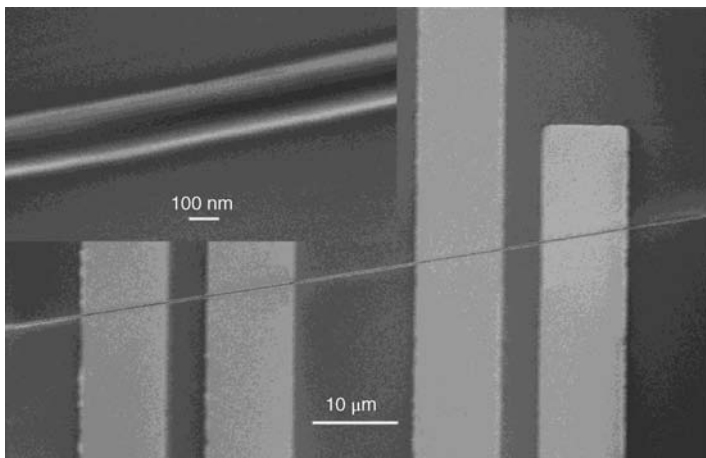


Figure 9.17 SEM image indicating a single polyaniline nanofiber lying on top of the electrode surface. (Reprinted with permission from Ref. [131]. Copyright 2004, American Chemical Society.)

to detect NH_3 gas at concentrations as low as 0.5 ppm with rapid response and recovery times.

9.5

Summary and Outlook

Conductive polymer nanostructures benefit on one hand from their high surface area-to-volume characteristics and thus the ability to react very sensitively to external agents [130,132,133]. On the other hand, conductive polymers exhibit attractive mechanical properties, such as flexibility and processing advantages [134,135]. Thus, functionalized nanostructures of conducting polymers in the size of 1–100 nm have received great attention in nanosciences and nanotechnology and lead to various new (possible) applications and devices. As already mentioned, conductive polymer nanostructures show enhanced surface area-to-volume characteristics, and the electrical properties can be reversibly changed by doping and dedoping processes, which make them highly sensitive to environment with faster response times with respect to their bulk counterparts. Thus, conductive polymer nanostructures are of high interest in the exploration as electrochemical, biological, and optical sensors [62,78,136–139]. In addition to detect chemical vapors, nanostructured conductive polymers have proved to be useful in detecting biological molecules [140–143]. Moreover, progresses have been made in fabricating different devices, such as field effect transistors, optoelectronic devices, supercapacitors, batteries, integrated circuits, memory devices, photodetectors, and so on [61,144–151].

Before conductive polymer nanostructures could find their way in major applications, several challenges, including the consistent and efficient preparation of various nanostructures with uniform, nondisperse, and well-controlled morphology and size need to be met; the precisely positioning of nanostructures into desired locations with ordered structures for device integration, the orientation and alignment control of conducting polymer chains in nanostructures, and the realization of multifunctional polymeric nanosystems. To address these issues and answer the open questions, increased research activities and the involvement of industry will be needed and they are on the way.

References

- 1 Shirakawa, H. (2001) The discovery of polyacetylene film: the dawning of an era of conducting polymers (Nobel Lecture). *Angew. Chem., Int. Ed.*, **40** (14), 2575–2580.
- 2 MacDiarmid, A.G. (2001) “Synthetic metals”: a novel role for organic polymers (Nobel Lecture). *Angew. Chem., Int. Ed.*, **40** (14), 2581–2590.
- 3 Heeger, A.J. (2001) Semiconducting and metallic polymers: the fourth generation of polymeric materials (Nobel Lecture). *Angew. Chem., Int. Ed.*, **40** (14), 2591–2611.
- 4 Bao, Z.N. *et al.* (1997) High-performance plastic transistors fabricated by printing techniques. *Chem. Mater.*, **9** (6), 1299–1301.
- 5 Garnier, F. *et al.* (1994) All-polymer field-effect transistor realized by printing techniques. *Supramol. Sci.*, **265** (5179), 1684–1686.
- 6 Yu, G., Zhang, C., and Heeger, A.J. (1994) Dual-function semiconducting polymer devices: light-emitting and photodetecting diodes. *Appl. Phys. Lett.*, **64** (12), 1540–1542.
- 7 Burroughes, J.H. *et al.* (1990) Light-emitting diodes based on conjugated polymers. *Nature*, **347** (6293), 539–541.
- 8 Virji, S., Kaner, R.B., and Weiller, B.H. (2006) Hydrogen sensors based on conductivity changes in polyaniline nanofibers. *J. Phys. Chem. B*, **110** (44), 22266–22270.
- 9 Wang, Y.G., Li, H.Q., and Xia, Y.Y. (2006) Ordered whiskerlike polyaniline grown on the surface of mesoporous carbon and its electrochemical capacitance performance. *Adv. Mater.*, **18** (19), 2619–2623.
- 10 Oyama, N. *et al.* (1995) Dimercaptan– polyaniline composite electrodes for lithium batteries with high energy density. *Nature*, **373** (6515), 598–600.
- 11 Baker, C.O. *et al.* (2008) Monolithic actuators from flash-welded polyaniline nanofibers. *Adv. Mater.*, **20** (1), 155–158.
- 12 Tseng, R.J. *et al.* (2005) Polyaniline nanofiber/gold nanoparticle nonvolatile memory. *Nano Lett.*, **5** (6), 1077–1080.
- 13 Wang, C.-C. *et al.* (2008) Enhancement of electrical properties of ferroelectric polymers by polyaniline nanofibers with controllable conductivities. *Adv. Funct. Mater.*, **18** (8), 1299–1306.
- 14 Long, Y. *et al.* (2010) Electrical conductivity studies on individual conjugated polymer nanowires: two-probe and four-probe results. *Nanoscale Res. Lett.*, **5** (1), 237–242.
- 15 Arico, A.S. *et al.* (2005) Nanostructured materials for advanced energy conversion and storage devices. *Nat. Mater.*, **4** (5), 366–377.
- 16 Simon, P. and Gogotsi, Y. (2008) Materials for electrochemical capacitors. *Nat. Mater.*, **7** (11), 845–854.
- 17 Abidian, M.R. *et al.* (2012) Neural tissue engineering: hybrid conducting polymer–hydrogel conduits for axonal growth and neural tissue engineering (*Adv. Healthcare Mater.* 6/2012). *Adv. Healthc. Mater.*, **1** (6), 681–1681.
- 18 Abidian, M.R. and Martin, D.C. (2009) Multifunctional nanobiomaterials for

- neural interfaces. *Adv. Funct. Mater.*, **19** (4), 573–585.
- 19** Peng, H. *et al.* (2007) DNA hybridization detection with blue luminescent quantum dots and dye-labeled single-stranded DNA. *J. Am. Chem. Soc.*, **129** (11), 3048–3049.
- 20** Ates, M. (2013) A review study of (bio) sensor systems based on conducting polymers. *Mater. Sci. Eng. C*, **33** (4), 1853–1859.
- 21** Eftekhari, A. (2010) *Nanostructured Conductive Polymers*, John Wiley & Sons, Inc., New York.
- 22** Pan, L. *et al.* (2010) Conducting polymer nanostructures: template synthesis and applications in energy storage. *Int. J. Mol. Sci.*, **11** (7), 2636–2657.
- 23** Li, D., Huang, J., and Kaner, R.B. (2008) Polyaniline nanofibers: a unique polymer nanostructure for versatile applications. *Acc. Chem. Res.*, **42** (1), 135–145.
- 24** Zhou, C., Han, J., and Guo, R. (2008) Dilute anionic surfactant solution route to polyaniline rectangular sub-microtubes as a novel nanostructure. *J. Phys. Chem. B*, **112** (16), 5014–5019.
- 25** Kim, H.S. *et al.* (2007) Doped and dedoped polypyrrole nanowires by using a BMIMPF₆ ionic liquid. *Synth. Met.*, **157** (22), 910–913.
- 26** Zhu, Y. *et al.* (2007) Conducting and superhydrophobic rambutan-like hollow spheres of polyaniline. *Adv. Mater.*, **19** (16), 2092–2096.
- 27** Jang, J., Ha, J., and Cho, J. (2007) Fabrication of water-dispersible polyaniline-poly(4-styrenesulfonate) nanoparticles for inkjet-printed chemical-sensor applications. *Adv. Mater.*, **19** (13), 1772–1775.
- 28** Yang, M. *et al.* (2005) General synthetic route toward functional hollow spheres with double-shelled structures. *Angew. Chem., Int. Ed.*, **44** (41), 6727–6730.
- 29** Zhang, Z., Wan, M., and Wei, Y. (2006) Highly crystalline polyaniline nanostructures doped with dicarboxylic acids. *Adv. Funct. Mater.*, **16** (8), 1100–1104.
- 30** Shin, M.K. *et al.* (2008) Enhanced conductivity of aligned PANi/PEO/MWNT nanofibers by electrospinning.
- Sens. Actuator B Chem.*, **134** (1), 122–126.
- 31** Ko, S. and Jang, J. (2006) A highly efficient palladium nanocatalyst anchored on a magnetically functionalized polymer-nanotube support. *Angew. Chem.*, **118** (45), 7726–7729.
- 32** Jang, J., Li, X.L., and Oh, J.H. (2004) Facile fabrication of polymer and carbon nanocapsules using polypyrole core/shell nanomaterials. *Chem. Commun.*, (7), 794–795.
- 33** Jang, J., Oh, J.H., and Stucky, G.D. (2002) Fabrication of ultrafine conducting polymer and graphite nanoparticles. *Angew. Chem., Int. Ed.*, **41** (21), 4016–4019.
- 34** Wan, M. (2009) Some issues related to polyaniline micro/nanostructures. *Macromol. Rapid Commun.*, **30** (12), 963–975.
- 35** Jang, J., Bae, J., and Park, E. (2006) Selective fabrication of poly(3,4-ethylenedioxythiophene) nanocapsules and mesocellular foams using surfactant-mediated interfacial polymerization. *Adv. Mater.*, **18** (3), 354–358.
- 36** Zhou, C., Han, J., and Guo, R. (2009) Polyaniline fan-like architectures of rectangular sub-microtubes synthesized in dilute inorganic acid solution. *Macromol. Rapid Commun.*, **30** (3), 182–187.
- 37** Jang, J. and Yoon, H. (2005) Formation mechanism of conducting polypyrrole nanotubes in reverse micelle systems. *Langmuir*, **21** (24), 11484–11489.
- 38** Yoon, H., Hong, J.Y., and Jang, J. (2007) Charge-transport behavior in shape-controlled poly(3,4-ethylenedioxythiophene) nanomaterials: intrinsic and extrinsic factors. *Small*, **3** (10), 1774–1783.
- 39** Zhang, X. *et al.* (2006) Chemical synthesis of PEDOT nanotubes. *Macromolecules*, **39** (2), 470–472.
- 40** Jang, J. and Yoon, H. (2003) Facile fabrication of polypyrrole nanotubes using reverse microemulsion polymerization. *Chem. Commun.*, (6), 720–721.
- 41** Martin, C.R. (1995) Template synthesis of electronically conductive polymer

- nanostructures. *Acc. Chem. Res.*, **28** (2), 61–68.
- 42** Xiao, R. *et al.* (2007) Controlled electrochemical synthesis of conductive polymer nanotube structures. *J. Am. Chem. Soc.*, **129** (14), 4483–4489.
- 43** Hernandez, S.C. *et al.* (2007) Single polypyrrole nanowire ammonia gas sensor. *Electroanalysis*, **19** (19–20), 2125–2130.
- 44** Cai, Z. and Martin, C.R. (1989) Electronically conductive polymer fibers with mesoscopic diameters show enhanced electronic conductivities. *J. Am. Chem. Soc.*, **111** (11), 4138–4139.
- 45** Woodson, M. and Liu, J. (2006) Guided growth of nanoscale conducting polymer structures on surface-functionalized nanopatterns. *J. Am. Chem. Soc.*, **128** (11), 3760–3763.
- 46** Niu, Z. *et al.* (2007) Assembly of tobacco mosaic virus into fibrous and macroscopic bundled arrays mediated by surface aniline polymerization. *Langmuir*, **23** (12), 6719–6724.
- 47** Martin, C.R. *et al.* (1990) Template synthesis of organic microtubules. *J. Am. Chem. Soc.*, **112** (24), 8976–8977.
- 48** Lin, M. *et al.* (2012) Functionalized polypyrrole nanotube arrays as electrochemical biosensor for the determination of copper ions. *Anal. Chim. Acta*, **746**, 63–69.
- 49** Andjelkovic, D.D. and Larock, R.C. (2006) Mechanical properties of novel rubbers from the cationic copolymerization of soybean oil and dicyclopentadiene. *Polym. Prepr.*, **47** (1), 28.
- 50** Zhang, L. and Liu, P. (2008) Facile fabrication of uniform polyaniline nanotubes with tubular aluminosilicates as templates. *Nanoscale Res. Lett.*, **3** (8), 299–302.
- 51** Zuo, S. *et al.* (2013) Preparation of polyaniline–polypyrrole binary composite nanotube using halloysite as hard-template and its characterization. *Chem. Eng. J.*, **228**, 1092–1097.
- 52** Yang, W. *et al.* (2013) Epitaxial growth of single-domain graphene on hexagonal boron nitride. *Nat. Mater.*, **12** (9), 792–797.
- 53** Joo, J. *et al.* (2005) Fabrication and applications of conducting polymer nanotube, nanowire, nanohole, and double wall nanotube. *Synth. Met.*, **153** (1–3), 313–316.
- 54** Ramanathan, K. *et al.* (2005) Bioaffinity sensing using biologically functionalized conducting-polymer nanowire. *J. Am. Chem. Soc.*, **127** (2), 496–497.
- 55** Martin, C.R. (1994) Nanomaterials: a membrane-based synthetic approach. DTIC document.
- 56** Demoustier-Champagne, S. and Stavaux, P.-Y. (1999) Effect of electrolyte concentration and nature on the morphology and the electrical properties of electropolymerized polypyrrole nanotubules. *Chem. Mater.*, **11** (3), 829–834.
- 57** Delvauz, M. *et al.* (2000) Chemical and electrochemical synthesis of polyaniline micro-and nano-tubules. *Synth. Met.*, **113** (3), 275–280.
- 58** Yan, H. *et al.* (2006) Synthesis, property and field-emission behaviour of amorphous polypyrrole nanowires. *Nanotechnology*, **17** (14), 3446.
- 59** Kim, B. *et al.* (2005) Synthesis, characteristics, and field emission of doped and de-doped polypyrrole, polyaniline, poly(3,4-ethylenedioxythiophene) nanotubes and nanowires. *Synth. Met.*, **150** (3), 279–284.
- 60** Park, S. *et al.* (2004) Self-assembly of mesoscopic metal-polymer amphiphiles. *Supramol. Sci.*, **303** (5656), 348–351.
- 61** Park, S., Chung, S.-W., and Mirkin, C.A. (2004) Hybrid organic–inorganic, rod-shaped nanoresistors and diodes. *J. Am. Chem. Soc.*, **126** (38), 11772–11773.
- 62** Cao, Y. *et al.* (2008) Electrical transport and chemical sensing properties of individual conducting polymer nanowires. *Nano Lett.*, **8** (12), 4653–4658.
- 63** Bangar, M.A. *et al.* (2009) Magnetically assembled multisegmented nanowires and their applications. *Electroanalysis*, **21** (1), 61–67.
- 64** Lee, J.I. *et al.* (2008) Highly aligned ultrahigh density arrays of conducting polymer nanorods using block copolymer templates. *Nano Lett.*, **8** (8), 2315–2320.

- 65** Lim, J.H. and Mirkin, C.A. (2002) Electrostatically driven dip-pen nanolithography of conducting polymers. *Adv. Mater.*, **14** (20), 1474–1477.
- 66** Noy, A. *et al.* (2002) Fabrication of luminescent nanostructures and polymer nanowires using dip-pen nanolithography. *Nano Lett.*, **2** (2), 109–112.
- 67** Su, M. *et al.* (2004) Dip-pen nanopatterning of photosensitive conducting polymer using a monomer ink. *Appl. Phys. Lett.*, **84** (21), 4200–4202.
- 68** Xu, P. and Kaplan, D.L. (2004) Nanoscale surface patterning of enzyme-catalyzed polymeric conducting wires. *Adv. Mater.*, **16** (7), 628–633.
- 69** Luo, X., Pedrosa, V.A., and Wang, J. (2009) Enzymatic nanolithography of polyaniline nanopatterns by using peroxidase-modified atomic force microscopy tips. *Chem. Eur. J.*, **15** (21), 5191–5194.
- 70** Maynor, B.W. *et al.* (2002) Direct-writing of polymer nanostructures: poly (thiophene) nanowires on semiconducting and insulating surfaces. *J. Am. Chem. Soc.*, **124** (4), 522–523.
- 71** Yang, M. *et al.* (2006) Direct writing of a conducting polymer with molecular-level control of physical dimensions and orientation. *J. Am. Chem. Soc.*, **128** (21), 6774–6775.
- 72** Aydemir, N. *et al.* (2013) Direct writing of conducting polymers. *Macromol. Rapid Commun.*, **34** (16), 1296–1300.
- 73** Nakashima, H. *et al.* (2011) Liquid deposition patterning of conducting polymer ink onto hard and soft flexible substrates via dip-pen nanolithography. *Langmuir*, **28** (1), 804–811.
- 74** Jang, S.-Y., Marquez, M., and Sotzing, G. A. (2004) Rapid direct nanowriting of conductive polymer via electrochemical oxidative nanolithography. *J. Am. Chem. Soc.*, **126** (31), 9476–9477.
- 75** Jiang, L., Wang, X., and Chi, L. (2011) Nanoscaled surface patterning of conducting polymers. *Small*, **7** (10), 1309–1321.
- 76** Tran, H.D., Li, D., and Kaner, R.B. (2009) One-dimensional conducting polymer nanostructures: bulk synthesis and applications. *Adv. Mater.*, **21** (14–15), 1487–1499.
- 77** Jang, J. (2006) Conducting polymer nanomaterials and their applications, in *Emissive Materials Nanomaterials*, Springer, pp. 189–260.
- 78** Chen, Y. and Luo, Y. (2009) Precisely defined heterogeneous conducting polymer nanowire arrays: fabrication and chemical sensing applications. *Adv. Mater.*, **21** (20), 2040–2044.
- 79** Lee, I. *et al.* (2008) Highly reproducible single polyaniline nanowire using electrophoresis method. *Nano*, **3** (2), 75–82.
- 80** Xue, M. *et al.* (2008) Processing matters: *in situ* fabrication of conducting polymer microsensors enables ultralow-limit gas detection. *Adv. Mater.*, **20** (11), 2145–2150.
- 81** Beh, W.S. *et al.* (1999) Formation of patterned microstructures of conducting polymers by soft lithography, and applications in microelectronic device fabrication. *Adv. Mater.*, **11** (12), 1038–1041.
- 82** Jung, M.-H. and Lee, H. (2008) Patterning of conducting polymers using charged self-assembled monolayers. *Langmuir*, **24** (17), 9825–9831.
- 83** Shi, F. *et al.* (2002) Layer-by-layer self-assembly of reactive polyelectrolytes for robust multilayer patterning. *Adv. Mater.*, **14** (11), 805–809.
- 84** He, H., Li, C., and Tao, N. (2001) Conductance of polymer nanowires fabricated by a combined electrodeposition and mechanical break junction method. *Appl. Phys. Lett.*, **78** (6), 811–813.
- 85** He, H. *et al.* (2001) A conducting polymer nanojunction switch. *J. Am. Chem. Soc.*, **123**, 7730–7731.
- 86** Yun, M. *et al.* (2004) Electrochemically grown wires for individually addressable sensor arrays. *Nano Lett.*, **4** (3), 419–422.
- 87** Ramanathan, K. *et al.* (2007) *In situ* fabrication of single poly(methyl pyrrole) nanowire. *Electroanalysis*, **19** (7–8), 793–797.
- 88** Peng, C.-Y. *et al.* (2003) Formation of nanostructured polymer filaments in

- nanochannels. *J. Am. Chem. Soc.*, **125** (31), 9298–9299.
- 89 Peng, C.-Y. *et al.* (2005) A “grow-in-place” architecture and methodology for electrochemical synthesis of conducting polymer nanoribbon device arrays. *Nano Lett.*, **5** (3), 439–444.
- 90 Ramanathan, K. *et al.* (2004) Individually addressable conducting polymer nanowires array. *Nano Lett.*, **4** (7), 1237–1239.
- 91 Chiang, C.-H. and Wu, C.-G. (2010) Fabrication of sub-100nm conducting polyaniline wire on a polymer substrate based on friction nanolithography. *Chem. Commun.*, **46** (16), 2763–2765.
- 92 Lock, J.P., Im, S.G., and Gleason, K.K. (2006) Oxidative chemical vapor deposition of electrically conducting poly(3,4-ethylenedioxythiophene) films. *Macromolecules*, **39** (16), 5326–5329.
- 93 Im, S.G. *et al.* (2007) Grafted conducting polymer films for nano-patterning onto various organic and inorganic substrates by oxidative chemical vapor deposition. *Adv. Mater.*, **19** (19), 2863–2867.
- 94 Dong, B. *et al.* (2005) Patterning of conducting polymers based on a random copolymer strategy: toward the facile fabrication of nanosensors exclusively based on polymers. *Adv. Mater.*, **17** (22), 2736–2741.
- 95 Dong, B. *et al.* (2006) Fabrication of high-density, large-area conducting-polymer nanostructures. *Adv. Funct. Mater.*, **16** (15), 1937–1942.
- 96 Dong, B. *et al.* (2005) Fabrication of polypyrrole wires between microelectrodes. *Small*, **1** (5), 520–524.
- 97 Jiang, L. *et al.* (2011) Enhanced electrical conductivity of individual conducting polymer nanobelts. *Small*, **7** (14), 1949–1953.
- 98 Bocharova, V. *et al.* (2005) Polypyrrole nanowires grown from single adsorbed polyelectrolyte molecules. *Angew. Chem., Int. Ed.*, **44** (39), 6391–6394.
- 99 Ma, Y. *et al.* (2004) Polyaniline nanowires fabricated on S(surfaces with DNA templates. *J. Am. Chem. Soc.*, **22**, 7097–7101.
- 100 Eichen, Y. *et al.* (1998) Self-assembly of nanoelectronic components and circuits using biological templates. *Acta Polym.*, **49** (10–11), 663–670.
- 101 Nickels, P. *et al.* (2004) Polyaniline nanowire synthesis templated by DNA. *Nanotechnology*, **15** (11), 1524.
- 102 Dong, L. *et al.* (2007) Synthesis, manipulation, and conductivity of supramolecular polymer nanowires. *Chem. Eur. J.*, **13** (3), 822–828.
- 103 Carpick, R.W. and Salmeron, M. (1997) Scratching the surface: fundamental investigations of tribology with atomic force microscopy. *Chem. Rev.*, **97** (4), 1163–1194.
- 104 Liu, G.-Y., Xu, S., and Qian, Y. (2000) Nanofabrication of self-assembled monolayers using scanning probe lithography. *Acc. Chem. Res.*, **33** (7), 457–466.
- 105 Berger, R. *et al.* (2007) Nanowear on polymer films of different architecture. *Langmuir*, **23** (6), 3150–3156.
- 106 Hirtz, M. *et al.* (2009) Structured polymer brushes by AFM lithography. *Small*, **5** (8), 919–923.
- 107 Jones, A.G. *et al.* (2006) Highly tunable, high-throughput nanolithography based on strained regioregular conducting polymer films. *Appl. Phys. Lett.*, **89** (1), 013119.
- 108 Li, L. *et al.* (2010) Patterning of polymer electrodes by nanoscratching. *Adv. Mater.*, **22** (12), 1374–1378.
- 109 Barret, M., Sanaur, S., and Collot, P. (2008) Inkjet-printed polymer thin-film transistors: enhancing performances by contact resistances engineering. *Org. Electron.*, **9** (6), 1093–1100.
- 110 Sirringhaus, H. *et al.* (2000) High-resolution inkjet printing of all-polymer transistor circuits. *Supramol. Sci.*, **290** (5499), 2123–2126.
- 111 Zielke, D. *et al.* (2005) Polymer-based organic field-effect transistor using offset printed source/drain structures. *Appl. Phys. Lett.*, **87** (12), 123508.
- 112 Li, D. and Guo, L.J. (2006) Micron-scale organic thin film transistors with conducting polymer electrodes patterned by polymer inking and stamping. *Appl. Phys. Lett.*, **88** (6), 063513.
- 113 Menard, E. *et al.* (2007) Micro-and nanopatterning techniques for organic

- electronic and optoelectronic systems. *Chem. Rev.*, **107** (4), 1117–1160.
- 114** Sengupta, S. *et al.* (2012) Biosupramolecular nanowires from chlorophyll dyes with exceptional charge-transport properties. *Angew. Chem., Int. Ed.*, **51** (26), 6378–6382.
- 115** Zhang, F., Nyberg, T., and Inganäs, O. (2002) Conducting polymer nanowires and nanodots made with soft lithography. *Nano Lett.*, **2** (12), 1373–1377.
- 116** Hu, Z. *et al.* (2007) High-throughput fabrication of organic nanowire devices with preferential internal alignment and improved performance. *Nano Lett.*, **7** (12), 3639–3644.
- 117** Kim, J., You, J., and Kim, E. (2010) Flexible conductive polymer patterns from vapor polymerizable and photo-cross-linkable EDOT. *Macromolecules*, **43** (5), 2322–2327.
- 118** Lasagni, A. *et al.* (2008) Advanced design of conductive polymeric arrays with controlled electrical resistance using direct laser interference patterning. *Appl. Phys. A*, **91** (3), 369–373.
- 119** Jung, Y.S. *et al.* (2008) Nanowire conductive polymer gas sensor patterned using self-assembled block copolymer lithography. *Nano Lett.*, **8** (11), 3776–3780.
- 120** Huang, C. *et al.* (2009) A strategy for patterning conducting polymers using nanoimprint lithography and isotropic plasma etching. *Small*, **5** (5), 583–586.
- 121** Huang, C. *et al.* (2010) A simple method for the fabrication of high-resolution conducting polymer patterns. *Langmuir*, **26** (11), 9142–9145.
- 122** Lipomi, D.J. *et al.* (2008) Fabrication of conjugated polymer nanowires by edge lithography. *Nano Lett.*, **8** (7), 2100–2105.
- 123** Reneker, D.H. and Yarin, A.L. (2008) Electrospinning jets and polymer nanofibers. *Polymer*, **49** (10), 2387–2425.
- 124** Shenoy, S.L. *et al.* (2005) Role of chain entanglements on fiber formation during electrospinning of polymer solutions: good solvent, non-specific polymer–polymer interaction limit. *Polymer*, **46** (10), 3372–3384.
- 125** Luzio, A. *et al.* (2014) Electrospun polymer fibers for electronic applications. *Mech. Compos. Mater.*, **7** (2), 906–947.
- 126** Dall'Acqua, L. *et al.* (2006) Vapour phase polymerisation of pyrrole on cellulose-based textile substrates. *Synth. Met.*, **156** (5), 379–386.
- 127** Zhang, Y. *et al.* (2012) Electrical conductivity of electrospun polyaniline and polyaniline-blend fibers and mats. *Macromolecules*, **45**, 4238–4246.
- 128** Tu, D. *et al.* (2010) Single light-emitting polymer nanofiber field-effect transistors. *Nanoscale*, **2** (10), 2217–2222.
- 129** Pinto, N. *et al.* (2003) Electrospun polyaniline/polyethylene oxide nanofiber field-effect transistor. *Appl. Phys. Lett.*, **83** (20), 4244–4246.
- 130** Liu, H.Q. *et al.* (2004) Polymeric nanowire chemical sensor. *Nano Lett.*, **4** (4), 671–675.
- 131** Liu, H.Q. *et al.* (2004) Polymeric nanowire chemical sensor. *Nano Lett.*, **4**, 671–675.
- 132** Matyba, P. *et al.* (2010) Graphene and mobile ions: the key to all-plastic, solution-processed light-emitting devices. *ACS Nano*, **4** (2), 637–642.
- 133** Arter, J.A. *et al.* (2010) Virus-PEDOT nanowires for biosensing. *Nano Lett.*, **10** (12), 4858–4862.
- 134** Cuenot, S., Demoustier-Champagne, S., and Nysten, B. (2000) Elastic modulus of polypyrrole nanotubes. *Phys. Rev. Lett.*, **85** (8), 1690.
- 135** Arinstein, A. *et al.* (2007) Effect of supramolecular structure on polymer nanofibre elasticity. *Nat. Nanotechnol.*, **2** (1), 59–62.
- 136** Yoon, H., Chang, M., and Jang, J. (2007) Formation of 1D poly(3,4-ethylenedioxythiophene) nanomaterials in reverse microemulsions and their application to chemical sensors. *Adv. Funct. Mater.*, **17** (3), 431–436.
- 137** Shirsat, M.D. *et al.* (2009) Polyaniline nanowires–gold nanoparticles hybrid network based chemiresistive hydrogen sulfide sensor. *Appl. Phys. Lett.*, **94** (8), 083502.
- 138** Pringsheim, E., Zimin, D., and Wolfbeis, O.S. (2001) Fluorescent beads coated with polyaniline: a novel nanomaterial for optical sensing of pH. *Adv. Mater.*, **13** (11), 819–822.

- 139 Gu, F. *et al.* (2008) Polymer single-nanowire optical sensors. *Nano Lett.*, **8** (9), 2757–2761.
- 140 He, H. and Tao, N.J. (2004) Electrochemical fabrication of metal nanowires, in *Encyclopedia of Nanoscience and Nanotechnology*, American Scientific Publishers, pp. 755–772.
- 141 Xie, H., Luo, S.C., and Yu, H.H. (2009) Electric-field-assisted growth of functionalized poly (3,4-ethylenedioxythiophene) nanowires for label-free protein detection. *Small*, **5** (22), 2611–2617.
- 142 Herland, A. and Inganäs, O. (2007) Conjugated polymers as optical probes for protein interactions and protein conformations. *Macromol. Rapid Commun.*, **28** (17), 1703–1713.
- 143 Huang, Y. *et al.* (2005) Enantioselective organo-cascade catalysis. *J. Am. Chem. Soc.*, **127** (43), 15051–15053.
- 144 Tang, J. *et al.* (2005) Rapid and reproducible fabrication of carbon nanotube AFM probes by dielectrophoresis. *Nano Lett.*, **5** (1), 11–14.
- 145 Liu, H., Reccius, C.H., and Craighead, H. (2005) Single electrospun regioregular poly(3-hexylthiophene) nanofiber field-effect transistor. *Appl. Phys. Lett.*, **87** (25), 253106.
- 146 Briseno, A.L. *et al.* (2008) Self-assembly, molecular packing, and electron transport in n-type polymer semiconductor nanobelts. *Chem. Mater.*, **20** (14), 4712–4719.
- 147 Nyström, G. *et al.* (2009) Ultrafast all-polymer paper-based batteries. *Nano Lett.*, **9** (10), 3635–3639.
- 148 Liu, R. and Lee, S.B. (2008) MnO₂/poly (3,4-ethylenedioxythiophene) coaxial nanowires by one-step coelectrodeposition for electrochemical energy storage. *J. Am. Chem. Soc.*, **130** (10), 2942–2943.
- 149 Qi, P. *et al.* (2004) Miniature organic transistors with carbon nanotubes as quasi-one-dimensional electrodes. *J. Am. Chem. Soc.*, **126** (38), 11774–11775.
- 150 Granström, M., Berggren, M., and Inganäs, O. (1995) Micrometer-and nanometer-sized polymeric light-emitting diodes. *Supramol. Sci.*, **267** (5203), 1479–1481.
- 151 Boroumand, F.A., Fry, P.W., and Lidzey, D.G. (2005) Nanoscale conjugated-polymer light-emitting diodes. *Nano Lett.*, **5** (1), 67–71.

10

DNA-Induced Nanoparticle Assembly

Anne Buchkremer and Ulrich Simon

10.1

Introduction

Deoxyribonucleic acid (DNA) is the molecule of life, a naturally occurring polymer that carries information on the development and function of living organisms. It is composed of two purine bases adenine (A) and guanine (G) and two pyrimidine bases thymine (T) and cytosine (C) [1], called nucleobases, that are aligned on a deoxyribose–phosphate backbone. As a subunit, nucleotides are composed of a nucleobase as well as a deoxyribose and a phosphate group. Two nucleotide strands run antiparallel to each other to form a double helix via the formation of sterically and thermodynamically favorable hydrogen bonds of A to T and C to G, called Watson–Crick base pairing (bp). Due to the fact that G and C are connected via three hydrogen bonds, their interaction is stronger than those between A and T, with only two interconnecting hydrogen bonds. The binding event of two bases across the double strand (dsDNA) is called a base pairing and the respective process is called hybridization. Nucleotides can be aligned in multiple combinations. Depending on the sequence of the nucleotides, the respective DNA strands can serve in different fields of operation. Due to the self-recognition abilities of DNA, it is involved in regulating cellular processes, transmitting genetic information, and fulfilling structural purposes [2,3]. Further structural motives in DNA architecture, such as triplex and quadruplex secondary structures, are accessible by the design of specific DNA sequences and by exploiting supramolecular forces in DNA [4], which led scientists to use DNA as a construction material for complex functional assemblies involving, for example, colloidal metal particles on nano- and microscales [1,5–8].

The field of metal colloids and bioconjugates is, due to the possibility of interfering with biological processes, considered as one of the most scientifically and industrially significant areas with recent examples of commercial applications, including biomedicine tests, contrast media, and cancer treatment. One of the most prominent examples of such metal–bio hybrid systems is the combination of DNA and colloidal metal nanoparticles. Due to the combination of optically or magnetically addressable nanoparticles with the molecular recognition

capabilities of oligonucleotides, DNA-functionalized nanoparticles and aggregates composed of them are the subject of recent research [9–12]. Applications of these systems in intracellular messenger RNA detection, biodiagnostics, and antisense gene regulation and as delivery systems are already in use today or seem within reach in the near future [13–16].

The most prominent example of such advanced hybrid systems is the combination of gold nanoparticles (AuNPs) and DNA, which is highly stable due to the formation of a covalent gold–sulfur bond that can be formed with commercially available thiol-modified DNA strands. Since the introduction of DNA-mediated gold nanoparticle assemblies in 1996 by Mirkin *et al.* [17] and Alivisatos *et al.* [18], great progress has been made in the field of structural and thermodynamic analyses.

In addition to the most commonly presented spherical AuNPs, different geometries such as anisotropic gold nanorods, gold nanoplatelets, and nanoprisms as well as hollow gold nanospheres have also been introduced, which opened up a whole new building block system for extended as well as defined, intermediate, and functional nano- and microstructures. More recently, magnetic nanoparticles, composed of, for example, iron oxide have also been introduced and were interconnected by DNA as well, allowing different kinds of manipulation by external stimuli. Also, so-called spherical nucleic acids (SNA), synthesized via DNA functionalization of metal nanoparticles and subsequent dissolving of the metal core, have been used that display a biological system bypassing a class of materials with promising potential in biomedicine [19].

Through combinations of metal- or semiconductor nanoparticles with different DNA strands, researchers were able to construct periodically ordered, extended superstructures, displaying various crystal lattices [12,20]. These kind of lattices can be controlled by changing reaction parameters such as the ratio of DNA length to particle diameter, ambient ionic strength, and additives. On the other hand, model structures such as precisely formed dimers, trimers, and tetramers could be synthesized and their optical as well as biomedical application potential was evaluated [21]. Tools to synthesize such defined and highly desirable structures are next to PCR synthesis enzymatic ligation and complex ligand exchange reactions, followed by extensive purifying steps involving, for example, high-performance liquid chromatography (HPLC) and gel electrophoresis. Consequently, the network and template morphology and physical properties can be adjusted. By varying the combined ratios of complementary functionalized nanoarchitectures, the overall network size can be further controlled, and the complex internal structure of such finite-sized aggregates can be quantified using a combination of sophisticated analytical methods.

The self-recognition of DNA not only allows a controlled network assembly but also represents a carrier for drugs based on DNA-intercalating dyes, to which class most cytostatic medications belong. Once intercalated into DNA

close to the nanoparticle, the respective drugs are expected to be released contactlessly by external stimuli, such as photo- and magnetothermal heating or environment-induced changes in solvation. Furthermore, the biomolecule DNA displays inherent biocompatibility. In combination with the optical properties of metal nanoparticles, various promising biodiagnostic methods have been introduced based on similar hybrid systems. The knowledge and full understanding of the basic physical effects taking place on a molecular length scale, in combination with the directed synthesis and structuring of novel contrast agents on the nanoscale, therefore, hold great potential. To generate additional functionalities on the system's periphery, a coupling to conventional polymers was recently shown, enabling multiple stimuli responsiveness [22].

This chapter aims at describing synthetic strategies based on versatile DNA architectures to generate nano- and microstructures and assemblies with defined and desirable sizes, shapes, and functionalities. According to Figure 10.1, differentiation is made between structures based on DNA templates onto which nanoparticles can be arranged (Chapter 10.2) and structures that can be generated using DNA as a linking ligand (Chapter 10.3). The chapter concludes with an overview of applications that arise from the availability of such hybrid constructs and a short summary.

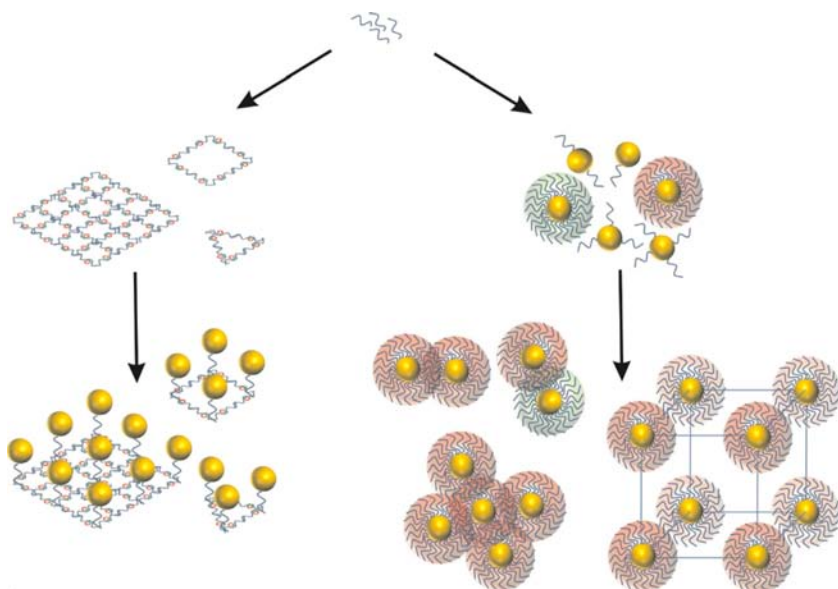


Figure 10.1 Schematic illustration of methodologies developed for DNA-mediated assembly of metal nanoparticles. DNA is thereby used either as a template (left pathway) or as a structure-guiding ligand (right

pathway) to form either finite-size or extended aggregates or superstructures. (Reproduced with permission from The Royal Society of Chemistry [23].)

10.2

DNA as a Template Material

10.2.1

On Modified Linear DNA Strands

Complex DNA strands are suitable templates for linear and 3D assemblies of metal nanoparticles that can bind either via electrostatic interactions [24,25] or via Watson–Crick base pairing of complementary designed targets [26,27]. Importantly, the required building blocks are readily available due to the versatile PCR synthesis routes and thus specific and functional fragments can be inserted into DNA. Due to their size-dependent electrical properties, one-dimensional assemblies of small nanoparticles on DNA are of particular interest for nanoelectronic applications and have been introduced in the late 1990s [18,28–40]. Structures are realized using techniques such as the electrostatic binding of positively charged particles to the negatively charged deoxyribose–phosphate backbone [41,42], the hybridization of single-stranded oligonucleotide-modified nanoparticles to complementary single-stranded oligonucleotide templates [26,43], or via a DNA binding complex such as *cis*-Pt [44] in which the Pt²⁺ ion serves as a binding site for amine-functionalized nanoparticles. Such spatially defined assemblies of aggregated nanoparticles are likely to exhibit quantized electron transport phenomena at room temperature, which could be utilized for switching and charge storage devices.

Approaches such as the controlled deposition of single-stranded DNA between lithographically defined electrodes by dip-pen nanolithography and the subsequent deposition of a complementary functionalized AuNP have been described [45]. Compared with a metal island, the simplest form of a charge quantization electronic device, the addition of a defined number of nanoparticles to such a gap in a spatially controlled way and with tunable interparticle distances can lead to more sophisticated switching and charge storage devices. Artificial DNA bases with defined alkyne-modified thymine bases can serve as binding sites to generate programmable DNA templates for spatially controlled nanoparticle assemblies [38]. The AuNP is functionalized with a glutathione azide derivative and can hence selectively bind to artificial DNA bases, via PCR synthesized alkyne-modified DNA duplexes, as seen in Figure 10.2a. The reaction follows a copper(I)-catalyzed Huisgen cycloaddition, known as “click chemistry.” This way, one-dimensional nanoparticle arrangements were obtained that show a dense coverage of the DNA template with equidistantly placed AuNPs, as seen in the representative (transmission electron microscopy) TEM image in Figure 10.2b. Furthermore, uniform bimetallic Au–Ag nanowires that are tunable in size can be constructed based on similar DNA templates. In these templates, the cytosines are alkyne modified and thus serve as addressable metal binding sites after conversion to a sugar triazole derivative via click chemistry and subsequent Tollens reaction [38]. Ag⁰ is generated by the sugar-modified DNA and the Tollens reagent, which leads in a later enhancement step using

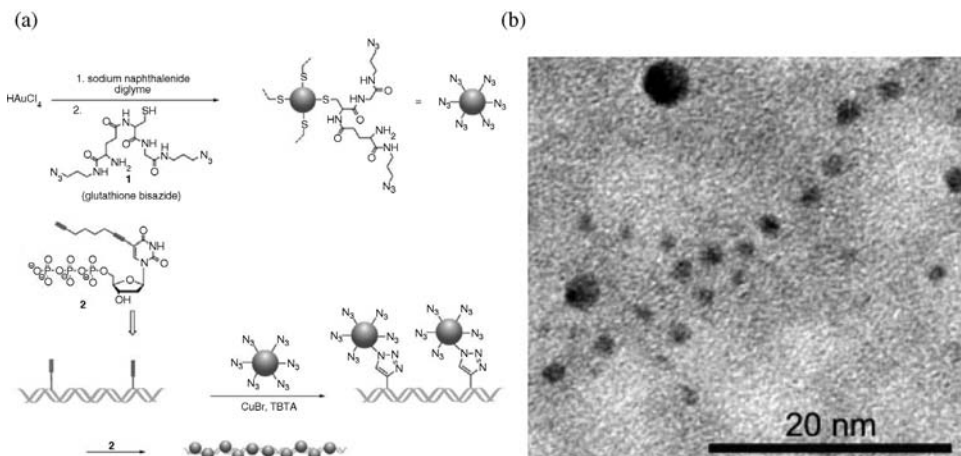


Figure 10.2 (a) Schematic presentation of the two-step AuNP synthesis: (1) the reduction of the gold precursor, dissolved in diglyme, by sodium naphthalenide; (2) the stabilization of the AuNP by the addition of azide-modified glutathione. Schematic of the immobilization of the azide-terminated AuNP to alkyne-

modified DNA strands via a “click” reaction. DNA was synthesized utilizing the alkyne-modified triphosphate (2). (b) TEM micrograph of one-dimensional equidistantly assembled nanoparticles on DNA. (Reproduced with permission from The Royal Society of Chemistry [38].)

gold to the formation of nanowires with dimensions smaller than 10 nm in diameter. The process involves the formation of small silver clusters Ag_n ($n = 2, 4, 6, \dots$), which are formed in a redox reaction between Ag^+ in solution and the aldehyde groups present on the DNA. Based on the stoichiometry of the process, one aldehyde group can reduce two silver ions, leading to Ag_2 clusters. In functionalizing DNA with *cis*-3,4-dihydroxypyrrolidin units and directly cleaving them on the DNA strand with sodium periodate, DNA with dialdehyde moieties is constructed [46]. The dialdehyde DNA has proven much more efficient in reducing Ag^+ ions, leading to the formation of particularly stable Ag nanoclusters and subsequent gold nanowire formation after enhancement. Following this two-step procedure, highly selective and spatially defined nanowires can be synthesized.

Further variation of this synthetic route can be achieved by the introduction of Pd [47], Pt [48], Cu [49], or Co [50] to the biomolecule template. All in common is the most critical initial nucleation step, because the spatial distribution of the metal complexes defines the homogeneity of the resulting device.

Although the described approaches enable to metallize DNA in a programmed manner, the resulting nanowires are fragile when handled and they lack specific affinity to stabilizing substrates, which is required for the integration into future electronic devices. Therefore, multifunctional DNA can be constructed that, on the one hand, enables programmable metallization and, on the other hand, carries functional groups to be covalently immobilized on technically relevant

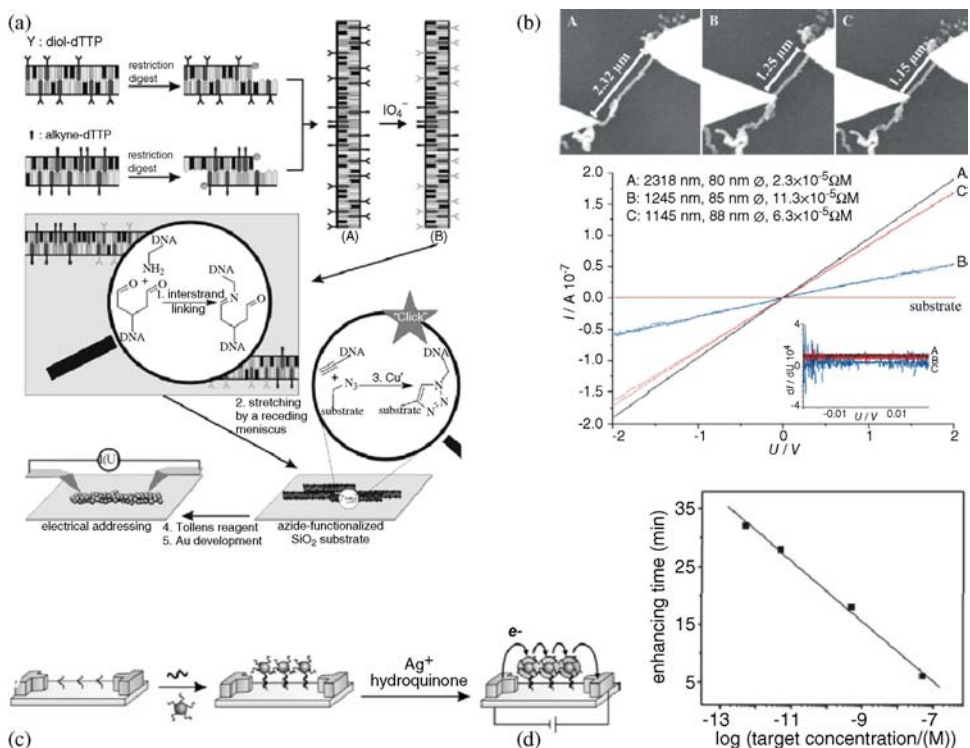


Figure 10.3 (a) Bifunctional DNA template synthesized by treatment with restriction digest. (b) Alkyne dialdehyde DNA was synthesized following an application of periodate solution. The products can be stretched onto an azide-functionalized Si-substrate. SEM images of the metallized DNA and the corresponding I/U characteristics that were measured *in situ* and show linear characteristics. (Reprinted from Ref. [51]. Copyright 2013,

Wiley-VCH Verlag GmbH.) (c) Schematic illustration of the electrical detection of DNA involving the deposition of silver onto nanoparticles deposited in a gap. (Reproduced with permission from Ref. [53].) (d) Graph of the silver-enhancing time required to reach a resistance value of $100 \text{ k}\Omega$ as a function of target concentration showing that target can be detected in the 50 nM to 500 fM concentration range by adjusting silver-enhancing time.

substrates such as silicon wafers, or is able to form intermolecular links that allow the formation of multistrands with enhanced structural integrity (Figure 10.3a) [51]. The covalent immobilization on a substrate can be realized by alkyne-functionalized DNA sequences that bind to azide-functionalized Si surfaces through copper-catalyzed alkyne–azide cycloaddition. Dialdehyde functions of the DNA not only lead to highly efficient Ag^+ reduction in Tollens reagent but also enable aldehyde-mediated interstrand linking analogous to the glutaraldehyde cross-linking in proteins [52]. By applying a receding meniscus technique, stretched DNA structures with lengths in the micrometer range can

be generated and observed in AFM as structures with the respective orientations. To assess the electrical properties of such structures, an *in situ* measuring setup delivered ohmic conductance behavior.

Figure 10.3b shows a different approach to introduce conductive devices based on DNA assembly, which is modified for analytical purposes by a detection method in which the binding of oligonucleotides and AuNP leads to conductivity changes associated with specific target samples that bind or do not bind to the device [53]. The binding events trap AuNPs in an electrode gap, and the number of trapped nanoparticles can be derived from the respective capacitance or conductivity measurement. The sensitivity of the device can be significantly increased by introducing a solution of Ag^+ and hydroquinone, as known from photographic developing solution. Using this device, an unusual salt concentration-dependent hybridization behavior associated with these DNA nanoparticle probes could be quantified with the detection of DNA concentrations down to as low as 500 fM.

10.2.2

On DNA Origami Structures

A different example of how DNA can direct the assembly of metal nanoparticles into complex chiral structures is presented by the attachment of nanoparticles to a helical DNA origami scaffold in Figure 10.4a [54]. The resulting, highly accurate chiral 3D structures exhibit defined circular dichroism (CD) responses and optical rotator dispersion effects at wavelengths in the visible region due to the specific plasmonic properties.

The presented example shows how linear DNA-induced nanoparticle assembly can lead to highly conductive and defined electrochemical devices. By expanding the system with more complex DNA structures such as DNA origami sheets [56], highly interesting and promising approaches for the construction of DNA-templated nanoelectronic circuitry and molecular lithography are conceived. More extended hybrid systems can be generated by nonlinear arrangements on DNA templates of AuNPs functionalized with single-stranded DNA that can be attached to form various 3D architectures, as shown in Figure 10.4b. This way stacked rings to single, double, and nested spirals of nanoparticle-covered DNA are accessible, in which the nanoparticles control the tube conformation through size-dependent steric repulsion effects [55].

Further extended periodic structures can be generated by embedding AuNPs in 2D DNA sheets, which can be assembled consisting of differently sized nanoparticles that decorate DNA tiles or are bound to sticky ends, as shown in Figure 10.5a [57,58]. From an application viewpoint, it is feasible to separate the as-prepared structures from the substrate. Therefore, freestanding monolayered DNA-functionalized AuNP superlattice sheets have been fabricated applying a microhole-confined dewetting process (Figure 10.5b) [59].

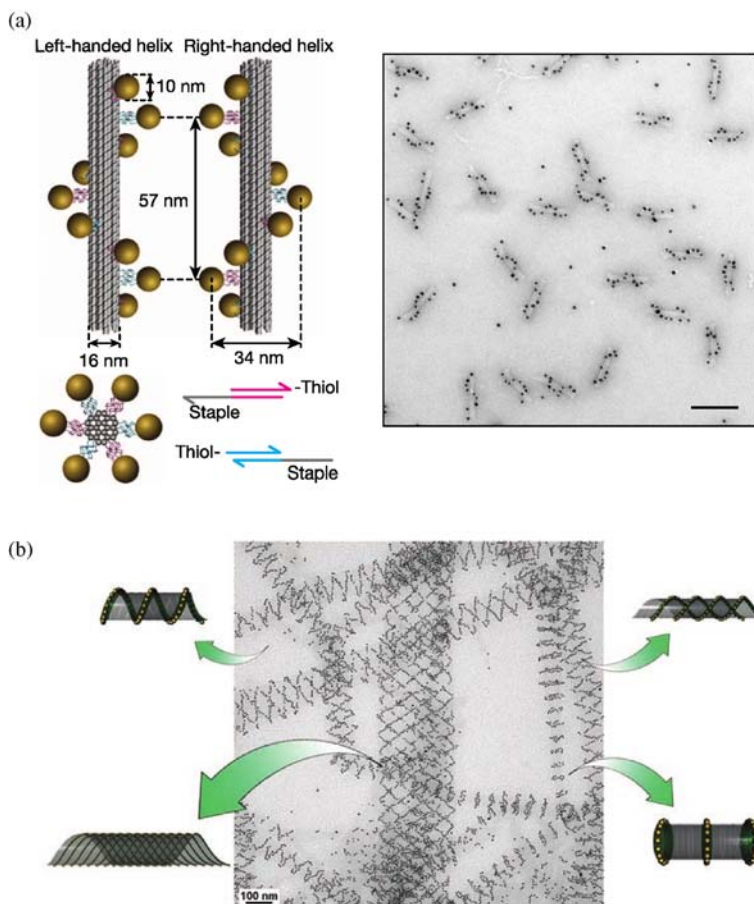


Figure 10.4 (a) Principle of chiral nanoparticle assembly using left- and right-handed nanohelices and DNA-functionalized gold nanoparticles, as well as the corresponding TEM images (scale bar 100 nm). (Reprinted with

permission from Ref. [54]. Copyright 2012, Macmillan Publishers Ltd.) (b) Tubular structures designed on DNA tiles following different tube designs and the corresponding TEM image. (Reprinted with permission from Ref. [55].)

10.2.3

On Geometrically Tailored DNA

The construction of finite-size assemblies with a discrete number of nanoparticles, such as mono-, di-, or trimers, can also be realized using a DNA template. Examples involving hybridization of the complementary components include triangular scaffolds onto which AgNP and nanorods can be arranged in controllable interparticle distances on prefabricated DNA templates, as shown in Figure 10.6 [60,61]. Also, defined hexagonal patterns of different metal nanoparticles can be designed and synthesized in a stepwise manner [62].

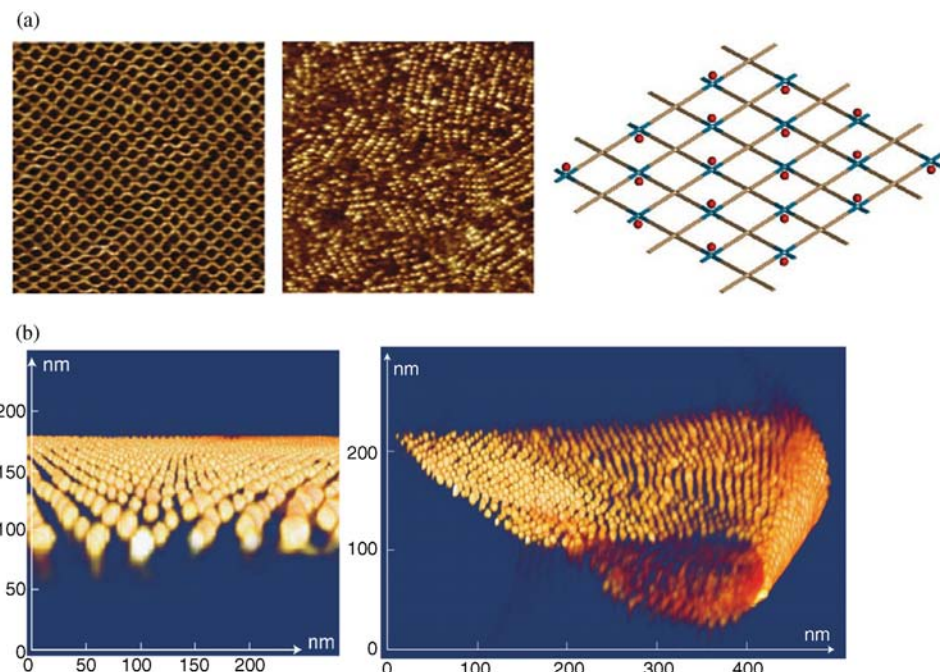


Figure 10.5 (a) Assembly of DNA–AuNPs on a DNA template using origami structures. (Reprinted with permission from Ref. [57]. Copyright 2006, Macmillan Publishers Ltd.) (b) Freestanding nanoparticle superlattices

consisting of a folded DNA sheet decorated with gold nanoparticles. (Reprinted with permission from Ref. [59]. Copyright 2009, Macmillan Publishers Ltd.)

10.3 DNA as Ligand

10.3.1

DNA Functionalization of Gold Nanoparticles and Network Formation

All syntheses of networks comprised of DNA-mediated AuNPs in common is the functionalization of AuNPs with thiol-modified ssDNA. “Spacers” are introduced, which are either several adenine or thymine bases or short polyethylene glycol (PEG) chains that increase the distance between metal surface and recognition base sequence. Therefore, they allow a less hindered DNA hybridization in following self-assembly reactions [63]. By changing the electric environment of the particles during DNA functionalization, it is possible to control the amount of ssDNA on the particle surface [64]. High ambient ionic strength induces less electronic repulsion between neighboring DNA strands and allows a higher ssDNA surface coverage due to reduced osmotic pressure. In addition, by increasing the particle size, the surface curvature of spheres is

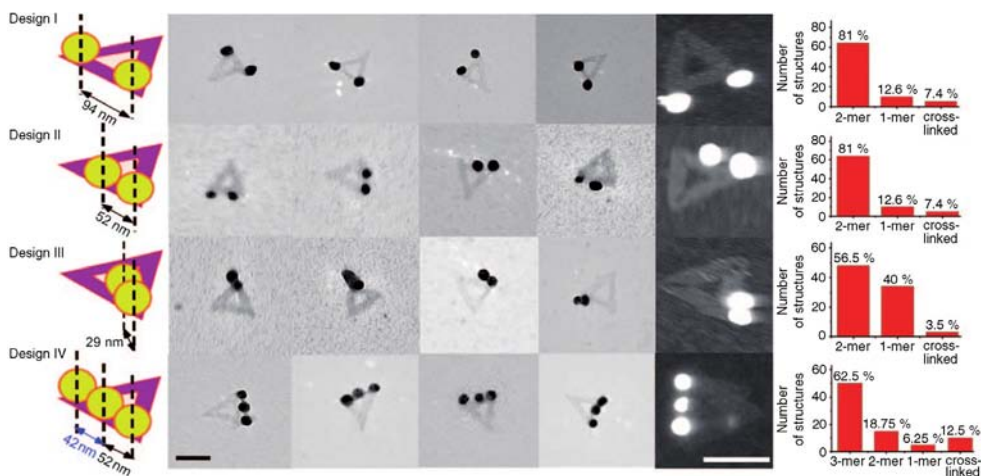


Figure 10.6 Triangle-shaped DNA origami decorated with AgNPs with variations in position and interparticle distances. (Reprinted with permission from Ref. [60].)

decreased, leading to considerably less oligonucleotides being packed into a given area due to electrostatic repulsion. This is schematically shown in Figure 10.7.

The number of DNA strands on the particle surface can be determined by functionalizing the AuNP with fluorophore-labeled ssDNA and subsequently performing a ligand exchange reaction with the dithiol dithiothreitol (DTT), which results in particle aggregation via cross-linking. The subsequent release of the fluorophore-labeled ssDNA makes it feasible to quantify the amount of DNA [66,67].

DNA-functionalized AuNPs can be coupled by DNA hybridization to form networks following two ways of assembly. For one, two batches of non-complementary ssDNA-functionalized AuNPs (DNA-A-AuNP and DNA-B-AuNP, respectively, shown in Figure 10.8a) can be connected via the addition of a free DNA strand A'B' that is complementary to DNA-A and DNA-B and is called linker DNA. Furthermore, two AuNP batches can be functionalized with complementary ssDNA, resulting in network formation upon



Figure 10.7 Sketch of DNA immobilized on a spherical gold nanoparticle (a), an egg-shaped gold nanoparticle (b), and a flat gold surface (c). (Adapted with permission from Ref. [65]. Copyright 2009, American Chemical Society.)

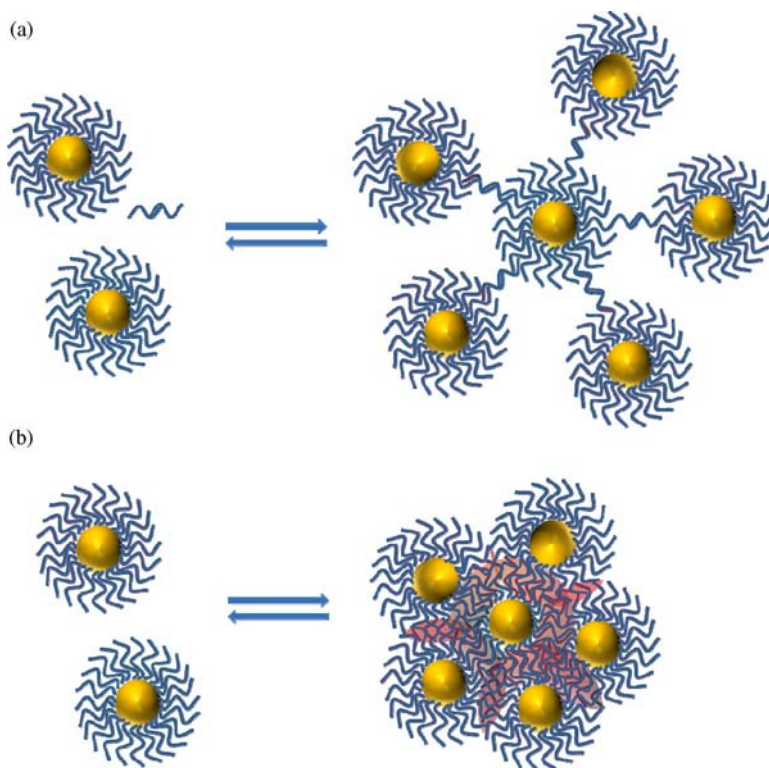


Figure 10.8 Sketch of network formation using DNA-functionalized gold nanoparticles. (a) Two different batches of DNA-functionalized gold nanoparticles are connected by linker DNA that is

complementary to both types of particles.
 (b) Two batches of gold nanoparticles functionalized with complementary DNA are mixed to form networks via direct Watson–Crick base pairing.

combination [17,68], as shown in Figure 10.8b. In DNA-assembled AuNP networks, electrostatic forces are expected to be significant in imparting attractive interactions between complementary DNA strands and repulsive particle–particle forces [69,70].

Due to the thermal addressability of the DNA double strands within the networks, the networks can be dissociated by increasing the temperature. By comparing the melting behavior of free DNA and DNA-mediated AuNP networks, a significantly higher and sharper melting temperature within the networks is observed, which is attributed to a cooperative melting mechanism. Not only the length of the particle-bound DNA and the ambient salt concentration, but also the DNA surface coverage and the particle size affect the melting temperature [63,64]. Also, for differently sized networks built out of AuNPs of the same size, a decrease of T_m and a broadening of the melting transition with decreasing network size were observed, which is explained by more hybridization events

taking place in larger networks that further stabilize the aggregate [11,64,70]. While partially noncomplementary DNA parts (mismatches) decrease T_m , the T_m value of DNA may be increased by introducing DNA intercalating molecules, which also applies to DNA–AuNP aggregates [2,71].

The network assembly can be followed by several analytical methods. The spectral position of the plasmon peak and its width are affected by the proximity of particles due to the interaction of the particle dipoles. In Figure 10.9a, one can see that as time progresses, this results in a redshift of the plasmon peak maximum λ_{\max} when networks assemble based on DNA hybridization [11,17]. Simultaneously, a decrease in optical absorption at a wavelength of 260 nm takes place due to hybridization of ssDNAs into dsDNA helices. Moreover, the networks size increases, which can be detected in time-evolving dynamic light scattering experiments by measuring the hydrodynamic radius R_H . A correlation of optical data with this obtained by dynamic light scattering during network growth depicts a simultaneous redshift of λ_{\max} and an increase in hydrodynamic radius R_H with time progressing after combination of the complementary components [72].

The advantages of using DNA as building block to construct networks are that it exhibits the possibility of tuning the interparticle distance [69,73] and also enables a spatially directed assembly of AuNPs [74]. The most established

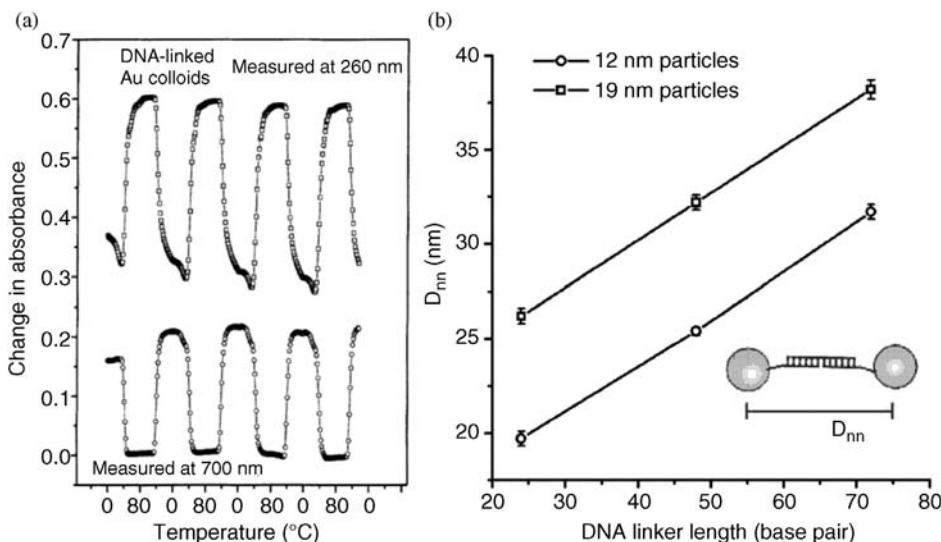


Figure 10.9 (a) Extinction in dependency of temperature plotted for DNA-functionalized gold nanoparticle networks measured at 260 nm (extinction maximum of DNA) and 700 nm (extinction high for goldnanoparticle networks. (Reprinted with permission from Ref. [17].) (b) Center-to-center interparticle

distances measured in DNA-mediated gold nanoparticle networks using SAXS. Different interparticle distances can be generated by using different particle sizes and lengths of linker DNA. (Reprinted with permission from Ref. [69]. Copyright 2004, American Chemical Society.)

method to obtain structural information is small-angle X-ray scattering (SAXS). A contribution of 0.25 nm per connecting base pair could be quantified, as seen in Figure 10.9b, which is less than that of free dsDNA with 0.34 nm per base pair [69]. Furthermore, electron microscopy has been established as a method of choice to overview assemblies [70,75], but it needs to be mentioned that the network appearance may be affected by sample preparation and measurement condition since 3D aggregates are visualized in only two dimensions.

10.3.2

Extended Superstructures

When DNA-mediated AuNP networks are assembled at temperatures just below the melting temperature of the dsDNA within the networks, a decrease of the initial growth rate is observed. A larger redshift of λ_{\max} for a certain R_H were measured at elevated temperatures, which is a hint toward formation of more compact internal structures, compared with those measured at lower assembly temperatures due to rearrangement processes [11,72]. By applying this annealing method, over the past years Mirkin, Gang, and their coworkers have established protocols for the syntheses of DNA nanoparticle hybrid structures to form highly ordered, crystalline extended architectures [12,20]. Parameters determining the kind of lattice are the particle size, particle composition, shape, and functionality as well as the length of connecting DNA strands. Synthetically programmable DNA–AuNP crystallization was demonstrated to the extent that the growth of periodic, micrometer-sized, for example, face-centered cubic (fcc) or body-centered cubic (bcc), crystal structures was directed [76–78]. Also, more sophisticated structures such as hcp, CsCl, AlB₂, Cr₃Si, Cs₆C₆₀ lattices, and others are observed, as shown in Figure 10.10.

Progress has been made by understanding that the weak interactions of short complementary DNA sequences are enhanced in the sense that within the polyvalently in connected AuNP aggregates, the system self-corrects its own defects when annealed and thus initially disordered aggregates transform into highly ordered and energetically favorable structures. Under these conditions, a high number of linkages hold the aggregate together, while the individual bonds are weak enough to de- and rehybridize to iterate the structure [19]. The structures were analyzed by SAXS as they showed characteristic scattering patterns after crystallization, as well as a visualization using TEM of resin-embedded superlattices was performed (Figure 10.10) [77]. Depending on the appropriate use of the respective building blocks, a new construction kit for aligning nanoparticle-based 3D architectures, which reminds of a nanoparticle-based analogue of the periodic table of elements, has been introduced that lead to nanoparticle-based programmable atom equivalents (PAEs) arranged into superlattices [79]. As a critical parameter, the ratio of DNA length to particle core size was identified, and, based on previous experiments, high ratios of DNA length to particle diameter and a decrease in local salt concentration as well as binding partners result in less binding events [19]. A set of rules was established to predict the structure

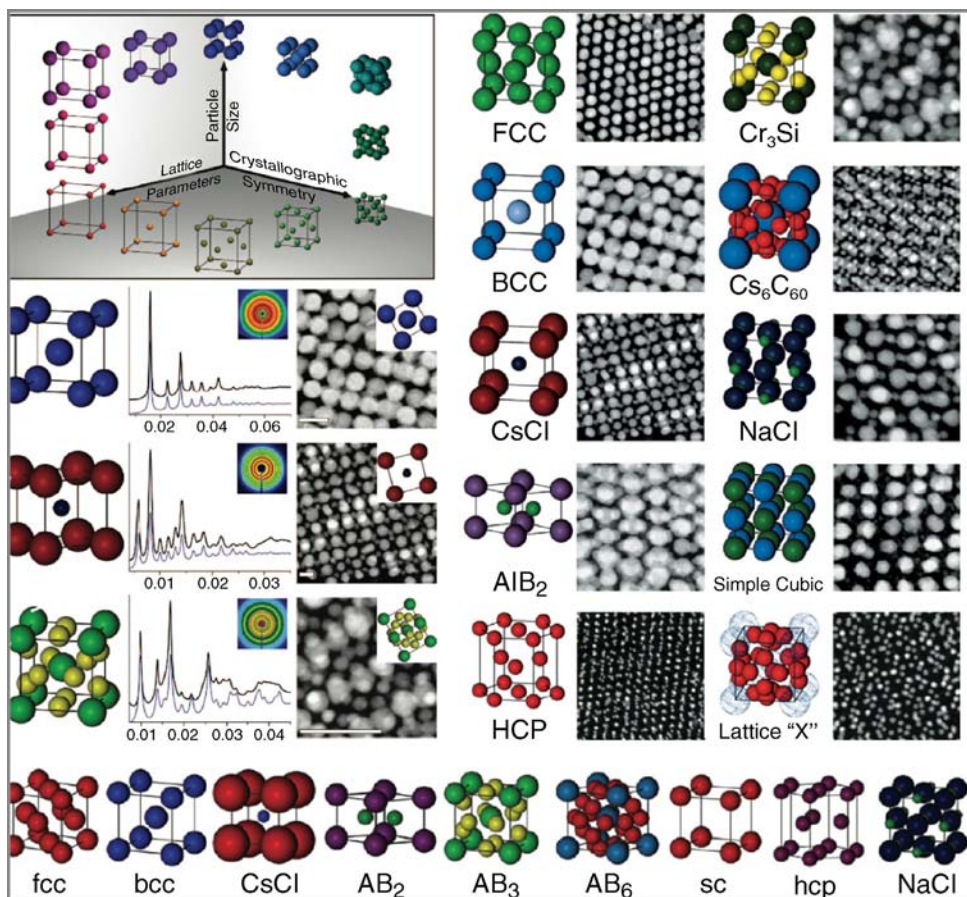


Figure 10.10 Different crystal structures based on nanoparticle–DNA superlattices and corresponding SAXS patterns and TEM images. (Reprinted with permission from Refs [19,77,79]. Copyright 2012–13, American Chemical Society and Wiley-VCH Verlag GmbH.)

that is to be obtained. Rule 1 states that the most stable crystal structure maximizes all possible types of DNA hybridizations, while rule 2 is for the special case that all DNA–AuNPs have the same hydrodynamic radius. If that is the case, the thermodynamic favorable product will maximize the number of nearest neighbors. The overall size of the DNA–AuNP and not the hydrodynamic elongation of either metal nanoparticle or DNA strands is dictating (rule 3). Rule 4 states that in a binary system the number of each complementary DNA sequences will be equivalent throughout the unit cell. Rule 5 implies that two systems comprising the same ratio of size and DNA length deliver the same thermodynamic product, and rule 6 is the extension to otherwise inaccessible structures via more than one kind of oligonucleotide per unit. Rule 7 includes hollow spherical nucleotides as spacer elements within nanoparticle superlattices,

which allows accessing symmetries that are not accessible with the core-filled structures and rule 8 includes anisotropic units [19,79,80]. These rules can be extended for anisotropic materials, leading to a dependency of the resulting structure on the number of binding events between the respective particles, which again are dependent on the particle geometry [79,81]. A phase diagram is introduced, based on experimental findings, that states that the number of linkages between nanoparticles for long DNA strands should be more than that for short DNA strands [82].

Another way to tune the interparticle distance of AuNPs within networks is to use different DNA conformations. Networks and multiple gold nanoparticle architectures connected with intramolecular complementary hairpin DNA have been investigated. Examples are shown in Figure 10.11, where the assembly of nanoparticles into 3D superlattices is presented. Using reconfigurable hairpin DNA, the superlattices can be modified by the addition of complementary DNA single strands, and their interparticle distances have been shown to elongate in the range of 15–25% (Figure 10.11a) [78,83]. Similar observations were made for hairpin DNA-functionalized hydrogels, which swelled in response to added fuel DNA [84]. This way the incorporation of such structures into functional devices is eased since these functional materials have the ability to adjust to the spatial requirements of the device.

Although the structures shown in Figure 10.11a can be switched between two distinct and rigid states, significant hysteresis is observed for the transition to flexible configurations within such superlattices. A reversible and rapid procedure to switch between such states can be realized by introducing allosteric effectors by the addition of complementary DNA and the withdrawal of these DNA strands by further complementary segments (Figure 10.11b) [85].

10.3.3

Finite Size DNA–AuNP Assemblies

The combinability of DNA-linked AuNPs enables the tailoring of network sizes not only up to several hundred nanometers [86] but also down to defined dimer, trimers, and so on [83]. In order to gain control over the size of DNA–AuNP conjugates and networks, synthetic protocols have been developed that are based either on the anisotropic functionalization of the AuNPs or on the reaction control via the concentration ratio of the reaction partners. Mirkin and coworkers introduced an approach to control the number of reacting DNA single strands by anisotropic functionalization of the AuNP based on thermal addressability of dsDNA [87]. DNA-functionalized AuNPs are linked to DNA-functionalized silica particles via hybridization to form satellite structures. The interconnecting DNA double strands are individually addressable at their melting temperatures at the two different sites facing the AuNP and the silica particle. This allows the temperature-induced release of the modified AuNP with the linker intact, yielding anisotropically functionalized particles due to the exposed “sticky end” (Figure 10.12a).

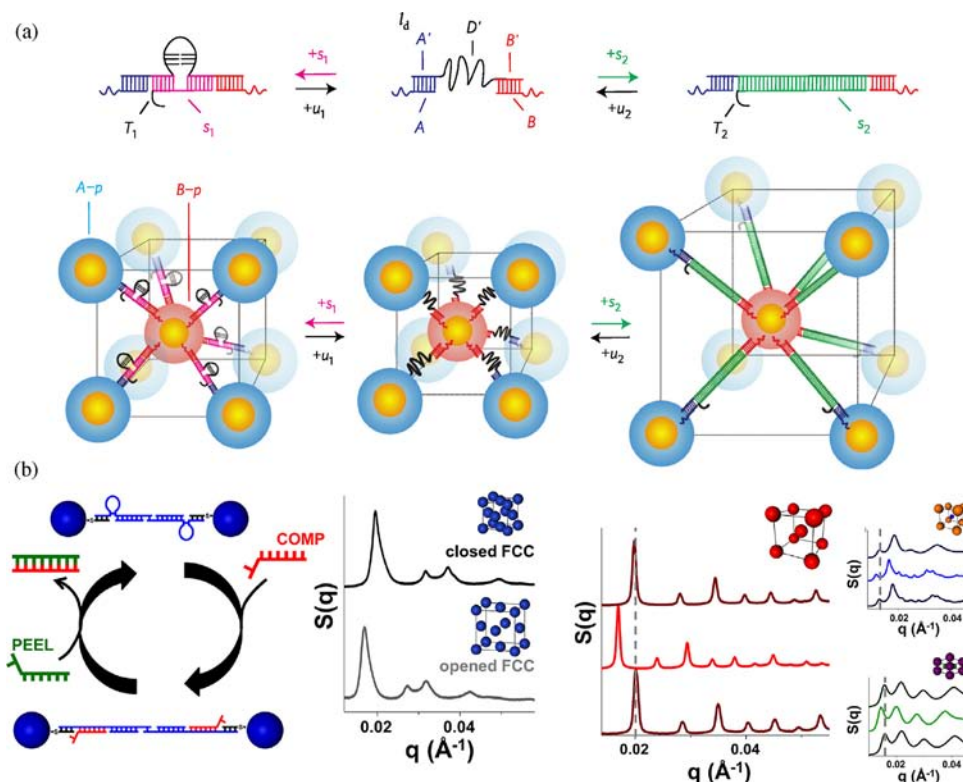


Figure 10.11 (a) Sketch of hairpin DNA-mediated gold nanoparticle networks that expand upon temperature increase due to DNA dehybridization and can be further elongated by the addition of a complementary DNA strand. (Reprinted with permission from Ref. [78]. Copyright 2010, Macmillan Publishers Ltd.) (b) Sketch of the opening and closing of

hairpin DNA-mediated gold nanoparticle superlattices, involving the addition of complementary “comp” and “peel” strands to generate a reversible aggregate formation as well as the corresponding SAXS patterns. (Reprinted with permission from Ref. [85]. Copyright 2013, American Chemical Society.)

Solution-based reactions are limited and typically yield a mixture of products, ranging from monomers and dimers and so on to multimers. A stepwise high-throughput method utilizing a solid support delivers ordered clusters of defined sizes and structure [88]. By anisotropically functionalizing the primary particles with different DNA strands, realized by immobilizing them on the solid support, they can be linked to isotropically functionalized DNA–AuNPs in a later reaction step, as seen in Figure 10.12b. The final structures can be visualized by electron microscopy. Another way to constructing Janus-type aggregates is by introducing Janus-type polystyrene nanoparticles that have a gold hemisphere after amino-functionalization and metal evaporation [89], followed by anisotropic DNA functionalization based on the different surface modifications. As shown in Figure 10.12c, the degree and reversibility of the assembly process of

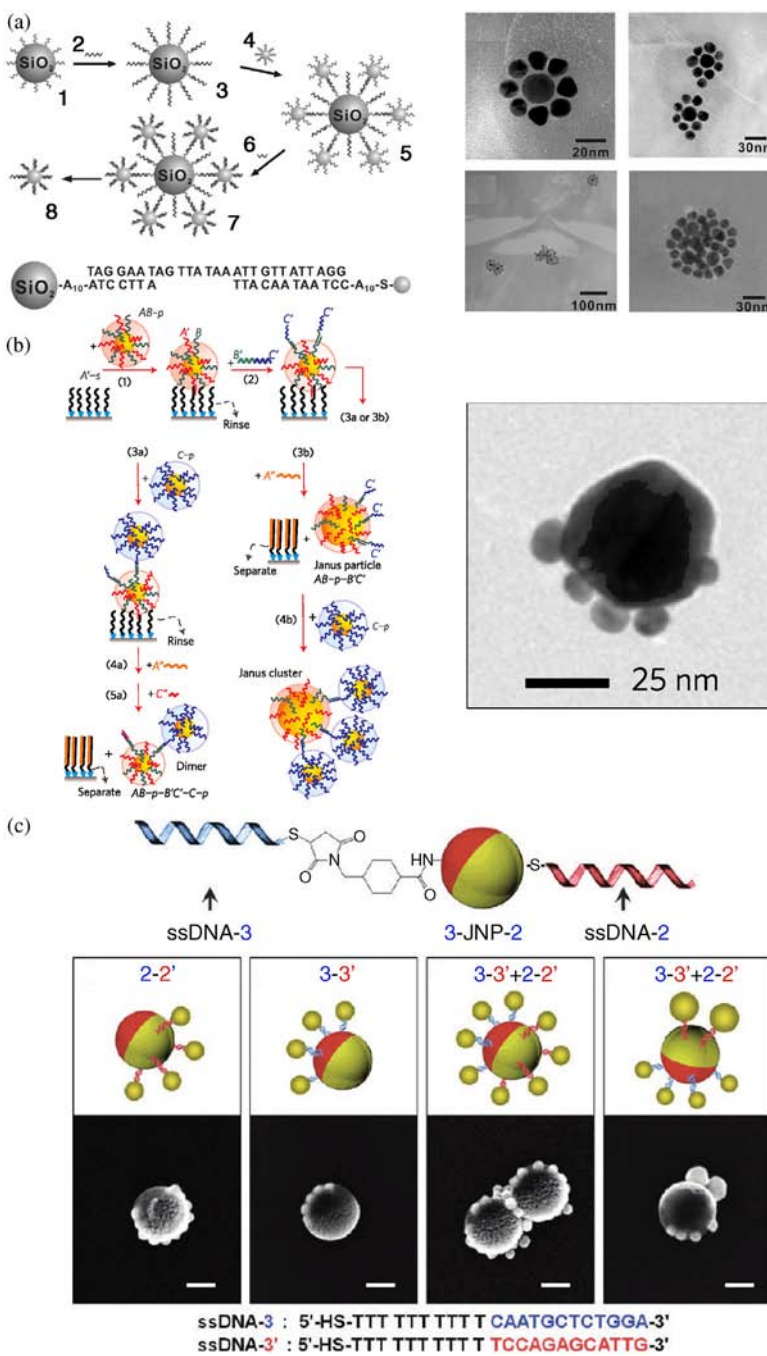


Figure 10.12 (a) Sketch for the asymmetric functionalization of nanoparticles with DNA utilizing silica particles and TEM images

of the resulting core–shell structures.
 (Reprinted with permission from Ref. [87].
 Copyright 2006, Wiley-VCH Verlag GmbH.)

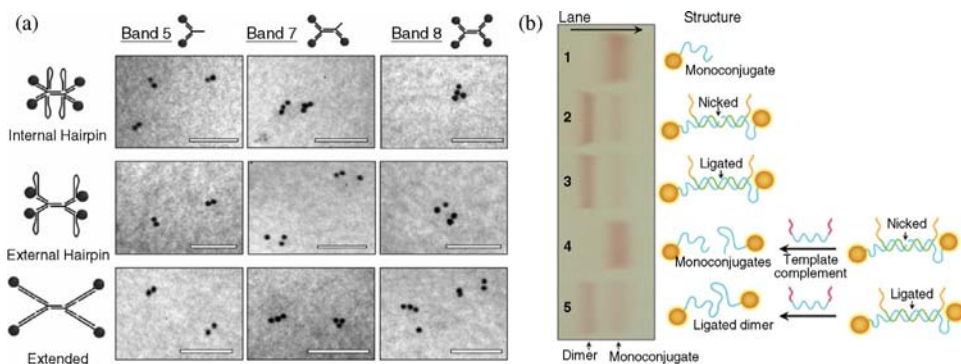


Figure 10.13 (a) TEM images of purified dimer, trimer, and tetramer structures generated using anisotropically functionalized DNA–gold nanoparticles. (Reprinted with permission from Ref. [21]. Copyright 2005, American

Chemical Society.) (b) Electrophoretic analysis of enzymatically ligated DNA connecting gold nanoparticles. (Reprinted with permission from Ref. [83]. Copyright 2008, American Chemical Society.)

the aggregates can be controlled, resulting in a wide range of structures associated with tailored optical properties.

The partial passivation of the nanoparticle surface with different ligands is a different approach to synthesize anisotropic nanoparticles. An approach presented by Alivisatos and coworkers describes the challenging synthesis of AuNPs with only a small number of DNA strands per particle achieved by passivation of the remaining particle surface with PEG ligands [21,83]. Purification via HPLC or gel electrophoresis and subsequent reaction based on DNA hybridization of complementary components enable the formation of discrete DNA–AuNP conjugates dependent on the absolute number of ssDNA present on the particle surface [83,90]. In this way, mono-, di-, and trifunctionalized particles can be separated and merged into branched discrete AuNP assemblies like dendrimers. Examples are shown in Figure 10.13a and b. Multiple tetramer architectures were investigated, showing hairpin DNA–gold nanoparticle conjugates with varying secondary structural motives based on conformational changes of the hairpin DNA.

DNA that was demonstrated to function as a single-stranded linker in AuNP dimers after enzymatic ligation directed nanoparticle assembly, which could be followed by SAXS and TEM. The DNA retained its sequence-specific properties, and could further be hybridized with analogous counterparts in a controlled fashion to yield larger discrete assemblies such as hexamers.

(b) Surface-encoded structures for the anisotropic functionalization of DNA-nanoparticles. (Reprinted with permission from Ref. [88]. Copyright 2009, Macmillan Publishers Ltd.)
 (c) Sketch of the coupling chemistry of amine-

modified Janus nanoparticles and corresponding TEM images of the generated anisotropic structures. (Reprinted with permission from Ref. [89]. Copyright 2012, American Chemical Society.)

To generate networks of larger but still defined dimensions, multicomponent systems have been synthesized varying the ratio of linker DNA or additive to both DNA-functionalized AuNP and complementary functionalized DNA–AuNP. The resulting networks were investigated by DLS concerning their hydrodynamic radius [70,72,91–93], OES [76,93–95], or SAXS concerning their average interparticle distance [69,70,72]. Larger networks predominantly experience attractive interactions based on Watson–Crick base pairing, leading to a shorter average interparticle distance, while in smaller networks repulsive interactions also exist that lead to an elongation of the average interparticle distance [70]. Electrodynamic calculations have been established to predict the optical properties of gold nanoparticle aggregates, considering different network sizes and levels of short-range order as well as the volume fractions of AuNP. The aggregation-induced redshift and broadening of the plasmon peak increase with aggregate size and polydispersity. Also, scattering becomes significant and absorption decreases as screening prevents the network interior from being fully accessible [96].

Since accurate calculations are challenging for larger systems, a thorough characterization using optical and scattering methods is especially necessary to gain knowledge of the inner structure of networks. A way to achieving a limited growth of defined DNA–gold nanoparticle clusters is the addition of the strongly binding DTT, which to a certain extent leads to particle agglomeration based on bridging of particles after ligand exchange reactions, as demonstrated in Figure 10.14a [66,67,93]. The sizes of the synthesized clusters can be adjusted by varying the molar ratio of DTT and DNA, leading to mostly narrow size distributions and a multitude of optical properties that are dominated by plasmon resonances [93]. Furthermore, increased cooperativity of the melting process can be observed with increasing network size.

The internal structure of such networks is of interest to explore the potential for biomedical applications, such as drug release systems. A profound knowledge of the internal structure is essential for developing quantitative models and for e.g., designing photothermal heating experiments and simulating heat distribution properties. Furthermore, it is desirable to precisely and quickly synthesize tailored networks of confined dimensions to channel the amount of gold and DNA introduced with the respective networks. Therefore, the amount of drug molecules intercalated can also be adjusted.

First steps to elucidate the structure have been done using SAXS, which can be used to determine the interparticle distance within aggregates [12]. In addition, SAXS is able to determine whether the DNA that is connecting the gold nanoparticles is double stranded or single stranded, adsorbed on the particle surface or freestanding. Nonhybridizing DNA on the particle surface, for example, can be used as a tool for steric repulsion and thus allows the control over a range of interaction energies [70]. This and the variation of ratios of complementary components, as presented in Figure 10.14b, besides the addition of additives such as DTT, lead to further control over the resulting aggregate size. With increasing size, the polydispersity of such networks increases, due to less

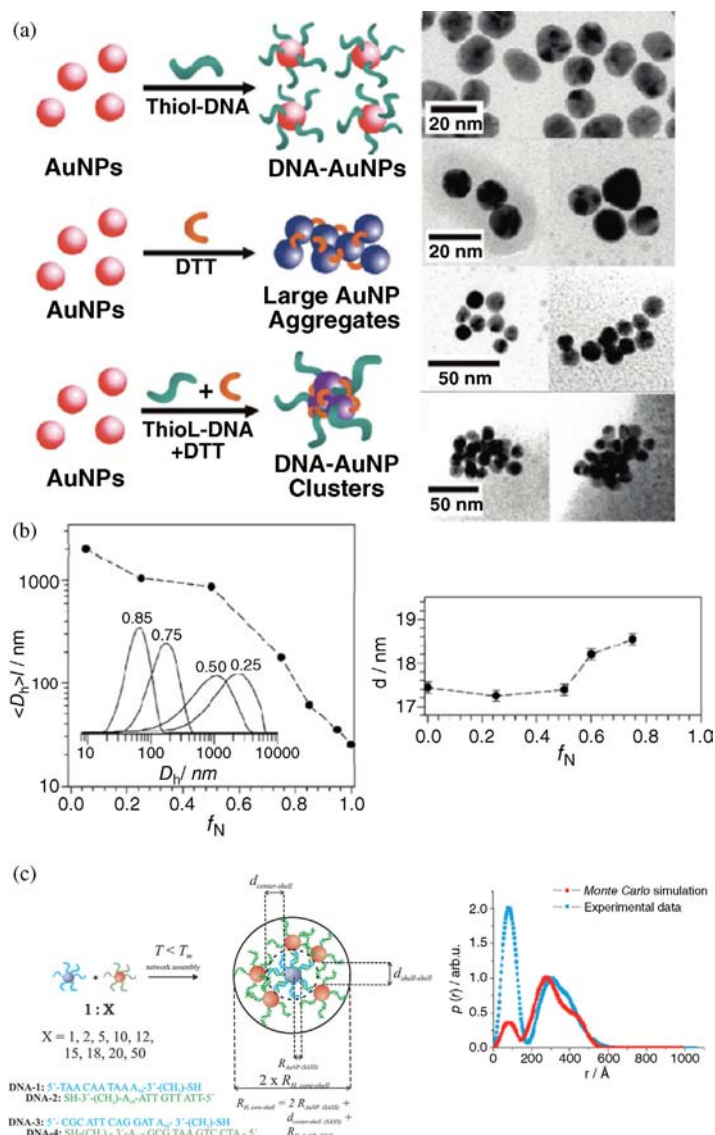


Figure 10.14 (a) Sketch of the synthesis of DNA-gold nanoparticle clusters that are mediated using DTT as well as the corresponding TEM images. (Reprinted with permission from Ref. [93]. Copyright 2009, American Chemical Society.) (b) Quantification of the size and interparticle distances within DNA-gold nanoparticle assemblies using DLS and SAXS. (Reprinted with permission from Ref. [70].)

Copyright 2006–2007, Wiley-VCH Verlag GmbH.) (c) Sketch of the synthesis of defined gold nanoparticle network using two sets of DNA. The interparticle distances could be quantified using a combination of SAXS and Monte Carlo simulations. (Reprinted with permission from Ref. [97]. Copyright 2014, American Chemical Society.)

homogeneous hybridization and thus a broader mixture of aggregates. With less binding events within a network, the interparticle distance also increases, leading to closely packed large and polydisperse networks compared to small and almost monodisperse networks with larger interparticle distances. To fully investigate the internal structure of finite-size networks, an elaborate combination of DLS, SAXS, and OES with Monte Carlo simulations of pair distance distribution function (PDDF) curves and generalized Mie theory simulations as well as *in situ* TEM is used to analyze the internal structure of finite-size assemblies [97]. Reaction mixtures of complementary functionalized DNA–AuNP between 1:15 and 1:20 display monodisperse networks of hydrodynamic radii associated with core–shell structures, for which the number of shell particles can be quantified to be about 10, with the exact number depending on the linking DNA double strand. Examples are shown in Figure 10.14c. A similar method to elucidate the internal structure is also used for assemblies in the micrometer range [86], which has proven useful for the construction and application of such systems as external stimulus-responsive materials. Due to the temperature sensitivity of the DNA within the networks, temperature changes, either induced thermally or photothermally, lead to switching between specific sizes associated with, for example, hierarchical superstructures, intermediate aggregates, and primary particles. The structural changes in size are likely to be accompanied by changes in macroscopic properties such as viscosity or conducting behavior.

10.3.4

Aggregates Composed of Different Particle Geometries and Morphologies

Although spherical AuNPs have proven useful in constructing DNA–nanoparticle assemblies, further functionalities can be introduced by varying the metal core material and/or geometry or by even introducing hollow components. For example, silver nanoparticles (AgNP) can be protected from surface oxidation using cyclic disulfides coupled to DNA [98], iron oxide nanoparticles bear DNA after a copper-catalyzed alkyne-azide click reaction [99], and CdSe quantum dots can be transferred to the aqueous phase by functionalization with 3-mercaptopropionic acid and later DNA functionalization [100] or via a peptide linker [101]. These examples are shown in Figure 10.15a and a further approach using click chemistry to functionalize nanoparticles independently on their material, for example, Pt nanoparticles, is shown in Figure 10.15b.

Introducing AgNP molecular diagnostic labels, synthons in programmable materials synthesis and devices for nanoelectronics and plasmonics can be fabricated, while the known cooperativity in oligonucleotide melting on metal nanoparticle surfaces and plasmonic coupling mechanisms are maintained [98]. On the other hand, superparamagnetic DNA-covered iron oxide and platinum nanoparticles can be stimulated using external magnetic fields while also displaying the properties that materials densely covered with oligonucleotides possess [99,102,103]. These particles, as their gold homologues, are also able to

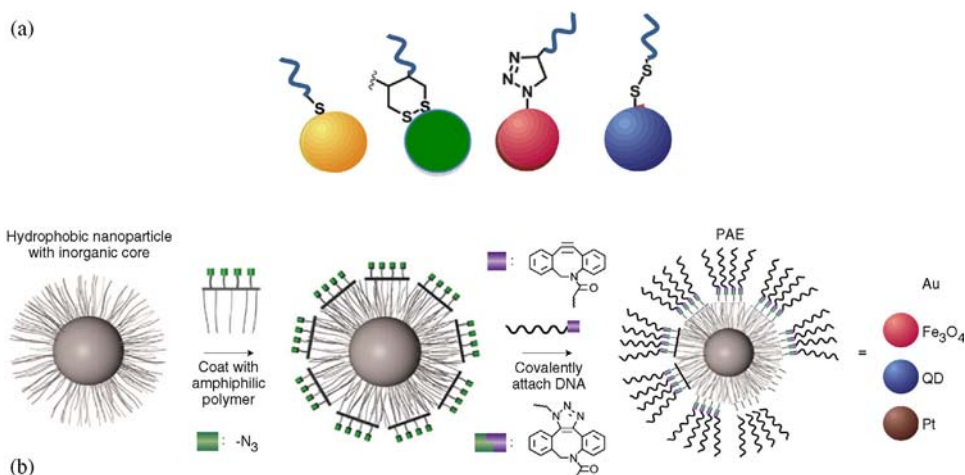


Figure 10.15 (a) Nanoparticles of different materials functionalized with DNA. (Reproduced with permission from The Royal Society of Chemistry [23].) (b) Synthetic route for the functionalization of various materials with

DNA utilizing amphiphilic polymers and click chemistry. (Reprinted with permission from Refs [102,103]. Copyright 2013, Macmillan Publishers Ltd.)

cross cervical cancer cell membranes without transfection agents and can function as magnetic resonance imaging (MRI) contrast agents and in electronic memory devices. These particles can further be aligned to exhibit similar superstructures as their gold homologous counterparts [102]. Also, silica or hollow nucleic acid structures can be synthesized that are constructed by cross-linking AuNP–DNA aggregates as presented earlier and dissolving the metal cores by the addition of potassium cyanide (KCN) in a subsequent reaction step, as shown in Figure 10.16a. This way the biomolecules are not affected and the resulting structures can be seen as three-dimensional biocompatible nontoxic spacers [80,104]. Due to the distinct luminescent, electronic, and chemical properties of quantum dots, these functionalities are coupled with the self-recognition properties, thus exhibiting biocompatibility of oligonucleotide-functionalized nanoparticles [100].

Interesting and versatile secondary superstructures can be generated when incorporating geometries that differ from the simplest spherical nanoparticles. The above presented crystal superlattices can be modified into one-, two-, or three-dimensional structures by introducing rods, triangular prisms, rhombic dodecahedra, and octahedrals as primary building blocks, as shown in Figure 10.16b [106]. Importantly, the resulting secondary structure depends on the geometry of the building blocks, since the anisotropy directs the bonding interactions, thus displaying inherent shape-directed crystallization when functionalized with complementary oligonucleotides. Anisotropy can be generated in two ways: particles are anisotropically either functionalized or aligned, based on

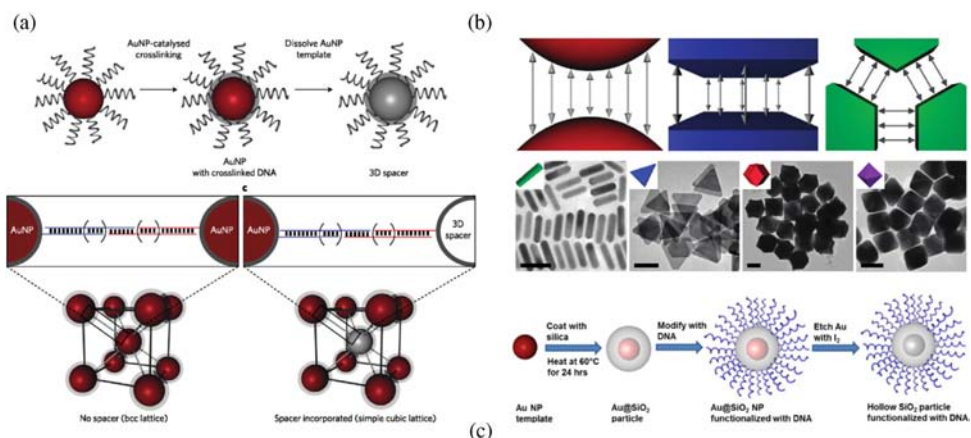


Figure 10.16 (a) Sketch of the synthesis of DNA hollow spheres via the dissolution of previously introduced gold nanoparticles. (Reprinted with permission from Ref. [80]. Copyright 2012, Macmillan Publishers Ltd.) (b) By introducing different nanoparticle geometries, further anisotropic structures can

be generated. (Reprinted with permission from Ref. [105]. Copyright 2010, Macmillan Publishers Ltd.) (c) Hollow structures can be synthesized by subsequent etching of previously introduced gold nanoparticles. (Reprinted with permission from Ref. [104]. Copyright 2010, American Chemical Society.)

their anisotropic shape. Hollow elements with additional silica shells further increase the structural complexity, as shown in Figure 10.16c. To create a periodic table-like particle equivalent of atoms, morphological diversity was introduced into structures made from DNA-functionalized silica spheres by generating particles with several symmetrically positioned patches that precisely mimic atomic orbital arrangements and molecular structures [105].

Introducing two kinds of particle geometries within one structure can generate further complexity. Phase separation based on particle geometries is observed, for example, when trigonal prisms and spherical particles are aligned using DNA [104,106]. The interplay of attractive depletion and repulsive electrostatic forces leads to one-dimensional lamellar crystals in solution with distinct interparticle spacings. These can be attributed to stacking interactions with the additionally introduced surfactant cetyltrimethylammonium bromide (CTAB), leading to parameters such as surfactant concentration, temperature, ionic strength, and prism geometry, and to an effective strategy to separate spherical from trigonal particles. This is shown in Figure 10.17a. Also, gold nanorods can be functionalized with DNA. Their anisotropy offers the possibility to selectively functionalize either the transversal or the longitudinal part of the rods with DNA, which in turn leads to different alignments when combined with complementary material (Figure 10.17b) [107]. End, side, and satellite structures can be generated that possess distinct optical properties with two plasmonic actuators and surface-enhanced Raman spectroscopy (SERS) signals.

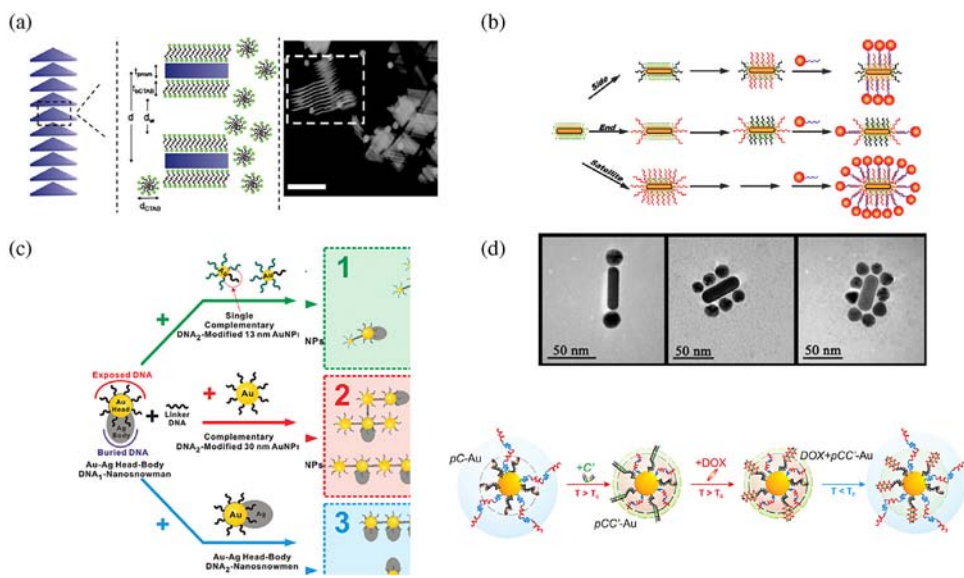


Figure 10.17 (a) Lamellar superstructures using nanoprisms that are mediated by DNA and the corresponding TEM image. (Reprinted with permission from Ref. [104].) (b) Regiospecific DNA–gold nanorod formation and the corresponding TEM images to show the anisotropic functionalization with DNA. (Reprinted with permission from Ref. [107]. Copyright 2012, American Chemical Society.)

(c) Directional assembly of DNA–nanosnowmen and the corresponding TEM images. (Adapted with permission from Ref. [108]. Copyright 2012, American Chemical Society.) (d) Gold nanoparticle functionalization steps toward multistimuli-responsive microgel–DNA hybrid systems. (Reprinted with permission from Ref. [22]. Copyright 2013, American Chemical Society.)

Nanoscale building blocks can further be synthesized to consist of two different kinds of metals, which are arranged via anisotropic DNA functionalization on the particle surface [108]. With adjustment of the salt concentration in the solution of DNA–NPs, Au–Ag head–body nanosnowmen structures can be generated after addition of Ag precursor-loaded polymers, as seen in Figure 10.17c. Polymers can also function to introduce an independent stimulus response when incorporated on the nanoparticle surface (Figure 10.17d) [22]. PNIPAAm-*co*-pAAm polymers shrink when temperatures are high enough and thus enable DNA that is shorter than the elongated polymer to hybridize at these elevated temperatures. Therefore, the polymers regulate the hybridization kinetics of the specific DNA, which can in later reaction steps function as drug-release systems.

10.4 Applications

DNA–AuNP aggregates display a fortunate combination of optical addressability and bio-recognition properties. Furthermore, manifold architectures and

versatile melting properties help to tailor the aggregates for various specific applications. In the field of biomedical applications in intracellular messenger RNA detection, biodiagnostics, antisense gene regulation, and delivery systems, great progress has been made [13–15]. It has to be mentioned that, although AuNP have been investigated thoroughly, the ability to deliver them into cells and specifically target them is still rather undeveloped. Quantitative descriptions on kinetics, amount, mechanisms, and trajectories of AuNP uptake are widely unexplored [109]. For *in vivo* applications, biological barriers such as undesired immune responses have to be overcome before the targeted cells can take up the particles [109,110].

Recently, many works are dedicated to understand how DNA–nanoparticle architectures interact with biological cells. The polyanionic charge of the DNA polymers is, under certain circumstances, the first obstacle to be overcome. Nevertheless, polyvalent nucleic acid nanostructures have been shown to be capable of high cellular uptake without the need of a cationic cocarrier after catalytic cross-linking [19]. These structures are also resistant toward nucleases that have to be encountered within biological cells. One reason for the high unexpected cellular uptake due to the charge of the DNA is the fact that extracellular proteins adsorb on the DNA–AuNP surface, as sketched in Figure 10.18a [111]. The amount of adsorbed proteins scales with the surface coverage of the AuNP with DNA. The protein adsorption reflects in a change in size and surface charge of the nanoparticles. A difference in cellular uptake patterns and cell line-specific behavior was observed for AuNP aggregates compared with single particles, suggesting a strong effect of aggregation on targeting and intracellular trafficking [112].

Within biological cells, the DNA–AuNPs encounter media with different biological and physical properties that lead to further processes such as the exposure to degrading enzymes. A systematic investigation revealed that the stability toward enzymatic degradation also increases with the DNA coverage on the nanoparticle surface (Figure 10.18b) [113]. Charge and local salt concentration are the main factors that scale with the amount of DNA on the surface. Polyvalency has not been shown to prevent enzyme binding; rather it has been shown to inhibit enzyme-catalyzed hydrolysis to the extent that DNA–AuNP species exhibit a 4.3 fold greater half-life time in cells than the molecular DNA. Recently, functional antibody–DNA–AuNPs were designed for HERG targeting that demonstrated cell-type selectivity concerning uptake and gene knockdown, compared with the analogous antibody-free materials, as seen in Figure 10.18c [114]. Also, these materials are able to freely penetrate the mouse skin and human epidermis *in vivo*, almost completely within hours after application [115]. Once internalized into cells, DNA–AuNPs are able to interfere with cellular processes, such as protein expression [14,111,116,117], and the neutralization of oncogene expression in GBM (glioblastoma multiforme), which led to increased intratumoral apoptosis [118]. Due to the recognition properties of DNA–AuNPs with specially designed oligonucleotide sequences, they can bind or release binding sequences complementary to natural DNA and thus “knock

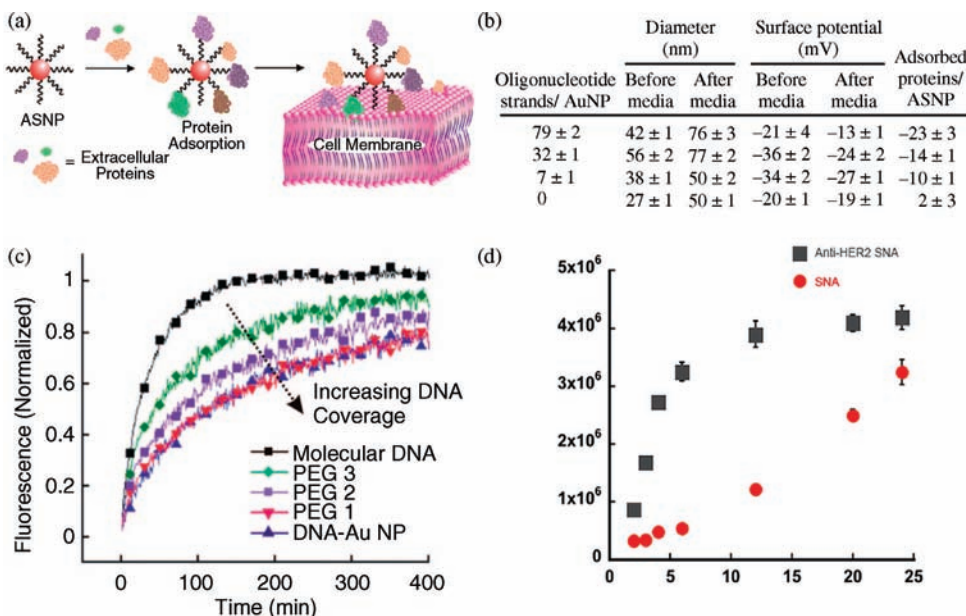


Figure 10.18 (a) Sketch of the adsorption of proteins on the DNA–gold nanoparticles to facilitate cellular uptake and effect on particle surface and particle surface charge. (Reprinted with permission from Ref. [111]. Copyright 2007, American Chemical Society.) (b) Fluorescence-based curves that show the cellular uptake dependence on the particle coverage

with DNA. (Reprinted with permission from Ref. [113]. Copyright 2009, American Chemical Society.) (c) Difference in cellular uptake as seen by SNA and antibody-SNA nanoparticles as a function of time. (Reprinted with permission from Ref. [114]. Copyright 2012, American Chemical Society.)

out” certain transfection species, resulting in a function called intracellular gene regulation. Furthermore, due to their sensitivity toward even smallest amounts of complementary DNA, these DNA–AuNP architectures are used as, for example, scanometric microRNA platform for the detection of relatively low-abundance miRNAs with high specificity and reproducibility [119] or as pregnancy tests [98,120] based on colorimetric, electronic, and Raman scattering-related biodetection strategies, of which some are admitted by the US Food and Drug Administration [111].

The DNA double helix can also function as a carrier system for small organic molecules that bind to the DNA strands either during or post DNA hybridization. These molecules can bind electrostatically with the negatively charged phosphate backbone, form a complex with the major or minor groove, or stack between base pairs [3,121–124]. The third form of interaction is called intercalation.

Prominent examples of DNA-intercalating molecules are ethidium bromide and 4'6-diamidino-2-phenylindol (DAPI) [121,122]. Since these are optically

active, they are commercially used as detection agents for double-stranded DNA. Since intercalating molecules interact with DNA, this cannot function in all cell processes anymore and intercalating molecules are therefore cytotoxic. This has opened up applications as cytostatic drugs in chemotherapy as well as in elucidating DNA function [2,68,125]. The change in melting temperature with increasing amount of the DNA-intercalating molecule DAPI can be seen in a systematic investigation in Figure 10.19a, as well as the proven specific affinity of DAPI to certain base sequences and DNA double strands [68,126]. When DNA double strands are dehybridized, DAPI is eventually released and thus DNA–AuNP architectures can function as drug delivery systems, providing the additional option to be photothermally triggered due to the plasmonic properties of the gold nanoparticles.

Photothermal heating is based on the absorption of light of the maximum absorption wavelength by AuNP. By irradiating AuNP architectures with laser light of this specific wavelength, the particles convert the absorbed light into heat. The generated heat is subsequently delivered to the immediate surroundings of the nanoparticle via heat transfer across the nanoparticle–solvent interface [128–131]. Since the described processes take place on the order of fractions of a second, photothermal heating can be assumed to be instantaneous upon irradiation. The

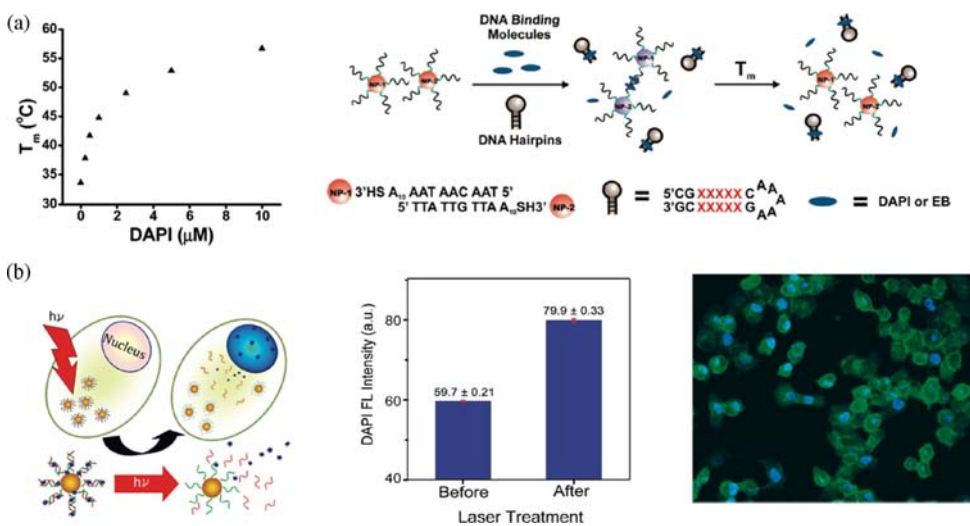


Figure 10.19 (a) Sketch elucidating the sequence selectivity of DNA binding molecules involving DNA-functionalized gold nanoparticles and the effect of DNA binding molecules on the melting temperature of networks formed from DNA–gold nanoparticles. (Reprinted with permission from Ref. [126]. Copyright 2007, American Chemical Society.)

(b) Sketch of the light-triggered release of DAPI from DNA nanoshells, the difference of DAPI fluorescence intensity before and after the laser treatment, and a microscopy image showing the uptake of the DNA-nanoshells in cells. (Reprinted with permission from Ref. [127]. Copyright 2012, American Chemical Society.)

process is further locally confined, which allows selectively influencing reactions close to the gold nanoparticle surface [132–134]. DAPI was photothermally released in living cells using DNA-loaded silica–gold nanoshells [127], and it was shown that the intercalating molecule diffuses to the nucleus and associates with the endogenous DNA of the cell, as seen in Figure 10.19b. By applying low laser powers and irradiation times, the viability of the cell was not inhibited. In future works in cancer research, this can be extended to develop delivery systems for intercalating molecules that inhibit the momentarily uncontrollable replication of tumor cells.

Compared with single DNA–AuNPs, this photothermal heating effect is enhanced within DNA–AuNP aggregates since they accumulate heat in between the individual particles. It was shown by irradiating DNA–AuNP aggregates with nanosecond laser pulses that it can be distinguished between a perfectly matching and a point-mutated DNA sequence in less than 1 ms in a rapid high-throughput analysis suitable for pathogen detection [135]. Although by using high-intensity pulsed laser irradiation, the gold–sulfur bond between AuNP and thiol-modified DNA in DNA-mediated AuNP networks has been broken [136], a continuous wave approach yields quantitative information on photothermally controlled experiments on DNA–AuNP aggregates. A first step toward the evaluation of the potential to reversibly photothermally control AuNP assemblies has been taken by observing the reassembly of DNA–AuNP networks after photothermally induced dissociation at different laser intensities. In doing so, the intact functionality of the DNA strands after laser irradiation was confirmed. The reversible process was proved to be locally confined to the microscopic dimensions of the laser beam, and the induced temperature difference between the integral and the photothermal heating was also shown by interferometric measurements [132].

10.5

Summary

This chapter summarizes synthetic strategies to generate DNA–nanoparticle assemblies with defined and desirable sizes, shapes, and functionalities. Two conceptually different methodologies have been introduced, which either apply DNA as a template, so that the preformed DNA template dictates the final assembly structure or morphology, or where DNA is used as a structure-guiding ligand for metal nanoparticles, whereas the DNA in conjunction with the particle is decisive for structure formation. While the first approach reflects the virtue of DNA assembly, culminating in hierarchical 3D structures, formed, for example, by DNA origami, the second approach allows fabricating fundamentally new architectures, that is, superlattices, that can resemble, for example, nanoscale analogues to ionic crystals. While most of these concepts have been developed for AuNP, very recent works have extended this to a general approach for achieving superlattices that are self-assembled from variable inorganic

nanoparticles. New coupling motives, which go beyond the gold–sulfur coupling chemistry, open up new perspectives for structure formation of nanoparticle-based solids as well as for technologically relevant applications in, for example, intracellular delivery.

References

- 1 Watson, J.D. and Crick, F.H.C. (1953) *Nature*, **171**, 737–738.
- 2 Nelson, D., Cox, M., and Held, A. (2001) *Lehninger Biochemie*, Springer, Berlin.
- 3 Stryer, L. (1985) *Biochemie*, Vieweg Teubner Verlag, Wiesbaden.
- 4 Burge, S., Parkinson, G.N., Hazel, P., Todd, A.K., and Neidle, S. (2006) *Nucleic Acids Res.*, **34**, 5402–5415.
- 5 Seeman, N.C. (2007) *Mol. Biotechnol.*, **37**, 246–257.
- 6 Seeman, N.C. (2010) *Annu. Rev. Biochem.*, **79**, 65–87.
- 7 Zhang, D. and Seelig, G. (2011) *Nat. Chem.*, **3**, 103–113.
- 8 Rothmund, P.W.K. (2006) *Nature*, **440**, 297–302.
- 9 (a) Katz, E. and Willner, I. (2004) *Angew. Chem.*, **116**, 6166–6235. (b) Katz, E. and Willner, I. (2004) *Angew. Chem., Int. Ed.*, **43**, 6042–6018.
- 10 (a) Niemeyer, C.M. (2001) *Angew. Chem.*, **113**, 4254–4287. (b) Niemeyer, C.M. (2001) *Angew. Chem., Int. Ed.*, **40**, 4128–4158.
- 11 Storhoff, J.J., Lazarides, A.A., Mucic, R.C., Mirkin, C.A., and Letsinger, R.L. (2000) *J. Am. Chem. Soc.*, **122**, 4640–4650.
- 12 Park, S.J., Lytton-Jean, A.K.R., Lee, B., Weingand, S., Schatz, G.C., and Mirkin, C.A. (2008) *Nature*, **451**, 553–556.
- 13 Nam, J.-W., Thaxton, C.S., and Mirkin, C.A. (2003) *Science*, **301**, 1884–1886.
- 14 Rosi, N.L., Giljohann, D.A., Thaxton, C.S., Lytton-Jean, A.K.R., Han, M.S., and Mirkin, C.A. (2006) *Science*, **312**, 1027–1030.
- 15 Braun, G.B., Pallaro, A., Wu, G., Missirikis, D., Zasadinski, J.A., Tirrell, M., and Reich, N.O. (2009) *ACS Nano*, **3**, 2007–2015.
- 16 Giljohann, D.A., Seferos, D.S., Prigodich, A.E., Patel, P.C., and Mirkin, C.A. (2009) *Am. Chem. Soc.*, **131** (6), 2072–2073.
- 17 Mirkin, C.A., Letsinger, R.L., Mucic, R.C., and Storhoff, J.J. (1996) *Nature*, **382**, 607–609.
- 18 Alivisatos, A.P., Johnsson, K.P., Peng, X., Wilson, T.E., Loweth, C.J., Brunchez, L.P., and Schultz, P.G. (1996) *Nature*, **382**, 609–611.
- 19 Cutler, J.I., Auyeung, E., and Mirkin, C.A. (2012) *J. Am. Chem. Soc.*, **134**, 1376–1391.
- 20 Nykypanchuk, D., Maye, M.M., van der Lelie, D., and Gang, O. (2008) *Nature*, **451**, 549–552.
- 21 Claridge, S.A., Mastroianni, A.J., Au, Y.B., Liang, H.W., Micheel, C.M., Fréchet, J.M.J., and Alivisatos, A.P. (2008) *J. Am. Chem. Soc.*, **130**, 9598–9605.
- 22 Hamner, K.L., Alexander, C.M., Coopersmith, K., Reishofer, D., Provenza, C., and Maye, M.M. (2013) *ACS Nano*, **7**, 7011–7020.
- 23 Kumar, A., Hwang, J.-H., Kumar, S., and Nam, J.-M. (2013) *Chem. Commun.*, **49**, 2597–2609.
- 24 Warner, M.G. and Hutchison, J.E. (2003) *Nat. Mater.*, **2**, 272–277.
- 25 Wang, G. and Murray, R.W. (2004) *Nano Lett.*, **4**, 95–101.
- 26 Deng, Z., Tian, Y., Lee, S.-H., Ribbe, A.E., and Mao, C. (2005) *Angew. Chem., Int. Ed.*, **44**, 3582–3585.
- 27 Beyer, S., Nickels, P., and Simmel, F.C. (2005) *Nano Lett.*, **5**, 719–722.
- 28 Schmid, G. and Simon, U. (2005) *Chem. Commun.*, 697–710.
- 29 Semrau, S., Schoeller, H., and Wenzel, W. (2005) *Phys. Rev. B Condens. Matter Mater. Phys.*, **72**, 205443.
- 30 Richter, J. (2003) *Phys. E (Amsterdam, Neth.)*, **16**, 157–173.

- 31** Niemeyer, C.M. and Simon, U. (2005) *Eur. J. Inorg. Chem.*, 3641–3655.
- 32** Winfree, E., Liu, F., Wenzler, L.A., and Seeman, N.C. (1998) *Nature*, **394**, 539–544.
- 33** He, Y., Ye, T., Su, M., Zhang, C., Ribbe1, A.E., Jiang, W., and Mao, C. (2008) *Nature*, **452**, 198–202.
- 34** Weizmann, Y., Patolsky, F., Popov, I., and Willner, I. (2004) *Nano Lett.*, **4**, 787–792.
- 35** Richards, C.I., Choi, S., Hsiang, J.-C., Antoku, Y., Vosch, T., Bongiorno, A., Tzeng, Y.-L., and Dickson, R.M. (2008) *J. Am. Chem. Soc.*, **130**, 5038–5039.
- 36** Weizmann, Y., Braunschweig, A.B., Wilner, O.I., Cheglakov, Z., and Willner, I. (2008) *Proc. Natl. Acad. Sci. USA*, **105**, 5289–5294.
- 37** Aldaye, F.A. and Sleiman, H.F. (2007) *J. Am. Chem. Soc.*, **129**, 4130–4131.
- 38** Fischler, M., Simon, U., Nir, H., Eichen, Y., Burley, G.A., Gierlich, J., Gramlich, P.M.E., and Carell, T. (2007) *Small*, **3**, 1049–1055.
- 39** Feldkamp, U. and Niemeyer, C.M. (2006) *Angew. Chem.*, **118**, 1888–1910.
- 40** Ma, N., Sargent, E.H., and Kelley, S.O. (2008) *Mater. Chem.*, **18**, 954–964.
- 41** Braun, G., Inagaki, K., Estabrook, R.A., Wood, D.K., Levy, E., Cleland, A.N., Strouse, G.F., and Reich, N.O. (2005) *Langmuir*, **21**, 10699–10701.
- 42** Woehrle, G.H., Warner, M.G., and Hutchison, J.E. (2004) *Langmuir*, **20**, 5982–5988.
- 43** Storhoff, J.J., Elghanian, R., Mucic, R.C., Mirkin, C.A., and Letsinger, R.L. (1998) *J. Am. Chem. Soc.*, **120**, 1959–1964.
- 44** Noyong, M., Blech, K., Rosenberger, A., Klocke, V., and Simon, U. (2007) *Meas. Sci. Technol.*, **18**, N84–N89.
- 45** Chung, S.-W., Ginger, D.S., Morales, M.W., Zhang, Z., Chandrasekhar, V., Ratner, M.A., and Mirkin, C.A. (2005) *Small*, **1**, 64–69.
- 46** Wirges, C.T., Timper, J., Fischler, M., Sologubenko, A.S., Mayer, J., Simon, U., and Carell, T. (2009) *Angew. Chem., Int. Ed.*, **48**, 219–223.
- 47** Richter, J., Seidel, R., Kirsch, R., Mertig, M., Pompe, W., Plaschke, J., and Schackert, H.K. (2000) *Adv. Mater.*, **12**, 507–510.
- 48** Seidel, R., Ciacchi, L.C., Weigel, M., Pompe, W., and Mertig, M. (2004) *J. Phys. Chem. B*, **108**, 10801–10811.
- 49** Monson, C.F. and Woolley, A.T. (2003) *Nano Lett.*, **3**, 359–363.
- 50** Gu, Q., Cheng, C., and Haynie, D.T. (2005) *Nanotechnology*, **16**, 1358–1363.
- 51** Timper, J., Gutsmiedl, K., Wirges, C., Broda, J., Noyong, M., Mayer, J., Carell, T., and Simon, U. (2012) *Angew. Chem., Int. Ed.*, **51**, 7586–7588.
- 52** Porro, M., Viti, S., Antoni, G., and Saletti, M. (1982) *Anal. Biochem.*, **127**, 316–321.
- 53** Park, S.-J., Taton, T.A., and Mirkin, C.A. (2002) *Science*, **295**, 1503–1506.
- 54** Kuzyk, A., Schreiber, R., Fan, Z., Pardatscher, G., Roller, E.-M., Hogege, A., Simmel, F.C., Govorov, A.O., and Liedl, T. (2012) *Nature*, **483**, 311–314.
- 55** Sharma, J., Chhabra, R., Cheng, A., Brownell, J., Liu, Y., and Yan, H. (2009) *Science*, **323**, 112–116.
- 56** Lin, C., Liu, Y., and Yan, H. (2009) *Biochemistry*, **48**, 1663–1674.
- 57** Sharma, J., Chhabra, R., Liu, Y., Ke, Y., and Yan, H. (2006) *Angew. Chem., Int. Ed.*, **45**, 730–735.
- 58** Zhang, J., Liu, Y., Ke, Y., and Yan, H. (2006) *Nano Lett.*, **6**, 248–251.
- 59** Cheng, W., Campolongo, M.J., Cha, J.J., Tan, S.J., Umbach, C.C., Muller, D.A., and Luo, D. (2009) *Nat. Mater.*, **8**, 519–525.
- 60** Pal, S., Deng, Z., Ding, B., Yan, H., and Liu, Y. (2010) *Angew. Chem., Int. Ed.*, **49**, 2700–2704.
- 61** Pal, S., Deng, Z., Wang, H., Zou, S., Liu, Y., and Yan, H. (2011) *J. Am. Chem. Soc.*, **133**, 17606–17609.
- 62** Aldaye, F.A. and Sleiman, H.F. (2006) *Angew. Chem., Int. Ed.*, **45**, 2204–2209.
- 63** Park, S.J., Lytton-Jean, A.K.R., and Mirkin, C.A. (2006) *Anal. Chem.*, **78**, 8313–8318.
- 64** Jin, R., Wu, G., Li, Z., Mirkin, C.A., and Schatz, G.C. (2003) *J. Am. Chem. Soc.*, **125**, 1643–1654.

- 65 Cederquist, K.B. and Keating, C.D. (2009) *ACS Nano*, **3**, 256–260.
- 66 Demers, L., Mirkin, C.A., Mucic, R.C., Reynolds, R.A., Letsinger, R.L., Elghanian, R., and Viswanadham, G. (2000) *Anal. Chem.*, **72**, 5535–5541.
- 67 Lee, J.-S., Stoeva, S.I., and Mirkin, C.A. (2006) *J. Am. Chem. Soc.*, **1128**, 8899–8903.
- 68 Han, M.S., Lytton-Jean, A.K.R., Oh, B.-K., Heo, J., and Mirkin, C.A. (2006) *Angew. Chem.*, **118**, 1839–1842.
- 69 Park, S.-J., Lazarides, A.A., Storhoff, J.J., Pesce, L., and Mirkin, C.A. (2004) *J. Phys. Chem. B*, **108**, 12375–12380.
- 70 Maye, M.M., Nykypanchuk, D., van der Lelie, D., and Gang, O. (2007) *Small*, **3**, 1678–1682.
- 71 Berman, H.M. and Young, P.R. (1981) *Ann. Rev. Biophys. Bioeng.*, **10**, 87–114.
- 72 Witten, K.G., Bretschneider, J.C., Eckert, T., Richtering, W., and Simon, U. (2008) *Phys. Chem. Chem. Phys.*, **10**, 1870–1875.
- 73 Slocik, J.M., Tam, F., Halas, N.J., and Naik, R.R. (2007) *Nano Lett.*, **7**, 1054–1058.
- 74 Tan, S.J., Campolongo, M.J., Luo, D., and Cheng, W. (2011) *Nat. Nanotechnol.*, **6**, 269–276.
- 75 Mucic, R.C., Storhoff, J.J., Mirkin, C.A., and Letsinger, R.L. (1998) *J. Am. Chem. Soc.*, **120**, 12674–12675.
- 76 Park, S.-J., Lazarides, A.A., Mirkin, C.A., and Letsinger, R.L. (2001) *Angew. Chem., Int. Ed.*, **40**, 2909–2912.
- 77 Macfarlane, R.J., Jones, M.R., Senesi, A.J., Young, K.L., Lee, B., Wu, J., and Mirkin, C.A. (2010) *Angew. Chem.*, **122**, 4693–4696.
- 78 Maye, M.M., Kumara, M.T., Nykypanchuk, D., Sherman, W.B., and Gang, O. (2010) *Nat. Nanotechnol.*, **5**, 116–120.
- 79 Macfarlane, R.J., OBrien, M.N., Hurst Petrosko, S., and Mirkin, C.A. (2013) *Angew. Chem., Int. Ed.*, **52**, 5688–5698.
- 80 Auyeung, E., Cutler, J.I., Macfarlane, R.J., Jones, M.R., Wu, J., Liu, G., Zhang, K., Osberg, K.D., and Mirkin, C.A. (2012) *Nat. Nanotechnol.*, **7**, 24–28.
- 81 Jones, M.R., Osberg, K.D., Macfarlane, R.J., Langille, M.R., and Mirkin, C.A. (2011) *Chem. Rev.*, **111**, 3736–3827.
- 82 Xiong, H., van der Lelie, D., and Gang, O. (2009) *Phys. Rev. Lett.*, **102**, 015504.
- 83 Claridge, S.A., Goh, S.L., Fréchet, J.M.J., Williams, S.C., Micheel, C.M., and Alivisatos, A.P. (2005) *Chem. Mater.*, **17**, 1628–1635.
- 84 Murakami, Y. and Maeda, M. (2005) *Biomacromolecules*, **6**, 2927–2929.
- 85 Kim, Y., Macfarlane, R.J., and Mirkin, C.A. (2013) *J. Am. Chem. Soc.*, **135**, 10342–10345.
- 86 Buchkremer, A., Linn, M.J., Reismann, M., Eckert, T., Witten, K.G., Richtering, W., von Plessen, G., and Simon, U. (2011) *Small*, **7**, 1397–1402.
- 87 Huo, F., Lytton-Jean, A.K.R., and Mirkin, C.A. (2006) *Adv. Mater.*, **18**, 2304–2306.
- 88 Maye, M.M., Nykypanchuk, D., Cuisinier, M., van der Lelie, D., and Gang, O. (2009) *Nat. Mater.*, **8**, 388–391.
- 89 Xing, H., Wang, Z., Xu, Z., Wong, N.Y., Xiang, Y., Liu, G.L., and Lu, Y. (2012) *ACS Nano*, **6**, 802–809.
- 90 Claridge, S.A., Liang, H.W., Basu, S.R., Fréchet, J.M.J., and Alivisatos, A.P. (2008) *Nano Lett.*, **8**, 1202–1206.
- 91 Dai, Q., Liu, X., Coutts, J., Austin, L., and Huo, Q. (2008) *J. Am. Chem. Soc.*, **130**, 8138–8139.
- 92 Miao, X.-M., Xiong, C., Wang, W.-W., Ling, L.-S., and Shuai, X.T. (2011) *Chem. Eur. J.*, **17**, 11230–11236.
- 93 Kim, J.-Y. and Lee, J.-S. (2009) *Nano Lett.*, **9**, 4564–4569.
- 94 Han, G., Xing, Z., Dong, Y., Zhang, S., and Zhang, X. (2011) *Angew. Chem.*, **123**, 1–5.
- 95 Park, H.-G., Oh, J.-H., and Lee, J.-S. (2011) *Anal. Chem.*. doi: dx.doi.org/10.1021/ac200764a
- 96 Lazarides, A.A. and Schatz, G.C. (2000) *J. Phys. Chem. B*, **104**, 460–467.
- 97 Buchkremer, A., Linn, M.J., Timper, J.U., Eckert, T., Mayer, J., Richtering, W., von Plessen, G., and Simon, U. (2014) *J. Phys. Chem. C*, **118**, 7174–7184.
- 98 Lee, J.-S., Lytton-Jean, A.K.R., Hurst, S.J., and Mirkin, C.A. (2007) *Nano Lett.*, **7**, 2112–2115.

- 99** Cutler, J.I., Zheng, D., Xu, X., Giljohann, D.A., and Mirkin, C.A. (2010) *Nano Lett.* doi: 10.1021/nl100477m.
- 100** Mitchell, G.P., Mirkin, C.A., and Letsinger, R.L. (1999) *J. Am. Chem. Soc.*, **121**, 8122–8123.
- 101** Medintz, I.L., Berti, L., Pons, T., Grimes, A.F., English, D.S., Alessandrini, A., Facci, P., and Mattoussi, H. (2007) *Nano Lett.*, **7**, 1741–1748.
- 102** Zhang, C., Macfarlane, R.J., Young, K.L., Choi, C.H.J., Hao, L., Auyeung, E., Liu, G., Zhou, X., and Mirkin, C.A. (2013) *Nat. Mater.*, **12**, 741–746.
- 103** Simon, U. (2013) *Nat. Mater.*, **12**, 694–696.
- 104** Young, K.L., Scott, A.W., Hao, L., Mirkin, S.E., Liu, G., and Mirkin, C.A. (2012) *Nano Lett.*, **12**, 3867–3871.
- 105** Jones, M.R. and Mirkin, C.A. (2013) *Angew. Chem.*, **125**, 2958–2963.
- 106** Jones, M.R., Macfarlane, R.J., Lee, B., Zhang, J., Young, K.L., Senesi, A.J., and Mirkin, C.A. (2010) *Nat. Mater.*, **9**, 913–917.
- 107** Xu, L., Kuang, H., Xu, C., Ma, W., Wang, L., and Kotov, N.A. (2012) *J. Am. Chem. Soc.*, **134**, 1699–1709.
- 108** Lee, J.-H., Kim, G.-H., and Nam, J.-M. (2012) *J. Am. Chem. Soc.*, **134**, 5456–5459.
- 109** Chou, L.Y.T., Ming, K., and Chan, W.C.W. (2010) *Chem. Soc. Rev.* doi: 10.1039/C0CS00003E
- 110** Giljohann, D.A., Seferos, D.S., Daniel, W.L., Massich, M.D., Patel, P.C., and Mirkin, C.A. (2010) *Angew. Chem.*, **122**, 3352–3366.
- 111** Giljohann, D.A., Seferos, D.S., Patel, P.C., Millstone, J.E., Rosi, N.L., and Mirkin, C.A. (2007) *Nano Lett.*, **7**, 3818–3821.
- 112** Albanese, A. and Chan, W.C.W. (2011) *ACS Nano*. doi: 10.1021/nn2007496
- 113** Seferos, D.S., Prigodich, A.E., Giljohann, D.A., Patel, P.C., and Mirkin, C.A. (2009) *Nano Lett.* doi: 10.1021/nl802958f
- 114** Zhang, K., Hao, L., Hurst, S.J., and Mirkin, C.A. (2012) *J. Am. Chem. Soc.*, **134**, 16488–16491.
- 115** Zheng, D., Giljohann, D.A., Chen, D.L., Massich, M.D., Wang, X.-Q., Iordanov, H., Mirkin, C.A., and Paller, A.S. (2012) *Proc. Natl. Acad. Sci. USA*. doi: 10.1073/pnas.1118425109
- 116** Prigodich, A.E., Alhasan, A.H., and Mirkin, C.A. (2010) *J. Am. Chem. Soc.* doi: dx.doi.org/10.1021/ja110833r
- 117** Massich, M.D., Giljohann, D.A., Schmucker, A.L., Patel, P.C., and Mirkin, C.A. (2010) *ACS Nano*. doi: 10.1021/nn102228s
- 118** Jensen, S.A., Day, E.S., Ko, C.H., Hurley, L.A., Luciano, J.P., Kouri, F.M., Merkel, T.J., Luthi, A.J., Patel, P.C., Cutler, J.I., Daniel, W.L., Scott, A.W., Rotz, M.W., Meade, T.J., Giljohann, D.A., Mirkin, C.A., and Stegh, A.H. (2013) *Sci. Transl. Med.*, **5**, 209.
- 119** Alhasan, A.H., Kim, D.Y., Daniel, W.L., Watson, E., Meeks, J.J., Shad Thaxton, C., and Mirkin, C.A. (2012) *Anal. Chem.*, **84**, 4153–4160.
- 120** Torabia, S.-F. and Lu, Y. (2011) *Faraday Discuss.*, **149**, 125–157.
- 121** Ihmels, H. and Otto, D. (2005) *Top. Curr. Chem.*, **258**, 161–204.
- 122** Armitage, B.A. (2005) *Top. Curr. Chem.*, **253**, 55–76.
- 123** Chaires, J.B., Dattagupta, N., and Crothers, D.M. (1982) *Biochemistry*, **21**, 3933–3940.
- 124** Nguyen, B., Neidle, S., and Wilson, W.D. (2009) *Acc. Chem. Res.*, **42**, 11–21.
- 125** Jamieson, E.R. and Lippard, S.J. (1999) *Chem. Rev.*, **99**, 2467–2498.
- 126** Hurst, S.J., Han, M.S., Lytton-Jean, A.K. R., and Mirkin, C.A. (2007) *Anal. Chem.*, **79**, 7201–7205.
- 127** Huschka, R., Neumann, O., Barhoumi, A., and Halas, N.J. (2010) *Nano Lett.*, **10**, 4117–4122.
- 128** Kreibig, U. and Vollmer, M. (1995) *Optical Properties of Metal Clusters*, Springer, Berlin.
- 129** Skirtach, A.G., Dejugnat, C., Braun, D., Susha, A.S., Rogach, A.L., Parak, W.J., Möhwald, H., and Sukhorukov, G.B. (2005) *Nano Lett.*, **5**, 1371–1377.
- 130** Chou, C.-H., Chen, C.-D., and Wang, C.R.C. (2005) *J. Phys. Chem. B*, **109**, 11135–11138.

- 131 Pissuwan, D., Valenzuela, S.M., and Cortie, M.B. (2006) *Trends Biotechnol.*, **24**, 62–67.
- 132 Reismann, M., Bretschneider, J.C., von Plessen, G., and Simon, U. (2008) *Small*, **4**, 607–610.
- 133 Bretschneider, J.C., Reismann, M., von Plessen, G., and Simon, U. (2009) *Small*, **5**, 2549–2553.
- 134 Link, S. and El-Sayed, M.A. (1999) *J. Phys. Chem. B*, **103**, 4212–4217.
- 135 Stehr, J., Hrelescu, C., Sperling, R.A., Raschke, G., Wunderlich, M., Nichtl, A., Heindl, D., Kurzinger, K., Parak, W.J., Klar, T.A., and Feldmann, J. (2008) *Nano Lett.*, **8**, 619–623.
- 136 Jain, P.K., Eustis, S., and El-Sayed, M.A. (2006) *J. Phys. Chem. B*, **110**, 18243–18253.

11

Nanostructured Substrates for Circulating Tumor Cell Capturing

Jingxin Meng, Hongliang Liu, and Shutao Wang

11.1

Introduction

Metastasis, a complicated biological process, is responsible for most cancer-related deaths. Paget explained this process via the famous “seed and soil” theory in 1889 [1]. Briefly, tumor cells first detach from the primary tumor, then travel in the peripheral bloodstream, next arrive at distant organs, and finally form new tumor colonies. However, arrival at the distant organs does not ensure proliferation of tumor cells [2]. Only a small percentage of these tumor cells will ultimately grow into micrometastases and even macrometastatic lesions. More importantly, this metastatic process of tumor cells usually occurs in parallel to the development of the primary tumor and often before the initial detection of solid tumor. Therefore, the metastatic tumor cells, namely, circulating tumor cells (CTCs), can be considered as a “liquid biopsy” of the primary and disseminated tumors, which provide a promising alternative for early diagnosis of metastases, cancer prognosis, and personalized therapy. Interestingly, the CTC-based approaches also show their unique advantages such as noninvasive serial monitoring during tumor therapy, which are far better than the traditional harmful detections and treatments of cancer such as radiographic imaging and surgical operation.

However, the relative low number of CTCs in the blood samples (as few as one in the background of 10^6 – 10^9 hematologic cells) [3] should be solved before CTCs were used as the promising biomarkers for the diagnosis and prognosis of cancer patients. Prior to the detection process of CTCs, many enrichment methods have been widely utilized such as cell separation based on cell density, cell filtration based on cell size [4], and immunomagnetic selection based on cell surface antigens [5]. However, some unavoidable problems from the enrichment methods itself, such as migration of cells in different density layers, wide distribution of cell sizes, and varied expression of cell surface antigens, result in the false-positive or false-negative results. After the enrichment of CTCs, some representative detection methods have been well developed, including immunocytochemical approaches and nucleic acid-based methods. Immunocytochemical

approaches are used to identify CTCs based on immunostaining with specific antibodies against antigens [6]. Not only epithelium-specific antigens such as cytokeratin (CK) and epithelial cell adhesion molecule (EpCAM), but also organ-specific markers, including prostate-specific antigen (PSA), carcinoembryonic antigen (CEA), and human epidermal growth factor receptor (EGFR), are widely used markers for tumor cell identification and detection despite variable rates of false-positive and false-negative staining as these markers are not present in all tumor cells. Reverse transcription polymerase chain reaction (RT-PCR) technologies, a kind of nucleic acid-based methods, have also been developed, which rely on the amplification of specific genes associated with CTCs. However, this technique is unable to provide a precise assessment of the number of tumor cells present in the sample due to the variability in the transcription rate between tumor cells. The advantages and disadvantages of recent CTC enrichment and detection approaches have been well discussed in many excellent reviews [6,7]. To further improve sensitivity and specificity of CTC capturing for routine clinical analysis and diagnosis, great effort and pioneering work still need to be done.

Compared with pure molecule-level interactions (e.g., affinity between antibody and antigen), the further introduction of topographic interaction between target cells and nanostructured substrates is much easier to achieve the goal of improving efficiency and specificity of CTC capture. This strategy certainly provides a fast and convenient way to identify and capture target CTCs. Therefore, here we will summarize three-dimensional (3D) nanostructured substrates for CTC capturing, which are assembled by low-dimensional building blocks such as nanoparticles, nanofractals, nanowires, nanoposts/pillars, nanotubes, and nanofibers, especially the new emerging nanopores (Figure 11.1). The potential cell-capture mechanisms of these nanostructured substrates, great challenges, and future directions for CTC isolation are also discussed in this chapter.

11.2

Nanostructured Substrates for CTC Capturing

Although there are many kinds of approaches for improving the specificity and sensitivity of CTC detection, the introduction of nanostructures is absolutely essential for its feasibility and accessibility. To get nanostructured substrates with satisfactory capture performance of CTCs, it is believed that structure design is the first and most important step. How can we find appropriate structural models to direct the design of CTC-capture substrates? Fortunately, nature gives us the best answers and inspires us to regulate cell adhesion (e.g., CTCs) and realize cell functions in an optimized way. Therefore, a few 3D nanostructured substrates have been designed and utilized for CTC capture, which are assembled from low-dimensional building blocks such as nanoparticles, nanofractals, nanowires, nanoposts/pillars, nanotubes, and nanofibers, as well as nanopores, which are thoroughly discussed in this chapter.

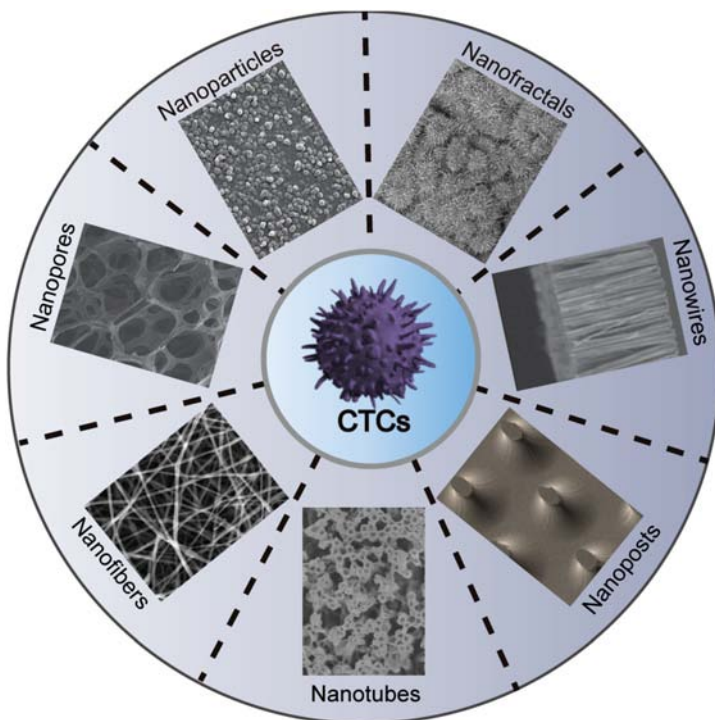


Figure 11.1 Circulating tumor cells can be efficiently and specifically captured by the three-dimensional nanostructured substrates, which are assembled from low-dimensional building blocks. Some representative

examples are exhibited here such as nanoparticles, nano fractals, nanowires, nanoposts/nanopillars, nanotubes, and nanofibers, as well as nanopores.

11.2.1

Nanoparticles

Nanoparticles, one of the most common building blocks, can be readily deposited or assembled on substrates (i.e., glass slides or silicon wafers) to fabricate nanoparticle-based substrates. Compared to flat substrates, the nanoparticle-based substrates can further improve the sensitivity and specificity of CTC detection because these nanostructures not only provide more contact area but also offer more recognition molecules.

Polymer nanoparticles can be employed for higher cell-capture capability, which may come from the synergistic effect of their nanostructured surfaces, recognition molecules, and soft nature. For example, Sekine *et al.* fabricated a polymer nanodot-based substrate by electrodepositing poly(3,4-ethylenedioxy) thiophenes (PEDOT) onto the surface of indium tin oxide (ITO) glasses (Figure 11.2b (i)) [8]. They found that amplification of voltage led to larger sizes and lower densities of PEDOT nanoparticles. Surface roughness initially increased

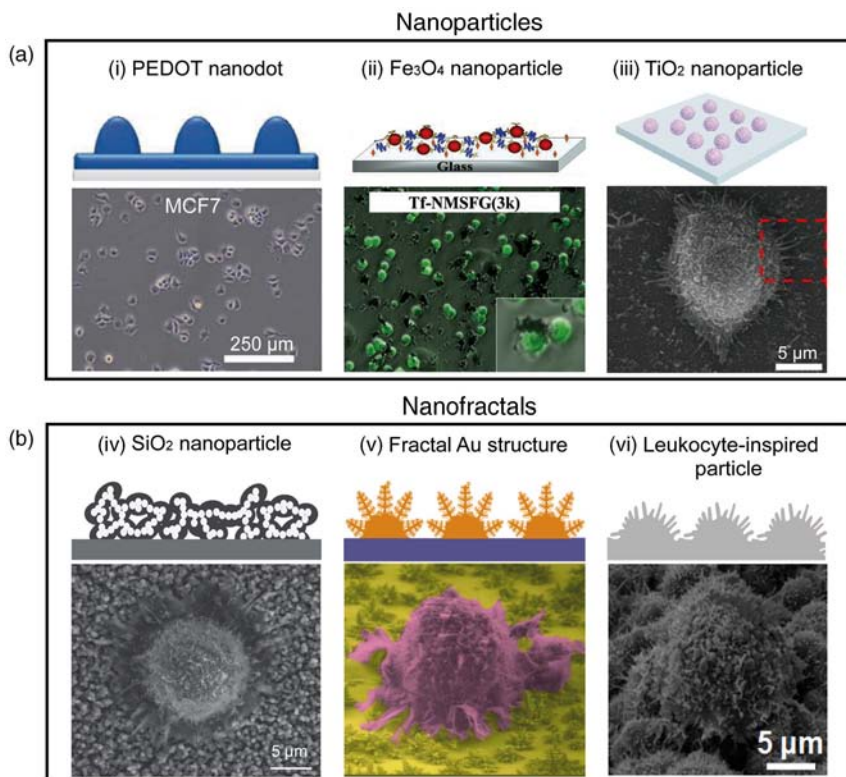


Figure 11.2 The schematic view (top) and the images of cell-substrate interaction (bottom) on (a) nanoparticle-based substrates such as (i) PEDOT nanodot, (ii) Fe₃O₄

nanoparticle and (iii) TiO₂ nanoparitlce, and (b) nanofractal-based substrates such as (iv) SiO₂ nanoparticle, (v) fractal Au structure and (vi) leukocyte-inspired particle.

with voltage and finally reached a maximum value due to the fusion of PEDOT nanoparticles, thus achieving a series of substrates with roughness ranging from 2.0 ± 0.1 to 41.3 ± 1.8 nm. Through the sequential chemical modification, it is easy to conjugate biotinylated anti-EpCAM on these carboxylated PEDOT nanoparticles. Then, the PEDOT nanodot-based substrates showed increased capture of EpCAM-positive cells (i.e., MCF7 breast cancer cells and T24 bladder carcinoma cells) compared to flat surfaces, but low cell capturing yields of EpCAM-negative cells (i.e., HeLa cervical cancer cells, Daudi Burkitt's lymphoma cells, and Jurkat human T cells) on both nanodot-based and flat surfaces, implying the synergistic effect of nanostructures and recognition molecules. More interestingly, the soft nature of conducting polymers (i.e., lower Young's modulus) also played a key role in improving cell-capture performance.

In addition to polymer nanoparticles, inorganic nanoparticles (e.g., Fe₃O₄ and TiO₂) can also be used to construct nanoparticle-based substrates. For example, Khandare and coworkers reported a Fe₃O₄ nanoparticle-based substrate for

capturing tumor cells by attaching a PEG–Fe₃O₄ 3D matrix on silanized glass (Figure 11.2b (ii)) [9]. In this system, Fe₃O₄ nanoparticles played a significant role in the formation of the 3D architecture. Transferrin (Tf) was used as the recognition molecules to specifically identify cancer cells overexpressing transferrin receptors (TfRs). In this report, HCT116 (overexpressing TfRs) and Caco-2 (low-expressing TfRs) were selected as model cells to explore the interaction between tumor cells and Fe₃O₄ nanoparticle-based substrates. The experimental results confirmed that the large surface area and the 3D topography benefit for the specific and enhanced interaction of nanostructured substrates and HCT116 cells. In another report, Zhao and coworkers prepared biocompatible TiO₂ nanoparticle-based substrates for the isolation of CTCs (Figure 11.2b (iii)) [10]. For the EpCAM-positive cancer cells (i.e., HCT116 cells), the device with surface roughness of 85 nm can reach the highest cell capture efficiencies. After spiking target HCT116 cells into PBS solution and healthy blood samples, increased topographic interaction led to 80 and 50% capture efficiency of target cells, respectively. Using these nanostructured substrates, CTCs can be isolated from the peripheral blood samples in cancer patients and further identified by a three-color immunostaining method.

11.2.2 Nanofractals

In comparison to above-mentioned nanoparticles, nanofractals with complex fractal dimensions can provide a more efficient way for cell–substrate interaction by increasing contact area and offering more recognition molecules. Some requirements (i.e., transparency) and some biological phenomena (i.e., fractal morphology of cancer cells and leukocytes) inspired us to fabricate nanofractal-based substrates for the improvement of cell-capture efficiency and sensitivity.

To directly monitor captured cancer cells, our group prepared underwater-transparent SiO₂ nanoparticle-based substrates (Figure 11.2b (iv)) [11]. To achieve these substrates, we first deposited candle soot on a quartz substrate. Then, a silica shell was coated on the candle soot template by chemical vapor deposition of SiCl₄. Finally, SiO₂ nanoparticle-based substrates with nanodendritic features could be produced by further heating. The higher sensitivity of these transparent substrates is derived from the enhanced topographic interaction between nanodendritic structures and surface components of target cells. In addition, the unique underwater transparency of the SiO₂ nanoparticle-based substrates allows for directly monitoring captured cells that may derive from the perfect match of reflective index between silica ($n \approx 1.46$) and water ($n \approx 1.33$). The outstanding underwater-transparent property endows these widespread substrate applications.

Recent knowledge has revealed that cancer cell surface possesses larger fractal dimension than the normal cell surface, which may be connected with cancer cell–microenvironment interactions and the stages of cancer. Inspired by this,

we electrochemically deposited fractal Au nanostructures on ITO-conducting glasses (Figure 11.2b (v)) [12]. To systematically study the influence of fractal dimension on cell–substrate interaction, we here adjusted the fractal dimension of Au nanostructures by altering the electrochemical deposition parameters such as potential and ion concentration. The results revealed that higher fractal dimension resulted in increased specific cell–substrate interactions, suggesting a potential design principle of programmable 3D nanostructured substrates. Furthermore, through the electrochemical cleavage of Au–S bonds, about 98% cells were released without damage from Au surfaces. Therefore, fractal Au nanostructures were capable of dynamic and controlled cell adhesion and detachment through the connecting and breaking of Au–S bonds.

It is well known that leukocytes play a crucial role in specific recognition and elimination of CTCs in immune systems. This inspired us to design hierarchical biointerfaces assembled by leukocyte-inspired particles (LIPs) (Figure 11.2b (vi)) [13]. By integrating a thermal oxidation and a chemical vapor deposition, LIPs could be produced with nanofiber lengths similar to that of the median microvillar length of leukocytes. The hierarchical biointerfaces exhibited efficient specific recognition of cancer cells from whole blood by introducing the synergistic effect of molecular recognition and hierarchical topographic interaction. Both the focal adhesions and morphologies of captured MCF7 cells demonstrated that the micro/nanohierarchical topographic interaction played a crucial role in the improvement of the cell-capture efficiency. On one hand, rough substrates with a microscale bump could match the microscale spherical parts of the targeted cells. On the other hand, nanoscale nanofibers, which are perpendicular to the spherical parts of LIPs, provide more contact sites and further match with the nanoscale surface components of the cancer cells (e.g., microvilli).

11.2.3

Nanowires

Inspired by the surface components of cells, the nanowire-based substrates have been designed and utilized to alter the surface adhesion of the cells and aid in the capture of CTCs in blood samples. For example, our group first employed anti-EpCAM-coated Si nanowire (SiNW) substrates to identify and capture CTCs (Figure 11.3a) [14]. Using a wet chemical etching approach, we prepared densely packed nanowires of 100–200 nm in diameter on silicon wafers. By altering etching times, the length of these nanowires can be easily controlled. To test the cell-capture efficiency of the SiNWs, cell suspension solution of MCF7 cells (an EpCAM-positive cell line) was introduced into the SiNWs and flat silicon surfaces for 1 h. It was found that more cells were captured on SiNWs (45–65%) than that on flat silicon substrates (4–14%). This suggests that 3D nanowires are responsible for enhanced cell capture, which can be explained by morphology differences of captured cells. It was found that SiNWs were able to capture cells with over 40% yields of artificial CTC blood samples compared to some commercially available technologies. In addition to SiNWs, quartz nanowires

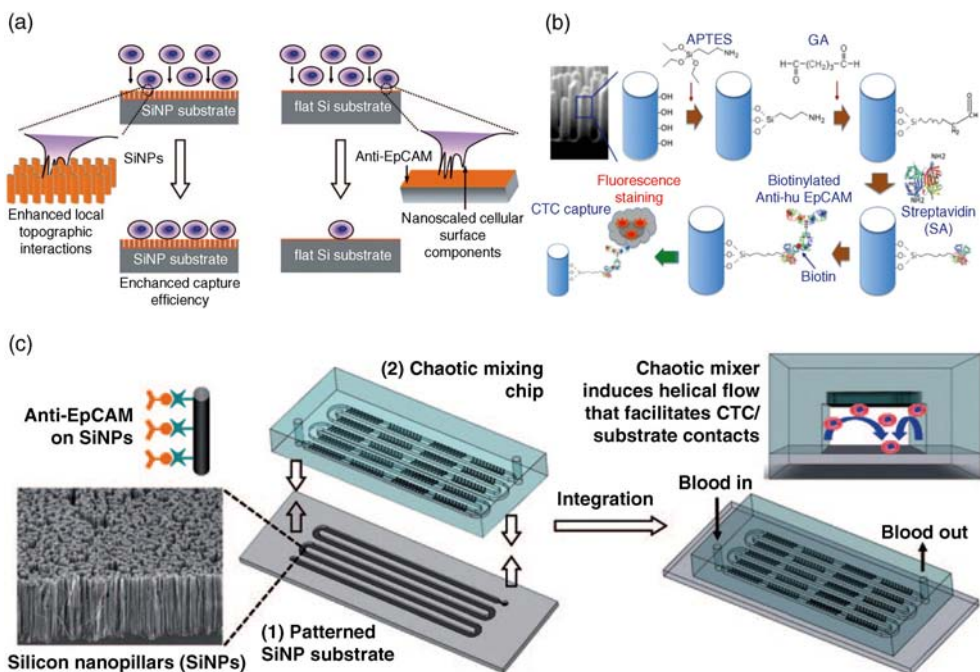


Figure 11.3 The schematic view of the nanowire-based substrates for CTC capturing including (a) silicon nanowires, (b) quartz nanowires, and (c) integrate nanowires with microfluidic device.

(QNWs) could also be used to identify and capture CTCs, which was reported by Fan and coworkers (Figure 11.3b) [15]. By integrating nanoparticle coating, metal deposition, pattern transfer, and deep reactive ion etching (RIE), QNWs were successfully fabricated with nanowire diameter in the range of 80–100 nm and length in the range of 250–350 nm. After coating anti-EpCAM, QNWs and flat glass surface exhibited 89 and 23% capture efficiency of target A549 cells (lung cancer cells) in PBS solution, respectively. To demonstrate the clinical applicability of QNW detection platform, 9 of 15 and 6 of 10 A549 cells were successfully captured by QNWs from spiked peripheral blood mononuclear cells in culture medium and the lysed peripheral blood samples, respectively. The increase contact frequency of cell–nanowire substrate is an effective way to further improve capture efficiency. In a relative report, we integrated SiNWs into a microfluidic device with serpentine chaotic micromixers, obtaining a nearly 100% capture efficiency (Figure 11.3c). Three cancer cell lines, MCF7, T24, and PC3 (prostate cancer cells), were spiked in concentrations ranging from 50 to 1000 cells ml^{-1} into four kinds of solutions, including culture medium, whole blood, lysed blood, and PBS. When flow rate did not exceed 2 ml h^{-1} , we found that the isolation efficiency of target cancer cells in all cases was more than 95%, opening up opportunities for early detection of cancer metastasis and isolation of other rare cells.

11.2.4

Nanoposts/pillars

The nanoposts/pillars-based substrates discussed here are considered as ordered nanowires, including round, elliptical, and octagonal posts. Moreover, nanoposts can be embedded into microfluidic device for efficient CTC capture and even integrated with magnetic nanoparticles (MNPs) for releasing captured cells.

Nagrath *et al.* pioneered a CTC chip integrating anti-EpCAM-coated Si microposts with a microfluidic device for the capture of CTCs from cancer patient blood samples (Figure 11.4a) [16]. The optimal flow rate (1–2 ml h⁻¹) was achieved with the maximal capture efficiency of 60% for NCI-H1650 cells (non-small cell lung cancer cell line) spiked into whole blood samples. The normalized number of CTCs in samples was counted from 68 patients with non-small cell lung (*n* = 55), prostate (*n* = 26), pancreatic (*n* = 15), breast (*n* = 10), and colon (*n* = 10) cancers, which were correlated with the efficacy of treatment. Through fluorescent staining methods, the cells stained with DAPI+/CK+/CD45 were recognized as CTCs and 115 of 116 (about 99%) samples were detected. While the number of CTCs in a patient sample did not reflect the size of the primary tumor, it did correspond to the patient's response to specific treatment. Because of its high yield, sensitivity, specificity, and clinical relevance, this chip represented great strides in the field of CTC isolation.

Sheng *et al.* demonstrated an aptamer-mediated microfluidic device with elliptical glass microposts in the glass substrate (Figure 11.4b) [17]. The glass substrate was isotropically wet-etched using a mixture of HF/HNO₃/H₂O to fabricate microposts. Biotinylated aptamers were used to conjugate with avidin on the surface of the glass microposts to specifically capture CTCs spiked into whole blood samples. They found that the capture efficiency of the device was significantly better than the flat channel that was derived from the following two aspects: (i) the increased surface area via microposts enhanced the loading capacity of aptamers and (ii) the row shift of microposts and channel geometry significantly increased the probability of cell encounters with aptamers on the surfaces. Therefore, the as-prepared device achieved cell-capture efficiency of about 95% and cell viability of about 93%.

In addition to directly capturing CTCs with post-based substrate, other nanostructures such as MNPs could be integrated to provide unique properties. Guo and coworkers developed a micropost device decorated with graphite oxide-coated MNPs for magneto-controllable capture and release of cancer cells (Figure 11.4c) [18]. Graphite oxide-coated Fe₃O₄ MNPs are synthesized by solution mixing and functionalized with a specific antibody, followed by the immobilization of such modified MNPs on the designed microposts device. Taking HCT116 cells as target cells, the high-density packing of antibody-modified MNPs on the microposts increases the local concentration of antibody, as well as the topographic interactions between cancer cells and microposts under magnetic field. The flow rate and the microposts geometry are optimized by

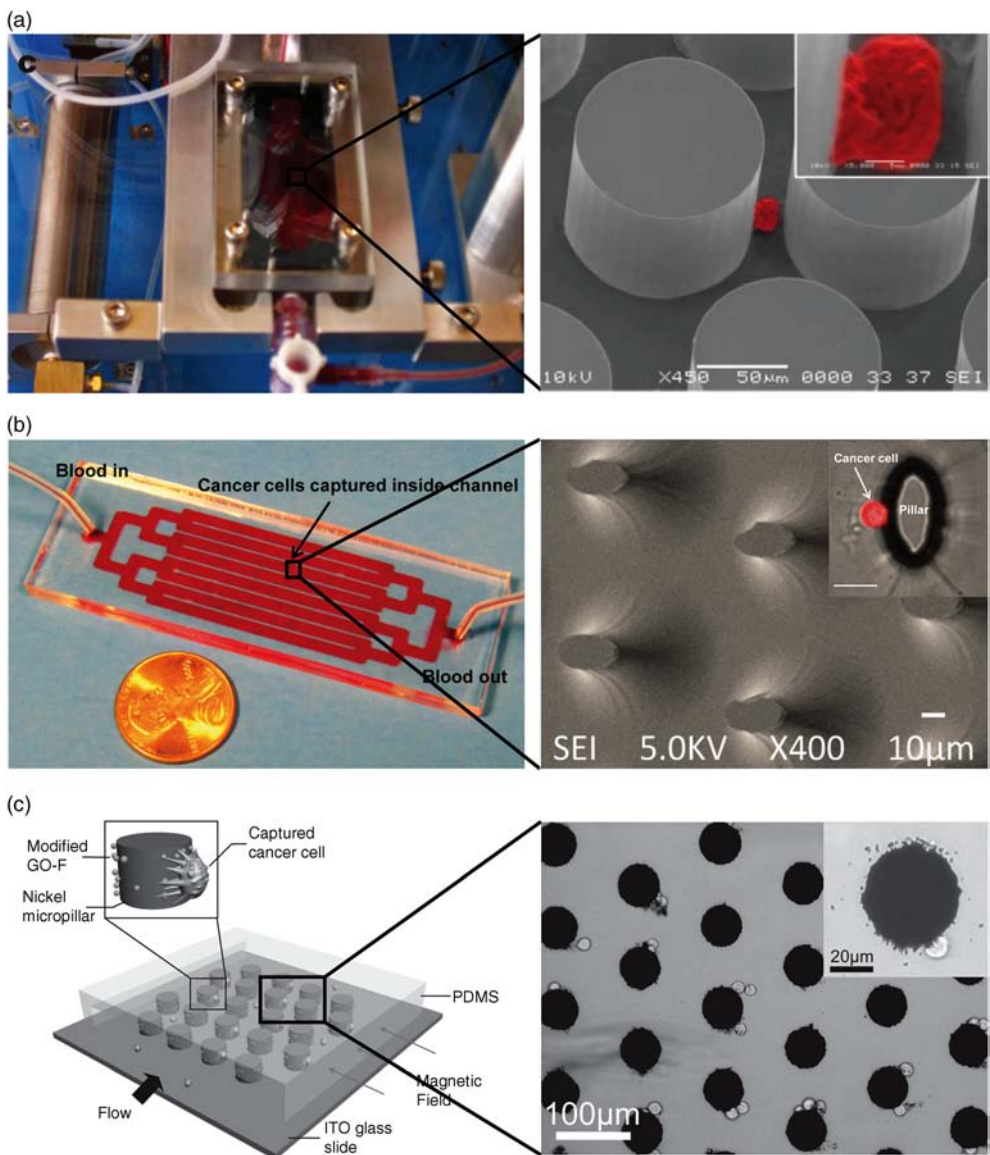


Figure 11.4 The schematic view (left) and the images of cell–substrate interaction (right) on nanopost-based substrates such as (a) round nanoposts, (b) elliptical nanoposts, and (c) integrate nanoposts with magnetic particles.

exploring their effects on capture efficiency. Then, the spiked HCT116 cells can be recognized and captured with the efficiency of about 70% in culture medium and about 40% in blood sample. Moreover, the captured cells are able to be released from the microposts with a saturated efficiency of 92.9% upon the

removal of applied magnetic field, and it is found that 78% of the released cancer cells are viable, making them suitable for subsequent biological analysis.

11.2.5

Nanotubes

Using 3-aminophenylboronic acid (APBA)-functionalized multiwalled carbon nanotube (MWCNT) films, Xu and coworkers developed an electrochemical cell sensor for the determination of K562 cells (leukemia cells) (Figure 11.5a) [19]. They prepared the films by covalent coupling between $-\text{NH}_2$ groups in APBA and $-\text{COOH}$ groups in acid-oxidized MWCNTs. As a result of the sugar-specific affinity interactions, the K562 cells are firmly bound to the APBA-functionalized MWCNTs film via boronic acid groups. Compared to electropolymerized APBA films, the presence of MWCNTs not only provides abundant boronic acid domains for cell capture but their high electrical conductivity also makes the film suitable for electrochemical sensing applications. The resulting modified

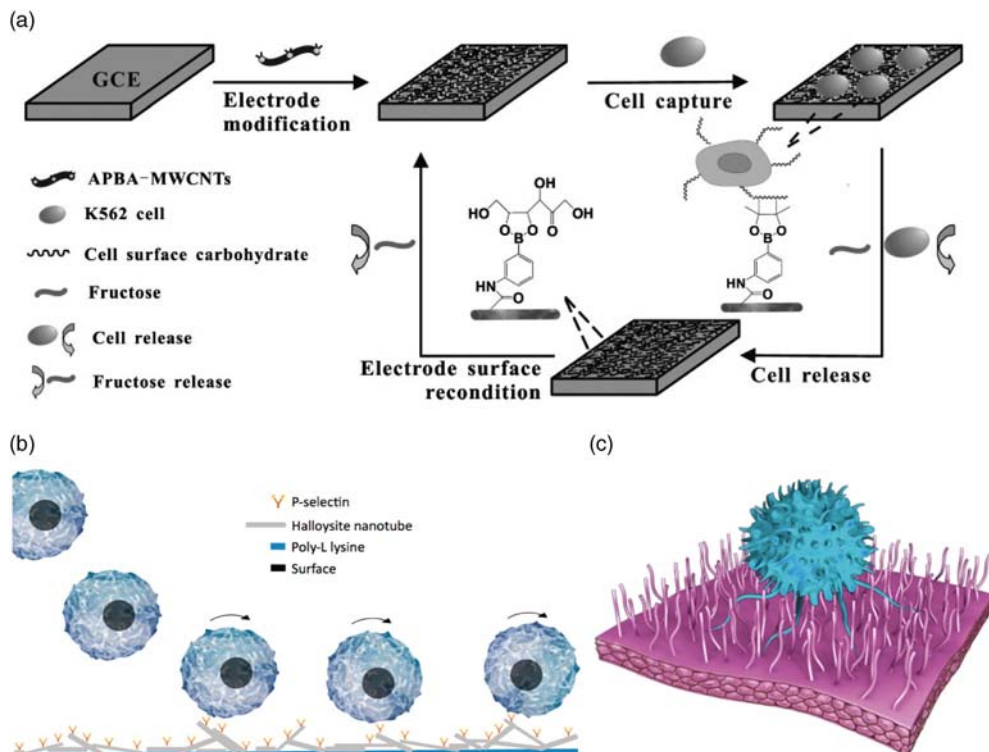


Figure 11.5 The schematic view of cell recognition on nanotube-based substrates such as (a) carbon nanotubes, (b) halloysite nanotubes, and (c) polystyrene nanotubes.

electrodes are tested as cell detection sensors. This work presents a promising platform for effective cell capture and reusable cytosensors.

Hughes and King explored a method to more efficiently capture leukemic and epithelial cancer cells from flow by altering the nanoscale topography of the inner surface of P-selectin-coated microtubes (Figure 11.5b) [20]. This functionalized topography was achieved by attaching naturally occurring halloysite nanotubes to the microtube surface via a monolayer of poly-L-lysine, followed by functionalization with recombinant human selectin protein. The capture efficiency of leukemic cells could be increased by halloysite nanotube coatings and mainly affected by halloysite content and selectin density. Ultimately, selectin-functionalized nanotube coatings should provide a way for enhanced cancer cell isolation from whole blood and other mixtures of cells.

Previous studies have demonstrated that the stiffness of materials is very important for biological studies and applications. Inspired by the soft nature of cell microenvironments, we designed soft polystyrene nanotube (PSNT) arrays via replication using anodic aluminum oxide (AAO) as a template (Figure 11.5c) [21]. The diameter of PSNTs can be tuned by AAO pores. By controlling the time of template etching, the length of PSNTs can be adjusted from several micrometers to dozens of micrometers. As PSNTs are soft, they aggregate when the length increases, but without large influence on cell–substrate interactions. Under the optimal conditions, the PSNT substrates provide a high value (about 70%) of target cells and negligible capture of nontarget cells in a shorter capture time (20 min) compared with inorganic cell-capture systems (more than 45 min). This soft substrate provides a soft platform to study the cooperative influence of stiffness, molecule, and topography to specific cell recognition and adhesion. Other polymer nanostructure arrays can also be developed by employing this replication method, which may offer an effective strategy for the fabrication of soft 3D nanostructured substrates.

11.2.6

Nanofibers

Inspired by extracellular matrix (ECM) scaffolds, nanofiber-based substrates have been fabricated and well developed for their efficient CTC capture efficiency. Different materials such as TiO₂, cholesteryl-succinyl silane (CSS), and poly(lactic-*co*-glycolic acid) (PLGA) can be electrospun to form desired nanofibers with controllable diameters and lengths.

In recent years, Zhang *et al.* fabricated TiO₂ into nanofibers of 100–300 nm diameter from a spun composite of titanium *n*-butoxide and polyvinyl pyrrolidone (Figure 11.6a) [22]. By coating anti-EpCAM onto the surface, specific cell capture can be processed. Performance was verified using samples from gastric and colorectal cancer patients. SEM imaging displayed cell spreading and the interaction of cellular structures with the nanostructures on the surface of substrates.

In another report, Wu and coworkers employed a biomimetic strategy to functionalize electrospun organic–inorganic CSS nanofibers with membrane-bound

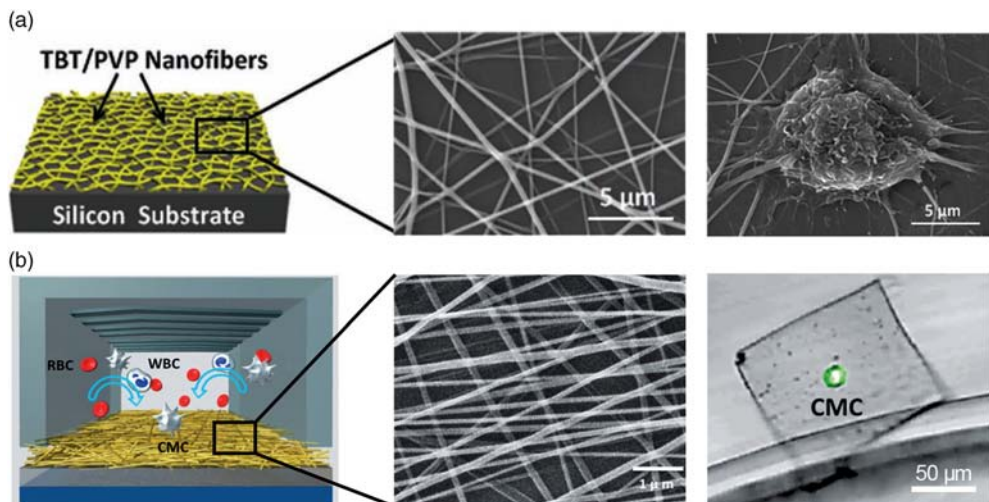


Figure 11.6 The schematic view (left) and images (right) of cell-specific recognition on nanofiber-based substrates, and the corresponding SEM images (middle) of nanofiber-based substrates such as (a) TiO_2 nanofibers and (b) PLGA nanofibers.

molecules, including NBD-conjugated phospholipids and antibodies-containing transmembrane domains [23]. An insert-and-tighten mechanism was proposed for the immobilization of membrane-bound molecules on the CSS nanofibers. Subsequently, the anti-CD20-functionalized CSS nanofibers displayed a greater ability to capture Granta-22 cells (human mantle cell lymphoma cell line) than their film counterparts, suggesting that surface topography play an important role in antibody immobilization and cell capture.

Hou *et al.* developed a PLGA nanofiber-embedded chip, which can not only capture CTCs with high efficiency but also enable highly specific isolation of single melanoma cell immobilized on the nanosubstrate (Figure 11.6b) [24]. To replace the nontransparent SiNW substrate with a transparent one, PLGA nanofibers were electrospun onto a commercial laser microdissection (LMD) slide and subsequently linked by a melanoma-specific antibody (i.e., anti-CD146). The unique combination of PLGA nanofibers and an LMD slide enables single-cell isolation using a highly accurate LMD technique. Furthermore, a four-color immunocytochemistry method was established to specifically identify CTCs among nonspecifically captured WBCs.

11.2.7

Nanopores

Nanopores open up a new opportunity in single-cell level-based disease diagnosis and personalized medicine screening. For example, Lin and coworkers developed a novel microfluidic platform integrated with aptamer-encoded microwells

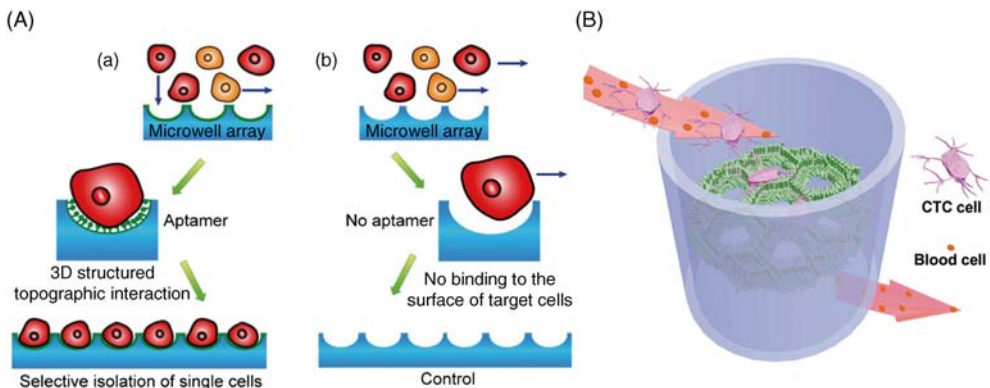


Figure 11.7 The schematic view of cell-specific recognition on nanopore-based substrates such as (a) microwell arrays and (b) micropores.

(Figure 11.7a) [25]. This platform can isolate single tumor cells with satisfied single-cell occupancy and unique bioselectivity. The designed microwell structures encourage strong 3D local topographic interactions of the target cell surface with biomolecules and regulate the single-cell resolution. Under the optimized size of microwells (i.e., 18 μm in diameter and 5 μm in height), the single-cell occupancy was significantly enhanced from 0.5 to 88.2% through the introduction of the aptamer. Importantly, such an aptamer-enabled microfluidic device shows an excellent selectivity for target single-cell (i.e., Ramos) isolation compared with three control cells (i.e., HepG2, CCRF-CEM, and MCF7). Subsequently, targeted isolation and analysis of single tumor cells were demonstrated by using artificial complex cell samples at simulated conditions, and various cellular carboxylesterases were studied by time-course measurements of cellular fluorescence kinetics at individual cell level.

More interestingly, the advantage of micropores for cell capture can be further extended by integrating other nanostructures such as nanorods. In a recent report, Chen and coworkers reported a 3D hierarchical graphene platform that combines microporosity from reduced graphene oxide foam with anti-EpCAM-coated ZnO nanorod array (Figure 11.7b) [26]. The advantage of this novel composite structure stems from its high density of ZnO nanorods, which increases cell–substrate contact frequency, as well as its microporosity, which lets through normal red blood cells but specifically captures CTCs due to the introduction of anti-EpCAM. When thickness of the foam reaches 5 mm, the cell-capture yield is more than 80%, implying that the potential CTC captures capability for the clinical blood samples.

Furthermore, the captured cells can be readily released from pits by introducing antibody-coated glass beads (GBs). For example, Iqbal and coworkers reported a Hele-Shaw microfluidic device integrated with array of pits and anti-EGFR aptamer-functionalized GBs [27]. Target tumor cells could be captured on

GBs from a mixture of human glioblastoma (hGBM) and normal cells. Thereafter, GBs in the pits were readily released in solution by reversing the device. The GBs were collected and then about 92% cancer cells were detached from GBs by combining gentle shaking and antisense RNA molecules. The antisense, called release molecule, competitively hybridized with the aptamer, thus reducing its affinity to EGFR. This device provides an important platform that can possibly be used to isolate CTCs from peripheral blood samples.

11.3

Nanostructured Substrates for Other Cells Capturing

Besides the CTCs, many other cells associated with human such as normal human dermal fibroblasts (NHDFs) [28], human mesenchymal stem cells (hMSCs) [29], and human umbilical vein endothelial cells (HUVECs) [30] have also been captured by these nanostructured substrates. For example, Aoyagi and coworkers developed a smart nanofiber web by electrospun copolymers of *N*-isopropylacrylamide (NIPAAm) with a UV-reactive benzophenone (BP)-conjugated comonomer [28]. The nanofiber web showed the ability to capture and release NHDFs in response to changes of web size. Then, Griffin and Kasko prepared hydrogel scaffolds integrating with photodegradable *ortho*-nitrobenzyl (*o*-NB) groups [29]. Taking hMSCs as model cells, these cells can be easily entrapped and subsequently released through the photodegradation of hydrogel. In a recent report, Qu and coworkers developed a 3D macroporous structures based on graphene oxide-pNIPAAm derivative hydrogel [30]. By adjustment of temperature, the porous size of hydrogel can be changed, which could be used for reversibly capturing and releasing cells (i.e., HUVEC). Although these nanostructured substrates did not take CTCs as the model cells, they could readily be used to specifically recognize and capture CTCs by modifying functional molecules, greatly expanding the relative investigation of CTCs.

11.4

Conclusions and Perspectives

In this chapter, we have summarized the recent progress of 3D nanostructured substrates as a promising platform for CTCs detection, which are assembled from many low-dimensional building blocks such as nanoparticles, nanofractals, nanowires, nanoposts/pillars, nanotubes, and nanofibers, as well as nanopores. Most of these building blocks were inspired by nature such as leukocyte-inspired nanoparticles, microvilli-inspired nanowires, ECM-inspired nanofibers, and so on. The cell-capture capability can be greatly enhanced through the topographic interaction between nanostructured substrates and surface components of target cells (i.e., microvilli or pseudopodia). In addition, the recognition molecules and responsive molecules bring in the specificity and responsiveness of

nanostructured substrates for cells that make the substrates capture only target cells and face complicated external environments. More interestingly, some nanostructured substrates have been successfully used for isolation and detection of other cells, greatly expanding the significance of CTC-related research. However, many problems remain unsolved, such as recycling of CTC-capture substrates for cost reduction and optimization of structural models for higher capture yield, and need more relative researches.

References

- 1 Paget, S. (1889) *Lancet*, **133**, 571–573.
- 2 Chambers, A.F., Groom, A.C., and MacDonald, I.C. (2002) *Nat. Rev. Cancer*, **2**, 563–572.
- 3 Mostert, B., Sleijfer, S., Foekens, J.A., and Gratama, J.W. (2009) *Cancer Treat. Rev.*, **35**, 463–474.
- 4 (a) Hosokawa, M., Hayata, T., Fukuda, Y., Arakaki, A., Yoshino, T., Tanaka, T., and Matsunaga, T. (2010) *Anal. Chem.*, **82**, 6629–6635; (b) Zheng, S., Lin, H., Liu, J.-Q., Balic, M., Datar, R., Cote, R.J., and Tai, Y.-C. (2007) *J. Chromatogr. A*, **1162**, 154–161.
- 5 (a) Wu, C.H., Huang, Y.Y., Chen, P., Hoshino, K., Liu, H.Y., Frenkel, E.P., Zhang, J.X.J., and Sokolov, K.V. (2013) *ACS Nano*, **7**, 8816–8823; (b) Medley, C.D., Bamrungsap, S., Tan, W., and Smith, J.E. (2011) *Anal. Chem.*, **83**, 727–734.
- 6 Gerges, N., Rak, J., and Jabado, N. (2010) *Br. Med. Bull.*, **94**, 49–64.
- 7 Danova, M., Torchio, M., and Mazzini, G. (2011) *Expert Rev. Mol. Diagn.*, **11**, 473–485.
- 8 Sekine, J., Luo, S.C., Wang, S., Zhu, B., Tseng, H.R., and Yu, H.H. (2011) *Adv. Mater.*, **23**, 4788–4792.
- 9 Banerjee, S.S., Paul, D., Bhansali, S.G., Aher, N.D., Jalota-Badhwari, A., and Khandare, J. (2012) *Small*, **8**, 1657–1663.
- 10 He, R., Zhao, L., Liu, Y., Zhang, N., Cheng, B., He, Z., Cai, B., Li, S., Liu, W., Guo, S., Chen, Y., Xiong, B., and Zhao, X.Z. (2013) *Biomed. Microdevices*, **15**, 617–626.
- 11 Yang, G., Liu, H.L., Liu, X.L., Zhang, P.C., Huang, C., Xu, T.L., Jiang, L., and Wang, S.T. (2014) *Adv. Healthc. Mater.*, **3**, 332–337.
- 12 Zhang, P.C., Chen, L., Xu, T.L., Liu, H.L., Liu, X.L., Meng, J.X., Yang, G., Jiang, L., and Wang, S.T. (2013) *Adv. Mater.*, **25**, 3566–3570.
- 13 Meng, J., Liu, H., Liu, X., Yang, G., Zhang, P., Wang, S., and Jiang, L. (2014) *Small*. doi: 10.1002/smll.201400215.
- 14 Wang, S.T., Wang, H., Jiao, J., Chen, K.J., Owens, G.E., Kamei, K., Sun, J., Sherman, D.J., Behrenbruch, C.P., Wu, H., and Tseng, H.R. (2009) *Angew. Chem., Int. Ed.*, **48**, 8970–8973.
- 15 Lee, S.K., Kim, G.S., Wu, Y., Kim, D.J., Lu, Y., Kwak, M., Han, L., Hyung, J.H., Seol, J.K., Sander, C., Gonzalez, A., Li, J., and Fan, R. (2012) *Nano Lett.*, **12**, 2697–2704.
- 16 Nagrath, S., Sequist, L.V., Maheswaran, S., Bell, D.W., Irimia, D., Ulkus, L., Smith, M.R., Kwak, E.L., Digumarthy, S., Muzikansky, A., Ryan, P., Balis, U.J., Tompkins, R.G., Haber, D.A., and Toner, M. (2007) *Nature*, **450**, 1235–1239.
- 17 Sheng, W.A., Chen, T., Katnath, R., Xiong, X.L., Tan, W.H., and Fan, Z.H. (2012) *Anal. Chem.*, **84**, 4199–4206.
- 18 Yu, X., He, R., Li, S., Cai, B., Zhao, L., Liao, L., Liu, W., Zeng, Q., Wang, H., Guo, S.-S., and Zhao, X.-Z. (2013) *Small*, **9**, 3895–3901.
- 19 Zhong, X., Bai, H.-J., Xu, J.-J., Chen, H.-Y., and Zhu, Y.-H. (2010) *Adv. Funct. Mater.*, **20**, 992–999.
- 20 Hughes, A.D. and King, M.R. (2010) *Langmuir*, **26**, 12155–12164.
- 21 Liu, X.L., Chen, L., Liu, H.L., Yang, G., Zhang, P.C., Han, D., Wang, S.T., and Jiang, L. (2013) *NPG Asia Mater.*, **5**, e63.
- 22 Zhang, N.G., Deng, Y.L., Tai, Q.D., Cheng, B.R., Zhao, L.B., Shen, Q.L., He, R.X., Hong, L.Y., Liu, W., Guo, S.S., Liu, K.,

- Tseng, H.R., Xiong, B., and Zhao, X.Z. (2012) *Adv. Mater.*, **24**, 2756–2760.
- 23** Zha, Z.B., Jiang, L.N., Dai, Z.F., and Wu, X.Y. (2012) *Appl. Phys. Lett.*, **101**, 193701.
- 24** Hou, S., Zhao, L., Shen, Q., Yu, J., Ng, C., Kong, X., Wu, D., Song, M., Shi, X., Xu, X., OuYang, W.-H., He, R., Zhao, X.-Z., Lee, T., Brunicardi, F.C., Garcia, M.A., Ribas, A., Lo, R.S., and Tseng, H.-R. (2013) *Angew. Chem., Int. Ed.*, **52**, 3379–3383.
- 25** Chen, Q.S., Wu, J., Zhang, Y.D., Lin, Z., and Lin, J.M. (2012) *Lab Chip*, **12**, 5180–5185.
- 26** Yin, S., Wu, Y.-L., Hu, B., Wang, Y., Cai, P., Tan, C.K., Qi, D., Zheng, L., Leow,
- W.R., Tan, N.S., Wang, S., and Chen, X. (2014) *Adv. Mater. Interfaces*, **1**, 1300043.
- 27** Wan, Y., Liu, Y.L., Allen, P.B., Asghar, W., Mahmood, M.A.I., Tan, J.F., Duhon, H., Kim, Y.T., Ellington, A.D., and Iqbal, S.M. (2012) *Lab Chip*, **12**, 4693–4701.
- 28** Kim, Y.-J., Ebara, M., and Aoyagi, T. (2012) *Angew. Chem., Int. Ed.*, **51**, 10537–10541.
- 29** Griffin, D.R. and Kasko, A.M. (2012) *J. Am. Chem. Soc.*, **134**, 13103–13107.
- 30** Li, W., Wang, J., Ren, J., and Qu, X. (2013) *Adv. Mater.*, **25**, 6737–6743.

12

Organic Nano Field-Effect Transistor

Yonggang Zhen and Wenping Hu

12.1

Introduction

Contrary to inorganic semiconductors, the organic semiconductors are lightweight, cheaper, flexible, and easy to prepare, involving different kinds of organic materials with a wide range of properties. In addition, organic semiconductors possess well-ordered molecular structures and its material properties can be designed and adjusted artificially, the advantages that inorganic semiconductors lack. Accordingly, organic semiconductors have attracted greater attention in recent years. Organic field-effect transistor (OFET) has been an important research area as it is one of the basic components of the circuit in organic semiconductors. The organic thin film is usually used as an active layer in organic field-effect transistors; a large number of structural defects and grain boundaries however exist in the organic thin film, as its particles can be bound or scattering, reducing the performance of the device. So, the intrinsic semiconductor characteristic of the materials cannot be reflected. In organic crystals, in which grain boundaries do not exist, molecular arrangement is of long-range order, and charge trap density is reduced to a minimum, are able to solve the problem effectively. However, most organic single crystals are nanostructures, and as such large organic crystal growth is difficult and it cannot meet the circuit miniaturization and integration. Therefore, if we can use organic nanocrystal as the active layer, not only can we overcome the difficulties of large organic crystal growth, but also retain all the advantages of organic single crystals, providing an effective characterization of the intrinsic properties of organic semiconductors, and make devices to meet the requirements of miniaturization and integration, thereby achieving the integration of organic crystals and nanodevices.

Organic nano field-effect transistor, which use nanomaterials (mainly organic nanocrystalline material) as channel materials, is mainly used to study the mechanism of charge transport in organic semiconductors and the relationship between molecular structure and the nature of organic semiconductors, thereby revealing the intrinsic properties of the charge transport of the organic semiconductor material.

12.2

The Fabrication of Organic Semiconductor Nanostructures

Organic semiconductors in nanoscale are the foundation to constructing nano OFETs. Until now, the making of nano-organic semiconductors involves several methods, including vapor- and liquid-phase methods (see Table 12.1).

12.2.1

Vapor-Phase Method

Vapor-phase method mainly includes physical vapor transport (PVT) growth method, hot wall epitaxial method, and others. For physical vapor transport growth method, the growth of organic semiconductors normally takes place in a horizontal tube furnace, which is always equipped with a vacuum system. Figure 12.1 is a schematic diagram of such system. In such system, organic semiconductor material/precursor is located in the high-temperature region. The growth of nano-organic semiconductors also occurs in the low-temperature region, the range of temperature being relatively narrow. When the organic semiconductor material/precursor sublimate in the high-temperature region, they will be transported by the carrier gas to the low-temperature region, where the growth of nano-organic semiconductors with crystal structures will take place. Inert gases of high purity always act as the carrier gas. For organic semiconductor materials/precursor containing impurities, the vapor pressure of heavy impurities is smaller than that of the pure organic semiconductors, thus the heavy impurities will deposit on the region of the source material in the high-temperature region. For light impurities, its vapor pressure is higher than that of the pure organic semiconductors, thus the light impurities will deposit on the region beyond the growth region of the semiconductor in the low-temperature region. The process of semiconductor growth is also a material purification process.

The key parameters in the physical vapor transport growth method for the growth of organic single crystal in nanoscale are the temperature of the deposition region, the flow rate of the carrier gas, and the vacuum degree of the chamber. The optimal parameters for the growth of the semiconductor vary according

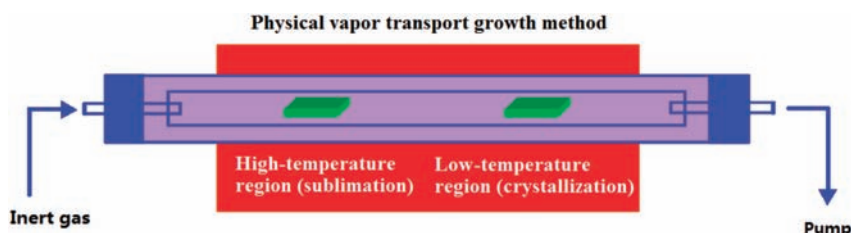


Figure 12.1 Schematic diagram of a physical vapor transport growth system for organic crystal growth.

Table 12.1 Organic semiconducting materials for nano-FETs.

Growth method	Material	Type	Mobility	ν_T	Insulating layer	Width	Length	Transfer method
PVT	PET [29]	P	0.8	-6	SiO ₂	1.8	>200	<i>In situ</i> growth
	BP2T [30]	P	0.42	-2.4	SiO ₂	1	Hundreds	Wetting transfer
	CuPc [22]	P	0.1–0.2	-2.4 to 2.9	SiO ₂	0.15–0.5	15–100	Mechanical probe
	CuPc [23]	P	0.1–0.5	-0.2 to 0.6	SiO ₂	0.05–0.15	15–100	<i>In situ</i> growth
	F ₁₆ CuPc [24]	N	0.2	-5.5	SiO ₂	0.3–0.4	15–100	<i>In situ</i> growth
	CuPc [81]	Ambipolar	0.1	—	Air gap	0.5	>20	Wetting transfer
	F ₁₆ CuPc [81]		0.17	—		0.225	>20	
	BNVBP [86]	P	2.49	-28	SiO ₂	0.3–100	>30	<i>In situ</i> growth
	DBTDT [25]	P	1.8	—	OTS/SiO ₂	10–20	10–20	<i>In situ</i> growth
	F-NDI [26]	N	0.7	2.2	OTS/SiO ₂	Several to dozens	Several to dozens	<i>In situ</i> growth
Liquid phase method	PBBTZ 1 [27]	P	3.6	-9 to 13	OTS/SiO ₂	Zero a few to several	Dozens to hundreds	<i>In situ</i> growth
	DCP [28]	P	9	-8 to 1	OTS/SiO ₂	—	—	<i>In situ</i> growth
	RRP3 HT [54]	P	0.02	—	SiO ₂	0.015	0.2–5	<i>In situ</i> growth
	Oligoarene [58]	P	0.005–0.01	-18 to 31	SiO ₂	0.5–1	30–100	<i>In situ</i> growth
	HTP [80]	P	0.27	-0.62	SiO ₂	0.15–1	>20	<i>In situ</i> growth
	PTCD [61]	N	0.01	—	SiO ₂	0.08–0.315	>10	<i>In situ</i> growth
	HBC [43]	P	0.02	—	SiO ₂	0.25	>14	Imprinted transfer
	P3HT [55]	P	—	—	OTS	1–3	30–500	<i>In situ</i> growth
	TIPS-PEN [60]	P	1.42	-10 to -22	SiO ₂	4–10	32–41	<i>In situ</i> growth
	BPE-PTCDI [33]	N	0.62 ± 0.41	—	OTS/SiO ₂	Dozens of nanometers to several micrometers	Dozens to thousands	Wetting transfer

(continued)

Table 12.1 (Continued)

Growth method	Material	Type	Mobility	V_T	Insulating layer	Width	Length	Transfer method
Oligothiophene derivatives [34]	P	6.2	-9		OTS/SiO ₂	1–5	600	Elastomeric stamp
C ₆₀ [49]	N	11	—		BCB/SiO ₂	—	—	<i>In situ</i> growth
C8-BTBT [35]	P	9.1	-19.9		PMMA	6–25	400	<i>In situ</i> growth
c12-4Cl <i>d</i> PBI [36]	N	4.65	—		OTS/SiO ₂	—	—	<i>In situ</i> growth
H2 TP [62]	P	0.85	5		OTS/SiO ₂	—	—	<i>In situ</i> growth
ZnTP [62]	P	2.9	2		OTS/SiO ₂	—	—	<i>In situ</i> growth
CDT-BTZ [56]	P	5.5	—		HMDS/SiO ₂	0.3–0.6	5–20	<i>In situ</i> growth
PY-4(THB) [78]	P	0.7	-10		OTS/SiO ₂	3–5	30–100	<i>In situ</i> growth
DTT-8 [46]	P	10.2	—		PMMA/SiO ₂	4–50	Hundreds	<i>In situ</i> growth
DTT-12 [46]	P	1.8	—		PMMA/SiO ₂	Dozens to hundreds	Dozens to hundreds	<i>In situ</i> growth
PTz [37]	P	0.46	-19		OTS/SiO ₂	0.08–0.25	—	<i>In situ</i> growth
DTBDT [38]	P	3.2	-24		HMDS/SiO ₂	2	200	<i>In situ</i> growth
TIPS-TAP [39]	N	1.77	-6.3 to 19.9		OTMS/SiO ₂	—	—	<i>In situ</i> growth
TESAN-BT [40]	P	1.28	-2		SiO ₂	9–10	—	<i>In situ</i> growth
TESAN-TT [40]	P	0.67	-9		SiO ₂	8–9	—	<i>In situ</i> growth
TIPS-Pentacene [28]	P	0.19	-23 to 5		SiO ₂	—	—	<i>In situ</i> growth

Other methods	PEO [70]	P	1.4×10^{-4}	—	SiO ₂	0.12–0.3	>100	<i>In situ</i> fabrication
	RRP3 HT [73]	P	0.03	—	SiO ₂	0.1–0.5	>100	<i>In situ</i> fabrication
	F-T3-F [75]	P	0.5×10^{-4}	—	SiO ₂	0.1–0.2	>20	<i>In situ</i> fabrication

RRP3HT: poly(3-hexylthiophene); PET: perylo[1,2-*b,c*]thiophene; CuPc: copper phthalocyanine; F₁₀CuPc: copper hexadecafluorophthalocyanine; HTP: hexathiapentacene; PTCDI: perylene-tetracarboxylic diimide; HBC: hexabenzocoronene; P3HT: poly(3-hexylthiophene); DCP: 6,13-dichloropentacene TIPS-PEN: trisopropylsilyl ethynyl pentacene; OTS: octadecyltrichlorosilane; PEO: polyaniline/polyethylene oxide; BPE-PTCDI: *N,N'*-bis(2-phenylethyl)-perylene-3,4;9,10-tetracarboxylic diimide; BNPBP: 4,4'-bis(*E*)-2-(naphthalen-2-ylvinyl)-1,1'-biphenyl; DBTDT: dibenz[*d,d'*]thieno[3,2-*b*,4,5-*b'0*]dithiophene; F-NDI: NDI with a certain fluoroalkyl chain; PBBTZ 1-3: 6*H*-pyrrolo-[3,2-*b*:4,5-*b'*]bis[1,4]benzothiazine and its 6-substituted derivatives; TIPS-pentacene: trisopropylsilyl ethynyl-substituted pentacene; C8-BTF: diocylbenzothienobenzothiophene; c12-4ClBPB: tetrachlorinated dipyrenyl bisimide; CDT-BTZ: cyclopentadiethiophene-benzothiadiazole copolymer; PY-4(THB): 1,3,6,8-tetraakis(4-hexyl phenyl)ethynyl pyrene; PTz: bithiazole-thiazolothiazole; DTBDT: dithieno[2,3-*d*:2',3'd']benzo[1,2-*b*:4,5'*b'*]thiophene; TIPS-TAP: 6,13-bis(trisopropylsilyl)ethynyl-5,7,12,14-tetraazapentacene; TESAN-BT: 2,6-di(20-bithiophenyl)-9,10-bis-[(triethylsilyl)ethynyl]-anthracene; TESAN-TT: 2,6-di(20-thienothiophenyl)-9,10-bis-(triethylsilyl) ethynyl-anthrancene.

Unit: mobility – cm²V⁻¹s⁻¹; threshold voltage – V; crystal width and crystal length – μm.

to the materials. The temperature of sublimation region (high-temperature region) normally equals to the threshold temperature of the material sublimation. Temperature gradient is crucial to the growth of single crystal as it directly affects the quality, size, and distribution density of crystal. Generally, small temperature gradient is more advantageous to the growth of large-sized single crystal. On the contrary, large temperature gradient is more advantageous for the growth of organic semiconductor in nanoscale. The growth of organic nanostructure generally lasts for more than 10 min to a few days, depending on the materials type, expected shape, and size of the crystal. For many kinds of materials, slower crystal growth rate will result in higher quality and higher mobility. One typical example is rubrene. On the other hand, the type of carrier gas is also very important. For linear polycyclic aromatic compounds such as pentacene, tetracene, and so on, argon gas of ultrahigh purity should be used as carrier gas to obtain nano single crystal with high mobility [1,2]. For rubrene, hydrogen is the most ideal carrier gas [3–5]. So far, however, the specific reason of the influence of carrier gas on the quality of the crystal is not clear [6]. Besides, the vacuum degree of the system and the purities of the source material play an important role in determining the quality of the crystal. High-quality nano-organic crystal, as a general rule, will be obtained with high-vacuum degree and high-purity precursor.

The morphology of the crystal mainly depends on the molecular structures of its own and their particular arrangement in the crystal, especially the magnitude of intermolecular interaction force and its anisotropy. As a general rule, the fastest growth happens along the direction where the intermolecular force is the strongest. For example, the crystal is inclined to grow along the direction of the $\pi-\pi$ interaction. The size of single crystal along one dimension can reach centimeters scale, with thickness ranging from several nanometers to several micrometers, which can be adjusted by controlling the crystal growth process.

Copper phthalocyanine (CuPc) is a kind of organic semiconductor material that has been widely studied. It shows excellent thermal and chemical stability, as well as good performance of the thin-film transistor constructed from it [7–21]. In 2006, Hu and coworkers reported the growth of CuPc single-crystal nanobelt on aluminum oxide substrate through a homemade tubular resistance furnace with two temperature control regions by physical vapor transport growth method [22,23]. The preferential growth direction of the single-crystal CuPc nanobelt is along the *b*-axis, and FETs based on single-crystal CuPc nanobelt are also constructed. The homemade tubular resistance furnace with two temperature control regions can result in a larger temperature gradient with controllable distribution, which is favorable for the growth of organic nanostructures. From distinct electron diffraction analysis by transmission electron microscopy, a single-crystal structure can be identified with preferential growth direction along the *b*-axis. Such crystals reached microscale with width range of 20 nm to several micrometers and exhibited good flexibility (Figure 12.2). Later, same method and equipment were used and some other single-crystal semiconductors [24–28] were successfully fabricated, such as copper

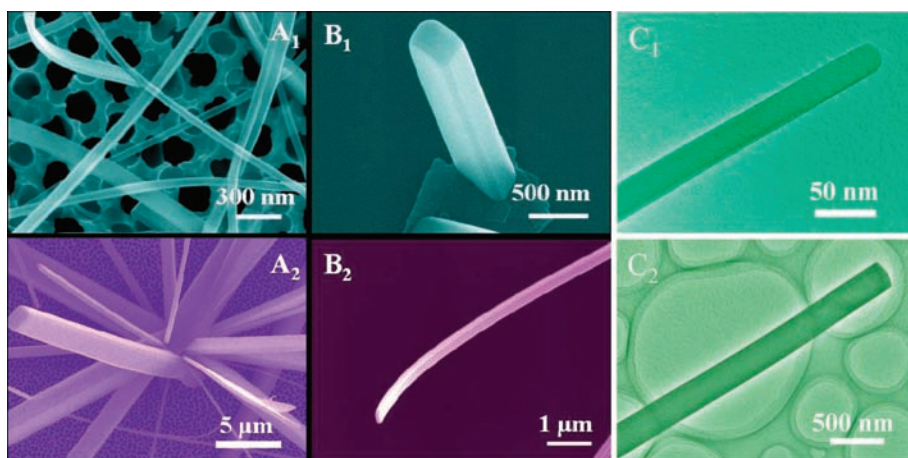


Figure 12.2 SEM and TEM images of CuPc nanostructures grown by physical vapor transport growth method.

hexadecafluorophthalocyanine ($F_{16}CuPc$), one of the few n-type semiconductors stable in ambient atmosphere [24]. These examples show that such method and equipment can be used as a universal approach for the growth of single-crystal semiconductors in nanoscale.

In 2007, Wang and coworkers synthesized derivatives of perylene, perylo[1,12-*b,c,d*]thiophene (PET) [29]. The molecules orientation along the long axis of the crystal shows a π - π stacking style, and there is strong S-S interactions among the molecules. The solid-state packing arrangement and the weak interaction between molecules make it easier for the PET molecules to grow into single crystal in nanoscale by self-assembly. Through physical vapor transport growth method, PET single crystals in nanoscale were obtained on Si/SiO₂ substrate by adjusting sublimation temperature and growth time. As shown in Figure 12.3, by vacuum deposition technology, metal electrodes were fabricated on the PET single crystal, and top contact-type FETs were obtained, with which a mobility up to $0.8\text{ cm}^2\text{ V}^{-1}\text{ s}^{-1}$ can be achieved, an order of magnitude higher than that of PET thin-film transistors ($0.05\text{ cm}^2\text{ V}^{-1}\text{ s}^{-1}$). In 2012, naphthalene bis(dicarboximide) was synthesized by Wang and coworkers [26]. With the cooperation of Hu and coworkers, a single crystal-based n-type FETs were constructed with the mobility of $0.7\text{ cm}^2\text{ V}^{-1}\text{ s}^{-1}$.

The principle of hot wall epitaxial method is similar to that of physical vapor transport growth method in terms of that the organic source materials/precur-sors sublime under high temperature in vacuum, deposit in low-temperature region, and grow into organic semiconductors, as shown in Figure 12.4. It differs from physical vapor transport growth method in that there is no carrier gas to transport the organic molecules and the system can maintain in a higher vacuum degree, thus allowing the organic molecule to move freely in space with a larger mean free path. After the absorption of organic molecules on the substrate,

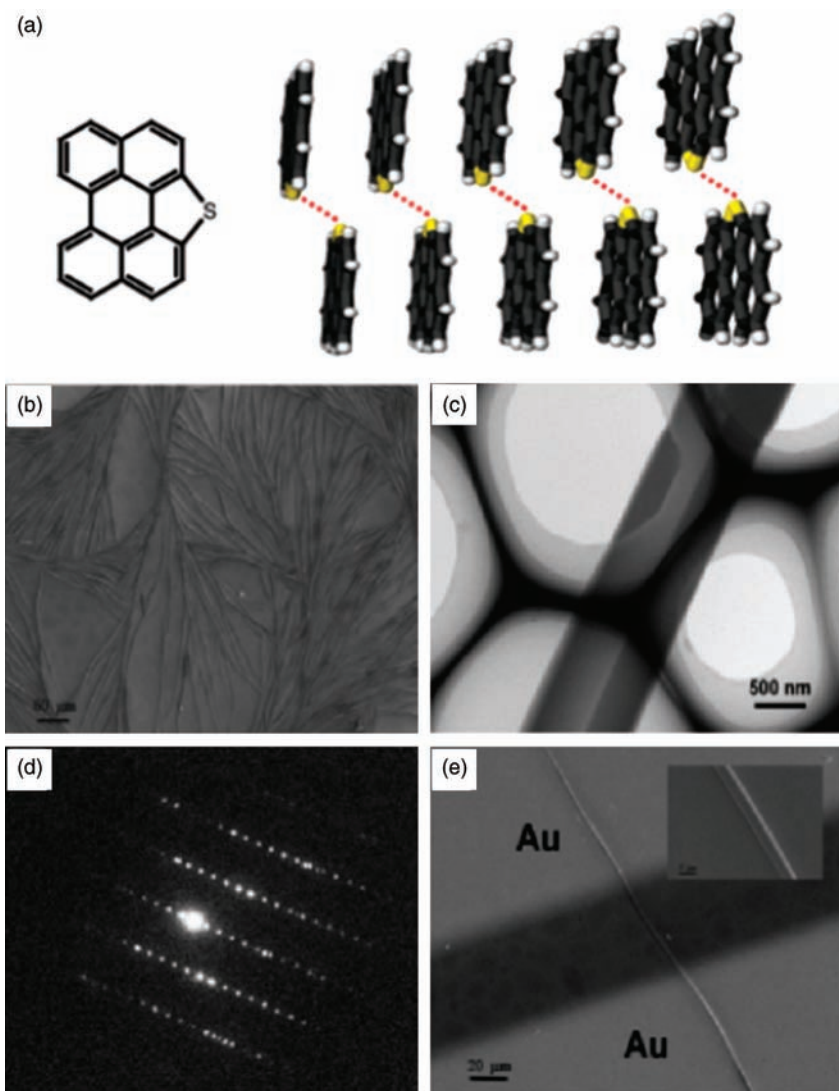


Figure 12.3 (a) Chemical structure and crystal packing view of PET. (b) Images of the large-area PET. (c) TEM image of a single-crystal PET wire. (d) The corresponding electron

diffraction pattern. (e) Micrograph of an individual PET wire and the electrodes formed by a gold wire mask.

single crystals begin to grow. There are relatively fewer reports on this method. For these few reports, KCl crystals were always used as substrate for crystal lattice-induced epitaxial growth of organic crystal nanostructures. For example, vapor hot wall epitaxial method was adopted by Ichikawa *et al.* [30–32] for the growth of nano single crystal of thiophene/phenylene co-oligomer (BP2T)

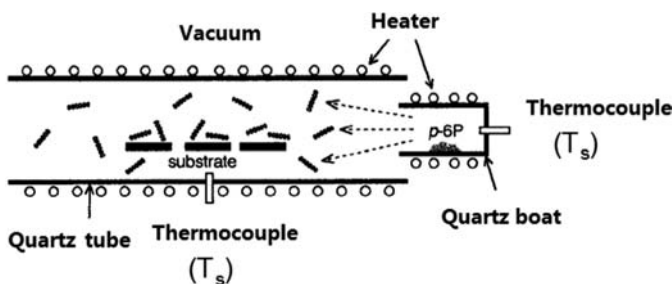


Figure 12.4 Schematic diagram of a hot wall epitaxial system for organic crystal growth.

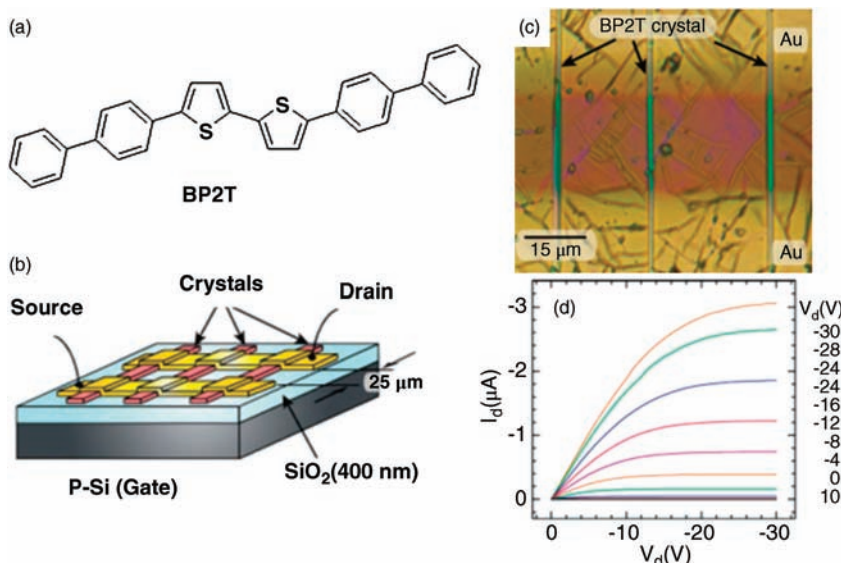


Figure 12.5 (a) Chemical structure of thiophene/phenylene co-oligomer (BP2T). (b) Schematic illustration of the FET devices. (c) Optical microscopy image of the FET device. (d) Drain current I_d versus source-drain voltage V_d curves.

on KCl single-crystal substrate and devices were constructed, as shown in Figure 12.5.

12.2.2

Solution Process

Solution process is one of the most simple and convenient approaches for organic nanostructure preparation. Good solubility in solvent is a prerequisite for organic semiconductor materials, which could be prepared by solution process. Organic semiconductor material dissolved in solvent can precipitate and

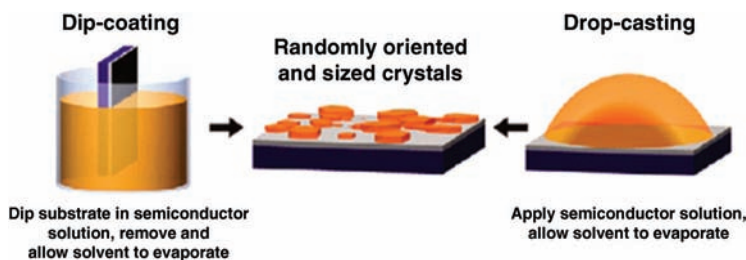


Figure 12.6 Schematic representations of dip coating (left) and drop casting (right).

grow into nanostructures by evaporating the solvent and by cooling or adding a poor solvent to obtain saturation solution. Compared with the physical vapor transport method, solution process is more suitable for low-cost and efficient production with broader commercial applications. However, the quality of crystals obtained from the solution process is not as good as the vapor-phase method crystals because of the residual solvent that becomes crystal impurities adversely affecting the properties of semiconductor materials. As a result, solution-processed nanocrystals-based field-effect transistors usually have poorer property than that obtained from the vapor transport method. In addition, most of the organic semiconductor materials are difficult to dissolve in conventional organic solvents, so this method has many limitations with relatively a narrow range of applications. In recent years, a variety of new high-performance soluble organic semiconductor molecules have been synthesized, and the application of solution process is increasing [33–40].

Solvent evaporation method includes drop casting and dip coating (as shown in Figure 12.6). Drop casting method drops organic semiconductor solution directly onto the substrate, and organic semiconductor material nanostructure are formed after the solvent is evaporated. The dip coating process involves immersing of substrate into organic semiconductor material solution, pulling up of substrate, and ultimately depositing the organic semiconductor material, the nanostructures will be formed directly on the substrate after evaporation of solvents. In the continuous process, the steps are carried out directly after each other. Crystal size depends on the evaporation rate, solvent used, the semiconductor molecular and crystal structures, and solution concentration. Typically, the saturated steam atmosphere of organic solvent can minimize the solution evaporation rate, thereby contributing to a larger crystal size.

Mas-Torrent *et al.* [41,42] first reported the preparation of dithiophene-tetra-thiafulvalene (DT-TTF) nanocrystal through solution process, and studied the field-effect transistor carrier transport properties of DT-TTF crystals in 2004. First of all, the electrodes were fabricated by electron beam lithography on a 200 nm thick oxidized silicon wafer, then a warm saturated solution of DT-TTF in chlorobenzene was poured over the electrodes, and finally the solvent evaporated at room temperature. This process, called drop casting, resulted in the formation of long, thin crystals, some of which connected two microfabricated gold

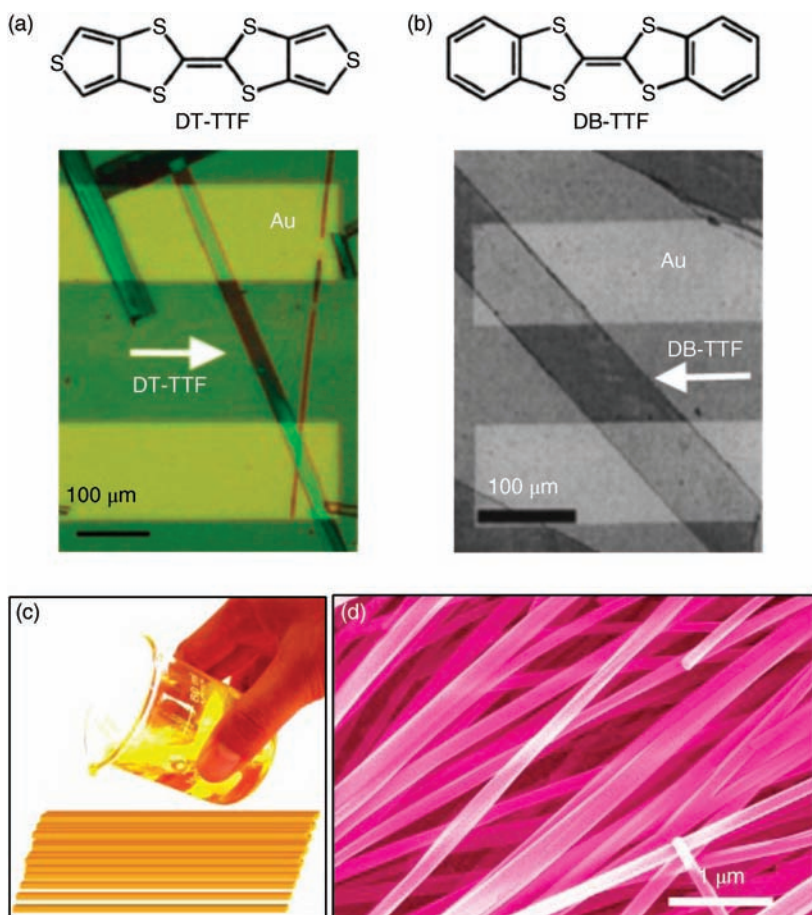


Figure 12.7 (a) Solution-processed DT-TTF. (b) DB-TTF. (c) Anthracene derivative single-crystal transistor. (d) Nanowire prepared by drop casting method.

electrodes. The formation of large regular crystals implies that the molecules are well ordered within the crystals (Figure 12.7a). In 2005, they fabricated dibenzotetrathiafulvalene (DB-TTF) single-crystal field-effect transistors by using similar method (Figure 12.7b).

Nuckolls and coworkers [43] grew hexabenzocoronene (HBC) nanowire by drop casting method, and fabricated single nanowire field-effect transistors in 2006. In 2007, Hu and coworkers [44] synthesized the crystals of α - and β -phase TTF separately under accurate control and fabricated bottom-contact field-effect transistors. They found that submicrometer TTF crystals with dimension up to several hundred nanometers could be obtained by using n-heptane as solvent, while large crystals of TTF could be obtained by using chlorobenzene as solvent by slow crystallization (more than 24 h) in a sealed container at room

temperature on octadecyltrichlorosilane (OTS)-modified substrates, their dimension being beyond 1 mm. TTF crystals from n-heptane were pure α -phase, while the products from chlorobenzene were pure β -phase; different TTF crystal phases could be obtained by simple selection of the solvents. Jiang *et al.* [45] also reported drop-casted anthracene derivative single-crystal nanowires (see Figure 12.7c and d). They synthesized single-crystalline nanowires and ultralong microwires of organic semiconductor in large scale through simple drop casting method. The size and orientation of these wires were easily controlled by changing solution concentration and other conditions. A series of research have been studied based on this method [38,46,47]. Besides growing nano single crystals based on one organic semiconductor, cocrystals based on mixed organic semiconductors are also adequate for this method. Xu and coworkers [48] presented the ambipolar transport behavior of a crystal of neutral donor–acceptor complex formed by *meso*-diphenyl tetrathia[22]annulene[2,1,2,1] (DPTTA) and tetracyanoquinodimethane (TCNQ) in 1:1 ratio with a width from several micrometers to tens of micrometers and a length from tens to hundreds of micrometers was obtained by evaporating a drop of a mixture of DPTTA and TCNQ in chlorobenzene solution.

Drop casting method is not only simple and feasible but can also obtain crystal arrays by controlling growth conditions. In 2012, Bao and coworkers [49] drop a C₆₀ solution composed of mixed solvents of *m*-xylene and carbon tetrachloride on a BCB-covered highly doped Si substrate with 300 nm SiO₂. The substrate placed a patch of Si wafer in advance and a droplet was dropped completely surrounding it (Figure 12.8a). Needle crystals were grown when the solution composed of only *m*-xylene was evaporated; in contrast, ribbon crystals were formed in the solution of mixed solvents of *m*-xylene and carbon tetrachloride. During drying of a droplet of semiconductor solution, crystals nucleated near the contact line and then grew along the receding direction of the droplet. The small Si wafer on the substrate made the contact line recede along the vertical direction of its edge. One-dimensional C₆₀ crystals were induced to arrays shown in Figure 12.8. This method can fabricate large-area crystal arrays with the largest area up to 100 mm. The highest electron mobility of fabricated FET was up to 11 cm² V⁻¹ s⁻¹. An average electron mobility (μ) of 5.2 cm² V⁻¹ s⁻¹ was achieved for the needles and an average electron mobility (μ) of 3.0 cm² V⁻¹ s⁻¹ was obtained for ribbons. They also use a similar method to fabricate p–n junction [50], exhibiting excellent ambipolar characteristics. Apart from the small Si wafer, capillary can also be used to grow crystal arrays [51]. Multiple drop casting method was another more simple way to prepare single-crystal arrays, which was developed by Tang and coworkers in 2014 [52]. They continuously and quickly dropped two droplets of DB-TTF solution on the substrate. The distance between two droplets was optimum distance. When the solution evaporated, DB-TTF nanowire crystal arrays were formed (Figure 12.9). The longest length of nanowire was up to 400 μ m with width from several hundred nanometers to a few micrometers. The whole area can be up to 0.5 \times 2 mm². The forming of crystal arrays is closely related to the number of droplets and the distance among

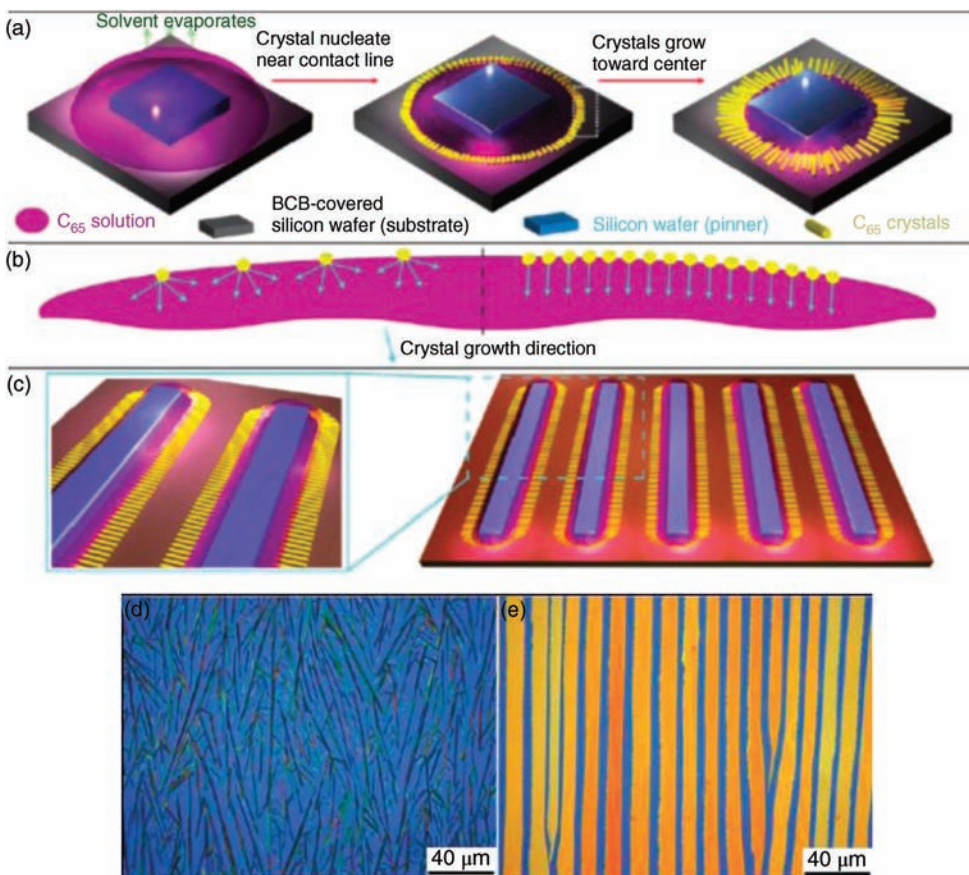


Figure 12.8 Schematic representations of the DPC method and morphologies and crystalline structures of well-aligned C₆₀ needle.

them. The success rate can be up to 94% when using multiple drop casting method, far more than using a single droplet (60%).

Not only small-molecule semiconductors, but also polymer semiconductors can be made with nano single crystals by solvent evaporation method. In 2004, Merlo and Frisbie [53,54] fabricated solution-processable RRP3HT (poly(3-hexylthiophene)) nanofiber that exhibits mobility of $0.02 \text{ cm}^2 \text{ V}^{-1} \text{ s}^{-1}$ and on/off ratio of 10^6 . In 2012, Guo and coworkers [34] present two liquid crystalline oligothiophene derivatives: one-dimensional microribbons from a CHCl₃ solvent via a slow solvent evaporation process and their OFET devices that show very high average field-effect mobility of $4.0 \text{ cm}^2 \text{ V}^{-1} \text{ s}^{-1}$ with the highest up to $6.2 \text{ cm}^2 \text{ V}^{-1} \text{ s}^{-1}$. In 2006, Cho and coworkers reported the preparation and properties of high-quality, 1D single-crystal P3HT microwires grown by a facile self-assembly process in dilute solution (Figure 12.10) [55]. Single-crystal microwires

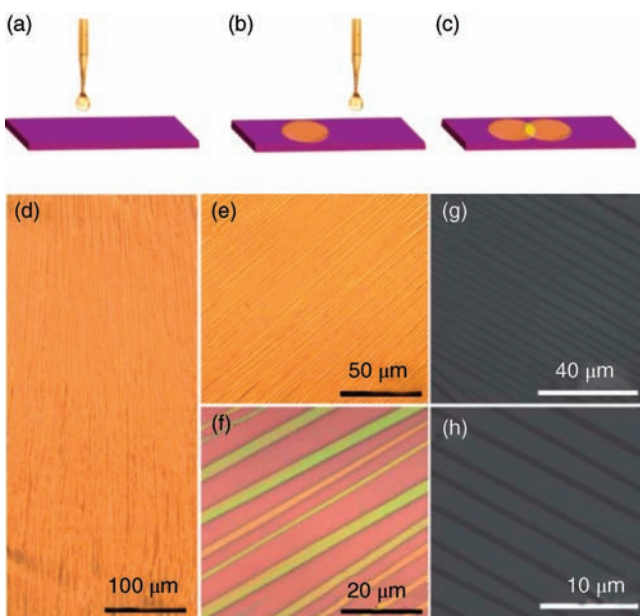


Figure 12.9 (a–c) Schematic illustration of the multiple drop casting method for the growth of oriented DB-TTF nanowire arrays on the substrate. (d–h) Optical microscopy and SEM images of oriented nanowires grown on the silicon substrate.

were prepared from a 0.1 mg ml^{-1} dilute solution in CHCl_3 using a seeding temperature of 40°C and a crystallization temperature of 10°C over a period of 3 days. A supersaturated solution was poured onto the highly doped silicon substrates modified with the CH_3 -functionalized self-assembled monolayer (SAM) dielectric in a closed jar and allowed to dry at 60°C for 10 h under vacuum. During the solution crystallization process, the P3HT chains self-organized via van der Waals interactions. As for the structure of single-crystal P3HT microwires, the extended P3HT chains are packed parallel to each other, with their long chain axis perpendicular to the long wire axis. In 2012, Pisula and coworkers [56] also grew single copolymer fibers of cyclopentadithiophene-benzothiadiazole copolymer (CDT-BTZ) using drop casting and solvent vapor annealing.

For many organic semiconductors, the solubility changes greatly along with the temperature in some specific solvent. Taking advantage of this point, researchers prepare a hot saturated solution, also called supersaturated solution, for organic semiconductors and then cool them down. This process would lead to crystallization, forming nanosized single crystals. For example, in 2007, Bao and coworkers [57] used cyclohexyl-substituted quaterthiophene (CH_4T) soluble in bromobenzene at high temperatures ($100\text{--}130^\circ\text{C}$) forming a supersaturated solution and slowly cooled down to prepare CH_4T single crystals (Figure 12.11). Besides, different size of crystals can be obtained by modulating the cooling rate. In the same year, Pei and coworkers [58] prepared organic

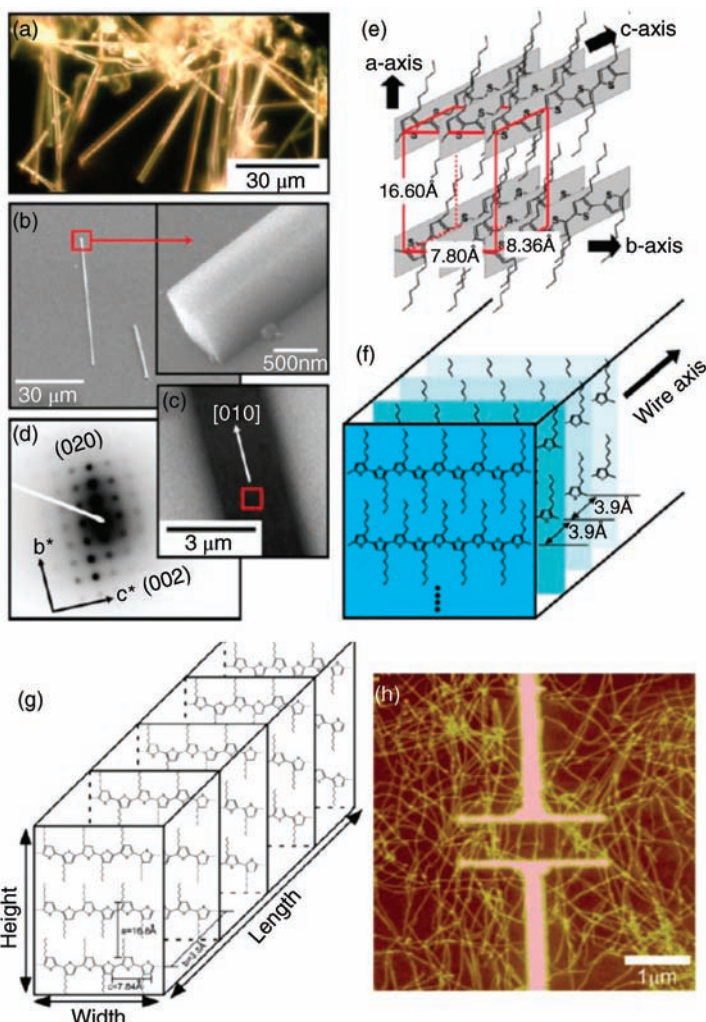


Figure 12.10 Morphological features and structure characterization of single-crystal P3HT microwires (a–f).

semiconductor nanowires on SiO_2/Si substrates using the similar method and dispersed them by a solution method to construct the bottom-gate top-contact nanowire field-effect transistors. The highest mobility was up to $0.01 \text{ cm}^2 \text{ V}^{-1} \text{ s}^{-1}$. In 2013, Bao and coworkers [33] combined supersaturated solution and poor solvent method to grow *N,N'*-bis(2-phenylethyl)-perylene-3,4:9,10-tetracarboxylic diimide (BPE-PTCDI) nanowires (Figure 12.12) and study their performance as field-effect transistors and phototransistors.

Supersaturation and precipitation in the organic semiconductor solution are the first steps for crystal growth. As already described, both evaporation of the

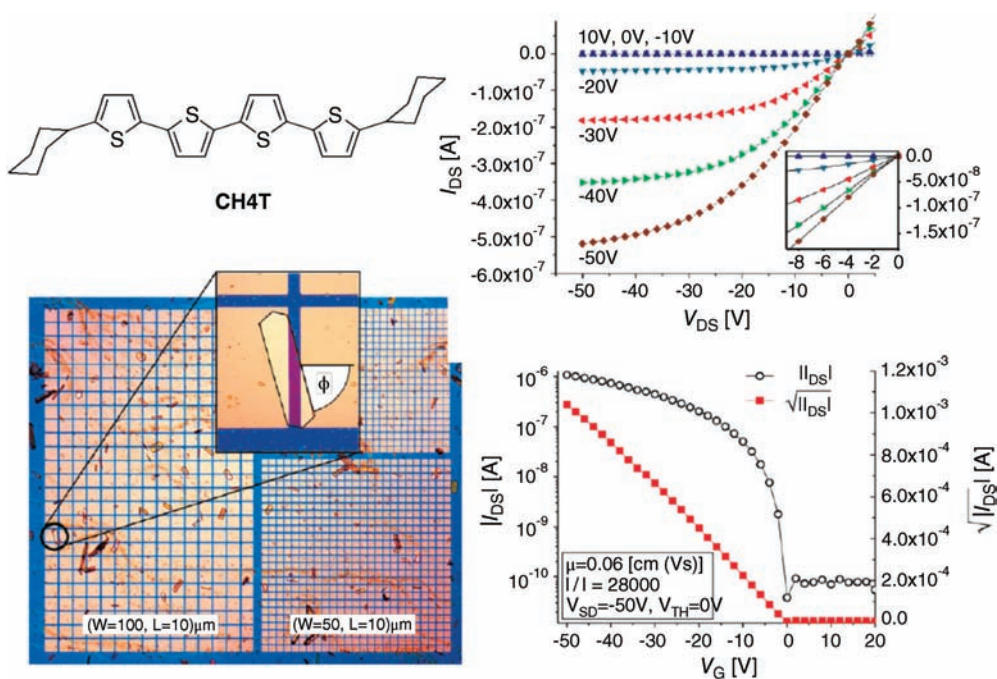


Figure 12.11 Drop-casted CH₄T bottom-contact single-crystal transistors.

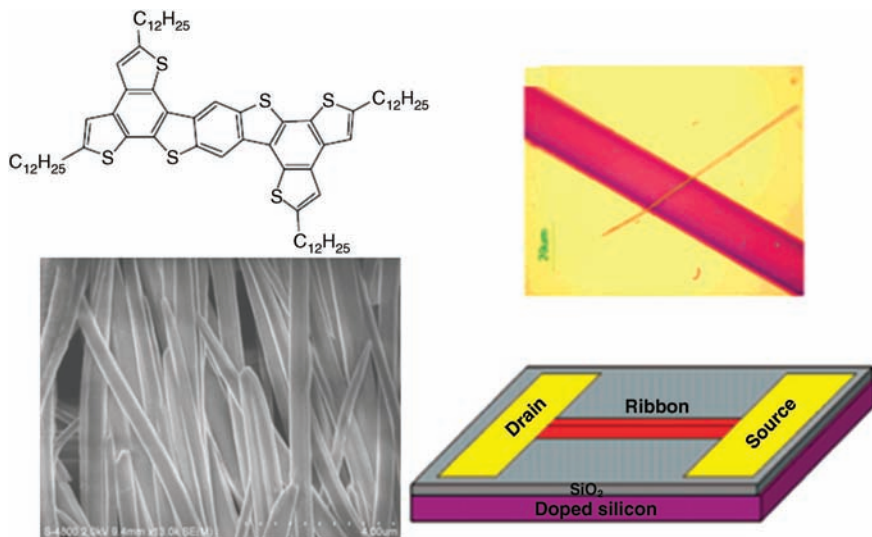


Figure 12.12 Solution-processed organic semiconductor nanoribbons and its top-contact field-effect transistor.

solvent and cooling the solution can achieve this. On the other hand, adding a poor solvent to the saturated solution leads to the precipitation, which is called “the solvent exchange” method. This common method is often used in the preparation single-crystalline micro/nanostructures of organic semiconductors. In 2007, Cho and coworkers [59,60] used the solvent exchange method to *in situ* grow the triisopropylsilyl ethynyl pentacene (TIPS-PEN) (pentacene derivative) single-crystalline nanobelts and tubes on the Si/SiO₂ substrate. In a typical experiment, TIPS-PEN was first dissolved in a good solvent such as toluene. Then a small amount of toluene solution was rapidly injected into a large volume of acetonitrile solvent. The interactions between acetonitrile and TIPS-PEN molecules are so weak that $\pi-\pi$ intermolecular interactions are dominant, which is responsible for the 1D growth of single-crystalline nanobelts. Remarkably, the highest mobility of obtained belt was $1.4 \text{ cm}^2 \text{ V}^{-1} \text{ s}^{-1}$, while that of the tube was $1.73 \text{ cm}^2 \text{ V}^{-1} \text{ s}^{-1}$. In the same year, Bao and coworkers [61] prepared PTCDI-C_n single-crystalline nanostructures by adding methanol into chloroform solution. Also in 2012, Lee and coworkers [62,63] prepared microcrystals of a porphyrin derivative with the similar method and fabricated the OFET devices.

In 2007, Yamao *et al.* [64] combined falling temperature with dipping method to prepare a series of thiophene-biphenyl-type single crystals and fabricate nano-sized single-crystal field-effect transistors with bottom-contact device configuration. The growth device was provided in Figure 12.13. Specific process was as follows: First, supersaturated solution was obtained at high temperatures by heating the bottom. Then, SiO₂/Si substrate with pattern source and drain electrode was fixed on an iron radiator. Different substrate temperatures could be achieved through adjusting the radiator. A temperature gradient was formed between substrate and solution and gave rise to crystal growth on the substrate. In the process of crystal growth, upper and lower convection occurred in the saturated solution caused by the substrate in saturated ambience all the time, in favor of achieving large-area, high-quality organic single crystals. They *in situ* fabricated very thin single-crystal devices that had a good contact with the electrode surface (large bulk crystals can be obtained only by using other methods for some organic semiconductors), indicating that this method had a certain universality. However, the performance achieved by this method was lower than that achieved by physical vapor method, showing the impact of solvent on device performance was not negligible.

Czochralski method is commonly used to prepare single crystal in microelectronics industry, which has been developed in the 1960s. For example, the silicon single crystal used in the integrated circuit has been prepared by the Czochralski method. In a typical process, a cylindrical silicon single-crystal ingot is formed by slowly pulling it out from the high-purity molten polycrystalline silicon. Although the Czochralski process is a traditional method, introducing this classical technique to the growth of organic micro/nanostructures is very new, which is somehow related to the dip coating method. Evaporating organic solvents in the pulling process, the Czochralski method can achieve orientation arrangement of micro/nanowires on the target substrate. Actually, there are so

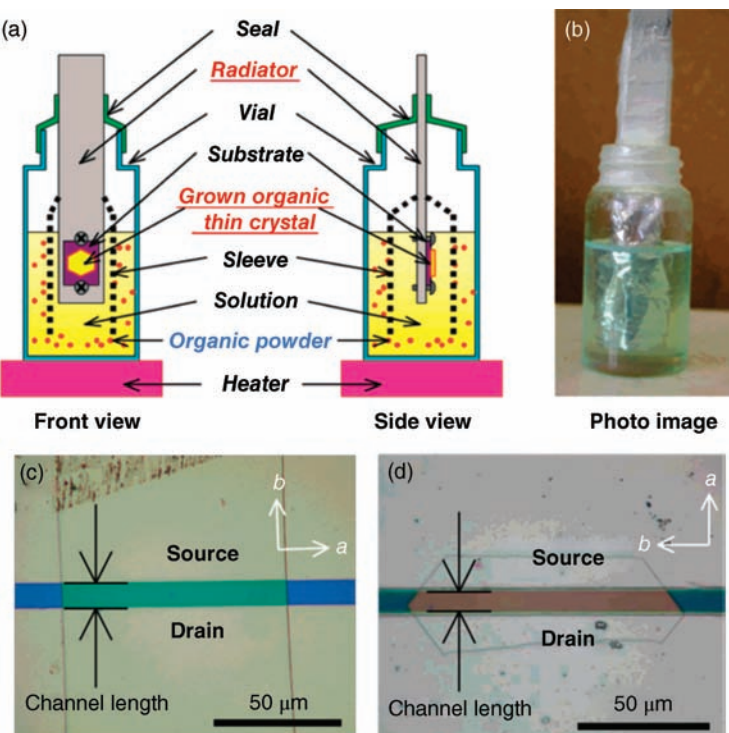


Figure 12.13 (a) Schematic diagram of the liquid-phase-growth apparatus. (b) Photograph of the apparatus. (c) Micrograph of the FET device made up of a BP3T thin crystal. (d) AC5 thin crystal.

many limitations that only 4–5 research groups attempt to prepare micro/nanostructures by this approach. For example, Pei and coworkers tried to use this method to grow micro/nanowires of a benzothiophene derivatives in 2009 [65]. In 2005, Müllen and coworkers obtained disk-shaped organic macromolecule densely packed fibers by this method [66]. In 2009, Tong *et al.* [67] found that by adjusting the pulling speed and solution concentration, they could obtain oriented, segregated, and long micro/nanowires of dichloroanthracene (DBA) and TTF materials (see Figure 12.14). Compared with the results of other research groups, these micro/nanowires are more conducive to fabrication universal, large-scale, low-cost devices. For example, good orientation is in favor of controllable preparation of electrodes. The smooth surface of these segregated and linear micro/nanowires reduces defects during device operation capture, and the long micro/nanowire greatly reduces the difficulty of preparing the electrodes. These arrays of micro/nanostructures exhibited very good optical transistor performance. Besides this work, another research group also conducted the similar studies and achieved good results [68].

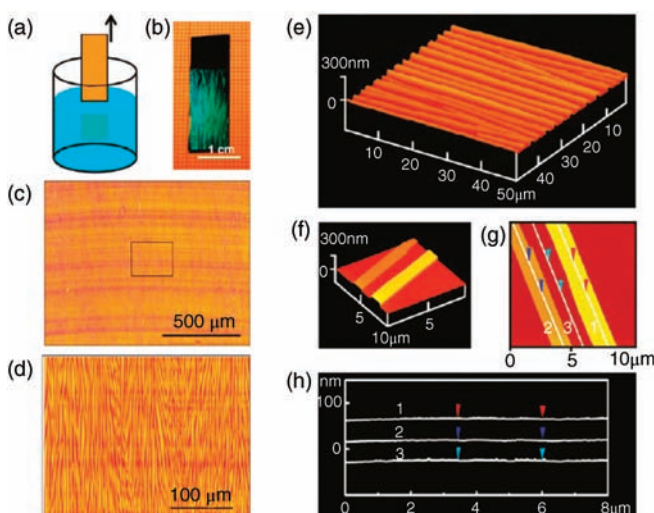


Figure 12.14 Oriented nanowires grown by the pulling method. (a) Schematic illustration of the pulling method for the growth of oriented nanowires on a vertical substrate from an organic solution. (b-d) Photograph and optical microscopy images of a typical sample. (e-h) AFM images of arrayed nanowires.

In 2011, Tsukagoshi and coworkers [35] developed a solvent vapor annealing (SVA) method. Organic semiconductor thin film was dissolved with saturated solvent vapor and then molecules moved on to the substrate surface followed by recrystallization, obtaining higher quality microcrystals compared with the crystalline quality obtained by direct heat treatment of thin film in the air. In a typical experiment, they first spin-coated dioctylbenzothienobenzothiophene (C8-BTBT) chlorobenzene solution onto the PMMA/SiO₂ substrate to obtain a polycrystalline thin film (see Figure 12.15a and b). The sample was then placed in a saturated vapor of chloroform for 10 h at room temperature, leading to small irregular crystals on the SiO₂/Si substrate (see Figure 12.15d) and long crystals on the PMMA substrate (see Figure 12.15e). This is due to the polarity of SiO₂ lower than that of the PMMA substrate that enabled C8-BTBT molecules to migrate more easily to the PMMA surface. Because PMMA was also soluble in chlorobenzene, spin-coating of C8-BTBT made PMMA surface rougher, leading to the smaller size of grown crystals. Based on this, they spin-coated mixed chlorobenzene solution of C8-BTBT and PMMA and then heat treated to obtain 1D crystals with a length of 400 μm, width of 6–25 μm, and thickness of 80–140 nm. The single crystal-based field-effect transistor exhibited excellent performance, up to a maximum mobility of 9.1 cm²V⁻¹s⁻¹, and the mobility of the device increased while the temperature decreased, showing the strip charge transportation behavior.

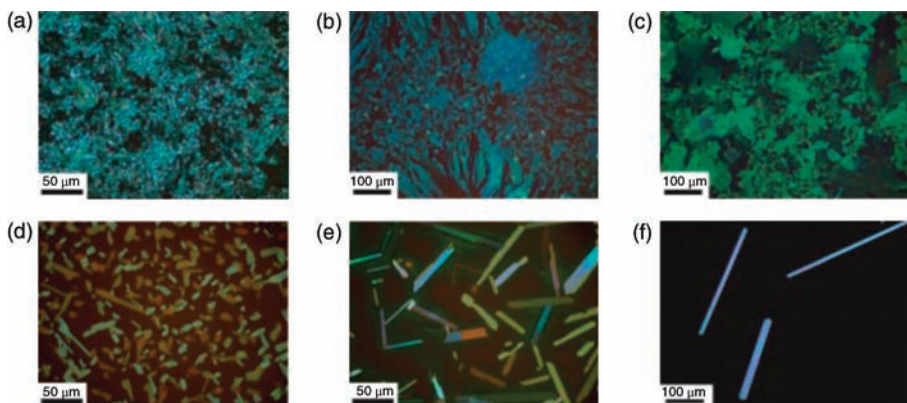


Figure 12.15 (a–f) Optical images of films taken by microscope before (a–c) and after solvent vapor annealing (d–f): C8-BTBT on SiO₂ (a and d); C8-BTBT on PMMA (b and e); and the mixture of C8-BTBT and PMMA (c and f).

12.2.3

Other Methods

Not all of the organic semiconductors may be (gas or solution) crystallized under certain conditions to form a single-crystalline nanostructure. Therefore, a number of other methods have been employed to prepare the nanostructure, such as electrospinning, drawing, self-assembly, and LB film method. Although these methods have some limitations such as a relatively narrow range of applications, these methods also have many advantages and characteristics that the conventional methods do not have.

Different from organic small-molecule semiconductors, polymer semiconductor materials in nanostructure can not be prepared by using physical vapor transport method, and the vast majority cannot be crystallized in the solution to form nanostructures, but it is actually good materials for electrospinning method. Preparation of superfine fiber by electrospinning is through static electricity as traction. Figure 12.16 is the schematic diagram of electrospinning apparatus. As shown, in the electrostatic spinning process, high-voltage of tens to thousands of volts are imposed on the polymer melt or solution, thereby generating a strong electric field force between the capillary and the grounded receiving ends leading to the extrusion of capillary polymer solution or melt and generating the jets. Before the flight of the solution jet to the collector, jet solvent evaporation, or curing, the receiving apparatus can collect the fine fibers. Due to the electric field, the surface of the polymer solution will have charges.

Same charge repulsion leads to the electric force in the direction opposite to the surface tension of the liquid. Thus, when the electric field force is applied to the surface of the liquid, an outward force is produced, as for a hemispherical droplet this outward force is opposite to the direction of the surface tension. If

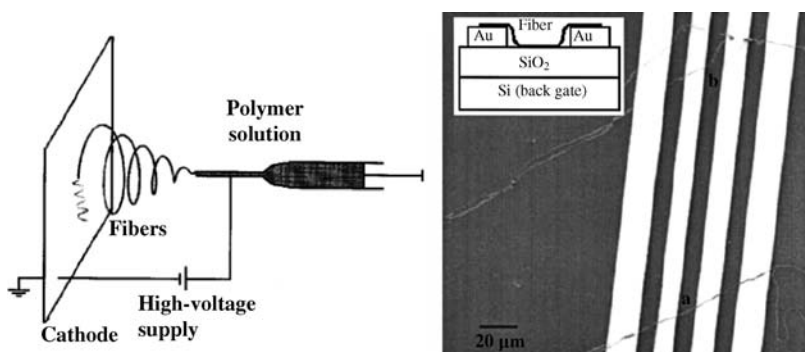


Figure 12.16 Schematic diagram of preparation of nanofibers and field-effect transistors based on the as-prepared fibers.

the size of the electric force is equal to the surface tension of the polymer solution or melt, charged droplet hangs at the end of the capillary in a equilibrium state. With the increase of electric force, the droplet at the hemispherical end of the capillary will be drawn into a cone shape under the force of electric field strength, which is Taylor cone. When the electric field force exceeds a critical value, the exclusion of the electric force will overcome the surface tension of the droplet and form the jets. The discharged polymer jet becomes very thin and long through an unstable jet drawing process; meanwhile, the solvent is volatilized to obtain charged polymeric fibers. This technique can be applied to a variety of polymer and with good generality, but the as-prepared fibers are not single crystal [69]. Polymer nanofiber fabricated by the electrostatic spinning method is much thinner than that prepared by traditional method, and the fiber is generally tens to thousands of nanometers in diameter. In 2003, Pinto *et al.* [70] prepared doped polyaniline/polyethylene oxide (PEO) nanofiber by electrospinning method (Figure 12.16), and this nanofiber has been used to build field-effect transistors. In 2005, they also prepared P3HT nanofiber field-effect transistors by using the same process [71]. In the same year, Jenekhe and coworkers [72] studied in detail the morphology, optical properties, and the properties of the doped conjugated nanofiber prepared by the electrospinning method (Figure 12.17). In 2005, Liu *et al.* [73] prepared RRP3HT nanofiber with a diameter of 100–500 nm on SiO₂/Si substrate using electrostatic spinning method (Figure 12.18), and the field-effect transistor was fabricated by using a single nanofiber as the channel – the measured mobility was $0.03 \text{ cm}^2 \text{ V}^{-1} \text{ s}^{-1}$.

In addition to preparing nanostructure by electrospinning technology, polymers can also self-assemble under special conditions. In 2005, Lin and Grannick [74] placed two pieces of mica sheets with fresh surface and curved arc vertically and across, the smallest distance between the two mica sheets being about 500 μm . A small drop of toluene solution of MEH-PPV was dropped at the nearest place, and then the two pieces of mica surface were brought into

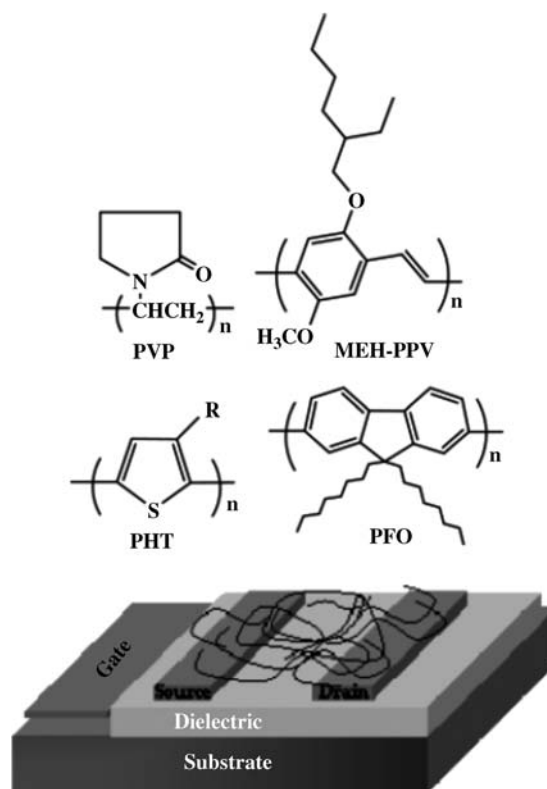


Figure 12.17 Doped conjugated nanofiber field-effect transistor fabricated by electrospinning method.

contact. After the solvent evaporated spontaneously, neatly arranged annular stripe formed on the mica surface (see Figure 12.19).

Small-molecule semiconductors can also adopt similar approach for self-assembly, but using different templates. In 2005, Müllen and coworkers [75] tightly pressed the polymer stamp that have parallel projection stripes on the 150 nm thick gold electrode crossing between the stamp and the substrate with a clearance. The F-T3-F solution was added dropwise at the junction of the stamp and the substrate; under the action of the capillary force, the solution entered into the bottom of the stamp, self-assembled into a parallel array of nanostripes formed by self-assembly at the bottom of the stamp, and after evaporation of the solvent both ends of the stripes connected to the gold electrode to form the device (Figure 12.20).

Organic semiconductors are of great variety with different properties; therefore, there is no universal technology for preparing nanostructures for all semiconductors. However, there are many ways of preparing nanostructures for organic semiconductors; so meeting a variety of special needs and becoming

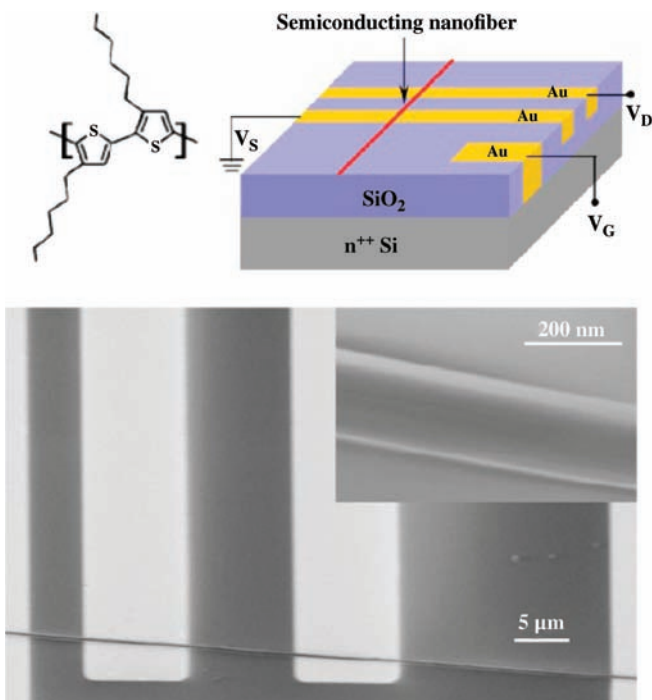


Figure 12.18 Field-effect transistor based on the RRP3HT nanofiber.

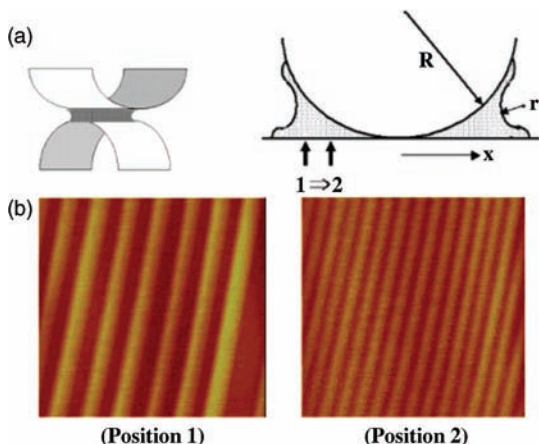


Figure 12.19 (a) Schematic diagram of the MEH-PPV self-assembly stripes. (b) AFM images of MEH-PPV self-assembly stripes.

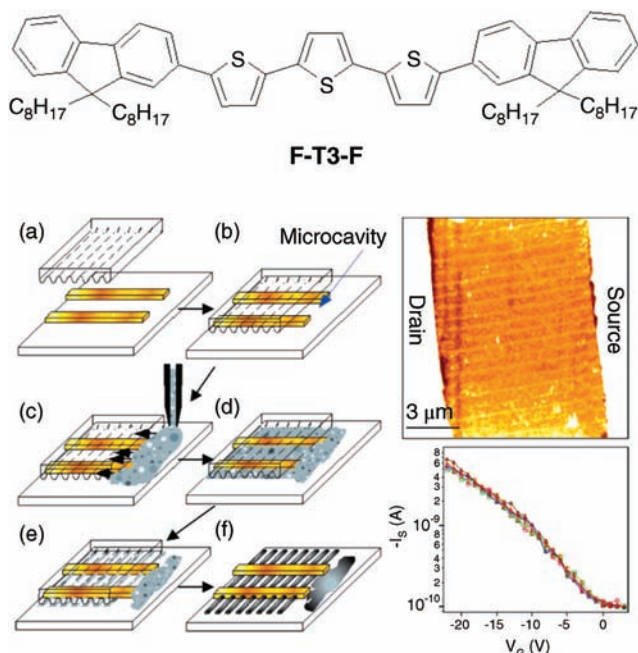


Figure 12.20 Schematic diagram of fabrication of top-contact nanostripe field-effect transistor using self-assembly.

more and more perfect in the preparation of nanostructures for most organic semiconductors is not a problem.

12.3

Device Structures of Organic Nano Field-Effect Transistor

The device structures of organic nano-FETs are the same as the corresponding thin film devices, which can be classified as bottom-gate-bottom-contact (BGBC) and bottom-gate-top-contact (BGTC) mode, as illustrated in Figure 12.21. Usually the nanocrystals are too fragile, it is difficult to fabricate dielectric layer on

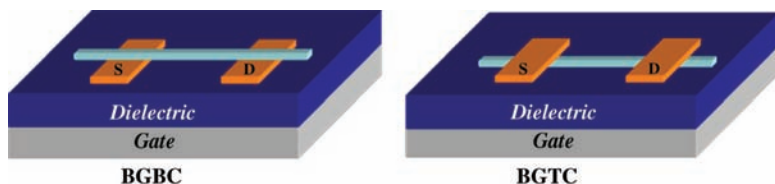


Figure 12.21 Schematic illustrations of nanocrystal device structures.

top of the crystals without causing any damage; thus, top-gate geometry has never been used in the micro/nanocrystal device.

The preparation process of BGBC-type device is relatively easy. The steps mainly involved are as follows: first, gate electrode, insulating layer, and the source and drain electrodes were fabricated respectively on a substrate, and then the prepared micro/nanostructures either by physical vapor deposition (PVD) or by solution process were transferred to (or directly prepared on) the intermediate of the electrodes; under the action of van der Waals forces, the nanostructures could form intimate contact with the source and drain electrodes and the insulating layer, thus forming a transistor device. Highly doped silicon was widely used as substrate on which an insulating layer of silicon dioxide was grown by thermal oxidation, and photolithography and vacuum vapor deposition processes were used to prepare the source and drain electrodes. The advantages of bottom-contact devices are (i) flexible plastic substrates could be used, on which flexible devices could be fabricated; (ii) the preparation of the electrodes was before the organic semiconductor nanostructures fabrication process, which avoids the damage that could be brought by electrode deposition and more complex electrode structure could be expected and also the four-probe structure could be prepared to study the intrinsic property of the device; and (iii) the anisotropy properties could be easily studied by adjusting the position of organic crystals. The disadvantage of this technique is that certain requirements should be taken into consideration while selecting organic semiconductor nanostructures; only sheet, ribbon, or linear nanostructures can be used, otherwise it is difficult to form good contact with the insulating layer and the electrodes. Moreover, electrodes were prepared directly on the insulating layer, thus the stepped structure is easily formed, which could bring voids at the crystal/electrodes/insulating interface at the step (corresponding to the introduction of a defect in the conduction channel) and the performance could be severely affected. Frisbie and coworkers [76] solved this problem by etching the insulating layer, and then the source and drain electrodes are deposited on the etched groove (Figure 12.22). In 2004, Podzorov and coworkers directly constructed rubrene single-crystal field-effect transistor (shown in Figure 12.23) by using air as insulating layer [77],

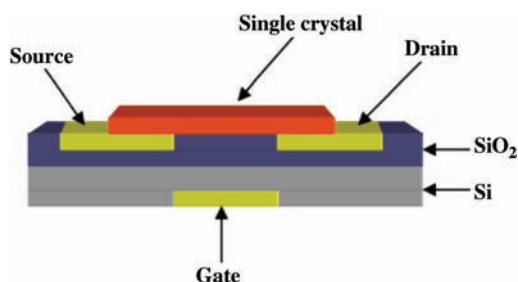


Figure 12.22 Structure diagram of source and drain electrodes deposited on the insulating layer in the etched bottom-contact-type field-effect transistor.

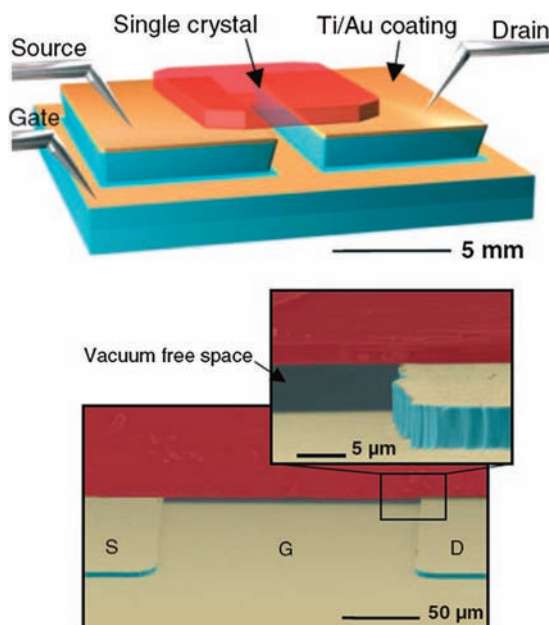


Figure 12.23 Schematic diagram of bottom-contact FET device using air as insulating layer.

which can easily avoid the step problem in the bottom-contact configuration, but possess all the advantages of bottom-contact configuration. These processes mentioned herein are widely used for large organic crystals, but could also be applied to the preparation of organic nanocrystal devices.

The fabrication of BGTC-type organic nano-FET device starts with the preparation of organic nanostructures (PVT or solution process) *in situ* on the insulating layer (e.g., Si/SiO₂ substrate) and then the source and drain electrodes were deposited at both ends of the nanostructures to finish the FET device. The advantages of this approach are (i) devices can be fabricated on flexible substrates; (ii) organic semiconductor nanostructures located on the flat surface of the insulating layer, which facilitates the formation of an intimate semiconductor/insulator interface, which can improve the device performance; (iii) since there is no convex structure formation, the device can be made to nanoscale. Typically, for the same semiconducting material, better performance could be expected for top-contact geometry. However, this structure has its own drawbacks: thermal evaporation has always been used for the fabrication of source/drain electrodes in top-contact devices and the heat radiation inevitably causes some damage to the nanostructures, and also it is difficult to build complex electrodes structure in this geometry. Furthermore, the carriers need to pass through the thickness of the crystal twice to connect the conducting channel and the electrodes, which, to certain extent, will have a negative impact on the performance of the device; thus, the selection of nanostructures with reasonable

thickness is crucial; too thick crystals will cause injection problems, thereby reducing the performance of the device.

12.4

The Preparation of Organic Nano Field-Effect Transistor

12.4.1

The Transfer of Organic Nanocrystals

In order to prepare nano-OFETs, it is important to transfer nanocrystals to substrates with top-contact or bottom-contact device configurations. Growing crystals directly on the substrate is the most facile way. This simple method can grow crystals on electrodes in advance of substrates or prepare crystals on the substrate and then deposit electrodes. It is widely used in solution-processed nanocrystals in bottom-contact devices. For instance, DT-TTF and DB-TTF were prepared by Mas-Torrent *et al.* [41,42], α - and β -phase TTF were reported by Hu and coworkers [44], RRP3HT fibers were made by Merlo and Frisbie [53,54], CH₄T and BPE-PTCDI were synthesized by Bao and coworkers [33,57], and thiophene-biphenyl was demonstrated by Yamao *et al.* [64]. More complex electrode structure devices such as four-point probe also can be fabricated by this method. However, devices were randomly scattered on the substrate, could not be manipulated, and exhibited lower device performance. As for top-contact device configurations, Cho and coworkers [55,59] fabricated poly(3-hexylthiophene) (P3HT) crystalline fibers and TIPS-PEN nanoribbon on substrates, and then deposited electrode using a mask.

In bottom-contact configurations, electrodes generally rose from the dielectric surface. It is difficult for crystals to form good contact between the electrode and the substrate grown by vacuum deposition. Therefore, it is preferred that nanocrystals are first prepared on the substrates, followed by deposition of the electrodes to form top-contact configurations. Wang and coworkers [29] grew perylo[1,12-*b,c,d*]thiophene (PET) nanocrystals on Si/SiO₂ by a vacuum process. Electrodes were further deposited by a mask method. In fact, many nanocrystals prepared by vacuum deposition did not grow along the substrate horizontally, and they inclined on the substrate surface at angles such as CuPc. To make devices, crystals need to be transferred to horizontal substrates.

Seed-mediated growth is a better way developed by Hu and coworkers to solve this problem [23]. They collected previously prepared CuPc single-crystalline submicrometer-sized ribbons, immersed it in ethanol, and sonicated to obtain a CuPc nanocrystal suspension. The larger nanocrystals deposited on the bottom after standing and the smaller one was suspended in the supernatant. Then, Si/SiO₂ substrates treated with oxygen plasma were dipped into the suspension to predeposit CuPc nanocrystals on their surface. The predeposited SiO₂/Si substrates were transferred into a physical vapor transport system to grow CuPc nanoribbons extending along the surface of the substrate (Figure 12.24). It was

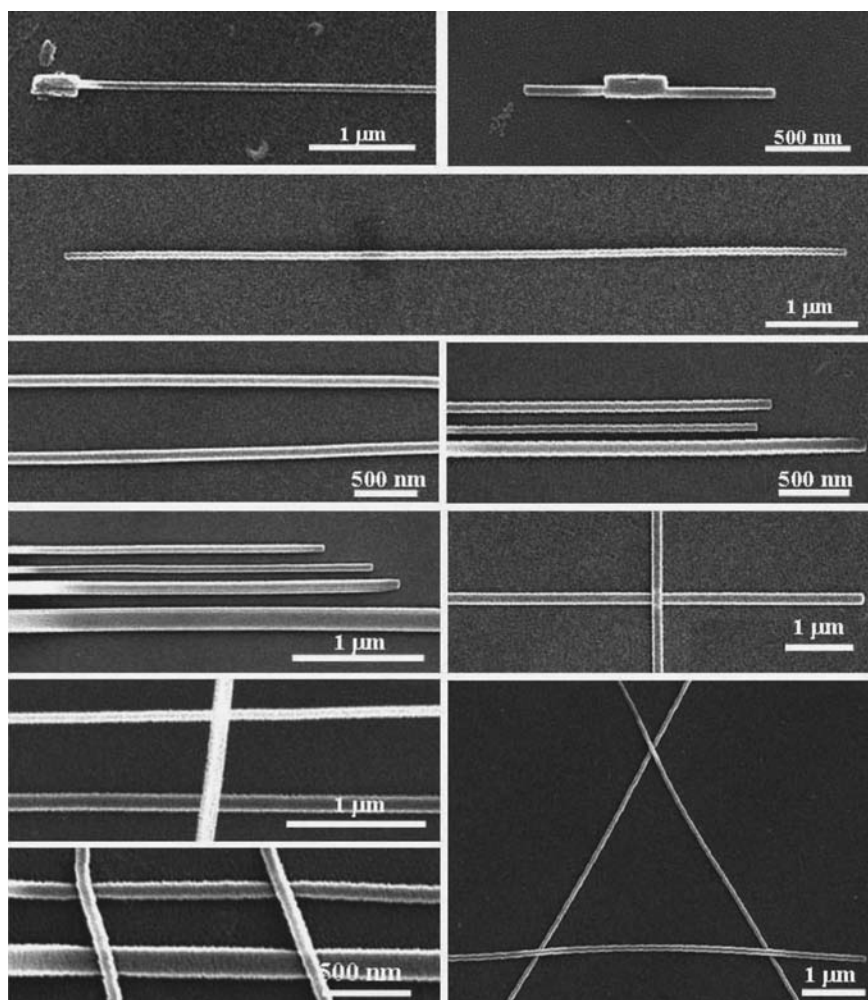


Figure 12.24 CuPc single-crystal nanoribbons extending along the surface of substrates grown by seed-mediated growth.

easier to grow nanocrystals *in situ* by directly dropping solution on substrates or putting substrates in solution. Recently, many soluble and high-performance organic semiconductor molecules have been synthesized, and they were widely used in the solution-processed nanocrystals [35–38,47,49,56,62,78].

Tang *et al.* developed a new method to transfer nanocrystals by mechanical probes under an optical microscope at magnifications of 400–1000 \times [22]. The probes on a highly precise mechanical prober can take crystals grown on the substrate with an angle and then place them on a target portion of the substrate. The accuracy of location was less than 20 μm . The mobility of single-crystal

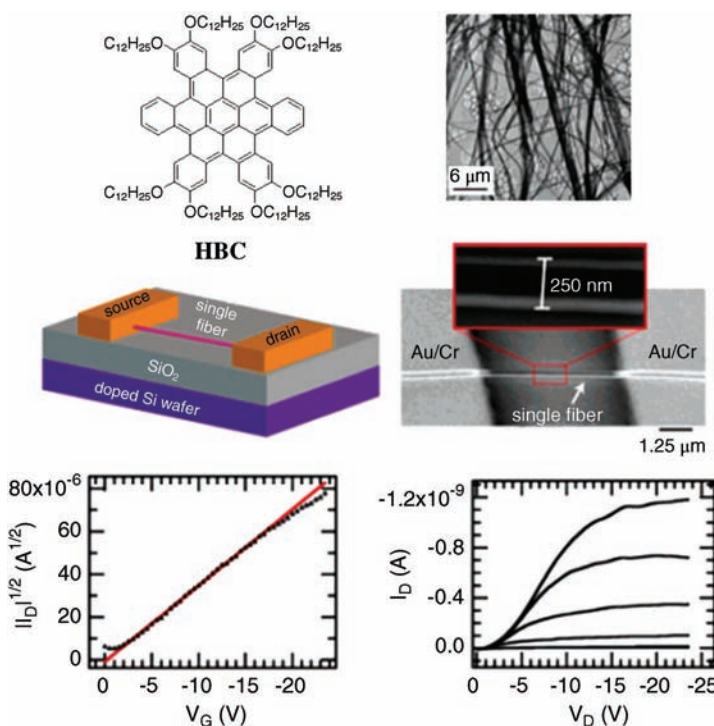


Figure 12.25 Solution-processed assembly of HBC nanocrystals and its corresponding OFETs.

OFETs based on CuPc submicrometer belt was over $0.1 \text{ cm}^2 \text{ V}^{-1} \text{ s}^{-1}$. The advantage of this method was that the interest crystals were selected arbitrarily and accurately put on the substrate. The assembly of more complex patterns can also be carried out, which was very difficult with other approaches. However, the efficiency was low since individual crystals were transferred at a time and there was high requirement for operation.

In view of the transfer of carbon nanotubes, Nuckolls and coworkers [43] introduced elastomer stamps technology to move nanocrystals (Figure 12.25). HBC nanofibers were grown by drop casting and then a piece of PDMS was pressed gently on the nanofibers. Parts of nanofibers adhered to the PDMS and these stamps were pressed into a substrate. A few nanofibers were shifted to the substrate. Next, they fabricated devices in both top-contact and bottom-contact device configurations and found that top-contact one showed superior performance to the bottom-contact one. Nevertheless, the carrier mobility was only up to $0.02 \text{ cm}^2 \text{ V}^{-1} \text{ s}^{-1}$ even in the top-contact one. In 2012, Guo and coworkers [34] loaded the thiophene derivative microribbons by a nondestructive elastomer-based transfer technique onto OTS-treated silicon wafers with the highest mobility up to $6.2 \text{ cm}^2 \text{ V}^{-1} \text{ s}^{-1}$. This value was far above the value of $0.2 \text{ cm}^2 \text{ V}^{-1} \text{ s}^{-1}$ of the corresponding thin-film devices. This technology can effectively

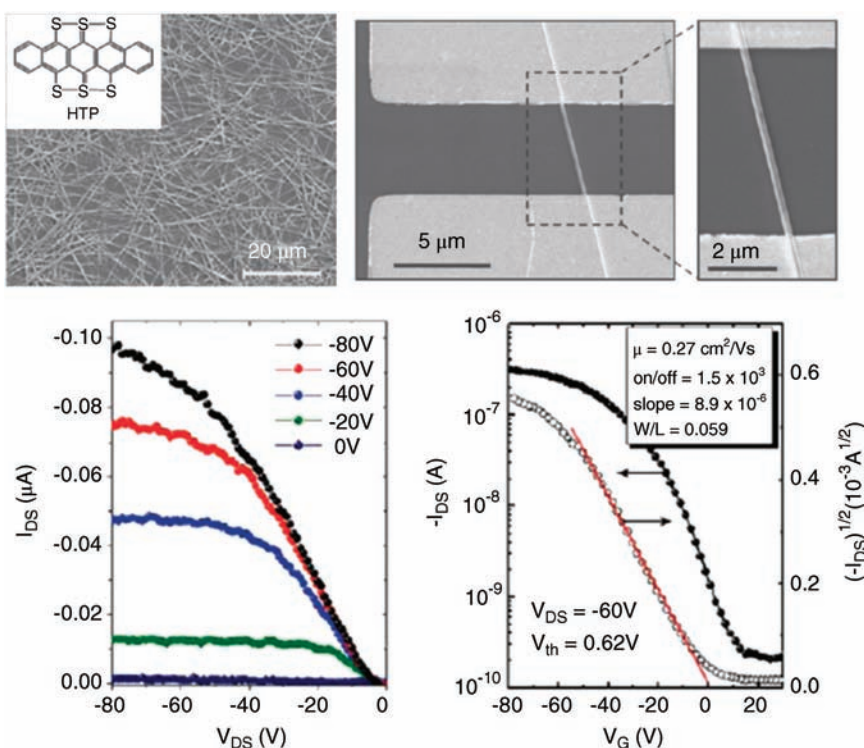


Figure 12.26 Typical OFETs from HTP single-crystalline nanowires.

disperse dense crystals in solution or on substrates to the substrate, which was advantageous in constructing devices. Crystals can also grow on the PDMS stamps and it would be transferred to the substrate directly [79]. But the transferring process was random and crystals cannot be diverted to accurate location.

For the transfer of inorganic semiconductor nanocrystals, crystals first dispersed in volatile organic solvents. Then a small volume of suspension was dropped on the substrate upon which crystals could grow with time. However, it is difficult to transfer organic crystals in such way as most of the organic crystals were easily aggregated. Usually, ultrasonic treatment was used to disperse inorganic crystals, but it was not suitable for scattering organic crystals as the ultrasonic treatment could destroy organic crystals, turning them into fragments. This approach may work for relatively dispersed organic crystals. Bao and co-workers made single-crystal OFETs based on HTP molecules in this way [80]. The previously prepared HTP single-crystalline nanowires were decentralized in ethanol and then dropped on the Si/SiO₂ substrate to fabricate bottom-contact OFETs (Figure 12.26). Ichikawa *et al.* [30–32] adopted similar method to prepare single-crystal devices on the basis of thiophene–benzene copolymer BP2 T prepared by a hot wall epitaxy technology. KCl crystal covered with nanocrystals

was immersed in water. Nanocrystals were separated from the KCl crystal and next was shifted to a Si/SiO₂ substrate (Figure 12.5). However, this easy method had limited scope of application and could not tune the transferring process.

12.4.2

Electrode of Organic Semiconductor Nanocrystal Field-Effect Transistor

Due to the sensitivity of organic semiconductor to solvent and radiation, lithography and electron beam exposure commonly used in inorganic nanodevice were not suitable in organic electronic device fabrication. As more and more research efforts have been made in organic nanocrystal field-effect transistors, multiple kinds of fabrication procedures have been developed to overcome these problems.

Source and drain electrode with bottom-contact configuration fabricated with conventional lithography and electron beam exposure is the most simple and suitable method. Multiple kinds of patterns were prepared on the substrate with this traditional preparation procedure, and a thin film of Ti or Ni (1.5–5 nm) was thermally evaporated on the substrate as adhesion layer. Gold thin film was thermally evaporated as the conductive layer. Gold is chemically stable, resistant to oxidation, highly conductive, and the work function of gold matches well with the highest occupied molecular orbital (HOMO) level of many organic semiconductors. All of these make gold one of the most desirable electrode materials. However, the adhesion ability of gold was rather poor, gold film directly evaporated onto the substrate was easily exfoliated in solution. Therefore, it is necessary to evaporate thin layer of Ti or Ni as adhesion layer to enhance to adhesion ability of bottom-contact electrode. Bao and coworkers [57,80], Mas-Torrent *et al.* [41,42], and Yamao *et al.* [64] have adopted this method to fabricate organic electronic device. However, this bottom-contact electrode configuration included step structure that influences the device fabrication. Some of the research groups used lithography method to etch thin layer of SiO₂ and evaporate metal thin film onto the groove to eliminate the influence of step. Liu *et al.* [73] fabricated rrP3HT nanofiber organic field-effect transistor using this method (Figure 12.22).

Shadow mask is another commonly used method in fabricating organic semiconductor nanodevice. Briefly, the middle of organic nanostructure was covered by mask and both ends were exposed, and then the metal electrode or other kind of material was thermally evaporated under vacuum chamber. The electrode covered the exposed area of nanostructure with conducting channel left. So far, shadow mask used in this procedure includes ultrathin gold wire, copper grid, and custom-made mask.

Tang *et al.* [22,23] have developed multiple times gold wire shadow mask method. First, individual single-crystal CuPc nanowire was transferred onto SiO₂ substrate across the pre-evaporated electrodes (Figure 12.27). Second, ultrathin gold wire was located on the CuPc nanowire with gold wire parallel to electrode. The gold wire was fixed with silver paste. With delicate control of gold nanowire, suitable area of nanowire was chosen as conducting channel. Finally,

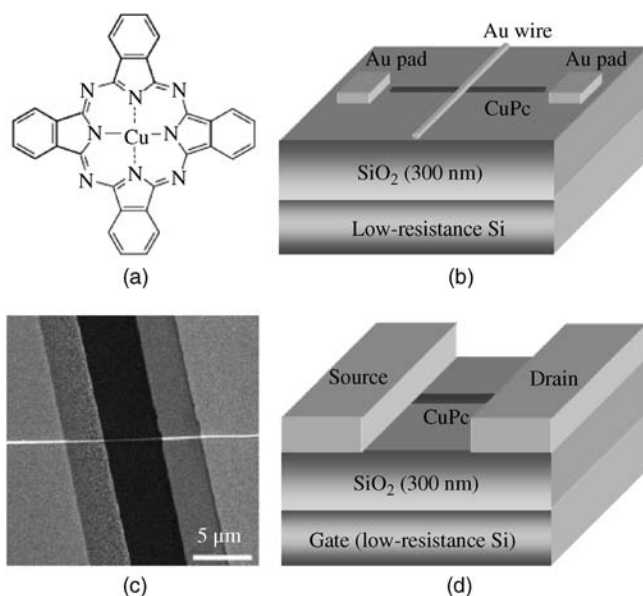


Figure 12.27 Top-contact CuPc nano field-effect transistor.

the substrate was thermally evaporated with gold as the electrode. Gold wire acted as shadow during the evaporation procedure. CuPc nanowire covered by the gold wire was defined as the conducting channel. The area left behind that evaporated with gold was defined as the drain and source electrodes. After the first evaporation completed, the gold wire could be slightly moved under optical microscopy with manipulator and a second layer of metal was evaporated. This process could repeat for several times to minimize the conducting channel length effectively. Furthermore, organic CuPc single crystals were grown *in situ* on Si/SiO₂ from crystal seeds to fabricate the devices with high performance.

Shadow mask using multiple time movement is used in fabricating not only symmetric drain and source electrodes but also the asymmetrical electrode. Tang *et al.* [24] prepared F₁₆CuPc single-crystal nanobelt with physical vapor transport method. Gold wire was used as shadow mask to define drain and source electrodes. After the gold deposition, the gold wire was slightly moved and silver was thermally evaporated. Asymmetrical electrode was completed as shown in Figure 12.28. As the work function of both gold and silver did not match with the lowest unoccupied molecular orbital (LUMO) level of F₁₆CuPc, the introduction of this unique asymmetrical electrode facilitated the injection and transport of charge carrier. It turned out that F₁₆CuPc single-crystal device with asymmetrical configuration showed improved device performance with highest mobility reported to date.

As the location of ultrathin gold wire could be precisely controlled with relatively high success rate, it is an ideal method to fabricate nanodevice. In addition,

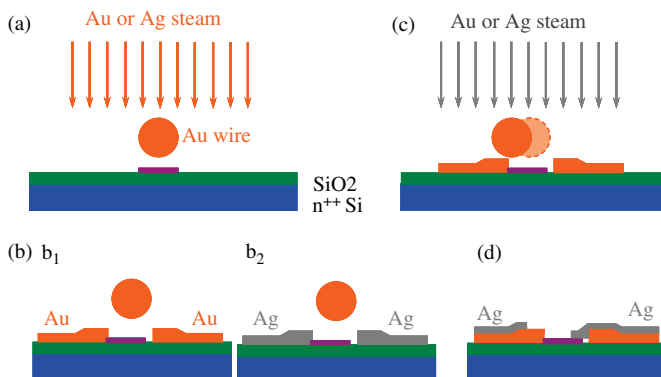


Figure 12.28 Fabrication procedure of top-contact nano field-effect transistor with asymmetrical configuration. (a and b) Deposition of gold electrode. (c and d) Deposition of silver.

this method does not involve expensive equipment such as lithography and electron beam exposure, and hence the cost is rather low. No solvent was needed, and therefore no contamination was introduced. However, the efficiency was relatively low and delicate experimental technique was needed.

Copper grid is a commercially available, regular-patterned metal grid that is often used in transmission electron microscope (TEM). It could also be used as shadow mask in fabricating electrode of organic semiconductor nanodevice. In 2006, Cho and coworkers [55] fabricated poly(3-hexylthiophene) crystalline nanofiber device with copper grid (Figure 12.23). Copper grid is easy to access and process, and a highly regular pattern is achieved facilely with this method. However, the size of the copper grid is relatively large ($>35\text{ m}$), so the length of the conducting channel is rather high and unable to adjust. The devices prepared using this method are random.

Gold wire and copper grid are simple and convenient solutions in the fabrication of electrode patterns. However, the electrode patterns of the drain and the source are rather limited. Complicated pattern is unable to fabricate using this method. Merlo and Frisbie [53,54] prepared shadow mask using a different method, as shown in Figure 12.29. First, Si_3N_4 was deposited on the Si wafer. Second, the pattern was prepared through lithography and Si_3N_4 was etched. Third, metal line was deposited and Si was etched with KOH. Finally, the second etch of Si_3N_4 was performed. Then, the shadow mask was used in thermal evaporation to complete the fabrication process. Complicated and ultrafine electrode pattern was prepared using this procedure. However, the fabrication procedure was complex and not easy to access by all the researchers.

Shadow mask could also be prepared using etch of stainless steel foil with laser or electroplating with Ni. During all of these preparation procedures, expensive equipment was needed.

Thermal evaporation was inevitable in metal film deposition during the fabrication procedure. The thermal irradiation during the process would influence

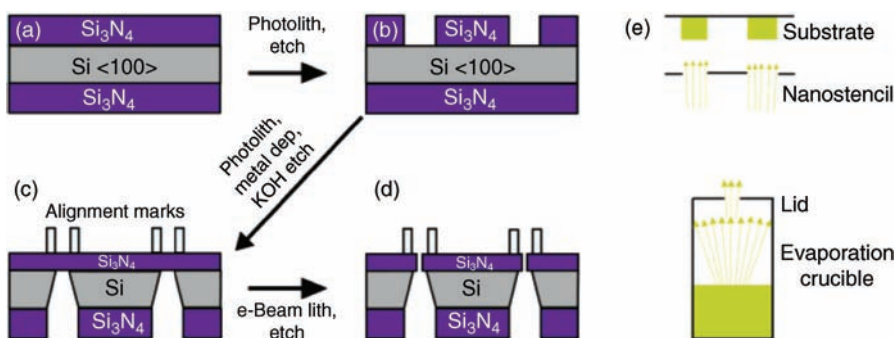


Figure 12.29 Preparation of Si shadow mask.

the packing of the surface molecules of organic single crystals, so the charge barrier was formed influencing the contact between the electrode and organic crystals. Furthermore, metal atoms would penetrate into organic semiconductor and influence the contact. In order to minimize the thermal damage of the thermal irradiation to organic semiconductor nanostructures, multiple kinds of methods were used. Tang *et al.* increased the distance between the evaporation source and the substrate, used as small as possible thermal evaporation source, and placed stainless steel between the evaporation source and the substrate to minimize the thermal irradiation. All of these methods increased the device performance.

Although the above-mentioned method could significantly reduce the thermal irradiation during the electrode deposition, they could not eliminate the thermal irradiation influence. In order to overcome this problem, Tang *et al.* [81,82] developed a gold thin film technique (Figure 12.30). First, gold thin film was thermally evaporated onto the Si wafer and the gold thin film was adhered to the substrate barely with van der Waals force. Second, gold thin film was sliced into small pieces, picked up with manipulator tip, and transferred onto the nanostructure. Due to the good flexibility and ductility of gold thin film, the gold film would adhere to the substrate and the nanostructure with good electronic

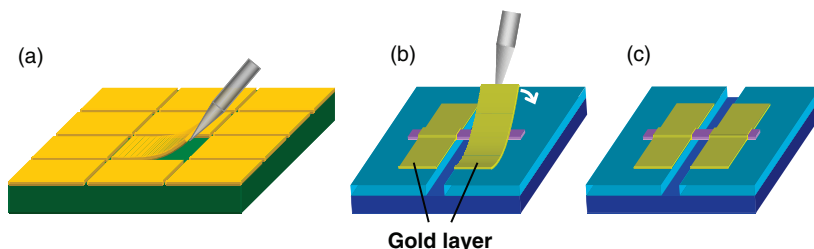


Figure 12.30 Preparation of organic single-crystal field-effect transistor with gold thin-film adhesion technique.

contact. In order to form good electronic contact between the organic semiconductor and the gold thin film, the surface of both the organic semiconductor and the gold thin needs to be first cleaned. The silicon wafer was carefully washed to remove contaminant. Organic single crystals used in this procedure, namely, CuPc and $F_{16}CuPc$, were prepared through physical vapor transport. Second, the bond between gold thin film and organic semiconductor was good. On one hand, the good flexibility and ductility of gold thin film ensured the good contact between the gold film and the organic semiconductors; on the other hand, nanostructure was slightly above the substrate that ensured the contact. All the above-mentioned methods ensured the good electric contact between the gold thin film and CuPc or $F_{16}CuPc$ nano single crystals. Bipolar organic single-crystal nanobelt transistor with air as dielectric layer was prepared using this technique, with hole mobility of $0.1\text{ cm}^2\text{ V}^{-1}\text{ s}^{-1}$ and electron mobility of $0.17\text{ cm}^2\text{ V}^{-1}\text{ s}^{-1}$, which were two orders of magnitude higher than the performance of bipolar organic thin film device [83–85]. This method has been utilized in preparing other kinds of organic single-crystal material devices and high performance was achieved [27,39].

These methods effectively improved the performance of the devices and revealed the intrinsic characteristics of organic semiconductors. However, these methods also have some limitations. For example, it requires that the crystal is one dimensional with length more than $20\mu\text{m}$. But many organic crystals did not meet this requirement. Fabricating devices on ultrashort organic crystals is still a great challenge so far. On the basis of already-mentioned shadow mask technology, Hu *et al.* have developed “organic ribbon mask” technique to deposit electrodes on organic crystals by using mechanical probes to transfer organic nanoribbon onto the surface of crystals. Figure 12.31 demonstrated the fabrication procedure of crystal device using an individual organic nanoribbon as shadow mask. The channel length was dependent on the width of the organic ribbon and could be scaled down to hundreds of nanometers, which opens a new cost-effective and facile way to fabricate organic single-crystal devices with a short conducting channel without lithography. Moreover, based on this technique, a “two-dimensional organic ribbon mask” technique was developed [25]. Electrode pairs were fabricated on an individual microcrystal to study the anisotropic charge transport along the different crystal axis directions. Hu and coworkers [25,26] and Tao and coworkers [86] conducted representative research work in this area. In 2009, Hu and coworkers reported that highly regular hexagonal single crystals of dibenzo[*d,d'0*]thieno[3,2-*b*;4,5-*b'0*]dithiophene (DBTDT) grown on Si/SiO₂ using physical vapor transport could be controlled. Electrode pairs were fabricated on an individual microcrystal with multiconducting channels along the different crystal axes and crystal planes with “multiorganic ribbon mask” technique. The transistors exhibited mobilities as high as $1.8\text{ cm}^2\text{ V}^{-1}\text{ s}^{-1}$ with on/off ratios typically $>10^7$. The mobility anisotropy along the *c*-axis was around 2–2.5 times than that along the *a*-axis. In 2012, Tao and coworkers [86] synthesized 4,4'-bis((E)-2-(naphthalen-2-yl)vinyl)-1,1'-biphenyl (BNVBP). BNVBP single crystals were obtained through physical vapor transport

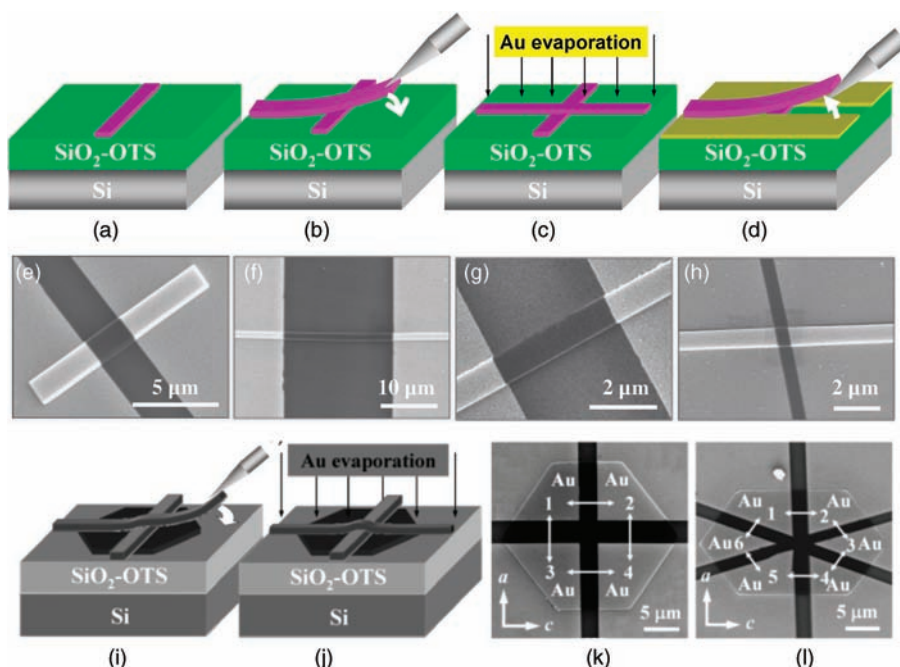


Figure 12.31 (a–d) Preparation of organic single-crystal field-effect transistor with nanowire shadow mask. (e–h) the SEM images of devices using “organic ribbon mask” method.

(i and j) Multiple time shadow mask deposition using nanowire mask. (k and l) SEM image with organic single-crystal field-effect transistor with anisotropic electrode pairs.

method. By controlling the growth conditions, single crystals were grown either on hexagonal plate or on 1D microrod. The charge mobility in hexagonal crystal [100] [110] [010] direction were 2.3, 0.6, and $1.1 \text{ cm}^2 \text{ V}^{-1} \text{ s}^{-1}$, while its charge mobility were only 0.4 and $0.016 \text{ cm}^2 \text{ V}^{-1} \text{ s}^{-1}$ in micrometer-sized rods single crystal [100] [001] directions. In conclusion, the mobility difference along the long and short axes of one-dimensional nanostructure were much larger than the corresponding two-dimensional crystal. The one-dimensional structure agrees well with its crystal structure, suggesting the intrinsic transport properties of these materials. Au thin film [81] can also be used as mask for deposition electrode to obtain good performance [28,36]. With this method, Hu and coworkers [36] fabricated c12-4Cl-diPBI single-crystal field-effect transistor with highest electron mobility up to $4.65 \text{ cm}^2 \text{ V}^{-1} \text{ s}^{-1}$. Li and coworkers [28] reported 6,13-Dichloropentacene (DCP) single-crystal field-effect transistor with highest hole mobility of $9 \text{ cm}^2 \text{ V}^{-1} \text{ s}^{-1}$.

Focused ion beam (FIB) is a common micromachining and microelectrode deposition technology in depositing electrode on inorganic nanodevices. During the deposition process, Pt and organic thin layer would form around electrodes that contaminated the device channel. In addition, electron or Ga ion imaging

was used in this technology and high-energy particle radiation would damage the semiconductor microstructure, decreasing the electrical properties. Tang *et al.* [22] demonstrated that high-energy electron radiation will decrease the performance of small-molecule organic nano single-crystal devices, so FIB technique is not suitable for the preparation of small-molecule organic nanodevices. In 2012, Pisula and coworkers [56] reported that CDT–BTZ polymer fiber field-effect transistor was fabricated using FIB technique with highest mobility of $5.5 \text{ cm}^2 \text{ V}^{-1} \text{ s}^{-1}$. This research demonstrated that OFETs based on individual CDT–BTZ copolymer fiber were embedded in SiO_2 protection layer before depositing two Pt electrodes using a focused ion beam can get better performance. All these results illustrated that Pt and organic do not mainly influence the device performance and that high-energy particle has less effect on the electric properties of polymer nanowires. This result was inconsistent with previous research. The possible explanations are (i) pollutants could not cover the entire channel because the conducting channel was long enough and (ii) inside the CDT–BTZ copolymer fiber, the conjugated molecular chain was long enough, and the high-energy particle may cause some part of the polymer chain deformation. But under the action of chain segment movement, it can quickly return to its original position. As long as the polymer chains were not broken by high-energy particle radiation, their electrical properties would not alter significantly. Different from conjugated polymers, molecules could not return to its original position after displacement in small-molecule organic nanocrystal under high-energy particle radiation and its electrical properties would decrease. From the experimental results, polymer organic semiconductor to the radiation resistance was strong enough and could be applied to some radiation environment.

12.5

Properties of Organic Nanoscale Field-Effect Transistor

Recently, great progress has been made in organic nano field-effect transistor with improved performance. Figure 12.32 shows the molecular structure of organic semiconductor materials commonly used in organic nano field-effect transistor.

Organic nano single crystals usually have superior properties than their film counterparts. Hu and coworkers have reported high-performance FET devices based on CuPc single crystal with mobility of $0.1\text{--}0.2 \text{ cm}^2 \text{ V}^{-1} \text{ s}^{-1}$. The best mobility can reach $0.5 \text{ cm}^2 \text{ V}^{-1} \text{ s}^{-1}$. The CuPc film FETs fabricated by Xiao [87] through controlling the substrate temperature however showed poor mobility of only $4.13 \times 10^{-3} \text{ cm}^2 \text{ V}^{-1} \text{ s}^{-1}$. Bao *et al.* reported the mobility of CuPc film FETs was $0.02 \text{ cm}^2 \text{ V}^{-1} \text{ s}^{-1}$ even with an optimized substrate temperature [10]. It can be seen that FET based on CuPc single crystal reveals high promoted properties than that based on CuPc film. It is thus easily comprehended that crystalline grain in film always has disorderly defects, which could trap the charges. And boundaries among crystal grains act as potential barriers that charges must conquer during transportation. On the contrary, the entire conducting channel in a

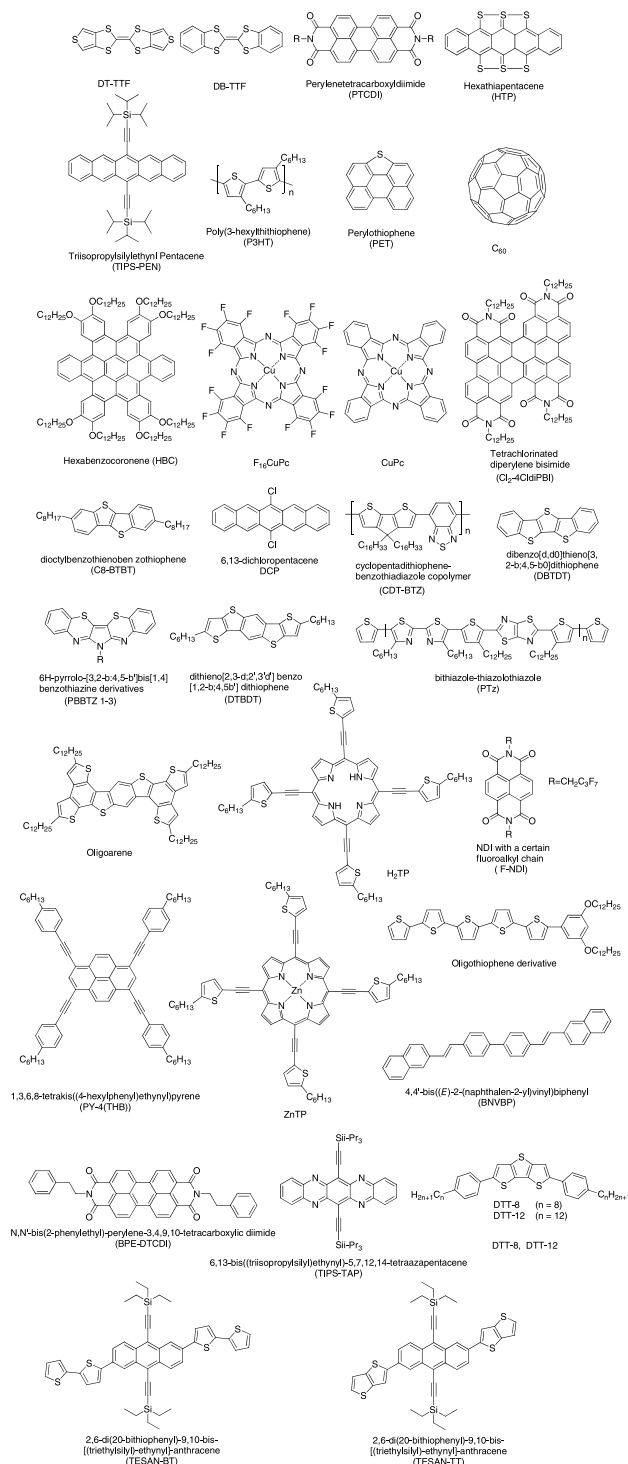


Figure 12.32 Molecular structure of commonly adapted organic semiconductor in organic nano field-effect transistor.

nano-FET device is made up of a single crystal, without grain boundaries and disorderly defects. This results in the high device performance. However, nano-FET devices exhibit lower capacities than that based on large crystal. Zeis *et al.* reported large-size CuPc single-crystal FET devices with $0.7\text{--}1.3\text{ }\mu\text{m}$ poly-*p*-xylene as dielectrics and aquadag as electrode, indicating mobility as high as $1\text{ cm}^2\text{ V}^{-1}\text{ s}^{-1}$ [9]. Reasons for these differences may lie in the strict fabrication conditions of nano-FET devices. Even very small fabrication defects, such as heat radiation and metal atoms diffusion when depositing electrodes and small flaws at the interface of organic semiconductor and dielectrics, can severely impact the properties. On the other hand, with more researchers entering the field and new fabrication techniques springing up, organic nano-FETs will be improved to the large-size devices level and manifest better application prospect.

12.6

Application of Organic Nano-FETs

To date, the organic nanocrystal field-effect transistors were mainly applied to investigate the relationship between the structure and the performance of the organic semiconductor materials and their intrinsic characteristics. Although the small working current of these devices limited their use in the drive circuits, it cannot forbid their application in other fields, such as sensor, photoswitch, logic circuit, and so on.

In 2006, Mas-Torrent and coworkers [88] first reported the photoresponsive behavior of TTF derivative DT-TTF nanoscale single crystal-based organic field-effect transistor, which was fabricated by the solution-processed method in a bottom-contact configuration. The light-to-dark-current ratio was up to 10^4 when irradiated with white light of 2.5 W cm^{-2} at $V_G=10\text{ V}$. But the devices exhibited obvious sustained photoconductive effect, namely, after withdrawal of the light, the photogenerated carriers would not be an entire recombination in a short time, but a part still contributed to the source-drain current (I_{SD}) that increased I_{SD} with respect to that before irradiation. The response time of optical field-effect transistor based on DT-TTF crystal they prepared exceeded 20 s, and only the very large gate voltage could induce the sustained photoconductive effect, but correspondingly the light response time was shortened to less than a few seconds.

Pei and coworkers cooperated to control the synthesis of a benzothiophene derivative nanowires [58], and further investigated the applications of these wires in optical devices, light-emitting diodes (LEDs), and TNT exploration, and achieved significant results [89].

In 2007, Tang *et al.* [90] found that F_{16}CuPc single-crystal nanoribbons possessed a good photoswitch property when studying the electrical property in the nanoribbons-based field-effect transistors (Figure 12.33). They found that when the gate voltage was zero and the source-drain voltage was held constant with or without the incident light, the device could be very well switched between the on

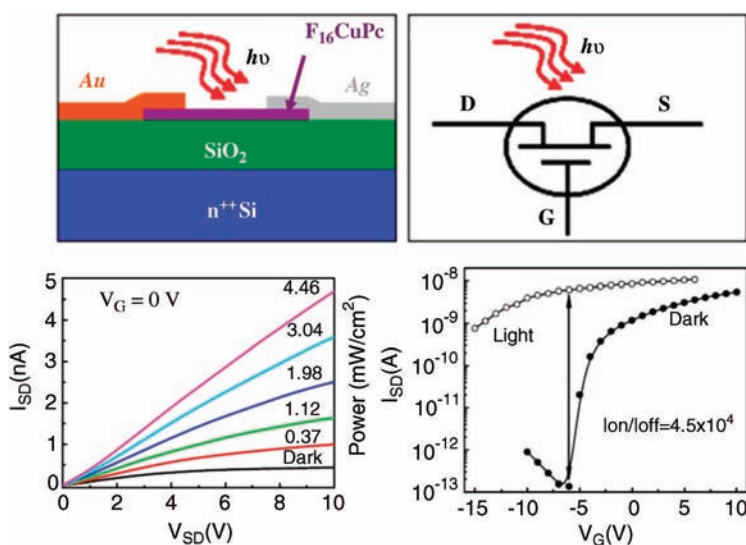


Figure 12.33 Diagram of work mode and output as well as transfer characteristics of optical OFET based on F₁₆CuPc single-crystal nanoribbons.

state (high current) and off state (low current), with the short response time, excellent reproducibility, and very good stability. They also found that CuPc single-crystal nanoribbons can also possess the light response characteristics. With respect to the CuPc devices, F₁₆CuPc devices exhibited a higher light-to-dark-current ratio (4.5×10^4), indicating that it was a more excellent photoconductor. They also investigated the work mode of optical field-effect transistor based on F₁₆CuPc single-crystal nanoribbons. The experimental results showed that with the fixed gate voltage, the obtained output curves under different light intensities were very similar to the output curves in the conventional enhanced field-effect transistor. With the fixed source–drain voltage, when studying the relationship between the output currents with different gate voltages and different light intensities, they found that the output curves were very similar to those obtained in the conventional depletion mode field-effect transistor. These results indicated that the light intensity can be used as the fourth gate electrode besides the source, drain, and gate electrodes to modulate the output properties of the devices. Furthermore, it was also a multifunctional device with the optical detection and the signal amplification functions. In 2013, Bao and coworkers [33] systematically compared the photoresponse properties of BPE-PTCDI nanowire- and thin film-based devices, and found that nanowire-based device exhibited much better photoelectric properties than the thin-film device, with an on-state photocurrent density higher than 10^4 . In addition, many other groups also conducted many works in this area [75,77,82].

The relatively small device operating current limited its application in the current drive circuit, but cannot affect the application in the circuits where voltage

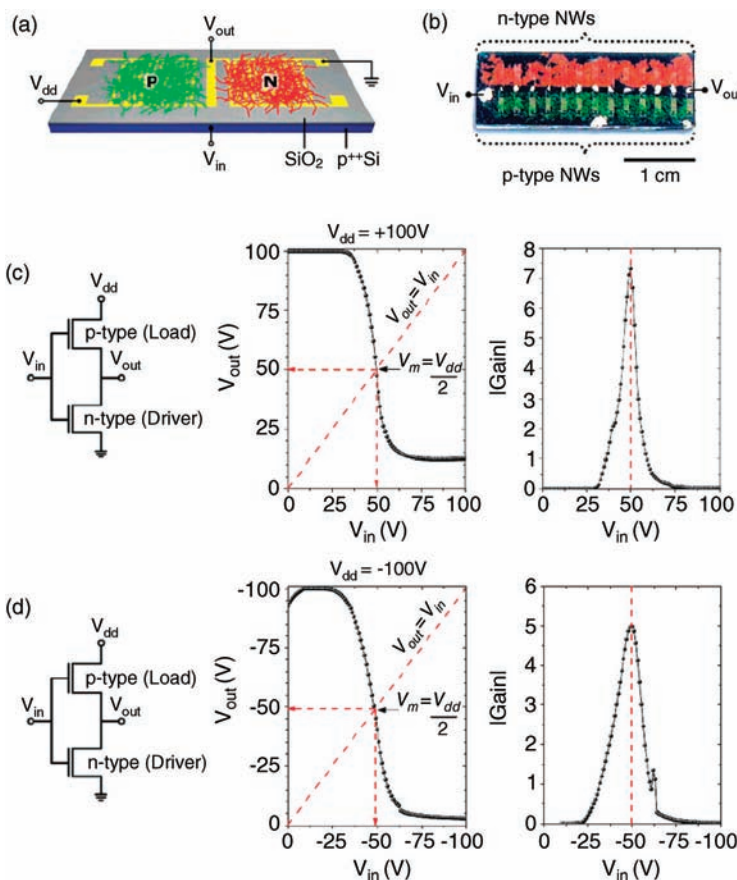


Figure 12.34 Organic nanowires-based inverter circuit.

was the primary signal, such as logic circuits. In this respect, Bao and coworkers cooperated to explore the research [61]. They made n-type organic semiconductor PTCDI-Cn nanowires-based device integrated with p-type organic semiconductor HTP nanowires-based device (Figure 12.34a) and fabricated a complementary symmetry inverter circuit (Figure 12.34c and d). Besides, they further studied their application in inverter circuits [91].

In OFET, as a field control device, its charge carriers were almost entirely concentrated within the very thin range of the semiconductor/insulator interface, so that even a tiny change in conducting channel environment would be enlarged, causing a great current change, which indicated that it is a good candidate for sensor. Organic field-effect gas sensor is an important branch of organic electronics. The large specific surface area of organic nanocrystal would improve the sensitivity, and the high crystalline quality is in favor of the investigation of the sensing mechanism. Therefore, it is more superior to apply the field-effect

devices in gas sensing. However, the conventional field-effect transistor usually adopts a solid dielectric layer and the conductive channel is sandwiched between the dielectric layer and the semiconductor, which cannot directly contact with the gas to be measured and limits the full action of the sensing function. In 2013, Tang and coworkers [92] employed air as an insulating layer to fabricate an organic field-effect transistor based on CuPc nanocrystal and applied it in SO₂ detection. The gas dielectric layer can make the test gas to directly contact with the conducting channel, which caused the device to have a lower detection limit and higher sensitivity as shown in Figure 12.35. It was for the first time that the semiconductor sensors were used to achieve a rapid detection of 0.5 ppm of SO₂ at room temperature, and the sensitivity was up to 100%, well above the solid insulated layer-based devices prepared under the same conditions (detection limit of 10 ppm and sensitivity of 20%).

12.7

Summary and Outlook

Until now, people have carried out multiparty exploration in the organic nano-device applications. Although it is still a relatively narrow range of applications, most of the performance has been able to meet the needs of the practical application, and certain aspects proposed can be compared with inorganic materials. With more researchers entering the field and developing a series of new technologies and methods, this area is becoming more and more mature.

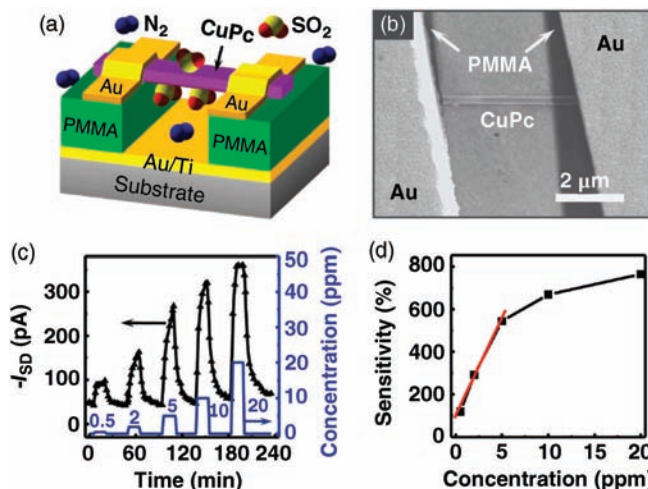


Figure 12.35 Schematic diagram (a) and scanning electron micrograph (b) of gas-insulated layer-based FETs SO₂ gas sensor. The current response (c) and gas response sensitivity (d) for different concentrations of SO₂.

References

- 1 Butko, V.Y., Chi, X., Lang, D.V., and Ramirez, A.P. (2003) Field-effect transistor on pentacene single crystal. *Appl. Phys. Lett.*, **83**, 4773.
- 2 Butko, V.Y., Chi, X., and Ramirez, A.P. (2003) Free-standing tetracene single crystal field effect transistor. *Solid-State Commun.*, **128**, 431.
- 3 Podzorov, V., Pudalov, V.M., and Gershenson, M.E. (2003) Field-effect transistors on rubrene single crystals with polyimide gate insulator. *Appl. Phys. Lett.*, **82**, 1739.
- 4 Podzorov, V., Sysoev, S.E., Loginova, E., Pudalov, V.M., and Gershenson, M.E. (2003) Single-crystal organic field effect transistors with the hole mobility $\sim 8 \text{ cm}^2 \text{V}^{-1} \text{s}^{-1}$. *Appl. Phys. Lett.*, **83**, 3504.
- 5 Sundar, V.C., Zaumseil, J., Podzorov, V., Menard, E., Willett, R.L., Someya, T., Gershenson, M.E., and Rogers, J.A. (2004) Elastomeric transistor stamps: reversible probing of charge transport in organic crystals. *Science*, **303**, 1644.
- 6 DeBoer, R.W.I., Gershenson, M.E., Morpurgo, A.F., and Podzorov, V. (2004) Organic single-crystal field-effect transistors. *Phys. Stat. Sol.*, **201**, 1302.
- 7 Simon, J. and Andre, J.J. (1985) Chapter 1, in *Molecular Semiconductors*, Springer, Berlin.
- 8 Leznoff, C.C. and Lever, A.B.P. (1993) Chapter 1, in *Phthalocyanines: Properties and Applications*, vol. 3 (eds C.C. Leznoff and A.B.P. Lever), Wiley-VCH Verlag GmbH, New York.
- 9 Zeis, R., Siegrist, T., and Kloc, C. (2005) Single-crystal field-effect transistors based on copper phthalocyanine. *Appl. Phys. Lett.*, **86**, 022103.
- 10 Bao, Z., Lovinger, A.J., and Dodabalapur, A. (1996) Organic field-effect transistors with high mobility based on copper phthalocyanine. *Appl. Phys. Lett.*, **69**, 3066.
- 11 Horowitz, G. (1998) Organic field-effect transistors. *Adv. Mater.*, **10**, 365.
- 12 Zhivkov, I., Nešpurek, S., and Schauer, F. (1999) Influence of oxygen on the parameters of a thin film copper phthalocyanine field effect transistor. *Adv. Mater. Opt. Electron.*, **9**, 175.
- 13 Kudo, K., Iizuka, M., Kuniyoshi, S., and Tanaka, K. (2001) Device characteristics of lateral and vertical type organic field effect transistors. *Thin Solid Films*, **393**, 362.
- 14 Xiao, K., Liu, Y., Yu, G., and Zhu, D. (2003) Influence of the substrate temperature during deposition on film characteristics of copper phthalocyanine and field-effect transistor properties. *Appl. Phys. A Mater. Sci. Process.*, **77**, 367.
- 15 Xiao, K., Liu, Y., Huang, X., Xu, Y., Yu, G., and Zhu, D. (2003) Field-effect transistors based on Langmuir–Blodgett films of phthalocyanine derivatives as semiconductor layers. *J. Phys. Chem. B*, **107**, 9226.
- 16 Zhang, J., Wang, J., Wang, H., and Yan, D. (2004) Organic thin-film transistors in sandwich configuration. *Appl. Phys. Lett.*, **84**, 142.
- 17 Okuda, T., Shintoh, S., and Terada, N. (2004) Copper-phthalocyanine field-effect transistor with a low driving voltage. *J. Appl. Phys.*, **96**, 3586.
- 18 Cherian, S., Donley, C., Mathine, D., LaRussa, L., Xia, W., and Armstrong, N. (2004) Effects of field dependent mobility and contact barriers on liquid crystalline phthalocyanine organic transistors. *J. Appl. Phys.*, **96**, 5638.
- 19 Ofuji, M., Ishikawa, K., and Takezoe, H. (2005) Crystallite size effect on the hole mobility of uniaxially aligned copper phthalocyanine thin-film field-effect transistors. *Appl. Phys. Lett.*, **86**, 062114.
- 20 Yasuda, T. and Tsutsui, T. (2005) Organic field-effect transistors based on high electron and ambipolar carrier transport properties of copper–phthalocyanine. *Chem. Phys. Lett.*, **402**, 395.
- 21 Zhang, J., Wang, H., Yan, X., Wang, J., Shi, J., and Yan, D. (2005) Phthalocyanine composites as high-mobility semiconductors for organic thin-film transistors. *Adv. Mater.*, **17**, 1191.
- 22 Tang, Q., Li, H., He, M., Hu, W., Liu, C., Chen, K., Wang, C., Liu, Y., and Zhu, D. (2006) Low threshold voltage transistors based on individual single-crystalline submicrometer-sized ribbons of copper phthalocyanine. *Adv. Mater.*, **18**, 65.

- 23** Tang, Q., Li, H., Song, Y., Xu, W., Hu, W., Jiang, L., Liu, Y., Wang, X., and Zhu, D. (2006) *In situ* patterning of organic single-crystalline nanoribbons on a SiO₂ surface for the fabrication of various architectures and high-quality transistors. *Adv. Mater.*, **18**, 3010.
- 24** Tang, Q., Li, H., Liu, Y., and Hu, W. (2006) High-performance air-stable n-type transistors with an asymmetrical device configuration based on organic single-crystalline submicrometer/nanometer ribbons. *J. Am. Chem. Soc.*, **128**, 14634.
- 25** Li, R., Jiang, L., Meng, Q., Gao, J., Li, H., Tang, Q., He, M., Hu, W., Liu, Y., and Zhu, D. (2009) Micrometer-sized organic single crystals, anisotropic transport, and field-effect transistors of a fused-ring thienoacene. *Adv. Mater.*, **2**, 4492.
- 26** Lv, A., Li, Y., Yue, W., Jiang, L., Dong, H., Zhao, G., Meng, Q., Jiang, W., He, Y., Li, Z., Wang, Z., and Hu, W. (2012) High performance n-type single crystalline transistors of naphthalene bis (dicarboximide) and their anisotropic transport in crystals. *Chem. Commun.*, **48**, 515.
- 27** Wei, Z., Hong, W., Geng, H., Wang, C., Liu, Y., Li, R., Xu, W., Shuai, Z., Hu, W., Wang, Q., and Zhu, D. (2010) Organic single crystal field-effect transistors based on 6H-pyrrolo[3,2-b:4,5-b']bis[1,4] benzothiazine and its derivatives. *Adv. Mater.*, **22**, 2458.
- 28** Wang, M., Li, J., Zhao, G., Wu, Q., Huang, Y., Hu, W., Gao, X., Li, H., and Zhu, D. (2013) High-performance organic field-effect transistors based on single and large-area aligned crystalline microribbons of 6,13-dichloropentacene. *Adv. Mater.*, **25**, 2229.
- 29** Sun, Y., Tan, L., Jiang, S., Qian, H., Wang, Z., Uan, D., Di, C., Wang, Y., Wu, W., Yu, G., Yan, S., Wang, C., Hu, W., Liu, Y., and Zhu, D. (2007) High-performance transistor based on individual single-crystalline micrometer wire of perylo[1,12-b,c,d]thiophene. *J. Am. Chem. Soc.*, **129**, 1882.
- 30** Ichikawa, M., Yanagi, H., Shimizu, Y., Hotta, S., Suganuma, N., Koyama, T., and Taniguchi, Y. (2002) Organic field-effect transistors made of epitaxially grown crystals of a thiophene/phenylene co-oligomer. *Adv. Mater.*, **14**, 1272.
- 31** Yanagi, H., Ashida, M., Harima, Y., and Yamashita, K. (1990) Photoelectrochemical properties of orientation-controlled thin film for 5,10,15,20-tetraphenylporphyrin. *Chem. Lett.*, **19**, 385.
- 32** Toda, Y. and Yanagi, H. (1996) Electroluminescence of epitaxial perylene films. *Appl. Phys. Lett.*, **69**, 2315.
- 33** Yu, H., Bao, Z., and Oh, J.H. (2013) High-performance phototransistors based on single-crystalline n-channel organic nanowires and photogenerated charge-carrier behaviors. *Adv. Funct. Mater.*, **23**, 629.
- 34** Dong, S., Zhang, H., Yang, L., Bai, M., Yao, Y., Chen, H., Gan, L., Yang, T., Jiang, H., Hou, S., Wan, L., and Guo, X. (2012) Solution-crystallized organic semiconductors with high carrier mobility and air stability. *Adv. Mater.*, **24**, 5576.
- 35** Liu, C., Minari, T., Lu, X., Kumatai, A., Takimiya, K., and Tsukagoshi, K. (2011) Solution-processable organic single crystals with bandlike transport in field-effect transistors. *Adv. Mater.*, **23**, 523.
- 36** Lv, A., Puniredd, S.R., Zhang, J., Li, Z., Zhu, H., Jiang, W., Dong, H., He, Y., Jiang, L., Li, Y., Pisula, W., Meng, Q., Hu, W., and Wang, Z. (2012) High mobility, air stable, organic single crystal transistors of an n-type diperylene bisimide. *Adv. Mater.*, **24**, 2626.
- 37** Liu, Y., Dong, H., Jiang, S., Zhao, G., Shi, Q., Tan, J., Jiang, L., Hu, W., and Zhan, X. (2013) High performance nanocrystals of a donor–acceptor conjugated polymer. *Chem. Mater.*, **25**, 2649.
- 38** Wang, S., Gao, P., Liebewirth, I., Kirchhoff, K., Pang, S., Feng, X., Pisula, W., and Müllen, K. (2011) Microribbon field-effect transistors based on dithieno[2,3-d;2',3'-d']benzo[1,2-b;4,5-b']dithiophene processed by solvent vapor diffusion. *Chem. Mater.*, **23**, 4960.
- 39** Wang, C., Liang, Z., Liu, Y., Wang, X., Zhao, N., Miao, Q., Hu, W., and Xu, J. (2011) Single crystal n-channel field effect transistors from solution-processed silylethynylated tetraazapentacene. *J. Mater. Chem.*, **21**, 15201.

- 40** Yun, H.-J., Chung, D.S., Kang, I., Park, J. W., Kim, Y.-H., and Kwon, S.-K. (2012) Novel triethylsilylethynyl anthracene-based organic semiconductors for high performance field effect transistors. *J. Mater. Chem.*, **22**, 24924.
- 41** Mas-Torrent, M., Durkut, M., Hadley, P., Ribas, X., and Rovira, C. (2004) High mobility of dithiophene-tetrathiafulvalene single-crystal organic field effect transistors. *J. Am. Chem. Soc.*, **126**, 984.
- 42** Mas-Torrent, M., Hadley, P., Bromley, S. T., Crivillers, N., Veciana, J., and Rovira, C. (2005) Single-crystal organic field-effect transistors based on dibenzotetrathiafulvalene. *Appl. Phys. Lett.*, **86**, 012110.
- 43** Xiao, S., Tang, J., Beetz, T., Guo, X., Tremblay, N., Siegrist, T., Zhu, Y., Steigerwald, M., and Nuckolls, C. (2006) Transferring self-assembled, nanoscale cables into electrical devices. *J. Am. Chem. Soc.*, **128**, 10700.
- 44** Jiang, H., Yang, X., Cui, Z., Liu, Y., Li, H., Hu, W., Liu, Y., and Zhu, D. (2007) Phase dependence of single crystalline transistors of tetrathiafulvalene. *Appl. Phys. Lett.*, **91**, 123505.
- 45** Jiang, L., Fu, Y., Li, H., and Hu, W. (2008) Single-crystalline, size, and orientation controllable nanowires and ultralong microwires of organic semiconductor with strong photoswitching property. *J. Am. Chem. Soc.*, **130**, 3937.
- 46** Yang, Y.S., Yasuda, T., Kakizoe, H., Mieno, H., Kino, H., Tateyama, Y., and Adachi, C. (2013) High performance organic field-effect transistors based on single-crystal microribbons and microsheets of solution-processed dithieno[3,2-*b*:2',3'-*d*]thiophene derivatives. *Chem. Commun.*, **49**, 6483.
- 47** Zhu, M., Luo, H., Wang, L., Guo, Y., Zhang, W., Liu, Y., and Yu, G. (2013) The synthesis of 2,6-dialkylphenyldithieno[3,2-*b*:2',3'-*d*]thiophene derivatives and their applications in organic field-effect transistors. *Dyes Pigm.*, **98**, 17.
- 48** Zhang, J., Geng, H., Virk, T.S., Zhao, Y., Tan, J., Di, C.A., Xu, W., Singh, K., Hu, W., Shuai, Z., Liu, Y., and Zhu, D. (2012) Sulfur-bridged annulene-TCNQ co-crystal: a self-assembled “molecular level heterojunction” with air stable ambipolar charge transport behavior. *Adv. Mater.*, **24**, 2603.
- 49** Li, H., Tee, B.C.-K., Cha, J.J., Cui, Yi., Chung, J.W., Lee, S.Y., and Bao, Z. (2012) High-mobility field-effect transistors from large-area solution-grown aligned C₆₀ single crystals. *J. Am. Chem. Soc.*, **134**, 2760.
- 50** Fan, C., Zoombelt, A.P., Jiang, H., Fu, W., Wu, J., Yuan, W., Wang, Y., Li, H., Chen, H., and Bao, Z. (2013) Solution-grown organic single-crystalline p–n junctions with ambipolar charge transport. *Adv. Mater.*, **25**, 5762.
- 51** Mukherjee, B., Sim, K., Shin, T.J., Lee, J., Mukherjee, M., Ree, M., and Pyo, S. (2012) Organic phototransistors based on solution grown, ordered single crystalline arrays of a p-conjugated molecule. *J. Mater. Chem.*, **22**, 3192.
- 52** Liu, Y., Zhao, X., Cai, B., Pei, T., Tong, Y., Tang, Q., and Liu, Y. (2014) Controllable fabrication of oriented nanowire arrays of dibenzotetrathiafulvalene by a multiple drop-casting method. *Nanoscale*, **6**, 1323.
- 53** Merlo, J.A. and Frisbie, C.D. (2003) Field effect conductance of conducting polymer nanofibers. *J. Polym. Sci. Part B Polym. Phys.*, **41**, 2674.
- 54** Merlo, J.A. and Frisbie, C.D. (2004) Field effect transport and trapping in regioregular polythiophene nanofibers. *J. Phys. Chem. B*, **108**, 19169.
- 55** Kim, D.H., Han, J.T., Park, Y.D., Jang, Y., Cho, J.H., Hwang, M., and Cho, K. (2006) Single-crystal polythiophene microwires grown by self-assembly. *Adv. Mater.*, **18**, 719.
- 56** Wang, S., Kappl, M., Liebewirth, I., Müller, M., Kirchhoff, K., Pisula, W., and Müllen, K. (2012) Organic field-effect transistors based on highly ordered single polymer fibers. *Adv. Mater.*, **24**, 417.
- 57** Mannsfeld, S.C.B., Locklin, J., Reese, C., Roberts, M.E., Lovinger, A.J., and Bao, Z. (2007) Probing the anisotropic field-effect mobility of solution-deposited dicyclohexyl- α -quaterthiophene single crystals. *Adv. Funct. Mater.*, **17**, 1617.
- 58** Zhou, Y., Liu, W.J., Ma, Y., Wang, H., Qi, L., Cao, Y., Wang, J., and Pei, J. (2007) Single microwire transistor of oligoarenes

- by direct solution process. *J. Am. Chem. Soc.*, **129**, 12386.
- 59** Kim, D.H., Lee, D.Y., Lee, H.S., Lee, W.H., Kim, Y.H., Han, J.I., and Cho, K. (2007) High-mobility organic transistors based on single-crystalline microribbons of triisopropylsilylethynyl pentacene via solution-phase self-assembly. *Adv. Mater.*, **19**, 678.
- 60** Kim, D.H., Lee, D.Y., Lee, S.G., and Cho, K. (2012) High-mobility organic single-crystal microtubes of soluble pentacene semiconductors with hollow tetragonal structures. *Chem. Mater.*, **24**, 2752.
- 61** Briseno, A., Mannsfeld, S., Reese, C., Hancock, J., Xiong, Y., Jenekhe, S., Bao, Z., and Xia, Y. (2007) Perylenediimide nanowires and their use in fabricating field-effect transistors and complementary inverters. *Nano Lett.*, **7**, 2847.
- 62** Hoang, M.H., Kim, Y., Kim, M., Kim, K.H., Lee, T.W., Nguyen, D.N., Kim, S.-J., Le, K., Lee, S.J., and Choi, D.H. (2012) Unusually high-performing organic field-effect transistors based on π -extended semiconducting porphyrins. *Adv. Mater.*, **24**, 5363.
- 63** Choi, S., Chae, S.H., Hoang, M.H., Kim, K.H., Huh, J.A., Kim, Y., Kim, S.-J., Choi, D.H., and Lee, S.J. (2013) An unsymmetrically π -extended porphyrin-based single-crystal field-effect transistor and its anisotropic carrier-transport behavior. *Chem. Eur. J.*, **19**, 2247.
- 64** Yamao, T., Miki, T., Akagami, H., Nishimoto, Y., Ota, S., and Hotta, S. (2007) Direct formation of thin single crystals of organic semiconductors onto a substrate. *Chem. Mater.*, **19**, 3748.
- 65** Liu, N., Zhou, Y., Wang, L., Peng, J., Wang, J., Pei, J., and Cao, Y. (2009) *In situ* growing and patterning of aligned organic nanowire arrays via dip coating. *Langmuir*, **25**, 665.
- 66** Kastler, M., Pisula, W., Wasserfallen, D., Pakula, T., and Müllen, K. (2005) Influence of alkyl substituents on the solution- and surface-organization of hexa-peri-hexabenzocoronenes. *J. Am. Chem. Soc.*, **127**, 4286.
- 67** Tong, Y., Tang, Q., Lemke, H.T., Moth-Poulsen, K., Westerlund, F., Hammershøj, P., Bechgaard, K., Hu, W., and Bjørnholm, P. (2010) Solution-based fabrication of single-crystalline arrays of organic nanowires. *Langmuir*, **26** (2), 1130.
- 68** Jang, J., Nam, S., Im, K., Hur, J., Cha, S.N., Kim, J., Son, H.B., Suh, H., Loth, M.A., Anthony, J.E., Park, J.-J., Park, C.E., Kim, J. M., and Kim, K. (2012) Highly crystalline soluble acene crystal arrays for organic transistors: mechanism of crystal growth during dip-coating. *Adv. Funct. Mater.*, **22**, 1005.
- 69** Wu, D., Du, Z., and Gao, X. (2003) *Nanofibers*, 1st edn, Chemical Industry Press, Beijing.
- 70** Pinto, N.J., Johnson, A.T., MacDiarmid, A.G., Mueller, C.H., Theofylaktos, N., Robinson, D.C., and Miranda, F.A. (2003) Electrospun polyaniline/polyethylene oxide nanofiber field-effect transistor. *Appl. Phys. Lett.*, **83**, 4244.
- 71** González, R. and Pinto, N.J. (2005) Electrospun poly(3-hexylthiophene-2,5-diyl) fiber field effect transistor. *Synth. Met.*, **151**, 275.
- 72** Babel, A., Li, D., Xia, Y., and Jenekhe, S.A. (2005) Electrospun nanofibers of blends of conjugated polymers: morphology, optical properties, and field-effect transistors. *Macromolecules*, **38**, 4705.
- 73** Liu, H., Reccius, C.H., and Craighead, H.G. (2005) Single electrospun regioregular poly(3-hexylthiophene) nanofiber field-effect transistor. *Appl. Phys. Lett.*, **87**, 253106.
- 74** Lin, Z. and Granick, S. (2005) Patterns formed by droplet evaporation from a restricted geometry. *J. Am. Chem. Soc.*, **127**, 2816.
- 75** Cavallini, M., Stolar, P., Moulin, J.-F., Surin, M., Leclère, P., Lazzaroni, R., Breiby, D.W., Andreasen, J.W., Nielsen, M.M., Sonar, P., Grimsdale, A.C., Müllen, K., and Biscarini, F. (2005) Field-effect transistors based on self-organized molecular nanostripes. *Nano Lett.*, **5**, 2422.
- 76** Newman, C.R., Chesterfield, R.J., Merlo, J.A., and Frisbie, C.D. (2004) Transport properties of single-crystal tetracene field-effect transistors with silicon dioxide gate dielectric. *Appl. Phys. Lett.*, **85**, 422.
- 77** Menard, E., Podzorov, V., Hur, S.H., Gaur, A., Gershenson, M.E., and Rogers, J.A. (2004) High-performance n- and p-type single-crystal organic transistors with free-

- space gate dielectrics. *Adv. Mater.*, **16**, 2097.
- 78** Kim, Y.S., Bae, S.Y., Kim, K.H., Lee, T.W., Hur, J.A., Hoang, M.H., Cho, M.J., Kim, S.J., Kim, Y., Kim, M., Lee, K., Lee, S.J., and Choi, D.H. (2011) Highly sensitive phototransistor with crystalline microribbons from new p-extended pyrene derivative via solution-phase self-assembly. *Chem. Commun.*, **47**, 8907.
- 79** Lee, K., Kim, J., Shin, K., and Kim, Y.S. (2012) Micropatterned crystalline organic semiconductors via direct pattern transfer printing with PDMS stamp. *J. Mater. Chem.*, **22**, 22763.
- 80** Briseno, A.L., Mannsfeld, S.C.B., Lu, X., Xiong, Y., Jenekhe, S.A., Bao, Z., and Xia, Y. (2007) Fabrication of field-effect transistors from hexathiapentacene single-crystal nanowires. *Nano. Lett.*, **7**, 668.
- 81** Tang, Q., Tong, Y., Li, H., Ji, Z., Li, L., Hu, W., Liu, Y., and Zhu, D. (2008) High-performance air-stable bipolar field-effect transistors of organic single-crystalline ribbons with an air-gap dielectric. *Adv. Mater.*, **20**, 1511.
- 82** Tang, Q., Tong, Y., Li, H., and Hu, W. (2008) Air/vacuum dielectric organic single crystalline transistors of copper-hexamethylbenzene phthalocyanine ribbons. *Appl. Phys. Lett.*, **92**, 083309.
- 83** Ye, R., Baba, M., Oishi, Y., Mori, K., and Suzuki, K. (2005) Air-stable ambipolar organic thin-film transistors based on an organic homostructure. *Appl. Phys. Lett.*, **86**, 253505.
- 84** Ye, R., Baba, M., and Mori, K. (2005) High-performance air-stable ambipolar organic thin-film transistor based on F₁₆CuPc and CuPc. *Jpn. J. Appl. Phys.*, **44**, L581.
- 85** Wang, J., Wang, H., Yan, X., Huang, H., Jin, D., Shi, J., Tang, Y., and Yan, D. (2006) Heterojunction ambipolar organic transistors fabricated by a two-step vacuum-deposition process. *Adv. Funct. Mater.*, **16**, 824.
- 86** He, T., Zhang, X., Jia, J., Li, Y., and Tao, X. (2012) Three-dimensional charge transport in organic semiconductor single crystals. *Adv. Mater.*, **24**, 2171.
- 87** Xiao, K., Liu, Y., Yu, G., and Zhu, D. (2003) Organic field-effect transistors using copper phthalocyanine thin film. *Synth. Met.*, **137**, 991.
- 88** Mas-Torrent, M., Hadley, P., Crivillers, N., Veciana, J., and Rovira, C. (2006) Large photoresponsivity in high-mobility single-crystal organic field-effect phototransistors. *Chem. Phys. Chem.*, **7**, 86.
- 89** Niu, Q., Zhou, Y., Wang, L., Peng, J., Wang, J., Pei, J., and Cao, Y. (2008) Enhancing the performance of polymer light-emitting diodes by integrating self-assembled organic nanowires. *Adv. Mater.*, **20**, 964.
- 90** Tang, Q., Li, L., Song, Y., Liu, Y., Li, H., Xu, W., Liu, Y., Hu, W., and Zhu, D. (2007) Photoswitches and phototransistors from organic single-crystalline sub-nanometer ribbons. *Adv. Mater.*, **19**, 2624.
- 91** Bao, Z., Lovinger, A.J., and Dodabalapur, A. (1996) Organic field-effect transistors with high mobility based on copper phthalocyanine. *Appl. Phys. Lett.*, **69**, 3066.
- 92** Shaymurat, T., Tang, Q., Tong, Y., Dong, L., and Liu, Y. (2013) Gas dielectric transistor of CuPc single crystalline nanowire for SO₂ detection down to sub-pm levels at room temperature. *Adv. Mater.*, **25**, 2269.

13

Advanced Dynamic Gels

Rekha G. Shrestha and Masanobu Naito

13.1

Introduction

Gel is a diverse system chemically and it stands somewhere between solid and liquid states. Simple vision on the gel is if it looks like “Jell-O,” it must be a gel! The gel itself has the mechanical properties of a solid, that is, it can maintain its form under the stress of its own weight, and under any mechanical stress, it shows the phenomenon of the strain referring to structural aspects of gels and their viscoelastic properties [1]. Gel is a coherent colloid disperse system of at least two components that exhibit mechanical properties characteristic of the solid state, and both the dispersed component and the dispersion medium extend themselves continuously throughout the whole system. While in Wikipedia a gel (coined by the nineteenth-century Scottish chemist Thomas Graham, by clipping from gelatine) is defined as a solid, jelly-like material that can have properties ranging from soft and weak to hard and tough (Douglas Harper, “Online Etymology Dictionary: gel,” *Online Etymology Dictionary*, retrieved December 9, 2013). By weight, gels are mostly liquid, although they behave like solids due to a three-dimensional cross-linked network within the liquid. It is the cross-linking within the fluid that gives a gel its structure (hardness) and contributes to the adhesive stick (tack). According to International Union of Pure and Applied Chemistry (IUPAC), gel is a nonfluid colloidal network or polymer network that is expanded throughout its whole volume by a fluid [2].

Based on these definitions, one can classify a substance as a gel (i) if it has a continuous microscopic structure with macroscopic dimensions that is permanent on the timescale of an analytical experiment and (ii) if it is solid-like in its rheological behavior despite being mostly liquid. There are several subclasses of gels, and each meets both of these basic criteria. There are different types of gels. As per Flory’s classification [3], gels can be classified as follows:

- (i) Lyotropic liquid-crystalline phases based on well-ordered structures.
- (ii) With cross-linked polymeric networks swollen with solvent. In these phases, the polymer chains are disordered.
- (iii) With polymer networks in which the chain-chain interactions are physical. The chains may be predominantly disordered, but the regions

of local order (especially where interchain interactions occur) may also exist. (iv) Those with disordered particulate structures, including materials in which the gel networks are comprised of fibrils. For instance, polymer gels are “cross-linked networks of polymers swollen with a liquid” and sol–gel glasses are 3D matrices of crystalline or amorphous solids with honeycombed channels. As such, their microscopic networks are present at all times and at all temperatures (below those at which irreversible decomposition occurs).

Different forms of gels are common in everyday life. Their applications range from personal care products (toothpaste, shampoo, deodorants, etc.) to foodstuffs, electronic devices, drug delivery, and tissue engineering [4]. They are used in the art restoration, weaving of a spider’s web by applying gels to the surface of oil paintings [5], pumping of gels into oil wells to increase the efficiency of crude oil recovery [6], and gelation of gasoline to make napalm [7]. The gels having the mechanical properties [8] can help protect the skyscrapers from crumbling during earthquakes.

13.2

Gels in Nature

Nature has exploited gel-like structures to impart unique properties to many macrobiological systems. Examples include fibrous actin [9] and clathrin [10], tubulin [11], keratin [12], insulin [13], collagen gels [14], silk processing by insects and spiders [15], amyloid fibrils that have been implicated in Alzheimer’s and other neurodegenerative diseases [16], sickle cell anemia hemoglobin in its deoxy state [17], and fibrinogen, the blood clotting factor [11,18]. Vision in animals depends on two hydrogels, the vitreous humor (the transparent mass in front of the retina that fills the eyeball) and the stroma (the thickest layer of tissue in the cornea) of eyes. Similarly, some species secrete gels that are effective in parasite control. For example, the long-finned pilot whale secretes an enzymatic gel that rests on the outer surface of this animal and helps prevent other organisms from establishing colonies on the surface of the bodies of these whales [19]. Gels existing naturally in the body include mucus, the vitreous humor of the eye, cartilage, tendons, and blood clots. Their viscoelastic nature results in the soft tissue component of the body, disparate from the mineral-based hard tissue of the skeletal system. Researchers are actively developing synthetically derived tissue replacement technologies derived from hydrogels, for both temporary implants (degradable) and permanent implants (nondegradable).

This chapter emphasizes mainly on the responsive properties of smart, intelligent, or advanced viscoelastic gels (VEGs): the gels that exhibit both viscous and elastic properties and can dynamically alter their structures and properties in response to environmental changes such as electric current, ultraviolet (UV)/visible (vis) light, temperature, pH, and so on [20]. The activation of the trigger changes the micellar structures and consequently alters the related rheological electrical, optical, thermal, or pH responses into chemical, biochemical, or physicochemical ones and vice versa. This alteration helps them regulate the transportation

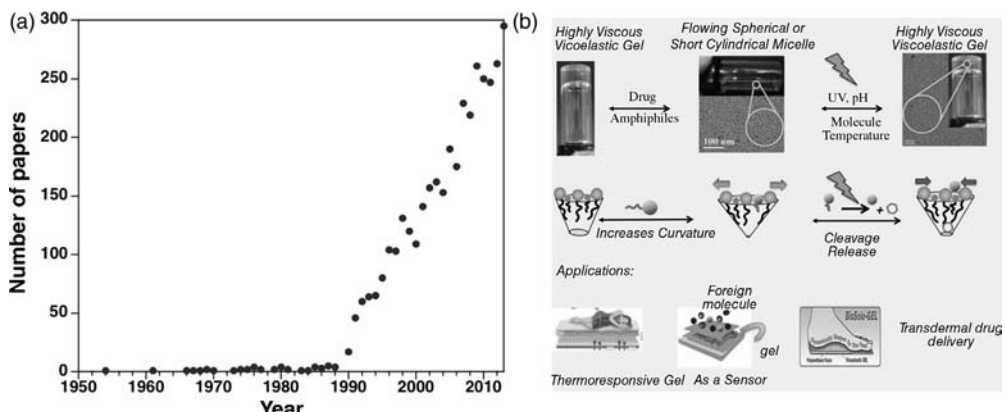


Figure 13.1 (a) Number of publications related with VEGs with the publication year. (ISI Web of Science, apps.webofknowledge.com/, July 7, 2014). (b) Schematic diagram

showing visual appearance, molecular arrangement being responsible for the texture and properties and their expected applications. (google.com).

of molecules near an oil–water interface [21] and alters wettability [22,23]. These functionalities and responsive changes in the aggregates provide a basis to design smart materials such as diagnostics, biosensors [24], drug delivery [25], tissue engineering [26], and smart optical systems [27], opening the door to a range of potential applications, including clutches [28], microfluidics, valves [29], vibration control [30], clean fracturing fluids [31], tissue engineering [32], and human muscle stimulators [33].

Figure 13.1 shows that the research related to viscoelastic gels started from the mid-1950s and a remarkable growth has been observed since 1990s. A detailed observation shows that this field has been of great interest to both theoreticians and experimentalists for their unique possession of viscous and elastic properties and finds applications in many fields. The huge number of research works ongoing in this field and the publications per year itself highlight the importance of these materials. We, therefore, believe that the review on VEGs should be documented.

13.3 Characterization of VEGs

There are several techniques of characterizing the gels. A few of these important techniques are discussed in the following sections:

13.3.1

Rheometer

Rheology is one of the main techniques to characterize a gel. VEGs show peculiar flow properties. Many polymer solutions and VEGs display rheological properties

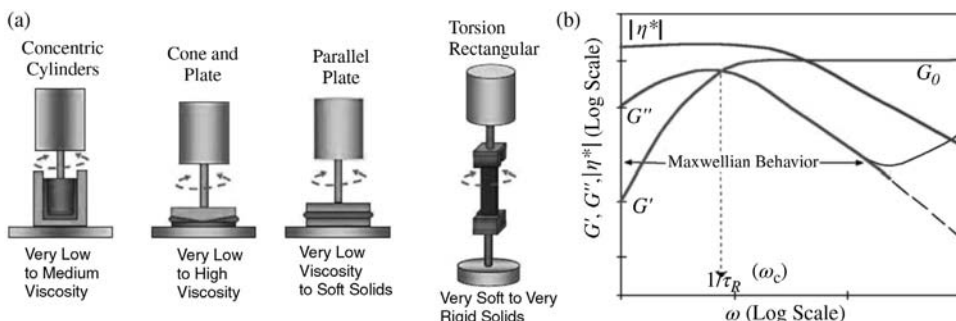


Figure 13.2 (a) Schematic view of the different geometry of rheometers used to get information on the rheological properties of the micellar solutions, and (b) frequency (ω) dependence of the storage (G') and loss moduli (G'') for VEGs following the Maxwellian

behavior. At low and medium oscillatory shear frequencies, the system shows the Maxwellian behavior. However, at high frequency, deviation from the Maxwellian behavior is observed. (The extract of the related theory has been included in Section 13.10). (google.com).

in which the response to mechanical perturbation involves both elastic deformation and viscous flow, and rheology deals with how a system responds to a mechanical perturbation in terms of elastic deformation and viscous flow.

The use of rheometer allows one to record the sample “flow curve” that relates its response (or deformation rate) to the mechanical stress subjected to it. Dynamic measurements in the oscillatory mode give the elastic and viscous contributions that are defined by the dynamic elastic and loss moduli, G' and G'' , respectively. These two moduli are usually measured as a function of oscillation frequency ω . A gel is considered to be a viscoelastic material when there is a crossover between G' and G'' around frequencies of practical interest (typically 100 rad s^{-1}) (Figure 13.2).

13.3.2

Small-Angle Scattering

The information about microscopic structures of VEGs is important to understand gels and their related phenomena. Scattering techniques such as (small-angle X-ray scattering (SAXS) and small-angle neutron scattering (SANS) have been extensively employed to characterize polymer networks and VEGs. The properties of VEGs are dependent on the shape, the size of micelles, and the interaction between these micelles. It is capable of probing a sufficiently broad range of length scales of micelles that build up the VEGs to extract the relevant structural information and correlate the structure–property relationships. In addition to study gels under atmospheric conditions, the effects of temperature, concentration, and pH can be easily controlled according to the requirements of the experiments. In a scattering measurement, the scattering vector $q = (4\pi n/\lambda_0) \sin(\theta/2)$, where θ is the scattering angle. The length scale d probed in the

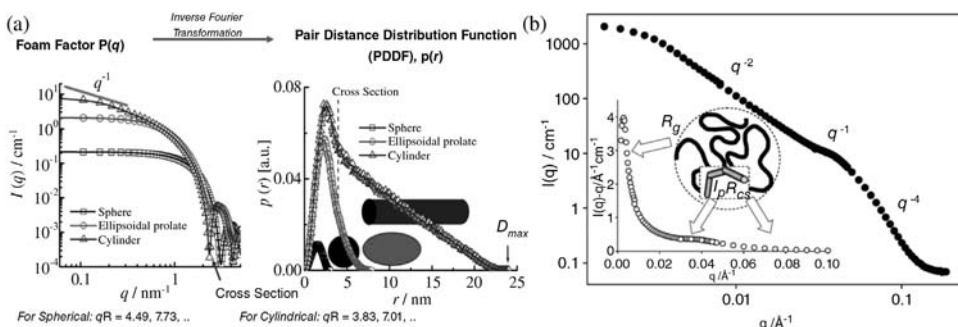


Figure 13.3 (a) The representative plots of scattering function and the corresponding pair distance distribution function PDDF, that is, the structure of the particle in real space obtained by treating the experimental data with generalized indirect Fourier transformation (GIFT). Judging from the shape of the PDDF curves, one can have an idea of the shape, size, and inhomogeneity of the particle. (b) SANS pattern obtained for nonionic worm-like micelles formed in mixtures of poly(oxyethylene)

cholesterol ether (1 wt%) and poly(oxyethylene) dodecyl ether (0.3 wt%). The scattering shows the characteristic q^{-2} dependence at low q (Gaussian chain), q^{-1} at intermediate q (rod-like), and q^{-4} at high q values, corresponding to the scattering from a sharp interface. *Inset:* Holzter plot of the data and schematic representation of the characteristic dimensions corresponding to the different regions. (Part b reprinted with permission from Ref. [92]. Copyright 2007, Royal Society of Chemistry.)

experiment is related to q by $d \sim 2\pi/q$; therefore, each q -region is correlated with a characteristic dimension of the system. In the low- q or the so-called Guinier region, the overall size of the chain is observed. At higher q , the random walk configuration of the chain is measured. At intermediate q , shorter length scales are probed and the stiffness of the chain appears as a q^{-1} behavior (typical of rod-like structures). In the high- q region, the scattering arises solely from the local cross section, leading to a Guinier behavior and a strong decrease in the intensity. A combination of static light scattering (SLS) and SAXS (or SANS) experiments is usually needed to access the whole range of length scales (Figure 13.3). An extract of the principle involved (mainly SAXS) and the related references have been presented in Section 13.10.

13.3.3

Transmission Electron Microscopy

The unique rheological properties of VEGs are the result of supramolecular aggregates that can be regular or irregular, homogeneous or very diverse. For this reason, cryo-TEM (transmission electron microscopy) is more useful to image the range of nanostructures present in the systems. The direct images of a suggested or a theoretically predicted model of branched micelles [34], the shape of the “end-caps” of thread-like micelles [35,36], can be obtained from the cryo-TEM technique that helps to explain the correlated mechanism and reason for the different rheological behaviors on imposing different stimuli.

13.4

Redox-Responsive VEGs

Redox-responsive VEGs or viscoelastic electrorheological (ER) gels are the gels whose rheology can be controlled by applying an electric potential [30]. They are applied in valves and clutches for transmission and precise control of mechanical positioning and are regarded as one of the most versatile materials available for building smart structures and machines. They can be made by dispersing solid particles within a liquid. When an alternating electric field is applied to such gels, the dispersed particles align to form strings in the direction parallel to the field due to the attraction of induced dipoles, increasing the viscosity in the direction perpendicular to the field. The conventional ER fluids, however, have many disadvantages. In particular, a high voltage and a high particle concentration are required and their stability is usually poor; this has hampered their industrial applications. In order to overcome such shortcomings, a novel, stable ER fluid in a mixture of 11-ferrocenylundecyltrimethylammonium bromide (FTMA) (Figure 13.4) and sodium salicylate (NaSal), whose viscoelasticity can be controlled using a “Faradaic (redox) reaction,” has been reported [37]. The system involves a cationic “redox-switchable” ferrocenyl surfactant, FTMA, that self-assembles into VEGs in the presence of NaSal. The authors have characterized solutions containing 50 mM FTMA in the presence of various concentrations of NaSal. Figure 13.4 provides clear images of the effect of the oxidation state of the FTMA on the rheological properties of this system. Figure 13.4a (i) and (ii) shows that in the absence or presence of 10 mM NaSal, the viscosity of the solutions of FTMA is almost similar to water. On increasing the concentration to 20 mM NaSal, a highly viscous solution (Figure 13.4 (iii)) is formed. Electrochemical oxidation of FTMA to FTMA^+ (see scheme in Figure 13.4b) in the presence of 20 mM NaSal resulted in the reappearance of flow behaviors comparable to those seen in the absence of NaSal (Figure 13.4 (iv)). The qualitative observations already described were accompanied by rheological measurements, as a function of concentration of NaSal and oxidation state of FTMA. The

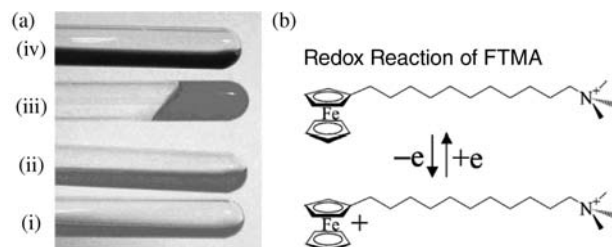


Figure 13.4 (a) Images showing the appearance of aqueous FTMA (reduced form) (50 mM)/NaSal mixture at molar ratio (i) 0, (ii) 0.2, and (iii) 0.4 and (iv) FTMA (oxidized form)/NaSal mixtures at molar ratio 0.4 after

electrolytic oxidation. (b) Scheme showing the redox reaction of FTMA. (Reprinted with permission from Ref. [37]. Copyright 2004, American Chemical Society.)

viscosity of a solution containing reduced FTMA and 20 mM NaSal was 15 Pa s. Electrochemical oxidation of FTMA to FTMA^+ resulted in a decrease in viscosity (four orders of magnitude) to 0.0025 Pa s. The freeze-fracture electron microscopy (not shown) showed long flexible cylindrical micelles in solutions containing 50 mM reduced FTMA and 20 mM NaSal. Attempts to recover the initial solution viscosity by electrochemically reducing a solution containing FTMA^+ back to FTMA were hindered by gel formation near the electrode surface, which dramatically reduced the diffusion rate of surfactant to the electrode. Ferrocenyl surfactants, FTMA has a redox-active ferrocenyl group positioned at the end of its alkyl chain. The ferrocenyl group in the reduced form is hydrophobic, while the ferricinium cation (oxidized form) acts as a hydrophilic group. This causes a remarkable change in the hydrophilic–lipophilic balance of FTMA, thereby altering its aggregation state. A redox-responsive VEG is formulated in an aqueous mixture of FTMA/NaSal by tuning the degree of entanglement of long cylindrical micelles through redox reaction of FTMA.

This gel presents numerous advantages over conventional ER fluids, and has great potential to be applied to inkjet printer inks and the controlled release of dyes and perfumes.

13.5

pH-Responsive VEGs

A control on the micellar aggregation and thereby the bulk properties of VEGs can be introduced by altering the pH of the solution [38]. Most of the pH-responsive VEGs so far reported involve mainly zwitterionic alkyldimethylamine oxide $C_n\text{DMAO}$ [39].

The alkyldimethylamine oxides exist either as a nonionic or a cationic (protonated form) species depending on the pH of their aqueous solution. At neutral pH, they are zwitterionic surfactants carrying no net charge and spontaneously self-organizing into a transient network of long and flexible micelles without any additives because of the weak repulsion between the head groups. It has been widely reported that near the point of half-ionization ($\alpha=0.5$, where α is the degree of ionization) alkyldimethylamine oxides exhibit a characteristic maximum in micellar size and weight, bulk viscosity (in $C_{14}\text{DMAO}$), a minimum in critical micelle concentration (cmc), and surface tension. Rathman and Christian reported formation of H-bonds between protonated and unprotonated alkyldimethylamineoxide (in $C_{12}\text{DMAO}$) [40] as supported by infrared spectra. This bond has been reported as maximum at equal number of protonated and unprotonated species [41].

Cationic surfactant solutions can also form pH-responsive VEGs by incorporating hydrotopes [42] and other surfactants [43]. Zhao *et al.* [44a] have reported pH-responsive VEGs, based on a simple ammonium surfactant *N*-cetyl-*N,N*-dihydroxyethylammonium bromide (CDHEAB). It is a weak acid and, therefore, CDHEAB and its counterpart CDHEA coexist in the solution, the relative ratio being dependent on the pH. A concentrated NaOH is used to alter the pH of the

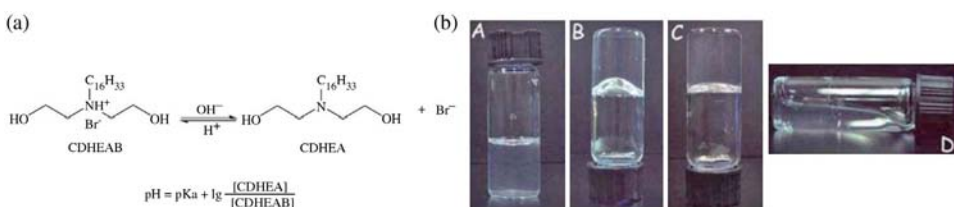


Figure 13.5 (a) Schematic diagram showing structural transition of CDHEAB induced by pH. (b) Images of aqueous solution of 100 mM CDHEAB at (A) pH = 3.31, (B) pH = 5.35, (C) pH = 5.53, and (D) pH = 5.63. (Reprinted with permission from Ref. [44]. Copyright 2012, Royal Society of Chemistry.)

solution. An aqueous solution of CDHEAB is clear at pH range = 3.31–4.97. From 4.97 to 5.53 (Figure 13.5b), the viscosity increases sharply up to 10^6 -fold. The rheological measurements confirm the presence of transient network of cylindrical micelles. The viscosity, however, decreases at pH 5.63. The variation of rheological behavior has been attributed to the molecular structure that allows the combination of strong hydrophobic interactions and effective hydrogen bonding upon protonation at higher pH.

In yet another unique report [44b], Sakai *et al.* have reported pH-responsive VEGs in a complex formed by an amino acid-based surfactant dodecanoylglutamic acid (C_{12}Glu), an alkyl dicarboxylic acid, and a secondary alkylamine dodecylmethylamine (C_{12}MA) and a tertiary alkylamine dodecyldimethylamine (C_{12}DMA). C_{12}Glu forms a stoichiometric 1:1 complex with C_{12}DMA and C_{12}MA . Rheological measurements have suggested that the complex systems yield VEGs and the rheological behavior is strongly dependent on the pH of the solution. This pH-dependent behavior results from the structural transformation of the viscoelastic micelles occurring in the narrow pH range of 5.5–6.2 (in the case of C_{12}Glu – C_{12}DMA system); that is, positive curved aggregates such as spherical or rod-like micelles tend to be formed at high pH values.

13.6

Temperature-Responsive VEGs

Temperature is one of the important triggers for gels. The rheology of VEGs is responsive to the temperature. A change in temperature can either help form highly viscoelastic gels or destroy the transient network depending upon the system.

Nonionic surfactant solutions especially of C_mEO_n type, where C_m denotes a saturated alkyl chain containing m carbon atoms and EO_n denotes a head group composed of ethylene oxide groups, can undergo temperature- or concentration-induced micellar growth through adequate modulation of the specific surface area and the interfacial curvature [45–47]. These temperature-dependent behaviors of C_mEO_n surfactants have been attributed to the balance of ethylene–ethylene oxide

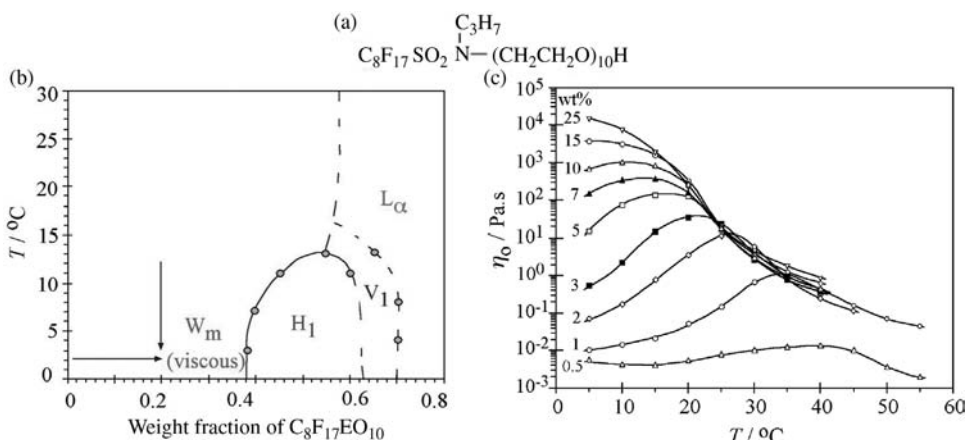


Figure 13.6 (a) Molecular structure of $C_8F_{17}EO_{10}$, (b) Partial phase diagram of $C_8F_{17}EO_{10}/H_2O$ binary system. W_m , H_1 , V_1 , and L_α stand for micellar, hexagonal, bicontinuous cubic, and lamellar liquid crystalline phases, respectively. The arrows in the W_m domain show the direction in which the viscosity increases for the systems at surfactant concentration of 15 wt% and above. At lower

concentrations, viscosity increases and then decreases with increasing temperature, and (c) variation of zero-shear viscosity (η_0) as a function of temperature at different concentrations (in wt%) of $C_8F_{17}EO_{10}$ in water at different temperatures. (Reprinted with permission from Ref. [48]. Copyright 2006, American Chemical Society.)

and ethylene oxide–water interaction. At higher temperatures, the ethylene oxide head group dehydrates, making the critical packing parameter, CPP increase and favoring compact arrangement of surfactant leading to the spherical–cylindrical micelle transition.

Among them, fluorocarbon surfactants $C_8F_{17}SO_2(C_3H_7)N(CH_2CH_2O)_{10}H$ is one of the nonionic fluorocarbon surfactants that show interesting temperature-dependent behavior [48]. Figure 13.6a shows that it forms a micellar solution over a wide range of compositions (up to 38 wt% at 5 °C) at low temperatures. Hexagonal (H_1), bicontinuous cubic (V_1), and lamellar (L_α) liquid crystalline phases are formed successively with an increase in surfactant concentration. Micellar solutions at low temperatures transform into highly viscous solutions with increasing surfactant concentration. Small-angle X-ray scattering patterns support the presence of long cylindrical micelles in the solution. The viscosity of the solutions gradually decreases with the increasing temperature and, ultimately, a less viscous easily flowing isotropic solution is formed. At further higher temperatures, clouding behavior is observed.

Figure 13.6c shows the variation of η_0 of $C_8F_{17}EO_{10}$ with temperature for concentrations between 1 and 7 wt%. With the increasing temperature, the viscosity shows a maximum for all concentrations. The low surface area of fluorinated surfactant favors micellar growth and an onset of the overlapping of worm-like micelle leading to η_0 increase even at low concentration; the η_0 of 2 wt% $C_8F_{17}EO_{10}/H_2O$ is about four orders of magnitude higher than that of water.

The η_0 of 1 wt% C₈F₁₇EO₁₀/H₂O increases by about two orders of magnitude on increasing the temperature from 5 to 35 °C. The temperature for viscosity maximum ($T_{\eta\text{-max}}$) shifts to lower values with increasing surfactant concentration. The viscosity of the micellar solution is very responsive to the concentration at low temperatures, but at and above 25 °C, the viscosity is nearly the same over a wide range of concentrations (2–25 wt%). At high surfactant concentration, the degree of hydration of the EO chain decreases. This reduces the specific surface area and increases aggregation numbers, inducing decrease in the spontaneous curvature of the aggregate and favoring 1D micellar growth, increasing the viscosity. Upon an increase in concentration, the formation of micellar joints with faster relaxation is expected to take place at lower temperatures, which can explain the gradual shift of $T_{\eta\text{-max}}$ toward lower temperatures.

VEGs have been reported in the poly(oxyethylene) cholesterol and poly(oxyethylene) phytosterol ethers [49]. Ahmed and Aramaki [50] have studied the temperature-dependent rheology of the VEGs formed in an aqueous mixture of poly(oxyethylene) cholesteryl ether (ChEO₁₅) and tri(ethyleneglycol) mono-*n*-dodecyl ether (C₁₂EO₃) or monolaurin. On increasing the poly(oxyethylene) chain length of ChEO_{*m*}, the temperature sensitivity of the viscosity of the solution is reduced. For, C₁₂EO₃ as a cosurfactant, the temperature sensitivity is lower at lower temperatures and higher at higher temperatures and at higher cosurfactant mixing fraction. For monolaurin, the temperature sensitivity increased with cosurfactant mixing fraction in the viscous region. The temperature-dependent rheology has been explained in terms of the reduction of the average curvature of micellar interface with temperature due to dehydration of the poly(oxyethylene) chain and formation of branches in long micelles. The same group extended their work to the aqueous nonionic VEGs formed by C₁₄EO₃ and Tween-80 [51].

Shrestha *et al.* have reported temperature-dependent VEGs in an aqueous mixture of poly(oxyethylene) cholesteryl ether (ChEO₂₀) and cocamid monoethanolamide (C-11 S) [49]. The rheological measurements of VEGs formed by 10% ChEO₂₀/H₂O + 5.7% C-11 S (corresponding to the maximum viscosity) over a wide temperature range showed that the viscosity changed by orders of magnitude upon a small change in temperature. The η_0 increased with the rise of temperature from 5 °C, to 25 °C to the micellar elongation and its entanglement. In aqueous systems of poly(oxyethylene)-type hydrocarbon or fluorocarbon nonionic surfactants, micellar growth is expected upon heating due to dehydration of the hydrophilic head group. Dehydration causes an increase in the CPP value, and aggregates with less positive curvatures are likely to form. Formation of hemispherical endcaps in the cylindrical aggregates becomes unfavorable due to the high energy cost and, consequently, one-dimensional micellar growth takes place; that is, the contour length L_c of long cylinders increases with temperature. The entanglement of these long cylindrical micelles forming a network structure increases the τ_R . A faster relaxation and viscosity drop above 25 °C have been explained by the predominance of the formation of a threefold junction within the already formed networks. Thus, from the dynamic rheology results, the fall in viscosity of the systems (Figure 13.7a) with temperature rise

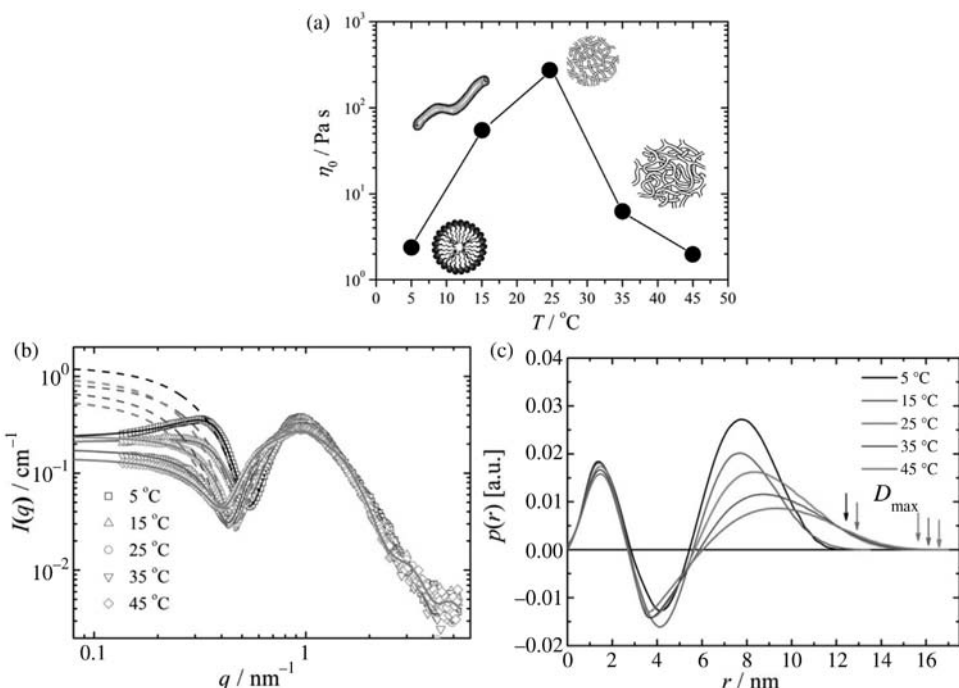


Figure 13.7 Variation of (a) zero-shear viscosity (η_0), (b) normalized X-ray scattered intensities $I(q)$ obtained in absolute scales, and (c) the corresponding $p(r)$ functions for the 10% ChEO₂₀/H₂O + 5.7% C-11 S system at different temperatures (5, 15, 25, 34, and 45 °C). The solid and broken lines in part

(b) represent the GIFT fit and the calculated form factor for n -particles existing in unit volume, $nP(q)$, respectively. Arrows in higher r -side of part (c) represent the maximum dimension of the micelles. (Reprinted with permission from Ref. [49]. Copyright 2011, American Chemical Society.)

can be ascribed to an increase in micellar junction density due to curvature reduction.

The authors have further explained the temperature-dependent rheology with SAXS measurements on the 10% ChEO₂₀/H₂O + 5.7% C-11 S sample. Figure 13.7b shows the scattering functions $I(q)$ and the corresponding $p(r)$ curves for the 10% ChEO₂₀/H₂O + 5.7% C-11 S system at different temperatures (5–45 °C). The shift of the position of the minimum toward the low- q side and an increase of the low- q slope in the $I(q)$ curves with the rise of temperature can be taken as evidence of temperature-induced micellar growth. The scattering functions show a monotonous micellar growth with the rise of temperature from 5 to 45 °C. A similar feature can be seen in the $p(r)$ curves (Figure 13.7c). All $p(r)$ curves exhibit a local maximum and minimum in the low- r side, indicating the core–shell micellar structure. The inflection point in the low- r side remains practically unchanged with the increase in temperature; however, D_{max} increases continuously showing the temperature-induced 1D micellar growth. An increase in temperature from 5 to 15 °C only slightly modulates the micellar

shape as judged from the only slightly asymmetric $p(r)$ curve. Above this temperature a long tailing in the high side of the $p(r)$ function appears, indicating the formation of elongated cylindrical micelles. These observations well support the rheology data that the viscosity increases with the increase of temperature from 5 to 25 °C are caused by the micellar growth (Figure 13.7a). Although micelles are increasing, viscosity shows a decreasing trend above 25 °C. Correlating with the rheological study, the authors have demonstrated that the viscosity decay above 25 °C is possibly due to the branching of the already existing entangled micelles.

Moitzi *et al.* have reported that on increasing the temperature of viscoelastic solution containing ChEO_m (where $m=10$ and 15) and C_{12}EO_3 , transition of transient network of long micelles to vesicles occurred on the basis of SANS measurements [52].

Further clear pictures on the effects of temperature on the aqueous VEGs formed by poly(oxyethylene) alkyl ether and C_{12}EO_3 were provided by Talmon and coworkers [53]. At lower temperatures, 8 °C, the aqueous micellar solutions of C_{12}EO_3 showed spherical and short rod-like micelles (<50 nm) (Figure 13.8a). The

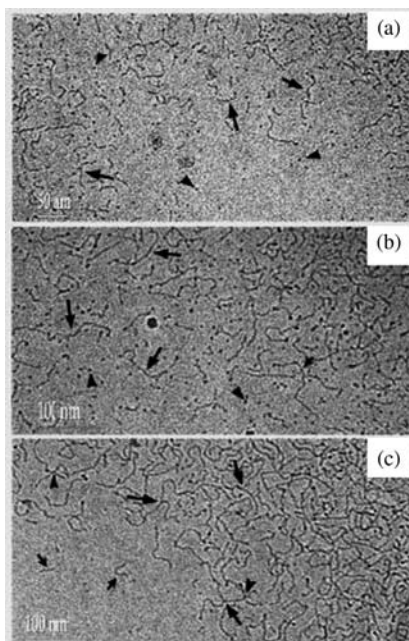


Figure 13.8 Cryo-TEM images of a 0.5 wt% aqueous C_{12}E_5 solution at three different temperatures. At 8 °C (a), spheroidal (arrowheads) and rather short (<50 nm) viscoelastic (arrows) coexist. At 18 °C (b), the coexistence of spheroidal (arrowheads) and cylindrical micelles (arrows) is again identified, but the worms are

longer (50–100 nm) and threefold junctions (small arrow) are present. At 29 °C (c), the worms are much longer (>100 nm), and the density of the threefold junctions (larger arrows) is higher. (Reprinted with permission from Ref. [53]. Copyright 2000, American Chemical Society.)

longer flexible cylindrical micelles with contour length (50–100 nm) were formed with a small number of threefold junction or branching points at 18°C (Figure 13.8b). With further increase of temperature to 29°C, longer micelles (>100 nm) and the higher density threefold junctions were observed (Figure 13.8c).

VEGs formed by ionic surfactants also show temperature sensitivity. One of the first studies on rod-like and VEGs were carried out by Debye and Anacker [54]. Thermoresponsive VEGs have mainly been reported in aqueous cationic surfactants such as cetyltrimethylammonium 3-hydroxynaphthalene-2-carboxylate (CTAHNC) by Manohar and coworkers [55]. They prepared CTAHNC by mixing CTAB and sodium 3-hydroxynaphthalene-2-carboxylate (SNHC) removing the counterions Na^+ and Br^- . On the basis of rheological study, optical microscopy, SANS experiments, DSC measurements, and cryo-TEM images, it was confirmed that the turbid vesicular solutions – clear viscoelastic gel transition – occurred on increasing the temperature [56].

Raghavan and coworkers reported low-viscous water-like fluid-to-viscoelastic gel transformation on increasing the temperature in an aqueous mixture of erucyl bis(hydroxyethyl)methylammonium chloride (EHAC) and SHNC [57]. They further developed another thermoresponsive VEG based on simple mixing of CTAB and hydrotope 5-methyl salicylic acid (5 mS) [58].

Sreejith *et al.* reported another thermoresponsive viscoelastic gel with CTAB and C_8OH in the presence of KBr [59]. The authors ascribed the temperature-induced vesicle-to-VEGs transition on the basis of rheological measurements, dynamic light scattering (DLS), and cryo-TEM observations. The temperature-induced thermothickening mechanism is assigned to a modification in the micellar aggregation.

Anionic surfactants are also known to form thermoresponsive VEGs. Kalur and Raghavan [60] report an exponential decay of viscosity with an increase in temperature for VEGs formed by an aqueous mixture of sodium oleate (NaOA) and potassium chloride (KCl) or triethylamine hydrochloride (Et_3NHCl). The temperature-induced decrease in the viscosity of the system has been attributed to the reduction in the micellar length on the basis of rheological and SANS measurements. A mixture of NaOA and Et_3NHCl displays cloud point upon heating, similar to nonionics.

Surfactants with hybrid fluorocarbon–hydrocarbon tails, sodium 1-oxo-1-[4-(tri-decafluorohexyl)phenyl]-2-hexanesulfonate (FC6-HC4), have shown temperature-induced VEGs (20 °C) to bilayer (40 °C) to continuous lamellar phase (60 °C) [61].

13.7

Photoresponsive VEGs

Light-responsive surfactants provide interesting opportunities to create stimuli-responsive VEGs because illumination of the solution can be easily patterned and modulated. The benefits of using light as a trigger include miniaturization and limited chemical contamination of the solution, promoting the development

of green sustainable systems [62]. Some VEGs that contain a light-responsive group respond to light by changing their rheological properties. The first report includes by Wolff and coworkers. They have reported that the substituted polyaromatic group such as anthracene [63], acridizinium salts [64], and coumarin [65]-containing compounds when added to micellar solutions of CTAB form light-responsive highly viscoelastic gels. On UV irradiation, the rheological properties changed by several orders. They have explained that the photodimerization of polyaromatic compound formed on UV irradiation is responsible for the different rheological behaviors.

Likewise, incorporation of several other photoresponsive groups in the solution such as azobenzene [66], stilbene [67], spiropyran [68], and also cinnamic acid and its derivatives [29,69] can form light-responsive VEGs. There are reports on reversible change in viscoelastic properties of micellar solutions as a result of the *trans-cis* photoisomerization of azobenzene-modified cationic surfactants [70], effect of light on self-assembly of aqueous mixtures of sodium dodecyl sulfate and a cationic, bolaform surfactant containing azobenzene [71]. The change in viscoelastic properties of gels has been confirmed as a result of the *trans-cis* photoisomerization of photoresponsive molecules present in the solution.

Recently, Aikawa *et al.* [72] have reported that an addition of a novel photocleavable surfactant C4-C-N-PEG9 to an aqueous mixture of 2.4 wt% tetraoxyethylene dodecyl ether C₁₂EO₄ and 4.9 wt% poly(oxyethylene) phytosterol ether PhyEO₂₀ that forms highly VEGs with high viscosity of ~10 Pa s decreases the viscosity. Viscosity decreased with C4-C-N-PEG9 concentration reaching ~0.003 Pa s at 2.5 wt% of C4-C-N-PEG9. However, upon UV irradiation, viscosity of the C4-C-N-PEG9 incorporated system increased significantly (~200 times at 1.5 wt% of C4-C-N-PEG9 system). Small-angle X-ray scattering studies have shown that the addition of C4-C-N-PEG9 favors long cylinders-to-sphere-type micellar transition in the structure. On the other hand, UV irradiation in the C4-C-N-PEG9 incorporated system causes 1D micellar growth. Since C4-C-N-PEG9 has relatively bigger head group than C₁₂EO₄, addition of C4-C-N-PEG9 into viscoelastic micelles reduces the critical packing parameter resulting in the formation of spherical aggregates. The authors have explained, as confirmed by the UV-vis spectrometry and HPLC measurements, Figure 13.9 that C4-C-N-PEG9 experiences a photocleavage through UV-induced cyclization in aqueous solution, yielding a less surface-active coumarin derivative (7-butoxy-2H-chromen-2-one) and an aminated poly(oxyethylene) compound, and it is due to this transformation that UV irradiation induces 1D micellar growth.

Photoresponsive nonaqueous dynamic gels can also be formed by phospholipid-based surfactants in nonaqueous solvents. One of the most common systems to form nonaqueous dynamic gels is a ternary mixture of phospholipids, oil, and H₂ [73] or phospholipids, oil, and substituent for water-like urea, sucrose fatty acid esters [74], sugars of RNA and DNA, polyglycerol [75], bile salt, and sodium deoxycholate [76]. Phospholipid with two alkyl chains forms globular or ellipsoidal micelles in a variety of organic solvents. A trace amount of water or substituting additives into the micellar solution can form hydrogen bonds with

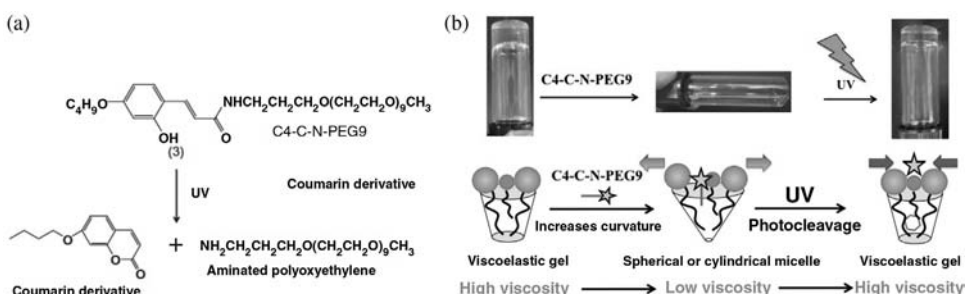


Figure 13.9 The VEGs formed by 4.9 wt% PhyEO₂₀/H₂O + 2.4 wt% C₁₂EO₄ system and the effect of C4-C-N-PEG9 and UV irradiation are schematically represented. PhyEO₂₀ molecule is shown as bigger spherical head and

black tail, C₁₂EO₄ molecule with a bigger spherical head and black tail, while the C4-C-N-PEG9 star shaped head and black tail. (Reprinted with permission from Ref. [72]. Copyright 2013, American Chemical Society.)

the phosphate group of phospholipids reducing the interfacial curvature of molecular assembly inducing an axial growth of micelles and leading to the formation of VEGs [77]. The η_0 increases by several orders of magnitude. The increase depends upon the molar ratio of water to phospholipids.

Raghavan and coworkers have reported the formation of UV responsive VEGs in a ternary mixture of lecithin, *p*-coumaric acid, and oils [69a]. Recently, Shrestha *et al.* have further illustrated a detailed study on photoinduced rheological changes in nonaqueous photoresponsive gels obtained with 1,2-diacyl-*sn*-glycero-3-phosphocholine-based nonaqueous VEGs, 1-palmitoyl-2-oleophosphatidylcholine (POPC)/cyclohexane/H₂O, POPC/isooctane/H₂O, and L- α -dioleophosphatidylcholine (DOPC)/isooctane/H₂O systems [78]. Initially, the mixtures form highly viscoelastic fluids of long, reverse viscoelastic micelles as confirmed by the rheological measurements. In order to impart viscoelasticity, they have added *trans*-CA to these mixtures, exhibit photosensitivity, and the viscoelasticity increased that decreased on UV irradiation. They have further reported the effect of nature of the substituent on the benzene ring of *trans*-CA on rheology. When hydroxycinnamic acid (HCA) (hydrophilic, -OH group attached to the benzene ring of CA) was added to DOPC/isooctane/H₂O phase separation occurred; the addition of methoxycinnamic acid (MOCA) and methylcinnamic acid (MCA) (hydrophobic groups, -OCH₃, and -CH₃ attached to the benzene ring of CA, respectively) to the same phase led to higher viscoelasticity. The study on the effects of position of the substitution on CA revealed that the viscosity enhancement is on the order of *p*->*m*->*o*-isomers. The different geometries obtained because of the substitution and photoinduced *trans*-*cis* isomerization responsible for the different rheology as confirmed by the dynamic rheology, the UV absorption, and the ¹H NMR spectra. The ¹H NMR spectra revealed a change in the solubilization site of CA with irradiation. *cis*-CA (high solubility in water) is solubilized in the vicinity of water (at the hydrophilic end of DOPC) compared with *trans*-CA. This disrupts the 3D networks of reverse viscoelastic micelles, decreasing the viscoelasticity of the solution (Figure 13.10).

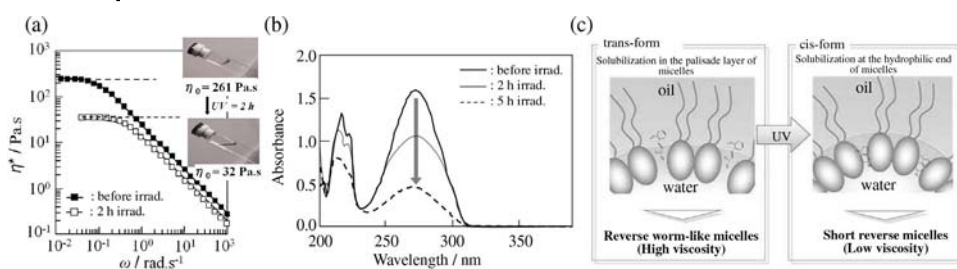


Figure 13.10 (a) Frequency-dependent complex viscosity $|\eta^*|$, (b) the corresponding UV-vis absorption spectra for DOPC (50 mM)/iso-octane/H₂O (150 mM)/CA (10 mM) solution before and after UV irradiation at 25 °C, and (c) diagrammatic view of change in solubilization sites of *trans*- and *cis*- isomers in micellar solution responsible for different rheology on UV irradiation. (Reprinted with permission from Ref. [78]. Copyright 2014, Springer.)

Raghavan and coworkers [79] have further reported VEGs combining the phospholipid lecithin and the bile salt sodium deoxycholate (SDC) in a nonpolar organic solvent such as cyclohexane (formed long cylinders, diameter ~4.4 nm and contour length >140 nm, as determined by small-angle neutron scattering). These cylinders entangle to form a transient network imparting viscoelasticity to the fluid. To impart photoresponsive properties to this gel, they added a small concentration of the spiropyran (SP) derivative 1',3',3'-trimethyl-6-nitrospiro[1(2H)-benzopyran-2,2'-indoline]. Initially, the lecithin/SDC/SP mixtures formed highly viscoelastic fluids. SPs are well-known photochromic compounds that can be reversibly photoisomerized between the colorless SP form and the colored merocyanine (MC) formed by the irradiation at different wavelengths of light, as shown in Figure 13.11. The closed SP form is hydrophobic and nonionic, whereas the open MC form is zwitterionic and hydrophilic. These two photoisomers are known to interact differently with the head groups of lecithin. Under UV irradiation, the SP was isomerized to the open MC form, causing the fluid viscosity to decrease by 10-fold. When the



Figure 13.11 (a) Sample containing 100 mM lecithin, 35 mM SDC, and 15 mMSP in cyclohexane. (b) After UV irradiation, the viscosity of the sample decreased and its color changed from yellow to red. (c) When the UV irradiation was stopped, the sample viscosity and color reverted to their initial states. This cycle could be repeated several times. Scheme

components of a reversible PR fluid: the phospholipid lecithin is combined with the bile salt SDC and an SP derivative. The SP is initially in a closed form but can be photoisomerized to the open (MC) form by UV irradiation. This can be reversed by visible-light irradiation or heating. (Reprinted with permission from Ref. [79]. Copyright 2011, American Chemical Society.)

UV irradiation was switched off, the MC reverted to the SP form, and the viscosity recovered its initial value. This cycle could be repeated several times without loss of response. The rheological transitions are believed to reflect changes in the length of the cylinders. This leads to reversible light-induced changes in the rheological properties of the solutions.

13.8 Applications

The field of stimuli-responsive gels has grown considerably over the past decade [80]. A lot of “intelligent” nanostructured systems have emerged and have been proposed for a wide range of applications, for instance, in electronic devices, as “smart” optical systems [81], microelectromechanical systems, in coatings, and quite significantly in the biomedical field for drug delivery, diagnostics, as biosensors, for bioseparation and artificial organs and tissues. Traditionally, these materials have predominantly been based on polymers; however, VEGs displaying substantial viscoelasticity [32,82] provide an opportunity for capture and release, particularly relevant to the areas of drug delivery [83], the release of perfumes, and cleaning processes. It is still a very young field, their applications as such are still largely speculative. Responsive viscoelastic gels could provide an alternative to conventional polymer-based materials for biomedical applications; they are easier to degrade and therefore likely to be more biocompatible; they are more amenable to being responsive to a range of various triggers particularly relevant to the biomedical field, because they often appear as the result of a pathology, including pH, temperature, and redox potential [84]. They naturally incorporate a hydrophobic core, which could serve as a solubilization locus for pharmaceutical oils and drugs [85]. In tissue engineering, scaffolds that gel upon exposure to body temperature offer the significant advantage of avoiding surgical procedures and complications associated with implants [84b]. The incorporation of stimuli responsiveness in “intelligent” materials addresses some of the systemic and intracellular delivery barriers. In addition, external stimuli can also be envisaged to target delivery to specific sites, in particular via the application of (localized) light, ultrasound, or magnetic field. They have potential as vehicles for controlled and targeted delivery. One could also envisage imparting responsiveness to chemical and biological stimuli such as glucose concentration for the treatment of diabetes [86] or the presence of metabolites [87]. Light-responsive gels provide the additional benefit of precise localization, making it useful in numerous nanotechnological applications, sensor systems, nanoelectronics, microfluidics, molecular devices, logic gates, and information storage devices [88]. Applications in bioseparation and capillary electrophoresis are anticipated as they are likely to tolerate the addition of electrolytes, macromolecules, or nanoparticles [69b,89]. The pH stimulus is of interest particularly in pharmaceutical, biomedical, and related fields. It is often triggered in the controlled release of encapsulated drugs. The VEGs whose

viscosity increases with increase in pH of the solution and degrade on coming in contact with hydrocarbons are advantageous over the polymer that generally has a narrow pH window and degrades with a temperature increase in the extraction process of CaCO_3 in calcite or MgCO_3 in dolomite.

In oil industry, controllable rheology of gels can be extensively used in different stages of oil production process, from drilling, gravel packing, fracturing fluid, and self-diverting acidizing [90] to tertiary oil recovery [91]. They have long been used as cleaning and personal care products [92]. Conventional VEGs have long been found to be superior to polymers as drag-reducing (DR) agents, because they reform after being broken down by high shear stresses, and the long micellar chains may help damp small turbulent eddies and reduce the dissipation of turbulent energy, and the alignment of thread-like micelles along the flow may cause anisotropic resistance to turbulent vortices resulting in suppressed flow fluctuations in the direction normal to the flow [93]. Responsive VEGs can further overcome poor heat-transfer capability by being able to switch on demand from a short aggregate structure (thus low viscosity and high heat-transfer capacity) to a long structure (thus high viscoelasticity and high DR state). The DR capability could thus be switched “off” at the inlet of the heat exchanger in a recirculating system, and switched back “on” at its exit. Recently, Zakin and coworkers demonstrated a very promising approach to developing effective drag reducing systems for use in cooling and heating installations [94]. Several researchers have exploited the “sol–gel” transition and network structure of VEGs to build up nanofibers [95], silica nanoparticles [96], as building blocks for the fabrication of smart surface coatings [97], and porous nanostructured materials [98]. It could be envisioned as optical sensors by mixing with solvatochromic species or aggregachromic dyes [27]. In order to implement VEG into the actual applications, studying the effects of various stimuli on rheology is essential.

13.9

Conclusions

Advanced dynamic gels that are responsive to external stimuli can be formed in aqueous or nonaqueous solution of surfactants. Experimental techniques such as rheology, small-angle X-ray scattering, and cryo-TEM provide evidences on the change in morphology and size and the dynamics of the systems, which show several relaxation and diffusion mechanisms, associated with micellar breaking, reptation, and entanglement. The molecular packing in micellar aggregates is affected by adding cosurfactant, altering the temperature, pH, and electrical stimulant. The basic principle relies on an introduction of a responsive surfactant or additive unit, either chemically to the gelling system or by adding a responder into the surfactant solutions. The modification of the critical packing parameter is triggered by the appropriate stimulus, inducing a spontaneous reorganization of the surfactants from highly viscoelastic gels to spheres, short

rods, or vesicles, and vice versa leading to the modification of the rheological properties. The responsive VEGs expand the field of applications and provide new insights into the study of living polymers. Due to their versatility and yet simplicity in designing principles, stimuli-responsive advanced dynamic gels have drawn interest over recent years and a range of gel systems have been reported, which respond to light, temperature, pH, redox reaction, and hydrocarbons. These gels can find real applications in a very diverse range of applications such as sensors, in microfluidics, drug delivery, biomedical applications, nanostructured materials, and in the oil industry. Future trends in this field may see an expansion toward multistimuli-responsive VEGs, as triggers to ultrasounds, microwaves, and magnetism. The hybridization of stimuli-responsive gels with polymers, colloids, nanoparticles, biomaterials, and any other functional materials could also open a facile way to fabricate stimuli-responsive hybrid materials. Responsive VEGs on aqueous or nonaqueous media have largely unexplored and may become the focus of further interest.

13.10 Theory

In 1913, McBain proposed the idea of self-assembly of amphiphiles in aqueous solution [99]. An amphiphile is made up of two different types of moieties: hydrophilic (affinity toward aqueous environment) and hydrophobic (affinity toward nonaqueous environment). Due to this, they have distinctly opposite affinity toward the solvents used. This amphiphilicity, therefore, is one of the main driving forces for self-assembly of surfactants. The thermodynamics of the micellization depend on the balance of repulsive interaction between the surfactant hydrophilic groups and van der Waals attractive forces between the hydrocarbon chains [100,101].

The packing free energy per molecule, f , is given by the sum of the average interaction (steric and/or electrostatic) energy per molecule resulting from the hydrophilic group repulsion, f_h , the surface energy associated with the hydrocarbon–water interface, f_s , and the chain (hydrocarbon tail) contribution to the free energy, f_t , as follows:

$$f = f_h + f_s + f_t \quad (13.1)$$

The three terms, f_h , f_s , and f_t , depend on the average cross-sectional area of the hydrophilic group per molecule at the interface, a_s , and on the local interfacial curvatures [102]. The thermodynamic properties of amphiphiles in solution are, therefore, controlled by the tendency of hydrophobic tails to avoid direct contact with water (i.e., hydrophobicity). This unfavorable interaction can be minimized by the self-assembly of amphiphilic molecules into micelles in which the hydrophilic domains become exposed to water and the hydrophobic parts are shielded. This is called micellization [6]. Furthermore, the segregated hydrocarbon chains of amphiphiles interrupt the hydrogen bonding between water molecules, which

are entropically unfavorable. In order to avoid this disruption of the water structure, entropically more favorable aggregated structures (micelles) are formed [7,8]. They form micelles that occur usually above a certain concentration known as the critical micelle concentration. The geometry of self-assembled structures formed by an amphiphile may be predicted by the critical packing parameter of an amphiphilic molecule, $\text{CPP} = v/a_s l_c$, where v is the volume of the lipophilic chain having maximum effective length, l_c and a_s . Generally, hydrophilic amphiphiles having large head group self-assemble into spherical micelles ($\text{CPP} \leq 1/3$) in dilute aqueous regions. A reduction in a_s , namely, an increase in the CPP, tends to induce micellar growth. Certain surfactants and polymers show an enormous micellar growth in one dimension. Depending on the nature of the surfactant, such micellar growth can be induced by change in concentration, temperature, adding cosurfactants, or specific counterions. These cylindrical micelles commonly consist of a cylindrical body and two hemispherical endcaps [103,104]. The molecules packed at the hemispherical ends have excess free energy called “endcap energy,” a thermodynamic driving force for the linear growth [54a], reaching a few nanometers to micrometers in length. When the number density of these long aggregates exceeds a certain threshold value, they entangle with each other to form a transient network called worm-like micelles, viscoelastic gels, or giant micelles [105] that exhibit viscoelastic properties. Above a system-dependent concentration, these long micelles are entangled to form a transient network that exhibits viscoelastic behavior.

A system exhibiting an elastic property characteristic of a solid material has a Hookean constant G_0 called the shear modulus, while those having a viscous property have a zero shear viscosity η_0 . The viscoelastic fluids or gels exhibit both these properties. In such cases, the rheological properties can be interpreted in terms of the Maxwell model of a viscoelastic fluid [106,107], consisting of an elastic spring with the Hookean constant G_0 and a dashpot with viscosity η_0 . Rheological criteria involving the magnitudes and ratios of the elastic (G') and loss (G'') moduli and viscosity are probably the most useful and physically quantifiable criteria. They allow a differentiation between a “true” gel and a jelly. The variation of elastic (storage) modulus (G') and viscous (loss) modulus (G'') with shear frequency ω is given by the following equations:

$$G'(\omega) = \frac{\omega^2 \tau_R^2}{1 + \omega^2 \tau_R^2} G_0, \quad (13.2)$$

$$G''(\omega) = \frac{\omega \tau_R}{1 + \omega^2 \tau_R^2} G_0, \quad (13.3)$$

where τ_R is the Maxwellian relaxation time.

In the low-frequency region $\omega \ll \omega_c$, G' and G'' relate with ω according to $G' \propto \omega^2$ and $G'' \propto \omega$. In the high-frequency region $\omega \gg \omega_c$, however, G' attains a plateau value equal to G_0 , whereas G'' shows a monotonic decrease. The shear frequency corresponding to $G'-G''$ crossover is $\omega_c = 1/\tau_R$. For worm-like micellar solutions, the τ_R and G_0 give information about the average micellar length

and the number density of the entanglements in the transient network, respectively. A $G'(\omega)$ versus $G''(\omega)$ (Cole–Cole) plot would give a semicircle for Maxwellian behavior. The G_0 , τ_R , and η_0 are related as follows:

$$\eta_0 = G_0 \tau_R. \quad (13.4)$$

Alternatively, η_0 is also related to the complex viscosity values ($|\eta^*|$) as follows:

$$|\eta^*| = \frac{(G'^2 + G''^2)^{1/2}}{\omega} = \frac{\eta_0}{\sqrt{1 + \omega^2 \tau_R^2}}. \quad (13.5)$$

When the equilibrium condition for viscoelastic system is disturbed, it tries to relax and restore the equilibrium condition within a definite relaxation time τ_R . In many cases, there is only one characteristic τ_R for viscoelastic micellar systems.

The viscoelastic micelles are often called *living polymers* as they break and reform spontaneously, which fluctuate their molecular weight with time [108], while the covalently bonded repeat units of conventional polymers keep their molecular weight constant. According to the mean field model developed by Cates and coworkers [109], the rheological behavior of viscoelastic gels is dictated by the competition between the two processes: reptation (reptile-like motion of the micelle along its own contour) and reversible scission of micelles, taking place at two timescales, namely, reptation time τ_{rep} and breaking time τ_b . It is assumed that when a chain breaks, the two resulting chains become uncorrelated and recombine with the micellar end in a random way. For fast scission kinetics ($\tau_b \ll \tau_{rep}$), a single-exponential stress decay is observed, and the viscoelastic behavior of such systems in the low-frequency region follows the Maxwell model with a single relaxation time τ_R given by $(\tau_b \cdot \tau_{rep})^{1/2}$. Although the Maxwell equations predict a monotonic decrease of G'' in the high-frequency region, viscoelastic gel usually deviates from this behavior, showing an increase of G'' in the high-frequency region and a deviation from the semicircle predicted by the Maxwell model in the G'' versus G' (Cole–Cole) plot. This deviation is often associated with the stress relaxation by additional “faster” processes such as Rouse modes of cylindrical micelles, analogous to polymer chains. The minimum value of G'' in the high-frequency region is related to contour length L according to the following relation:

$$\frac{G''_{min}}{G_0} \approx \frac{l_e}{L}, \quad (13.6)$$

where l_e is the entanglement length, that is, the contour length of the section of viscoelastic micelles between two entanglement points. For flexible micelles, the correlation length ξ , which gives the mesh size of the micellar network, is related to l_e :

$$l_e = \frac{\xi^{5/3}}{l_p^{2/3}}. \quad (13.7)$$

The persistence length l_p gives an estimate of micellar flexibility. Even though the micelles are flexible, at a small length scale (comparable to l_p), they behave

as rigid rods. The correlation length ξ is related to T and G_0 as follows:

$$\xi \approx \left(\frac{kT}{G_0} \right)^{1/3}. \quad (13.8)$$

The combination of Eqs. (13.7) and (13.8) yields an equation that relates l_e to G_0 :

$$G_0 \approx \frac{kT}{l_e^{9/5} l_p^{6/5}} \quad (13.9)$$

For $\tau_b \ll \tau_{\text{rep}}$, the living polymer model predicts the following scaling laws for the viscoelastic parameters [110]: $G_0 \approx \phi^{2.25}$, $\tau_R \approx \phi^{1.25}$, $\eta_0 \approx \phi^{3.5}$, and $G''_{\min}/G_0 \approx \phi^{-1.75}$. When $\tau_b \gg \tau_{\text{rep}}$, the micelles behave like ordinary polydisperse unbreakable polymers, and the stress relaxation function is strongly nonexponential. For neutral or highly screened ionic micelles [111], the zero-shear viscosity scales as $\eta_0 \propto \phi^{5.25}$. For branched or interconnected micelles, the exponents of the scaling laws are significantly different [112,113]. For saturated interconnected network, $G''_{\min}/G_0 \approx \phi^{-0.75}$ has been proposed [114].

Most of the already discussed fundamental structural quantities can be obtained from the rheological measurements.

The analysis of small-angle scattering data using indirect Fourier transformation (IFT) followed by deconvolution [115] allows us to extract information about the shape and the internal structure of the aggregate without having a prior assumption of the model. Here, only an extract of the principle involved is presented.

The overall scattering intensity $I(q)$ for the systems of monodisperse spherical particles is given by

$$I(q) = nP(q)S(q), \quad (13.10)$$

where $P(q)$ is the intraparticle contribution, known as form factor, and $S(q)$ is the interparticle contribution or structure factor. When the system is sufficiently dilute, $S(q) \approx 0 \leftarrow 1$, the spatially averaged $I(q)$ is given by

$$I(q) = 4\pi \int_0^\infty p(r) \frac{\sin(qr)}{qr} dr, \quad (13.11)$$

where $p(r)$ is the pair-distance distribution function (PDDF), which enables the overall information about the shape of the scattering particles such as micellar aggregates. The Fourier transform of $p(r)$ gives $P(q)$. The PDDF for a particle of an arbitrary shape with a scattering density difference of $\Delta\rho(r)$ is given by

$$p(r) = r^2 \Delta\tilde{\rho}^2(r), \quad (13.12)$$

where $\Delta\tilde{\rho}^2(r)$ is the convolution square of $\Delta\rho(r)$ averaged for all directions in space. The form factor and the structure factor can be determined by *generalized indirect Fourier transformation* (GIFT) technique [116–118] simultaneously from the scattering data without any assumption for the form factor, whereas we

need appropriate assumptions for the interparticle interaction potential for the structure factor. A hard-sphere interaction model is the common choice. The detailed theoretical description of the method has been reported elsewhere. It has been observed that when particle geometry deviates from an ideal spherical symmetry, the output parameters from $S(q)$ analysis are no longer exact. Nevertheless, the GIFT approach efficiently suppresses the influence of the interparticle interference scattering in the calculation of $p(r)$ and allows us to deduce a sufficiently reliable $p(r)$ value.

References

- 1 Kruyt, H.R. (1949) Chapter XII, in *Colloid Science*, vol. II, Elsevier, Amsterdam, p. 484.
- 2 Jones, R.G., Edward, S., Wilks, W., Metanomski, V., Kahovec, J., Hess, M., Stepto, R., and Kitayama, T. (2009) *Compendium of Polymer Terminology and Nomenclature: IUPAC Recommendations 2008*, 2nd ed., RSC Publishing, p. 464. ISBN 978-0-85404-491-7.
- 3 Flory, P. (1974) *Discuss. Faraday Soc.*, **57**, 7–18.
- 4 Wallace, D.G. and Rosenblatt, J. (2003) *Adv. Drug Deliv. Rev.*, **55**, 1631–1649.
- 5 (a) Jin, H.-J. and Kaplan, D.L. (2003) *Nature*, **424**, 1057–1061; (b) Valluzzi, R., Jin, H.-J., and Park, J. (2004) PCT Int. Appl. WO 41,845 (Cl. C07K), May 21, 2004.
- 6 Clark, J.B. (1952) Treatment of wells. U.S. Patent 2,596,844, May 13, 1952.
- 7 Fieser, L.P., Harris, G.C., Hershberg, E.B., Morgana, M., Novello, F.C., and Putnam, S.T. (1946) *Ind. Eng. Chem.*, **38**, 768–773.
- 8 Ingber, D.E. (1998) *Sci. Am.*, **278**, 48–57.
- 9 Greer, S.C. (2002) *Annu. Rev. Phys. Chem.*, **53**, 173–200.
- 10 Kirchhausen, T. (2000) *Annu. Rev. Biochem.*, **69**, 699–727.
- 11 (a) Tuszyński, J.A., Brown, J.A., and Sept, D. (2003) *J. Biol. Phys.*, **29**, 401–428; (b) Oakley, B.R. and Akkari, Y.N. (1999) *Cell Struct. Funct.*, **24**, 365–372.
- 12 (a) Fuchs, E. (1995) *Annu. Rev. Cell Dev. Biol.*, **11**, 123–153; (b) Smack, D.P., Korge, B.P., and James, W.D. (1994) *J. Am. Acad. Dermatol.*, **30**, 85–102.
- 13 (a) Waugh, D.F. (1946) *J. Am. Chem. Soc.*, **68**, 247–250; (b) Jiminez, J.L., Nettleton, E.J., Bouchard, M., Robinson, C.V., and Dobson, C.M. (2002) *Proc. Natl. Acad. Sci. USA*, **99**, 9196–9201.
- 14 Caria, A., Bixio, L., Kostyuk, O., and Ruggiero, C. (2004) *IEEE Trans. Nanobiosci.*, **3**, 85–89.
- 15 (a) Jin, H.-J. and Kaplan, D.L. (2003) *Nature*, **424**, 1057–1061; (b) Valluzzi, R., Jin, H.-J., and Park, J. (2004) PCT Int. Appl. WO 41,845 (Cl. C07K), May 21, 2004.
- 16 (a) Jimenez, J.L., Nettleton, E.J., Bouchard, M., Robinson, C.V., Dobson, C.M., and Saibil, H.R. (2002) *Proc. Natl. Acad. Sci. USA*, **99**, 9196–9201; (b) Liu, W., Prausnitz, J.M., and Blanch, H.W. (2004) *Biomacromolecules*, **5**, 1818–1823; (c) Nilson, M.R. (2004) *Methods*, **34**, 151–160; (d) Waterhouse, S.H. and Gerrard, J.A. (2004) *Aust. J. Chem.*, **57**, 519–523.
- 17 Galkin, O. and Vekilov, P.G. (2004) *J. Mol. Biol.*, **336**, 43–59.
- 18 (a) Drukman, S. and Kavallaris, M. (2002) *Intern. J. Oncol.*, **21**, 621–628; (b) Reinhart, W.H. (2001) *Biorheology*, **38**, 203–212.
- 19 Dee, E.M., McGinley, M., and Hogan, C.M. (2010) Long-finned pilot whale, in *Encyclopedia of Earth* (eds P. Saundry and C. Cleveland), National Council for Science and the Environment, Washington, DC.
- 20 Chu, Z., Dreiss, C.A., and Feng, Y. (2013) *Chem. Soc. Rev.*, **42**, 7174–7203.
- 21 Liu, Y., Jessop, P.G., Cunningham, M., Eckert, C.A., and Liotta, C.L. (2006) *Science*, **313**, 958–960.
- 22 Lahann, J., Mitragotri, S., Tran, T.-N., Kaido, H., Sundaram, J., Choi, I.S., Hoffer,

- S., Somorjai, G.A., and Langer, R. (2003) *Science*, **299**, 371–374.
- 23** Xin, B. and Hao, J. (2010) *Chem. Soc. Rev.*, **39**, 769–782.
- 24** Tokarev, I. and Minko, S. (2009) *Adv. Mater.*, **21**, 241–247.
- 25** Bajpai, A.K., Shukla, S.K., Bhanu, S., and Kankane, S. (2008) *Prog. Polym. Sci.*, **33**, 1088–1118.
- 26** Lee, K.Y. and Mooney, D. (2001) *J. Chem. Rev.*, **101**, 1869–1879.
- 27** Pucci, A., Bizzarri, R., and Ruggeri, G. (2011) *Soft Matter*, **7**, 3689–3700.
- 28** Hartsock, D.L., Novak, R.F., and Chaundy, G.J. (1991) *J. Rheol.*, **35**, 1305–1326.
- 29** Ketner, A.M., Kumar, R., Davies, T.S., Elder, P.W., and Raghavan, S.R. (2007) *J. Am. Chem. Soc.*, **129**, 1553–1559.
- 30** Stanway, R., Sproston, J.L., and El-Wahed, A.K. (1996) *Smart Mater. Struct.*, **5**, 464–482.
- 31** Boek, E.S., Jusufi, A., Löwen, H., and Maitland, G.C. (2002) *J. Phys. Condens. Matter*, **14**, 9413–9430.
- 32** Chu, Z. and Feng, Y. (2011) *Chem. Commun.*, **47**, 7191–7193.
- 33** Bohon, K. and Krause, S. (1998) *J. Polym. Sci. B Polym. Phys.*, **36**, 1091–1094.
- 34** Danino, D., Talmon, Y., Levy, H., Beinert, G., and Zana, R. (1995) *Science*, **269**, 1420–1421.
- 35** Bernheim-Groswasser, A., Zana, R., and Talmon, Y. (2000) *J. Phys. Chem. B*, **104**, 4005–4009.
- 36** Zheng, Y., Won, Y.Y., Bates, F.S., Davis, H.T., Scriven, L.E., and Talmon, Y. (1999) *J. Phys. Chem. B*, **103**, 10331–10334.
- 37** Tsuchiya, K., Orihara, Y., Kondo, Y., Yoshino, N., Ohkubo, T., Sakai, H., and Abe, M. (2004) *J. Am. Chem. Soc.*, **126**, 12282–12283.
- 38** Chu, Z. and Feng, Y. (2010) *Chem. Commun.*, **46**, 9028–9030.
- 39** (a) Kawasaki, H., Souda, M., Tanaka, S., Nemoto, N., Karlsson, G., Almgren, M., and Maeda, H. (2002) *J. Phys. Chem. B*, **106**, 1524–1527; (b) Maeda, H., Yamamoto, A., Souda, M., Kawasaki, H., Hossain, K.S., Nemoto, N., and Almgren, M. (2001) *J. Phys. Chem. B*, **105**, 5411–5418; (c) Maeda, H., Tanaka, S., Ono, Y., Miyahara, M., Kawasaki, H., Nemoto, N., and Almgren, M. (2006) *J. Phys. Chem. B*, **110**, 12451–12458;
- (d) Majhi, P.R., Dubin, P.L., Feng, X., and Guo, X. (2004) *J. Phys. Chem. B*, **108**, 5980–5988; (e) Brinchi, L., Germani, R., Profio, P.D., Marte, L., Savelli, G., Oda, R., and Berti, D. (2010) *J. Colloid Interface Sci.*, **346**, 100–106.
- 40** Rathman, J.F. and Christian, S.D. (1990) *Langmuir*, **6**, 391–395.
- 41** (a) Maeda, H. (1996) *Colloids Surf. A*, **109**, 263–271; (b) Zhang, H., Dubin, P.L., and Kaplan, J.I. (1991) *Langmuir*, **7**, 2103–2107; (c) Mille, M. (1981) *J. Colloid Interface Sci.*, **81**, 169–179.
- 42** (a) Lin, Y., Han, X., Huang, J., Fu, H., and Yu, C. (2009) *J. Colloid Interface Sci.*, **330**, 449–455; (b) Yan, H., Zhao, M., and Zheng, L. (2011) *Colloids Surf. A*, **392**, 205–212; (c) Verma, G., Aswal, V.K., and Hassan, P. (2009) *Soft Matter*, **5**, 2919–2927; (d) Ali, M., Jha, M., Das, S.K., and Saha, S.K. (2009) *J. Phys. Chem. B*, **113**, 15563–15571.
- 43** (a) Lin, Y., Han, X., Cheng, X., Huang, J., Liang, D., and Yu, C. (2008) *Langmuir*, **24**, 13918–13924; (b) Ghosh, S., Khatua, D., and Dey, J. (2011) *Langmuir*, **27**, 5184–5192; (c) Johnsson, M., Wagenaar, A., and Engberts, J.B.F.N. (2003) *J. Am. Chem. Soc.*, **125**, 757–760; (d) Johnsson, M., Wagenaar, A., Stuart, M.C.A., and Engberts, J.B.F.N. (2003) *Langmuir*, **19**, 4609–4618; (e) Jaeger, D.A., Li, G., Subotkowski, W., and Carron, K.T. (1997) *Langmuir*, **13**, 5563–5569; (f) Graf, G., Drescher, S., Meister, A., Dobner, B., and Blume, A. (2011) *J. Phys. Chem. B*, **115**, 10478–10487.
- 44** (a) Zhao, L., Wang, K., Xu, L., Liu, Y., Zhai, S., Li, Z., Yan, Y., and Huang, J. (2012) *Soft Matter*, **8**, 9079–9085; (b) Sakai, K., Nomura, K., Shrestha, R.G., Endo, T., Sakamoto, K., Sakai, H., and Abe, M. (2012) *Langmuir*, **28**, 17617–17622.
- 45** Kato, T., Terao, T., and Seimiya, T. (1994) *Langmuir*, **10**, 4468–4474.
- 46** Schurtenberger, P., Cavaco, C., Tiberg, F., and Regev, O. (1996) *Langmuir*, **12**, 2894.
- 47** Arrigo, G.D. and Briganti, G. (1998) *Phys. Rev. E*, **58**, 713–723.
- 48** Acharya, D.P., Sharma, S.C., Rodriguez-Abreu, C., and Aramaki, K. (2006) *J. Phys. Chem. B*, **110**, 20224–20234.

- 49** (a) Jerke, G., Pedersen, J.S., Egelhaaf, S.U., and Schurtenberger, P. (1998) *Langmuir*, **14**, 6013–6024; (b) Acharya, D.P. and Kunieda, H. (2003) *J. Phys. Chem. B*, **107**, 10168–10175; (c) Ahmed, T. and Aramaki, K. (2008) *J. Colloid Interface Sci.*, **327**, 180–185; (d) Shrestha, R.G., Sharma, S.C., Sakai, K., Sakai, H., and Abe, M. (2012) *Colloid Polym. Sci.*, **290**, 339–348; (e) Kunieda, H., Rodriguez, C., Tanaka, Y., Kabir, Md. H., and Ishitobi, M. (2004) *Colloids Surf. B*, **38**, 127–130; (f) Acharya, D.P., Hossain, Md. K., Feng, J., Sakai, T., and Kunieda, H. (2004) *Phys. Chem. Chem. Phys.*, **6**, 1627–1631; (g) Sato, T., Hossain, Md. K., Acharya, D.P., Glatter, O., Chiba, A., and Kunieda, H. (2004) *J. Phys. Chem. B*, **108**, 12927–12939; (h) Hashizaki, K., Tamaki, N., Taguchi, H., Saito, Y., Tsuchiya, K., Sakai, H., and Abe, M. (2008) *Chem. Pharm. Bull.*, **56**, 1682–1686; (i) Sharma, S.C., Shrestha, L.K., Tsuchiya, K., Sakai, K., Sakai, H., and Abe, M. (2009) *J. Phys. Chem. B*, **113**, 3043–3050; (j) Shrestha, R.G., Sakai, K., Sakai, H., and Abe, M. (2011) *J. Phys. Chem. B*, **115**, 2937–2946; (k) Shrestha, R.G., Abezgauz, L., Danino, D., Sakai, K., Sakai, H., and Abe, M. (2011) *Langmuir*, **27**, 12877–12883.
- 50** Ahmed, T. and Aramaki, K. (2009) *J. Colloid Interface Sci.*, **336**, 335–344.
- 51** Varade, D., Ushiyama, K., Shrestha, L.K., and Aramaki, K. (2007) *J. Colloid Interface Sci.*, **312**, 489–497.
- 52** Moitzi, C., Freiberger, N., and Glatter, O. (2005) *J. Phys. Chem. B*, **109**, 16161–16168.
- 53** Bernheim-Groswasser, A., Wachtel, E., and Talmon, Y. (2000) *Langmuir*, **16**, 4131–4140.
- 54** (a) Debye, P. and Anacker, E. (1951) *J. Phys. Chem.*, **55**, 644–655; (b) Nash, T. (1958) *J. Colloid Sci.*, **13**, 134–139.
- 55** Salkar, R.A., Hassan, P.A., Samant, S.D., Valaulikar, B.S., Kumar, V.V., Kern, F., Candau, S.J., and Manohar, C. (1996) *Chem. Commun.*, 1223–1224.
- 56** (a) Hassan, P.A., Valaulikar, B.S., Manohar, C., Kern, F., Bourdieu, L., and Candau, S.J. (1996) *Langmuir*, **12**, 4350–4357; (b) Narayanan, J., Mendes, E., and Manohar, C. (2002) *Int. J. Mod. Phys. B*, **16**, 375–382; (c) Mendes, E., Oda, R., Manohar, C., and Narayanan, J. (1998) *J. Phys. Chem. B*, **102**, 338–343; (d) Horbaschek, K., Hoffmann, H., and Thunig, C. (1998) *J. Colloid Interface Sci.*, **206**, 439–456.
- 57** Kalur, G.C., Frounfelker, B.D., Cipriano, B.H., Norman, A.I., and Raghavan, S.R. (2005) *Langmuir*, **21**, 10998–11004.
- 58** Davies, T.S., Ketner, A.M., and Raghavan, S.R. (2006) *J. Am. Chem. Soc.*, **128**, 6669–6675.
- 59** Sreejith, L., Parathakkat, S., Nair, S.M., Kumar, S., Varma, G., Hassan, P.A., and Talmon, Y. (2011) *J. Phys. Chem. B*, **115**, 464–470.
- 60** Kalur, G.C. and Raghavan, S.R. (2005) *J. Phys. Chem. B*, **109**, 8599–8604.
- 61** (a) Tobita, K., Sakai, H., Kondo, Y., Yoshino, N., Iwahashi, M., Momozawa, N., and Abe, M. (1997) *Langmuir*, **13**, 5054–5059; (b) Tobita, K., Sakai, H., Kondo, Y., Yoshino, N., Kamogawa, K., Momozawa, N., and Abe, M. (1998) *Langmuir*, **14**, 4753–4757; (c) Danino, D., Weihs, D., Zana, R., Orädd, G., Lindblom, G., Abe, M., and Talmon, Y. (2003) *J. Colloid Interface Sci.*, **259**, 382–390.
- 62** Yang, D., Piech, M., Bell, N.S., Gust, D., Vail, S., Garcia, A.A., Schneider, J., Park, C.-D., Hayes, M.A., and Picraux, S.T. (2007) *Langmuir*, **23**, 10864–10872.
- 63** Wolff, T. and Kerperin, K. (1993) *J. Colloid Interface Sci.*, **157**, 185–195.
- 64** Lehnberger, C. and Wolff, T. (1999) *J. Colloid Interface Sci.*, **213**, 187–192.
- 65** Yu, X. and Wolff, T. (2003) *Langmuir*, **19**, 9672–9679.
- 66** (a) Shang, T., Smith, K.A., and Hatton, T.A. (2006) *Langmuir*, **22**, 1436–1442; (b) Sakai, H., Orihara, Y., Kodashima, H., Matsumura, A., Ohkubo, T., Tsuchiya, K., and Abe, M. (2005) *J. Am. Chem. Soc.*, **127**, 13454–13455; (c) Sakai, H., Matsumura, A., Yokoyama, S., Saji, T., and Abe, M. (1999) *J. Phys. Chem. B*, **103**, 10737–10740; (d) Hubbard, F.P., Jr., Santonicola, G., Kaler, E.W., and Abbott, N.L. (2005) *Langmuir*, **21**, 6131–6136; (e) Lee, C.T., Smith, K.A., and Hatton, T.A. (2005) *Biochemistry*, **44**, 524–536; (f) Orihara, Y., Matsumura, A., Saito, Y., Ogawa, N., Saji, T., Yamaguchi, A., Sakai,

- H., and Abe, K. (2001) *Langmuir*, **17**, 6072–6076; (g) Shin, J.Y. and Abbott, N.L. (1999) *Langmuir*, **15**, 4404–4410; (h) Bradley, M., Vincent, B., Warren, N., Eastoe, J., and Vesperinas, A. (2006) *Langmuir*, **22**, 101–105.
- 67** (a) Eastoe, J., Dominguez, M.S., Wyatt, P., Beeby, A., and Heenan, R.K. (2002) *Langmuir*, **18**, 7837–7844; (b) Eastoe, J., Dominguez, M.S., Wyatt, P., and Heenan, R.K. (2004) *Langmuir*, **20**, 6120–6126; (c) Kozlecki, T. and Wilk, K.A. (1996) *J. Phys. Org. Chem.*, **9**, 645–651; (d) Kozlecki, T., Wilk, K.A., and Syper, L. (1998) *Prog. Colloid. Polym. Sci.*, **110**, 193–198.
- 68** (a) Sun, C., Arimitsu, K., Abe, K., Ohkubo, T., Yamashita, T., Sakai, H., and Abe, M. (2004) *Mater. Technol.*, **22**, 229–232; (b) Liu, S., Fujihira, M., and Saji, T. (1994) *J. Chem. Soc. Chem. Commun.*, **16**, 1855–1856.
- 69** (a) Kumar, R., Ketner, A.M., and Raghavan, S.R. (2010) *Langmuir*, **26**, 5405–5411; (b) Kumar, R. and Raghavan, S.R. (2009) *Soft Matter*, **5**, 797–803.
- 70** Sakai, H., Orihara, Y., Kodashima, H., Matsumura, A., Ohkubo, T., Tsuchiya, K., and Abe, M. (2005) *J. Am. Chem. Soc.*, **127**, 13454–13455.
- 71** Hubbard, F.P. Jr. and Abbott, N.L. (2007) *Langmuir*, **23**, 4819–4829.
- 72** Aikawa, S., Shrestha, R.G., Ohmori, T., Fukukita, Y., Tezuka, Y., Endo, T., Torigoe, K., Tsuchiya, K., Sakamoto, K., Sakai, K., Abe, M., and Sakai, H. (2013) *Langmuir*, **29**, 5668–5676.
- 73** (a) Shchipunov, Y.A. (2001) *Colloid Surf. A*, **183–185**, 541–554; (b) Willard, D.M., Riter, R.E., and Levinger, N.E. (1998) *J. Am. Chem. Soc.*, **120**, 4151–4160; (c) Scartazzini, R. and Luisi, P.L. (1988) *J. Phys. Chem.*, **92**, 829–833.
- 74** (a) Hashizaki, K., Taguchi, H., and Saito, Y. (2009) *Colloid Polym. Sci.*, **287**, 1099–1105; (b) Hashizaki, K., Chiba, T., Taguchi, H., and Saito, Y. (2009) *Colloid Polym. Sci.*, **287**, 927–932.
- 75** (a) Hashizaki, K., Taguchi, H., and Saito, Y. (2009) *Chem. Lett.*, **38**, 1036–1037; (b) Hashizaki, K., Sakanishi, Y., Yako, S., Tsusaka, H., Imai, M., Taguchi, H., and Saito, Y. (2012) *J. Oleo Sci.*, **61**, 267–275.
- 76** (a) Tung, S.H., Huang, Y.E., and Raghavan, S.R. (2006) *J. Am. Chem. Soc.*, **128**, 5751–5756; (b) Tung, S.H., Huang, Y.E., and Raghavan, S.R. (2007) *Langmuir*, **23**, 372–376.
- 77** (a) Schurtenberger, P., Scartazzini, R., Magid, L.J., Leser, M.E., and Luisi, P.L. (1990) *J. Phys. Chem.*, **94**, 3695–3701; (b) Schurtenberger, P., Magid, L.J., King, S.M., and Lindner, P. (1991) *J. Phys. Chem.*, **95**, 4173–4176.
- 78** Shrestha, R.G., Agari, N., Tsuchiya, K., Sakamoto, K., Sakai, K., Abe, M., and Sakai, H. (2014) *Colloid Polym. Sci.*, **292**, 1599–1609.
- 79** Lee, H.Y., Diehn, K.K., Sun, K., Chen, T., and Raghavan, S.R. (2011) *J. Am. Chem. Soc.*, **133**, 8461.
- 80** Peppas, N.A., Hiltz, J.Z., Khademhosseini, A., and Langer, R. (2006) *Adv. Mater.*, **18**, 1345–1360.
- 81** Löwik, D.W.P.M., Leunissen, E.H.P., van den Heuvel, M., Hansen, M.B., and van Hest, J.C. M. (2010) *Chem. Soc. Rev.*, **39**, 3394–3412.
- 82** (a) Raghavan, S.R. and Kaler, E.W. (2001) *Langmuir*, **17**, 300–306; (b) Chu, Z. and Feng, Y. (2010) *Soft Matter*, **6**, 6065–6067; (c) Kumar, R., Kalur, G.C., Ziserman, L., Danino, D., and Raghavan, S.R. (2007) *Langmuir*, **23**, 12849–12856.
- 83** (a) Meng, F., Zhong, Z., and Feijen, J. (2009) *Biomacromolecules*, **10**, 197–209; (b) Xiong, W., Wang, W., Wang, Y., Zhao, Y., Chen, H., Xu, H., and Yang, X. (2011) *Colloids Surf. B*, **84**, 447–453; (c) Su, J., Chen, F., Cryns, V.L., and Messersmith, P.B. (2011) *J. Am. Chem. Soc.*, **133**, 11850–11853.
- 84** (a) Ganta, S., Devalapally, H., Shahiwala, A., and Amiji, M. (2008) *J. Control. Release*, **126**, 187–204; (b) Kretlow, J.D., Klouda, L., and Mikos, A.G. (2007) *Adv. Drug Deliv. Rev.*, **59**, 263–273; (c) You, Y.-Z., Zhou, Q.-H., Manickam, D.S., Wan, L., Mao, G.-Z., and Oupicky, D. (2007) *Macromolecules*, **40**, 8617–8624.
- 85** (a) Afifi, H., Karlsson, G., Heenan, R.K., and Dreiss, C.A. (2011) *Langmuir*, **27**, 7480–7492; (b) Afifi, H., Karlsson, G., Heenan, R.K., and Dreiss, C.A. (2012) *J. Colloid Interface Sci.*, **378**, 125–134.
- 86** Wu, Q., Wang, L., Yu, H., Wang, J., and Chen, Z. (2011) *Chem. Rev.*, **111**, 7855–7875.

- 87 El-Hamed, F., Dave, N., and Liu, J. (2011) *Nanotechnology*, **22**, 494011.
- 88 Ferri, V., Elbing, M., Pace, G., Dickey, M.D., Zharnikov, M., Samori, P., Mayor, M., and Rampi, M.A. (2008) *Angew. Chem., Int. Ed.*, **47**, 3407–3409.
- 89 (a) Baglioni, P., Braccalenti, E., Carretti, E., Germani, R., Goracci, L., Savelli, G., and Tiecco, M. (2009) *Langmuir*, **25**, 5467–5475; (b) Pereira, M., Leal, C.R., Parola, A.J., and Scheven, U.M. (2010) *Langmuir*, **26**, 16715–16721.
- 90 Kefi, S., Lee, J., Pope, T.L., Sullivan, P., Nelson, E., Hernandez, A.N., Olsen, T., Parlar, M., Powers, B., Roy, A., Wilson, A., and Twynam, A. (2004) *Oilfield Rev.*, **16** (4), 10–23.
- 91 Sullivan, P., Nelson, E.B., Anderson, V., and Hughes, T. (2007) Oilfield applications of giant micelles, in *Giant Micelles: Properties and Applications* (eds R. Zana and E.W. Kaler), CRC Press, Boca Raton, FL, pp. 453–472.
- 92 Dreiss, C.A. (2007) *Soft Matter*, **3**, 956–970.
- 93 Zakin, J.L., Zhang, Y., and Ge, W. (2007) Drag reduction by surfactant giant micelles, in *Giant Micelles: Properties and Applications* (eds R. Zana and E.W. Kaler), CRC Press, Boca Raton, FL, pp. 473–492.
- 94 Shi, H.F., Wang, Y., Fang, B., Talmon, Y., Ge, W., Raghavan, S.R., and Zakin, J.L. (2011) *Langmuir*, **27**, 5806–5813.
- 95 Li, G. and Zhang, Z. (2004) *Macromolecules*, **37**, 2683–2685.
- 96 (a) Tan, B., Dozier, A., Lehmler, H.-J., Knutson, B.L., and Rankin, S.E. (2004) *Langmuir*, **20**, 6981–6984; (b) Nagamine, S., Kurumada, K.-I., and Tanigaki, M. (2001) *Adv. Powder Technol.*, **12**, 145–156; (c) Broz, P., Driamov, S., Ziegler, J., Ben-Haim, N., Marsch, S., Meier, W., and Hunziker, P. (2006) *Nano Lett.*, **6**, 2349–2353.
- 97 Sakai, K., Smith, E.G., Webber, G.B., Baker, M., Wanless, E.J., Bütün, V., Armes, S.P., and Biggs, S. (2006) *Langmuir*, **22**, 8435–8442.
- 98 Choi, D. and Kumta, P.N. (2007) *J. Power Sources*, **163**, 1064–1069.
- 99 McBain, J.W. (1913) *Trans. Faraday Soc.*, **9**, 99.
- 100 Debye, P. (1949) *J. Phys. Colloid Chem.*, **53**, 1–8.
- 101 Tanford, C. (1973) *The Hydrophobic Effect*, John Wiley & Sons, Inc., New York.
- 102 May, S., Bohbot, Y., and Ben-Shaul, A. (1997) *J. Phys. Chem. B*, **101**, 8648–8657.
- 103 McMullen, W.E., Ben-Shaul, A., and Gelbart, W.M. (1984) *J. Colloid Interface Sci.*, **98**, 523–536.
- 104 Vila-Romeu, N. and Taddei, G. (1999) *Colloid Polym. Sci.*, **277**, 1093–1097.
- 105 Porte, G. (1983) *J. Phys. Chem.*, **87**, 3541–3550.
- 106 Larson, R.G. (1999) *The Structure and Rheology of Complex Fluids*, Oxford University Press, New York.
- 107 Marin, G. (1998) *Rheological Measurement*, 2nd edn (eds A.A. Collyer and D.W. Clegg), Chapman and Hall, London.
- 108 Candau, S., Hirsch, E., and Zana, R. (1985) *J. Colloid Interface Sci.*, **105**, 521–528.
- 109 (a) Cates, M.E. and Candau, S.J. (1990) *J. Phys. Condens. Matter*, **2**, 6869–6892; (b) Granek, R. and Cates, M.E. (1992) *J. Chem. Phys.*, **96**, 4758–4767; (c) Cates, M.E. (1988) *J. Phys. Fr.*, **49**, 1593–1600.
- 110 Berret, J.F., Appell, J., and Porte, G. (1993) *Langmuir*, **9**, 2851–2854.
- 111 Magid, L.J. (1998) *J. Phys. Chem. B*, **102**, 4064–4074.
- 112 Drye, T.J. and Cates, M.E. (1993) *J. Chem. Phys.*, **98**, 9790–9797.
- 113 Lequeux, F. (1992) *Europhys. Lett.*, **19**, 675–681.
- 114 Khatory, A., Lequeux, F., Kern, F., and Candau, S.J. (1993) *Langmuir*, **9**, 1456–1464.
- 115 (a) Glatter, O. (1977) *J. Appl. Crystallogr.*, **10**, 415–421; (b) Glatter, O. (1981) *J. Appl. Crystallogr.*, **14**, 101–108; (c) Strey, R., Glatter, O., Schubert, K.V., and Kaler, E.W. (1996) *J. Chem. Phys.*, **105**, 1175–1188.
- 116 Brunner-Popela, J. and Glatter, O. (1997) *J. Appl. Crystallogr.*, **30**, 431–442.
- 117 Weyerich, B., Brunner-Popela, J., and Glatter, O. (1999) *J. Appl. Crystallogr.*, **32**, 197–209.
- 118 Bergmann, A., Fritz, G., and Glatter, O. (2000) *J. Appl. Crystallogr.*, **33**, 1212–1216.

14

Micro/Nanocrystal Conversion beyond Inorganic Nanostructures

Jiansheng Wu, Li Junbo, and Qichun Zhang

14.1

Introduction

Low-dimensional organic and organic/inorganic hybrid micro/nanostructures, including particles, rods, wires, and tubes, have emerged as an exciting research area in both materials and chemistry science owing to their unique and highly tailororable properties, which make them potential applications in highly efficient catalysis, biomedical imaging, chemical sensors, drug delivery, gas storage, optics, optoelectronics, and high-density information storage [1–4]. Although a lot of methods [5–10] including solution processing, template fabrication, vapor deposition, direct writing method, laser ablation deposition, and electrospinning preparation have been employed to create different morphologies of organic micro/nanomaterials, using organic particles as starting materials to generate novel organic micro/nanostructures through chemical conversion/transformation is rare. Since it has been widely demonstrated that the preformed inorganic nanoparticles can be converted into more complicated nanocrystalline solids through chemical reaction [11–13], it should be reasonable to predict that organic particles could also possess this ability to perform chemical conversion. Nevertheless, the present reports for organic particles focus only on synthesis (shape/size control) and applications [4–6]. The chemical transformation of organic particles into derivative materials is rare.

In this chapter, we will summarize the current progress in the chemical conversion field among organic micro/nanocrystals as well as inorganic–organic hybrid micro/nanostructures. In addition, the changes of physical properties of as-prepared micro/nanomaterials will also be reviewed.

14.2

Micro/Nanostructure Conversion through Charge Transfer Complex Formation

TTF–TCNQ is a well-known organic charge-transfer (CT) salt that has a well-defined quasi-one-dimensional structure with a high electronic conductivity [14].

Recent researches have also shown the metallic conductivity property at the interfaces between two crystals of TTF and TCNQ through direct mechanical contact [15]. The amazing properties on the bulk TTF–TCNQ and the interfaces between the TTF and TCNQ crystals led to the attempts toward conversion between TTF and TCNQ nanostructures. Zhang and coworkers first studied the postchemistry between aqueous TTF microparticles and TCNQ microstructures [16]. The aqueous TTF microparticles and TCNQ microstructures were prepared as follows: the TTF or TCNQ acetonitrile solution was added to aqueous solution containing poly(ethylene glycol)-block-poly(propylene glycol)-block-poly(ethylene glycol) (P123) nonionic surfactant with stirring. The size of the TTF microparticles and TCNQ microstructures is about 500 nm to 1.2 μm and 500–800 nm, respectively (Figure 14.1a and b). When TTF microparticles

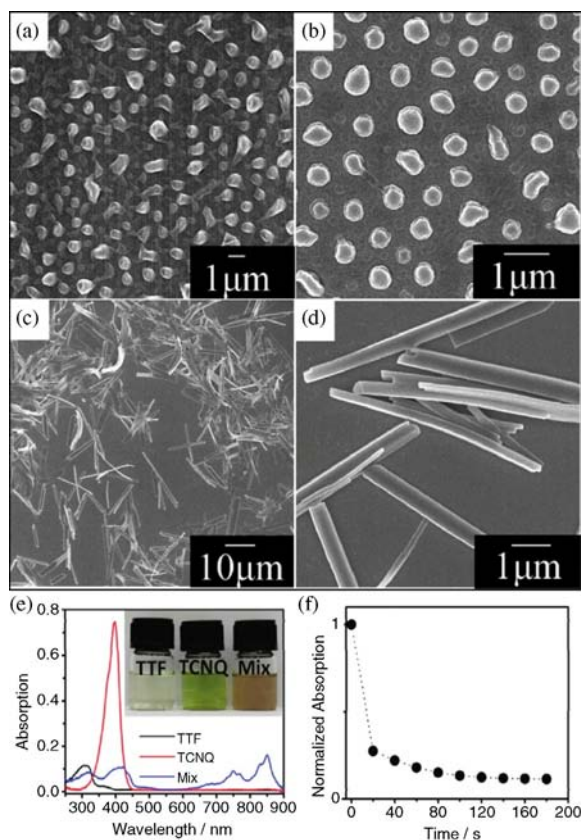


Figure 14.1 SEM images of (a) TTF microparticles, (b) TCNQ microstructures, and (c and d) TTF–TCNQ nanowires. UV-vis absorption spectra of (e) TCNQ microstructures (red), TTF microparticles (black), and TTF–TCNQ nanowires (blue). The inset shows that their

photographs were dispersed in aqueous solution. (f) Absorption of TCNQ microstructures as a function of reaction time after mixing of the TTF microparticles and TCNQ microstructures. (Reprinted with permission from Ref. [16]. Copyright 2010, American Chemical Society.)

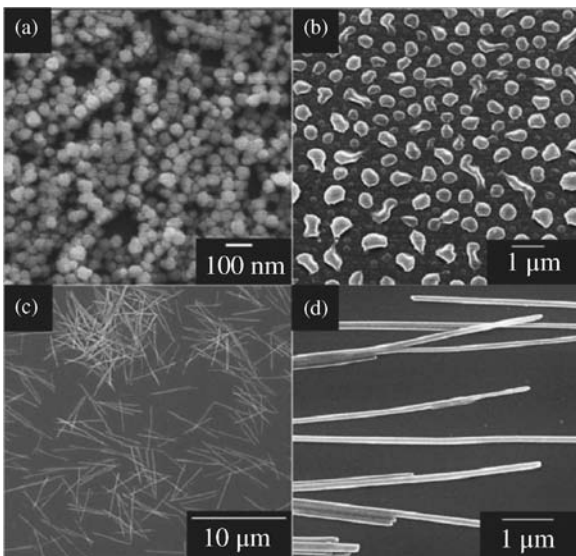


Figure 14.2 SEM images of (a) Ag nanoparticles, (b) TCNQ microparticles, and (c and d) Ag-TCNQ nanowires. (Reprinted from Ref. [21]. Copyright 2011, Wiley-VCH Verlag GmbH.)

were added to TCNQ microstructures in aqueous solution, the color of the TCNQ solution immediately changed from yellow-green to brown (Figure 14.1e, inset), and TTF-TCNQ nanowires were formed. The diameters and lengths of the TTF-TCNQ nanowires were 300–700 nm and about 10 μm (Figure 14.1c and d). From the UV-vis absorption spectra (Figure 14.1e and f), it can be found that the reaction between TTF and TCNQ is very fast. The as-synthesized TTF-TCNQ nanowires showed good performance in nonvolatile memory devices with multiple write-read-erase-read (WRER) cycles in air.

Continuing on this strategy, Zhang and coworkers also demonstrated that the chemical reaction between the inorganic Ag nanoparticles and organic TCNQ microparticles could also be realized in aqueous solution [17], although Ag-TCNQ nanowires have been prepared by many methods, including the spontaneous electrolysis technique [18], chemical vapor deposition [19], solution processes [20], and the photocrystallization approach [21]. In Zhang and coworkers' research [17], the Ag-TCNQ nanowires were formed by adding an aqueous solution of Ag nanoparticles into TCNQ aqueous solution with stirring of the mixed solution for 2 h (Figure 14.2) and an obvious color change of the mixed solution from green to blue was observed in 6 min (Figure 14.3a, inset).

A possible formation mechanism of Ag-TCNQ nanowires has been studied through the UV-vis spectroscopy and scanning electron microscopy (SEM). As shown in Figure 14.3, the SEM images of the samples collected at different reaction times (20 s, 40 s, 2 min, 4 min, and 15 min) clearly indicated that (i) in the early state, Ag nanoparticles and TCNQ microparticles aggregated, (ii) followed by a solid-state reaction between Ag and TCNQ particles, and (iii) leading

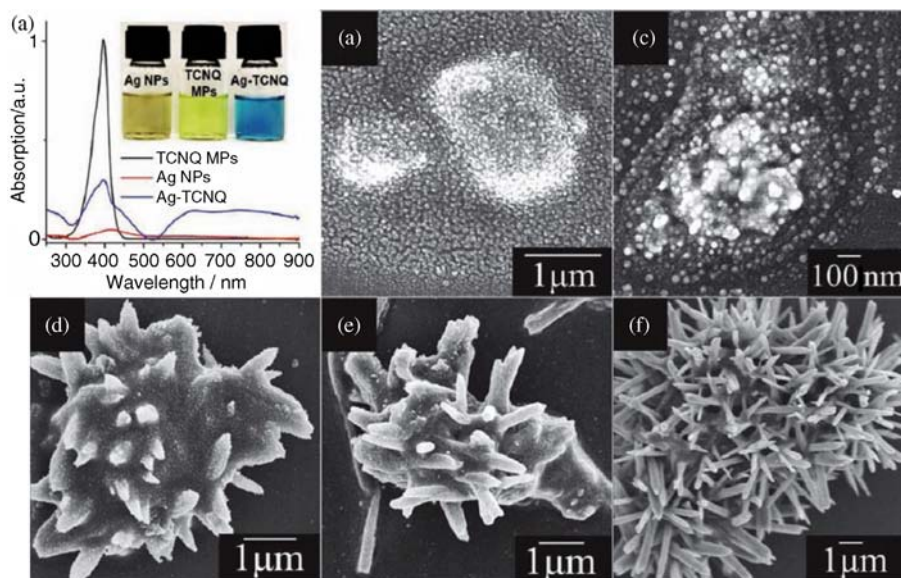


Figure 14.3 (a) UV-vis spectra of TCNQ microparticles, Ag nanoparticles, and Ag-TCNQ nanowires. The inset shows that their photographs were dispersed in aqueous

solution. (b–f) The SEM images of the products at 20 s, 40 s, 2 min, 4 min, and 15 min, respectively. (Reprinted from Ref. [21]. Copyright 2011, Wiley-VCH Verlag GmbH.)

to the formation of Ag-TCNQ nanowires. The as-synthesized semiconducting Ag-TCNQ nanowires show good performance in nonvolatile memory devices with multiple WRER cycles in air.

14.3

Micro/Nanostructure Conversion through Ion and Ligand Exchange

Ion exchange as well as ligand exchange is one of the most important strategies to construct new micro/nanoparticles. The successful nanostructure conversion through ligand exchange [22] and ion exchange in inorganic nanocrystals has been reported recently [23]. It is highly desirable that organic coordination complex nanostructures possess the ability to convert their micro/nanostructures with ion/ligand exchange.

Oh and Mirkin reported a method that could allow one particle to transform into another micro/nanostructure through cation exchange without significantly affecting the morphology of the particle structures (Figure 14.4) [24]. In their research, they first prepared the infinite coordination polymer particles, which consist of metal-bis-metallo-tridentate Schiff base (BMSB) building blocks and Zn(II) interconnecting nodes (named Zn-BMSB-Zn particles). The average diameter of microparticles is about 1.6 μm. Then, a mixture of dispersed

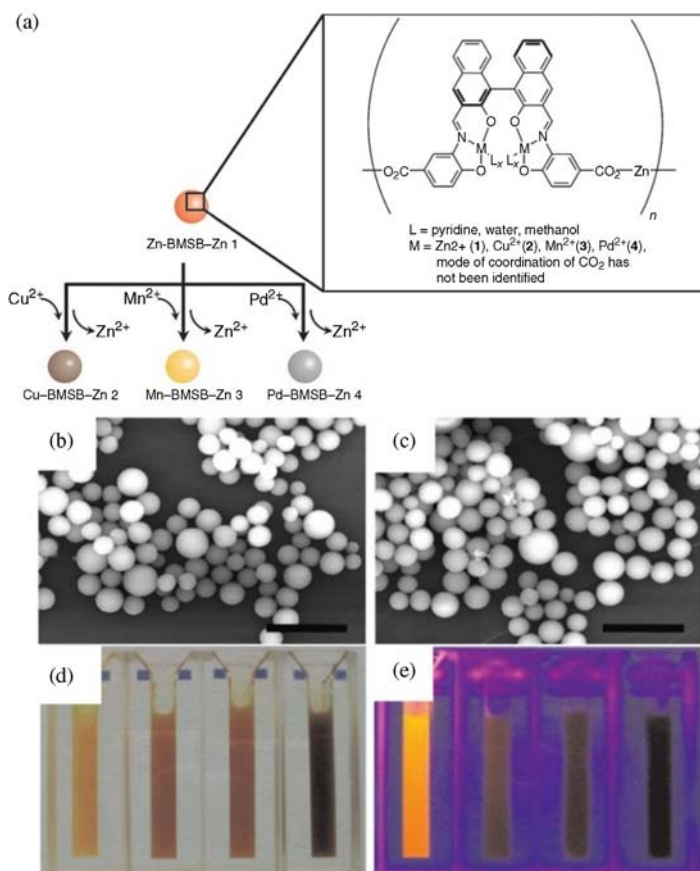


Figure 14.4 (a) Schematic representation of ion exchange reactions. (b and c) SEM images of Zn-BMSB-Zn and Cu-BMSB-Zn spherical microparticles. Scale bars = 5 μ m. (d and e) Digital photographs of a series of

nanoparticles (left to right: Zn-BMSB-Zn, Cu-BMSB-Zn, Mn-BMSB-Zn, Pd-BMSB-Zn) without and with UV irradiation. (Reprinted from Ref. [24]. Copyright 2006, American Chemical Society.)

Zn-BMSB-Zn particles with copper acetate was stirred at room temperature. Within 5 min, most of the Zn-BMSB-Zn particles had been transformed into the Cu-BMSB-Zn particles, and the reaction was completed after 60 min. During the ion exchange process, the particles retain their shape and size. Fluorescence quenching was found due to the Zn(II) ions replaced by the Cu(II) ions providing another evidence of effective ion exchange. It is worth noting that exchange does not occur at the carboxylate nodes. Moreover, this type of exchange process also works for other salts, including Mn(II), Pd(II), and Ni(II).

Recently, Zhang and coworkers reported their discovery of the submicrospherical particles of three-dimensional Zn(SPh)₂ networks (SPh = thiophenol group),

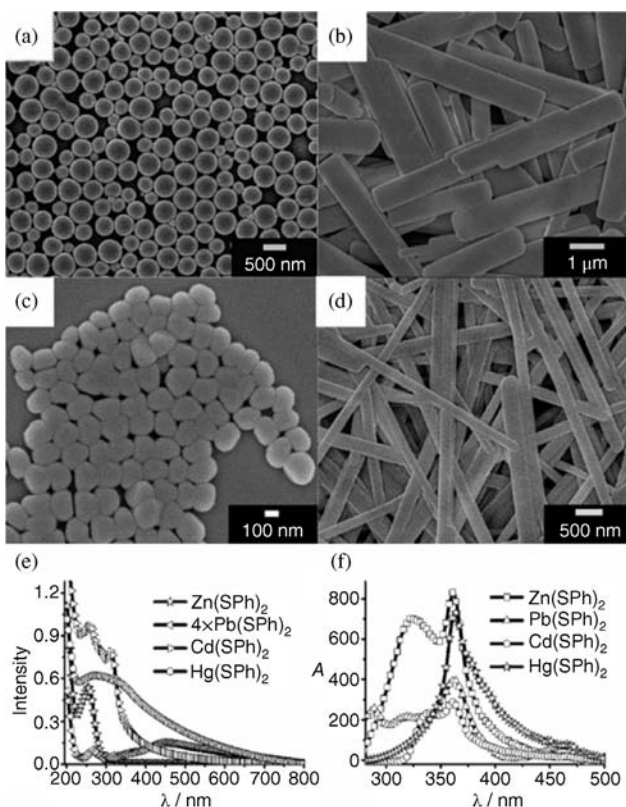


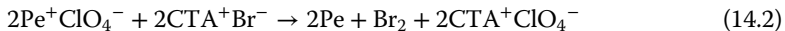
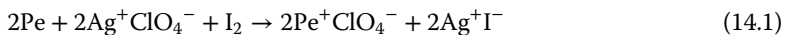
Figure 14.5 The SEM images of (a) $\text{Zn}(\text{SPh})_2$, (b) $\text{Pd}(\text{SPh})_2$, (c) $\text{Cd}(\text{SPh})_2$, and (d) $\text{Hg}(\text{SPh})_2$. (e) The UV/vis absorption spectra of different particles in aqueous solution. (f) Photoluminescence (PL) spectra of different particles. (Reprinted from Ref. [25]. Copyright 2011, Wiley-VCH Verlag GmbH.)

which could perform a metal–cation exchange in aqueous solution and transform into crystalline nanoparticles and nanowires [25]. Generally, to a well-dispersed aqueous solution containing spherical particles of $\text{Zn}(\text{SPh})_2$, heavy metal sources such as Pd^{2+} , Cd^{2+} , and Hg^{2+} ions were added and the Zn^{2+} ions in the spherical particles could be exchanged by these heavy metals to form different structures, including wires, ribbons, or pebble-like particles (Figure 14.5). The average diameter of $\text{Zn}(\text{SPh})_2$ spherical particles is about 300 nm. After the ion exchange, the widths of $\text{Pb}(\text{SPh})_2$ ribbons and $\text{Hg}(\text{SPh})_2$ wires were in the range of 500 nm to 1 μm and 200–500 nm, respectively. Their lengths are however similar (about 10 μm). Interestingly, the structure of the $\text{Cd}(\text{SPh})_2$ is very different from those of $\text{Pb}(\text{SPh})_2$ and $\text{Hg}(\text{SPh})_2$. The average size of pebble-like $\text{Cd}(\text{SPh})_2$ particles is about 200 nm. All of these particles were stable in water and in the dried state. The UV-vis absorption and photoluminescence of $\text{Pd}(\text{SPh})_2$, $\text{Cd}(\text{SPh})_2$, and $\text{Hg}(\text{SPh})_2$ are also different from $\text{Zn}(\text{SPh})_2$ (Figure 14.5e and f).

14.4

Micro/Nanostructure Conversion through Reduction

Yao and coworkers developed a colloid chemical reaction method to prepare the nanoparticles and nanobelts/square nanorods by using reduction of perylene perchlorate by Br^- anions in the presence of cetyltrimethylammonium bromide (CTAB) in acetonitrile (Eqs (14.1) and (14.2)) [26].



where Pe is perylene. In this method, different structures of perylene were achieved by changing the molar ratio of CTAB to perylene perchlorate. The different sizes of perylene nanoparticles were obtained when the molar ratio (N) of CTAB to perylene perchlorate was <1 . Furthermore, if the molar ratio is >1 , perylene forms nanobelts or square nanorods. Figure 14.6 displays the morphology, formation processes, and spectroscopic properties of the different perylene micro/nanostructures. The diameter of the perylene spherical nanoparticles is about 25 nm (Figure 14.6a). The width and length of the square nanorods are about 400 nm and 50 μm , respectively (Figure 14.6c). Although the compositions of the different perylene micro/nanostructures are same, their absorption and emission spectra have obvious difference (Figure 14.6e and f), which suggests that the morphologies have strong effect on the physical properties.

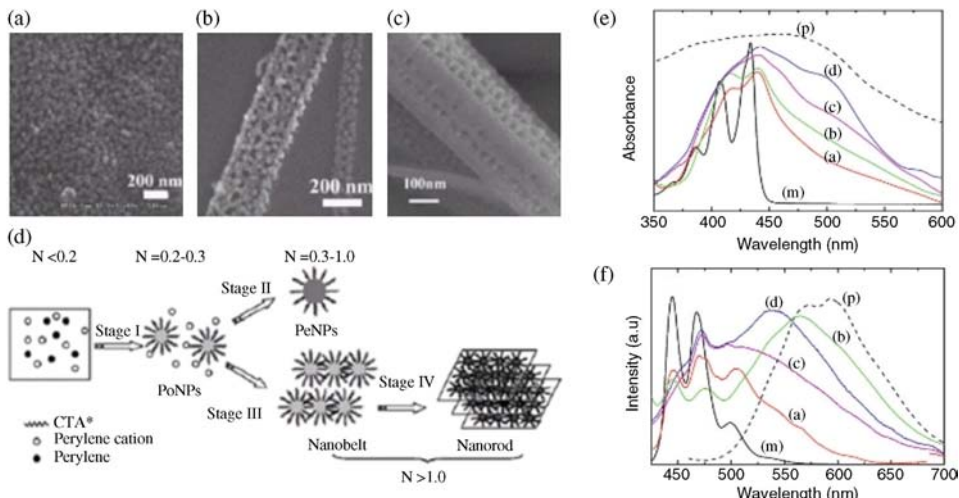


Figure 14.6 SEM images of perylene (a) quasi-spherical nanoparticles ($N = 0.3$), (b) nanobelts ($1.0 < N < 1.2$), and (c) square nanorods ($N > 2.0$). (d) Schematic illustration representing formation of the perylene nanoparticles. Stage I: nucleation; stage II: growth; stages III and IV: 1D–3D organization. (e) Absorption and (f) emission spectra of different perylene structures. (Reprinted from Ref. [26]. Copyright 2007, American Chemical Society.)

nucleation; stage II: growth; stages III and IV: 1D–3D organization. (e) Absorption and (f) emission spectra of different perylene structures. (Reprinted from Ref. [26]. Copyright 2007, American Chemical Society.)

14.5

Micro/Nanostructure Conversion through Photoinduced Reaction

The reversible or irreversible photochemical conversions can occur in many organic molecules such as the *cis-trans* conversion of stilbene [27] and azobenzene [28], photoinduced cycloaddition reaction [29], photoinduced CC polymerization [30], and so on. Here, the transformation in micro/nanostructures of the organic molecules by photoinduced reaction is focused and described.

For crystal materials, the bulk crystals are easy to be destroyed after the photo-induced chemical reaction, but the same photoreaction sometimes cannot destroy the micro/nanocrystals. In 2002, Nakanishi and coworkers showed that the photo-polymerization of a diolefin derivative resulted in the disintegration of bulk crystals, but the nanocrystals were not destroyed [31]. Bučar and MacGillivray and Garcia-Garibay and coworkers have also reported the ability of nano- and microcrystals to survive photochemical transformations with their morphology intact [32,33]. This stability enables the photoinduced nanostructure conversion. Bardeen and coworkers thoroughly studied the photoinduced micro/nanocrystals conversions with anthracene derivatives [4]. In 2006, Bardeen and coworkers reported that crystalline nanorods composed of an anthracene (*9-tert*-butylanthroate (9-TBAE)) derivative could expand up to 15% driven by a crystal-to-crystal photodimerization reaction (Figure 14.7) [34]. Moreover, simply removing the *tert*-butyl group from 9TBAE yields 9-anthracene carboxylic acid (9AC), which crystallizes in a head-to-head *syn*-arrangement. They monitored the expansion and subsequent contraction of individual 9AC rods using AFM [35]. After light exposure, an individual rod briefly expands by 1–3%, but then returns to its original shape. To induce more useful types of motion, they used spatially localized photoexcitation on isolated rods in aqueous solution. They found that a single rod, irradiated in its central region, instantly bends under the influence of light beam (Figure 14.8). After 2–5 min in the dark, the bent rod returned to its original shape. This sequence could be repeated for multiple cycles, the rod bending under illumination and then straightening in the dark.

Bardeen and coworkers also showed that the solid-state [4 + 4] photodimerization reaction could change the shape of 9-methylanthracene (9MA) microneedles and microribbons (Figure 14.9) [36]. The microneedles and microribbons of

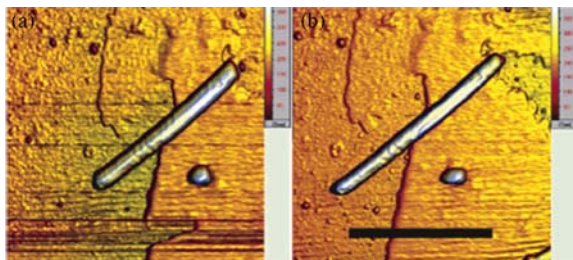


Figure 14.7 (a) AFM image of a single nanorod before illumination and (b) after illumination with 365 nm. (Reprinted from Ref. [34]. Copyright 2006, American Chemical Society.)

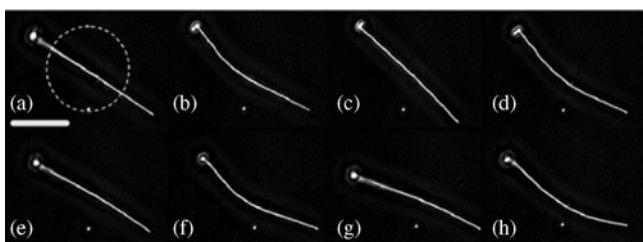


Figure 14.8 Single 200 nm diameter nanorod of 9AC (60 μm long) briefly exposed to 365 nm light in a 50% solution of phosphoric acid in water. The dotted circle shows the illuminated region (35 μm in diameter). The nanorod repeatedly flexes back and forth (after UV

illumination = panels b, d, f, and h; after dark period = panels a, c, e, and g). The time required to revert back is around 2 min at room temperature. Scale bar = 20.7 μm . (Reprinted from Ref. [35]. Copyright 2007, Wiley-VCH Verlag GmbH.)

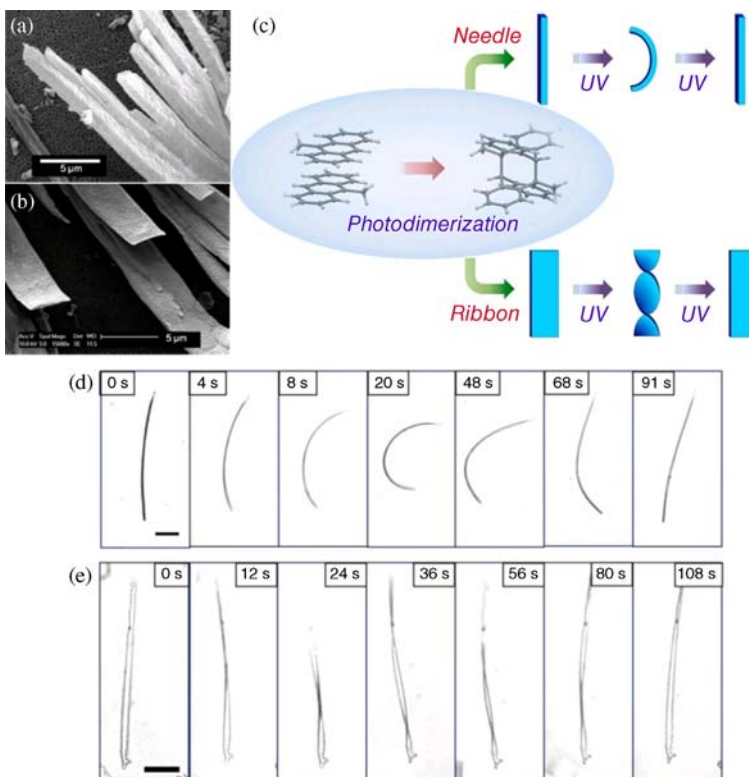


Figure 14.9 (a and b) SEM images of 9MA microneedles and 9MA microribbons. (c) Schematic representation of photodimerization reaction. (d and e) Optical microscope images of bending and unbending of a 9MA

microneedle and twisting and untwisting of a 9MA microribbon during 365 nm UV irradiation. Scale bar: 20 μm . (Reprinted from Ref. [36]. Copyright 2014, American Chemical Society.)

9MA were prepared by using the floating drop method from various solvents on a clean water surface (Figure 14.9a and b). When the 9MA needles and ribbons were exposed on 365 nm UV irradiation from a mercury lamp, the needles underwent a bending motion during irradiation, but then returned to their original shape with time (Figure 14.9d). A similar sequence of events was also observed for the microribbons (Figure 14.9e). In both crystal shapes, the maximum deformation occurred at roughly the midpoint of the reaction, while further dimerization caused the crystals to return to their original shapes.

14.6

Micro/Nanostructure Conversion through Thermal-induced Reaction

Zhang and coworkers first used organic microrod precursors as starting materials to generate conducting polymer micro/nanomaterials in water through thermal polymerization [37]. They chose 2,5-dibromo3,4-ethylenedioxythiophene (DBEDOT) as the precursor, which has been reported to perform solid-state polymerization through simply heating crystalline bulk monomers to produce highly conductive self-doped semicrystalline poly(3,4-ethylenedioxythiophenene) (PEDOT) [38]. The DBEDOT microrods were prepared by addition of an ethanol solution of DBEDOT (1 mM) to water with stirring. The samples for

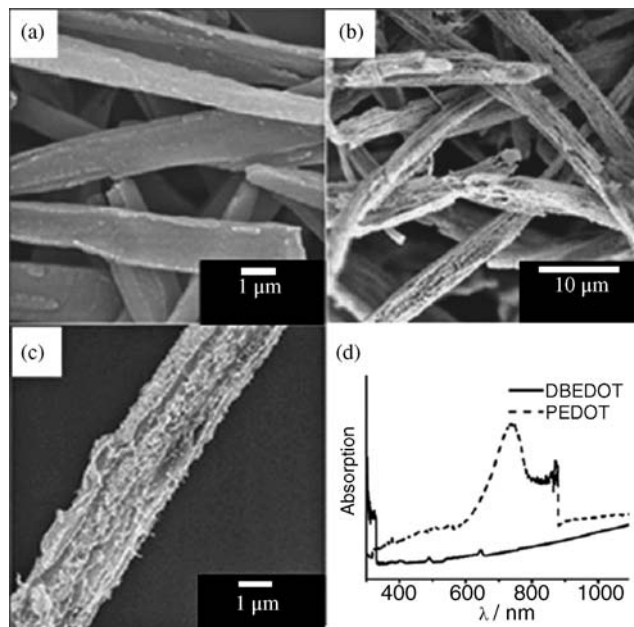


Figure 14.10 SEM images of DBEDOT microrods (a) before polymerization, (b) after polymerization, and (c) the magnification of single microrod after polymerization; (d) UV-vis

absorption of DBEDOT microrods before (black line) and after (dashed line) polymerization. Reprinted from Ref. [37]. Copyright 2011, Wiley-VCH Verlag GmbH.

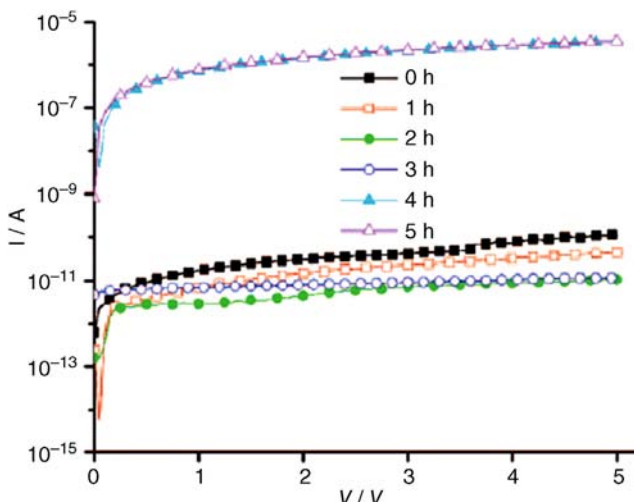


Figure 14.11 Current–voltage (I – V) measurements for different single microrods (Au/microrod/Au junction). *Top group:* After polymerization. *Bottom group:* Before polymerization. Reprinted from Ref. [37]. Copyright 2011, Wiley-VCH Verlag GmbH.

solid-state polymerization were obtained by dispersing the as-prepared microrod precursors in water and heating at 75 °C for 4 h. DBEDOT shows a typical microstructure with diameters in the range of 13 µm and lengths of about 15 µm. The surface of the DBEDOT microrods is very smooth (Figure 14.10a). After polymerization in water, the surface became rough and a lot of defects were observed (Figure 14.10b and c). The polymerization was further confirmed by XRD. However, after polymerization, the UV-vis absorption spectra show a new broad peak at approximately 710 nm. Figure 14.11 shows the typical I – V characteristics of microrods before and after polymerization. The resistance of microrods after polymerization (based on two different single microrods) is about 10^5 smaller than that of microrods before polymerization.

14.7

Properties and Applications

In addition to controlling the morphology of organic and organic/inorganic hybrid micro/nanostructures, their optical, electronic, and mechanical properties can also be tuned. It is necessary to discuss the properties and applications of as-fabricated micro/nanostructures.

14.7.1

Optical Properties

As already mentioned, the optical properties of organic and organic/inorganic hybrid micro/nanostructures are very special, because the intermolecular interactions in organic materials are based on weak types, such as hydrogen bonds, π – π

stacking, van der Waals interactions, and even charge-transfer interactions. Therefore, the UV-vis absorption and photoluminescence properties would change with the changing of composition and structure. For example, although the morphology of the particles (Figure 14.4) underwent no change after the Zn–BMSB–Zn particles were transformed into Cu–BMSB–Zn, Mn–BMSB–Zn, and Pd–BMSB–Zn particles through ion exchange, the colors of the ion-exchanged particles became dark and the fluorescence was quenched due to ion exchanges [24]. In addition, the size-dependent optical properties were also investigated in organic and organic/inorganic hybrid micro/nanostructures [26]. For example, the different perylene structures show different absorption and emission spectra in Figure 14.6 [26].

14.7.2

Electronic Properties and Information Storage

Organic and organic/inorganic hybrid micro/nanostructure semiconductors have various electronic properties. In the previous section, we mentioned that the TTF–TCNQ [16] and Ag–TCNQ [21] nanowires could be prepared by chemical reaction between the related nanoparticles. The electronic properties of TTF–TCNQ and Ag–TCNQ nanowires were also measured by metal–semiconductor–metal junctions. The structure of the device is shown in the inset of Figure 14.12a. The device is electronically stable, and all of the measurements

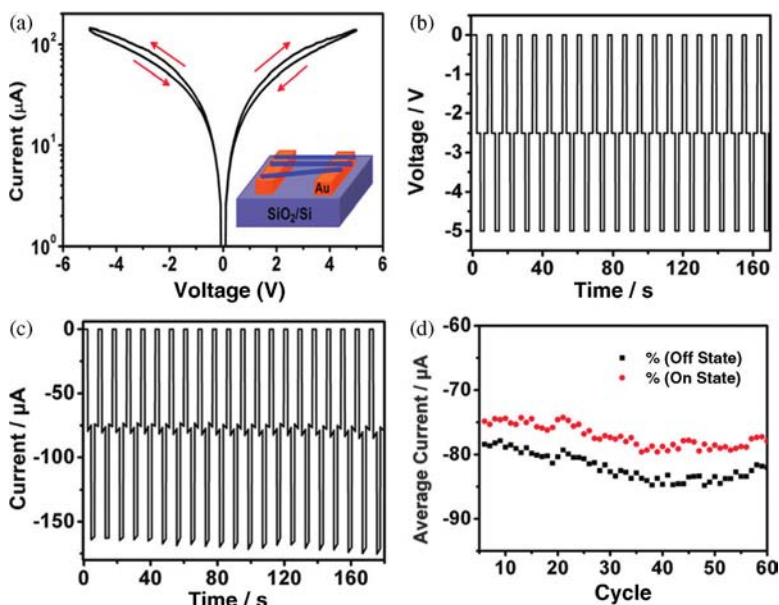


Figure 14.12 (a) Typical I – V curves for a network of TTF–TCNQ nanowires. The inset is a schematic of memory device. (b and c) WRER cycles of a network of TTF–TCNQ nanowires

for a rewritable data storage application. (d) Current in the on and off states with 60 WRER cycles. (Reprinted from Ref. [16]. Copyright 2010, American Chemical Society.)

were performed under an air atmosphere. Figure 14.12a shows the typical $I-V$ characteristics of the TTF-TCNQ nanowires/Au junction. The obvious conductivity-switching behavior makes it possible for the nonvolatile rewritable organic memory devices. The stability of the devices was tested under a pulsed voltage sequence with a WRER cycle (Figure 14.12b and c). The stable high/low (on/off) conductivity-switching behavior under multiple current measurements at -2.5 V showed no significant degradation of the device with respect to either on/off current or voltage after 60 write-erase cycles in air (Figure 14.12d). The Ag-TCNQ nanowires also showed similar properties under the same measurements. Such stable switching behavior suggests that the material has great potential for nonvolatile memory applications.

14.7.3

Mechanical Properties and Photomechanical Actuator

Many organic molecules can directly absorb the photons and convert their energies into chemical reactions. Since the chemical changes are usually accompanied by a geometrical rearrangement, the organic and organic/inorganic hybrid micro/nanostructures are ideal transducers to transfer light into motion. In many cases, the process can be repeated because the photochemical reaction is reversible. Bardeen and coworkers reported several works in this field. For example, the microneedles of 9MA can bend and unbend, while microribbons of 9MA can twist and untwist during 365 nm UV irradiation (Figure 14.9d and e) [36]. Furthermore, the microribbons of 9-anthracenecarboxylic acid could rapidly twist when they were exposed to spatially uniform light irradiation. After the light is turned off, they relax back to their original shape over the course of minutes [36].

14.8

Summary and Outlook

In this chapter, we introduced the chemical reactions among organic and organic/inorganic hybrid micro/nanostructures and the recent progress on construct organic and organic/inorganic hybrid micro/nanostructures by using chemical reaction method. In addition, the properties and applications of the organic and organic/inorganic hybrid micro/nanostructures have been presented as well.

The conversion of organic and organic/inorganic hybrid micro/nanostructures could offer a new route for preparing new organic and organic/inorganic hybrid micro/nanostructures and tuning their physical properties through the ions or organic ligands exchange or phototransformation. We believe that this concept can provide a more powerful tool for designing and synthesizing organic and organic/inorganic hybrid micro/nanomaterials for further applications.

References

- 1 Cui, Q.H., Zhao, Y.S., and Yao, J. (2014) Tailoring the structures and compositions of one-dimensional organic nanomaterials towards chemical sensing applications. *Chem. Sci.*, **5**, 52–57.
- 2 Yan, Y. and Zhao, Y.S. (2014) Organic nanophotonics: from controllable assembly of functional molecules to low-dimensional materials with desired photonic properties. *Chem. Soc. Rev.*, **43**, 4325–4340.
- 3 Xu, H., Chen, R., Sun, Q., Lai, W., Su, Q., Huang, W., and Liu, X. (2014) Recent progress in metal–organic complexes for optoelectronic applications. *Chem. Soc. Rev.*, **43**, 3259–3302.
- 4 Kim, T., Zhu, L., Al-Kaysi, R.O., and Bardeen, C.J. (2014) Organic photomechanical materials. *ChemPhysChem*, **15**, 400–414.
- 5 Horn, D. and Rieger, J. (2001) Organic nanoparticles in the aqueous phase: theory, experiment, and use. *Angew. Chem., Int. Ed.*, **40**, 4330–4361.
- 6 Spokony, A.M., Kim, D., Sumrein, A., and Mirkin, C.A. (2009) Infinite coordination polymer nano- and microparticle structures. *Chem. Soc. Rev.*, **38**, 1218–1227.
- 7 Zhao, Y.S., Fu, H., Peng, A., Ma, Y., Xiao, D., and Yao, J. (2008) Low-dimensional nanomaterials based on small organic molecules: preparation and optoelectronic properties. *Adv. Mater.*, **20**, 2859–2876.
- 8 Zhao, Y.S., Fu, H., Peng, A., Ma, Y., Liao, Q., and Yao, J. (2009) Construction and optoelectronic properties of organic one-dimensional nanostructures. *Acc. Chem. Res.*, **43**, 409–418.
- 9 Oh, M. and Mirkin, C.A. (2006) Ion exchange as a way of controlling the chemical compositions of nano- and microparticles made from infinite coordination polymers. *Angew. Chem., Int. Ed.*, **45**, 5492–5494.
- 10 Liu, Y., Boey, F., Lao, L.L., Zhang, H., Liu, X., and Zhang, Q. (2011) Postchemistry of inorganic–organic hybrid particles in aqueous solution: metal–cation exchange. *Chem. Asian J.*, **6**, 1004–1006.
- 11 Sun, Y.G. and Xia, Y.N. (2002) Shape-controlled synthesis of gold and silver nanoparticles. *Science*, **298**, 2176–2179.
- 12 Yin, Y.D., Rioux, R.M., Erdonmez, C.K., Hughes, S., Somorjai, G.A., and Alivisatos, A.P. (2004) Formation of hollow nanocrystals through the nanoscale Kirkendall effect. *Science*, **304**, 711–714.
- 13 Vasquez, Y., Henkes, A.E., Bauer, J.C., and Schaak, R.E. (2008) Nanocrystal conversion chemistry: a unified and materials-general strategy for the template-based synthesis of nanocrystalline solids. *J. Solid State Chem.*, **181**, 1509–1523.
- 14 Ferraris, J., Cowan, D.O., Walatka, V. Jr., and Perlstein, J.H. (1973) Electron transfer in a new highly conducting donor–acceptor complex. *J. Am. Chem. Soc.*, **95**, 948–949.
- 15 Alves, H., Molinari, A.S., Xie, H.X., and Morpurgo, A.F. (2008) Metallic conduction at organic charge-transfer interfaces. *Nat. Mater.*, **7**, 574–580.
- 16 Xiao, J., Yin, Z., Li, H., Zhang, Q., Boey, F., Zhang, H., and Zhang, Q. (2010) Postchemistry of organic particles: when TTF microparticles meet TCNQ microstructures in aqueous solution. *J. Am. Chem. Soc.*, **132**, 6926–6928.
- 17 Xiao, J., Yin, Z., Wu, Y., Guo, J., Cheng, Y., Li, H., Huang, Y., Zhang, Q., Ma, J., Boey, F., Zhang, H., and Zhang, Q. (2011) Chemical reaction between Ag nanoparticles and TCNQ microparticles in aqueous solution. *Small*, **7**, 1242–1246.
- 18 Ren, L., Fu, L., Chen, S.L., and Liu, Z.F. (2009) Electrochemical synthesis of high-quality AgTCNQ nanowires using carbon nanotube electrodes. *Adv. Mater.*, **21**, 4742–4746.
- 19 Liu, H.B., Zhao, Q., Li, Y.L., Liu, Y., Lu, F.S., Zhuang, J.P., Wang, S., Jiang, L., Zhu, D.B., Yu, D.P., and Chi, L.F. (2005) Field emission properties of large-area nanowires of organic charge-transfer complexes. *J. Am. Chem. Soc.*, **127**, 1120–1121.
- 20 Fang, Z.Y., Mo, X.L., Lou, C.F., Yao, Y., Wang, D.W., Chen, G.R., and Lu, J.G. (2005) Structures and electrical properties

- of Ag-tetracyanoquinodimethane organometallic nanowires. *IEEE Trans. Nanotechnol.*, **4**, 238–241.
- 21** O'Mullane, A.P., Fay, N., Nafady, A., and Bond, A.M. (2007) Preparation of metal-TCNQ charge-transfer complexes on conducting and insulating surfaces by photocrystallization. *J. Am. Chem. Soc.*, **129**, 2066–2073.
- 22** Pyle, A.M., Rehmann, J.P., Meshoyrer, R., Kumar, C.V., Turro, N.J., and Barton, J.K. (1989) Mixed-ligand complexes of ruthenium(II): factors governing binding to DNA. *J. Am. Chem. Soc.*, **111**, 3051–3058.
- 23** Son, D.H., Hughes, S.M., Yin, Y.D., and Alivisatos, A.P. (2004) Cation exchange reactions in ionic nanocrystals. *Science*, **306**, 1009–1012.
- 24** Oh, M. and Mirkin, C.A. (2006) Ion exchange as a way of controlling the chemical compositions of nano- and microparticles made from infinite coordination polymers. *Angew. Chem., Int. Ed.*, **45**, 5492–5494.
- 25** Liu, Y., Boey, F., Lao, L.L., Zhang, H., Liu, X., and Zhang, Q. (2011) Postchemistry of inorganic–organic hybrid particles in aqueous solution: metal–cation exchange. *Chem. Asian J.*, **6**, 1004–1006.
- 26** Kang, L., Wang, Z., Cao, Z., Ma, Y., Fu, H., and Yao, J. (2007) Colloid chemical reaction route to the preparation of nearly monodispersed perylene nanoparticles: size-tunable synthesis and three-dimensional self-organization. *J. Am. Chem. Soc.*, **129**, 7305–7312.
- 27** Waldeck, D.H. (1991) Photoisomerization dynamics of stilbenes. *Chem. Rev.*, **91**, 415–436.
- 28** Kumar, G.S. (1989) Photochemistry of azobenzene-containing polymer. *Chem. Rev.*, **89**, 1915–1925.
- 29** Huang, C.M., Zheng, M.M., Xu, J.H., and Zhang, Y. (2013) Photoinduced cycloaddition reactions of α -diketones and transformations of the photocycloadducts. *Molecules*, **18**, 2942–2966.
- 30** Chen, X.Q., Zhou, G.D., Peng, X.J., and Yoon, J.Y. (2012) Biosensors and chemosensors based on the optical responses of polydiacetylenes. *Chem. Soc. Rev.*, **41**, 4610–4630.
- 31** Takahashi, S., Miura, H., Kasai, H., Okada, S., Oikawa, H., and Nakanishi, H. (2002) Single-crystal-to-single-crystal transformation of diolefin derivatives in nanocrystals. *J. Am. Chem. Soc.*, **124**, 10944–10945.
- 32** Bučar, D.K. and MacGillivray, L.R. (2007) Preparation and reactivity of nanocrystalline cocrystal formed via sonocrystallization. *J. Am. Chem. Soc.*, **129**, 32–33.
- 33** Kuzmanich, G., Gard, M.N., and Garcia-Garibay, M.A. (2009) Photonic amplification by a singlet-state quantum chain reaction in the photodecarbonylation of crystalline diarylcyclopropenones. *J. Am. Chem. Soc.*, **131**, 11606–11614.
- 34** Al-Kaysi, R.O., Muller, A.M., and Bardeen, C.J. (2006) Photochemically driven shape changes of crystalline organic nanorods. *J. Am. Chem. Soc.*, **128**, 15938–15939.
- 35** Al-Kaysi, R.O. and Bardeen, C.J. (2007) Reversible photoinduced shape changes of crystalline organic nanorods. *Adv. Mater.*, **17**, 1276–1280.
- 36** Kim, T., Zhu, L., Mueller, L.J., and Bardeen, C.J. (2014) Mechanism of photoinduced bending and twisting in crystalline microneedles and microribbons composed of 9-methylanthracene. *J. Am. Chem. Soc.*, **136**, 6617–6625.
- 37** Xiao, J.C., Kusuma, D.Y., Wu, Y.C., Boey, F., Zhang, H., Lee, P.S., and Zhang, Q.C. (2011) Postchemistry of organic microrods: thermopolymerization in aqueous solution. *Chem. Asian J.*, **6**, 801–803.
- 38** Meng, H., Perepichka, D.F., and Wudl, F. (2003) Facile solid-state synthesis of highly conducting poly(ethylenedioxythiophene). *Angew. Chem., Int. Ed.*, **42**, 658–661.

15

Self-Healing Electronic Nanodevices

Li Zhang, Bevita K. Chandran, and Xiaodong Chen

15.1

Introduction

With the explosive development of electronic products, more and more people are sick of having to work their way through a series of broken electronic devices, dulled (or dead) batteries, and an endless thread of replacement of cell phones. This, in turn, has resulted in dreams of electronic devices of the future, which could self-repair tiny cracks or breaks in their circuitry. Such a capability will result in enhanced durability and lifetime of the device and, consequently, reduce electronic waste.

Self-healing, defined as the ability to repair damage spontaneously, is an important survival feature in nature that increases the lifetime of most living creatures. Inspired by the intrinsic self-repairing ability of biological systems, one class of artificial “smart” materials, called self-healing materials, that can repair internal or external damages has been developed over the past decade [1]. Besides restoring the mechanical and structural properties of the material, recovery of functional properties after damage has recently been emphasized, and this has been successfully achieved in several functional materials [2,3]. For example, anticorrosive, antifouling, superhydrophobic, and electrically conductive materials with self-healing properties have been developed [4–10]. Due to these breakthroughs, self-healing materials are highly promising for the development of robust functional devices with long lifetimes. However, fabrication of integrated functional devices with self-healing features, that is, the integration of these self-healing functional materials into electronic devices still remains a challenge [7]. This chapter summarizes the various approaches used to develop self-healing materials for electronic devices, particularly for applications such as electrical conductors, energy storage, and electronic skin (E-skin).

15.2

Self-Healing Materials

Self-healing, as mentioned earlier, can be defined as the ability of a material to heal (recover/repair) damages automatically and autonomously, that is, without any external intervention. Many common terms such as self-repairing, autonomic healing, and autonomic repairing are used to define such a property in materials. However, self-healing action in man-made materials, in most cases, cannot be induced without the help of an external trigger [1]. Thus, healing materials can be autonomic or nonautonomic, depending on whether or not an external trigger such as heat or light is required.

For decades, self-healing materials have been intensively researched, but the focus was largely on designing unique, stimulus-responsive polymer systems for the restoration of mechanical properties. In their review, Bao and coworkers have summarized that artificial mechanically self-healing systems are mainly divided into two categories: (i) composites of polymers and capsules or pipelines loaded with healing agents (healants) and (ii) polymers that contain dynamic reversible bonds, including covalent and noncovalent reversible bonds [23]. These smart material systems are tremendously useful for enhancing structural safety [11], enabling new biological applications [12,13], creating long-lived superhydrophobic coatings [14,15], increasing the lifespan of materials, and improving environmental sustainability [11,16,17]. Some specific examples are as follows, where the first four examples can be classified into category 2 and the last two examples belong to category 1.

- 1) In the area of fault-tolerant soft electrons, Yuan and colleagues first demonstrated the use of high-strain-capable carbon nanotube electrodes that can selectively combust or “self-clear” in localized short circuits to maintain constant operation of the dielectric elastomer actuators [16,18].
- 2) Wudl and coworkers have used the dynamic covalent bond between furan and maleimide moieties to demonstrate the first self-healing plastic that can be self-healed upon heating [11].
- 3) By incorporating hydrogen bonds into a polymer matrix, Leibler and coworkers have demonstrated the first room-temperature self-healing elastomer [19].
- 4) The first UV-triggered self-healing polymer (SHP) was reported by Ghosh and Urban using oxetane-substituted chitosan polyurethane networks [20].
- 5) White *et al.* have demonstrated the first example of a self-healing material incorporating a microencapsulated healing agent and a catalytic chemical trigger within an epoxy matrix. Upon damaging the material, the healant at the wounded area is released and the polymerization of the healing agent is triggered by contact with the embedded catalyst, subsequently repairing the damage [21].
- 6) Recently, by spraying PAH–SPEEK complexes, PAA, and healing agents with low surface energy, Sun and coworkers have developed a facile

spraying method for the fabrication of mechanically robust, self-healing superhydrophobic coatings. The resultant coatings can autonomically and repetitively restore their superhydrophobicity after damage in a slightly humid environment. These self-healing superhydrophobic coatings are anticipated to have important practical applications because of their satisfactory mechanical stability, self-healing ability, and convenient use in outdoor and large-scale fabrications [22].

In spite of the great promise these systems provide, there is one striking omission in their properties – the lack of high bulk electrical conductivity in the self-healing materials. This shortcoming limits their potential use in electronic applications. To be able to apply these polymers to electronic devices, the limiting challenge would be incorporating electrical properties into materials while retaining the self-healing capability. In the following sections, the new contributions to the development of self-healing conductors are introduced.

15.3

Self-Healing Electrical Conductors

Many people know the familiar wince when a cell phone or laptop hits the floor. The failure of electronic devices due to mechanical fracture limits the lifetime and reliability of the devices and leads to an increasing amount of electronic waste. Healable electronics are being explored as a strategy that could help alleviate these problems. So far, healable electronic conductors, a key component in healable electronic devices, have been reported in several publications.

William and coworkers first fabricated the semiconductor-level conductive films of organometallic polymers, comprising *N*-heterocyclic carbenes and transition metals, that had the ability to heal mechanical damage on thermal treatment [6] (Figure 15.1). However, in this case, the conductivity ($\sim 10^{-3}$ S cm $^{-1}$) was too low to be effectively used as electrodes. In addition, the requirements of high temperature (200 °C) and solvent vapor for healing are difficult to attain for practical usages in electronic devices.

Apart from direct synthesis of self-healing conductive polymers, another approach is to incorporate inorganic conductive materials into nonconductive polymers. Sun and coworkers have demonstrated a self-healing conductor by casting silver conductive nanowires (AgNWs) onto polyelectrolyte multilayer (PEM)

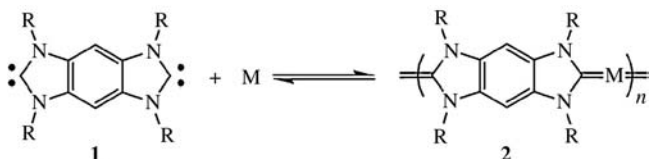


Figure 15.1 Self-healing organometallic polymer and the dynamic covalent chemistry in the polymer. (Adapted with permission from Ref. [6].)

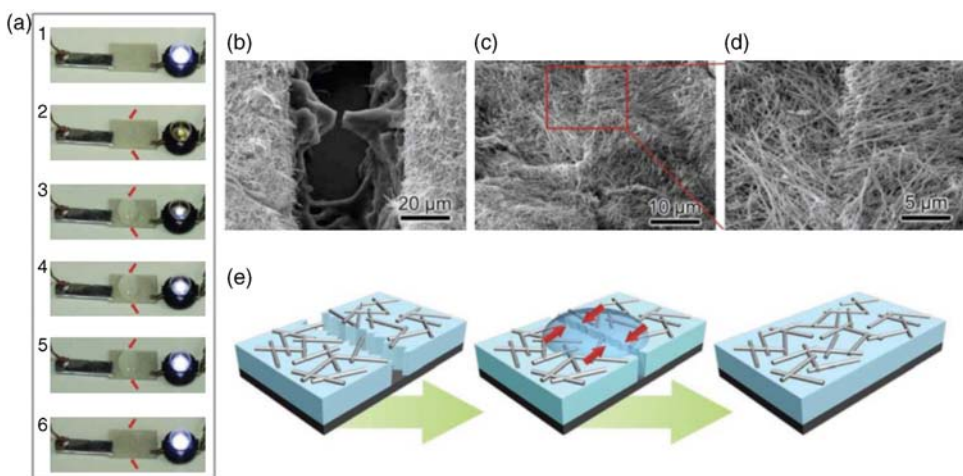


Figure 15.2 (a) Time profiles of healing a cut on a AgNWs/(bPEI/PAA-HA)*50 film connected in a circuit with an LED bulb: (a1) as-prepared film; (a2) the film is cut; (a3–a5) deionized water is dropped on the cut to enable healing of the conductivity; (a6) water is removed after completion of the healing process. The arrows indicate the cuts. (b–d) SEM

images of AgNWs/(bPEI/PAA-HA)*50 film with a cut before (b) and after (c and d) being healed. (d) Magnified view of healed cut in part (c) marked with a square. (e) Schematic illustration of the self-healing conductor using polyelectrolyte multilayers coated with silver nanowires. (Adapted with permission from Ref. [2].)

films to enable healing capability (Figure 15.2) [2]. The healable PEM film consists of a layer-by-layer (LbL) assembled branched poly(ethylenimine) (bPEI) and poly(acrylic acid)-hyaluronic acid (PAA-HA) blend (denoted as (bPEI/PAA-HA)) on a silicon or PET substrate. A layer of AgNWs was then drop casted onto the PEM film as the conductive layer. The hydrogen bonding interactions between carboxylic acid groups on the surface of the bPEI/PAA-HA film and the pyrrolidone groups of the PVPOON-decorated AgNWs enable strong interactions between the two layers. Therefore, even if the film is immersed in water, the AgNWs will not delaminate from the PEM film. Upon contact with water, the PEM film simply swells and causes the fractured surface to heal by reforming the dynamic ionic bonds. The strong interaction between the PEM film and the AgNWs also drives the movement and contact of the conductive layer, and hence restores the electrical conductivity (Figure 15.2). Thus, the system can recover both its conductivity and structural integrity when deionized water is dropped onto the crack. However, the use of water in electronic systems may cause other problems such as short circuit, water leakage, and so on in the applications. Efforts toward solving these problems are currently in progress.

Similarly, by the combination of highly conductive AgNWs with mechanically strong and transparent Diels–Alder (DA) polymers, Pei and coworkers reported the synthesis of a semitransparent composite conductor comprising a layer of AgNW percolation network inlaid in the surface layer of a DA-based healable polymer

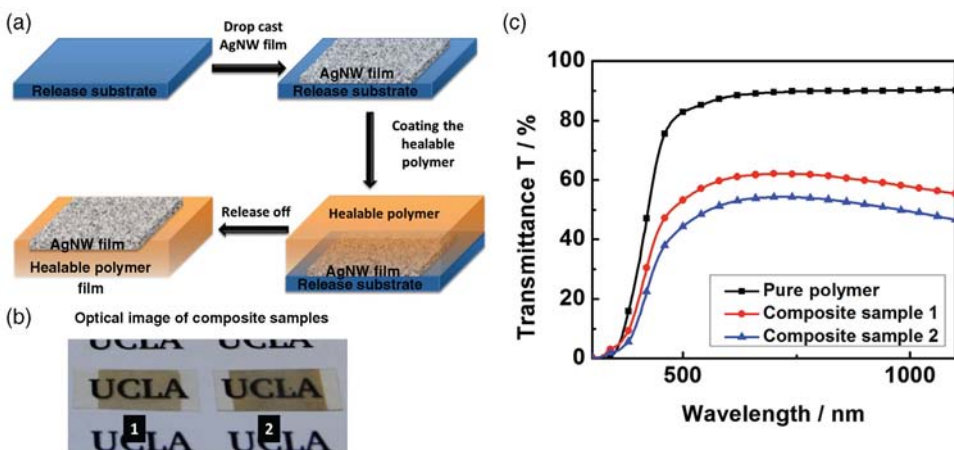


Figure 15.3 (a) Schematic illustration of the fabrication of a healable composite conductor based on AgNWs and MDPB-FGEEDR copolymer. (b) Photographs of composite conductor samples 1 and 2 with different

thicknesses of AgNW layer. (c) Transmittance spectra of pure MDPB-FGEEDR copolymer of 113 μm thickness and composite conductor samples of the same thickness. (Adapted with permission from Ref. [3].)

film [3] (Figure 15.3). The semitransparent composite conductor has a highly conductive surface with sheet resistance as low as $9.5 \Omega \text{sq}^{-1}$ and shows very good flexibility. The composite film is capable of both structural and electrical healing via heating. A cut crack can heal quickly and efficiently as the DA polymer matrix reforms to bring together the silver nanowires, which reforge and restore the percolation network. A crack cut on the conductive surface can heal upon heating at 110°C . As much as 97% of the surface conductivity can be recovered in 5 min. The healing is repeatable at the same location over multiple cycles of cutting and healing without significant loss of surface conductivity (Figure 15.4). For practical

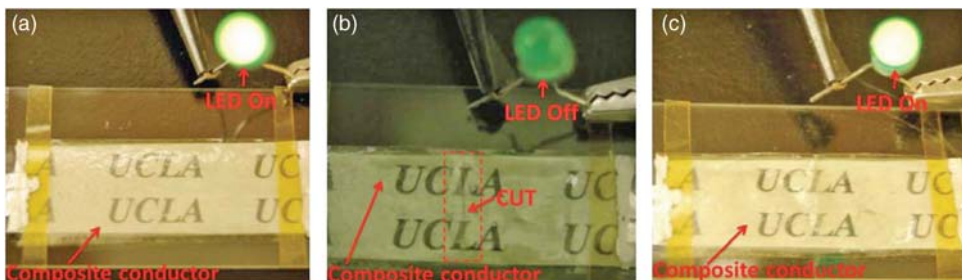


Figure 15.4 (a) A composite conductor specimen connected in series with a lit LED. The specimen was fixed on a glass substrate. A pizza paper with UCLA logos was placed in between for convenient removal of the specimen from the glass slide and also to show the

transparency of the composite conductor. (b) The specimen was cut across its width to break the circuit (see the darker gray line as indicated by the red arrow). (c) The LED was lit again after the cut specimen was healed upon heating. (Adapted with permission from Ref. [3].)

applications, the composite conductor needs to be further improved to increase its transparency, and it would be ideal if the healing could be done at room temperature, without the requirement of heat, so that the materials can “self-heal” autonomously. It is believed that healable transparent conductors can open new vistas for the fabrication of healable and intelligent optoelectronic devices.

An intrinsically self-healing and conductive composite that self-heals without external aids such as heat, light, or solvents is then desired to obtain electrodes for electronic devices. To achieve this, uniform electrical properties and facile processing are required. However, intrinsically self-healing conductors are difficult to be realized. A composite becomes conductive only when the amount of conductive fillers exceeds the percolation threshold. Therefore, chemical compatibility and adequate surface area are important. Moreover, the ratio of the inorganic fillers will also affect the physical property of the composite as well as the self-healing capability.

Recently, Bao and coworkers have demonstrated the first example of intrinsic self-healing conductive composite that can self-heal at room temperature (Figure 15.5) [7]. The polymer host is a hydrogen-bonded network modified from the classical synthetic route demonstrated by Leibler and coworkers [19]. Nickel microparticles (μ Ni particles) with flower-like nanostructures were chosen as conductive fillers. The μ Ni particles are normally covered with a thin oxide layer, which can form hydrogen bonds with the polymer network. Therefore, the μ Ni particles are compatible with the polymer host. The content of μ Ni particles in the composite can reach a volume percentage of 31% without any agglomeration. The percolation threshold in this case is \sim 15% volume fraction of the μ Ni particles. Above the percolation threshold, the conductivity can reach as high as 40 S cm^{-1} . Even at a high volume fraction of μ Ni particles (\sim 30%), the composite still displays both the mechanical and the electrical self-healing capability at room temperature. After being damaged, the material can quickly be healed to 90% of its original conductivity in 15 s at room temperature. It should be noted that the flower-like nanostructure is of high importance for its high conductivity and self-healing capability. The flower-like nanostructures provide adequate surface area and good wetting to facilitate the self-healing. Moreover, the nanostructures greatly enhance the quantum tunneling effect, leading to high conductivity.

Furthermore, a self-healing conductor using capsules with charge transfer salts was reported by White and coworkers. The poly(urea-formaldehyde) core-shell microcapsules were separately loaded with solutions of TTF-TCNQ (tetrathiafulvalene–tetracyanoquinodimethane) in various solvents [9]. The mixed capsules were then plated into the gaps between gold electrodes. Upon mechanical damage, the polymer capsules ruptured and TTF and TCNQ components, which were initially in individual capsules before being damaged, mixed together to form a conductive charge transfer salt. The conductive charge transfer salt then filled up the gaps and subsequently restored the electrical conductivity (Figure 15.6).

Using a similar approach, White and coworkers developed another self-healing conductor using EGaIn as the healant [24]. In this case, mixing of different types of healants is not required. Simply, micrometer-sized capsules with conductive

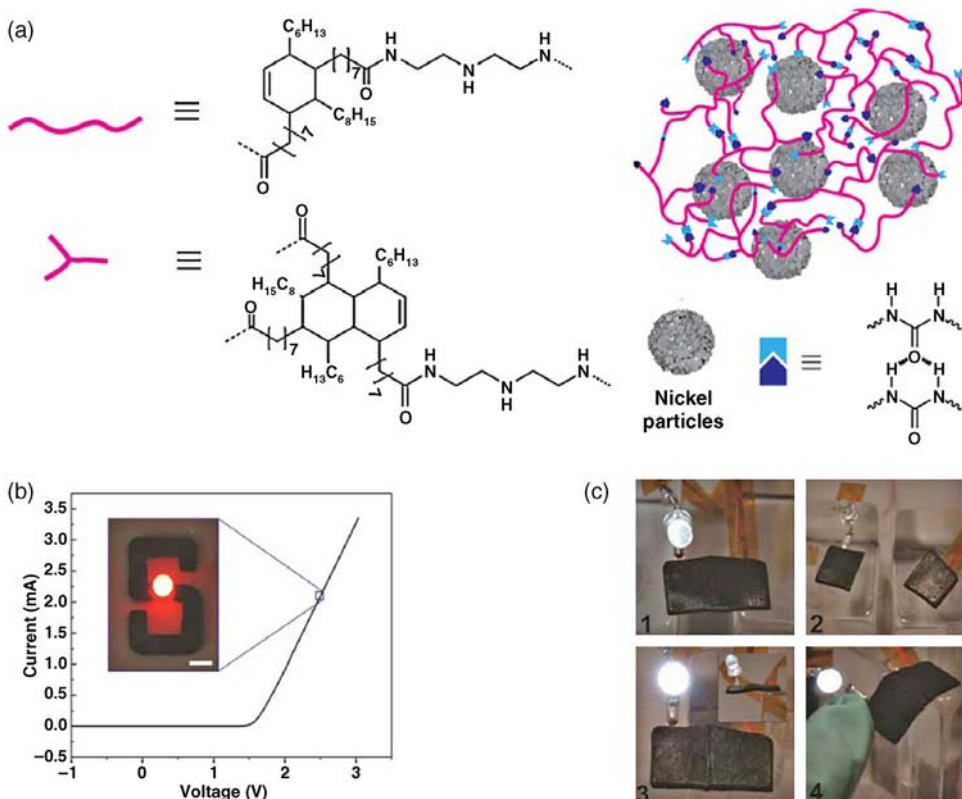


Figure 15.5 Self-healing conductor based on a composite of self-healing polymer and metal particles. (a) Illustration of the self-healing composite. Pink lines represent linear and branched polymers that form the randomly branched network; blue and purple shapes represent urea groups at the ends of the branched polymers that form the primary

hydrogen bonds between the polymer chains.

- A current–voltage curve of a commercial LED using self-healing electrically conductive composite wire molded into an “S” shape.
- Healed film being flexed to show its mechanical strength and flexibility after only 5 min of healing at room temperature.
(Adapted with permission from Ref. [7].)

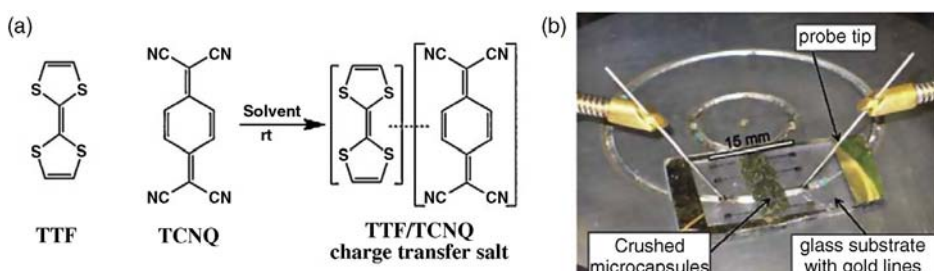


Figure 15.6 (a) TTF and TCNQ can form conductive charge transfer salts. (b) Image of the self-healing circuit. (Adapted with permission from Ref. [9].)

liquid metals were embedded into a conductive circuit. When a mechanical damage was exerted on the area, the microcapsules were ruptured and the encapsulated liquid metal was released and introduced to the damaged parts, hence restoring its electrical conductivity. Notably, this healing process is observed to be fast and efficient. Specifically, an average capsule diameter of $10\text{ }\mu\text{m}$ can restore nearly 100% of its initial conductivity in $160\text{ }\mu\text{s}$. In addition, silver ink can also be used as a healant for restoring conductivity [8]. Obviously, the advantage of a self-healing conductor capsule is its autonomous nature and rapid healing speed. Healing can be triggered automatically at the damaged area without the need of any stimulus. However, these conductive healing agents do not allow simultaneous structural healing. Another disadvantage of the microcapsule self-healing system is that the healing is not repeatable at the same damage location.

15.4

Self-Healing in Energy Storage Devices

The self-healing feature is particularly desirable for energy storage because the lifetimes of many rechargeable batteries are limited by the mechanical fractures over the cycling process. Electrochemical reactions in battery materials during the cycling process normally result in structural changes, which may cause degradation and damage, and ultimately cause the battery to be nonfunctional [25–28]. Next-generation electrode materials for lithium ion batteries are especially susceptible to these failure mechanisms because they react with greater amounts of lithium and thus undergo more drastic structural changes [26,29–33]. For example, silicon, which has a theoretical specific capacity 10 times higher than that of conventional graphite anodes, usually suffers from fast capacity decay and short lifetime. This is mainly because silicon expands volumetrically by up to three times on full lithium insertion (lithiation) and contracts significantly on lithium extraction (delithiation). These extreme volumetric changes can cause cracking and pulverization in the electrode, which lead to loss of electrical contact and excessive solid electrolyte interphase (SEI) growth [25,34,35]. Even after incorporating the silicon materials with metal alloys or high-modulus polymer binders, mechanical fractures and damages still occur.

Silicon microparticles (SiMPs) are more promising as electrode materials toward practical industrial applications because they are cheap and readily commercially available. However, all previously reported pure SiMP anodes have an extremely short lifetime over deep galvanostatic cycling [34] because of the significant fracture and particle detachment in the electrodes [36–39].

Recently, Bao and coworkers used a chemical approach to improve the cycling lifetime of SiMPs by coating the microparticles with a thin layer of hydrogen bonding-directed SHP [42]. Compared with traditional polymer binders, the self-healing chemistry is designed to enable spontaneous repair of the mechanical damage in the electrode and thus increase the lifetime of the SiMP anode. In this design (Figure 15.7), the silicon electrode is coated with a thin layer of soft

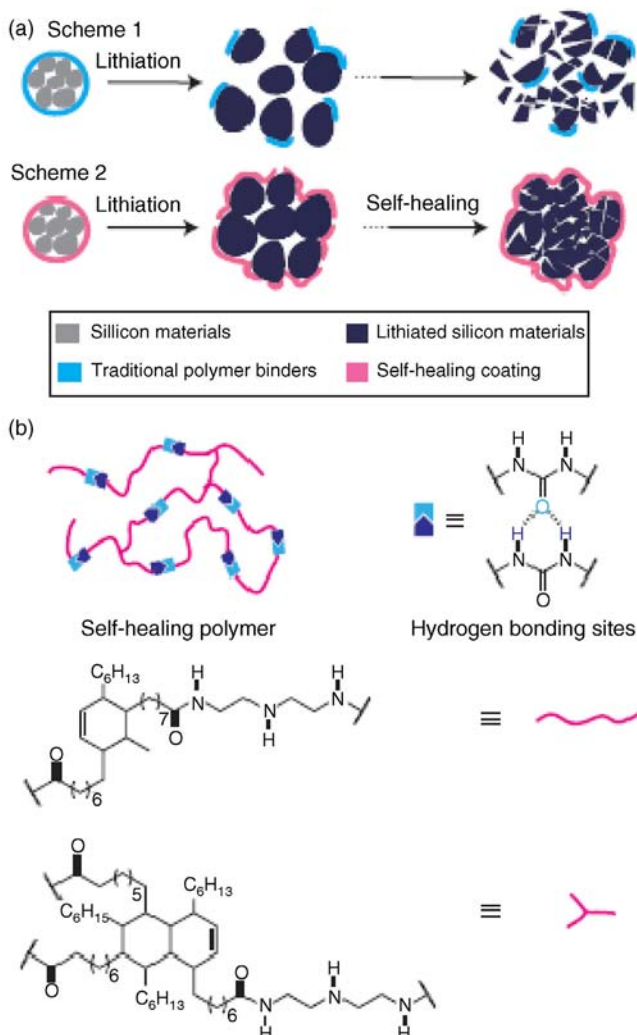


Figure 15.7 Design and structure of the self-healing electrode. (a) Schematic illustration of the design and behavior of a conventional silicon electrode that shows failure of the electrode because of cracking in particles and polymer binder, which results in loss of electrical contact. Scheme 2 Schematic illustration of the design and behavior of the stretchable

self-healing electrode that shows the maintaining of electrical contact between the broken particles and no cracks in the polymer binder because of the stretchability and incorporation of self-healing chemistry. (b) Chemical structure of the SHP. Magenta lines, polymer backbones; light-blue and dark-blue boxes, hydrogen bonding sites. (Adapted with permission from Ref. [42].)

SHP. Different from the conventional polymer binders, the SHP is stretchable and can spontaneously repair the mechanical damage and cracks in the electrode, which results in more stable mechanical and electrical connections among the silicon particles.

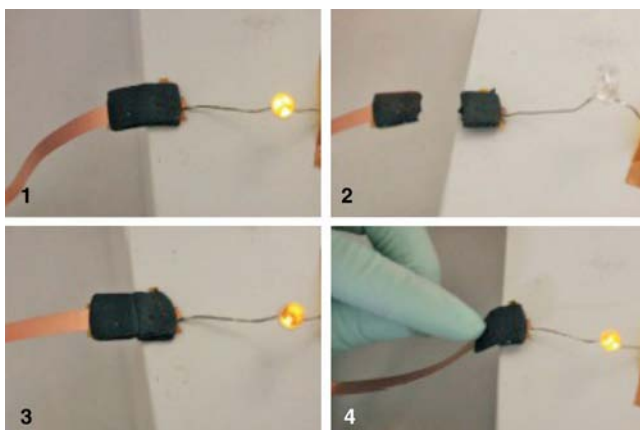


Figure 15.8 Demonstration of the electrical and mechanical self-healing capability of the conductive composite using a battery-powered circuit with the composite SHP as the conductive pathway that connects the LED to the battery. (Adapted with permission from Ref. [42].)

The SHP is a randomly branched hydrogen bonding polymer, synthesized and fabricated using an approach modified from previous reports [7,19,40]. Its molecular structure is shown in Figure 15.7. Particularly, a hydrogen bonding-directed [41] SHP is most advantageous as the coating layer allows the cracks to heal autonomously and repeatedly at room temperature [7]. The SHP is made conductive ($\sim 0.25 \text{ S cm}^{-1}$) by uniformly dispersing conductive carbon black (CB) nanoparticles into the polymer. The composite undergoes simultaneous mechanical and electrical self-healing at room temperature. The self-healing capability is demonstrated in Figure 15.8, which shows that, after an electrical circuit is broken, when the two pieces of SHP acting as the conductors are brought together, the circuit is completed in about 1 min, and the light-emitting diode (LED) illuminates again. At the same time, the composite can withstand mechanical bending at the healed location, which indicates the quick electrical and mechanical healing at room temperature. The cross-linked network of our SHP enables good mechanical stretchability as well, which allows the polymer to accommodate potential expansion of silicon to avoid nonhealable damage, for example, large cracks or delamination. SHP can be stretched to three times its initial length without breaking.

Moreover, they fabricated the self-healing silicon electrodes by sealing SiMPs inside a SHP/CB composite coating. Coin cells with metallic lithium counter-electrodes were employed to evaluate the electrochemical performance of the electrodes. The superior cycling stability and the high capacity of the SiMP/SHP/CB electrodes are highly repeatable. Owing to its superior mechanical stretchability as well as its strong interactions with the silicon surface, the SHP/CB coating can better withstand the large volumetric changes of SiMPs during lithiation/delithiation to bring the shrunken silicon particles into contact with the polymer binder and at the same time avoid large nonhealable cracks in the polymer binder. When the SHP/CB composite coating does undergo fracture, it

can proceed to self-heal. These two unique features of our SHP allow the electrode structure to be maintained over repeatable cycling processes.

Besides the successful demonstration of self-healing chemistry in battery application, this new concept of a self-healing electrode may also be useful for other materials that suffer from mechanical issues during electrochemical reactions, including electrode materials for fuel cells, water splitting, and catalysis.

Supercapacitors, another promising class of energy storage devices, are drawing much attention due to their fast charge and discharge rates, high power density, and long lifetimes [43–60]. Recently, to meet the requirements of miniaturized portable electronic devices, great efforts have been devoted to flexible and lightweight supercapacitors [61–68]. However, most of these supercapacitors suffer from mechanical fragility when they are subjected to practical applications; the electrode materials become susceptible to structure fractures under bending or during charge and discharge processes, while the polymeric flexible substrates may possibly undergo mechanical damage due to deformation over time or by accidental cutting [69–73]. Both of these failures would seriously limit the reliability and lifetime of the supercapacitors, resulting in the wholesale breakdown of electronic devices and generation of excessive electronic waste and causing safety hazards [69–73]. Hence, supercapacitors that can, after being subjected to mechanical damages, not only retain high capacitance and portability but also be endowed with impressive properties such as the capability for prevention of structural fractures in electrode materials and restoration of configuration integrity and electrical properties of the device after mechanical damage. As current research comprises striking omissions in the mechanical sustainability of these supercapacitors, it should be of scientific and technological importance to explore robust supercapacitors with the capability for damage management.

With the concept of integration of appropriate self-healing materials into supercapacitor devices, which could prevent the structural fractures of electrode materials, as well as restore the configuration integrity and electrical properties of the devices after mechanical damage, our group reported a mechanically and electrically self-healing supercapacitor for the first time (Figure 15.9) [74]. In this supercapacitor configuration, the electrodes are fabricated by spreading single-walled carbon nanotube (SWCNT) films onto self-healing substrates. Upon subjection to mechanical damage, lateral movement of the self-healing composite layer brings the separated areas of the SWCNT layer into contact, hence enabling the restoration of the device's configuration and conductivity. The as-prepared supercapacitors exhibited excellent electrochemical self-healing performance, and the specific capacitance can be restored up to 85.7% of its original value even after the fifth cutting.

The manufacturing process of an integrated self-healing supercapacitor device is illustrated in Figure 15.9. The self-healing substrates are composed of a supramolecular network with the low glass transition temperature (T_g) below room temperature and hierarchical flower-like TiO_2 nanostructures. This is achieved through the assembly of molecules to form both chains and cross-links via a large amount of hydrogen bond acceptors and donors, which are also able to

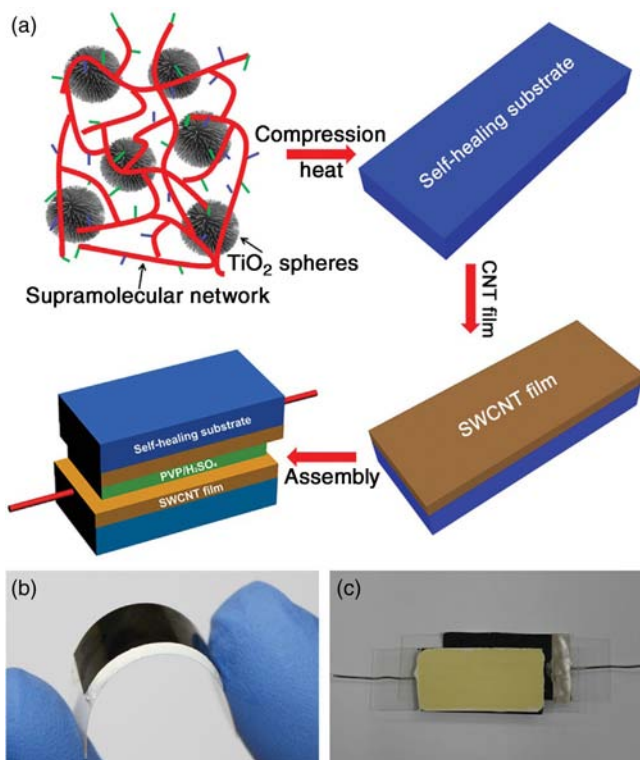


Figure 15.9 (a) The design and manufacturing process flow of a flexible, electrically and mechanically self-healing supercapacitor. The self-healing composite is composed of hierarchical flower-like TiO₂ nanostructures (black spheres) and a supramolecular network (red wires) with a large amount of hydrogen bond acceptors (blue rods) and donors (green rods), which is then compressed under heat to form

a self-healing substrate. CNT films are deposited on the self-healing substrates, which are then assembled to form the sandwiched supercapacitors. (b) Optical image of a flexible self-healing substrate on PET sheet after deposition of the CNT film. (c) Optical image of an integrated self-healing supercapacitor. (Adapted with permission from Ref. [74].)

dynamically associate at room temperature and manifest as a self-healing property by bringing together fractured surfaces in the event of a cut or breakage [75,76]. The rutile flower-like TiO₂ nanospheres, with an average size about 400 nm, were uniformly dispersed and incorporated into the as-synthesized oligomers by vigorous mechanical stirring, followed by thermal cross-linking with urea. An integrated supercapacitor device was fabricated in which SWCNT films serve as active materials and current collectors, while PVP-H₂SO₄ gel serves as both electrolyte and separator. When damaged, lateral movement of the underlying self-healing composition layer brings the separated areas of the SWCNT layer into contact and enables restoration of its conductivity. In addition, PVP gel is a self-adhering material and can self-heal to some extent.

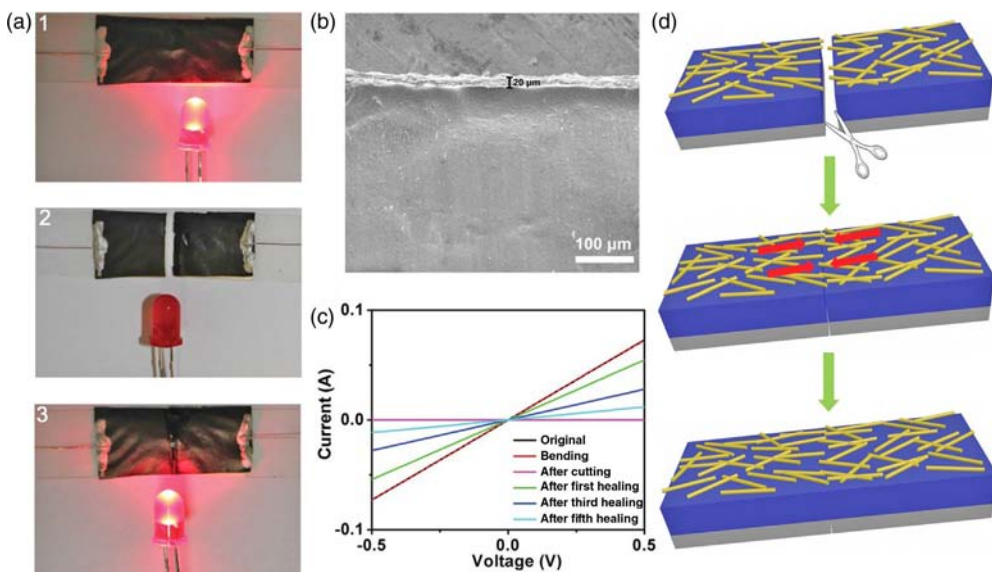


Figure 15.10 The self-healing of electrical conductivity of the as-prepared SWCNT films spread on self-healing substrates. (a) Optical images of as-prepared SWCNT films spread on self-healing substrates in a circuit with an LED bulb. (1): The original; (2): after cutting; and (3): after healing. (b) The cross-sectional SEM image of as-prepared SWCNT films spread on self-healing substrates. (c) Current–voltage

curves of SWCNT films spread on self-healing substrates under bending (an inward $\sim 45^\circ$ bending angle), cutting, and after healing for different times. (d) Schematic representation of self-healing capabilities of electrical conductivity of as-prepared SWCNT films spread on self-healing substrates. (Adapted with permission from Ref. [74].)

A commercially available light-emitting diode bulb was employed for monitoring the conductive behavior of the electrode in a tandem circuit. As shown in Figure 15.10, the electrode was cut with a knife and the lighted LED was immediately extinguished. If a gentle pressure was applied within 20 s, bringing together the two halves of the bifurcated electrode, the LED would light up again as that of the original intact SWCNT films. Furthermore, as a proof of concept, the electrochemical performance of the two-electrode symmetrical flexible supercapacitor cells based on the as-prepared electrically self-healing SWCNT films was investigated. Remarkably, nearly no degradation was observed for the supercapacitors before cutting, and only 3.6% decay in specific capacitance was observed for the supercapacitors after the fifth healing, which demonstrates the excellent electrochemical stability of the self-healing supercapacitors.

By spreading functionalized SWCNT films on self-healing substrates, we have designed and fabricated the first integrated, mechanically and electrically self-healing supercapacitor. The specific capacitance can be restored by up to 85.7% even after the fifth cutting. It is certain that the restoration performance could be further improved through the optimization of operation techniques or replacing the nonconductive self-healing substrates by the conductive self-healing

composites such as micro-nickel particles-incorporated supramolecular networks [7]. The successful preparation of this self-healing supercapacitor may provide a way to expand the lifetime of future energy storage devices and empower them with desirable economic and human safety attributes. Our work may be a stepping-stone toward the design and fabrication of various next-generation self-healing electronic devices in the future.

15.5

Self-Healing Electronic Skin

Sensing is an important feature of the human skin. Developing self-healing sensor materials is an important step toward developing self-healing skin. However, due to the challenge of combining repeatable self-healing, force sensitivity, and high bulk electrical conductivity, so far few self-healing tactile sensors have been reported [1,77].

Bao and coworkers recently demonstrated the first repeatable, room-temperature self-healing electronic sensor skin, using a supramolecular organic–inorganic composite [7]. The method used is similar to the one described previously for a self-healing conductor [7]; self-healing hydrogen bonding networks and nanostructured μ Ni particles were chosen as the components. As stated previously, when the volume content of μ Ni particles is above the percolation threshold, the composites are electrically conductive. However, when the volume percentage is below the percolation threshold and the particles are spaced farther apart, the materials can be made to sense external forces. The larger particle spacing allows a more significant change in resistance as the compressive forces bring the μ Ni particles closer within the matrix. At μ Ni concentrations near the percolation threshold (15 vol%), the composite material can be used to sense mechanical forces such as tactile pressure (Figure 15.11a) and flexion (Figure 15.11b). When the composite material was flexed, compressive stresses were built up at the inner curvature. Thus, the μ Ni particles came closer and thereby reduced the composite's resistance, further serving as a flexion sensor. Pressure exerted on the material can have a similar effect, which can serve as a tactile sensor. The sensor materials can be integrated with the conductors into an all-self-healing E-skin, where both the conductive electrodes and the pressure sensor can self-heal. The material can be molded into a flat piece or mounted onto PET substrate into a flexion sensor. A tactile sensor was completely constructed from self-healing materials by employing a parallel plate structure with the piezoresistive composite sandwiched between the conductive composite with its piezoresistive response. The sensors were then integrated onto a humanoid mannequin. The sensors were located on the palm and the elbow joint in the path of electric circuits using the light intensity of LEDs as indicators of mechanical forces. They demonstrated the ability to detect varying pressures and changing positions of the limbs, that is, proprioception. At different pressures and different flexion angles, the LED was shown to have different intensities, as it responds to

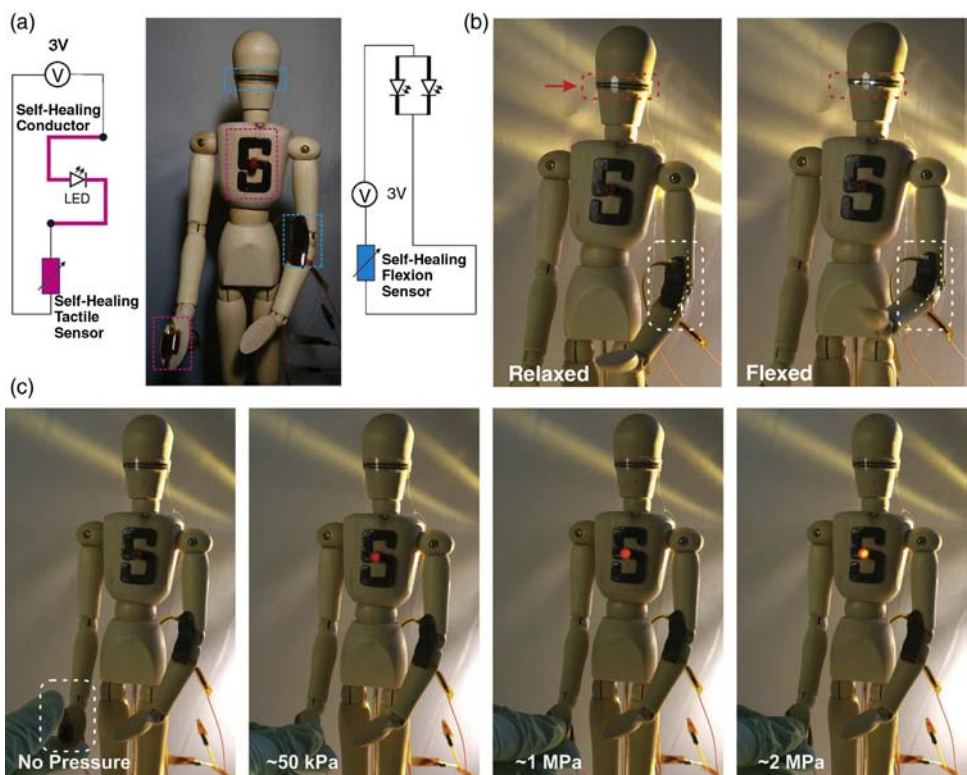


Figure 15.11 Humanoid mannequin showing integration of E-skin. LEDs placed on the mannequin light up at varied intensities based on the movements and magnitude of the inflicted perturbations. (Adapted with permission from Ref. [7].)

different forces and movements. These results are shown in Figure 15.11. Self-healing capability in E-skin has been the driving force for the development of self-healing electronic materials. Although the concept of a total self-healing E-skin has already been demonstrated, further developments are still needed. Specifically, for practical and multiple uses, the electrical materials need to be simultaneously stretchable and capable of self-healing. Furthermore, the sensitivity and stability of the sensors need to be improved. Hence, self-healing elastomers and related composites are both logical challenges in generating the next generation of self-healing sensors.

15.6 Conclusive Remarks and Outlook

People have been dreaming of self-healing materials since the dawn of science fiction. In practice, the development of such materials and further self-healing

devices is a great challenge. Researchers have previously investigated self-healing materials, ranging from rubber to remixed concrete and paint; self-repairing electronic devices could represent one of the best ventures yet.

In this chapter, several recent efforts toward self-healing electronics devices were discussed. While flexible organic electronic devices are already prevalent, the need for stretchable and self-healing electronics nonetheless remains necessary and/or desirable for many emerging applications, for example, electronics, displays, energy, environment, and medicine.

Many of us have experienced anxious moments upon inadvertently dropping an electronic device such as a mobile phone or a laptop as we rush to see whether our beloved device has survived the fall. In future, with the development of such “self-healing first-aid kit-embedded electronic systems” that could stop circuit failure and lead to safer, longer lasting batteries, the researchers in the world will make such incidents a little less distressing. There is also potential for the technology to be used in batteries to restore the electrical conductivity of damaged battery electrodes, thereby preventing a short circuit that could lead to explosion of the battery.

References

- 1 Ghosh, S.K. (2009) *Self-Healing Materials: Fundamentals, Design Strategies, and Applications*, Wiley-VCH Verlag GmbH, Germany.
- 2 Li, Y., Chen, S.S., Wu, M.C., and Sun, J.Q. (2012) *Adv. Mater.*, **24**, 4578–4582.
- 3 Gong, C.K., Liang, J.J., Hu, W., Niu, X.F., Ma, S.W., Hahn, H.T., and Pei, Q.B. (2013) *Adv. Mater.*, **25**, 4186–4191.
- 4 Zheng, Z., Huang, X., Schenderlein, M., Borisova, D., Cao, R., Möhwald, H., and Shchukin, D. (2013) *Adv. Funct. Mater.*, **23**, 3307–3314.
- 5 Zheludkevich, M.L., Shchukin, D.G., Yasakau, K.A., Mohwald, H., and Ferreira, M.G.S. (2007) *Chem. Mater.*, **19**, 402–411.
- 6 Williams, K.A., Boydston, A.J., and Bielawski, C.W. (2007) *J. R. Soc. Interface*, **4**, 359–362.
- 7 Tee, B.C.K., Wang, C., Allen, R., and Bao, Z.N. (2012) *Nat. Nanotechnol.*, **7**, 825–832.
- 8 Odom, S.A., Chayanupatkul, S., Blaiszik, B.J., Zhao, O., Jackson, A.C., Braun, P.V., Sottos, N.R., White, S.R., and Moore, J.S. (2012) *Adv. Mater.*, **24**, 2578–2581.
- 9 Odom, S.A., Caruso, M.M., Finke, A.D., Prokup, A.M., Ritchey, J.A., Leonard, J.H., White, S.R., Sottos, N.R., and Moore, J.S. (2010) *Adv. Funct. Mater.*, **20**, 1721–1727.
- 10 Andreeva, D.V., Fix, D., Mohwald, H., and Shchukin, D.G. (2008) *Adv. Mater.*, **20**, 2789–2794.
- 11 Chen, X., Dam, M.A., Ono, K., Mal, A., Shen, H., Nutt, S.R., Sheran, K., and Wudl, F.A. (2002) *Science*, **295** (5560), 1698–1702.
- 12 Nakahata, M., Takashima, Y., Yamaguchi, H., and Harada, A. (2011) *Nat. Commun.*, **2**, 511–516.
- 13 Phadke, A., Zhang, C., Arman, B., Hsu, C.C., Mashelkar, R.A., Lele, A.K., Tauber, M.J., Arya, G., and Varghese, S. (2012) *Proc. Natl. Acad. Sci. USA*, **109**, 4383–4388.
- 14 Li, Y., Li, L., and Sun, J. (2010) *Angew. Chem., Int. Ed.*, **122**, 6265–6269.
- 15 Wong, T.-S., Kang, S.H., Tang, S.K.Y., Smythe, E.J., Hatton, B.D., Grinthal, A., and Aizenberg, J. (2011) *Nature*, **477**, 443–447.
- 16 Yuan, W., Hu, L.B., Yu, Z.B., Lam, T., Biggs, J., Ha, S.M., Xi, D., Chen, B., Senesky, M.K., Grüner, G., and Pei, Q.B. (2008) *Adv. Mater.*, **20**, 621–625.
- 17 Wang, Q., Mynar, J.L., Yoshida, M., Lee, E., Lee, M., Okuro, K., Kinbara, K., and Aida, T. (2010) *Nature*, **463**, 339–343.

- 18** Brochu, P. and Pei, Q. (2010) *Macromol. Rapid Commun.*, **31**, 10–36.
- 19** Cordier, P., Tournilhac, F., Soulie-Ziakovic, C., and Leibler, L. (2008) *Nature*, **451**, 977–980.
- 20** Ghosh, B. and Urban, M.W. (2009) *Science*, **323**, 1458–1460.
- 21** White, S.R., Sottos, N.R., Geubelle, P.H., Moore, J.S., Kessler, M.R., Sriram, S.R., Brown, E.N., and Viswanathan, S. (2001) *Nature*, **409**, 794–797.
- 22** Li, Y., Chen, S.S., Wu, M.C., and Sun, J.Q. (2014) *Adv. Mater.*, **26**, 3344–3348.
- 23** Benight, S.J., Wang, C., Tok, J.B.H., and Bao, Z. (2013) *Prog. Polym. Sci.*, **38**, 1961–1977.
- 24** Blaiszik, B.J., Kramer, S.L.B., Grady, M.E., McIlroy, D.A., Moore, J.S., Sottos, N.R., and White, S.R. (2012) *Adv. Mater.*, **24**, 398–401.
- 25** Beaulieu, L.Y., Eberman, K.W., Turner, R.L., Krause, L.J., and Dahn, J.R. (2001) *Electrochem. Solid-State Lett.*, **4**, A137–A140.
- 26** Goodenough, J.B. and Kim, Y. (2009) *Chem. Mater.*, **22**, 587–603.
- 27** Tarascon, J.M. and Armand, M. (2001) *Nature*, **414**, 359–367.
- 28** Cheng, Y.-T. and Verbrugge, M.W. (2008) *J. Appl. Phys.*, **104**, 083521.
- 29** Besenhard, J.O., Yang, J., and Winter, M. (1997) *J. Power Sources*, **68**, 87–90.
- 30** Kang, B. and Ceder, G. (2009) *Nature*, **458**, 190–193.
- 31** Zhang, W.J. (2011) *J. Power Sources*, **196**, 13–24.
- 32** Arico, A.S., Bruce, P., Scrosati, B., Tarascon, J.-M., and van Schalkwijk, W. (2005) *Nat. Mater.*, **4**, 366–377.
- 33** Lee, Y.J., Yi, H., Kim, W.-J., Kang, K., Yun, D.S., Strano, M.S., Ceder, G., and Belcher, A.M. (2009) *Science*, **324**, 1051–1055.
- 34** Hatchard, T.D. and Dahn, J.R. (2004) *J. Electrochem. Soc.*, **151**, A838–A842.
- 35** Wu, H., Chan, G., Choi, J.W., Ryu, I., Yao, Y., McDowell, M.T., Lee, S.W., Jackson, A., Yang, Y., Hu, L., and Cui, Y. (2012) *Nat. Nanotechnol.*, **7**, 309–314.
- 36** Kasavajjula, U., Wang, C., and Appleby, A.J. (2007) *J. Power Sources*, **163**, 1003–1039.
- 37** Liu, W.R., Guo, Z.Z., Young, W.S., Shieh, D.T., Wu, H.C., Yang, M.H., and Wu, N.L. (2005) *J. Power Sources*, **140**, 139–144.
- 38** Obrovac, M.N. and Krause, L.J. (2007) *J. Electrochem. Soc.*, **154**, A103–A108.
- 39** Ryu, J.H., Kim, J.W., Sung, Y.E., and Oh, S.M. (2004) *Electrochem. Solid-State Lett.*, **7**, A306–A309.
- 40** Montarnal, D., Tournilhac, F.O., Hidalgo, M., Couturier, J.-L., and Leibler, L. (2009) *J. Am. Chem. Soc.*, **131**, 7966–7967.
- 41** Wang, L.Y., Wang, Z.Q., Zhang, X., Shen, J.C., Chi, L.F., and Fuchs, H. (1997) *Macromol. Rapid Commun.*, **18**, 509–514.
- 42** Wang, C., Wu, H., Chen, Z., McDowell, M.T., Cui, Y., and Bao, Z. (2013) *Nat. Chem.*, **5**, 1042–1048.
- 43** Chen, L.F., Zhang, X.D., Liang, H.W., Kong, M.G., Guan, Q.F., Chen, P., Wu, Z.Y., and Yu, S.H. (2012) *ACS Nano*, **6**, 7092–7102.
- 44** Chen, Z., Augustyn, V., Wen, J., Zhang, Y.W., Shen, M.Q., Dunn, B., and Lu, Y.F. (2011) *Adv. Mater.*, **23**, 791–795.
- 45** Fan, Z.J., Yan, J., Wei, T., Zhi, L.J., Ning, G.Q., Li, T.Y., and Wei, F. (2011) *Adv. Funct. Mater.*, **21**, 2366–2375.
- 46** Futaba, D.N., Hata, K., Yamada, T., Hiraoka, T., Hayamizu, Y., Kakudate, Y., Tanaike, O., Hatori, H., Yumura, M., and Iijima, S. (2006) *Nat. Mater.*, **5**, 987–994.
- 47** Hao, L., Li, X.L., and Zhi, L.J. (2013) *Adv. Mater.*, **25**, 3899–3904.
- 48** Liu, C., Li, F., Ma, L.P., and Cheng, H.M. (2010) *Adv. Mater.*, **22**, E28–E62.
- 49** Liu, F., Song, S.Y., Xue, D.F., and Zhang, H.J. (2012) *Adv. Mater.*, **24**, 1089–1094.
- 50** Reddy, A.L.M., Gowda, S.R., Shaijumon, M.M., and Ajayan, P.M. (2012) *Adv. Mater.*, **24**, 5045–5064.
- 51** Wen, Z.H., Wang, X.C., Mao, S., Bo, Z., Kim, H., Cui, S.M., Lu, G.H., Feng, X.L., and Chen, J.H. (2012) *Adv. Mater.*, **24**, 5610–5616.
- 52** Zhang, L.L. and Zhao, X.S. (2009) *Chem. Soc. Rev.*, **38**, 2520–2531.
- 53** Bae, J., Park, Y.J., Lee, M., Cha, S.N., Choi, Y.J., Lee, C.S., Kim, J.M., and Wang, Z.L. (2011) *Adv. Mater.*, **23**, 3446–3449.
- 54** Wang, Q., Wen, Z.H., and Li, J.H. (2006) *Adv. Funct. Mater.*, **16**, 2141–2146.
- 55** Zhu, Y.W., Murali, S., Stoller, M.D., Ganesh, K.J., Cai, W.W., Ferreira, P.J.,

- Pirkle, A., Wallace, R.M., Cychosz, K.A., Thommes, M., Su, D., Stach, E.A., and Ruoff, R.S. (2011) *Science*, **332**, 1537–1541.
- 56** Gao, W., Singh, N., Song, L., Liu, Z., Reddy, A.L.M., Ci, L.J., Vajtai, R., Zhang, Q., Wei, B.Q., and Ajayan, P.M. (2011) *Nat. Nanotechnol.*, **6**, 496–500.
- 57** Ren, J., Li, L., Chen, C., Chen, X.L., Cai, Z.B., Qiu, L.B., Wang, Y.G., Zhu, X.R., and Peng, H.S. (2013) *Adv. Mater.*, **25**, 1155–1159.
- 58** Chen, T., Qiu, L.B., Yang, Z.B., Cai, Z.B., Ren, J., Li, H.P., Lin, H.J., Sun, X.M., and Peng, H.S. (2012) *Angew. Chem., Int. Ed.*, **51**, 11977–11980.
- 59** Wang, G.P., Zhang, L., and Zhang, J.J. (2012) *Chem. Soc. Rev.*, **41**, 797–828.
- 60** Kaempgen, M., Chan, C.K., Ma, J., Cui, Y., and Gruner, G. (2009) *Nano Lett.*, **9**, 1872–1876.
- 61** Chen, P.C., Shen, G.Z., Shi, Y., Chen, H.T., and Zhou, C.W. (2010) *ACS Nano*, **4**, 4403–4411.
- 62** Lu, X.H., Wang, G.M., Zhai, T., Yu, M.H., Xie, S.L., Ling, Y.C., Liang, C.L., Tong, Y.X., and Li, Y. (2012) *Nano Lett.*, **12**, 5376–5381.
- 63** Niu, Z., Liu, L., Zhang, L., Zhu, B., Dong, H., and Chen, X. (2013) *Adv. Mater.*, **25**, 4035–4042.
- 64** Xu, Y., Lin, Z., Huang, X., Liu, Y., Huang, Y., and Duan, X. (2013) *ACS Nano*, **7**, 4042–4049.
- 65** Wang, X.F., Liu, B., Wang, Q.F., Song, W.F., Hou, X.J., Chen, D., Cheng, Y.B., and Shen, G.Z. (2013) *Adv. Mater.*, **25**, 1479–1486.
- 66** Wang, K., Wu, H.P., Meng, Y.N., Zhang, Y.J., and Wei, Z.X. (2012) *Energy Environ. Sci.*, **5**, 8384–8389.
- 67** El-kady, M.F., Strong, V., Dubin, S., and Kaner, R.B. (2012) *Science*, **335**, 1326–1330.
- 68** Meng, F.H. and Ding, Y. (2011) *Adv. Mater.*, **23**, 4098–4102.
- 69** Raymundo-Pinero, E., Cadek, M., Wachtler, M., and Beguin, F. (2011) *ChemSusChem*, **4**, 943–949.
- 70** Chen, Y.C., Hsu, Y.K., Lin, Y.G., Lin, Y.K., Horng, Y.Y., Chen, L.C., and Chen, K.H. (2011) *Electrochim. Acta*, **56**, 7124–7130.
- 71** Chan, C.K., Peng, H.L., Liu, G., McIlwrath, K., Zhang, X.F., Huggins, R.A., and Cui, Y. (2008) *Nat. Nanotechnol.*, **3**, 31–35.
- 72** Bian, C.Q., Yu, A.H., and Wu, H.Q. (2009) *Electrochem. Commun.*, **11**, 266–269.
- 73** Huang, L., Yi, N., Wu, Y., Zhang, Y., Zhang, Q., Huang, Y., Ma, Y., and Chen, Y. (2013) *Adv. Mater.*, **25**, 2224–2228.
- 74** Wang, H., Zhu, B., Jiang, W., Yang, Y., Leow, W.R., Wang, H., and Chen, X.D. (2014) *Adv. Mater.*, **26**, 3638–3643.
- 75** Tee, B.C.K., Wang, C., Allen, R., and Bao, Z.N. (2012) *Nat. Nanotechnol.*, **7**, 825–832.
- 76** Cordier, P., Tournilhac, F., Soulie-Ziakovic, C., and Leibler, L. (2008) *Nature*, **451**, 977–980.
- 77** Zhang, M.Q. and Rong, M.Z. (2011) *Self-Healing Polymers and Polymer Composites*, Wiley-VCH Verlag GmbH, Germany.

Index

a

ABC transporters, 110
 2-acetyl-6-dimethylaminonaphthalene, 140
 2-acetyl-6-methylaminonaphthalene, 140
 acridinium salts, 370
 ACT. *See* adoptive T-cell therapy (ACT)
 acyl chlorides, 5
 adoptive T-cell therapy (ACT), 187
 adsorption
 – and change in viscosity, 174
 – of CO₂ vapors, 105
 – enhanced, 102
 – geometries, 2
 – of ink molecules, 162
 – lysozyme, 102
 – physical, 238
 – protein, 283, 284
 – of proteins on DNA–gold nanoparticles to facilitate cellular uptake and, 284
 – selective, 177, 178
 adsorption–desorption equilibrium, 138
 AFM images of MEH-PPV self-assembly stripes, 331
 agglomeration, 9, 100, 277, 406
 aging time, 138
 Ag nanoparticles, 387, 388
 AgNWs/(bPEI/PAA-HA)^{*}50 film, LED bulb, 404
 AgNWs copolymer, 403–405
 Ag–TCNQ nanowires, 387, 388, 396, 397
 – formation mechanism, 387
 – UV-vis spectroscopy/scanning electron microscopy (SEM), 387
 aldol reaction, 62
 alkane polymerization, 6
 allergens, 163
 aluminum oxide, 138
 Alzheimer's β-amyloid peptide, 67

ambient atmosphere n-type semiconductors, 315
 3-aminophenylboronic acid (APBA), 302
 ammonia, 102, 249, 250
 amphiphiles, 33–35
 – Gemini, 37, 38
 – self-assembly, 375
 – supra, 40, 41
 – thermodynamic properties, 375
 – triangular, 38–40
 – typical, 35
 AMT-based BBB transport systems, 121
 angiogenesis, 79
 aniline, 102
 anisotropy, 144, 281
 anodic aluminum oxide (AAO), 303
 anthracene, 370
 9-anthracenecarboxylic acid, 397
 3-(anthracen-10-yl)-1-phenylpro-2-en-1-one (APO), 150
 antibodies-containing transmembrane domains, 304
 anticancer drug DOX, storage and release processes, 99
 anticorrosive conductive materials, 401
 anti-EpCAM-coated Si nanowire (SiNW) substrates, 298
 antifouling, 401
 antisense gene regulation, 260
 APC analogues, 187, 188
 APC surrogate system, bead-based, 187
 aquaporins, 70
 aqueous C₁₂E₅ solution, cryo-TEM images, 368
 astrocytes, 79, 112
 atomic force microscopes (AFMs), 97, 139, 161, 163, 238, 243, 246, 327, 392
 atomic layer deposition (ALD) technique, 220
 – applications, 221

- to control thickness of oxide layer with, 220
- atomic precision, 217, 219, 220, 222
- Au junction
 - I–V curves, 397
 - Au/microrod/Au junction
 - current–voltage (I–V) measurements, 395
 - azide–alkyne “click” reaction, 8
 - azide–alkyne cycloaddition, 6–9
 - reaction, 8
- N*-(4-azidophenyl)-4-ethynylbenzamide, 7
- azobenzene, 42, 54, 370, 392
 - -modified cationic surfactants, 370
 - photoresponsive groups, 370
- b**
- Bacillus subtilis*, 65
- bandgap, 2, 222, 233
- barrier tightness, regulation of, 112
- batteries, 250
- BBB. *See* blood-brain barrier (BBB)
- BCSFB. *See* blood-CSF barrier (BCSFB)
- benzene, 38–40, 45, 102, 104, 141, 371
- 3-(2-benzothiazoly)-7-diethylaminocoumarin (coumarin 6), 151
- benzothiophene derivatives, 326
- BGBC. *See* bottom-gate-bottom-contact (BGBC)
- BGTC. *See* bottom-gate-top-contact (BGTC)
- BGTC-type organic nano-FET device
 - fabrication of, 334
- bimetallic Au–Ag nanowires, 262
- biocompatibility, 46, 59, 77, 115, 120, 124, 172, 182, 261, 280
- biodegradability, 46, 59, 77
- biodiagnostics, 260, 283
- biofunctionalization, 194, 195, 203–205, 209, 212
- biological applications, 176, 177, 402
- biomedicine, 62, 75, 77, 155, 259, 260
- biomimetic lipid membranes, 162, 177, 178
- biomimetic membranes, 176
 - doped with biotin, 179
- bionics, 62
- bio-specific interactions, 101
- biotin, 174, 175, 178, 179
- bipolar organic single-crystal nanobelト transistor, 343
- N,N*-bis(acryloyl)cysteamine, 201
- 1,4-bis(1,2'-6',1''-bis(3-butyl-1*H*-3,4,5-triazolyl)pyridin-4'-yl)benzene nanostructures, 143
- 4,4'-bis((E)-2-(naphthalen-2-yl)vinyl)-1,1'-biphenyl (BNVBP), 311, 313, 343
- bis(iminopyrrole)benzene, 141
- 5,5'-bis(4'-methoxybiphenyl-4-yl)-2,2'-bithiophene (BP2T-OMe), 136
- N,N*-bis(2-phenylethyl)-perylene-3,4:9,10-tetracarboxylic diimide (BPE-PTCDI) nanowires, 323
- N,N*-bis(2-phenylethyl)-perylene-3,4:9,10-tetracarboxylic diimide (BPE-PTCDI) nanowires, 323
- 9,10-bis(phenylethynyl)anthracene (BPEA), 137, 144, 145, 151, 153
- bis(2,4,5-trichloro-6-carbopentoxyphenyl) oxalate (CPPO), 153
- bivalent cation, 179
- block copolymer micellar nanolithography (BCML), 189, 190
- blood–brain barrier (BBB), 109, 120–124
 - cells of neurovascular unit forming, 111
 - drug permeability across, 112, 113
 - endothelial, 110
 - surface functionalization of nanoparticles for, 120–122
 - transport routes across, 112, 113
 - *in vitro* models of, 114, 115
- blood-CSF barrier (BCSFB), 109, 110, 111, 112
 - *in vitro* models, 114, 115
- bolaamphiphiles, 35–37
- bolaform surfactant containing azobenzene, 370
- bone, 79
- boronic acid, 5
- bottom-contact FET device, 334
- bottom-contact-type field-effect transistor
 - source/drain electrodes, structure diagram of, 333
- bottom-gate-bottom-contact (BGBC)
 - advantages, 333
 - device structures of organic nano-FETs, 332
 - disadvantage, 333
 - preparation process, 333
- bottom-gate-top-contact (BGTC)
 - device structures of organic nano-FETs, 332
- bottom-up method, 133
- BPEA wire, 144
- BPE-PTCDI nanowire/thin film-based devices, 348
- brain, 110
- branched poly(ethylenimine) (bPEI), 404
- Br[−] anions, 391
 - cetyltrimethylammonium bromide (CTAB), 391
- bromobenzene, 322
- β-sheet-like structures, 69

c

cable-like optical waveguide sensing platform, 154
 cage-in-fiber-type nanoporous carbon sensor, 103
 calcite, 374
 camphorsulfonic acid-doped polyaniline/polyethylene oxide nanofiber, 247
 capacitors, 1
 carbohydrates, 118
 carbon black (CB) nanoparticles, 410
 carbon nanocage, 102
 carbon nanotubes, 77, 302
 carboxyfluorescein (CF)-loaded vesicles, 73
 carcino embryonic antigen (CEA), 294
 carrier-mediated transport, 113
 catalysis, 74, 75, 96, 385, 411
 catechin, 102
 C8-BTBT on SiO₂, 328
 C4-C-N-PEG9 concentration, 370
 C₆₀ crystals, one-dimensional, 320
 CD. *See* circular dichroism (CD)
 CDT-BTZ copolymer fiber, 345
 cell adhesion, 178, 298
 cell-penetrating peptides (CPPs), 121
 cell–substrate interaction, 301
 central nervous system (CNS), 109
 cerasome, 96–98
 cerasomes, 96, 97
 – Lbl films, 97
 cerebrospinal fluid (CSF), 109–111, 114
 cerebrovascular unit (CVU), 110, 112
 N-cetyl-*N,N*dihydroxyethylammonium bromide (CDHEAB), 363
 – schematic diagram, 364
 cetyltrimethylammonium bromide (CTAB), 53, 142, 281
 – in acetonitrile, 391
 – Br[–] anions, 391
 – micelles, 142
 – thermoresponsive viscoelastic gel, 369
 cetyltrimethylammonium 3-hydroxynaphthalene-2-carboxylate (CTAHNC), 369
 C₈F₁₇EO₁₀ molecular structure, 365
 C₈F₁₇SO₂(C₃H₇)N(CH₂CH₂)₁₀H, nonionic fluorocarbon surfactants, 365
 C₁₂Glu–C₁₂DMA system, pH-dependent behavior, 364
 charge transfer complexes, 40, 101, 385
 – micro/nanostructure conversion, 385–388
 chemical modification, 110, 296

CH₃-functionalized self-assembled monolayer (SAM), 322
 chitosan, 118, 123, 402
 chlorobenzene, 318–320, 327
 cholesterol ester, 63
 cholesteryl-succinyl silane (CSS), 303
 cinnamic acid, 370
 circular dichroism (CD), 43, 67, 265
 circulating tumor cells (CTCs), 293, 294, 306
cis-coordination processes, 223
 claudins, 110, 112
 cleavable camptothecin (CPT), 58
 click chemistry, 262
 C_mEO_n system nonionic surfactant solutions, 364
 CMK-3 nanochannel, 102
 coatings
 – microelectromechanical systems, 373
 – organic nanoparticles, 115
 combinatorial biomimetic lipid membranes, 178
 composite structures
 – fabricated from synergistic assembly of different molecules, 141, 142
 compressed CO₂ regulated self-assembled vesicle, 61
 condensation reactions, 5
 conducting polymer nanostructures
 – solution-based synthesis, 234
 – substrate-based fabrication, 237
 conductive polymers, 233, 235, 250, 251, 403
 conductivity, 233, 246, 265, 403, 404, 406
 – of electrospun conducting polymer nanofiber, 246, 248
 – measurement, 265
 – of nanofiber, 247
 – of polymer nanofiber as function of conducting polymer content, 248
 copper-catalyzed alkyne–azide cycloaddition, 264
 copper grid, 339
 – transmission electron microscope (TEM), 341
 copper hexadecafluorophthalocyanine (F₁₆CuPc), 313, 315
 copper(I)-catalyzed Huisgen cycloaddition, 262
 copper phthalocyanine (CuPc), 147, 313, 314
 – nano field-effect transistor, top-contact, 340
 – SEM and TEM images, 315
 – single-crystal nanowire, 339
 – SO₂ detection, 350
p-coumaric acid, 371

- covalent bonding, 2, 3, 11, 101, 240
- CPs. *See* cyclic peptides (CPs)
- critical size, 133
- cross-linked iron oxide nanoparticles (CLIO), 124
- cryo-TEM images, 368
- aqueous $C_{12}E_5$ solution at three different temperatures, 368
- crystal growth, 133, 224, 309–314, 317, 323, 325
- crystallization process, 41, 133, 271, 280, 322
- crystal morphology, depends on, 314
- Cu–BMSB–Zn particles, 389
- Cu(II) ions, 389
- Cu^{2+} -mediated nanotubular, 74
- CuPc nanobelt, 314
- CuPc nanocrystal
 - suspension, 335
- CuPc single crystal, 345
- FET devices, 347
- cyclic arginine–glycine–aspartic acid peptide (cRGDfK), 206
- cyclic peptides (CPs), 62, 65, 69, 73
 - nanotubes, 69
- cyclodehydrogenation, 2
- cyclohexane, 103, 104, 371, 372
- cyclohexyl-substituted quaterthiophene (CH_4 T), 322
- soluble, 322
- cyclopentadithiophene-benzothiadiazole copolymer (CDT-BTZ), 312, 313, 322, 345
- cysteine (Cys), 76, 211
- cytokeratin (CK), 294
- cytosines, 43, 259, 262
- Czochralski method, 325

- d**
- DAPI staining, 180
- DA polymer matrix, 405
- DBEDOT microrods, 394, 395
 - SEM images of, 394
- DB-TTF nanowire arrays, 320, 322
- decarboxylative polymerization, of acids, 13–16
- dedoping processes, 233, 242, 250
- dehalogenation, of chloro-substituted perylene, 3
- dehydrogenative polymerization, of *n*-dotriacontane, 7
- dendrimers, 55, 56
 - amphiphilic, based on L-glutamic acid pH-responsive self-assembly, 57
 - heterostructures, as optical routers, 146
- density functional theory (DFT), 2
- deoxyribonucleic acid (DNA), 259
 - aggregates composed of different particle geometries and morphologies, 279–282
 - applications, 282–286
 - lamellar superstructures using nanoprisms, 282
 - nanoparticles of materials functionalized with DNA, 280
 - bifunctional template synthesized by treatment with restriction digest, 264
 - correlation of optical data with dynamic light scattering, 270
 - dialdehyde, 263
 - dialdehyde functions, 264
 - extended superstructures, 271–273
 - crystal structures, 272
 - hairpin DNA-mediated gold nanoparticle networks, 274
 - finite size DNA–AuNP assemblies, 273–279
 - asymmetric functionalization of nanoparticles with DNA utilizing silica particles, 275
 - DNA–gold nanoparticle clusters mediated using DTT, 278
 - TEM images of purified dimer, trimer, and tetramer structures generated using, 276
 - functionalization of gold nanoparticles and network formation, 267–271
 - immobilized on a spherical gold nanoparticle, 268
 - inherent biocompatibility, 261
 - intercalating molecules, 284, 285
 - intercalators, 102
 - as ligand, 267
 - mediated assembly of metal nanoparticles, methodologies, 261
 - multifunctional, 263
 - network formation using DNA-functionalized gold nanoparticles, 269
 - self-recognition of, 260
 - as a template material, 262–267
 - on geometrically tailored, 266, 268
 - on modified linear DNA strands, 262–265
 - on origami structures, 265–267
 - T_m value, 269
 - triangle-shaped DNA origami decorated with AgNPs, 268
 - dephosphorylation, 112
 - dextran, 118
 - 3D growth, 170
 - 1D growth, of ADN, 141

- 1,2-diacyl-*sn*-glycero-3-phosphocholine-based nonaqueous VEGs, 371
- 4'6-diamidino-2-phenylindol (DAPI), 284, 285
- 1,5-diaminoanthraquinone (DAAQ), 139
- dibenzo[*d,d'*]thieno[3,2-*b*;4,5-*b'*]dithiophene (DBTDT), 343
- dibenzotetrathiafulvalene (DB-TTF), 319
- single-crystal field-effect transistors, 319
- 2,5-dibromo3,4-ethylenedioxythiphene (DBEDOT), 394
- dichloroanthracene (DBA), 326
- micro/nanowires, 326
- 6,13-dichloropentacene (DCP)
- single-crystal field-effect transistor, 344
- 4-(dicyanomethylene)-2-methyl-6-(*p*-dimethylaminostyryl)-4*H*-yan (DCM), 142
- 1,4-di(eicosyl)benzene, 6
- dielectric constant, 222
- Diels–Alder (DA) polymers, 404
- Diels–Alder reaction, 74
- 2-(*N,N*-diethylanilin-4-yl)-4,6-bis(3,5-dimethylpyrazol-1-yl)-1,3,5-triazine (DBPT), 135
- 1,4-diethynylbenzene, 11
- dimerization, 8
- aryl alkyne, 13
- dinitrophenol (DNP), 174
- diocetylbenzothienobenzothiophene (C8-BTBT) chlorobenzene solution, 327
- 1,2-dioleoyl-*sn*-glycero-3-phosphocholine (DOPC), 163, 168, 170, 172, 174, 177, 371, 372
- frequency-dependent complex viscosity, 372
- dip coating, 318, 325
- schematic representations of, 318
 - solvent evaporation method, 318
- diphenylalanine peptide, 67
- analogues, 68
- 9,10-diphenylanthracene (DPA), 149
- 1,5-diphenyl-1,4-pentadien-3-one (DPPDO), 135–137
- 1,3-diphenyl-2-pyrroline (DP), 142
- meso*-diphenyl tetrathia[22]annulene[2,1,2,1] (DPTTA), 320
- dipole–dipole interaction, 141
- dip-pen nanolithography (DPN), 161, 162, 190, 238, 262
- of diffusive inks, 165, 166
 - of lipid inks, 166–170
 - of liquid inks, 165
 - scheme of, 162
- dipping processes parameters, 190
- 2,6-dipyrazol-1-ylpyridine, 135
- dithiol dithiothreitol (DTT), 268
- dithiophene-tetra-thiafulvalene (DT-TTF)
- nanocrystal, 318
 - single-crystal field-effect transistors, 319
 - solution-processed, 319
- divalent metal ions, 77
- diyne polycyclotrimerization, 11
- DNA. *See* deoxyribonucleic acid (DNA)
- DNA–AuNP. *See* DNA-gold nanoparticles
- DNA-gold nanoparticles
- adsorption of proteins to facilitate cellular uptake, 284
 - aggregates display fortunate combination, 282
 - architectures, 285
 - assembly on DNA template using origami structures, 267
 - effect of DNA binding molecules on the melting temperature, 285
 - exposure to degrading enzymes, 283
 - finite size assemblies, 273
 - functional antibody–DNA–AuNPs designed for, 283
 - hydrodynamic radius, 272
 - intercalating molecules, and affect on T_m value, 270
 - photothermal heating effect, 286
 - scanometric microRNA platform for detection of, 284
 - synthetically programmable crystallization, 271
 - TEM images of purified dimer, trimer, and tetramer structures, 276
- 1D nanostructures, 23
- DNP-cap-PE lipid, 179
- N*-dodecanoyl-(D-/L-)serine, 65
- dolomite, 374
- MgCO₃, extraction process, 374
- doped conjugated nanofiber field-effect transistor, 330
- doped nanostructures, 149
- core/sheath structures, 153, 154
 - gradiently doped structures, 151–153
 - uniformly doped structures, 149–151
- doped polyaniline/polyethylene oxide (PEO) nanofiber, 329
- doping, 149, 233
- DPC method, schematic representations, 321
- 2D PEG-DA hydrogels, 189
- DPN. *See* dip-pen nanolithography (DPN)
- drag-reducing (DR) agents, 374
- drop-casted CH₄ T bottom-contact single-crystal transistors, 324

- drop casting, 318, 320
 - schematic representations of, 318
 - solvent evaporation method, 318
- drug delivery systems (DDS), 105
- drug encapsulation efficiency, 59
- dwell time, 171
- dynamic gels, advanced, 357
 - applications, 373, 374
 - classification, 357, 358
 - in nature, 358, 359
 - photoresponsive VEGs, 369–373
 - pH-responsive VEGs, 363, 364
 - redox-responsive VEGs, 362, 363
 - temperature-responsive VEGs, 364–369
 - theory, 375–379
 - VEGs, characterization, 359
 - – rheometer, 359, 360
 - – small-angle neutron scattering (SANS), 360, 361
 - – transmission electron microscopy, 361
- dynamic light scattering (DLS), 369

- e**
- e-beam lithography, 190
- EGaIn, self-healing conductor, 406
- elastic deformation, 171
- electrical conductivity, 233
- electrically conductive materials, 401
- electrochemical coupling, 101
- electrode of organic semiconductor nanocrystal field-effect transistor, 339–345
- electrolytes, 237
- electronic nanodevices, 75
- electronic properties, 1, 138, 145
- electronic skin. *See* E-skin
- electron microscopy, 271
- electroplating, 341
- electrospinning technique, 233, 246
 - carrier polymers utilized in, 247
 - of conducting polymer, 245–250
 - – structure, 247
 - diameter in range of, 246
 - doped conjugated nanofiber field-effect transistor fabricated by, 330
 - doped polyaniline/polyethylene oxide (PEO) nanofiber, 329
 - to fabricate polyaniline nanowires with diameters of, 249
 - polyaniline/polyethylene oxide (PEO) nanofiber, 329
 - schematic illustration of apparatus, 245
- electrospun conducting polymer nanofibers, 246

- electrostatic forces, 131
- electrostatic interaction, 220
- electrostatic repulsions, 76
- emission color, 142
- enamel, 79
- enantioselectivity, 62, 74
- endocytosis, 113
- energy balance, 170
- energy/charge transfer, 145
- energy storage, 401
- epithelial cell adhesion molecule (EpCAM), 294
- epithelium-specific antigens, 294
- EP–SPP coupling, 145
- erucyl bis(hydroxyethyl)methylammonium chloride (EHAC), 369
- E-skin, 401, 414, 415
- etched bottom-contact-type field-effect transistor, 333
- ethanol, 137, 178
- ethidium bromide, 284
- exciton polaritons (EPs), 132
- extracellular matrix (ECM), 109, 303

- f**
- fabricated rrP3HT nanofiber organic field-effect transistor, 339
- fabricating devices, on ultrashort organic crystals, 343
- fabrication, of uniformly doped structures, 150
- fac*-tris(2-phenylpyridine)iridium ($\text{Ir}(\text{ppy})_3$) compound, 143
- Faradaic (redox) reaction, 362
- F_{16}CuPc single-crystal nanoribbons, 347
 - optical OFET, diagram of, 348
- Fe_3O_4 nanoparticles, 297
- 11-ferrocenylundecyltrimethylammonium bromide (FTMA), 362, 363
 - electrochemical oxidation of, 363
 - electrolytic oxidation, 362
 - NaSal and oxidation state, 362
 - redox-responsive VEG, 363
- FETs. *See* field effect transistors (FETs)
- FIB technique, 345
- field effect transistors (FETs), 26, 233, 250, 323, 329
 - based on RRP3HT nanofiber, 331
 - nanoribbons-based, 347
 - schematic diagram, 329
 - flake-shell capsule, 98–100
 - formation, 98
 - storage and release processes of drug, 99
 - structural adjustments, 100

Flory's classification, 357
 flow rate, 245, 299, 300, 310
 – dynamic, 167, 168
 – parameters applied for stable droplet formation, 202
 fluorescein-labeled lipids, 177
 fluorescence-based techniques, 179
 fluorescence intensity, of selectively adsorbed proteins, 179
 fluorescence micrographs, of T cells selectively, 180
 fluorescent dyes, 61
 focused ion beam (FIB), 344
 – micromachining and microelectrode deposition technology, 344
 Förster resonant energy transfer (FRET), 70, 141, 146, 149
 Frenkel-type excitons, 132
 F-T3-F solution, 330
 functionalization, 54
 – of cerasome surface, 97
 – DNA, 260, 267, 274, 279, 282
 – droplets without, 207
 – nanotubes, 69
 – with recombinant human selectin protein, 303
 – sensor, 163
 – surface, 119, 120
 π -functionalized system, 51
 – molecular graphene, 53, 54
 – π -conjugated gelators, 54
 – porphyrin, 51–53

g
 gadolinium-based nanoparticles, 119
 gas sensing
 – capabilities, of LbL films, 104
 – selective, LbL film of graphene and ionic liquid for, 105
 gas sensors, 233, 249
 – organic field-effect, 349
 gelation, 26, 27, 70
 – instant, process of, 72
 gelators, 41
 – alkane- and fatty acid-based, 43
 – amino acid- and peptide-based, 45–50
 – carbohydrate-based, 50, 51
 – cholesterol-based, 41–43
 – nucleoside-based, 43–45
 gel electrophoresis, 260
 generalized indirect Fourier transformation (GIFT) technique, 378

GFP/pMHC-linked goldnanostructured droplets, fluorescence images, 211
 Glaser coupling, 9–13
 – of C20 and C22 molecules, 12, 13
 – – after UV irradiation on Ag(111), 14
 – of C38 molecule, 11
 glass transition temperature, 411
 glucocorticoid receptor (GR), 181
 glycolipids, 63, 64
 gold nanoparticles (GNPs), 31, 70, 120, 189, 190, 191, 192, 195, 206, 211, 267, 277, 281, 285
 gold-nanostructured PEG-DA hydrogel beads, 199
 gold–organic hybrids, 4
 gold–organic linear polymers, 3
 gold thin-film adhesion technique
 – organic single-crystal field-effect transistor preparation, 342
 gold wire
 – electrode patterns, fabrication, 341
 graphene, 104, 176
 – layer-by-layer assembly, 104
 graphene nanoribbons, 2
 graphite oxide-coated Fe₃O₄ MNPs, 300
 growth processes
 – dendritic organic–metal nanowire heterojunctions, 147
 – of fluorescent perylene nanocrystals, 25
 – nucleation and, 222
 Guinier behavior, 361

h
 β -hairpin-like conformation, 69
 halloysite nanotubes, 302
 HBC nanocrystals, solution-processed assembly of, 337
 HBC nanofibers, 337
 heterochiral cyclic peptides, 69
 heterogeneous conducting nanowires, 237
 1,1,1,3,3-hexafluoro-2-propanol (HFIP), 67
 hexahistidine (His6-tag) antibody-binding protein G, 189
 hierarchical structures, 101
 highest occupied molecular orbital (HOMO), 339
 – level, 339
 high-performance liquid chromatography (HPLC), 260
 His-tag chelator, 178
 HIV-1 transactivating transcriptor, 121
 homogeneous nanotubes, 69
 Hookean constant, 376

- hot wall epitaxial method, principle, 315
 HTP single-crystalline nanowires, 338
 human epidermal growth factor receptor (EGFR), 294
 human mesenchymal stem cells (hMSCs), 306
 human umbilical vein endothelial cells (HUVECs), 306
 humidity, 137, 162, 166, 172
 hydrogels, 76, 118, 189
 – divalent metal ions trigger, 76
 – shrinkable, 77
 hydrogen bonds, 22, 64, 101, 131, 135, 219, 370
 – interactions, 141
 hydrophilic drugs, 59
 hydrophobic
 – dipeptides, 67
 – drugs, 59
 – interactions, 64, 76
 – nanostructures, 77
 – surface effect, 144
 hydroquinone, 265
 hydroxycinnamic acid (HCA), 371
 2-hydroxy-4'-(2-hydroxyethoxy)-2-methylpropiophenone, 191
- i*
 IgE reactivity profile, on DNPGradient allergen arrays, 180
 IgE receptor, 181
 immune system, 187
 immuno-cytochemical approaches, 293
 immunological synapse (IS), 187
 indirect Fourier transformation (IFT), 378
 indium tin oxide (ITO), 295
 ink transfer models, 164, 165
 ink transport stages, in DPN, 169
 inorganic materials, 21, 100, 101, 116, 131, 133, 350
 inorganic nanomaterials, 21
 inorganic nanoparticles, 77, 118, 119
 integrated circuits, 250
 $\pi-\pi$ interactions, 131, 135, 141, 148, 151, 220
 interdigitated transducer (IDT) electrodes, 174
 intermolecular interactions, 131, 133
 – inherent, 133–137
 intralayer acid–anion interaction, 66
 ion exchange, 388
 – micro/nanostructure conversion, 388–390
 – schematic representation, 389
 ion exchange reactions, schematic representation, 389
 ionic covalent bonds, 223
 ionic liquids, 104
 – layer-by-layer assembly, 104
 ionic strength, 76
 iridium(III) bis(2-phenylbenzothiozolato-*N*, *C*²) acetylacetone ((BT)₂Ir(acac)), 149
 iron oxide, 260
 N-isopropylacrylamide (NIPAAm), 306
- j*
 Jell-O, 357
 junctional proteins, 112
- k*
 KCl crystals, 316, 317
 kinetic crystal growth model, of anatase and rutile TiO₂, 224
 kinetic energy, 167
- l*
 laminin, 79
 Langmuir–Blodgett (LB) technique, 23, 27–29
 lanthanides, 221
 layer-by-layer (LbL) assemblies, 29–31, 95, 101
 – of graphene and ionic liquids, 104
 layer-by-layer (LbL) films
 – applied to sensors based on electrical resistance, 105
 – of graphene and ionic liquid, for selective gas sensing, 105
 – of mesoporous silica capsule, for controlled release, 105–107
 – QCM sensor system with, 102
 LB film method, 328
 lecithin, 371
 leukocyte-inspired particles (LIPs), 298
 L-glutamic acid, 56
 Li batteries, 221
 ligand exchange, 388
 – micro/nanostructure conversion, 388–390
 light beam, bending, 392, 393
 light-emitting diodes (LEDs), 233, 347, 410
 light–matter interactions, 132
 lipid DPN (L-DPN), 162, 163
 – applications in sensing, 172–176
 – carrier ink, 163
 – on graphene, 176
 – nanobiological applications, 176–182
 – scheme on goblet WGM structures, 175
 lipid-encapsulated compounds, 182
 lipidic nanoparticles, 117
 lipids, 172
 liposomes, 96, 117, 121
 liquid crystalline oligothiophene derivatives, 321

liquid-phase-growth apparatus, 326
 lithium, 221
 lithography, 161
 living polymers, 377
 low-dimensional structures, 145
 lowest unoccupied molecular orbital (LUMO), 340

m

magnetic nanoparticles, 119
 magnetic resonance imaging (MRI), 122, 123
 mannose-6-phosphate receptor, 118
 mast cells, 181
 matrix metalloproteinases (MMP), 112
 Maxwell equations, 377
 Maxwellian relaxation time, 376
 Maxwell model, of a viscoelastic fluid, 376
 MBE. *See* molecular, beam epitaxy (MBE)
 MDPB–FGEDR copolymer, 405
 MEH-PPV self-assembly stripes, 331
 melting temperature, 221
 membrane proteins, 177
 memory devices, 250
 meniscus kinetics, 170
 mercury lamp, UV irradiation, 394
 merocyanine (MC), 372
 – formation, 372
meso-diphenyl tetrathia[22]annulene[2,1,2,1] (DPTTA), 320
 mesoporous carbon capsule, in layer-by-layer film, 103, 104
 mesoporous carbon, in hierarchical assembly, 101–103
 mesoporous silica capsules
 – automodulated (periodic On and Off) materials release from, 106
 – Lbl film of, 106
 messenger RNA detection, 260
 metal-bis-metalloc Tridentate Schiff base (BMSB) building blocks, 388
 metal coordination, 101
 metal–insulator transition, 233
 metal ions, 76, 223
 – divalent, 77
 metallic cells, 100, 101
 – practical applications, improvements, 101
 – preparation, 100
 – with superior catalytic activities, 100
 metal–ligand bonds, 61
 metallocendrimers, 61
 metal–organic polymers, 3
 metal oxides, 221
 metastasis, 293

methanol, 208
 methoxycinnamic acid (MOCA), 371
 9-methylanthracene (9MA)
 – microneedles and microribbons, 392
 – SEM images of, 393
 methylcinnamic acid (MCA), 371
 5-methyl salicylic acid, 369
 micelles, 117, 118
 microcontact printing (μ CP), 163
 microlaser sensing devices, 174
 micro/nanostructure conversion
 – charge transfer complex formation, 385–388
 – ion and ligand exchange, 388–390
 – photoinduced reaction, 392–394
 – reduction, 391
 – thermal-induced reaction, 394, 395
 microribbons, 392
 molecular
 – beam epitaxy (MBE), 217
 – diffusion models, 170
 – dynamics simulation, 76
 – planarity, 144
 – structure, of TMGE, 72
 molecular design, and building blocks, 33
 – amphiphiles, 33–41
 – dendrimers, 55, 56
 – π -functionalized system, 51–54
 – gelators, 41–50
 – typical building blocks for self-assembly, 34
 Moore’s law, 95, 221
 MTT assay, 59
 multilayer stacking, control of, 163
 multiorganic ribbon mask technique, 343
 multiple drop casting method
 – schematic illustration, 322
 multiplexed lipid patterning, 177, 178

n

nanobelts, 22
 – assembled from a PA containing, 75
 nanobiosensors, 177
 nanocrystal device structures, schematic illustrations, 332
 nanodots, 217
 nano-FET devices, 347
 nanofibers, 74–79, 303, 304
 – based substrates, 303
 – and field-effect transistors based on as-prepared fibers, 329
 – preparation, schematic diagram, 329
 nanofractals, 297, 298
 nanogels, 117, 118

- nanostructured materials. *See* inorganic materials; organic materials
- nanomicellar emulsions, 117, 118
- nanoparticles, 295
 - exhibiting different material properties, 116
 - and imaging, 122–124
 - nanopatterned APC surrogate systems, 188
 - impact on cellular analysis, 188, 189
 - nanopatterned hydrogels
 - efficiently functionalized with anti-CD3 antibody, 194
 - nanopatterned PEG-DA hydrogels
 - biofunctionalization, 194, 195
 - characterization, 191–193
 - fabrication, 191–193
 - nanophotonics, 131
 - nanopores, 217, 304–306
 - nanoposts/pillars-based substrates, 300–302
 - nanoreactors, 61
 - nanoribbons, 22, 137
 - nanoscience, 21
 - nanosensor, 249
 - nanosheet, 29, 41, 52, 98, 99, 143
 - triple-folded, 135
 - nanostructured PEG-DA hydrogel beads, 198–200
 - biofunctionalization, 204
 - characterization of, 203, 204
 - fabrication, by droplet-based microfluidics, 201–203
 - nanostructured polymer surfaces, fabrication steps, 244
 - nanostructured substrates
 - for cells capturing, 306
 - for CTC Capturing, 294, 295
 - nanostructures based on their dimensions, 23
 - nanostructures, classification of, 22
 - nanostructures, functions, 56
 - nanofibers, 74–79
 - nanotubes, 62–74
 - vesicles/hollow spheres, 56–62
 - nanostructures self-assembly method, for construction of, 23
 - nanotechnology, 28, 217
 - contribution, 95
 - supramolecular, 95
 - nanotubes, 22, 62, 65, 137, 302
 - functionalization of, 69–74
 - self-assembled lipid, 62–65
 - self-assembled peptide, 65–69
 - TEM and CLSM images, 72
 - nanowires, 22, 135, 137, 236, 237
 - arrays, 217
 - -based substrates, 298, 299
 - exposed to gas vapors, 154
 - heterojunctions, 145, 146
 - p–n Junctions as photoelectric transducers, 146–149
 - 2,6-naphthalenedicarboxylic acid (NDCA), 13
 - NBD-conjugated phospholipids, 304
 - NBD nanotubes, time-lapse fluorescence microscopic images, 71
 - needle crystals, 320
 - neural electrodes, 233
 - nickel microparticles, 406
 - Ni ions, 174
 - nitrilotriacetic acid (NTA), 179
 - chemistry, 189
 - noncontact atomic force microscopy (NC-AFM), 1
 - noncovalent interactions, 33
 - non-liquid inks, 171
 - normal human dermal fibroblasts (NHDFs), 306
 - n-type material (5,10,15,20-tetra(4-pyridyl) porphyrin, H₂TPyP), 147
 - nucleation, 9, 24, 133, 222
 - centers for the vertical epitaxial growth, 146
 - site-specific, 144
 - stage, 391
 - nucleic acid-based methods, 293

O

 - occludins, 110, 112
 - octadecyltrichlorosilane (OTS)-modified substrates, 320
 - OFET. *See* organic field-effect transistor (OFET)
 - ohmic conductance behavior, 265
 - oligo-2,6-naphthalene, 14
 - oligonucleotides, 260, 265
 - oligopeptide-based bolaamphiphiles, 65
 - one-dimensional (1D) nanostructures, 22
 - optical imaging, 123, 124
 - optical micrographs, of lipid patches, 176
 - optical properties, 132
 - of gradually doped 1D nanostructures, 152
 - optical triode, 153
 - optoelectronic devices, 233, 250
 - optoelectronic properties, 1
 - organic aggregates, 139
 - organic charge-transfer (CT) salt, 385
 - organic crystal nanostructures
 - crystal lattice-induced epitaxial growth of, 317
 - organic field-effect transistor (OFET)

- HTP single-crystalline nanowires, 338
 - from HTP single-crystalline nanowires, 338
 - overview of, 309
 - semiconductor nanostructures, fabrication
 - electrostatic spinning, 329, 330
 - physical vapor transport (PVT) growth, 328
 - solution process, 317–328
 - vapor-phase method, 310–317
 - temperature gradient, 310
 - thin film, 309
 - organic/inorganic hybrid micro/nanostructures
 - electronic properties and information storage, 396, 397
 - optical properties, 395, 396
 - organic materials, 133, 139, 155, 395
 - organic–metal nanowire heterojunctions, 145
 - organic molecules, 22
 - assemble into, 133
 - spiraling cognition of relationships among, 156
 - organic nano-FETs
 - application of, 347–350
 - device structures, 332–335
 - preparation
 - nanocrystals, transfer of, 335–339
 - semiconductor nanocrystal field-effect transistor, electrode of, 339–345
 - shadow mask, 339, 340, 341
 - semiconducting materials, 311–313
 - organic nano field-effect transistor, 309, 332
 - device structures, 332
 - molecular structure, 346
 - preparation of, 335–339
 - organic nanomaterials, 22, 132, 155
 - organic nanoparticles, 115
 - exhibiting material properties, 116
 - organic nanoscale field-effect transistor
 - properties of, 345, 347
 - organic nano single crystals, 345
 - organic nanostructures, 139
 - organic nanowires-based inverter circuit, 349
 - organic ribbon mask, two-dimensional, 343
 - organic semiconducting materials, for nanofETs, 311–313
 - organic semiconductor nanoribbons
 - solution-processed, 324
 - organic semiconductors, 315, 322
 - in organic nano field-effect transistor., 346
 - properties, 330
 - organic semiconductor solution
 - supersaturation and precipitation, 323
 - organic–silver nanowire heterojunction, 144
 - organic single crystals
 - field-effect transistor, preparation, 342, 344
 - thermal irradiation, 341
 - organic system
 - TTET upconversion and FRET downconversion, 149
 - osmotic homeostasis, 73
 - OTS-treated silicon wafers, 337
 - *o*-xylene, 190
- p**
- PAH–SPEEK complexes, 402
 - 1-palmitoyl-2-oleophosphatidylcholine (POPC), 371
 - PAMAM dendrimers, 55
 - PA nanofibers, 77
 - application, 77
 - to functionalize titanium implants, 79
 - TEM micrograph, 78
 - PANI–Ppy binary nanotubes, 236
 - paramagnetic inorganic nanoparticles, 119
 - paramagnetic ions, 120
 - passive diffusion, 110, 112
 - PBI–gold hybrid species, 5
 - Pb(SPh)₂ ribbons, 390
 - Pd(SPh)₂
 - SEM images of, 390
 - UV-vis absorption and photoluminescence, 390
 - PEG-*b*-PCPTM polyprodrug amphiphiles, 58
 - PEG-DA hydrogels, 193
 - properties, 191
 - pentacene, 314
 - pentadecafluorooctanoyl chloride, 208
 - peptide amphiphiles, 65
 - peptide lipid-based gelators, 66
 - peptide-loaded major histocompatibility complexes (pMHC), 210
 - peptide nanotube arrays, 68
 - peptides, as building blocks, 75
 - perfluorooctanyl-triethylene glycol (PFO-PEG), 208
 - perylene (Pe), 391
 - perylene perchlorate reduction
 - Br[–] anions, 391
 - perylene, perylo[1,12-*b,c,d*]thiophene (PET), 315
 - peryo[1,12-*b,c,d*]thiophene (PET), 315
 - chemical structure and crystal packing view, 316

- PFPE(7500)–PEG(350)–gold diblock copolymer surfactants, 207
- PFPE–PEG–PFPE triblock copolymer surfactant, 208
- phase transition initiation temperature, 223
- phenylazomethine dendrimers, 222, 223
- phosphate buffered saline (PBS), 192
- phospholipid lecithin, 372
- phospholipid membranes, 182
- phospholipids, 161, 177
- phosphorylation, 112
- photochromism, 149
- photodetectors, 233, 250
- photoelectrical transducers, 149
- photoexcitation, 222
- photoluminescence, 131, 144
 - aggregation-induced enhanced, 132
- photomechanical actuator
 - and mechanical properties, 397
- photonic devices, 145
- photonic properties
 - dendritic organic–metal nanowire heterojunctions, 147
- photoresponsive nonaqueous dynamic gels, 370
- phototransistors, 246, 323
- P3HT microwires, 1D single-crystal, 321
- P3HT nanofiber field-effect transistors, 329
- physical vapor deposition (PVD), 333
- physical vapor transport (PVT) growth, 310, 328
- physicochemical properties, 162
- planarity, 140
- plasma membrane
 - dynamics of GR at, 181
- plastic deformation, 171
- PLGA nanofibers, 304
- PMMA/SiO₂ substrate, 327
- polarized photoluminescence, 248
 - spectroscopy of single MEH-PPV nanofiber, 248
- polyamide condensation, 5
- polyaniline (PAN), 236, 249
- polyaniline/polyethylene oxide (PEO) nanofiber, 329
- poly(benzyl ether) dendritic organogelators, 57
- poly(benzyl ether) metallodendrimers, 61
- poly(oxyethylene) cholestryl ether (ChEO₁₅), 366
- polyelectrolyte (poly (diallyldimethylammonium chloride) (PDDA), 96
- polyelectrolyte multilayer (PEM), 403
- film, healing capability, 404
- poly(3,4-ethylenedioxy) thiophenes (PEDOT), 295, 296, 394
- polyethylene glycol (PEG), 58, 115, 267
- poly(ethylene glycol) (PEG)-based 2D and 3D APC surrogates, 188
- poly(ethylene glycol)-block-poly(propylene glycol)-block-poly(ethylene glycol) (P123), 386
- poly(ethylenimine) (bPEI)
 - layer-by-layer (LbL) assembled, 404
- poly(γ -benzyl-L-glutamate)-*b*-hyaluronan vesicles, 59
- polyglycerol, 370
- poly(3-hexylthiophene) crystalline nanofiber device, 341
- poly(acrylic acid)–hyaluronic acid (PAA–HA) blend, 404
- poly(lactic-*co*-glycolic acid) (PLGA), 303
- poly-L-lysine, 303
- polymeric nanoparticles, 116, 117
- polymerization, 5, 189, 192, 394, 395
 - decarboxylative, 13
 - electrochemical, 238
 - metal-catalyzed, 13, 15
 - NDCA, 15
 - microemulsion, 234
 - on-surface, alkanes, 6
- polymer nanofiber, 329
- polymer pen lithography (PPL), 161, 163, 164
 - ink transfer in, 170–172
- poly[2-methoxy-5-(2-ethylhexyloxy)-1,4-phenylenevinylene] (MEHPPV), 246
- poly(methyl methacrylate) (PMMA), 102
 - C8-BTBT, 328
 - optical images of films, 328
- poly(oxyethylene) alkyl ether, 368
- poly(oxyethylene) cholestryl ether (ChEO₂₀), 366
- poly(oxyethylene) phytosterol ether PhyEO₂₀, 370
 - viscoelastic gels (VEGs), 366
- polypeptide-based vesicles, 59
- poly-(*p*-phenylen-vinylen (PPV), 236
- polypyrrole nanowires synthesis, 236
- poly(sodium styrenesulfonate) (PSS), 104
- poly(styrene-*b*-dimethylsiloxane) diblock copolymer, 244
- polystyrene nanotube (PSNT) arrays, 303
- poly(urea-formaldehyde) core–shell
 - microcapsules, 406
- polyvinyl pyrrolidone, 303
- pore size, 5

- porphyrins nanomaterials, 52
potassium chloride (KCl), 369
potassium cyanide (KCN), 280
potassium ion channels, 70
precipitation, 65, 323, 325
proline, 61
prostate-specific antigen (PSA), 294
protein coupling strategies, 178
PS-*b*-P2VP characteristics, 190
P-selectin-coated microtubes, 303
p-type doped materials, 249
p-type material (copper phthalocyanine, CuPc), 147
pulling method, oriented nanowires, 327
- q**
QCM sensor system, 102
– LbL films of mesoporous carbon capsules, 104
quartz crystal microbalance (QCM), 97
quartz nanowires, 298, 299
quenching, 176
- r**
reactive ion etching (RIE), 299
recombinant proteins, 178
reflective index, 297
reflux time, 137
regioselectivity, 7, 9, 16
– of azide–alkyne cycloaddition, 9
relative humidity (RH), 162, 172
reprecipitation method, 24–26
reverse transcription polymerase chain reaction (RTPCR), 294
rheological transitions, 373
rheometers, schematic view, 360
rhodamine-labeled lipids, 177
rhodamine-tagged lipid, 182
RRP3HT (poly(3-hexylthiophene)) nanofiber, 321
RRP3HT nanofiber, field-effect transistor, 331
rubrene doping, 142
rutile flower-like TiO₂ nanospheres, 412
- s**
scanning electron microscopy (SEM), 99, 190
scanning tunneling microscopy (STM), 1, 218
seed-mediated growth, 335, 336
selective adsorption, 178
selectivity, tunable sensors, 103
self-assembled lipid nanotubes (LNTs), 62
self-assembled monolayer (SAM), 219
self-assembly
- of polyprodrug amphiphiles, 59
– in solution, 31, 32
self-healing
– conductive polymers, 403
– synthesis of, 403
– conductor
– advantage of, 408
– EGaIn, 406
– defined, 401
– elastomers, 415
– electrode, design and structure, 409
– electronic nanodevices, 414
– defined, 401
– electrical conductors, 403–408
– electronic skin, 414, 415
– in energy storage devices, 408–414
– material, 401–403
– overview of, 401
– electronic sensor skin, 414
– organometallic polymer, 403
– polymer, 407
– SHP electrical and mechanical capability, 410
– systems
– categories, 402
semiconducting organic molecules, 77
semiconductors, 223, 237, 321
– nanoparticles, 119, 120
– sensors, 75, 233, 350
SEM images
– Ag nanoparticles, 387
– and CuPc nanostructures, 315
– of perylene, 391
– polyaniline nanofiber bridging gap between metal electrodes, 249
– TCNQ microstructures, 386
– TTF microparticles, 386
– of vesicles, 60
– Zn(SPh)₂, 390
semitransparent composite conductor, 405
shadow mask, 339, 340, 341
β-sheet conformation, 76
SHP/CB composite coating, 410
shrinking behavior, 98
silicon microparticles (SiMPs), 408
– cycling lifetime of, 408
– self-healing silicon electrodes, 410
silicon oxide, 176
silicon wafers, 264
siloxane bonds, 96
silver conductive nanowires (AgNWs), 403
– polyelectrolyte multilayer (PEM), 403
silver ions, 263

- silver nanowires, 144, 405
 - DA polymer matrix, 405
- single-crystal nanostructures, 137
- single-crystal P3HT microwires
 - morphological features and structure characterization, 323
- single-walled carbon nanotube (SWCNT) films, 411
 - electrical conductivity, self-healing, 413
 - self-healing substrates, 413
- Si shadow mask, preparation, 342
- Si/SiO₂ substrate
 - PET single crystals, 315
- Si/SiO₂ substrate, 334
- site-selected assembly, on specific substrates, 138, 139
- Si wafer, 342
- size-dependent excitation, 233
- small-angle neutron scattering (SANS), 360
- small-angle X-ray scattering (SAXS), 271, 360
- small-molecule semiconductors, 330
- sodium deoxycholate (SDC), 372
- sodium 3-hydroxynaphthalene-2-carboxylate (SNHC), 369
- sodium 1-oxo-1-[4-(tri-decafluoroethyl phenyl]-2-hexanesulfonate (FC6-HC4), 369
- sodium salicylate (NaSal), 362
- soft cell-like structures, 96
- soft matter assembly
 - for atomically precise oxide layers, 220, 221
 - for constructing nanostructure with atomic precision, 219
- soft template synthesis, 234–236
- solar cells, 1
- “sol–gel” transition, 374
- solid electrolyte interphase (SEI), 408
- solid electrolyte interphase (SEI) growth, 408
- solubility, 24, 32, 41, 117, 138, 169, 317, 322, 371
- solution-based delivery, 182
- solution-based synthesis, 233
 - conducting polymer nanostructures, 234
 - hard template approach, 236, 237
 - soft template approach, 234–236
- solution-processed organic semiconductor nanoribbons
 - top-contact field-effect transistor, 324
- solvent effect, in assembly, 137
- solvent etching effect, 137
- solvent vapor annealing (SVA) method, 327
- sphere-like organometallic complex, 151
- spherical nucleic acids (SNA), 260
- spin casting processes parameters, 190
- spiropyran (SP), 370, 372
 - 1',3',3'-trimethyl-6-nitrospiro[1(2H)-benzopyran-2,2'-indoline], 372
- sputtering–annealing cycles, 6
- stability, 162
- “stamp” transport mode, 171
- static light scattering (SLS), 361
- stereocomplex formation, 101
- steric hindrance, 140, 151
- steroids, 63
- stilbene, 370
 - *cis-trans* conversion of, 392
- STM images
 - of AEB monomer deposition on Au(111), 8
 - of C22 dimers, 14
 - for polymerization of NDCA on Cu(111), 15
- streptavidin, 174, 178
- stress relaxation function, 378
- structural deformation, 144
- structure control, through intermolecular interactions, 140
 - structures obtained
 - from synergistic assembly of different compounds, 141, 142
 - via molecular design, 140, 141
 - structure modulation, through external factors, 143
 - heterostructures through site-specific epitaxial growth, 144, 145
 - structures *vs.* aging time, 143, 144
- substrate-based fabrication, 233
 - add to surface, 237
 - chemical polymerization, 240, 241
 - direct writing, 237, 238
 - electrochemical polymerization, 239
 - electrostatic assembly, 242
 - *in situ* synthesis or assembly, 238
 - conducting polymer nanostructures, 237
 - remove from surface, 242
 - etching, 243–245
 - nanoscratching, 242, 243
- substrate effect, on assembly of organic molecules in vapor phase, 138
- sumatriptan, 58
- supercapacitors, 250, 411–413
- superhydrophobic, 401
- supersaturation, 133
 - degree of the vaporized molecules, 138
- supported lipid bilayers (SLBs), 205
- supramolecular chemistry, 95
- supramolecular network
 - electrically and mechanically self-healing supercapacitor, 412

- surface acoustic wave (SAW) sensor, 174
 surface energy, 135, 170
 surface-enhanced Raman spectroscopy (SERS)
 signals, 281
 surface functionalization, of
 nanoparticles, 120–122
 surface tension, 138
 surfactants, 369
 – amphiphilic, 61
 – synthesis, 200, 201, 207, 208
- t**
- tannic acid, 102
 TAT-coupled polymeric micelles, 121
 Taylor cone, 246
 T cell–antigen-presenting cell (APC), 187
 T cell–APC interface, 187
 T-cells, 179, 180, 187, 189, 197, 199
 – activation, 188
 – differentiation, 187
 – isolation, 195
 – proliferation, 196
 – receptors, 188
 – stimulation, 195
 TEM micrograph, cell entrapped in
 nanofibrillar matrix, 78
 temperature, 138
 – programmed desorption (TPD), 2
 template-free method
 – for heterostructures with, 151
 template inorganic mineralization, 77
tert-leucine, 69
 tetracene, 314
 tetracyanoquinodimethane (TCNQ), 320, 385,
 386, 387
 – absorption of, 386
 – conductive charge transfer salts, 407
 – microstructures, 386
 – SEM images, 387
 – UV-vis spectra, 388
 – UV-vis spectra of, 388
 thermal diffusion, 222
 thermal irradiation, 341
 thermodynamics, 223
 thiophene/phenylene co-oligomer
 (BP2 T), 317
 – chemical structure of, 317
 three-dimensional (3D) nanostructures, 23
 TiO₂ nanofibers, 304
 TiO₂ nanostructures
 – electrically and mechanically self-healing
 supercapacitor, 412
 – glass transition temperature, 411
 tissue inhibitors of MMPs (TIMPs), 112
 titanium *n*-butoxide, 303
 titration curve, 58
 Tollens reaction, 262, 264
 toluene, 65
 top-contact CuPc nano field-effect
 transistor, 340
 top-contact nano field-effect transistor
 – fabrication procedure of, 341
 top-contact nanostripe field-effect transistor
 – schematic diagram of, 332
 TPP/rubrene molar ratio, 142
 transactivator of transcription (TAT), 121
trans–*cis* photoisomerization, 370
 transferrin (Tf), 121
 – receptor, 122
 transferrin receptors (TfRs), 297
 transistors, 1, 250
 transition temperature, 222
 transmission electron microscope (TEM), 96,
 341
 – CuPc nanostructures, 315
 triazoles, 9
 – derivative, 262
 1,4-triazoles, 7
 triblock microrods, 142
 triethylamine hydrochloride (Et₃NHCl), 369
 triethylene glycol, 208
 tri(ethyleneglycol) mono-*n*-dodecyl ether
 (C₁₂EO₃), 366
 triisopropylsilyl ethynyl pentacene (TIPS-PEN), 325
 – π – π intermolecular interactions, 325
 1',3',3'-trimethyl-6-nitrospiro[1(2H)-benzopyran-2,2'-indoline], 372
 2,4,5-triphenylimidazole (TPI), 150
 1,3,5-triphenyl-2-pyrazoline, 141
 triplet–triplet energy transfer (TTET),
 149
 tris(8-hydroxyquinoline)aluminum
 (Alq₃), 138
 TTF conductive charge transfer salts, 407
 TTF derivative DT-TTF nanoscale single
 crystal-based organic field-effect
 transistor, 347
 TTF materials, 326, 386
 – micro/nanowires, 326
 TTF-TCNQ (tetraphiafulvalene-tetracyanoquinodimethane), 406
 – nanowires, 386, 387, 396
 – – I–V curves, 396, 397
 – – *I*–V curves for a network of, 396
 tubular structures, 137

- two-component drug system, 76
 two-dimensional (2D) nanostructures, 23
- u**
 UCLA logos, 405
 Ullmann Coupling, 2–5
 ultrahigh vacuum (UHV) conditions, 1, 2
 ultraviolet irradiation, 203
 UV irradiation, 150, 370
 UV-triggered self-healing polymer (SHP), 402
- v**
 van der Waals forces, 9, 11, 131, 135, 151, 168, 342
 – interactions, 22, 322, 396
 VEGs. *See* viscoelastic gels (VEGs)
 vesicle-encapsulated microtubes, 66
 vesicles/hollow spheres, 56–62
 viscoelastic fluid, Maxwell model, 376
 viscoelastic gels (VEGs), 358
 – anionic surfactants, 369
 – C₁₄EO₃ and Tween-80, 366
 – characterization, 359
 – light-responsive surfactants, 369
 – number of publications, 359
 – photoresponsive, 369–373
 – pH-responsive, 364
 – PhyEO₂₀/H₂O, 371
 – poly(oxyethylene) alkyl ether and C₁₂EO₃, 368
 – poly(oxyethylene) cholesterol, 366
 – potassium chloride (KCl), 369
 – properties of, 358
 – redox-responsive, 362, 363
 – rheological properties, 361
 – rheology, 359, 360
 – rheometer, 359, 360
 – small-angle neutron scattering (SANS), 360, 361
 – temperature-responsive, 364–369
- transmission electron microscopy, 361
 viscoelastic gels, rheological behavior, 377
 viscoelasticity, 371
 viscoelastic micelles, 377
 viscosity, 174, 246, 368, 370
- w**
 water-in-oil emulsion, 205
 – biofunctionalization of nanostructured droplets, 209–211
 – cell experiments, 211–213
 – characterization of the gold nanostructured droplets of, 209
 – droplet-based microfluidics, 208
 – nanostructured and specifically biofunctionalized droplets, properties, 205–207
 – surfactant synthesis, 207, 208
 wetting properties, 162
 WGM-based sensors, 174
 worm-like micelles, 376
 write-read-erase-read (WRER) cycles, 387, 397
- x**
 X-ray photoelectron spectroscopy (XPS), 2
m-xylene, 320
- y**
 Young's modulus, 67, 188, 193, 296
- z**
 zero-dimensional (0D) organic nanoparticles, 22
 Zn–BMSB–Zn particles, 388, 389, 396
 Zn(II) interconnecting nodes, 388
 Zn²⁺ ions, 390
 ZnO nanorods, 305
 Zn(SPh)₂ networks, 389
 zonula occludens (ZO), 112

WILEY END USER LICENSE AGREEMENT

Go to www.wiley.com/go/eula to access Wiley's ebook EULA.